

Photophysics of Multicomponent Molecules under Dynamic Control

A PhD Thesis submitted to:

Newcastle University

School of Chemistry



Patrycja Stachelek

November 2016

To Maria & Tadeusz Gärtner

Acknowledgments

First of all I would like to express my gratitude to Professor Anthony Harriman for his endless patience and for being incredibly supportive over the past three years. The value of his advice cannot be overstated.

I would also like to acknowledge Dr Jerry Hagon for all of his advice, and all of the MPL group members and our collaborators: Dr Raymond Ziessel, Dr Sandra Rihn and Dr Julian Knight for providing me with the compounds studied within this thesis.

I must also thank my amazing family: my parents and my sisters for believing in me and encouraging me throughout my Master's degree and PhD studies. Last but not least, I would like to thank John for always motivating me to stay positive.

Abstract

This work focusses on seeking to gain a deep understanding of the photophysical processes inherent to multi-functional and/or multi-component supermolecules in the condensed phase. To do this, a variety of molecular systems have been subjected to spectroscopic examination, most commonly using steady-state and time-resolved emission spectroscopy to interrogate the samples. A common feature of all the molecular architectures examined herein relates to the possibility for structural motion on timescales of concern to the photophysical event. Furthermore, to provide a spectroscopic signature, most of the target dynamic systems comprise a donor covalently attached to a complementary acceptor. These systems possess the potential to be used as solar-energy concentrators or for specific sensing applications. However, attention is given only to the fundamental properties.

Chapter 1 provides a general introduction to the field of molecular rotors and to the concepts of energy and electron transfer in molecular systems. Key literature examples are used to illustrate the current state-of-the-art and to set the tone for later discussions. Each chapter includes a brief introduction to the specific topic under discussion while avoiding the generic details covered in the main introduction. The essential experimental details and underlying analytical protocols for all the studies described are provided in the final chapter.

Chapter 2 describes a new series of molecular rotors based on the boron dipyrromethene (BODIPY) structure. This series includes structurally-similar compounds that exhibit surprisingly disparate behaviours as putative probes for solvent viscosity. In fact, the results tend to challenge the conventional understanding of BODIPY-based molecular probes. In this chapter, we highlight the importance of asymmetry, question how it might be used to one's advantage in the design of next generation probes, and raise ideas about porosity of the excited-state potential energy surface.

By way of Chapter 3, we expand of the same subject but introduce a series of control compounds, bearing 5- or 6-membered straps at the boron atom intended to switch fluorescence according to the state of an appended amino donor. The design element was based on differences in ionisation potential of an amine and its corresponding amide. In fact, this series provided important insight into how substituents at the lower rim of the BODIPY nucleus affect the photophysical properties of the dye despite not being part of the conjugation pathway. Switching was possible by using a photo-acid but underlying structural factors introduce significant non-radiative pathways that were not anticipated.

Chapter 4 changes focus by introducing molecular dyads and triads built around BODIPY but equipped with secondary chromophores (i.e., diketopyrrolopyrrole) and triphenylamine units. This is an extension of the work covered in Chapter 3 but positions the redox-active components in a more popular (i.e., linear) geometrical pattern. An additional point of interest concerns moving towards BODIPY-based dyes with more extended conjugation pathways. The target compounds allow the interplay between energy- and charge-transfer processes, so critical in natural organisms, to be scrutinised. Competition between the various processes is affected by choice of excitation wavelength and environment (e.g., solvent polarity, temperature, and phase).

Continuing this approach in Chapter 5, a molecular a pentad is investigated; here, individual components comprising pyrene, BODIPY, extended-BODIPY, dithiocyclopentane, and triphenylamine units arranged in a linear but bifurcated geometry. The latter arrangement introduces a certain degree of redundancy in that certain units could corrode under illumination but without serious damage to the opto-electronic properties of the array. This leads us to raise questions about the practical usage of large conjugated dyes as solar collectors. To this end, the kinetics of photo-bleaching of the pentad were measured under continuous exposure to white light.

Chapter 6 examines an alternative supermolecule built from modules formed around N,N-dimethylaniline, BODIPY, extended-BODIPY, dithiocyclopentane and triphenylamine units. This provides an opportunity to explore in some detail the photo-stability of a multi-functional molecular assembly designed for a particular purpose (i.e., an optical pH probe). The importance of auto-catalysis is recognised here. A further point of interest concerns the stepwise breakdown of the overall molecule. This means that a well-designed supermolecule continues to be effective even after several components have degraded. In fact, our main target compounds shows an impressive turnover number of ten million.

By way of Chapter 7, we return to our main theme of exploring the molecular photophysics of donor-acceptors systems able to exchange conformation in the ground state. Rather than employ more rotors, we have examined dyads assembled around amide linkages that are subject to *cis-trans* isomerization. Amides have great relevance for biology and are used frequently as bridges for donor-acceptor systems. It is not often, however, that the geometry of the amide is taken into account. Using two sets of BODIPY-based dyads, we assess how the geometry around the amide linkage affects the dynamics of light-induced charge or energy transfer between appended BODIPY units in fluid solution. The essential point to emerge from this work is that the amide-containing linker facilitates an unusually broad distribution of separation distances between the chromophores.

Table of Contents

Acknowledgments	iii
Abstract	v
Chapter 1. Introduction	1
1.1 Why BODIPY?.....	4
1.2 Molecular Rotors	6
1.2.1 Theoretical Background.....	6
1.2.2 BODIPY-Based Molecular Rotors.....	8
1.2.3 The Physics of Rotors.....	13
1.2.4 Measurements and Calibration	25
1.3 Electronic Energy Transfer.....	28
1.3.1 Förster Resonance Energy Transfer (FRET)	29
1.3.2 Dexter Energy Transfer	31
1.3.3 Spectroscopic Gradient.....	33
1.4 References	36
Chapter 2. Fluorescent Molecular Rotors Based on the BODIPY Motif: Effect of Remote Substituents.....	43
2.1 Introduction.....	43
2.2 Results and Discussion	46
2.2.1 Spectroscopic Data.....	46
2.2.2 Temperature Dependence	49
2.2.3 Viscosity Dependence	54
2.3 Conclusions.....	59
2.4 References	60

Chapter 3. Rapid Internal Conversion in N,B,O-Strapped Boron Dipyrromethene Derivatives.....	63
3.1 Introduction	63
3.2 Results and Discussion	65
3.2.1 Spectroscopic Data	65
3.2.2 Electrochemistry.....	70
3.2.3 Fluorescence Quenching in the Glassy Matrix	77
3.2.4 Fluorescence Quenching in Liquid Solution	80
3.3 Conclusions	87
3.4 References	89

Chapter 4. Electronic Energy Transfer and Charge Transfer in Molecular Dyads and Triads Built Around a BODIPY-Based Dye.....	91
4.1 Introduction	91
4.2 Results and Discussion	96
4.2.1 Spectroscopic Data	96
4.2.2 Electronic Energy Transfer.....	99
4.2.3 Temperature Effect	102
4.2.4 Solvent Effects	107
4.3 Conclusions	116
4.4 References	118

Chapter 5. A Bifurcated Molecular Pentad Capable of Sequential Electronic Energy Transfer and Intramolecular Charge Transfer	121
5.1 Introduction	121
5.2 Results and Discussion	124
5.2.1 Photophysical Data	124
5.2.2 Photolysis.....	126
5.2.3 Charge Transfer	130

5.2.4 Electronic Energy Transfer	134
5.3 Conclusions.....	135
5.4 References	137
 Chapter 6. Stepwise Photoconversion of an Artificial Light-Harvesting Array Built from Extended BODIPY Units	 139
6.1 Introduction.....	139
6.2 Results and Discussion	141
6.2.1 Photophysical Properties	141
6.2.2 Cyclic Voltammetry	143
6.2.3 Computational Studies.....	144
6.2.4 Photochemical Degradation.....	147
6.3 Conclusions.....	153
6.4 References	155
 Chapter 7. Conformational Exchange in Closely-Spaced Dyads and the Effect on Electronic Energy Transfer	 157
7.1 Introduction.....	157
7.2 Results and Discussion	160
7.2.1 Spectroscopic Data.....	160
7.2.2 Photophysical Properties of 1,10-Phenanthroline Bridged Bichromophores in a Range of Solvents.....	161
7.2.3 Fluorescence Quenching of 1,10-Phenanthroline-Bridged Bichromophores.....	167
7.2.4 Energy Transfer in 1,2-Diaminocyclohexane-Bridged Dyads.....	172
7.3 Conclusions.....	181
7.4 References	183
 Chapter 8. Experimental Methods	 187
8.1 Materials.....	187

8.2 UV-Visible Absorption Spectroscopy	189
8.3 Fluorescence Spectroscopy.....	190
8.4 Lifetime Measurements	191
8.5 Temperature- Dependent Spectroscopic Studies	193
8.5.1 Low-Temperature	193
8.5.2 High-Temperature	193
8.6 Electrochemistry	194
8.7 Sample Preparation	196
8.8 Data Analysis.....	197
8.8.1 Fluorescence Quantum Yield	197
8.8.2 Radiative Rate Constant (k_{rad}).....	199
8.8.3 Electronic Energy Transfer Rate Constant.....	200
8.8.4 Energy Transfer Probability.....	202
8.8.5 Englman-Jortner Energy-Gap Law.....	203
8.8.6 Electron Transfer.....	204
8.9 Computational Methods	206
8.9.1 PeakFit- Spectral Analysis	206
8.9.2 Spartan'06.....	209
8.9.3 GAMESS.....	209
8.10 References	211
Appendix.....	215
List of Publications.....	217
Charge-Recombination Fluorescence from Push-Pull Electronic Systems Constructed around Amino-Substituted Styryl-BODIPY Dyes.....	219
Exciplex Emission From a Boron Dipyrromethene Bodipy Dye Equipped with a Dicyanovinyl Appendage.....	229
Fluorescent Molecular Rotors Based on the BODIPY Motif Effect of Remote Substituents	239

Stepwise Photoconversion of an Artificial Light Harvesting Array Built from Extended BODIPY Units	245
A Bifurcated Molecular Pentad Capable of Sequential Electronic Energy Transfer and Intramolecular Charge Transfer	255
Solvent-Driven Conformational Exchange for Amide-Linked Bichromophoric BODIPY Derivatives	263
Electronic Communication in Closely-Connected BODIPY-Based Bi- Chromophores.	275

Chapter 1. Introduction

Rheology, often simplified to refer specifically to viscosity, continues to be an important research subject in academia and industry alike. There are many recognised types of fluids; *pseudoplastic*, Newtonian and dilatant amongst many others, Figure 1.1. Once the type of fluid (Newtonian or non-Newtonian) is identified, one needs to consider how temperature, pressure and other environmental factors might affect the properties of solvents (or fluids in general). For example, can varying the temperature of the medium create the same effect as varying the pressure applied to the solvent molecules? All of the above make studying viscosity a very topical, meaningful and challenging subject.¹⁻⁴ There are, in fact, numerous ways to measure viscosity in the laboratory and in the workplace. Mostly, these methods are fairly empirical and measure relative viscosity. This is suitable for most industrial applications, such as paint spraying, but refer to some kind of local standard. In other applications, such as inkjet printing, the viscosity of the medium is critical for successful performance but it is too high to use flow methods for accurate determination. In such cases, rotating viscometers are used to measure the shear viscosity under application of a high load. Again, the result is rather empirical and based on local knowledge. Typical viscometers require a large volume of sample but can be made fully automatic. Even so, such methods cannot be used under remote or hazardous conditions. There are few, if any, adequate instruments for measuring viscosity in biological media, such as intact membranes, or to extract real information on how drugs or disease affect local viscosity.

Molecular probes, examples being dicyanovinyl julolidine (DCVJ), triphenylmethane (TPM) and boron dipyrromethene (BODIPY) dyes, have been identified as potential molecular-scale viscometers. All of these dyes have a rotating entity (such as an unhindered phenyl ring) that is credited with inducing the sensitivity towards viscosity. However, not every fluorophore with a rotating group can be a

molecular viscosity probe; examples of this are Rhodamine B/6G. Spinning of a molecular fragment in relation to the remaining structural scaffold needs to be accompanied by an easily registered event that can be quantified in real time. Many different spectroscopic detection protocols could be imagined, and indeed do work with molecular-scale viscometers, but are often time consuming or expensive. A simple and relatively inexpensive protocol can be built around fluorescence spectroscopy where a specific rotation is related to emission quenching. An obvious example of this situation relates to the so-called twisted internal charge-transfer (TICT) state, where excitation of a neutral molecule is followed by rapid intramolecular charge transfer. During the charge-transfer step, one (or both) of the redox partners undergoes a substantial change in geometry. Thus, the relative fluorescence yield measures indirectly the ability of the molecule to acquire the optimum geometry for charge transfer. In turn, the local environment imposes a barrier to conformational exchange and, with careful calibration, the amount of fluorescence detected under controlled conditions can be used to measure the local viscosity. It is rarely that easy in practice.

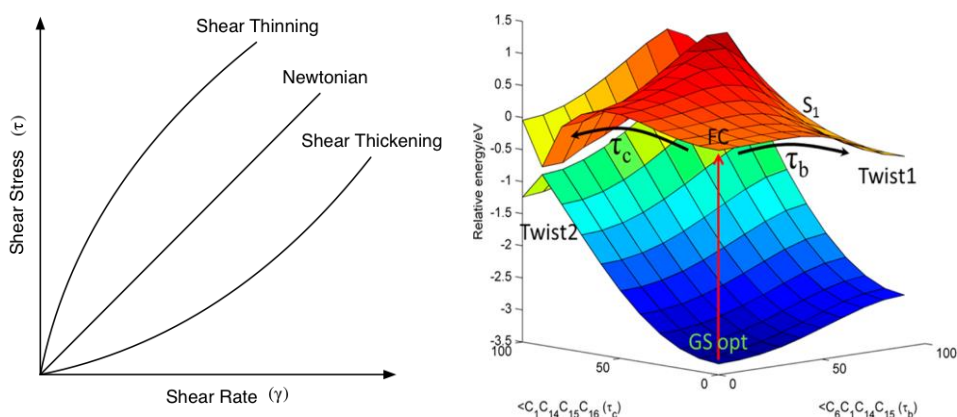


Figure 1.1. The panel on the left demonstrates different types of viscosity, whereas the panel on the right shows potential energy surfaces for one of the most popular commercially available viscosity probe, the DCVJ dye. The potential energy surfaces have been calculated by Yang and Han (J. Phys. Chem. A **2016**, 120, 4961–4965).

There has been a tremendous expenditure of effort in order to gain further understanding of the photophysics of these multi-component molecules under dynamic control. One example of this class of molecules concerns those BODIPY dyes possessing a phenyl ring attached at the *meso*-position. The prevailing wisdom is that the upper rim of the dye is crucial in controlling how these BODIPY-based viscosity probes actually respond to changes in the environment. This is entirely logical because the rotor is attached at the upper rim but, in trying to dig deeper into the sensory mechanism, we have sought to monitor the effects of different types of substituents. For example, we have been interested in probing the effect of ancillary substituents attached to the lower rim as well as trying to gain further understanding of the effects of charge-transfer (CT) and electronic energy transfer (EET) on BODIPY rotors. Another important factor of interest is the photochemical stability of the fluorophores, especially when used in living cells. Finally, we have become interested in how the solvent itself affects the dynamics of internal rotation of a probe; for example, we raise the question as to whether there is a difference in molecular dynamics of a molecule embedded in a hydrocarbon solvent as opposed to an alcohol with a comparable viscosity. This is a classical feature of physical chemistry and brings into play protic vs aprotic effects. Does hydrogen bonding exert an undue effect on the rotation dynamics? The same question can be asked about solvent and/or solute polarity. When we started this investigation, little was known about how or why gyration of the *meso*-phenyl ring in certain substituted boron dipyrromethene dyes caused severe loss of emission. Several examples of putative BODIPY-based molecular rotors had been proposed in the literature but, by-and-large, these were close analogues of the same basic molecular framework. In effect, the same is true for most other types of molecular-scale rotors and there does not exist a clear understanding of the mechanism responsible for emission quenching.

As already mentioned, there are many different methods available for viscosity measurements, like the rotational viscometer or capillary viscometer, however they all rely on bulk samples. The advantage of using a molecular rotor is that it can be used *in situ*. Great interest has been

generated in the possible use of small molecular probes to monitor viscosity in bio-systems. Changes in viscosity can have profound effects on cells and on the body itself, they are linked to multiple diseases like heart-disease⁵⁻⁷ and diabetes⁸ amongst others. It is immediately clear that a simple method for measuring viscosity effectively within living cells would be highly beneficial in medicine. However, it is just as easy to imagine a molecular rotor being used as a probe in the petrochemical industry or for environmental studies under remote or hazardous conditions. One example of this is the common use of fluorescence for leak detection in underwater oil wells; all that is required to find the origin of the leak is a UV light source. Taking into account all of the above, it is not surprising that fluorescent molecular probes are already of great relevance in industry.⁹ In such applications, it is often sufficient to know that the system works and there is less of a need to know the reasons why the probe acts as it does.

1.1 Why BODIPY?

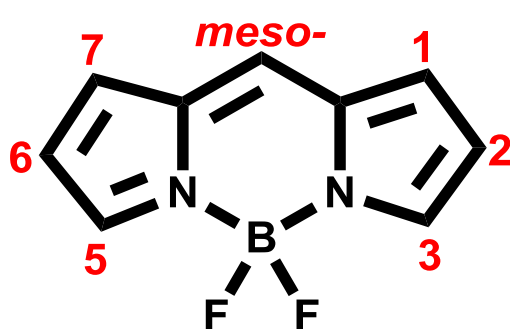


Figure 1.2. Molecular formula of the basic BODIPY framework, with numbering system.

4-Difluoro-4-bora-3a,4a-diaza-s-indacene, or BODIPY (Figure 1.2) was first described by Kreuzer and Treibs¹⁰ in 1968 and quickly gained popularity due to its excellent photophysical properties.¹¹ These are characterized by sharp, intense absorption and emission transitions, high emission quantum yields, small Stokes' shifts and relatively long excited-state lifetimes (nanosecond timescales).^{12,13} A

further point of interest for using BODIPY-based dyes is that the corresponding triplet-excited state is not formed to any appreciable extent by way of intersystem-crossing.

In addition, the basic BODIPY core can be modified easily in order to tune the properties to specific requirements. For example, the Stokes' shift can be increased, the transitions made broader, the extent of π -conjugation can be increased significantly and hence they are available in an inordinately wide range of colours. This is especially significant when monitoring live cells, since the BODIPY conjugation length can be extended so that its emission does not overlap with the intrinsic emission from biological samples (auto-fluorescence can be observed from approx. 300 to 700 nm).^{14,15} Importantly, they are also characterized by good levels of photochemical stability under exposure to visible light.^{16,17} Another advantage of using BODIPY dyes concerns their resistance to aggregation in solution, as well as high radiative rate constants (ca. 10^8 s^{-1}).¹⁸ Due to all of the above advantages, these dyes have already found multiple applications in many emerging technologies and are becoming important constituents in solar cells and specific ion detectors. New synthetic protocols, together with rapid purification procedures, have ensured that a wealth of BODIPY derivatives is now available, including optically resolved enantiomers. Other studies have successfully incorporated heteroatoms into the framework and extended the conjugation pathway by attaching a variety of aryl substituents to different parts of the BODIPY nucleus.

In recent years, there has been an upsurge of interest in using BODIPY-based rotors for intracellular imaging.¹⁹ One of the most important benefits of BODIPY as a molecular viscosity probe is that the dye is rarely affected by solvent polarity, unlike traditional TICT-based rotors. However, they can be modified easily to be sensitive towards local polarity if required. Once properly calibrated, the probe should work well in a range of media.²⁰ Additionally, BODIPY dyes have been used to stain live cells where a particular advantage is gained by their low cytotoxicity. However, as with so many areas of BODIPY chemistry, there has not been a conclusive study to examine the toxicity of this class of dyes.²¹⁻²³ The same is true for photostability. There are several claims that the dyes are resistant to photochemical degradation but few actual details are available.

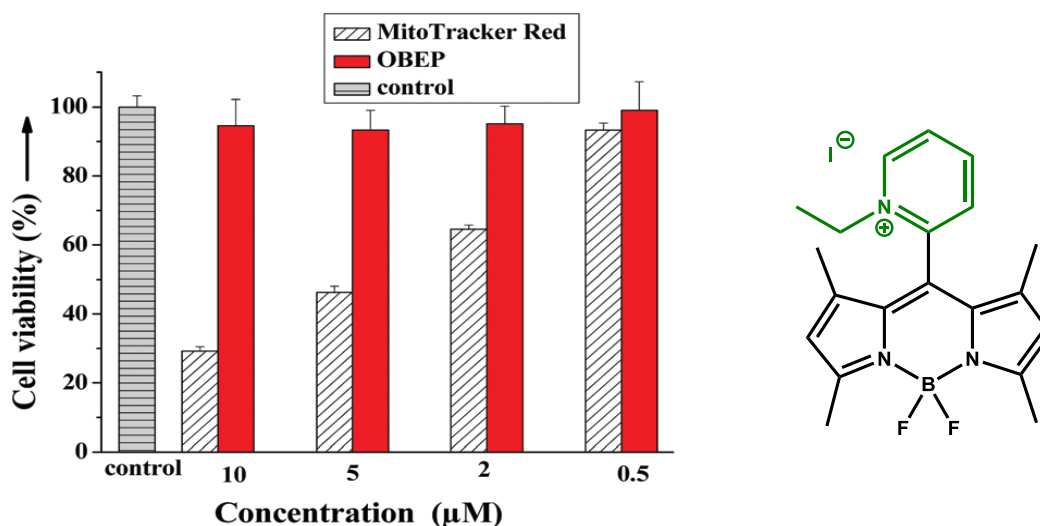


Figure 1.3. Figure adapted from *Org. Biomol. Chem.*, **2013**, *11*, 555, demonstrates cytotoxicity of BODIPY referred to as OBEP at different concentrations in living HeLa cells for 12 hours and directly compared to commercially available MitoTracker Red. On the right is shown the molecular formula of OBEP.

1.2 Molecular Rotors

1.2.1 Theoretical Background

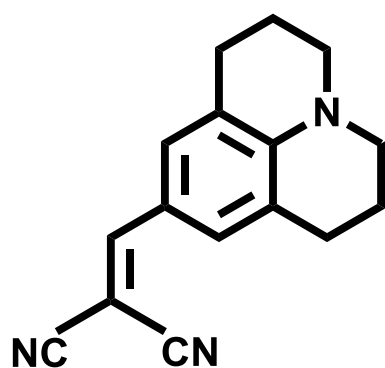


Figure 1.4. Molecular formula of 9-(2,2-dicyanovinyl) julolidine (DCVJ) dye.

Traditionally, molecular rotors were designed to operate by means of TICT formation, these are defined as molecules that form twisted conformations under illumination due to rotation of one particular fragment of the molecule with respect to the remaining part. A prototypic example, which was referred to earlier as being the industry standard, is DCVJ and its close derivatives, Figure 1.4.⁴ There is an excellent review that describes the TICT process written by Grabowski *et al.*²⁴ Here, it

is stressed that the light-induced conformational change is imposed on the molecule by the need to optimize stabilization of the charge-transfer state. Usually,

the ground state is neutral but the TICT state has an important dipole moment. It is quite clear that TICT formation cannot account for the rheological abilities of the *meso*-substituted BODIPY dyes. One theory hypothesizes that the rheological properties arise from the differences between the ground and the first-excited singlet state potential energy surfaces and that the photophysical behaviour of the BODIPY rotor can be explained using already existing models developed for light-driven isomerization reactions. In this context, we note that the so-called pinhole sink model is one of the theories used to explain the viscosity dependence for non-radiative decay of boron dipyrin dyes. The crucial difference between the DCVJ dyes and BODIPY rotors is that, with the latter compounds, the radiative rate constant (k_{RAD}) is not affected by gyration of the rotor. The rotation of the *meso*-ring and any subsequent bending out-of-shape of the BODIPY core, amplifies the non-radiative rate so that this pathway becomes competitive with radiative deactivation of the excited state. This being the case, it becomes crucial to better understand the non-radiative pathways.

As has been stressed earlier, viscosity can be linked to multiple diseases, but it is also important for drug delivery, metabolism and cell signalling since it is closely related to molecular diffusion. The latter is used to describe the diffusive transport of a single molecule. Indeed, the Stokes- Einstein equation reflects the relationship between the two terms, Equation 1.1.²⁵

$$D\eta = k_B T / 6\pi r_H \quad \text{Equation 1.1}$$

Here, D is the diffusion coefficient of a target species, T is the absolute temperature, k_B is the Boltzmann constant, η is the shear viscosity of the solvent and finally r_H is the hydrodynamic radius. Traditional methods of measuring viscosity are often impractical and need rather substantial volumes but they do measure the viscosity of the bulk solvent. In contrast, molecular-scale rotors are best suited to measure micro-rheology as opposed to macro-rheology (measured by mechanical methods).²⁶ The concept of micro-rheology has been introduced because the shear viscosity was unable to provide an accurate description of friction between solvent molecules and a gyrating rotor, Equation 1.2,²⁷ where η is viscosity, T_{rL} and

T_r refer to the reduced solvent and solute temperatures, respectively, r is the solute radii and r_L is solvent molecular radii. The viscosity, or in the case of molecular rotors micro-viscosity, effect arises because of frictional forces between the solute and the surrounding solvent. The solvent cage must be forced out of the way in order for the rotor to twist about the bond; the same principle applies to isomerization reactions. The size of the rotor becomes of importance here. The rate of rotation decreases with increased size due to the pressure exerted during rotation. Increasing the size of the rotor hinders the rotation process, thereby providing a simple means by which to control the rate, and thereby serves to shut down the non-radiative pathways. This can be used to one's advantage since, by manipulating the size of the rotor, a series of similar probes might be created for applications over narrow ranges of specific viscosities.

$$\eta_{\mu} = f\eta \quad \text{Equation 1.2}$$

$$f = (0.16 + 0.4^r/r_L)(0.9T_{rL} - 0.25T_r) \quad \text{Equation 1.3}$$

$$T_{rL} = \frac{T - T_m}{T_b - T} \quad \text{Equation 1.4}$$

1.2.2 BODIPY-Based Molecular Rotors

The simplest of all BODIPY-based molecular-scale rotors is undoubtedly ROBOD (see below for molecular formula), which is basically the unadorned *meso*-substituted boron-dipyrromethene core, Figure 1.5.²⁸ In terms of its sensitivity as a fluorescent reporter of viscosity changes, it is roughly 50% more effective than the standard dicyanovinyl julolidine dye (DCVJ) under closely comparable conditions.

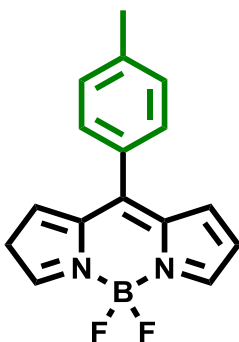


Figure 1.5. Molecular formula for the most basic of BODIPY rotors, referred to throughout as ROBOD.

The fluorescence quantum yield of ROBOD is 0.023 and the corresponding singlet lifetime is 0.15 ns in fluid solution at low viscosity. The radiative rate constant is $1.5 \times 10^8 \text{ s}^{-1}$ whereas the combined non-radiative rate constant is $65 \times 10^8 \text{ s}^{-1}$ in methanol at 20°C. The magnitude of the radiative rate constant is typical for this class of dye, reflecting the strong oscillator strength, but the non-radiative rate constant is greatly magnified compared to the sterically constrained BODIPY dye (2) where it is typically in the region of 10^7 s^{-1} .²⁹

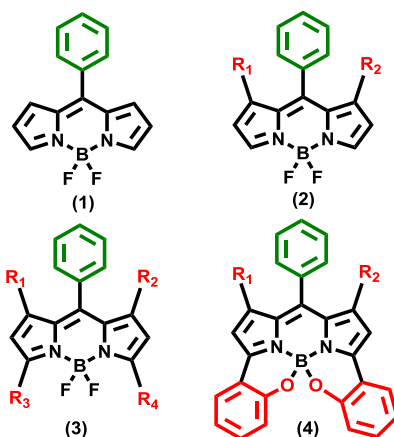


Figure 1.6. Molecular formulae for classical types of *meso*-substituted BODIPY dyes often encountered in the literature.

It is universally recognised that molecules like (2), where R_1 and R_2 are methyl groups or more bulky analogues, successfully hinder rotation of the *meso*-aryl ring and recover the fluorescence quantum yield. There has been

a lot of work carried out on modifying positions 1 and 7 and the effect of substitution in either of these sites is now well documented. In contrast, molecules such as (3), where R_1 and R_2 are hydrogen atoms but R_3 and R_4 are aryl groups that can extend the conjugation, have not received the same amount of attention. Constraining the geometry at the boron atom, exemplified by molecule (4), represents a further interesting instance that has not been subjected to any significant amount of consideration. A thought-provoking trend has been identified where substitution at positions 3 and 5 affects the non-radiative decay. Interestingly, the more conjugation added in either of these positions the smaller the effect of the molecular rotor, as exemplified by molecules (5) to (10).

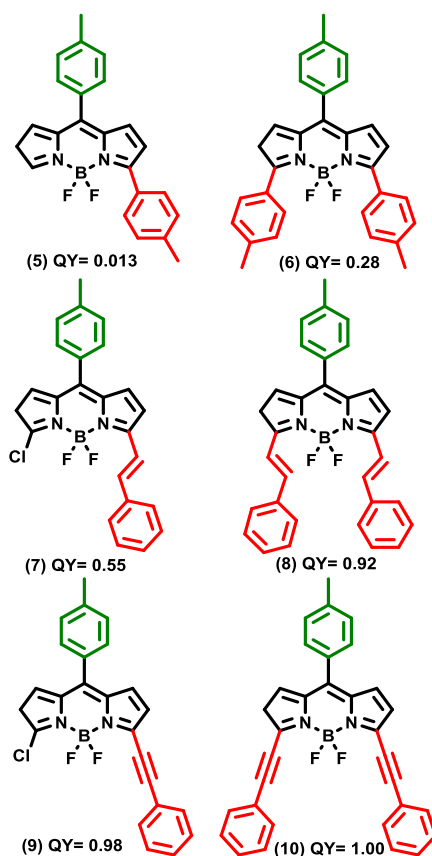


Figure 1.7. Molecular formulae for some of the more common BODIPY-based rotors reported in the literature. QY stands for fluorescence quantum yield. QY for (5) and (6) were reported by Harriman *et al.*,²⁹ whereas QY for (7)-(10) were reported by Loudet *et al.*¹⁹

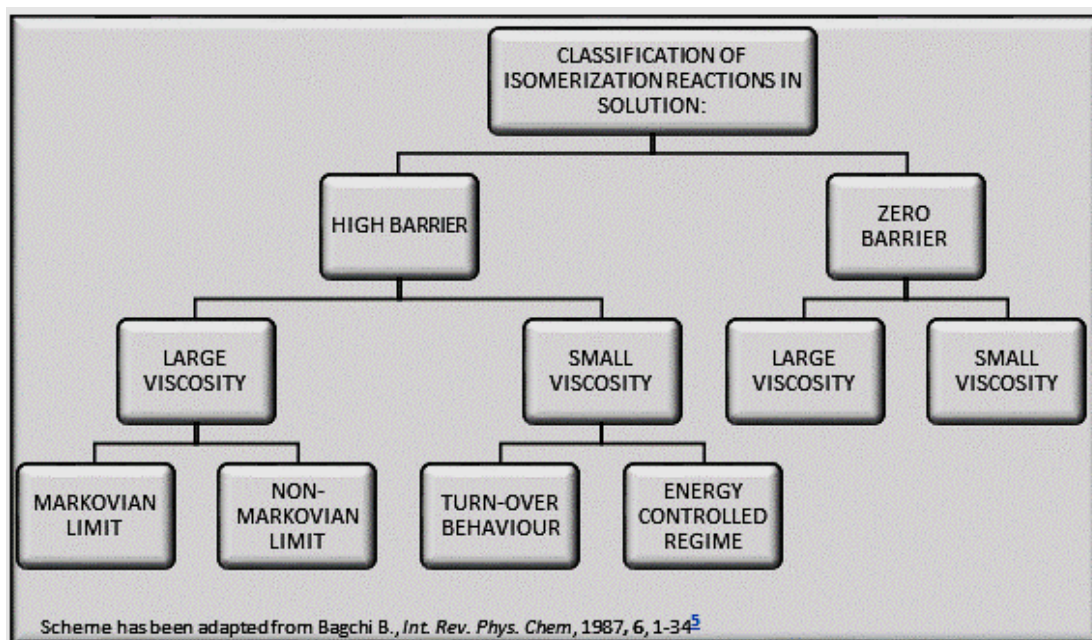


Figure 1.8 Diagram to demonstrate method of classification of isomerization reactions in solution.

Compound (5), this being the non-symmetrical derivative, has a fluorescence quantum yield in low viscosity solvents, that is even lower than that of ROBOD and therefore it can be reasoned that the non-radiative quenching event has been enhanced. However, it is quite remarkable to note that for the symmetrical dye (6) we observe that the fluorescence emission is increased significantly upon addition of the second tolyl ring. It appears that asymmetry plays a crucial role in establishing the photophysical properties of these seemingly simple compounds. It might be argued that, because of some kind of mechanical effect, asymmetry is able to amplify the consequences of gyration of the *meso*-aryl ring. Conversely, moving towards the symmetrical derivative curtails this effect and hinders the rotary motion of the same *meso*-aryl ring.

Here, we would like to draw a parallel between BODIPY dyes and the corresponding cyanine dyes. It has been shown that symmetrical cyanine dyes have higher rotational energy barriers, as well as larger energy gaps, when compared to their asymmetrical counterparts. This is the reason why the asymmetrical variants of cyanine dyes tend to have faster and more

efficient non-radiative decay rates.³⁰ One can observe a trend comparing molecules (7)- (10), it appears that once conjugation is further increased in either position 3 or 5 the emission increases. However, the emission quantum yield can be further increased upon attachment of the same group at the remaining position. In molecules (8), (9) and (10) the rotor effect is non-existent.

It is apparent that aryl substituents attached to the lower rim of the BODIPY dye increase π -conjugation and by doing so serve to push both absorption and emission transitions to the lower energy end of the visible spectrum. The substituents at the lower rim also appear to squeeze the upper rim and, by doing so, the space available for the *meso*-aryl rotor is affected. In turn, this leads to a modulation of the non-radiative rate for decay of the excited-singlet state. There clearly is disparity between the symmetrical and asymmetrical derivatives. It also appears that the bigger the group appended to the lower rim the more substantial becomes the 'squeezing effect' on the upper rim. This situation serves to reduce the non-radiative rate constant. However it is notable that the effect is not simply generated by the lack of symmetry although this appears to play an important role. In order to design the most sensitive rotors one needs to understand both effects.

1.2.3 The Physics of Rotors

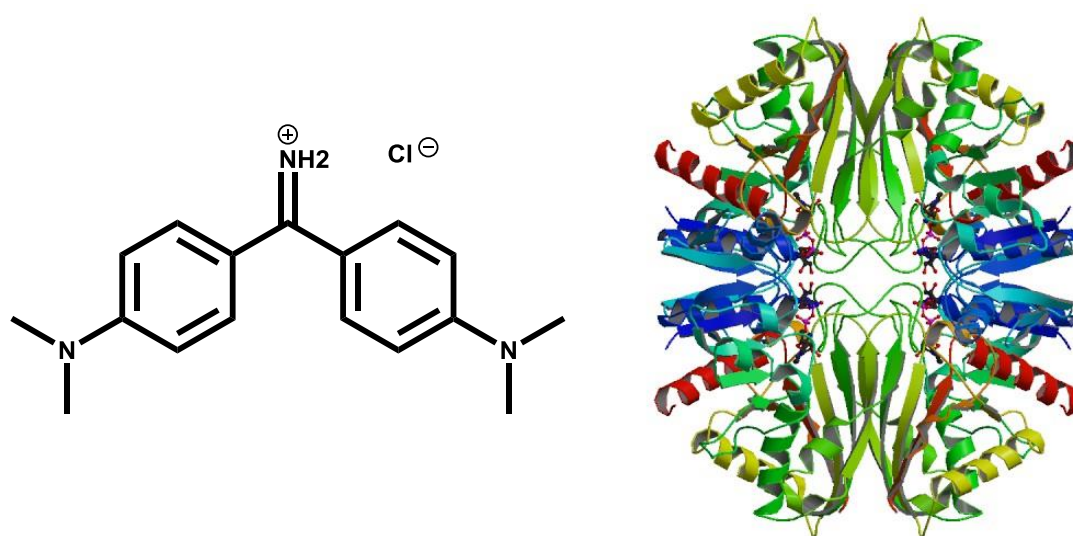


Figure 1.9. Molecular formula of Auramine O, a substituted diphenylmethane dye. It exhibits a viscosity dependence similar to that of triphenylmethane dyes; whereas on the right is a crystal structure of 3-phosphate dehydrogenase from *Thermus thermophilus* HB8 obtained by Ishijima and Yutani (DOI: 10.2210/pdb1vc2/pdb). Auramine O has been used to derive information about the surface and binding pocket of enzymes like that pictured.³¹

Meso-substituted boron dipyrin (BODIPY) dyes act as molecular rotors due to the distortion of their structure imposed by gyration of the aryl substituent. The net effect is loss of fluorescence due to the dramatically enhanced non-radiative route back to the ground state. Crucially, the rotary action bears no effect on the radiative rate constant. Rotation around a partially inhibited C-C bond resembles an isomerization reaction, at least in certain aspects. Numerous models have been proposed to explain the enhancement of the non-radiative decay in such BODIPY dyes. Most of those treatments propose that a non-radiative drain is coupled to S_0 and S_1 surfaces and that the wave packet moves along the surface until it reaches the drain.

Bagchi, Fleming and Oxtoby³² explored electronic relaxation for dyes with no activation barrier for internal rotation; e.g., certain triphenylmethane (TPM) dyes in low viscosity media. They argued that in those instances where there is no barrier, solvent-friction provides the only notable resistance to rotation at the excited-state level. They suggested that the rate of decay of the

excited state is set by a 'position-dependent sink'. They were able to identify three different types of sink: namely, pinhole, Gaussian and Lorentzian sinks. A somewhat related theory was introduced by Oster-Nishijama to account for internal rotation in diphenylmethane dyes, for which we use Auramine O as the main stereotype, Figure 1.9.^{33,34} An advantage of this compound as a fluorescent rotor is that it dissolves readily in water and can be used to interrogate biological systems, most notably enzymes.

The issue with employing a model developed for TPM dyes to account for rotations relevant to BODIPY-based molecular rotors is that there are some obvious structural differences between the two classes. Firstly, the main difference is that in TPM dyes there are three rotating phenyl rings, compared to one in most BODIPY-based rotors. Secondly, and most importantly, the rate of non-radiative decay of boron-dipyrrin dyes is 50-fold slower than that of the corresponding TPM dye. This suggests that there must be a barrier for accessing the non-radiative drain.²⁸ Both TPM dyes and BODIPY-based molecular rotors alike are believed to decay back to ground state due to vibronic coupling and not because of light-induced charge transfer. The vibration of interest is introduced by the gyrating aryl rings.³⁵

Lindsay *et al.*^{36,37} have argued that, after excitation to the S_1 state, the *meso*-phenyl ring is held at a dihedral angle of 180° to the plane of the BODIPY core. This is so the SOMO can be delocalized on to the ring, hence increasing conjugation. This is in contrast to the ground state, where the preferred dihedral angle is around 49° , at least this is so for ROBOD.²⁸ The drawback of Lindsey's model is that it does not account for the observed temperature dependence found for the excited-state deactivation of ROBOD. Nonetheless, the Lindsey publication was the first to address the mechanics of the rotary action for a BODIPY dye.

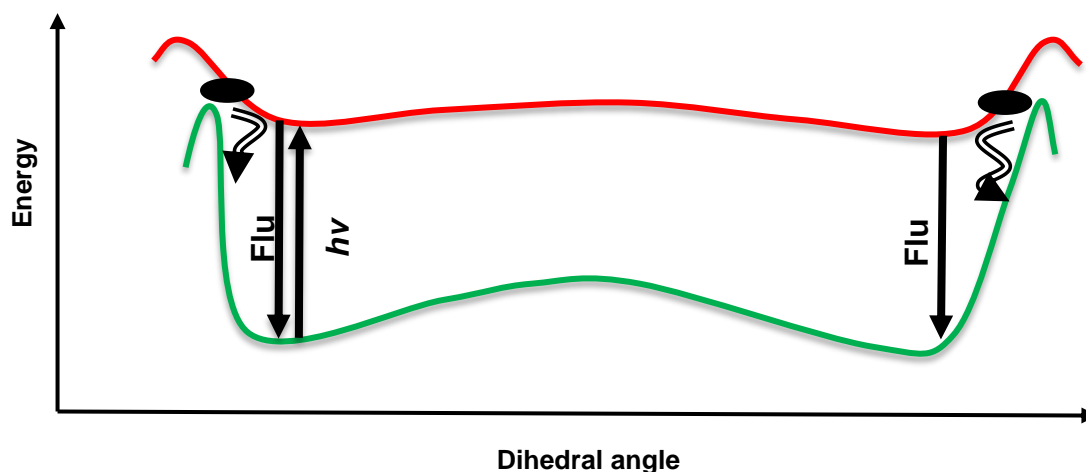


Figure 1.10. Potential energy diagram created for ROBOD by Harriman *et al.* (DOI: 10.1021/cm800702c) in order to explain the temperature effect on non-radiative decay of the first-allowed singlet-excited state. The red and green curves, respectively, refer to the excited- and ground-state potential surfaces for rotation around the *meso*-aryl ring.

Figure 1.10 is a pictorial representation of how the potential energy surface might look for a *meso*-aryl substituted boron-dipyrin dye. Quantum chemical calculations repeatedly point to structural distortion of the BODIPY core that accompanies *meso*-ring rotation. The landscape of the potential energy surface is usually adapted by positioning bulky groups at the upper rim so as to hinder rotation but this strategy provides little useful insight into the mechanics of the rotary action. In a clever modification of the norm, Fan *et al.*³⁸ synthesized a *meso*-substituted BODIPY dye where the substituent was an aldehyde group. They were able to compare the photophysical properties of this derivative with those of the corresponding compound where the aldehyde group was placed at the 2-position,³⁸ Figure 1.11.

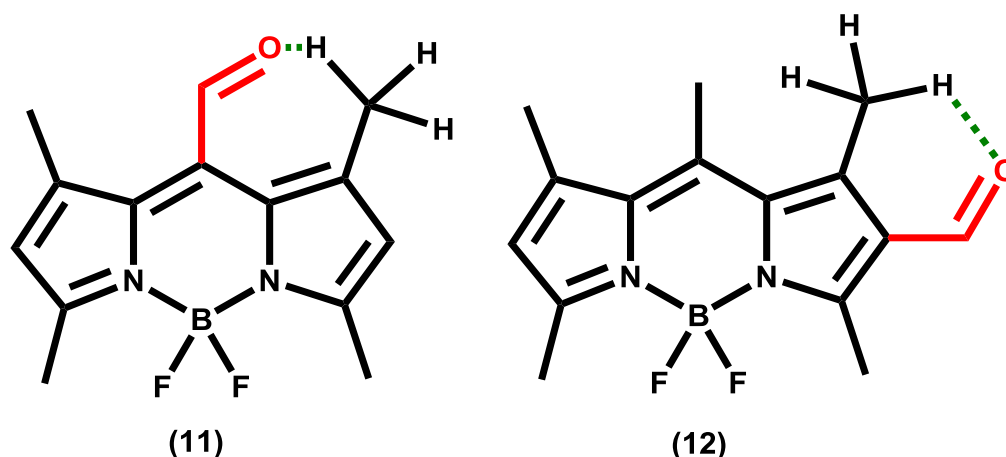


Figure 1.11. Molecular rotors designed by Fan *et al.*,³⁸ where the aldehyde group acts as the rotor and the dashed lines highlight the possibility of weak internal H-bonding. In the case of (11), H-bonding creates a 7-membered ring whereas for (12) it forms a more stable 6-membered cycle.

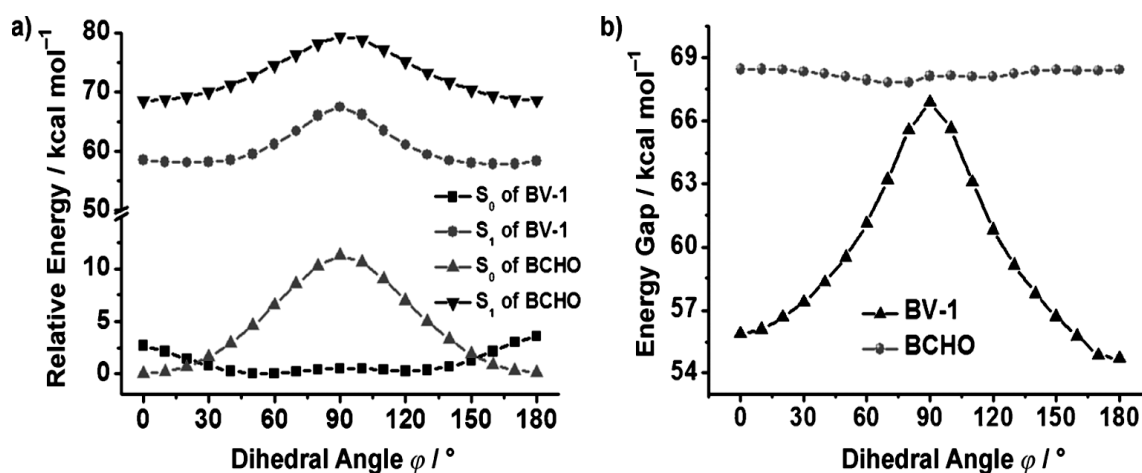


Figure 1.12. Figure adapted from a publication by Fan *et al.*,³⁸ (a) demonstrates potential-energy curves of BV-1 and BCHO at the S_0 and S_1 states with the dihedral angle around the C-C bond, whereas (b) demonstrates the energy gap between the S_0 and S_1 states of BV-1 (circle) and BCHO (triangle) with dihedral angles around the C-C bond. Calculations were performed by means of the DFT method [B3LYP/6-31G(d, p)]. BV-1 is molecule (11) whereas BCHO is molecule (12).

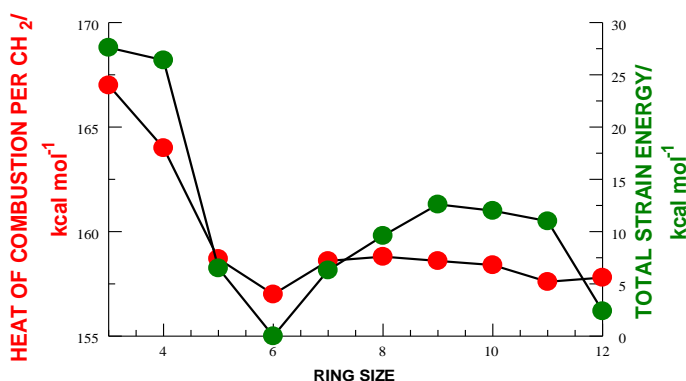


Figure 1.13. Graph adapted from Organic Chemistry, John McMurry-3rd edition ISBN 0-534-16218-5 to demonstrate the relationship between ring size and heat of combustion and total strain energy.

Molecule (11) behaves like a prototypic molecular-scale rotor whereas (12) does not follow suit. It is important to note that methyl groups had to be added at positions 1 and 7 in order to create the steric clash which leads to the desired structural distortion of the BODIPY core. Importantly, there is the likelihood for weak H-

bonding, for (11) this creates a 7-membered ring whereas for (12) it forms a more thermodynamically stable 6-membered ring, Figure 1.11. Fan *et al.*,³⁸ reported computational modelling studies to indicate that the BODIPY core remains planar, regardless of rotation of the aldehyde group at position 2. However, for molecule (11) their calculations were consistent with structural distortion of the dipyrin core when the aldehyde was at a torsional angle close to 180°. This particular geometry increases the conjugation and therefore the energy gap between the first-excited state and the ground state decreases. In turn, this enhances non-radiative decay because of the energy-gap law.^{39,40} No such claim can be made for (12). The authors concluded that the geometry at the excited state is crucial to the process of promoting non-radiative decay. This work appears to support the earlier research published by Lindsay *et al.* mentioned above. Crucially, this work demonstrates that, in terms of BODIPY derivatives, quenching of fluorescence is specific to rotation of groups appended at the *meso*-position.

The issue of a viscosity-dependent fluorescence quantum yield is not restricted to TPM, DCVJ dyes and BODIPY rotors. Sterically hindered stilbenes are further examples of fluorescent compounds where the emission quantum yield is highly dependent on the viscosity of the surrounding medium. At room temperature, it has been found that *trans*-stilbenes are weakly fluorescent whereas the corresponding *cis*-derivatives are non-

fluorescent.⁴¹ In the case of *cis*-stilbenes, steric interactions provide an incentive for the excited state to twist around the central C=C bond (i.e., light-induced isomerization). Rotation around a double bond is formally forbidden, nevertheless it occurs readily in fluid solution. The overall process is strongly temperature dependent and the rate varies proportionally with inverse viscosity of the surrounding medium. In the excited state, this twisting motion is responsible for arriving at the geometry from which the radiationless transition is favoured.

Separately, Velsko and Fleming^{42,43} in a classical publication investigated the photophysics of diphenylbutadiene (DPB) and observed two decay channels, one being associated with high temperatures and the other with low temperatures. This situation has not been reported for any BODIPY derivative.⁴³ However, with stilbenes there is another complication which appears in the form of accessible triplet states reached *via* intersystem crossing. In a 1971 paper by Muszkat and Sharafy,⁴⁴ it was proposed that internal conversion from S₁ to the S₀ state in stilbenes is due to a process of tunnelling for molecules twisted by 90° about the central double bond, Figure 1.16.^{44,45} However, it is important to note that in his original paper Kramers' dismisses "tunnel-effects" as a possibility.⁴⁶ In the same paper, these authors attributed the noted differences in how the emission properties depend on viscosity for the *trans*- and *cis*-derivatives to a difference in their molar volumes. Again, we foresee no real relevance of this work in terms of BODIPY-based rotors.

An empirical mathematical treatment based on the degree of the statistical free volume available in the solvent structure has been used with some success to describe the fluidity of liquids, Equation 1.5,⁴⁷ where k_{RED} is the reduced isomerization rate, D and α are constants and finally η is the viscosity.

$$k_{RED} = D/\eta^\alpha \quad \text{Equation 1.5}$$

Of course, this expression is rather crude and does not convey much scientific information,⁴⁷ other than the ability to compare coefficients between different systems. Interestingly, Brey *et al.*⁴⁸ carried out pressure effect studies on *trans*-stilbene and found that there was a more substantial effect in polar solvents than non-polar solvents with the same viscosity.^{48,49} They concluded that the observed activation energy in solution is affected by both internal and solvent contributions.⁴³ These experiments highlight the role played by the nature of the solvent and also demonstrate that a molecular rotor could be used as a pressure monitoring probe, under the right conditions.

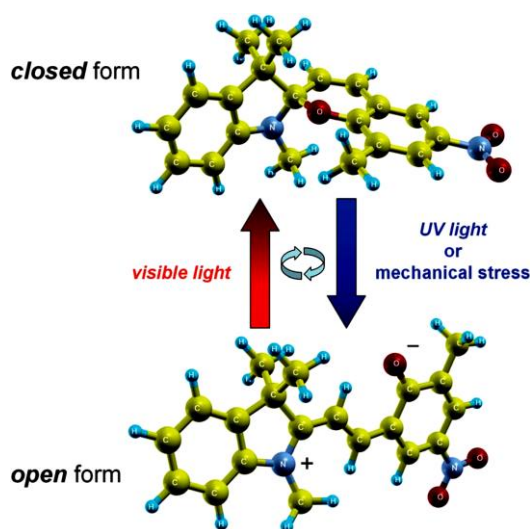


Figure 1.14. Molecular structures of open and closed-configuration of a merocyanine dye (spiropyran). The isomerization process is reversible upon irradiation with visible light, which restores the closed spiropyran form. Figure adapted from *Nanoscale*, **2012**, 4, 1321–1327.

Cyanine dyes, as mentioned earlier, represent a further example of fluorescent dyes where rotation around a C=C bond (i.e., light-induced isomerization) is viscosity dependent, Figure 1.14. As expected, the excited-state manifold of the cyanine dye decays *via* fluorescence (with low quantum yield) and predominately by way of internal conversion.^{30,50} Intersystem crossing to the triplet state is comparatively slow, in the absence of a spin-orbit coupler, and the triplet yield is negligible. Light-induced isomerization occurs with high probability in many cyanine dyes and the resultant isomer can be detected by transient absorption spectroscopy, which is an obvious

advantage for experimental studies. This allows the rate of isomerization to be measured under quite disparate conditions, thereby building up a wealth of information.

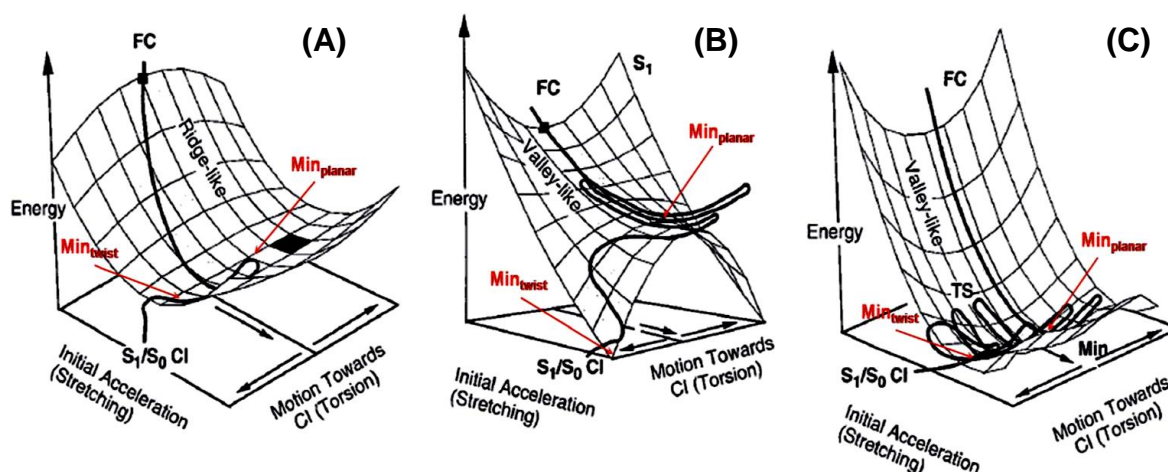


Figure 1.15. Cyanine dyes; two-mode excited state potential energy surface with ridge (A), ridge valley (B), and valley (C), picture adapted from *RSC Adv.*, **2016**, 6, 45210–45218. (A) represents barrierless isomerization, (B) demonstrates intermediate barrier, and (C) shows potential energy surface where there is a significant barrier to isomerization.⁵¹

Many cyanine dyes, however, are polar– the so-called merocyanine form – and this feature introduces certain complications for understanding the isomerization mechanism, Figure 1.15.⁵² For example, the rate of isomerization depends on solvent polarity, as well as viscosity.^{53–56} In some aspects, the dependence of the fluorescence quantum yield on solvent viscosity found for BODIPY-based rotors is comparable to the dependence of the isomerization rate constant observed with cyanine dyes; the reason for this is that both processes involve torsional motion of molecular fragments and crucially those movements are influenced by solvent friction.⁵⁷ The BODIPY rotors involve a more subtle internal motion than is pertinent to the cyanine dyes and, of course, there are no spectroscopic signatures by which to monitor the event in real time, other than by fluorescence.

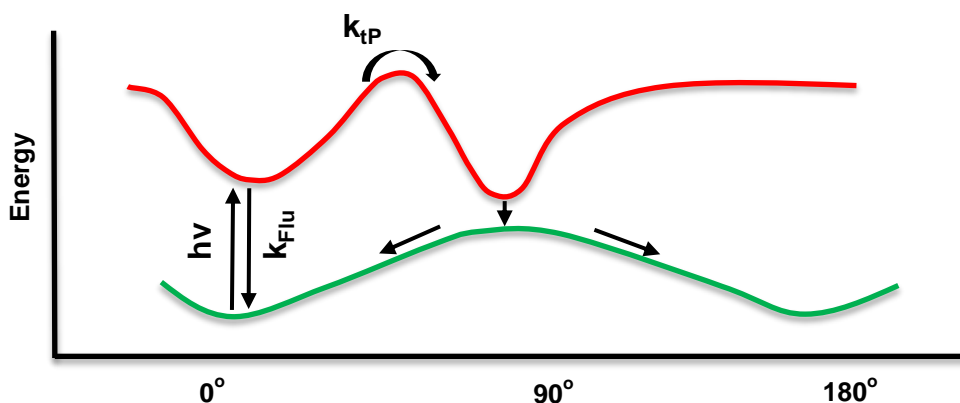


Figure 1.16. Potential energy diagram reported for a typical stilbene dye, adapted from Turro, N., University Science Books. The x-axis represents dihedral angle for the connecting double bond and the y-axis is total energy. The ground state potential surface is shown as a green curve while the corresponding excited-state surface is illustrated by the red curve.

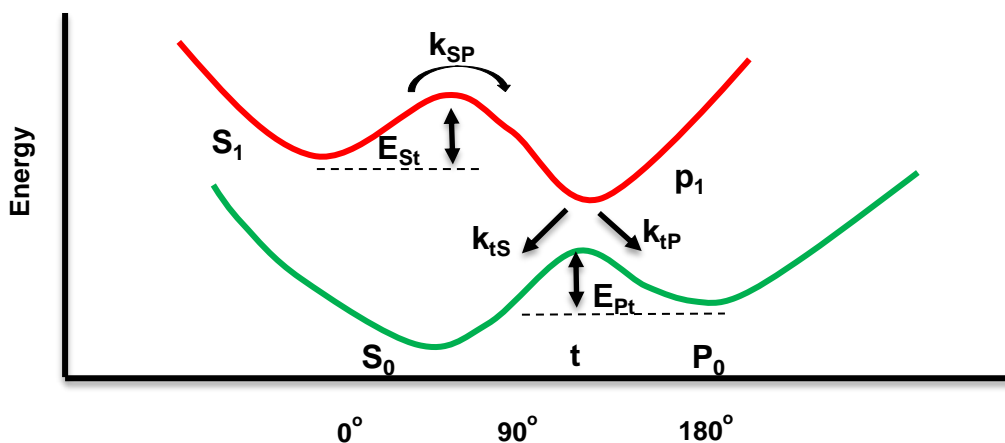


Figure 1.17. Potential energy diagram reported for certain cyanine dyes by Velsko and Fleming, *Chem. Phys.* **1982**, 65, 59. The x-axis represents dihedral angle for the connecting double bond and the y-axis is total energy. The ground state potential surface is shown as a green curve while the corresponding excited-state surface is illustrated by the red curve.

Figure 1.17 shows a pictorial representation of a potential energy diagram of the type frequently used to demonstrate the isomerization process relevant to cyanine dyes.⁵⁸ The symbol 't' is used to refer to a twisted intermediate along the isomerization pathway. It is characterized by fast deactivation to reform the ground state. In contrast, 'S₀' is the ground state for the normal conformer and 'P₀' refers to the photo-isomer. Kramers' treatment, also referred to as the Fokker-Planck equation, might be used to interpret the rates of isomerization, including non-radiative decay of BODIPY-based rotors.^{46,59} This theory has been popular with physicists for many decades and has proved to be applicable for cyanine dyes as well as certain stilbene derivatives. The treatment uses Brownian motion dynamics, which are driven by thermal forces, and by means of the fluctuation-dissipation theorem can be linked to temperature and friction.^{46,60,61} Activation restrictions for the twisting process undergone by cyanine dyes and stilbenes, which must accompany isomerization, bear certain resemblances to the rotation of the *meso*-aryl ring found with the BODIPY-based rotors. In particular, solvent viscosity will affect the rate at which solvent cages are able to rearrange so as to accommodate the twisting motion (i.e., internal rotation) and this means the solvent specific barrier, which is present in all media, is higher in more viscous solvents.⁶² Despite the possible similarities between isomerization and the so-called rotor effect, there have been no serious attempts to apply Kramers' theory to internal rotation in BODIPY dyes.

In certain cases, it has been demonstrated that, for a particular dye molecule, the emission lifetime depends not only on viscosity but also on the identity of the solvent when compared to different solvents having the same viscosity. This is known as an iso-viscosity plot. One reason for this situation might be because of specific solvent-solute interactions, such as H-bonding.⁶³ Clearly, this complicates interpretation of experimental kinetic data because it means that attention must be given to controlling temperature, pressure, polarity, viscosity and chemical composition of the solvent. For this reason, most studies that attempt to vary solvent viscosity do so by employing a homologous series of solvents, such as the linear alcohols. It might be

mentioned in passing that there have been very few studies where the solvent viscosity is increased by adding a soluble polymer.

$$k = (\omega_r/2\pi\omega_b)[((\xi^2/4) + \omega_b^2)^{1/2} - \xi/2] \exp(-E_0/RT) \quad \text{Equation 1.6}$$

Equation 1.6 above is known as Kramers' treatment. Here, ζ is the frictional parameter, ω_r is the frequency of the reactant well, ω_b is the barrier frequency, and finally E_0 is the activation energy for the rotation.^{58,64}

$$k(\zeta \rightarrow 0) \cong (E_0/k_bT)\zeta \exp(-E_0/k_bT) \quad \text{Equation 1.7}$$

Equation 1.7 corresponds to Kramers' estimate of what happens to the rate constant at very low friction. This latter expression predicts that ζ becomes smaller as the rate constant decreases. In order to analyse experimental results, it is common practice to relate ζ to shear viscosity, η .

$$k = k^{TST} = (\omega_r/2\pi) \exp(-E_0/k_bT) \quad \text{Equation 1.8}$$

Equation 1.8 is a transition state result, it applies when the frequency of the barrier (ω_b) is greater than the friction parameter (ξ). When the k^{TST} limit is reached, the barrier is sharp and therefore it is unlikely the particle will spend long enough on the barrier top to be affected by frictional forces. However, the situation when the friction parameter is significantly greater than ω_b is known as the Smoluchowski limit (SL), Equation 1.9.

$$k \equiv k^{SL} = (\omega_r\omega_b/2\pi\zeta) \exp(-E_0/k_bT) \quad \text{Equation 1.9}$$

The inverse friction dependence described in Equation 1.9 occurs when the barrier is relatively flat and the motion at the top of the barrier is pretty much diffusive.⁶⁴ However, it has been shown that the SL is not always observed.^{42,43} The activation energy (E_0) can be estimated from the slope of an Arrhenius-type plot of $1/T$ against $\ln(k)$. Reported deviations to Kramers'

theory are often attributed to differences between the bulk viscosity of the solvent and the local viscosity in the vicinity of the solute.^{62,65} This is a particular problem for large solutes or in cases where charge transfer is involved. Another commonly encountered challenge is set by non-Markovian friction and multiple models have been developed to try to overcome this issue, most notably the so-called Grote-Hynes approach.⁶⁶ One disadvantage of compensating for this situation is that additional terms are added to the basic equation to account for specific features. In the end, the treatment becomes cumbersome and even intractable.^{57,67}

Kramers' theory appears to break down at high viscosities; this was addressed by Grote and Hynes⁶⁶ (as well as the non-Markovian behaviour). These authors extended Kramers' theory by including the frequency reliance on friction.

$$k = (\lambda_r/\omega_b)(\omega_0/2\pi) \exp(-E_0/k_B T) \quad \text{Equation 1.10}$$

Where:

$$(\lambda_r/\omega_b) = (\omega_b/\lambda_r) + \int_0^\infty \xi(t) \exp(-\lambda_r t) dt = \kappa_{GH} \quad \text{Equation 1.11}$$

κ_{GH} is a transmission coefficient obtained by solving Equation 1.11, where I is the moment of inertia.

$$1 - \kappa^2 - (\kappa/I\omega_b)\zeta(\kappa\omega_b) = 0 \quad \text{Equation 1.12}$$

The parameters E_0 and ω_0 can be obtained by plotting $\ln(k(T)/\kappa(T))$ against $1/T$. In fact, E_0 can be estimated from the slope whereas ω_0 can be obtained from the intercept. The plot should be linear provided the intrinsic barrier is only weakly dependent on polarity.⁶⁸ Kramers' theory was not developed with molecular probes in mind. However, it is, to this day, the most

comprehensive theory available for analysis of the behaviour of molecular rotors such as ROBOD.

1.2.4 Measurements and Calibration

In order to quantify the degree of success of any particular molecular rotor, the most common procedure is to measure its emission quantum yield and/or excited-state lifetime in a series of solvents possessing similar chemical properties but differing viscosity. This protocol provides the simplest means by which to compare rates of non-radiative decay with solvent viscosity. It also provides access to the limiting 'on'/ 'off' levels of fluorescence that determine the ease of use of the rotor. A series of linear alcohols or linear alkanes is often used for these measurements. Viscosity is known to change with temperature and pressure and therefore it is necessary to fix these variables. Activation energies for the rotary process should be measured if at all possible and, in principle, this can be done by conventional Arrhenius-type studies. However, viscosity is strongly dependent on temperature, but not always in a linear manner. The solution to this problem is to select solvents where the viscosity is the same fixed value but at different temperatures. Now the temperature effect can be isolated from the viscosity effect. Because some rotors respond to changes in polarity, it is important to conduct trial studies to eliminate this effect. This is done by using solvents of the same polarity but disparate viscosity and vice-versa. Most studies in the literature have relied on empirical rate expressions to quantify the relationship between fluorescence yield and solvent viscosity.

For example, BODIPY-based molecular rotors have been established to be more sensitive viscosity probes than industry standards like 9-dicyanovinyl julolidine.⁶⁹

$$k_{NR} = v/\eta^\alpha \exp(-E_A/RT) \quad \text{Equation 1.13}$$

This claim is made on the basis of Equation 1.13,⁴² where η is viscosity, α is a coefficient that is used to determine the sensitivity towards viscosity, v is a limiting pressure exerted by the rotor, E_A is a barrier for internal rotation and finally T is the absolute temperature. This model allows for an additional activationless non-radiative decay channel to compete with emission and barrier-controlled rotation.⁴² The term α is crucial here as it determines the degree of sensitivity of the probe and is easily established from a log-log plot of viscosity vs. non-radiative decay rate constant. It has been shown that α for the simplest BODIPY-based rotor, i.e. ROBOD, is 0.41.²⁹ However, it is even higher for (5) ($\alpha=0.62$).²⁹ In contrast the same coefficient for the DCVJ dye mentioned above is approximately 0.3 under the same conditions.⁶⁹ We will show later that there is further opportunity to increase the sensitivity of BODIPY-based rotors as we explore the influence of substitution at the 3,5-positions. The Förster-Hoffmann equation⁷⁰ is another popular way of measuring the effectiveness of molecular viscometers, Equation 1.14.

$$\ln(\phi_f) = C + x \ln(\eta)$$

Equation 1.14

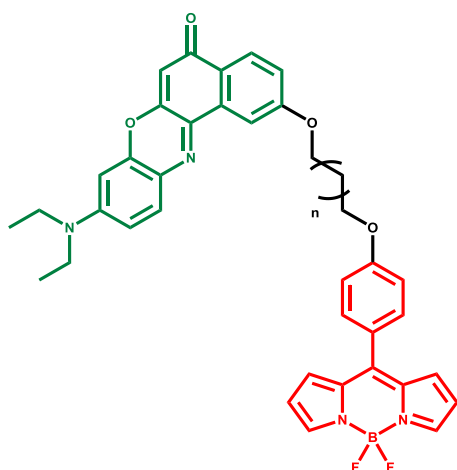


Figure 1.18 Molecular formula for the BODIPY- Nile Red ratiometric probe.

The experimental quantum yield can be replaced with the excited-state lifetime since the latter is easier to measure *in vivo*. In the Förster-Hoffmann equation, x is the sensitivity parameter. It is the slope of the log-log plot of viscosity vs. lifetime (or quantum yield). This approach predicts the perfect rotor to have an 'x' value of 0.6.⁷¹ However it is important to note that this is only a very crude estimate and Equation 1.13 gives a better

representation of the viscometer's behaviour.

There are two commonly used approaches to creating a calibration curve: notably using the excited-state lifetime or the relative emission intensity.

Intensity is the less reliable of these methods. This is simply because it is easily influenced by local conditions and by concentration. If intensity is the preferred way to measure the viscosity, one must use a reference dye that is known to be insensitive to changes in the local environment, such as temperature and viscosity. A common choice for the control emitter is the coumarin family of dyes.⁷² This allows for a ratiometric approach. Coumarin and BODIPY dyes will allow for two distinct emission spectral profiles, the emission from the latter will change with viscosity unlike that of the coumarin dye which is expected to remain constant. The ratio of emission intensities under controlled excitation conditions at preselected wavelengths is independent of probe concentration and therefore a ratiometric probe is self-referencing. A good example of this is provided by the work of Kang *et al.*⁷³ where Nile Red is used as a reference for a BODIPY-based rotor, Figure 1.18. Additionally, this bichromophore can be used to monitor polarity since Nile Red is sensitive to solvent polarity but the photophysics of BODIPY are independent of the solvent dielectric constant.

A more reliable method to monitor viscosity by means of fluorescence is to use the excited-state lifetime. The emission lifetime is concentration independent, however it is more difficult to analyse. This can be done using fluorescence lifetime imaging microscopy, FLIM.^{20,74} It provides images based on the time taken for decay from the excited state instead of relying on fluorescence intensity.⁷⁵ FLIM is capable of not only measuring the lifetime by time-correlated, single photon counting (TCSPC) but also anisotropy; time resolved fluorescence anisotropy imaging (TR-FAIM). With this method, it is straightforward to produce a calibration curve of viscosity against lifetime. However, the method has its disadvantages, for example it can be relatively time consuming. Also, lifetime decay curves are not always mono-exponential! Most importantly, the technique requires specialist equipment and a well-trained operator. Unlike measuring fluorescence intensity, lifetime or quantum yield, it is unlikely that this method can be used outside of a research environment.

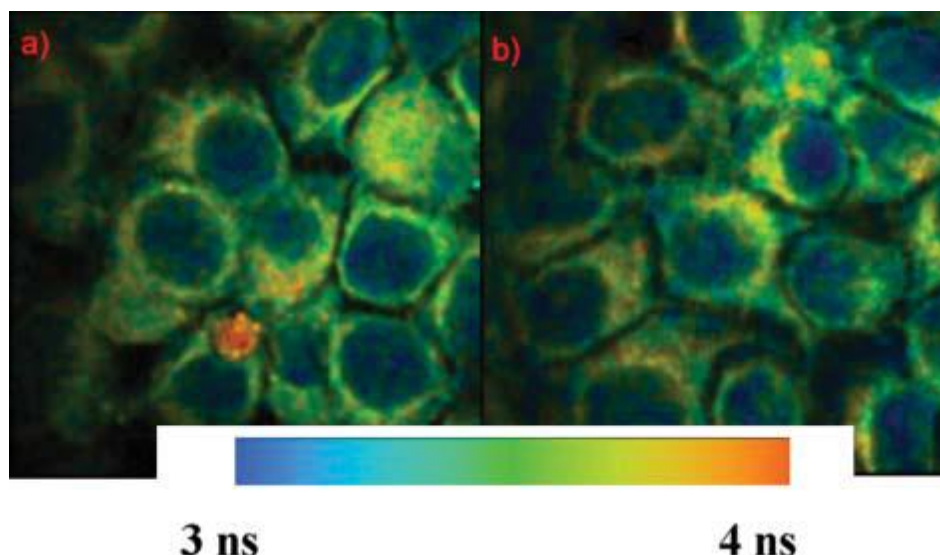


Figure 1.19. Examples of images taken of HeLa cells stained with a BODIPY dye collected using the FLIM technique. Pictures are reproduced from a publication by Ziessel *et al.*⁷⁶

1.3 Electronic Energy Transfer

Electronic energy transfer (EET) is an essential process in Nature in respect of photosynthesis and in DNA repair enzymes, amongst others.⁷⁷ Moreover, it has also found multiple applications in modern technologies like organic light-emitting diodes (OLEDs)⁷⁸ and artificial photon collecting systems. There are two common mechanisms: (1) Dexter-type EET (i.e., through-bond interactions) which is strongly distance dependent and involves significant overlap of wave-functions on donor and acceptor species. (2) Förster-type EET (i.e., through-space interactions) which can occur over longer distances and involves Coulombic coupling between remote reactants. The two mechanisms often contribute to the overall EET rate and resolving the individual processes can be a challenging process in some cases. The Dexter EET mechanism sometimes involves ‘super-exchange interactions’. This takes place when a bridge (B) in a donor-bridge-acceptor system is electronically conductive and able to delocalise and mix its orbitals with those of either D or A. In general, EET can be considered as the radiationless transfer of electronic energy from a donor (D) to an acceptor (A) at distances extending from 10 to 100 Å.⁷⁹ It can involve inter- or intramolecular processes. As a result of

efficient EET, emission originates exclusively from the acceptor and the singlet lifetime (τ_s) of the donor moiety is effectively reduced to zero.

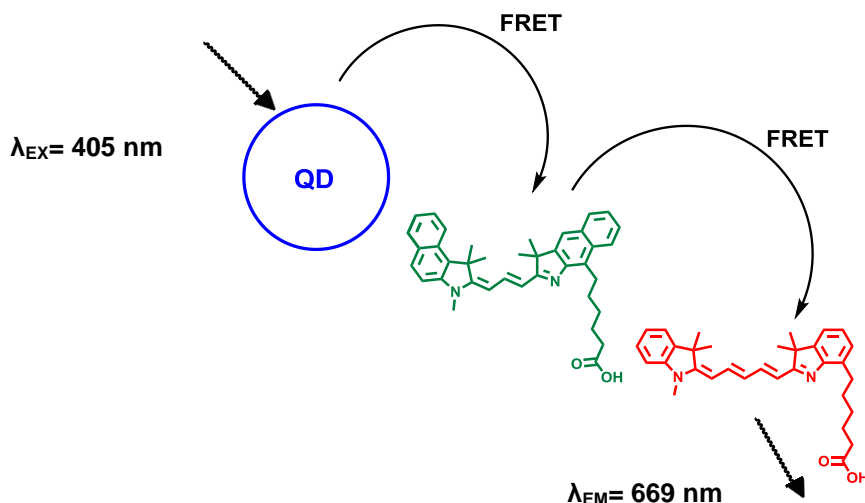


Figure 1.20. Example of an EET based sensing scheme adapted from *Chem. Commun.*, **2011**, 47, 611–631. A quantum dot (QD) with excitation energy of 405 nm, cyanine 3.5 (green) and cyanine 5 (red) dyes are arranged according to their excitation energy in order to facilitate efficient energy transfer. FRET refers to Förster Resonance Energy Transfer.

1.3.1 Förster Resonance Energy Transfer (FRET)

Förster Resonance Energy Transfer or FRET was proposed by Theodor Förster^{80,81} in 1946 as a dipole-dipole interaction between two chromophores, one acting as an energy donor and the other as an energy acceptor. The crucial condition for FRET to take place relates

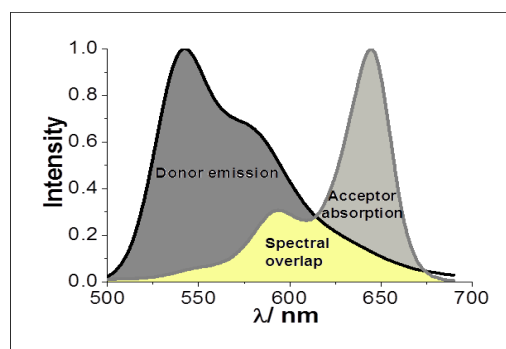


Figure 1.21. Illustration of the donor- acceptor spectral overlap.

to the overlap integral, J_{DA} , between the donor emission spectrum and the acceptor absorption spectrum; for a well-designed D-A system there is no overlap between the acceptor emission and donor excitation spectra (N.B. re-absorption leads to 'reverse' FRET). The term J_{DA} is a thermodynamic factor, it increases (and with it the rate of EET) with high molar absorption coefficient (ϵ) of the acceptor and small Stokes' shift (SS). The rate of

EET can be estimated by means of Fermi's Golden Rule (Equation 1.15) where V_{DA} is the coulombic electronic coupling matrix element (Equation 1.18), κ is the orientation factor, s is the screening factor (Equation 1.16) and J_{DA} is the overlap integral (Equation 1.17).

$$k_{EET} = \frac{2\pi}{\hbar} \times |v_{DA}|^2 \times |\kappa^2| \times s^2 \times J_{DA} \quad \text{Equation 1.15}$$

$$s = \frac{3}{2n^2 + 1} \quad \text{Equation 1.16}$$

$$J_{DA} = AB \int \frac{F_D(v)}{v^3} \times \frac{\epsilon_A(v)}{v} dv \quad \text{Equation 1.17}$$

$$V_{DA} = \frac{\mu_D \times \mu_A}{R_{DA}^3 \times (4\pi\epsilon_0)} \quad \text{Equation 1.18}$$

When the distribution of donor and acceptor orientations is random, κ^2 can be assumed to be equal to 2/3.⁸⁰ However, for D-B-A type systems it can be anywhere between 0 and 4. In fact, κ is at its highest when the transition dipole moments vectors are aligned parallel to each other and conversely at its lowest when they are orthogonal to each other. The rate of FRET is also dependent on the refractive index of the solvent (n), and the distance (R_{DA}) between the centres of the transition vectors associated with donor and acceptor.⁸² The rate of EET can be manipulated by changing the mutual orientation of these transition dipoles.

FRET has frequently been used as a 'molecular ruler' by which to measure distances in proteins, nucleic acids and many other biological structures.⁸³ This can be achieved because, according to Förster theory, the rate constant is proportional to the inverse sixth power of the distance ($1/R_{DA}^6$) between donor and acceptor.⁸² One of the main characteristics of FRET is the critical

Förster distance, R_0 . This is the distance at which the FRET efficiency is precisely 50%, Equation 1.19.⁸⁴

$$E\% = R_0^6 / (R_0^6 + R_{DA}^6) \quad \text{Equation 1.19}$$

The probability of EET is determined by taking a lifetime or quantum yield ratio of a donor-acceptor system and a corresponding isolated donor, Equation 1.20.

$$P_{EET} = 1 - (\tau_{D-A} / \tau_D) = 1 - (\phi_{D-A} / \phi_D) \quad \text{Equation 1.20}$$

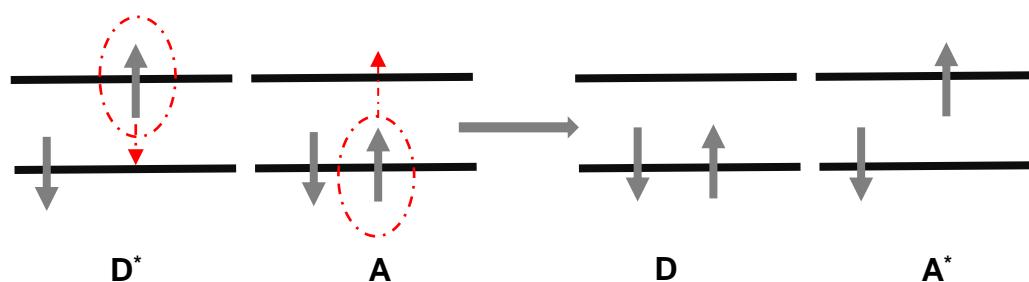


Figure 1.22. Frontier molecular orbital diagram for Förster-type electronic energy transfer.

1.3.2 Dexter Energy Transfer

Dexter-type electronic energy transfer is also referred to as 'electron exchange'⁸⁵ because it can be compared easily to Marcus theory.⁸⁶⁻⁸⁸ Figure 1.20 provides an example of a molecule that undergoes EET by way of the electron exchange mechanism. Such EET processes tend to occur over shorter distances than are often found for FRET, because of the demand for overlap of donor and acceptor wave-functions. However, when considered in terms of the super-exchange mechanism in donor-bridge-acceptor multi-component molecules, the length scale for Dexter-type EET is expanded by a considerable amount and distances in the

region of 50 Å are not uncommon. The Dexter mechanism can be applied to explain singlet-singlet energy transfer, but it is more commonly used to describe triplet-triplet EET events.

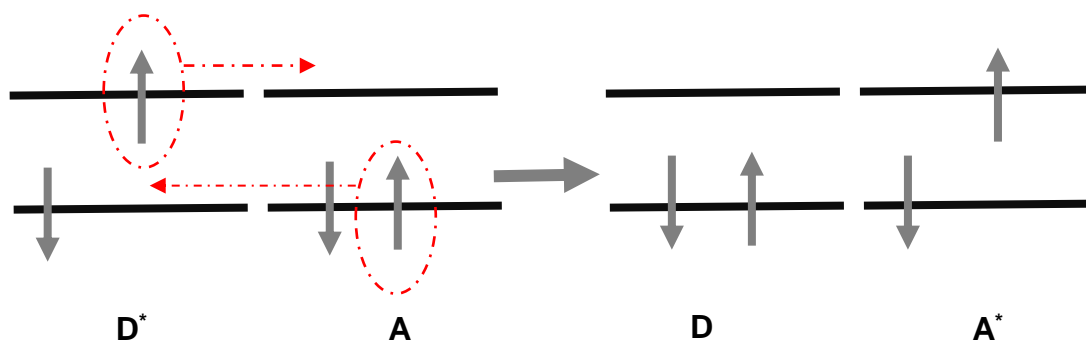


Figure 1.23. Frontier molecular orbitals to account for Dexter-type EET for the singlet-singlet mechanism.

Equation 1.21 describes the rate of EET according to the Dexter mechanism, where L is the sum of the van der Waals radii, J_{DA} is the spectral overlap integral and R_{DA} is the edge-to-edge distance between the donor and acceptor. The term V_{DA} describes electronic mixing between orbitals on donor and acceptor and is distance dependent, $V_{DA} \propto \exp((- \beta / 2) R_{DA})$. Here, β is referred to as an attenuation factor, it is dependent on the product of atomic orbital coefficients, γ , and on the energy difference between the donor orbital and the corresponding bridge orbital,⁸⁹ $\beta = 2 / R_0 \ln |\Delta E / \gamma|$. Through-bond EET such as that proposed by Dexter exchange is usually temperature dependent. This is because of a discrepancy between the reorganisation energy and the thermodynamic driving force.⁹⁰

$$k_{DEXTER} = \frac{2\pi}{\hbar} J_{DA} V_{DA} \exp(-2R_{DA}/L) \quad \text{Equation 1.21}$$

1.3.3 Spectroscopic Gradient

EET occurs from a chromophore absorbing at shorter wavelength (this being the donor) to one absorbing at longer wavelength (this being the acceptor). However, it is common, especially in natural systems and ever more frequently in artificial systems, that there are several layers of disparate chromophores arranged to facilitate a cascade of EET events. When the chromophores are arranged correctly, the net result is an energy funnel.^{91,92} A good example of such elaborate light-harvesting systems is provided by a multi-layered dendrimer.⁹¹ It is important that, on progressing from the exterior to the interior of the core, that each generation is bathochromically shifted compared to the preceding layer and that good spectral overlap is preserved at each interface. In general, one wants to take the same precautions as for simpler donor-acceptor systems to avoid back EET and loss of significant amounts of energy.

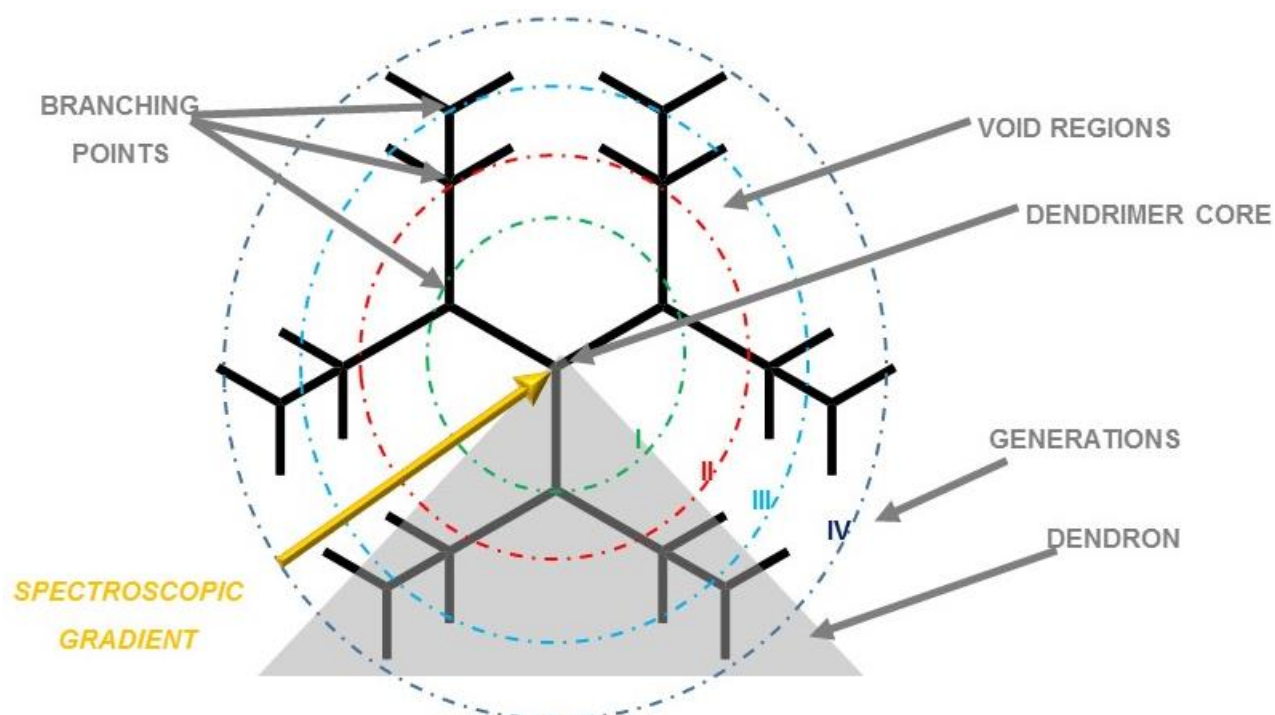


Figure 1.24. Schematic representation of a dendrimer engineered for multiple EET events from periphery to core, picture adapted from *Annu. Rep. Prog. Chem., Sect. C*, **2003**, 99, 177-241.⁹³

.....

This work focusses on seeking to gain a deep understanding of the photophysical processes inherent to multi-functional and/or multi-component supermolecules in condensed phase and attention is given only to the fundamental properties. Throughout this project we probed the photophysical behaviour of molecular rotors. At the beginning we focus on the structural effect of the BODIPY lower rim and on what happens when we constrain the geometry at the boron atom. We follow these studies with an investigation into the effect of electronic energy transfer and charge transfer on to the putative rotor. The photochemical stability of a large molecular assembly in condensed phase is also probed. Finally, we return to the solvent effect on large molecular assemblies.

The compounds investigated herein range from relatively small BODIPY-based molecules to large molecular assemblies (i.e., dyads, triads and pentads). The focus at the beginning is solely on the photophysics of molecular rotors based on BODIPY and how relatively small structural modifications can greatly enhance the non-radiative decay. We investigate the effect of asymmetry on the fluorescence quenching and follow these studies with a series of investigations into BODIPY dyes constrained at the boron atom. These are relatively new types of fluorophore and there is almost no prior information reported in the literature.

Fluorescence intensity is strongly concentration dependent; this is a major limitation for environmental sensing applications and for devices exposed to a large number of photons. Prolonged exposure to intense light gives rise to photobleaching of organic dyes and this in turn leads to loss of intensity. To date, there has not been a conclusive study into the photostability of BODIPY-based dyes. Hence we endeavour to shed more light onto the kinetics of photodegradation of such organic dyes. The photodegradation process is followed by a range of techniques, notably 700 MHz ^1H NMR and UV-vis spectroscopy.

Finally, we return to the study of molecular dynamics in condensed phase with two groups of closely-spaced bichromophores. We interrogate the effects of solvent on the photophysics of molecular assemblies of two BODIPY-based bichromophores bridged by 1,10-phenanthroline. In this case, we are able to show that the nature of the solvent controls the geometry of the assembly but that minor changes in the

molecular architecture are met by major changes in behaviour. This work has relevance to the folding of peptides and small proteins. Encouraged by this result, we investigated a second series of bichromophores where the connection is provided by a 1,2-diaminocyclohexane ring. The spacer unit is subject to conformational exchange and therefore can be probed by excitation energy transfer dynamics.

1.4 References

- (1) Haidekker, M. A.; Theodorakis, E. A. *Org. Biomol. Chem* **2007**, 5, 1669.
- (2) Kottas, G. S.; Clarke, L. I.; Horinek, D.; Michl, J. *Chem. Rev.* **2005**, 105, 1281.
- (3) Kuimova, M. K. *Chimia* **2012**, 66, 159.
- (4) *Advanced Fluorescence Reporters in Chemistry and Biology I: Fundamentals and Molecular Design*; Springer Science & Business Media, 2010.
- (5) Luby-Phelps, K. *Int. Rev. Cytol.* **2000**, 192.
- (6) Chien, S.; Usami, S.; Bertles, J. F. *J. Clin. Invest.* **1970**, 49, 623.
- (7) Lobo, A. J.; Jones, S. C.; Juby, L. D.; Axon, A. T. *J. Clin. Pathol.* **1992**, 45, 54.
- (8) Nadiv, O.; Shinitzky, M.; Manu, H.; Hecht, D.; Roberts, C. T.; LeRoith, D.; Zick, Y. *Biochem. J* **1994**, 298, 443.
- (9) Ryder, A. G. In *Reviews in Fluorescence 2005*; Geddes, C. D., Lakowicz, J. R., Eds.; Springer US: Boston, MA, 2005, p 169.
- (10) Treibs, A.; Kreuzer, F.-H. *Justus Liebigs Annalen der Chemie* **1968**, 718, 208.
- (11) Ulrich, G.; Ziessel, R.; Harriman, A. *Angew. Chem. Int. Ed. Engl.* **2008**, 47, 1184.
- (12) Ziessel, R.; Ulrich, G.; Harriman, A. *New J. Chem.* **2007**, 31, 496.
- (13) Harriman, A.; Izzet, G.; Ziessel, R. *J. Am. Chem. Soc.* **2006**, 128, 10868.
- (14) Schönenbrücher, H.; Adhikary, R.; Mukherjee, P.; Casey, T. A.; Rasmussen, M. A.; Maistrovich, F. D.; Hamir, A. N.; Kehrli, M. E.; Richt, J. A.; Petrich, J. W. *J. Agric. Food. Chem.* **2008**, 56, 6220.
- (15) Menter, J. M. *Photochem. Photobiol. Sci.* **2006**, 5, 403.

- (16) Harriman, A.; Stachelek, P.; Sutter, A.; Ziessel, R. *Photochem. Photobiol. Sci.* **2015**, *14*, 1100.
- (17) Hinkeldey, B.; Schmitt, A.; Jung, G. *Chemphyschem*: **2008**, *9*, 2019.
- (18) Ziessel, R.; Ulrich, G.; Haefele, A.; Harriman, A. *J. Am. Chem. Soc.* **2013**, *135*, 11330.
- (19) Loudet, A.; Burgess, K. *Chem. Rev.* **2007**, *107*, 4891.
- (20) Levitt, J. A.; Kuimova, M. K.; Yahiloglu, G.; Chung, P.-H.; Suhling, K.; Phillips, D. *J. Phys. Chem. C* **2009**, *113*, 11634.
- (21) Alford, R.; Simpson, H. M.; Duberman, J.; Hill, G. C.; Ogawa, M.; Regino, C.; Kobayashi, H.; Choyke, P. L. *Mol. Imaging* **2009**, *8*, 341.
- (22) Zhang, S.; Wu, T.; Fan, J.; Li, Z.; Jiang, N.; Wang, J.; Dou, B.; Sun, S.; Song, F.; Peng, X. *Org. Biomol. Chem.* **2013**, *11*, 555.
- (23) Li, Z.; Chen, Q.-Y.; Wang, P.-D.; Wu, Y. *RSC Adv.* **2013**, *3*, 5524.
- (24) Grabowski, Z. R.; Rotkiewicz, K.; Rettig, W. *Chem. Rev.* **2003**, *103*, 3899.
- (25) Brillo, J.; Pommrich, A. I.; Meyer, A. *Phys. Rev. Lett.* **2011**, *107*, 165902.
- (26) Khair, A. S.; Brady, J. F. *J. Rheol.* **2008**, *52*, 165.
- (27) Benniston, A. C.; Harriman, A. *J. Chem. Soc., Faraday Trans.* **1994**, *90*, 2627.
- (28) Alamiry, M. A. H.; Benniston, A. C.; Copley, G.; Elliott, K. J.; Harriman, A.; Stewart, B.; Zhi, Y.-G. *Chem. Mater.* **2008**, *20*, 4024.
- (29) Bahaidarah, E.; Harriman, A.; Stachelek, P.; Rihn, S.; Heyer, E.; Ziessel, R. *Photochem. Photobiol. Sci.* **2014**, *13*, 1397.
- (30) Cao, J.; Wu, T.; Hu, C.; Liu, T.; Sun, W.; Fan, J.; Peng, X. *Phys. Chem. Chem. Phys.* **2012**, *14*, 13702.
- (31) Ivanov, M. V.; Klichko, V. I.; Nikulin, I. R.; Asryants, R. A.; Nagradova, N. K. *Eur. J. Biochem.* **1982**, *125*, 291.

- (32) Bagchi, B.; Fleming, G. R.; Oxtoby, D. W. *J. Chem. Phys.* **1983**, 78, 7375.
- (33) Oster, G.; Nishijima, Y. *J. Am. Chem. Soc.* **1956**, 78, 1581.
- (34) Gautam, P.; Harriman, A. *J. Chem. Soc., Faraday Trans.* **1994**, 90, 697.
- (35) Duxbury, D. F. *Chem. Rev.* **1993**, 93, 381.
- (36) Kee, H. L.; Kirmaier, C.; Yu, L.; Thamyongkit, P.; Youngblood, W. J.; Calder, M. E.; Ramos, L.; Noll, B. C.; Bocian, D. F.; Scheidt, W. R.; Birge, R. R.; Lindsey, J. S.; Holten, D. *J. Phys. Chem. B* **2005**, 109, 20433.
- (37) Li, F.; Yang, S. I.; Ciringh, Y.; Seth, J.; Martin, C. H.; Singh, D. L.; Kim, D.; Birge, R. R.; Bocian, D. F.; Holten, D.; Lindsey, J. S. *J. Am. Chem. Soc.* **1998**, 120, 10001.
- (38) Zhu, H.; Fan, J.; Li, M.; Cao, J.; Wang, J.; Peng, X. *Chem. Eur. J.* **2014**, 20, 4691.
- (39) Bixon, M.; Jortner, J.; Cortes, J.; Heitele, H.; Michel-Beyerle, M. E. *J. Phys. Chem.* **1994**, 98, 7289.
- (40) Englman, R.; Jortner, J. *Mol. Phys.* **1970**, 18, 145.
- (41) Turro, N. J. *Modern Molecular Photochemistry*; University Science Books, 1991.
- (42) Velsko, S. P.; Fleming, G. R. *Chem. Phys.* **1982**, 65, 59.
- (43) Velsko, S. P.; Fleming, G. R. *J. Chem. Phys.* **1982**, 76, 3553.
- (44) Sharafy, S.; Muszkat, K. A. *J. Am. Chem. Soc.* **1971**, 93, 4119.
- (45) Whitten, D. G. *Acc. Chem. Res.* **1993**, 26, 502.
- (46) Kramers, H. A. *Physica* **1940**, 7, 284.
- (47) Korppi-Tommola, J. E. I.; Hakkarainen, A.; Hukka, T.; Subbi, J. *J. Phys. Chem.* **1991**, 95, 8482.
- (48) Brey, L. A.; Schuster, G. B.; Drickamer, H. G. *J. Chem. Phys.* **1979**, 71, 2765.

- (49) Brey, L. A.; Schuster, G. B.; Drickamer, H. G. *J. Am. Chem. Soc.* **1979**, *101*, 129.
- (50) Sanchez-Galvez, A.; Hunt, P.; Robb, M. A.; Olivucci, M.; Vreven, T.; Schlegel, H. B. *J. Am. Chem. Soc.* **2000**, *122*, 2911.
- (51) Ma, F.; Yartsev, A. *RSC Adv.* **2016**, *6*, 45210.
- (52) Wong, B. M.; Ye, S. H.; O'Bryan, G. *Nanoscale* **2012**, *4*, 1321.
- (53) C. Benniston, A.; Harriman, A. *J. Chem. Soc., Faraday Trans.* **1998**, *94*, 1841.
- (54) C. Benniston, A.; Harriman, A.; McAvoy, J. *J. Chem. Soc., Faraday Trans.* **1997**, *93*, 3653.
- (55) Harriman, A. *J. Photochem. Photobiol., A Chem.* **1992**, *65*, 79.
- (56) Benniston, A. C.; Harriman, A.; McAvoy, C. *J. Chem. Soc., Faraday Trans.* **1998**, *94*, 519.
- (57) Levitus, M.; Negri, R. M.; Aramendia, P. F. *J. Phys. Chem.* **1995**, *99*, 14231.
- (58) Aramendia, P. F.; Negri, R. M.; Roman, E. S. *J. Phys. Chem.* **1994**, *98*, 3165.
- (59) McCaskill, J. S.; Gilbert, R. G. *Chem. Phys.* **1979**, *44*, 389.
- (60) Hänggi, P.; Talkner, P.; Borkovec, M. *Rev. Mod. Phys.* **1990**, *62*, 251.
- (61) Pollak, E.; Talkner, P. *Chaos* **2005**, *15*, 026116.
- (62) Sun, Y. P.; Saltiel, J. *J. Phys. Chem.* **1989**, *93*, 8310.
- (63) Sundström, V.; Gillbro, T. *Chem. Phys.* **1981**, *61*, 257.
- (64) Bagchi, B. *Int. Rev. Phys. Chem.* **1987**, *6*, 1.
- (65) Harju, T. O.; Eroestyák, J.; Chow, Y. L.; Korppi-Tommola, J. E. I. *Chem. Phys.* **1994**, *181*, 259.
- (66) Grote, R. F.; Hynes, J. T. *J. Chem. Phys.* **1980**, *73*, 2715.

- (67) Skinner, J. L.; Wolynes, P. G. *J. Chem. Phys.* **1978**, 69, 2143.
- (68) Ferreira, J. A. B.; Costa, S. M. B.; Vieira Ferreira, L. F. *J. Phys. Chem. A* **2000**, 104, 11909.
- (69) Allen, B. D.; Benniston, A. C.; Harriman, A.; Rostron, S. A.; Yu, C. *Phys. Chem. Chem. Phys.* **2005**, 7, 3035.
- (70) Förster, T.; Hoffmann, G. *Z. Phys. Chem.* **1971**, 75, 63.
- (71) Raut, S.; Kimball, J.; Fudala, R.; Doan, H.; Maliwal, B.; Sabnis, N.; Lacko, A.; Gryczynski, I.; Dzyuba, S. V.; Gryczynski, Z. *Phys. Chem. Chem. Phys.* **2014**, 16, 27037.
- (72) Yoon, H.-J.; Dakanali, M.; Lichlyter, D.; Chang, W. M.; Nguyen, K. A.; Nipper, M. E.; Haidekker, M. A.; Theodorakis, E. A. *Org. Biomol. Chem.*, **2011**, 9, 3530.
- (73) Yang, Z.; He, Y.; Lee, J. H.; Chae, W.-S.; Ren, W. X.; Lee, J. H.; Kang, C.; Kim, J. S. *Chem. Commun.* **2014**, 50, 11672.
- (74) Kuimova, M. K.; Botchway, S. W.; Parker, A. W.; Balaz, M.; Collins, H. A.; Anderson, H. L.; Suhling, K.; Ogilby, P. R. *Nat. Chem.* **2009**, 1, 69.
- (75) Suhling, K.; French, P. M. W.; Phillips, D. *Photochem. Photobiol. Sci.* **2005**, 4, 13.
- (76) Didier, P.; Ulrich, G.; Mely, Y.; Ziessel, R. *Org. Biomol. Chem.*, **2009**, 7, 3639.
- (77) Alamiry, M. A. H.; Hagon, J. P.; Harriman, A.; Bura, T.; Ziessel, R. *Chem. Sci.* **2012**, 3, 1041.
- (78) Seino, Y.; Sasabe, H.; Pu, Y.-J.; Kido, J. *Adv. Mater.* **2014**, 26, 1612.
- (79) Speiser, S. *Chem. Rev.* **1996**, 96, 1953.
- (80) Forster, T. *Farad. Discuss.* **1959**, 27, 7.
- (81) Munoz-Losa, A.; Curutchet, C.; Krueger, B. P.; Hartsell, L. R.; Mennucci, B. *Biophys. J.* **2009**, 96, 4779.
- (82) Stryer, L.; Haugland, R. P. *Proc Natl Acad Sci U S A* **1967**, 58, 719.

367. (83) Woolley, P.; Steinhäuser, K. G.; Epe, B. *Biophys. Chem.* **1987**, 26,
- (84) Berney, C.; Danuser, G. *Biophys. J.* **2003**, 84, 3992.
- (85) Dexter, D. L. *J. Chem. Phys.* **1953**, 21, 836.
- (86) Marcus, R. A. *Rev. Mod. Phys.* **1993**, 65, 599.
- (87) Marcus, R. A.; Sutin, N. *Biochim. Biophys. Acta* **1985**, 811, 265.
- (88) Marcus, R. A. *Annu. Rev. Phys. Chem.* **1964**, 15, 155.
- (89) Eng, M. P.; Albinsson, B. *Chem. Phys.* **2009**, 357, 132.
- (90) Gust, D.; Moore, T. A.; Moore, A. L.; Devadoss, C.; Liddell, P. A.; Hermant, R.; Nieman, R. A.; Demanche, L. J.; DeGraziano, J. M.; Gouni, I. *J. Am. Chem. Soc.* **1992**, 114, 3590.
- (91) Andrews, D. L.; Bradshaw, D. S.; Jenkins, R. D.; Rodriguez, J. *Dalton Trans.* **2009**, 10006.
- (92) Andrews, D. L. *J. Mater. Res.* **2012**, 27, 627.
- (93) Juris, A. *Ann. Rep. Progr. Chem. C* **2003**, 99, 177.

Chapter 2. Fluorescent Molecular Rotors Based on the BODIPY Motif: Effect of Remote Substituents

2.1 Introduction

The fluorescence properties of boron dipyrromethene (BODIPY) dyes have been reported by many research groups and used to fabricate a diverse range of applications. As described in the introduction, one such application concerns using the fluorescent dye to monitor changes in local viscosity. This particular feat is achieved by designing a BODIPY-based dye to have a phenyl ring at the *pseudo-meso* position and to omit any alkyl substituents from the upper rim of the dipyrin. The phenyl ring can rotate, or at least gyrate, around the dipyrin unit but it is subject to some steric blocking by the 1,7-hydrogen atoms. In fact, the effects of the *meso*-phenyl ring on the fluorescence yield and lifetime for certain BODIPY derivatives have been well documented by many authors and a substantial number of research papers has been produced.¹⁻³ This strategy of modifying the degree of friction between the rotary phenyl ring and the 1,7-hydrogen atoms has formed the basis for all putative molecular rotors based on this type of dye. In particular, the effect of remote substituents on the BODIPY fluorescent rotors has attracted scant attention. As outlined in the introduction, it is well known that rotation of the *meso*-phenyl ring is not directly responsible for the enhanced non-radiative decay of the excited-singlet state. In essence, in order for the phenyl ring to complete a full rotation, the dipyrin backbone has to buckle slightly and it is this structural deformity that opens up the channel for radiationless return to the ground state. Realizing this, it becomes possible to design new molecular rotors by structural modification away from the *meso*-position. It might be mentioned that many

researchers have used substituents attached to the meso-phenyl ring to adapt the solubility and lipophilicity of the dye.⁴

As a starting point to designing a new range of molecular rotors, or more specifically, examining in more detail the mechanism for the rotor behavior, we studied the effect of adding bulky substituents in positions 3 and 5 of the BODIPY backbone (lower rim of the boron dipyrromethene unit). To our surprise, it was found that they can greatly influence the ability of the probe to assess the local rheology and indirectly to function as a crude temperature indicator.⁵ We will show that a BODIPY dye can be manipulated such that the *meso*-ring has no effect on the nonradiative decay.

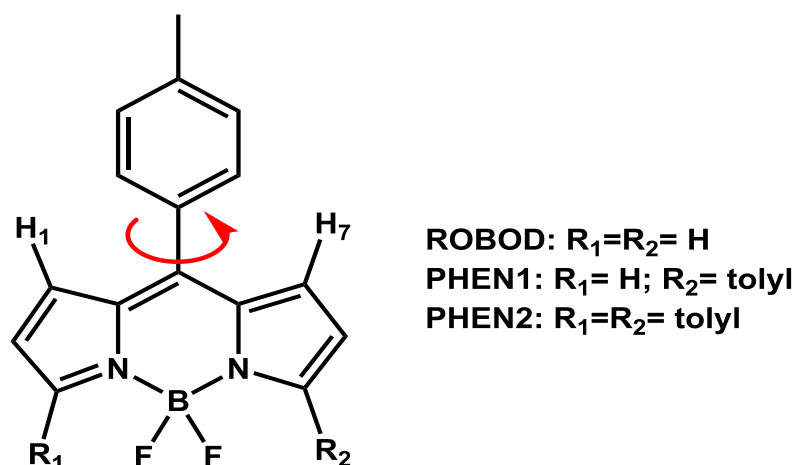


Figure 2.1. Molecular formulae of the compounds presented in this chapter.

Figure 2.1 shows the molecular formulae of the two compounds under investigation: **PHEN1** and **PHEN2**, as well as the popular control compound; **ROBOD** (fully characterized in *RSC Adv.*, **2012**, 2, 981-9859). Figure 2.2 shows molecular formulae of additional control compounds: **CORE** and **BOD** (**BOD** has been characterized by previous members of the MPL using the same technique and instrumentation).⁶ **CORE** is the only compound in this chapter that lacks the *meso*-phenyl group, however it has the ancillary tolyl groups at the 3,5-positions.

It is common knowledge that groups appended at positions 3 and 5 can increase conjugation and shift both absorption and emission wavelengths towards the red.⁷⁻

⁹ The effect of these substituents on the basic structure and more importantly on

the geometry of the dipyrryn upper rim has failed to attract much attention. We demonstrate here that the symmetry of a boron dipyrromethene dye is crucial for controlling the ability of the dye to probe the local environment.

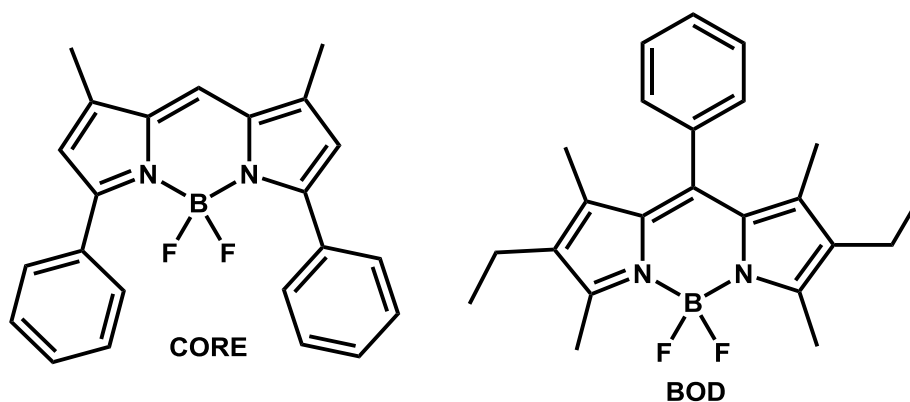


Figure 2.2. Molecular formulae of the compounds used as controls.

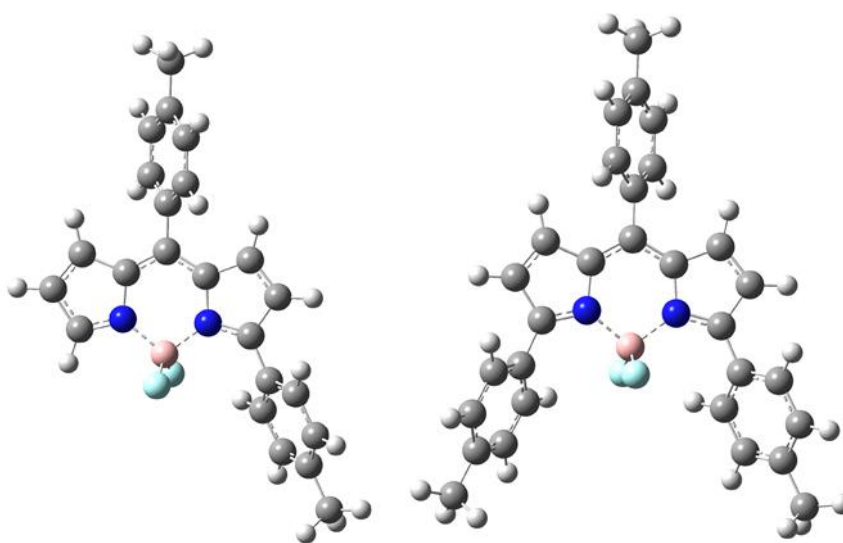


Figure 2.3. Energy-minimized geometries computed for **PHEN1**, left, and **PHEN2**, right.

2.2 Results and Discussion

2.2.1 Spectroscopic Data

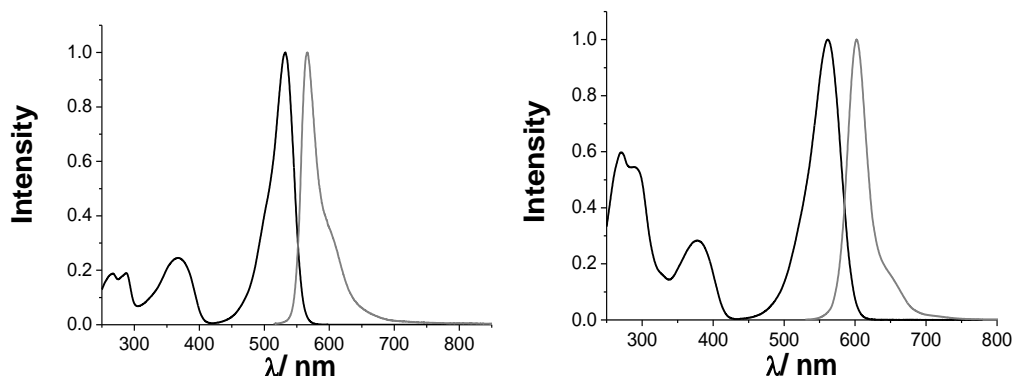


Figure 2.4. Absorption and emission spectra recorded for **PHEN1**, on the left, and **PHEN2**, panel on the right, in MTHF at room temperature.

The absorption and emission spectra recorded for **PHEN1** and **PHEN2** are shown below in Figure 2.4. Spectra were measured in 2-methyltetrahydrofuran (MTHF) at room temperature. The absorption and emission spectra for both **PHEN1** and **PHEN2** are typical for BODIPY dyes in fluid solution. A small Stokes' shift is observed for both dyes. There is a reasonably good mirror symmetry for **PHEN1**, however the lowest energy absorption transition for **PHEN2** appears to be somewhat broader than that of a typical BODIPY dye. This is a consequence of incorporating the second tolyl ring at the 5-position. The absorption and emission spectra recorded for **CORE** are very similar to those found for **PHEN1** and **PHEN2**, with the only significant difference being a slight broadening of the emission spectral profile as shown in Figure 2.5.

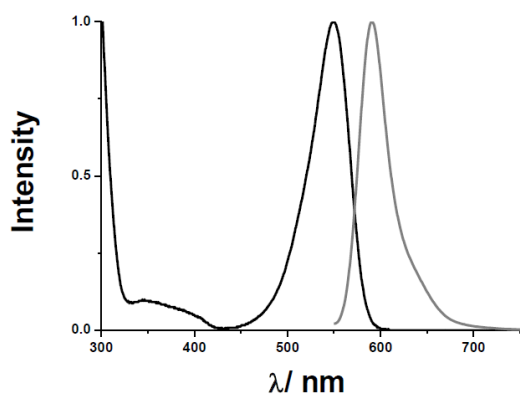


Figure 2.5 Absorption and emission spectra recorded for **CORE** in MTHF at room temperature.

The photophysical properties of all the compounds were measured in MTHF at room temperature and the main findings are collected in Table 2.1. Data were also collected under the same conditions in dichloromethane (DCM) and are included in Table 2.2, however there are no significant differences between the two solvents. At first glance, we observe that each tolyl ring shifts the absorption and emission maxima to the red by approximately 30 nm. This can be observed by comparing absorption maxima for **ROBOD**, which has no tolyl rings at the lower rim of the dipyrin unit, with the corresponding absorption maxima for **PHEN1** (one tolyl attached to the lower rim) and **PHEN2** (tolyl rings at positions 3 and 5). The molar absorption coefficients, ϵ , for all five compounds are comparable and typical of this class of dye. A modest Stokes' shift (SS) is observed for all the compounds studied here and remains independent of solvent polarity. While analyzing data in Table 2.1, **PHEN2** emerges as the most interesting compound. It has a *meso*-ring yet its photophysical properties are not too dissimilar from those of **CORE**. They are certainly unusual for a molecular rotor; **PHEN2** with a fluorescence quantum yield of 0.28 certainly would not be considered as an effective molecular probe, unlike **PHEN1**. The only structural difference between the two compounds concerns the one extra tolyl ring at the lower rim of the BODIPY core. It is important to note that **PHEN1** is actually a more efficient rotor than is **ROBOD**, this can be easily observed by comparing the respective non-radiative rate constants (k_{NR}). Thus, the non-radiative rate constant for **PHEN1** is nearly twice that of **ROBOD**. What is even more striking is the comparison of k_{NR} for **PHEN2**. It appears that substitution of BODIPY core at the 3,5- positions can have profound effects on the performance of the molecular rotor.

It might be stressed that we were not expecting this type of behavior. It is clear that the 3,5-aryl substituents should affect the absorption and fluorescence maxima because of increased conjugation.¹⁰ It is not obvious that these same substituents will affect the properties at the dipyrryn upper rim and, in particular, modulate the dynamics of *meso*-ring rotation. These dyes are essentially non-polar so we can eliminate charge-transfer effects from playing any role in the non-radiative decay processes. We can now examine in more detail the effects of the peripheral tolyl groups.

Table 2.1. Summary of the photophysical data recorded for the studied compounds in MTHF at room temperature.

	ROBOD	BOD	PHEN1	PHEN2	CORE
λ_{\max}/nm	502	525	531	559	547
$\epsilon_{\max}/\text{M}\cdot\text{cm}^{-1}$	71 000	74 000	59 100	62 235	62 100
$\lambda_{\text{Flu}}/\text{nm}$	530	547	564	602	588
SS/cm^{-1}	1050	765	1105	1280	1280
Φ_{Flu}	0.023	0.78	0.013	0.28	0.92
$\tau_{\text{S}}/\text{ns}$	0.15	5.4	0.092	2.1	6.6
$k_{\text{RAD}}/10^8\text{ s}^{-1}$	1.5	1.45	1.42	1.3	1.4
$k_{\text{NR}}/10^8\text{ s}^{-1}$	65	0.4	110	3.5	0.12

Table 2.2. Summary of the photophysical data recorded for the studied compounds in DCM at room temperature.

	ROBOD	BOD	PHEN1	PHEN2	CORE
λ_{\max}/nm	502	525	531	559	547
$\epsilon_{\max}/\text{M}\cdot\text{cm}^{-1}$	71 000	74 000	59 100	62 235	62 100
$\lambda_{\text{Flu}}/\text{nm}$	528	544	557	697	582
SS/cm^{-1}	980	665	880	1140	1100
Φ_{Flu}	0.021	0.77	0.01	0.24	0.87
$\tau_{\text{S}}/\text{ns}$	0.16	5.4	0.07	2.06	6.4
$k_{\text{RAD}}/10^8\text{ s}^{-1}$	1.31	1.43	1.43	1.16	1.36
$k_{\text{NR}}/10^8\text{ s}^{-1}$	61	0.43	141	3.7	0.2

2.2.2 Temperature Dependence

In order to investigate the effect of the 3,5-aryl substitution on a BODIPY-based molecular rotor, temperature dependence studies were carried out. These were performed in MTHF using an Oxford Instruments optical cryostat. The primary purpose of these experiments was to examine the variation of Φ_F as a function of temperature.¹¹ All results were corrected for solvent contraction during freezing.¹²

Small spectral shifts accompany freezing of the solvent but the vitrification of MTHF is not a simple physical process. Indeed, the solvent freezes over a small range of temperatures but also forms an isotropic syrup in addition to a clear optical glass. In general, not much is known about the freezing process. Now, Φ_F recorded for **CORE** is not affected by decreasing the temperature from

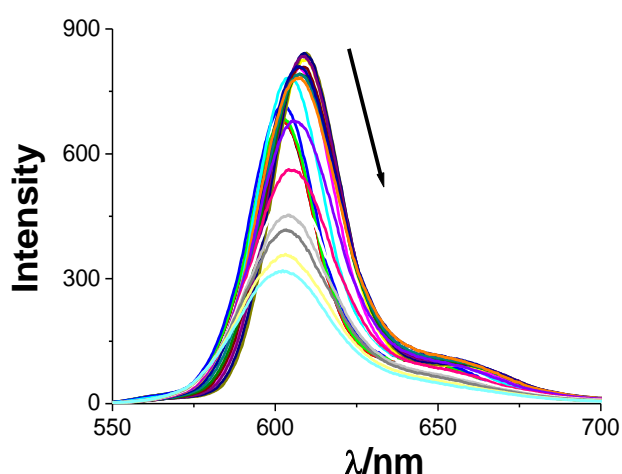


Figure 2.6. Temperature dependence observed for the emission spectra recorded for **PHEN2** in MTHF.

295K to 77K. On the other hand, Φ_F measured for **BOD** appears to be constant at temperatures below 200K but varies slightly at higher temperatures. It seems that there is a minor activated route for deactivation of the excited-singlet state for **BOD**. A similar conclusion was raised previously on the basis of pressure-dependent studies. The temperature effect on the non-radiative rate constants for the target compounds has been investigated under the same conditions as used for the reference compounds, Figure 2.7. It was found that lowering of the temperature had a far greater effect on the non-radiative rate constant (k_{NR}) for **PHEN1** than for **PHEN2**, Table 2.3. However, both of these compounds exhibit similar trends in the variation of Φ_F to that found for **ROBOD**. This finding tends to confirm the conclusion that these compounds operate as fluorescent rotors.

The total variation in Φ_{Flu} found for **PHEN1** over this temperature range is approximately 75-fold, in contrast to that of **PHEN2** is only about 3-fold. The variation of **PHEN1** is far greater than that recorded for **ROBOD**. For each studied compound, Φ_{F} approaches unity in the glassy matrix around 100K. The remaining compounds (**CORE**, **BOD**) show some increase of k_{NR} as the temperature increases, however the effect is of a much smaller magnitude. Figure 2.6 demonstrates this effect quite clearly; the non-radiative rate constants for **PHEN1** (dark blue) and **ROBOD** (yellow) clearly change significantly with temperature. These compounds display typical rotor behaviour (i.e. the non-radiative constant increases linearly with the temperature).¹¹ The insert shows in more detail what happens to the other three compounds **PHEN2** (grey), **BOD** (orange) and **CORE** (light blue) as the temperature changes. Looking closely at the behaviour of **PHEN2** it can be concluded that it is that of a molecular rotor; it follows the same trend as **PHEN1** and **ROBOD**. The only difference is the magnitude of the effect as described earlier.

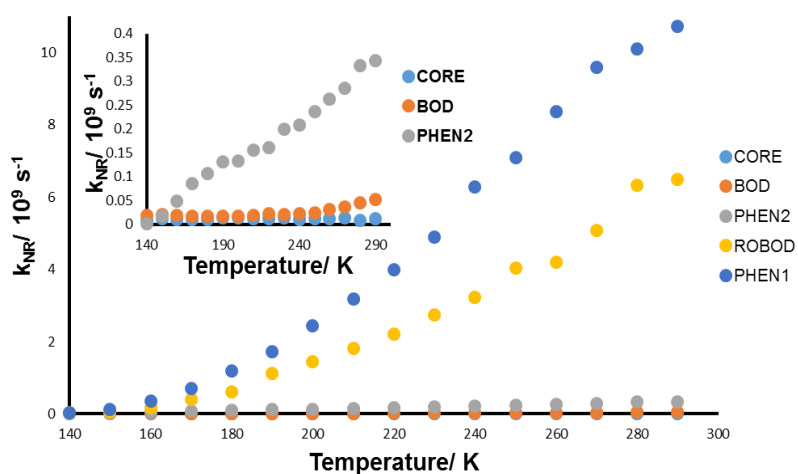


Figure 2.7. Effect of temperature on the nonradiative rate constant. The rate constants are expressed in units of 10^9 s^{-1} .

Table 2.3. Effect of temperature on the respective non-radiative rate constants. The rate constants are expressed in units of 10^9 s^{-1} .

Temp/ K	CORE	BOD	PHEN2	ROBOD	PHEN1
140	0.0085	0.0195	0.0015	0.022	0.03
150	0.012	0.021	0.017	0.065	0.12
160	0.0107	0.019	0.048	0.174	0.35
170	0.01	0.017	0.085	0.395	0.71
180	0.01	0.0175	0.106	0.616	1.2
190	0.013	0.017	0.1315	1.116	1.71
200	0.014	0.017	0.1335	1.438	2.43
210	0.012	0.0185	0.156	1.806	3.18
220	0.012	0.023	0.161	2.2	4
230	0.014	0.021	0.2	2.75	4.9
240	0.0096	0.023	0.208	3.22	6.28
250	0.0115	0.0245	0.236	4.03	7.1
260	0.0125	0.0305	0.263	4.19	8.37
270	0.013	0.037	0.286	5.08	9.6
280	0.009	0.046	0.3335	6.34	10.1
290	0.012	0.052	0.343	6.5	10.73

We can consider that increased π -electron delocalization between the BODIPY core and the ancillary tolyl rings in the 3,5- positions is the main reason for the observed red shifts for absorption and emission spectra. This behaviour is observed for both **PHEN1** and **PHEN2** as well as for **CORE** but is not evident for either of the compounds lacking the 3,5-tolyl rings, i.e. **ROBOD** and **BOD**. It can be supposed that the degree of conjugation between the respective π -systems will depend on the mutual orientations, being at a maximum when the dihedral angle is close to zero. For the target compounds studied here, the possibility of increased conjugation was examined by means of molecular orbital calculations carried out

at the B3LYP/6-31G+G(d)/PCM level. The main findings are summarized as follows: We found that the core aryl rings on the lower rim of the BODIPY core adopt a dihedral angle of approx. 50° for the lowest-energy conformation, this applies to all three derivatives (**PHEN1**, **PHEN2** and **CORE**). However, some modest instability can be observed at approx. 20° , caused by close proximity of the *ortho*-hydrogen atom on the tolyl ring(s) and a fluorine atom; 1.6 Å. The rotation at the connecting C-C bond is otherwise unconstrained. The barrier for complete rotation of the tolyl ring(s) introduced by the steric clash is approximately 50 kJ mol⁻¹. However, there is essentially no barrier for gyration of the aryl rings over a wide angular variation.

The electronic interaction between the aryl ring and the BODIPY nucleus depends on the mutual orientation, which is set in part by steric factors. This effect was studied in detail using a small series of BODIPY-based bichromophores, where the connection point was varied. It was found that the level of excitonic coupling, as determined by the splitting of the lowest-energy absorption transition into two peaks, varied markedly among the various bichromophores. For these compounds, rotation around the connection is more restricted than for the aryl-BODIPY derivatives because of the presence of alkyl substituents. [The results of this study are provided as part of the Appendix.] Here, we could show that the dihedral angle between the side-by-side bichromophores was largely responsible for the degree of excitonic splitting. There are clear analogies between the two sets of compounds, although the bichromophores provide the more obvious interactions. For the aryl-BODIPY derivatives, the dihedral angle will help determine the energy of the absorption and emission transitions.

Returning now to the effect of temperature on the fluorescence properties for the putative molecular rotors, we note that neither the Strickler-Berg expression nor the Englman-Jortner energy gap law allows for a strong temperature effect on the rate of decay of the excited state.^{13,14} The refractive index will change with temperature, as will the density of the solvent, but the effect is not so pronounced. Because the molecules are non-polar, there is no reason for the Stokes' shift to vary with temperature. Furthermore, it was found that, in all cases, the fluorescence quantum yield is essentially independent of temperature in the glassy region. To accommodate this latter effect, we introduce Equation 2.1; where k_0 refers to an

activationless rate constant, k_{ACT} is the corresponding activated term and T_G is the glass transition temperature of MTHF, 100 K. The activation barrier, E_B , is considered to contain important contributions from both changes in viscosity and internal rotation. It was found that Equation 2.1 gives a good representation of the experimental data for each compound, except **CORE**. For this latter compound, k_{NR} is essentially independent of temperature across the region of interest.

$$k_{NR} = k_0 + k_{ACT} \exp\left(-\frac{E_B}{R[T - T_G]}\right) \quad \text{Equation 2.1}$$

Table 2.4. Summary of the parameters associated with Equation 2.1. Data for **ROBOD** and **BOD** taken from literature.⁵

	ROBOD	BOD	PHEN1	PHEN2	CORE
$k_0 / 10^7 \text{ s}^{-1}$	17	1.8	12	1.9	1.2
$k_{ACT} / 10^9 \text{ s}^{-1}$	36.5	5.9	51.0	0.8	NA
$E_B / \text{kJ mol}^{-1}$	2.6	7.7	2.3	1.4	NA

Analysis of the experimental data (Table 2.4) demonstrates that there is a large activation barrier for **BOD**. Most likely, this is because the internal rotation is blocked due to the presence of the relatively bulky methyl groups. For the remaining compounds, the magnitude of the barrier height decreases with increasing effective mass of the dipyrroin unit. The core

tolyl groups, attached at the lower rim, cause slight curvature of BODIPY core, which is at its maximum as the two units become co-planar. Double substitution, and also electronic excitation, increases this curvature and forces the *meso*-aryl

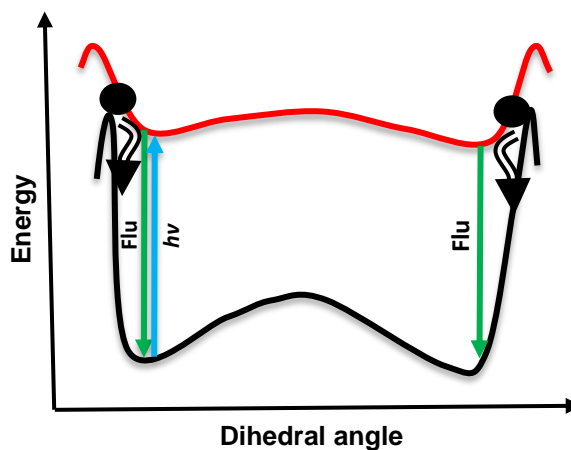


Figure 2.8. Pinhole sink model as adapted for BODIPY rotors.

ring out of the plane of symmetry. At the excited-state level, this structural distortion will stretch and eventually tear the S_1 surface so as to create a pinhole through which the exciton can escape back to the ground state, Figure 2.8.¹⁵ This pinhole is not equivalent to the transition state in isomerization reactions and as a consequence, it is difficult to characterize.¹⁶⁻¹⁹ Nevertheless the experimental evidence strongly supports this model. We will return to this point after consideration of how the solvent viscosity affects the photophysical properties of the molecular rotor.

2.2.3 Viscosity Dependence

The easiest way by which to vary the viscosity of the system is to use a series of similar solvents that vary in molecular mass. One such series is the linear alcohols, where the molar mass correlates nicely with the bulk viscosity. This is not an ideal way to vary viscosity but, in fact, all such experiments are flawed to various degrees.²⁰ For example, changing temperature or applied pressure are alternative strategies but cause other changes at the same time. Also, it should be stressed that bulk viscosity refers to interactions between adjacent solvent molecules whereas the fluorescence studies are intended to probe solvent-solute interactions. Concepts such as micro-viscosity have been introduced to overcome these limitations but, what looks like a straightforward experiment, can be difficult to analyze correctly.²¹

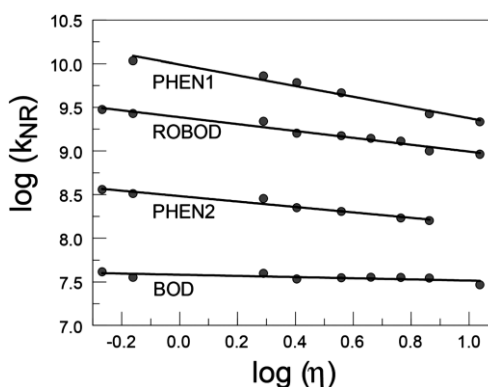


Figure 2.9. Effect of solvent viscosity on the non-radiative rate constant measured in a series of linear alcohols at room temperature.

The photophysics of **PHEN1** and **PHEN2** were recorded in a homologous series of linear alcohols at room temperature, Table 2.6. **ROBOD** and **BOD** were investigated by other group members using identical experimental techniques. Across the series of solvents, the shear viscosity can be changed by a factor of 6-fold.²² The target compounds are readily soluble in these solvents and exhibit no signs of self-association. Changes in viscosity have no obvious effect on the

photophysical properties derived for **BOD**. This compound is strongly fluorescent and behaves nicely across all the solvents. The weakly activated process identified from the temperature-dependence studies is not evident from the viscosity related work. For an effective molecular rotor, we anticipate that the changes in viscosity will lead to progressive increases in emission quantum yield and excited-state lifetime due to the increased frictional forces experienced by the gyrating phenyl ring. This behaviour is indeed observed for **ROBOD**, **PHEN1** and **PHEN2**.

Across this series of solvents, there is a reasonably linear relationship between k_{NR} and shear viscosity, η , as considered in the form of log-log plots, Figure 2.9 and Figure 2.10, but with differing gradients and intercepts. Indeed, the experimental data collected at 20 °C can be considered in terms of Equation 2.2,²³ where v corresponds to a limiting pressure exerted by the rotor, α is a coefficient that effectively describes the sensitivity towards viscosity, and E_A is a barrier for internal rotation.²⁴ It is possible to determine the value for α from the slope of the linear log-log plot, whereas E_A can be estimated from the intercept to the same plot. We observe that both **PHEN1** and **PHEN2** display small gradients, however it is quite clear that the gradient derived for **PHEN2** is steeper and therefore this compound is considerably more sensitive to changes in solvent viscosity. Because of the log-log plot, the derived parameters are subject to significant error and the analysis assumes a common value for v across the series of compounds. This latter point is difficult to verify by experiment and, in our understanding, the magnitude of v will depend on interactions between the rotor and solvent.^{25,26} The solute fits in a cavity within the solvent structure but we have not seen any indications for strong interaction between dye and solvent. In contrast, recent work with aza-BODIPY dyes where the N atom is substituted at the *meso*-position has shown that alcohols coordinate to the aza site and promote non-radiative decay.²⁷ Perhaps the 3,5-aryl groups serve to modify the shape of the cavity and thereby influence v but we are not able to address this possibility. Furthermore, there is no information in the literature that could be used to expand this discussion.

$$k_{NR} = \frac{v}{\eta^\alpha} \exp\left(-\frac{E_A}{RT}\right) \quad \text{Equation 2.2}$$

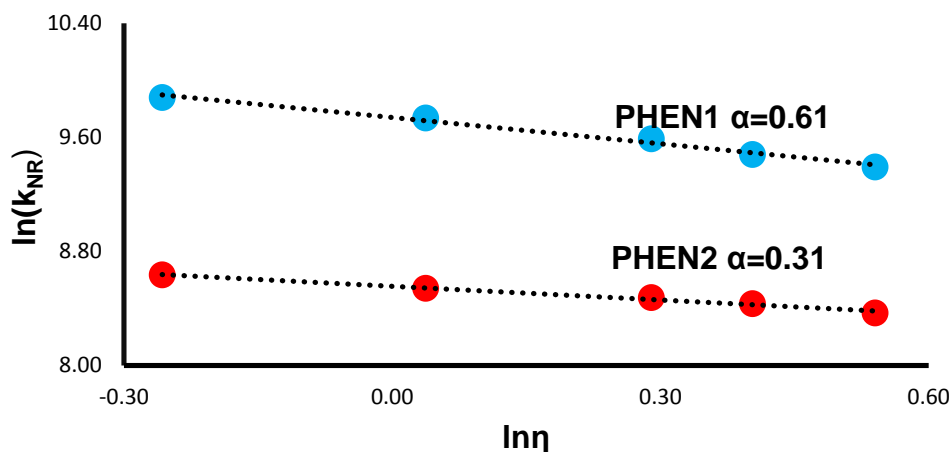


Figure 2.10. Effect of solvent viscosity on the non-radiative rate constant measured in a series of linear alcohols for **PHEN1** (blue) and **PHEN2** (red) at RT.

For the prototypic rotor **ROBOD**, α has a value of 0.41, which is similar to that determined earlier for a closely related dye,²⁸ but this falls to 0.31 for the symmetrical **PHEN2**. In contrast, α determined for the asymmetrical **PHEN1** is 0.62, which is the highest such value found for any BODIPY-based rotor and is far superior to that measured for the industry standard, DCVJ dye,²⁹ under the same conditions ($\alpha=0.31$).³⁰ Overall, **PHEN1** performs remarkably well as a fluorescent rotor, in marked contrast to **PHEN2**. The two control compounds, **CORE** and **BOD** show no significant viscosity dependence.

Table 2.5. Data collected in viscosity experiment for **PHEN1** at 20 °C.

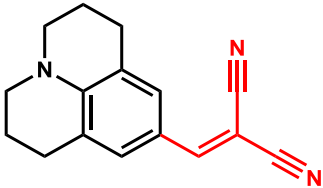
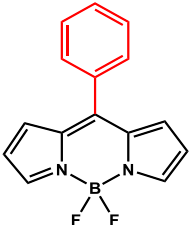
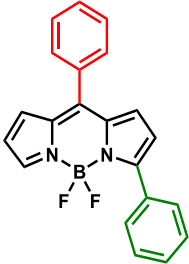
	log(η)	QY	τ / ns	$k_{\text{RAD}}/10^8 \text{ s}^{-1}$	$k_{\text{NR}}/10^9 \text{ s}^{-1}$	log(k_{NR})
Methanol	-0.257	0.014	0.13	1.11	7.58	9.88
Ethanol	0.037	0.021	0.18	1.15	5.44	9.74
Propanol	0.290	0.026	0.25	1.04	3.90	9.59
Butanol	0.403	0.035	0.32	1.08	3.02	9.48
Pentanol	0.540	0.040	0.39	1.02	2.46	9.39

Table 2.6. Data collected in viscosity experiment for **PHEN2** at 20 °C.

	log(η)	QY	τ / ns	$k_{\text{RAD}}/10^8 \text{ s}^{-1}$	$k_{\text{NR}}/10^9 \text{ s}^{-1}$	log(k_{NR})
Methanol	-0.257	0.25	1.74	1.44	4.31	9.88
Ethanol	0.037	0.31	2.0	1.53	3.47	9.74
Propanol	0.290	0.32	2.27	1.41	3.00	9.59
Butanol	0.403	0.38	2.3	1.64	2.71	9.48
Pentanol	0.540	0.44	2.4	1.83	2.34	9.39

Several parameters combine to define the performance of the dye in terms of its ability to function as a fluorescent rotor, including α . Table 2.7 demonstrates how the fluorescence quantum yield changes with viscosity for three dyes with different α value (DCVJ, **ROBOD** and **PHEN1**). The relative values determined for α can be considered as a crude measure of the volume of solvent that will be affected by the geometry change undertaken by the solute.³¹ Additionally, in the specific case of BODIPY dyes, only a few solvent molecules are affected and the geometry change is considered to be either minor or highly localized. Symmetrical dyes, such as **ROBOD** and **PHEN2**, are susceptible to buckling of the dipyrin core but this is mostly restricted to the upper rim. Asymmetrical dyes, such as **PHEN1**, undergo more substantial structural distortion during rotation and this will engage more solvent molecules.

Table 2.7. Effect of solvent viscosity on three dyes with different α value.

	α	QY		
		Methanol	Propanol	Pentanol
	0.3	0.0007	0.0009	0.0013
	0.4	0.038	0.057	0.082
	0.6	0.014	0.026	0.4

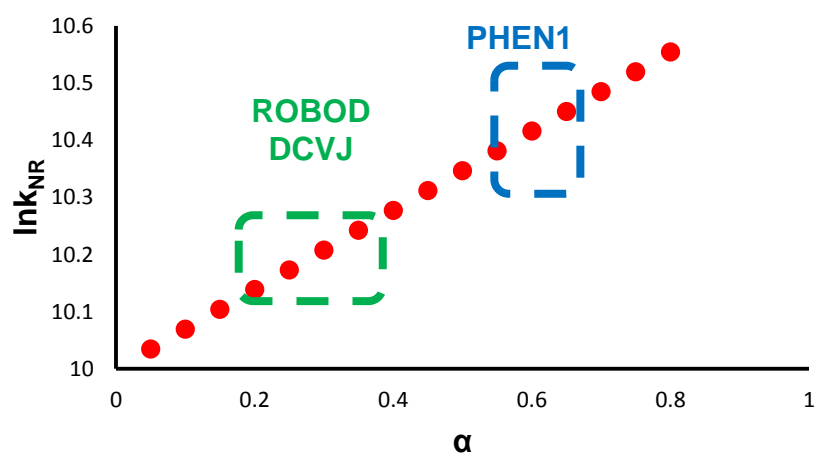


Figure 2.11 Simulation of the radiationless rate constants for rotors with differing α values, where both viscosity and the activation barrier remain constant.

2.3 Conclusions

Molecular-scale sensors based on fluorescence detection are recognized as being promising materials for certain applications where conventional devices might be inappropriate. We have considered the design of putative BODIPY-based dyes as sensors for the remote monitoring of changes in rheology, notably viscosity. Our interest has been to develop improved analogues by considering modifications to the molecular framework that might not be obvious candidates for affecting the rotary mechanics. The results outlined above indicate that improved performance might be achieved by incorporating substituents at remote sites on the BODIPY fluorophore. Aryl substituents attached at the lower rim of the dipyrroin unit serve to push the absorption and emission maxima towards the red region, via increased π -conjugation, and to squeeze the upper rim. The latter situation affects the space available for the meso-aryl rotor and applies some level of control for the rate of non-radiative deactivation of the first-excited singlet state. The disparity between the symmetrical and asymmetrical derivatives is most unexpected and clearly opens up the way to design new and improved sensors. By this route, one can imagine a range of targeted molecular rotors for high, medium and low viscosity regimes.

One of the key discoveries in the BODIPY field has been the recent introduction of strategies whereby the B-F bonds can be replaced with B-O or B-C bonds. This approach provides access to a rich variety of derivatives where secondary groups can be accommodated away from the dipyrroin unit. It also gives us the opportunity to engage the boron atom in cyclic structures that might be a unique way to apply stress to the dipyrroin upper rim. In this way, the dynamics for meso-aryl ring rotation might be addressed by structural variations at the boron atom. In particular, we raise the following question: Could tethering the boron atom with a rigid strap further enhance the non-radiative decay?

2.4 References

- (1) Ghiggino, K. P.; Hutchison, J. A.; Langford, S. J.; Latter, M. J.; Lee, M. A. P.; Lowenstern, P. R.; Scholes, C.; Takezaki, M.; Wilman, B. E. *Adv. Funct. Mater.* **2007**, *17*, 805.
- (2) Levitt, J. A.; Chung, P. H.; Kuimova, M. K.; Yahiloglu, G.; Wang, Y.; Qu, J. L.; Suhling, K. *Chemphyschem* **2011**, *12*, 662.
- (3) Zhu, H.; Fan, J.; Li, M.; Cao, J.; Wang, J.; Peng, X. *Chem. Eur. J.* **2014**, *20*, 4691.
- (4) Bahaidarah, E.; Harriman, A.; Stachelek, P.; Rihn, S.; Heyer, E.; Ziessel, R. *Photochem. Photobiol. Sci.* **2014**, *13*, 1397.
- (5) Kee, H. L.; Kirmaier, C.; Yu, L.; Thamyongkit, P.; Youngblood, W. J.; Calder, M. E.; Ramos, L.; Noll, B. C.; Bocian, D. F.; Scheidt, W. R.; Birge, R. R.; Lindsey, J. S.; Holten, D. *J. Phys. Chem. B* **2005**, *109*, 20433.
- (6) Benniston, A. C.; Copley, G.; Elliott, K. J.; Harrington, R. W.; Clegg, W. *Eur. J. Org. Chem.* **2008**, *2008*, 2705.
- (7) Ziessel, R.; Ulrich, G.; Harriman, A. *New J. Chem.* **2007**, *31*, 496.
- (8) Ulrich, G.; Ziessel, R.; Harriman, A. *Angew. Chem. Int. Ed. Engl.* **2008**, *47*, 1184.
- (9) Loudet, A.; Burgess, K. *Chem. Rev.* **2007**, *107*, 4891.
- (10) Jiang, X.-D.; Gao, R.; Yue, Y.; Sun, G.-T.; Zhao, W. *Org. Biomol. Chem.* **2012**, *10*, 6861.
- (11) Vu, T. T.; Meallet-Renault, R.; Clavier, G.; Trofimov, B. A.; Kuimova, M. K. *J. Mater. Chem. C* **2016**.
- (12) Zoon, P. D.; Brouwer, A. M. *Photochem. Photobiol. Sci.* **2009**, *8*, 345.
- (13) Strickler, S. J.; Berg, R. A. *J. Chem. Phys.* **1962**, *37*, 814.
- (14) Bixon, M.; Jortner, J.; Cortes, J.; Heitele, H.; Michel-Beyerle, M. E. *J. Phys. Chem.* **1994**, *98*, 7289.
- (15) Alamiry, M. A. H.; Bahaidarah, E.; Harriman, A.; Bura, T.; Ziessel, R. *RSC Advances* **2012**, *2*, 9851.

- (16) Bagchi, B. *Int. Rev. Phys. Chem.* **1987**, 6, 1.
- (17) Brinkman, H. C. *Physica* **1957**, 23, 82.
- (18) Brey, L. A.; Schuster, G. B.; Drickamer, H. G. *J. Am. Chem. Soc.* **1979**, 101, 129.
- (19) Harju, T. O.; Erostyák, J.; Chow, Y. L.; Korppi-Tommola, J. E. I. *Chem. Phys.* **1994**, 181, 259.
- (20) Laitinen, E.; Ruuskanen-Järvinen, P.; Rempel, U.; Helenius, V.; Korppi-Tommola, J. E. I. *Chem. Phys. Lett.* **1994**, 218, 73.
- (21) Benniston, A. C.; Harriman, A. *J. Chem. Soc., Faraday Trans.* **1994**, 90, 2627.
- (22) Garcia, B.; Alcalde, R.; Aparicio, S.; Leal, J. M. *Phys. Chem. Chem. Phys.* **2002**, 4, 1170.
- (23) Velsko, S. P.; Fleming, G. R. *Chem. Phys.* **1982**, 65, 59.
- (24) Levitt, J. A.; Kuimova, M. K.; Yahioğlu, G.; Chung, P.-H.; Suhling, K.; Phillips, D. *J. Phys. Chem. C* **2009**, 113, 11634.
- (25) Casey, K. G.; Quitevis, E. L. *J. Phys. Chem.* **1988**, 92, 6590.
- (26) Gautam, P.; Harriman, A. *J. Chem. Soc., Faraday Trans.* **1994**, 90, 697.
- (27) Karlsson, J. K. G.; Harriman, A. *J. Phys. Chem. A* **2016**, 120, 2537.
- (28) Alamiry, M. A. H.; Benniston, A. C.; Copley, G.; Elliott, K. J.; Harriman, A.; Stewart, B.; Zhi, Y.-G. *Chem. Mater.* **2008**, 20, 4024.
- (29) Haidekker, M. A.; Theodorakis, E. A. *Journal of Biological Engineering* **2010**, 4, 1.
- (30) Allen, B. D.; Benniston, A. C.; Harriman, A.; Rostron, S. A.; Yu, C. *Phys. Chem. Chem. Phys.* **2005**, 7, 3035.
- (31) Kuimova, M. K.; Botchway, S. W.; Parker, A. W.; Balaz, M.; Collins, H. A.; Anderson, H. L.; Suhling, K.; Ogilby, P. R. *Nat. Chem.* **2009**, 1, 69.

Chapter 3. Rapid Internal Conversion in N,B,O-Strapped Boron Dipyrromethene Derivatives

3.1 Introduction

Here we present three boron-dipyrromethene, BODIPY, derivatives constrained at the boron centre by means of a 5-membered strap (N,B,O-strap). An advantage of the N,B,O-strapped dyes is that the redox properties might be varied over a wide range by substitution at the N atom. This site also provides a simple means by which to anchor the dye to a surface or biological entity. With the strap in place, these new compounds are non-fluorescent even when light-induced charge transfer between dye and strap is highly unfavourable on thermodynamic grounds. The motivation for this project was based on recent publications by Raymo *et al.*,¹⁻⁴ where they propose charge transfer (CT) from a 5-membered catecholate ligand strapped to the BODIPY core at the boron atom as being responsible for the emission quenching. Our previous research has suggested that substitution at the lower rim, in conjunction with constraining the geometry at the upper rim, can have a significant effect on the photophysics of BODIPY dyes.⁵ Hence, we decided to investigate the interplay between geometry effects and charge transfer in compounds designed specifically for this purpose. The new compounds include a derivative strapped with an amine (i.e., 2-aminophenol as the bridging ligand) at the boron centre, which should quench the fluorescence by way of charge transfer. This compound is easily transformed with acetyl chloride to give the corresponding amide derivative (i.e., using 2-acetamidophenol as strap), which we expect to be fluorescent since light-induced charge transfer will be switched off. To confirm this type of behaviour, a second amide derivative was synthesized. Our expectations were not realized!

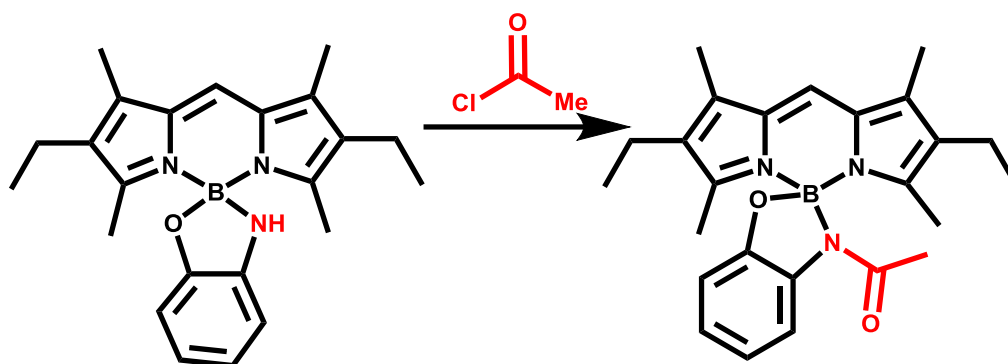


Figure 3.1. Molecular formulae of the two target compounds **AA27** on the left and on the right **AA112**.

In the case of **AA27**, the strap is built around an electron-donating amine, whereas both **AA55** and **AA112** possess straps constructed from an amide (Figure 3.1 and Figure 3.2). Otherwise, there are no significant changes in the structure. The compounds are reasonably soluble in common organic solvents and appear to be stable with respect to cleavage of the strap.

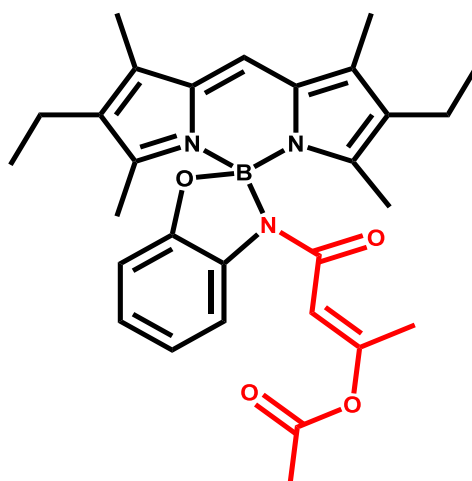


Figure 3.2. Molecular formulae of **AA55**, the additional amide-strapped compound studied in this chapter.

3.2 Results and Discussion

3.2.1 Spectroscopic Data

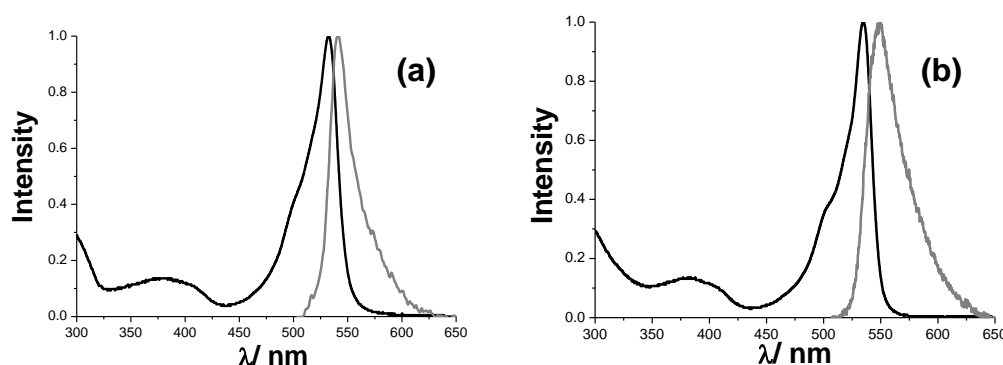


Figure 3.3. (a) Absorption and emission spectra of **AA27** in spectrophotometric grade MTHF at room temperature and (b) absorption and emission spectra of **AA112** recorded under the same conditions.

The absorption and emission spectra of all three compounds display the characteristics of a typical BODIPY chromophore; most notably, a sharp absorption band, $\lambda_{\text{max}} = 533$ nm, and a relatively small Stokes' shift indicating that emission occurs from an excited-singlet state S_1 having a comparable geometry to that of the ground state S_0 . Surprisingly, each of the three molecules demonstrates an unusually low fluorescence quantum yield, Table 3.1. All measurements were carried out in spectrophotometric grade MTHF but for **AA27** measurements were also performed in toluene. This was done to identify whether light-induced charge transfer might play a major role in quenching of the fluorescence.^{6,7} We observed no difference in the emission quantum yield measured in toluene compared to a more polar solvent like MTHF.⁸ This leads us to believe there are other underlying factors governing the emission quantum yield, at least for this compound.

Table 3.1 summarizes the main photophysical properties for these compounds. The molar absorption coefficients are much smaller than normally found for a BODIPY dye and these give rise to Strickler-Berg radiative rate constants that are about half what is regarded as typical for this class of dye; the low fluorescence yield might render the Strickler-Berg analysis somewhat doubtful.⁹ The low

emission yields are supported by short excited-state lifetimes. In fact, the emission decay profiles were complex, indicating a very short-lived species with a lifetime too close to the instrumental response function for proper analysis. The short component is estimated to be somewhat less than 50 ps in each case. The longer-lived component is present at low intensity and we are mindful of the possible involvement of fluorescent impurities. We will return to the possible involvement of a longer-lived species later in the chapter. Data analysis was advanced by the availability of an ultra-short LED excitation source (FWHM = 75 ps) from PTI-Horiba. Using this pulsed LED ($\lambda = 515$ nm) for excitation, the shorter-lived components in the decay records could be measured with more confidence (Table 3.1).

To accommodate the very low emission quantum yields and short lifetimes, we note that the non-radiative rate constants are unusually high for all three compounds. We also draw attention to the very small Stokes' shifts but note the reasonably good mirror symmetry between absorption and emission spectra. For each compound, it was possible to show good agreement between absorption and excitation spectra. It might also be noted that the synthetic chemist was requested to further purify these samples until we obtained consistent results.

Table 3.1. Spectroscopic data collected for the three N,B,O-strapped compounds in MTHF at room temperature; N.B. k_{SB} is the calculated radiative rate constant.

	$\lambda_{ABS}/$ nm	$\lambda_{EM}/$ nm	SS/ cm ⁻¹	QY_{FLU}	τ_{FLU}/ns	k_{RAD}/\times 10 ⁸ s ⁻¹	k_{NR}/\times 10 ¹⁰ s ⁻¹	k_{SB}/\times 10 ⁸ s ⁻¹	f	$\epsilon_{MAX}/$ M ⁻¹ cm ⁻¹
AA27	533	540	243	0.003	0.025	0.5	1.7	1.08	0.18	36 500
AA112	533	543	345	0.001	0.030	0.2	2.5	0.71	0.12	28 320
AA55	533	549	546	0.004	0.048	1	2.5	0.69	0.12	27 653

That the N,B,O strap participates in fluorescence quenching was confirmed by photo-acid treatment in MTHF solution. The photo-acid generator used here was N-Hydroxynaphthalimide triflate, which is activated by illumination with near-UV light. It was noted that strong fluorescence accompanies release of protons into the system. The photo-acid generator was added to the sample solution in methanol and sonicated until fully dissolved. The solutions were then exposed to UV light for a period of 30 seconds, Figure 3.5. All three samples have displayed significant recovery in terms of emission quantum yield and fluorescence lifetime; the QY_F of **AA27** increased to 86% whereas that of **AA55** to 27%, Table 3.2.

Table 3.2. Spectroscopic data collected for all three compounds in MTHF at room temperature after addition of photo-acid generator (N-Hydroxynaphthalimide triflate).

	$\lambda_{\text{ABS}} /$ nm	$\lambda_{\text{EM}} /$ nm	SS/ cm ⁻¹	QY _{FLU}	$\tau_{\text{FLU}} /$ ns
AA27	533	542	312	0.86	5.95
AA112	533	540	243	0.26	5.15
AA55	533	540	243	0.37	4.3

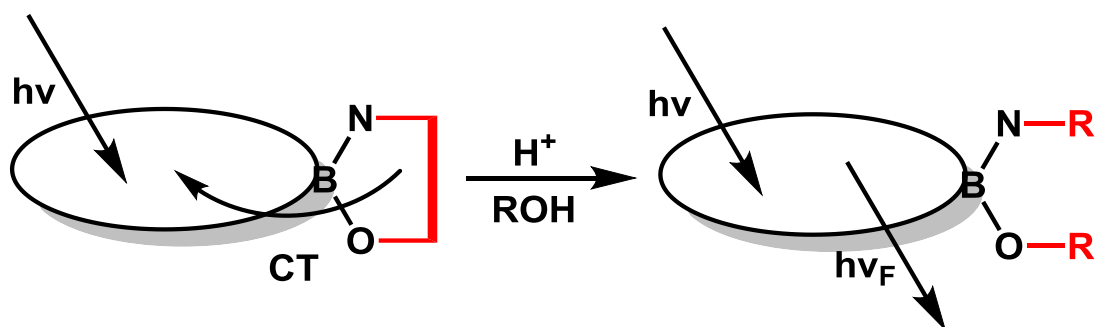


Figure 3.4. Cartoon representation of constrained (left-hand side) and unconstrained (right-hand side) BODIPY dyes where the redox-active strap eliminates fluorescence ($h\nu_F$) by virtue of intramolecular charge transfer (CT).

We also carried out an experiment where we created a room temperature glass using sucrose-octa-acetate. A concentrated solution of each of the three compounds in spectrophotometric grade acetone was prepared ready to be added to a sample vial full of sucrose octa-acetate powder placed in a water bath set to 100°C . Once the powder was fully melted, the sample was incorporated into the viscous, clear liquid. After dissolving, the sample vial was taken out of the water bath and placed in beaker full of cold water; this in turn solidified the solution creating a room-temperature glass. We expected to observe fluorescence recovery under those conditions, however this was not the case, Figure 3.6.¹⁰⁻¹²



Figure 3.5. On the left is the solution of **AA27** with and without photo-acid generator, whereas on the right is the equivalent experiment carried out with **AA55**.

In case of classical rotors the emission is recovered in a room-temperature glass because the non-radiative decay is strongly dependent on the gyration of a meso-phenyl ring, Figure 3.6.^{13,14} However, in the case of the strapped compounds studied here, the emission is not recovered; this combined with the results of the photo-acid test strongly suggests that the non-radiative pathway is due to a structural effect built into these molecules by the means of the 5-membered strap at the boron atom.

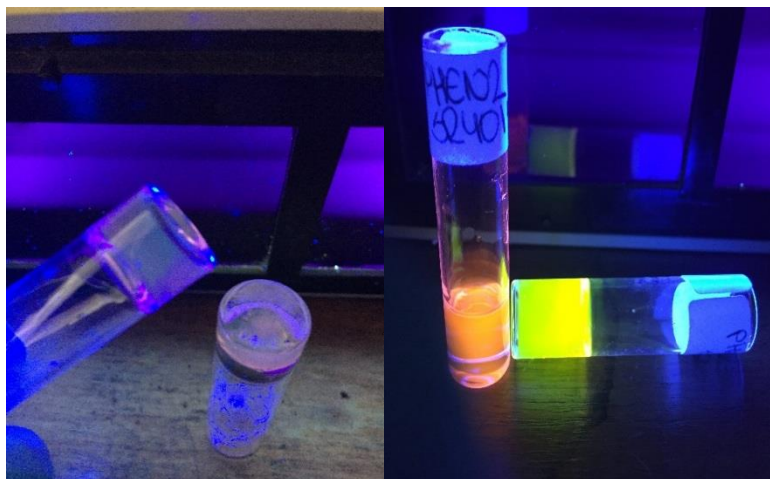


Figure 3.6. Picture on the left demonstrates the effect of immobilising **AA27** and **AA55** in a room temperature glass made with sucrose octa-acetate, whereas on the right we have the same glass formed in the presence of **PHEN1** and **PHEN2**. These latter compounds are known to function as molecular-scale rotors.

3.2.2 Electrochemistry

Light-induced, intramolecular charge transfer from the N,B,O strap to the excited state of the BODIPY unit offers a cursory explanation of the photophysics observed with these compounds. In order to calculate the thermodynamic driving force for intramolecular, light-induced charge transfer from the strap to the BODIPY core, cyclic voltammetry was carried out for all compounds dissolved in deaerated acetonitrile containing background electrolyte, Bu₄N.PF₆ (0.1M), at room temperature.¹⁵ A glassy carbon working electrode was used in conjunction with a platinum counter electrode and a Ag/Ag⁺ reference electrode. Ferrocene was used as internal calibration. The main results are summarized in Table 3.3.

Table 3.3. Summary of the electrochemical properties recorded for **AA27**, **AA55** and **AA112** in acetonitrile containing ⁿBu₄N.PF₆ as supporting electrolyte.

	E ⁰ (ox)/V	E ⁰ (red)/V		
	ΔE /mV	ΔE /mV	HOMO/ eV	LUMO/ eV
AA27	0.23 (irr.)			
	0.90 (irr.)	-1.58 (irr.)	5.65	3.17
AA55	0.77 (64)			
	1.17 (irr)	-1.46 (81)	5.52	3.28
AA112	0.80 (irr.)			
	1.29 (irr.)	-1.55 (210)	5.55	3.2

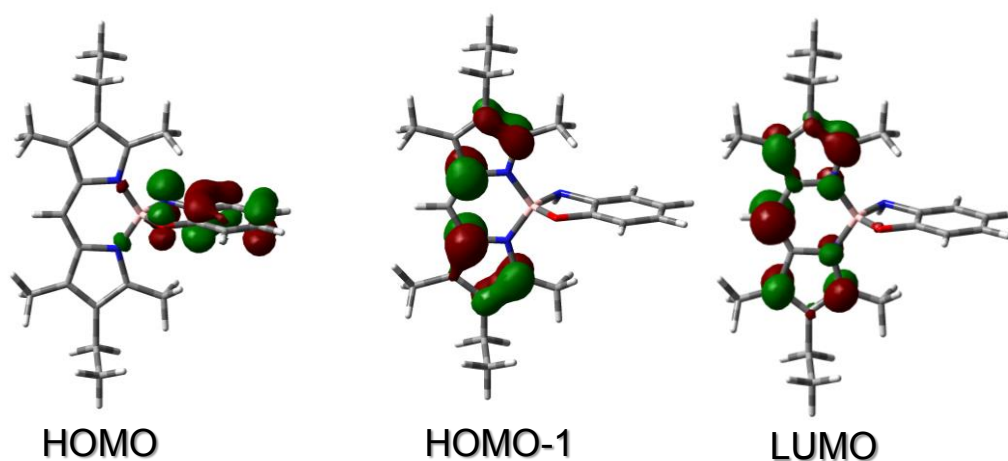


Figure 3.7. Kohn-Sham distributions computed for the relevant orbitals; running from left to right, HOMO, HOMO(-1) and LUMO for **AA27**.

On oxidative scans, **AA27** exhibits two irreversible waves with peaks at 0.23 V and 0.9 V vs Ag/Ag⁺. The first oxidative wave is clearly at too low potential to refer to oxidation of BODIPY and is unambiguously assigned to one-electron oxidation of the strap. Indeed, the second one-electron oxidation wave can be attributed to removal of an electron from the BODIPY core. The reductive process can be assigned to one electron reduction of the BODIPY core, this assignment is done with the aid of quantum mechanical calculations and literature data, Figure 3.7.^{16,17}

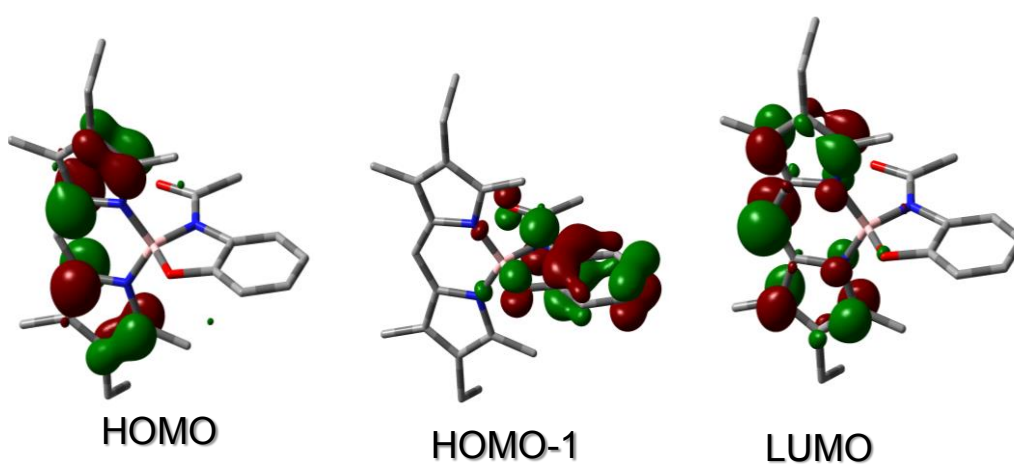


Figure 3.8. Kohn-Sham distributions computed for the relevant orbitals; running from left to right, HOMO, HOMO(-1) and LUMO for **AA112**.

AA55 exhibits two oxidative waves with peaks at 0.77 V and 1.73 V vs Ag/Ag⁺, the wave centred at the 0.77 V is electrochemically reversible with $\Delta E = 64$ mV. Quantum chemical calculations indicate that both the LUMO and HOMO are localized on the BODIPY unit while HOMO(-1) resides on the amide-based strap. In turn, **AA112** has two oxidative waves at 0.80 V and at 1.29 V and one quasi-reversible reductive wave at -1.55 V, $\Delta E = 210$ mV. Quantum chemical calculations again indicate that both the LUMO and HOMO are localized on the BODIPY unit while HOMO(-1) resides on the amide-based strap, Figure 3.8. This assignment is supported by the observation that the difference between E_{RED} and E_{OX} ($\Delta E_{\text{OP}} = 2.36$ eV) lies close to the optical transition energy ($\Delta E_{\text{XS}} = 2.29$ eV) measured as the crossover point between normalized absorption and emission spectra.

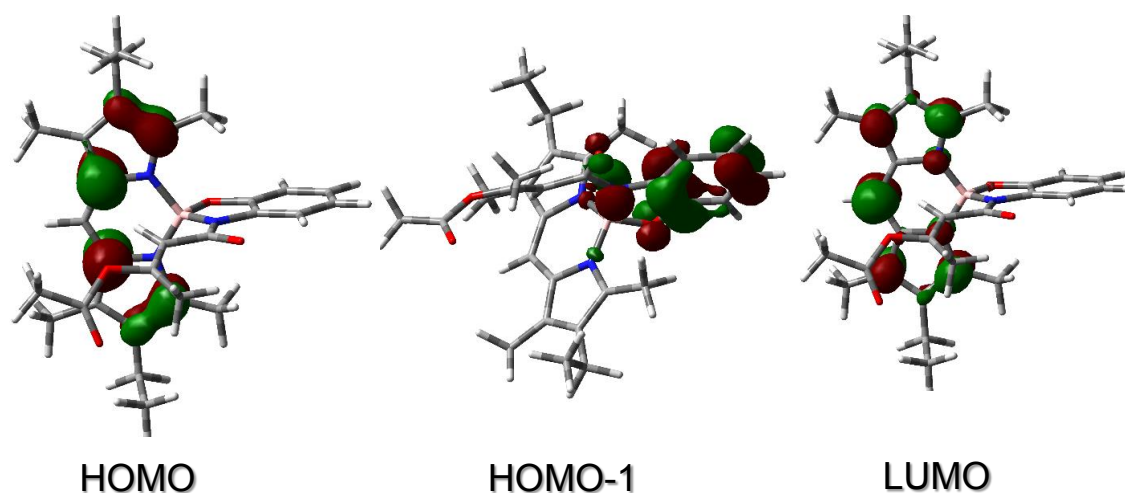


Figure 3.9. Kohn-Sham distributions computed for the relevant orbitals; running from left to right, HOMO, HOMO(-1) and LUMO for **AA55**.

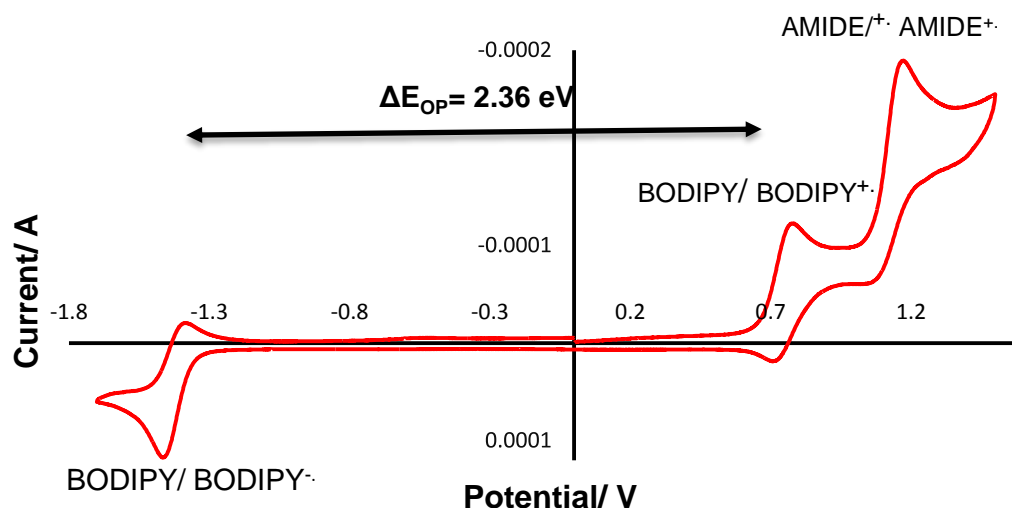


Figure 3.10. Cyclic voltammogram of **AA55** recorded in anhydrous deaerated acetonitrile (0.1M $n\text{BuN.PF}_6$). Scan rate 0.15 Vs^{-1} .

The cyclic voltammetry used in conjunction with spectroscopic data is used to determine the thermodynamic driving force (ΔG_{CT}) for light-induced charge-transfer in each of the three compounds. Using Equation 3.1 it was determined that the driving force for the charge transfer from the amine strap to the excited-singlet state of BODIPY¹⁸ for **AA27** is -0.48 eV , whereas for the amide-strapped BODIPY dyes it is equal to 0.38 eV and 0.56 eV for **AA55** and **AA112** respectively. Therefore, it can be concluded that light-induced charge transfer is only possible for **AA27**. Here the driving force is sufficient to promote effective charge transfer from the amine to the BODIPY core. It might be noted that the distance between these reactants is short but the geometry is not conducive for fast electron transfer.

$$\Delta G_{CT} = e(E_{ox} - E_{red}) - E_{xs} - E_{es} - E_{sol} \quad \text{Equation 3.1}$$

$$E_{es} = \frac{e^2}{(4\pi\epsilon_0)\epsilon_s R_{CC}} \quad \text{Equation 3.2}$$

$$E_{sol} = \frac{e^2}{8\pi\epsilon_0} \left(\frac{1}{R_D} + \frac{1}{R_A} \right) \left(\frac{1}{\epsilon_{ref}} - \frac{1}{\epsilon_s} \right) \quad \text{Equation 3.3}$$

The parameters used in Equation 3.1-Equation 3.3 include the excited-state energy, E_{xs} = 2.29 eV. This was derived from the intersection of normalized absorption and fluorescence spectra. There was no need to correct for the difference in solvent dielectric constant as all investigations were carried out in acetonitrile, $\epsilon_s = \epsilon_{ref} = 35.94$.⁸ The molecular dimensions were derived from X-ray structures obtained by our Crystallography Laboratory, Table 3.4.

Table 3.4. Compilation of intramolecular distances obtained using X-Ray structures, R_D is the radius of the donor, R_A is the radius of the acceptor whereas R_{CC} is the centre-to-centre distance between donor and acceptor.

	$R_D / \text{\AA}$	$R_A / \text{\AA}$	$R_{CC} / \text{\AA}$
AA27	1.16	2.98	4.64
AA55	1.43	2.98	4.3
AA112	2.12	2.36	4.05

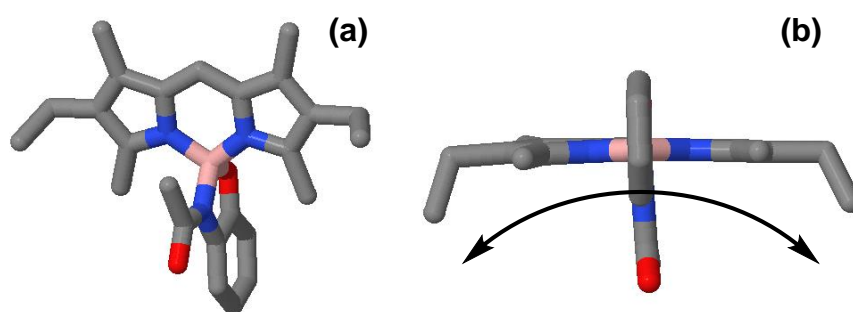


Figure 3.11. (a) X-Ray structure obtained for **AA112**; X-ray structures were used to calculate R_{cc} distances for all three samples investigated. (b) View from above of the same X-ray structure showing small curvature of the BODIPY core.

Aside from the unusual fluorescence properties, these strapped BODIPY analogues display small Stokes' shifts, low molar absorption coefficients and red-shifted absorption maxima when compared to an unsubstituted BODIPY dye. For a conventional BODIPY-based dye, successive replacement of the B-F bonds with B-OCH₃ groups has no effect on the energies of either absorption or fluorescence maxima.^{19,20} This realization points towards some important geometrical factor as being responsible for the weak absorption profile and it is important to recall that the X-ray structures indicate slight curvature of the dipyrin backbone, Figure 3.11. The quantum chemical calculations replicate this disruption from planarity of the BODIPY nucleus but it is difficult to identify a simple means by which to quantify the extent of curvature, especially since the distortion is not evenly spread over the dipyrin, Figure 3.12. The same studies carried out for the unsubstituted BODIPY dye indicate that it is planar and highly symmetrical. This slightly displaced geometry is expected to reduce connectivity along the conjugation path and thereby lower the absorption coefficient. However, the strap is not directly involved in the conjugation path and changing the nature of the strap does not affect the magnitude of the optical bandgap. As such, the basic conjugation length is considered to be much the same for each of the strapped compounds.

In fact, the calculations indicate a marked change in the internal electronic properties of the dipyrin units for the strapped analogues when compared to the unsubstituted BODIPY dye. This is conveniently registered by the Mulliken charge (μ_M) for the dipyrin N atoms. For an unsubstituted BODIPY dye, the charges are balanced and indicate electro-negative N atoms ($\mu_M = -0.303$) but for **AA112** ($\mu_M = -0.278$) the charges are raised to a less negative value. The amine derivative, **AA27**, leads to asymmetry for these charges due to the N lone pair being localized above the plane of the dipyrin nucleus. Here, the individual μ_M values are -0.277 and -0.247, both values being more positive than found for the unsubstituted BODIPY dye. Interestingly, the calculated charges for **AA55** ($\mu_M = -0.277$ and -0.270) differ slightly from those determined for **AA112** and indicate slight asymmetry caused by the side-chain positioning itself over the dipyrin. As such, the red-shifted absorption transition and low ϵ_{MAX} values found for the strapped analogues can be attributed to the changes in the atomic orbital coefficients for contributors to the effective conjugation length.

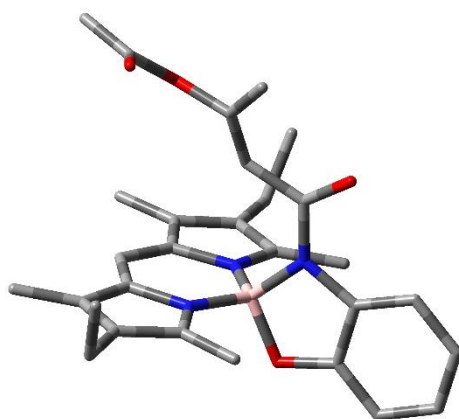


Figure 3.12. Computed molecular geometry for **AA55**.

3.2.3 Fluorescence Quenching in the Glassy Matrix

The fluorescence quantum yield determined for each of the strapped BODIPY derivatives is approximately constant in the rigid glass at temperatures below 110 K and the averaged values are collected in Table 3.5. These values range from 0.08 for **AA112** to 0.02 for **AA55** and show no correlation with the thermodynamic driving forces calculated for light-induced, intramolecular charge transfer in fluid solution. Our expectation that charge transfer for **AA27** will be switched off in the glassy matrix is based on the acceptance that the charge-transfer state will be subject to a destabilization energy of ca. 0.8 eV on vitrification of the medium, Figure 3.13.²¹ This value was determined experimentally for certain porphyrin-quinone dyads and confirmed for a *bis*-porphyrin dyad. It might not be considered relevant to the strapped BODIPY dyes investigated here, especially given the close proximity of the redox units. However, calculation of the destabilization energy expected for formation of a radical ion pair in MTHF at 80K using the procedure described by Wasielewski *et al.*,²¹⁻²³ which follows that introduced by Weller,²⁴ we reach a value of 0.83 eV. Thus, the poor emission yields determined for the strapped BODIPY dyes in the rigid glass are unlikely to be due to light-induced charge transfer.

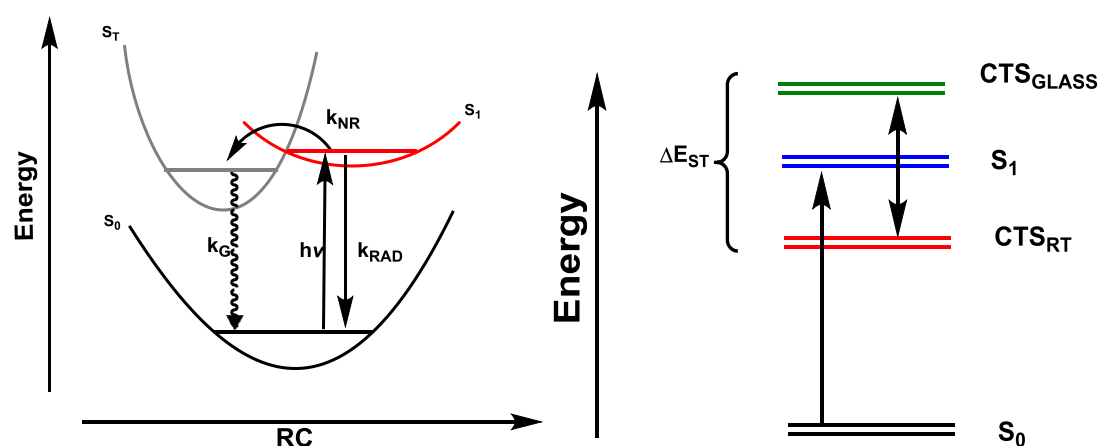


Figure 3.13. Potential energy diagram proposed to account for the photophysical properties determined for the strapped BODIPY-based in a rigid MTHF glass at low temperature and illustration of the effect of destabilization of the charge-transfer state on moving from fluid solution (CTS_{RT}) to the rigid glass (CTS_{GLASS}).

Each compound exhibits a small Stokes' shift, indicating that emission occurs from an excited-singlet state S_1 having a comparable geometry to that of the ground state S_0 . The observation that fluorescence in solution is thermally activated is most unusual and means that S_1 is being repopulated from a lower-energy trap S_T by way of a Boltzmann-type barrier crossing process.²⁵ To accommodate all the photophysical observations, we propose an S_1 potential energy surface with a shallow minimum corresponding to the S_0 geometry. Without this, it is difficult to explain the small Stokes' shift. The exciton can easily escape from the well to sample the potential surface but becomes trapped in a deeper well that is coupled in a radiationless manner to the ground state. The fluorescence yield now increases with increasing temperature, reflecting the fraction of entombed excitons able to return to the emissive trap. This situation will establish an equilibrium with the exciton shuttling between the two traps, with radiative decay from the shallow trap and radiationless decay occurring primarily from the deeper one. Since fluorescence is weak in all cases, it follows that internal conversion from the deeper trap is fast relative to re-population of the emitting state.

Because ϕ_F is essentially independent of temperature in the glassy matrix, we raise the general approximation that there is no significant thermal repopulation of the emitting state under these conditions. In other words, the observable fluorescence corresponds to prompt emission. In support of this hypothesis, it was found that time-resolved fluorescence decay profiles could be analyzed satisfactorily in terms of single-exponential fits for **AA112** and **AA55** in the glassy matrix. The derived lifetimes are included as part of Table 3.5 and appear to be in line with the quantum yields. For **AA112**, the emission lifetime at 80K is less than 60 ps. Now, taking k_{RAD} as being numerically identical to that measured in fluid solution and further assuming that there is no direct internal conversion from the shallow trap to the ground state, it becomes possible to estimate the rate constant (k_{NR}) for radiationless escape from the deeper trap, Figure 3.13. This simplified scheme, pertinent only to the glassy matrix, is illustrated by way of Figure 3.13 and the derived k_{NR} values are collected in Table 3.5. The magnitude of k_{NR} depends on the nature of the strap. Since k_{NR} determines the amount of prompt fluorescence, it follows that this rate refers to the process that populates the deeper trap and not

the actual rate (k_G) at which trapped excitons return to the ground state. Presumably, in the glassy matrix, k_G exceeds k_{NR} in each case.

Table 3.5. Parameters derived for deactivation of the excited-singlet state in the glassy matrix at temperatures below 120K.

	AA27	AA112	AA55
$\Delta G/ \text{eV}^{(a)}$	-0.56	+0.46	+0.25
$\Delta G/ \text{eV}^{(b)}$	+0.27	+1.29	+1.08
$\phi_F^{(c)}$	0.0017	0.084	0.020
$\tau_s/ \text{ns}^{(d)}$	<0.06	0.95	0.38
$k_{\text{RAD}} / 10^7 \text{ s}^{-1}$	5	7	7
$k_{\text{ESC}} / 10^8 \text{ s}^{-1}$	300	8	35

(a) Thermodynamic driving force for light-induced intramolecular charge transfer calculated for MTHF solution at 20 °C.

(b) Thermodynamic driving force for light-induced intramolecular charge transfer calculated for glassy MTHF at 80K.

(c) Fluorescence quantum yield measured at 80K for the compound in glassy MTHF.

(d) Fluorescence lifetime measure at 80K for the compound in glassy MTHF.

3.2.4 Fluorescence Quenching in Liquid Solution

The above model is not applicable to fluid solution because for each compound there is a gradual recovery of emission on raising the temperature. The most obvious case is that found for **AA27**, where ϕ_F increases progressively with temperature from the onset of melting, Figure 3.14.

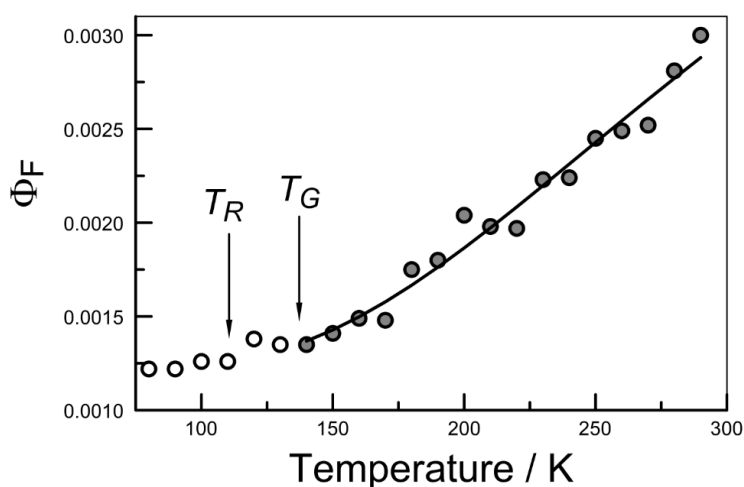


Figure 3.14. Effect of temperature on the fluorescence quantum yield measured for **AA27** in MTHF; the filled circles refer to measurements made above the glass transition temperature (T_G) while the empty circles refer to the glassy matrix. At temperatures below T_R , the glass is considered to be rigid. The solid line drawn through the data points represents a fit to Equation 3.7.

In the case of the two amide derivatives, the onset for thermally activated fluorescence is apparent at temperatures above the glass transition temperature, Table 3.6.^{26,27} To accommodate thermal repopulation of the emitting state, it is necessary to introduce an activated process that competes with emptying the deeper trap by way of internal conversion. This situation leads to the model illustrated in Figure 3.15. The only change from the low-temperature limit is to include reverse population of the S_1 level by way of barrier crossing, where ΔE is the barrier height and k_{DS} is the corresponding rate constant, which can be obtained from Equation 3.6. The fit to data collected for **AA27** is robust (Figure 3.16) and leads to the parameters collected in Table 3.6. In order to optimize the

fit, it is necessary to allow for recycling between the two traps. The actual number of cycles (\bar{n}) will increase with increasing temperature, at least according to the model and our simulations. The remaining parameters are allowed to float, allowing estimation of the barrier height as being 6 kJ/mol. The rates for occupying (k_{NR}) and emptying (k_G) the deeper trap are comparable but the key variable is the rate (k_{DS}) for return population of the emitting state. The importance of this latter term can be judged by the realization that ϕ_F increases by a factor of ca. 2-fold on progressing from the melting point to room temperature.

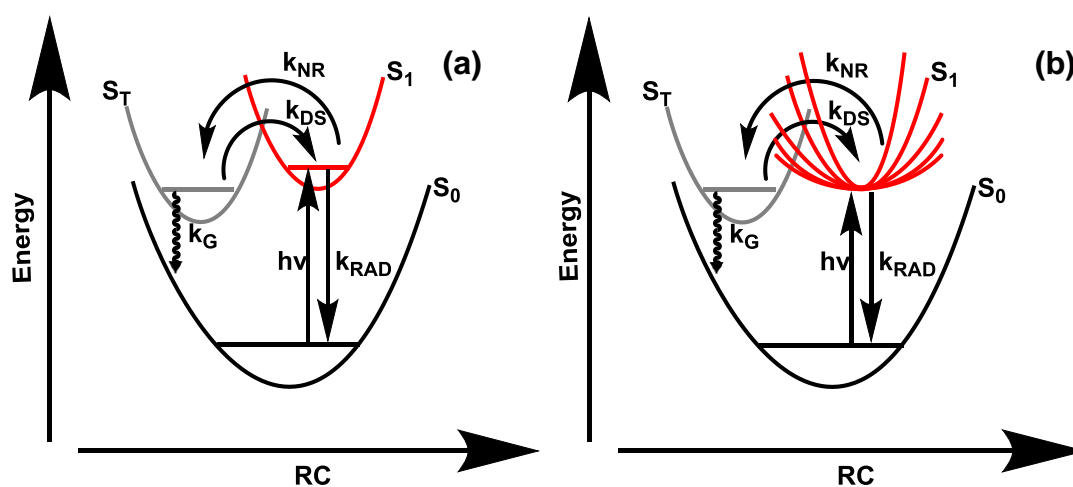


Figure 3.15. (a) A model proposed to accommodate an activated process that competes with emptying the deeper trap by way of internal conversion. (b) Here we demonstrate how the curvature of the S_1 state can vary and thereby modulate the barrier height and k_{DS} .

Table 3.6. Summary of the parameters derived from fitting the temperature dependent emission yields in fluid solution.

	$k_{NR} /$ ns^{-1}	$\Delta E /$ $J\ mol^{-1}$	$k_{DS} /$ ns^{-1}	$k_G /$ ns^{-1}	$\tau_p /$ $ps^{(a)}$	$\tilde{n}^{(b)}$
AA27	56	5 970	60	2.9	17 & 370	1.67
AA112	32	7 385	60	1.5	29 & 715	2.93
AA55	21	5 400	15	1.5	44 & 710	1.39

(a) τ_p predicted singlet lifetimes obtained using TADF model.

(b) \tilde{n} mean number of cycles at room temperature.

An important point emerging from the temperature dependence recorded for **AA27** is that passing from fluid solution to an isotropic glass ($T_G = 137\ K$) and finally to a rigid glass ($T_{RG} = 91\ K$) does not cause a marked change in ϕ_F . This indicates that the potential energy surface for the emitting state S_1 is essentially flat for this molecule.^{27,28} It is also apparent that the main cause of fluorescence quenching is not due to light-induced charge transfer and, instead, we attribute the fast deactivation of S_1 to a rupturing of the potential energy surface imposed by the N,B,O strap.

Before considering the other compounds, we will explain our fitting procedure: Equation 3.4 allows us to determine the mean number of cycles (\tilde{n}) at any individual temperature. Re-cycling is between the S_1 state and the trap, where ϕ_{FLU} is a quantum yield at the temperature of interest and ϕ_{FLU}^{LT} is the lower limit to the quantum yield found at low temperature. The number of cycles is also related to the probability of reaching the deeper trap (ϕ_T) and the probability that the exciton will return to the emitting state (ϕ_S). The non-radiative decay is first estimated using ϕ_{FLU}^{LT} and it is assumed to be activationless (Equation 3.5). Note that we have omitted direct internal conversion from the emitting state to the ground state as a means for simplifying the situation. Once the number of cycles is determined (\tilde{n})

for a range of temperatures it can be used to obtain the quantum yield for return to the emitting state at each temperature. This parameter is in turn used to obtain k_G , k_{DS} and ΔE by fitting data at all temperatures (Equation 3.6). In order to check the quality of our fit we used the above parameters to recover the lifetime values. This was done to ensure the fit is self-consistent.

After establishing crude values for the rate constants and barrier height, the next stage of analysis involved fitting the temperature dependent emission quantum yields determined in fluid solution. In so doing, we equate the (extrapolated) lower limit for emission in the fluid solvent as arising from prompt fluorescence. This number is needed to start the iterative fitting procedure since it forces a value for k_{NR} (Equation 3.8). The entire data set is now analysed in terms of Equation 3.7, which uses a Taylor expansion with up to 5 terms. Initial estimates for the unknown parameters are input according to the above analysis. Iteration was continued until convergence – see Figure 3.14 for an example. Again, the derived rate constants and barrier height were used to compute the two fluorescence lifetimes and, if two sets of values gave comparable statistical fits, a decision on the validity of the data was made on the basis of the agreement between observed and computed lifetimes.

$$\tilde{n} = \frac{\phi_{FLU}}{\phi_{FLU}^{LT}} - 1 = \frac{\phi_T \times \phi_S}{1 - \phi_T \phi_S} \quad \text{Equation 3.4}$$

$$\phi_T = \frac{k_{NR}}{(k_{NR} + k_{RAD})} \quad \text{Equation 3.5}$$

$$\phi_S = \frac{k_{DS} e^{-\Delta E/(RT)}}{k_G + k_{DS} e^{-\Delta E/(RT)}} \quad \text{Equation 3.6}$$

$$\phi_{FLU} = \phi_{PF} [1 + (\phi_T \phi_S) + (\phi_T \phi_S)^2 + (\phi_T \phi_S)^3 + \dots] \quad \text{Equation 3.7}$$

$$\phi_{PF} = \frac{k_{RAD}}{(k_{RAD} + k_{NR})} \quad \text{Equation 3.8}$$

In order to check the quality of our fit we used the above parameters to recover the lifetime values. If we assume there is no internal conversion from S_1 to the ground state (GS), the only processes available to S_1 are fluorescence (k_{RAD}) and escape to the trap (k_{NR}). The only activated process is repopulation of S_1 from the trap. The rate constant is k_{DS} and the barrier height is ΔE .

There should be two lifetimes. The shorter lifetime represents prompt fluorescence but includes a term for escape to the trap. The longer lifetime refers to repopulation of the S_1 state and is given as:

$$k_1 = \frac{1}{\tau_1} = \frac{k_G + k_{DS} \exp^{-\frac{\Delta E}{RT}} (1 - \phi_T)}{1 + k_{DS} \exp^{-\frac{\Delta E}{RT}} \chi} \quad \text{Equation 3.9}$$

Here, k_G refers to the rate constant for radiationless decay from the trap to the ground state. The other term is defined as:

$$\chi = \frac{1}{k_{RAD} + k_{NR}} \quad \text{Equation 3.10}$$

The other lifetime (i.e., the faster process) is given simply as:

$$k_2 = \frac{1}{\tau_2} = \frac{1}{\chi} + k_{DS} \exp^{-\frac{\Delta E}{RT}} \quad \text{Equation 3.11}$$

Table 3.7. Example of a simulation carried out for **AA112** using Equation 3.4 to obtain the mean number of cycles (\tilde{n}) at a particular temperature.

Temperature/ K	ϕ_{FLU}	\tilde{n}	ϕ_{s}
180	0.00024	0.1429	0.1255
190	0.00026	0.2381	0.1931
200	0.00031	0.4762	0.3239
210	0.00031	0.4762	0.3239
220	0.00033	0.5714	0.3651
230	0.00039	0.8571	0.4634
240	0.00056	1.6667	0.6275
250	0.00067	2.1905	0.6893
260	0.00064	2.0476	0.6746
270	0.00061	1.9048	0.6584

A likewise robust fit is obtained for **AA55** over the same temperature range (Figure 3.16), with the derived parameters being collected in Table 3.6. Again, it is necessary to allow for recycling between the two traps with a mean value obtained from Equation 3.4. Compared to **AA27**, the analytical fit suggests a slightly deeper trap, with ΔE increasing to 6.7 kJ/mol, but with minimum change among the derived rate constants. This is further confirmation that fluorescence quenching is not due to intramolecular charge transfer. Nonetheless, there is a 2.5-fold increase in ϕ_{F} between the glass melting and reaching room temperature, Figure 3.16. A notable difference between **AA55** and **AA27** relates to the observation that the former shows partial fluorescence recovery in the rigid glass. In fact, ϕ_{F} falls precipitously as the glass melts (Figure 3.16) and there is excellent accord between the loss of emission for **AA55** and the solvent reorientation time measured *via* the fluorescence properties of oxazine-4.^{29,30} We interpret this behaviour in terms of the S_1 potential surface being slightly more curved than that found for **AA27** such that the wave-packet encounters a slight barrier on the way to reaching the trap. Because of this curvature, the barrier appears marginally deeper and k_{DS} increases slightly.

The situation for **AA112** is more complex, despite the fact that there is minimal difference between the two amides in terms of structure. This compound is the least fluorescent, reaching a lower limit of 0.0002 at low temperature, but shows the most recovery (i.e., a factor of 4-fold) at room temperature. The inherently low ϕ_F , together with a common k_{RAD} , indicates that k_{NR} must be considerably higher than that derived for **AA55**, Table 3.6. Analysis of the high temperature regime (Figure 3.16) produces parameters differing from those derived above (Table 3.6), although the analysis is less robust because there are fewer data points. The main features of this analysis are: (i) the elevated barrier height derived, (ii) the higher k_{NR} , (iii) the higher k_{DS} , and (iv) the increased number of cycles. The second point is forced by the low fluorescence inherent to **AA112** while an unusually high k_{DS} is required to account for the relatively high drop of thermally-activated fluorescence. In turn, the mean recycling number is a consequence of the slow rate for emptying the trap. Thus, the derived values are highly correlated.

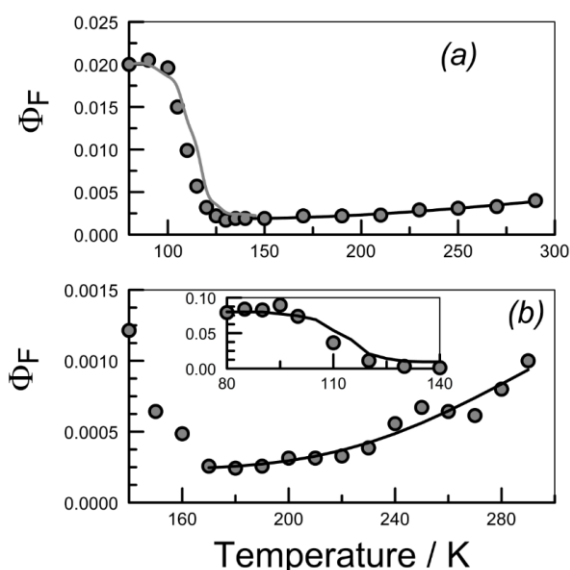


Figure 3.16. Effect of temperature on the fluorescence quantum yield measured for (a) **AA55** and (b) **AA112** in MTHF. For (a) the grey curve accompanying the low temperature data points is the solvent relaxation time determined using oxazine-4 to reflect the melting of the glass while the black curve running through the data points is a non-linear least-squares fit to Equation 3.7 with the parameters listed in Table 3.6. For (b), the solid black line running through the data points is a non-linear least-squares fit to Equation 3.7 while the inset shows the low temperature region with the solvent relaxation time accompanying the experimental data points.

One consequence of the thermally-activated repopulation of the emitting state is that the time-resolved emission profiles should exhibit short- and long-lived components.²⁶ This is not the case at 80K, where single-exponential decay records are recovered after deconvolution of the instrument response function. The analysis carried out for **AA27** at room temperature shows the presence of a longer-lived component with a lifetime of 390 ± 60 ps that contributes ca.15% to the total signal. Again, this slower component is attributed to thermally-activated, delayed fluorescence arising via repopulation of the shallow trap from the deeper trap. The reason for the poor precision regarding analysis of this latter component is because multiple recycling will extend the lifetime but complicate the fitting procedure.

The situation is similar for both **AA112** and **AA55** and there is a longer-lived component present in the time-resolved decay records. In both cases, the fractional contribution of the longer-lived component was small and could not be determined with much accuracy because the shorter-lived component is not well resolved from the instrument response function collected at room temperature. Both studies indicate a small amount of relatively long-lived emission, with lifetimes of 300 ± 120 and 635 ± 110 ps, respectively, for **AA112** and **AA55**. These components appear consistent with repopulation of the shallow trap but require more detailed analysis. Our choice of excitation wavelength is somewhat restricted and we are mindful of trace impurities complicating the signals.

3.3 Conclusions

The main finding to emerge from this investigation concerns the realization that the lack of fluorescence inherent to these strapped BODIPY-based chromophores is not a consequence of intramolecular charge transfer. In fact, the OFF signal for these proton-sensing probes is insensitive to the thermodynamic driving force for light-induced charge transfer from strap to BODIPY core. Our understanding of the photophysical properties of these compounds is based on the strap imposing steric constraints on the dipyrin unit that rupture the potential energy landscape for the excited state, thereby introducing pinholes that trap the migrating wave-packet.

Escape from the trap to the ground state potential surface appears to be fairly slow and allows return to the emitting state. The latter situation is characterized by thermally-activated, delayed fluorescence but the yield is kept low by the poor radiative probability of the excited state. An interesting observation relates to the effect that the strap has on the internal electronic properties of the BODIPY core. Effectively, the strap modulates both the energy and the oscillator strength of the absorption transition, thereby providing a novel approach for fine-tuning the optoelectronic properties of the chromophore. The compounds function as excellent fluorescent sensors for protons but cleavage of the strap is irreversible and is considered to be a practical option.

3.4 References

- (1) Shaban Ragab, S.; Swaminathan, S.; Deniz, E.; Captain, B.; Raymo, F. M. *Org. Lett.* **2013**, *15*, 3154.
- (2) Deniz, E.; Battal, M.; Cusido, J.; Sortino, S.; Raymo, F. M. *Phys. Chem. Chem. Phys.* **2012**, *14*, 10300.
- (3) Wijesinghe, C. A.; El-Khouly, M. E.; Blakemore, J. D.; Zandler, M. E.; Fukuzumi, S.; D'Souza, F. *Chem. Commun.* **2010**, *46*, 3301.
- (4) Wijesinghe, C. A.; El-Khouly, M. E.; Subbaiyan, N. K.; Supur, M.; Zandler, M. E.; Ohkubo, K.; Fukuzumi, S.; D'Souza, F. *Chem. Eur. J.* **2011**, *17*, 3147.
- (5) Bahaidarah, E.; Harriman, A.; Stachelek, P.; Rihn, S.; Heyer, E.; Ziesel, R. *Photochem. Photobiol. Sci.* **2014**, *13*, 1397.
- (6) Thilagar, P. *Inorg. Chem.* **2014**, *53*, 2776.
- (7) Wang, S.; Cai, J.; Sadygov, R.; Lim, E. C. *J. Phys. Chem.* **1995**, *99*, 7416.
- (8) Nano, A.; Ziesel, R.; Stachelek, P.; Harriman, A. *Chem. Eur. J.* **2013**, *19*, 13528.
- (9) Abboud, J. L. M.; Notario, R. *Pure Appl. Chem.* **1999**, *71*, 645.
- (10) Strickler, S. J.; Berg, R. A. *J. Chem. Phys.* **1962**, *37*, 814.
- (11) Jones, G.; Yan, D.; Hu, J.; Wan, J.; Xia, B.; Vullev, V. I. *J. Phys. Chem. B* **2007**, *111*, 6921.
- (12) Allen, B. D.; Benniston, A. C.; Harriman, A.; Mallon, L. J.; Pariani, C. *Phys. Chem. Chem. Phys.* **2006**, *8*, 4112.
- (13) Domingue, R. P.; Fayer, M. D. *J. Chem. Phys.* **1985**, *83*, 2242.
- (14) Alamiry, M. A. H.; Bahaidarah, E.; Harriman, A.; Bura, T.; Ziesel, R. *RSC Adv.* **2012**, *2*, 9851.
- (15) Alamiry, M. A. H.; Benniston, A. C.; Copley, G.; Elliott, K. J.; Harriman, A.; Stewart, B.; Zhi, Y.-G. *Chem. Mater.* **2008**, *20*, 4024.

- (16) Lambert, C.; Schelter, J.; Fiebig, T.; Mank, D.; Trifonov, A. *J. Am. Chem. Soc.* **2005**, *127*, 10600.
- (17) Qin, W. W.; Baruah, M.; Van der Auweraer, M.; De Schryver, F. C.; Boens, N. *J. Phys. Chem. A* **2005**, *109*, 7371.
- (18) Summers, G. H.; Lefebvre, J.-F.; Black, F. A.; Stephen Davies, E.; Gibson, E. A.; Pullerits, T.; Wood, C. J.; Zidek, K. *Phys. Chem. Chem. Phys.* **2016**, *18*, 1059.
- (19) Nano, A.; Ziessel, R.; Stachelek, P.; Alamiry, M. A. H.; Harriman, A. *Phys. Chem. Chem. Phys.* **2014**, *15*, 177.
- (20) Ziessel, R.; Ulrich, G.; Harriman, A. *New J. Chem.* **2007**, *31*, 496.
- (21) Ulrich, G.; Ziessel, R.; Harriman, A. *Angew. Chem. Int. Ed. Engl.* **2008**, *47*, 1184.
- (22) Harriman, A.; Heitz, V.; Ebersole, M.; van Willigen, H. *J. Phys. Chem.* **1994**, *98*, 4982.
- (23) Gaines, G. L.; O'Neil, M. P.; Svec, W. A.; Niemczyk, M. P.; Wasielewski, M. R. *J. Am. Chem. Soc.* **1991**, *113*, 719.
- (24) Wasielewski, M. R.; Johnson, D. G.; Svec, W. A.; Kersey, K. M.; Minsek, D. W. *J. Am. Chem. Soc.* **1988**, *110*, 7219.
- (25) Rosspeintner, A.; Kattnig, D. R.; Angulo, G.; Landgraf, S.; Grampp, G. *Chem. Eur. J.* **2008**, *14*, 6213.
- (26) dos Santos, P. L.; Dias, F. B.; Monkman, A. P. *J. Phys. Chem. C* **2016**, *120*, 18259.
- (27) Ward, J. S.; Nobuyasu, R. S.; Batsanov, A. S.; Data, P.; Monkman, A. P.; Dias, F. B.; Bryce, M. R. *Chem. Commun.* **2016**, *52*, 2612.
- (28) Baleizão, C.; Berberan-Santos, M. N. *Ann. N.Y. Acad. Sci.* **2008**, *1130*, 224.
- (29) Zoon, P. D.; Brouwer, A. M. *Photochem. Photobiol. Sci.* **2009**, *8*, 345.
- (30) Görlach, E.; Gygax, H.; Lubini, P.; Wild, U. P. *Chem. Phys.* **1995**, *194*, 185.

Chapter 4. Electronic Energy Transfer and Charge Transfer in Molecular Dyads and Triads Built Around a BODIPY-Based Dye

4.1 Introduction

Our investigations into the mechanics of BODIPY-based molecular rotors has resulted in the elaboration of several new principles relating to the general effects of constraining the boron atom within a cyclic structure. This type of confinement has important consequences for the optical properties of the chromophore due to changes in the effective conjugation length and the internal electronics. Indeed, the strap can be used to fine-tune the opto-electronic properties of the chromophore, thereby pushing the absorption transition towards lower energies. The latter is recognized as being significant for the future development of advanced prototypes that might offer practical applications as rheology sensors. As an alternative strategy, we now consider the advantages of designing multi-component molecular systems where the rotor is not illuminated directly. The main purpose of such an approach is to enlarge the Stokes' shift such that excitation and detection are made easier. It might be recalled that most BODIPY-based dyes, and especially the strapped analogues, are subject to a rather small Stokes' shift. This is not a problem in the laboratory but could cause difficulties if these compounds are to be used in industrial settings. Our reasoning here is to design new molecular systems where the BODIPY dye is activated indirectly by way of intramolecular electronic energy transfer (EET) from a suitable energy donor. This is not entirely original and there have been numerous studies of EET involving BODIPY-based dyes, both from our laboratory and from other research groups. As a refinement to the basic strategy, we sought to invoke the idea of competition between EET and light-induced charge transfer as a further means by which to improve the selectivity of the sensor (see Figure 4.1). Now, we address the first part of the project by

exploring EET and charge-transfer in some BODIPY-based molecular architectures.

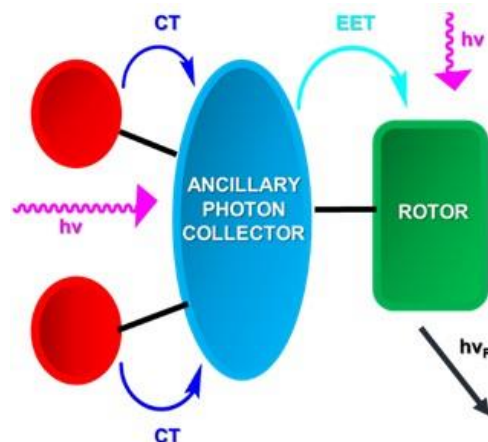


Figure 4.1. Pictorial representation of the prototypic rheology sensor based on indirect excitation and competing charge transfer.

In searching for a suitable energy donor to use with our BODIPY-based dyes, we have identified the diketopyrrolopyrrole (DPP) unit as being a promising candidate. These dyes are well known in industry as stable, light-fast materials that are used as pigments in many applications. The dyes are symmetrical and easily functionalised so as to generate a range of colours. Like many simple organic molecules, the DPP family of dyes are also electro-active. In starting the project, we obtained a small series of multi-component reagents built around an expanded BODIPY chromophore, equipped with a DPP residue, Figure 4.6. The basic building blocks are identified in Figure 4.4. The key component is **REF1**, which is a functionalised DPP dye that will act as the principle energy donor. It is interesting to note that **REF1** is highly fluorescent in the solid state, as shown opposite, which is quite unusual. In order to simulate light-induced charge transfer chemistry, a further two reference compounds have been examined, Figure 4.4. Here, redox-active terminals have been added to the basic DPP unit so as to construct a simple molecular dyad. The donor ability of the amino-based

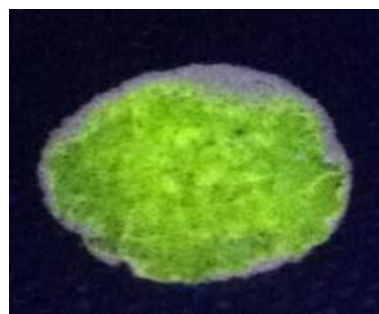


Figure 4.2. KBr disc prepared with addition of **REF1**.

terminal has been varied by the introduction of methoxy- groups. Both reference compounds make use of an ethyne bridge to interconnect the reactants.

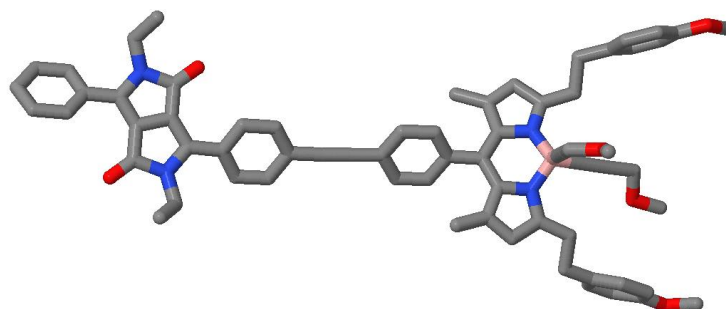


Figure 4.3. Computed structure obtained for **DYA1**, the basis set used was DFT/B3LYP/6-31G.

To extend the series, an expanded BODIPY dye has been identified as being a suitable partner, Figure 4.5. This compound is abbreviated throughout the chapter as **ACC**. It should be noted that the usual B-F bonds have been replaced with polyethylene glycol residues intended to assist solubility of the dye in organic solvents. The absorption maximum has been pushed towards longer wavelength by the simple strategy of attaching styryl groups to the 3,5-positions of the dipyrroin unit. The styryl units are further functionalised with solubilising groups. In fact, we have not encountered problems with dissolving **ACC** in weakly polar organic solvents but it is known that the DPP residue is not especially soluble. The solubilising groups, therefore, become important when considering the multi-component molecular systems comprising a boron-dipyrromethene dye covalently linked to a diketopyrrolopyrrole (DPP) derivative and triphenylamine (TPA) fragments, Figure 4.6. The final molecules are quite large and required extensive purification by column chromatography by our colleagues at Strasbourg. A critical design feature involved trying to ensure that each component retains its own identity so that fundamental photophysical processes, such as energy and charge transfer events, can be resolved. Understanding the mechanistic details for these crucial processes is essential for the successful design of viable molecular systems, for example functional cascade molecules designed to emulate photosynthetic systems¹ and artificial light collectors.² As illustrated above, DPP³ takes the role of secondary chromophore with the specific intention of extending

the Stokes' shift. In turn, molecular systems with larger Stokes' shifts prove themselves more useful for techniques like fluorescence microscopy and flow-cytometry.⁴

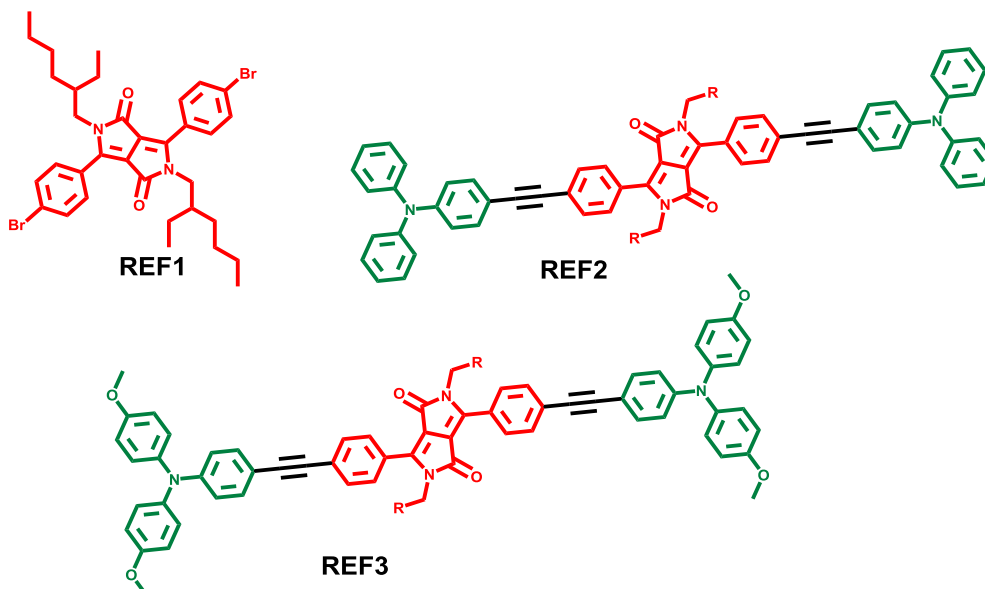


Figure 4.4. Molecular formulae for the three DPP-based donors discussed in this chapter. **REF1** is a synthetic precursor used to prepare the elongated versions. For **REF2** and **REF3**, R refers to the same solubilising function shown for **REF1**.

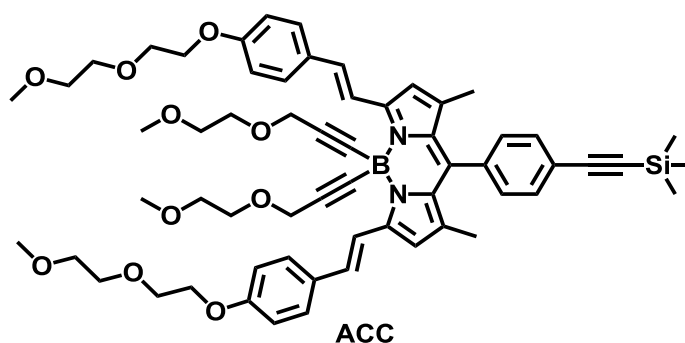


Figure 4.5. Molecular formula of the BODIPY-based energy acceptor studied in this chapter. The alkynylene-silyl function is used to assemble the molecular triads and, because it is attached at the pseudo-meso position, it is not expected to interfere with the photophysical properties of the BODIPY unit. The poly(ether) chains are added to assist solubility in organic solvents. Note that the styryl groups are intended to push the lowest-energy absorption transition to lower energy.

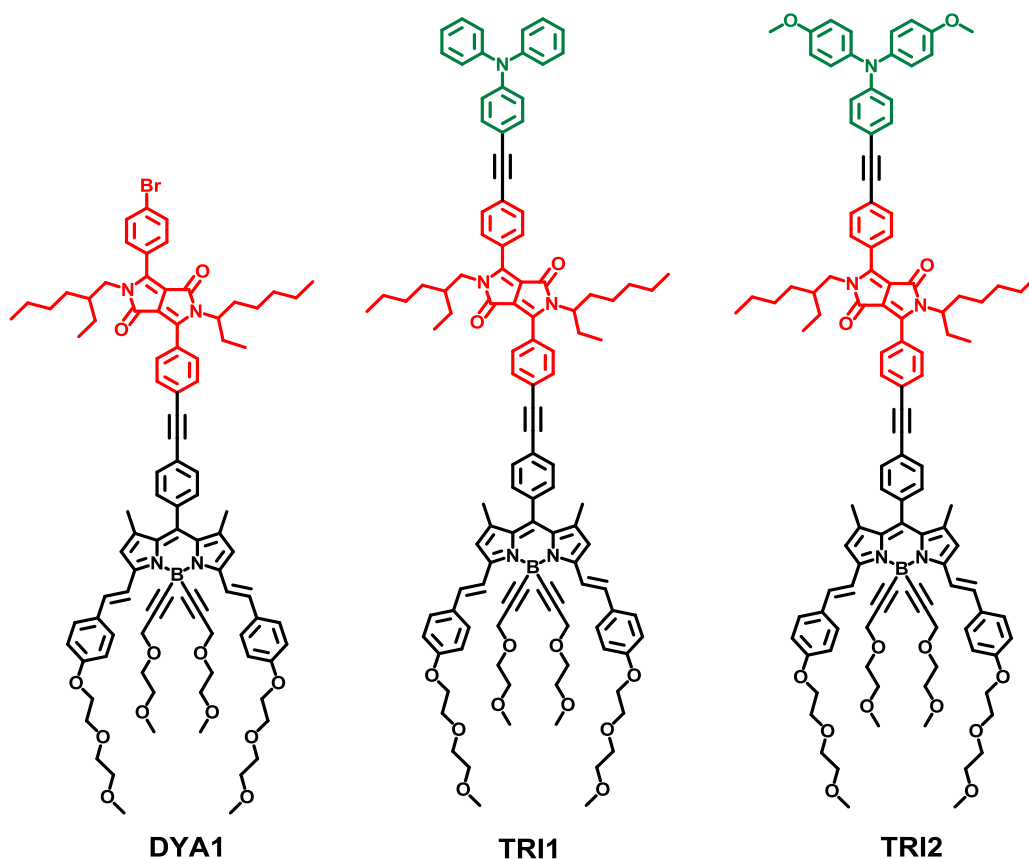


Figure 4.6. Molecular formulae of the BODIPY-based molecular dyad and the two corresponding molecular triads comprising a terminal BODIPY unit and a central DPP fragment. **DYA1** lacks the terminal redox-active donor. The two molecular triads differ in terms of the ionisation potential of the terminal electron donor. In all cases, the excitation energy of DPP lies well above that of **ACC**.

4.2 Results and Discussion

4.2.1 Spectroscopic Data

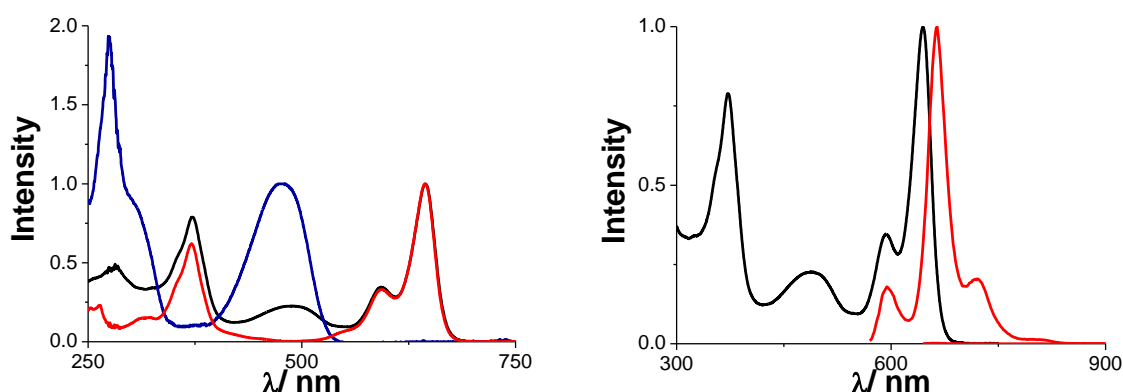


Figure 4.7. On the left-hand side we have normalised absorption spectra recorded for **REF1** (blue) **ACC** (red) and **DYA1** (black). On the right-hand side we have absorption and emission spectra recorded for **TRI2**. All spectra were measured at RT in spectrophotometric grade dichloromethane.

The molecular assemblies investigated herein were constructed by logical attachment of a DPP derivative (**REF1**), a blue BODIPY dye (**ACC**) and either triphenylamine (**REF2**) or methoxy-triphenylamine (**REF3**). The optical properties of the three molecular systems were recorded primarily in spectrophotometric-grade 2-methyltetrahydrofuran (MTHF). They were compared against the relevant reference compounds; specifically, **ACC** is used as a control compound by which to better understand the properties of the BODIPY unit and **REF1**, **REF2** and **REF3** were used as control compounds for the DPP residue. The lowest-energy absorption transition observed for **ACC** is relatively narrow and easily recognised in the spectrum, this is also the case for **DYA1**. This is to be expected as most BODIPY dyes are characterised by sharp absorption transitions. The emission spectrum is a reasonably good mirror image of the lowest-energy absorption transition.

Table 4.1: Photophysical measurements made for **ACC**, **DYA1**, **TRI1** and **TRI2** as well as for the DPP derivatives: **REF1**, **REF2** and **REF3**. All measurements were made using spectrophotometric grade MTHF. SS refers to the Stokes' shift.

	REF1	REF2	REF3	ACC	DYA1	TRI1	TRI2
$\lambda_{\text{ABS}}/\text{nm}$	475	498	511	644	645	645	644
$\lambda_{\text{EM}}/\text{nm}$	542	586	586	665	664	663	661
$\text{SS}/\text{cm}^{-1(\text{a})}$	2 600	3 020	2 500	490	440	420	400
$\epsilon/\text{M}^{-1}\text{cm}^{-1}$	17 400	51 900	51 200	145 500	114 641	138 680	93 410
Φ_{FLU}	0.84	0.43	0.7	0.67	0.28	0.29	0.05
τ/ns	6.9	3.3	2.4	4.8	4.7	4.6	4.8
$k_{\text{RAD}}/\text{x } 10^8 \text{ s}^{-1}$	1.2	2.2	2.9	1.4	0.6	0.6	0.09
$k_{\text{NR}}/\text{x } 10^8 \text{ s}^{-1}$	8.8	7.8	7.1	0.6	1.5	1.5	1.9

(a) Stokes' shift values quoted within margin error of $\pm 10 \text{ cm}^{-1}$.

The absorption and emission maxima recorded for the dyads are not red shifted relative to the BODIPY reference, as one might expect. The absorption spectrum of **DYA1** (Figure 4.7) appears to be a sum of the relevant individual components and therefore this suggests strongly to us that the donor and acceptor are not in significant electronic communication. The situation is a bit more complicated for both **TRI1** and **TRI2** (Figure 4.7) where absorption due to the TPA fragment overlaps with the high-energy absorption bands associated with BODIPY and DPP⁵⁻⁷ and this makes for a more challenging spectral deconstruction.

Table 4.1 summarizes the main photophysical data collected at room temperature for all the molecules. The emission maxima move towards higher energy ever so slightly (i.e. are blue shifted) along the series. The Stokes' shift (quoted in wavenumbers) decreases steadily as the structure of the dyad becomes more complicated. The molar absorption coefficients are consistent with those determined for many different BODIPY dyes.⁸ However, the molar absorption coefficient determined for **TRI2** is lower than that of the other two dyads and of that found for the BODIPY reference, **ACC**. In fact, the BODIPY reference dye has the strongest absorption coefficient. Lifetime measurements suggest there is no

quenching of the BODIPY-based first-excited singlet state since the singlet lifetimes for all molecular assemblies and the reference (**ACC**) are closely comparable.

The radiative rate constants for the dyads studied are smaller than those usually associated with BODIPY dyes and that of the BODIPY reference. The fluorescence quantum yields for the BODIPY-based acceptor present in the dyad and triads were determined experimentally; the excitation wavelength used was 490 nm, at this wavelength the BODIPY dye does not absorb appreciably. Therefore, all of the emission observed is due to electronic energy transfer from the complementary donor. It is worth pointing out that the DPP reference (**REF1**) does not respond to the internal heavy-atom effect, i.e. no reduction of either quantum yield (QY) or lifetime observed due to the presence of the bromine atoms. The heavy-atom effect promotes inter-system crossing and this in turn diminishes the emission from the singlet-excited state.^{9,10} The introduction of amino groups for compounds **TRI1** and **TRI2** might be expected to introduce intramolecular charge-transfer (CT) character. There does appear to be evidence for significant CT in **TRI2** as the QY has been severely quenched, but this does not appear to be the case for **TRI1**. The reason for this might be a superior electron-donating ability of TPA(OMe)₂ appended to DPP in **TRI2** compared to TPA alone, as is present in **TRI1**.⁵ However, no significant broadening of the S₀→S₁ transition can be observed.

As mentioned above, the fluorescence quantum yield measurements were made via indirect population of the emitting state. This implies efficient EET along the molecular axis. Indeed, this situation was confirmed by comparing excitation and absorption spectra recorded in MTHF solution at room temperature. In each case, absorption by the DPP donor results in emission by the BODIPY acceptor. We will return to this point at a later stage but it might be worth stressing that intramolecular EET provides a simple means for improving the fraction of the solar spectrum that can be harvested by the molecular dye. It is most unlikely that any single compound will collect a significant fraction of the solar region while a cocktail of dyes will function as a group of emitters. The notion of providing a cascade of EET events along a logical gradient is a synthetic strategy that overcomes the problems associated with a mixture of dyes.

4.2.2 Electronic Energy Transfer

The rates of electronic energy transfer have been analyzed using Equation 4.1 to Equation 4.4.¹¹⁻¹⁴ These equations are based on the Förster dipole-dipole interaction theory and provide the simplest approach to estimating rates of EET. To be valid, the reactants must be only weakly coupled and there must be no exchange interactions occurring by way of through-bond coupling. Our intention here is to enquire whether the coulombic mechanism can give a reasonable representation of the EET efficiency.

$$k_{EET} = \frac{2\pi}{\hbar} |V_{DA}| |\kappa^2| s^2 J_{DA} \quad \text{Equation 4.1}$$

$$V_{DA} = \frac{\mu_D \times \mu_A}{R_{DA}^3 \times (4\pi\epsilon_0)} \quad \text{Equation 4.2}$$

$$|\mu_A^2| = \frac{3000 \ln 10 \hbar c n}{8 N_A \pi^3 f^2} \int \left(\frac{\epsilon_A}{\tilde{\nu}} \right) d\tilde{\nu} \quad \text{Equation 4.3}$$

$$\kappa^2 = (\sin\theta_D \sin\theta_A \cos\phi - 2\cos\theta_D \cos\theta_A)^2 \quad \text{Equation 4.4}$$

Here, s is a screening factor in this case equal to 3.97, J_{DA} is the spectral overlap integral, μ_D is the transition dipole moment of the donor, μ_A is the transition dipole moment of the acceptor and finally R_{DA} is the centre-to-centre separation distance between the donor and acceptor. The orientation factor κ^2 is estimated using a computed structure.

Table 4.2. Summary of variables calculated for the **DY1**, **TRI1** and **TRI2** using Equation 4.1 to Equation 4.4.

	J_{DA}/cm^{-1}	$R_{DA}/\text{\AA}$	μ_D/D	μ_A/D	V_{DA}/cm^{-1}	κ^2	$k_{EET}/\times 10^{-12}\text{s}^{-1}$
DYA1	0.004	16	2.00	3.45	14	0.2	2.8
TRI1	0.006	16.6	3.09	3.45	20	0.2	9.7
TRI2	0.007	18.1	4.15	3.45	20	0.6	3.3

One of the key features of the Förster theory for EET that has proved to be invaluable over the decades is the sensitivity to molecular structure. This relates to the strong dependence of the rate of EET on the specific orientation of transition dipole moment vectors associated with donor and acceptor and with their mutual separation. This means that, provided the mechanism is valid for the system under study, the EET probability can be used to estimate structural features. Many biological entities have been examined in this way, although it might be stressed that the theory was not developed for the study of closely-spaced molecular dyads. Kuhn¹⁵ modified the basic theory to account for coulombic interactions between pairs of cyanine dyes and thereby introduced the concept of extended dipoles. This was done to avoid using the centre-to-centre distances since this could be misleading at short separations. The Kuhn approach has many uses in the field of conjugated polymers and long, linear molecules. As the reactants approach each other, there is less likelihood that conventional Förster theory will hold and several research groups have questioned the validity of using the ideal dipole approximation for molecular dyads. One way around this problem is to divide the transition dipole moment into individual contributions associated with the actual atoms on the donor and acceptor chromophores. This approach is good for cases where the vector is difficult to assign. The limiting case of this approach is the transition density cube method introduced by Fleming,^{16,17} where the transition dipole moment is divided into tiny cubes and a matrix is created to account for interaction between millions of cubes, Figure 4.8. Clearly, the reliability increases as the reliance on a single value is relaxed but the complexity of the calculation increases enormously.

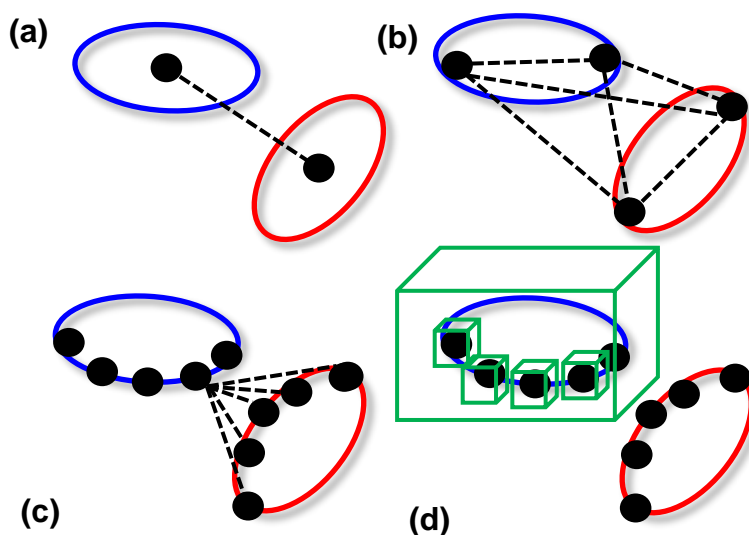


Figure 4.8. Cartoon to demonstrate different approaches to dealing with the specific orientation of transition dipole moment vectors associated with donor (blue) and acceptor (red) and with their mutual separation. (a) demonstrates the Förster ideal dipole approximation, (b) represents the Kuhn extended dipole approach, (c) scheme to demonstrate the approach based on dividing the transition dipole moment into individual contributions associated with the actual atoms on the donor and acceptor chromophores, and finally (d) the transition density cube method introduced by Fleming.

Excitation spectra recorded for the dyads and triads are highly suggestive of efficient EET along the molecular axis from DPP to **ACC**. Emission from the DPP fragment is largely quenched and EET appears to be fully competitive. In fact, it is estimated to be over 90% efficient. Analysis in the spectral region where donor emission is anticipated failed to identify a donor component, however it has been red-shifted relative to **REF1**, $\lambda_{\text{EM}} = 542$ nm, for isolated donor, whereas the emission from the donor substituent in **DYA1** is of lower energy, $\lambda_{\text{EM}} = 590$ nm. This points towards electronic interaction of the donor entity with the bridging unit. The emission quantum yields for the **ACC** component in **DYA1**, **TRI1** and especially **TRI2** appear lower than those of the isolated control compound. This is especially surprising when the EET is estimated to be very effectual. However there is a strong possibility for competing charge transfer from the terminal amine units to the DPP, this is discussed further at a later stage.

Returning now to the results of the calculations, we see that the ideal dipole approximation predicts very fast EET from DPP to **ACC** in these multi-component molecules. In each case, the rate is anticipated to exceed 1 ps^{-1} , in line with our

analysis of the excitation spectra. Thus, the molecules are ideally set up for efficient intramolecular EET and easily fulfill the requirement for an extended Stokes' shift. Within the confines of the ideal dipole approximation, it appears that EET is most efficient for **TRI1** followed by **TRI2** and finally by **DYA1**. **TRI1** has the highest rate of EET due to multiple contributing factors^{18,19} the optimal centre-to-centre distance and a more substantial spectral overlap integral due to increased conjugation. It is also interesting to note that there is less likelihood for light-induced charge transfer from the TPA unit to DPP for **TRI1** than for the analogous **TRI2**.

These qualitative results indicate that it is a viable proposition to equip a molecular rotor with an ancillary photon capturing facility. We note that DPP is far from ideal in this respect because its absorption spectral profile is relatively weak. None-the-less, it serves to demonstrate the potential use of such ancillary units as a means to separate excitation from emission. We now turn our attention to the acceptor unit and enquire as to the suitability of using this expanded BODIPY dye in molecular devices. Much less is known about the photophysical properties of these styryl-based BODIPY dyes compared to the conventional analogues. We have conducted a series of measurements aimed at clarifying the sensitivity of **ACC** to environmental effects.

4.2.3 Temperature Effect

The design of an effective molecular-scale rotor demands access to fluorophores that remain insensitive to all other environmental factors except the one of interest. In particular, in the absence of the rotor, the fluorophore must be highly tolerant of changes in temperature and solvent polarity. When dealing with a new fluorophore, it is important to assess the likelihood that these environmental effects could be problematic. It might be stressed that the Strickler-Berg²⁰ expression, as used to calculate the radiative rate constant, does not contain direct links to either temperature or solvent polarity. The refractive index does depend on temperature but the effect is rather shallow. However, the corresponding non-radiative rate constant could easily be sensitive to the nature of the environment.

To investigate the effect of temperature on the photophysical properties of **DYA1**, a solution was prepared using spectrophotometric grade MTHF and cooled to 80 K in an optical cryostat. The temperature effect is clear; the emission intensity increases steadily for both components as the temperature rises, Figure 4.9. A small red shift is observed over the temperature region where glassy MTHF melts, i.e. the amorphous phase between 110 and 140 K. However, a blue shift is observed once past the glass transition temperature.

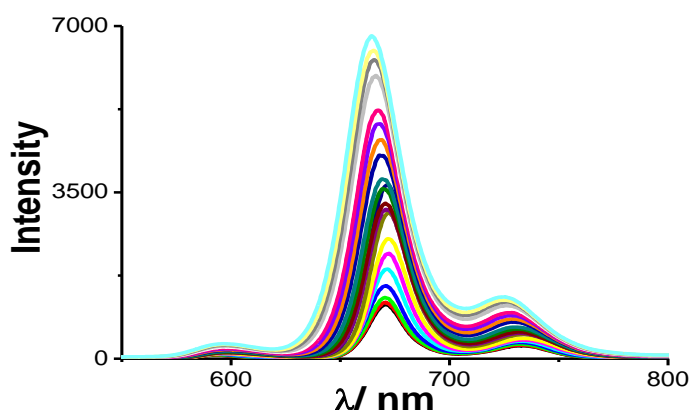


Figure 4.9. Temperature effect recorded for **DYA1** in MTHF over the range 80-290 K. The excitation wavelength was 465 nm, which corresponds to excitation into the DPP chromophore. The intensity increases with increasing temperature.

The fluorescence quantum yields were corrected for changes in density and refractive index as the temperature is varied.²¹ However, for the BODIPY-based acceptor there is a clear trend in that the emission quantum yield increases with increasing temperature. This is most unusual, as typically the opposite trend is observed. This is because processes competing with EET, such as light-induced electron transfer, are switched off at low temperature. The same tendency is observed for the DPP-based donor in MTHF. As the temperature falls slowly, the fluorescence intensity decreases and the emission peak becomes sharper. There is also a change in the emission maximum, recorded in units of wavenumber, as the temperature changes, Figure 4.10. Indeed, the emission maximum nicely tracks the melting of the solvent– the glass transition temperature is seen clearly as a minimum in the energy curve. In the high temperature region, where the solvent is fluid, there is a progressive increase in the energy of the transition as the

temperature rises. Similar effects have been reported previously for conducting polymers and attributed to temperature-induced changes in molecular conformation.

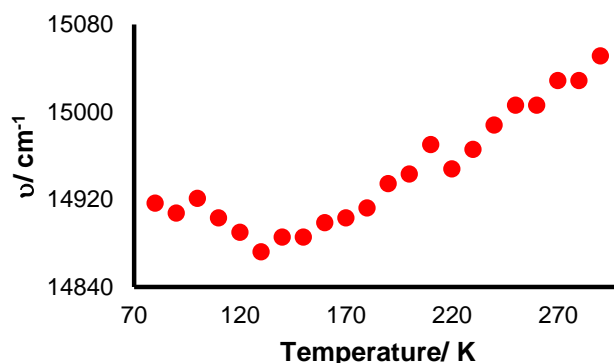


Figure 4.10. Effect of temperature on the emission energy recorded for the BODIPY-based acceptor unit present in **DYA1** in MTHF. The excitation wavelength was 475 nm.

Over the temperature range where MTHF remains fluid, there is a good correlation between the energy of the emission maximum and temperature as displayed in the form of Equation 4.5.^{22,23} Here, E_0 refers to the optical bandgap at low temperature and, from the fit (Figure 4.11), has a value of 1.83 eV. The term ΔE is a fitting parameter that is related to the effective conjugation length of the molecule in the high temperature limit.

$$E_{00}(T) = E_0 + \frac{\Delta E}{\exp(\frac{\epsilon}{k_B T})} \quad \text{Equation 4.5}$$

The form of Equation 4.5 has been developed for better understanding the temperature dependence of polymers and oligomers constructed from materials of interest in organic solar cells. The variation in the optical bandgap with increasing temperature can be ascribed to an increasing tendency for the styryl groups to move out of planarity with the dipyrin unit. It is interesting to note that further cooling after the freezing point ($T = 137$ K) causes the optical bandgap to increase slightly. The solvent hardens over the temperature range from 137 K to ca. 105 K

before forming a rigid glass at around 100 K. Our results suggest that the bandgap is independent of temperature in the rigid glass but slightly affected by the contraction of the solvent in the isotropic region.

An alternative explanation is that the emission maximum depends on solvent polarity. This possibility arises because the dielectric constant of the solvent evolves with temperature. To exclude this as being the factor responsible for the blue shift noted on increasing the temperature, a small series of solvents were used to study the photophysical properties of **ACC**. This study will be described later in the chapter.

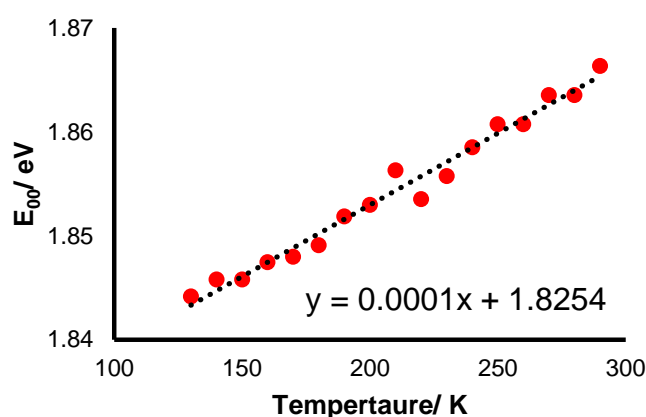


Figure 4.11. Correlation between the energy of the emission maximum (E_{00}) and temperature as displayed in the form of Equation 4.5.

Returning to the experimental data presented in Figure 4.9, we might suppose that there is some kind of solubility problem as the temperature decreases. This issue could be a consequence of the long polyethylene glycol chains attached to the BODIPY dye since we have not encountered the same problem with other dyes. It is possible that the polyethylene glycol chains are interacting with other BODIPY molecules forming small agglomerates. To this effect, we measured the fluorescence quantum yield for the BODIPY reference, **ACC**, over the same range of temperature. It follows the same pattern as found for the dyad. This further suggests that the polyethylene glycol chains might be responsible for inducing quenching of emission. It also indicates that the temperature effect is not

associated with changes in the EET probability. It might be noted that solutions of **ACC** in MTHF did not give rise to laser scattering.

In order to test this solubility hypothesis, a micellar solution of **DYA1** was prepared using Triton X-100 neutral micelles. The basic idea was that the BODIPY segment of the molecule would be incorporated into the interior of the micelle and this would prevent 'aggregation' of dye molecules. If this were so, we would expect to see an increase in the emission quantum yield. This however did not work as planned. The QY for **DYA1** embedded in the micelle solution turned out to be relatively low at 11%.

Another experiment designed to either prove or disprove this so-called solubility hypothesis involved depositing a solution of **DYA1** in a long chain alcohol solvent, in this case octanol, on a nylon membrane filter. The membrane was left to dry on top of an oven for a few hours and the emission spectrum of the compound was recorded. The pore size of the membrane filter was 0.2 μm . The molecules trapped inside the membrane pores are expected to quickly aggregate; this, in turn, would lead to diminishing emission from the fluorophore.

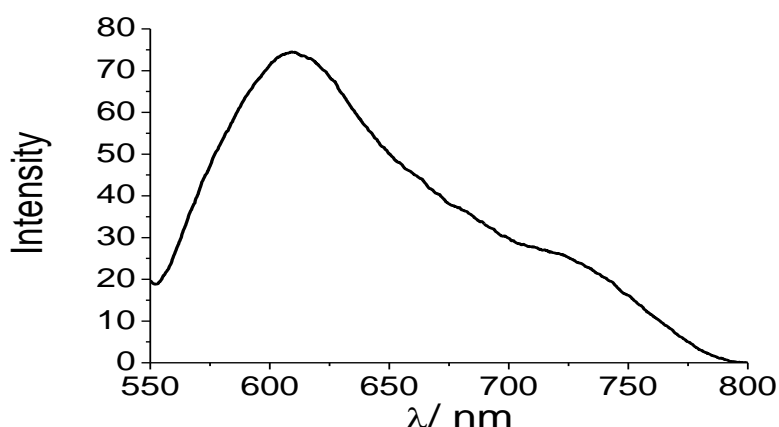


Figure 4.12. Emission spectrum recorded for **DYA1** after deposition on a nylon membrane.

The membrane-bound dye exhibits a broad emission spectrum with clear signs of scattering, Figure 4.12. The emission maximum lies at 610 nm, which is considerably red shifted in contrast to the donor reference compound, where the

peak is found at 542 nm. The peak is blue-shifted relative to fluorescence recorded for monomeric **ACC** in solution. One possibility for the emission spectral profile seen in the membrane is that the **ACC** units are in sufficiently close contact to undergo excitonic coupling. In this case, according to the Kasha theory,²⁴⁻²⁶ the monomer absorption transition is split into higher and lower energy transitions. Emission is usually observed only from the lower energy transition and could be responsible for the band seen at around 725 nm. This is red-shifted relative to the monomer emission found in solution. Forming a dimer would affect the fluorescence quantum yield and would also have important implications for EET from the DPP terminal. Since the fluorescence maximum found for DPP depends on the nature of the surrounding medium, it is possible that the 610 nm band found in the membrane is due to the donor.

4.2.4 Solvent Effects

The photophysical properties of the three dyads were investigated in a small range of solvents in order to examine the effect of solvent polarity on the emission quantum yield and excited-state lifetime. The experiments were performed by direct excitation into the DPP unit at 465 nm but with the emission being collected from the **ACC** residue at longer wavelength. The idea behind the experiment is that fast EET along the molecular axis will populate the excited-singlet state localised on **ACC**. In competition to intramolecular EET, the excited state of DPP might enter into charge-transfer interactions with the terminal amine donors. In this respect, **DYA1** can be considered to take the part of a control compound since it lacks the donor functions.

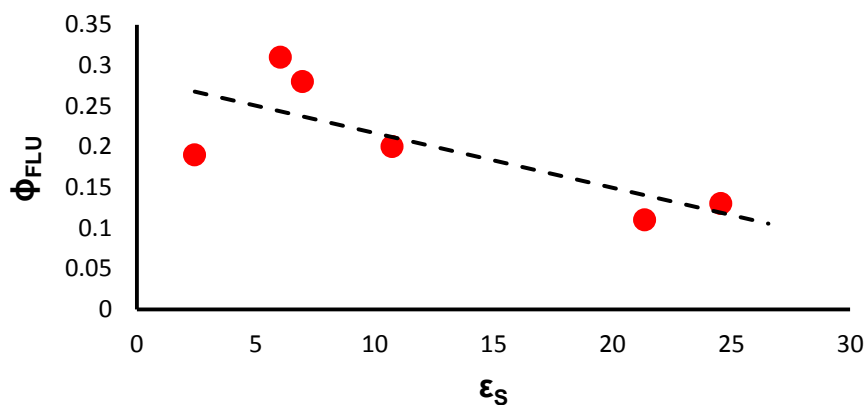


Figure 4.13. Relationship between the emission quantum yield (ϕ_{FLU}) and the solvent static dielectric constant (ϵ_S) as recorded for **DYA1** at room temperature. Excitation populates the DPP unit but emission is recorded for the **ACC** acceptor portion of the molecule. The line drawn through the data points bears no theoretical significance.

Figure 4.13 shows the relationship observed between solvent static dielectric constant (ϵ_S) and the fluorescence quantum yield as recorded for **DYA1**. As the solvent dielectric constant increases the measured quantum yield decreases. The relationship is approximately linear within the limited data set. This is supported by the experimentally determined excited-state lifetimes, Table 4.3. Over the same series of solvents, there are only minor changes in the energies of the absorption and fluorescence maxima and no real variation in the magnitude of the Stokes' shift (Table 4.3). Furthermore, the radiative rate constant remains essentially independent of solvent polarity, except for the situation found with heptyl cyanide which seems strangely anomalous, with a mean value of $11 \times 10^7 \text{ s}^{-1}$. As a consequence, it appears that the non-radiative decay rate constant is responsible for the observed loss of emission in more polar solvents (Table 4.3). The effect is relatively minor but, taken in terms of a molecular-scale rotor, undesirable since it introduces a sensitivity to the nature of the environment. The polarity effect is not caused by competing light-induced charge transfer and, since the quantum yield and lifetime vary in the same manner, it is related to the photophysics of the **ACC** unit. That is to say, the reduced quantum yield does not arise from partial switching-off of the intramolecular EET process. If this were the case, the quantum yield would appear to decrease but the lifetime would remain fixed.

Table 4.3. Photophysical data collected for **DYA1**. EtOAc stands for ethyl acetate, SS stands for Stokes' shift, ϵ is dielectric constant, QY is fluorescence quantum yield.

Solvent	ϵ^{27}	λ_{ABS} / nm	λ_{EM} / nm	SS/ cm ⁻¹	QY	τ / ns	$k_{\text{RAD}}/$ $\times 10^7$ s ⁻¹	$k_{\text{NR}}/$ $\times 10^8$ s ⁻¹
Toluene	2.4	650	665	347	0.19	4.3	4.4	1.9
Chloroform	4.9	648	664	372	0.26	4.9	5.3	1.5
EtOAc	6.0	642	660	425	0.31	4.8	6.5	1.4
MTHF	6.9	645	662	398	0.28	4.7	5.9	1.5
DCM	10.7	647	664	396	0.2	3.9	5.1	2.1
Heptyl Cyanide	17.3	645	666	489	0.23	2.1	10.9	3.7
Acetone	21.4	642	664	516	0.11	2.5	4.4	3.6
Butyronitrile	24.6	644	662	422	0.13	2.7	4.8	3.2

Table 4.3 summarizes the data obtained for **DYA1**. The lifetime decreases as the dielectric constant increases. The changes in absorption and emission maxima are negligible. We also observe only very small changes in the corresponding Stokes' shift. This suggests no substantial change in geometry and polarity between ground and excited states.²⁸ Since the Stokes' shift is independent of solvent polarity, it can be concluded that there is no CT character at the S₁ level of the acceptor.²⁹ There is no obvious trend emerging in either absorption or emission maxima. The small variations observed for **DYA1** due to multiple with its local environment like H-bonding, Figure 4.14.³⁰ The solvent effect might be expected to be more significant in the more complicated cases, shifts are expected in the emission spectrum. However, absorption spectra are not as sensitive to solvent effects.

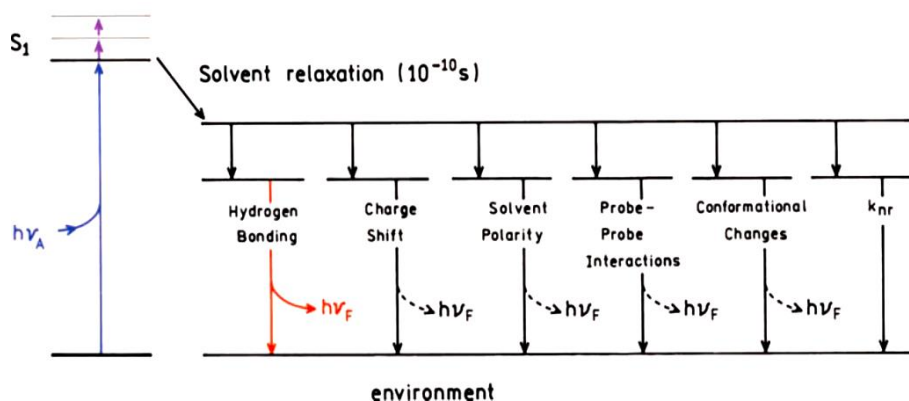


Figure 4.14. Illustration of the different ways solvent can affect the emission from a fluorophore. Image adapted from 'Principles of Fluorescence' by J.R. Lakowicz, 2006.³⁰

The quantum yields and lifetimes follow the same trend in as much as they increase as the solvent polarity decreases. Except for heptyl cyanide, which is clearly anomalous, the radiative rate constants are essentially independent of solvent polarity. This is not the case for the corresponding non-radiative rate constant, which increases steadily as the solvent polarity increases. Exactly the same trend is exhibited by the two more complicated dyads. We note that there are other ways to express solvent polarity but the scarcity and spread of data precludes a detailed comparison of the different quantitative measures of the solvent properties. The data, however restricted, can be used to argue that there is a competing process in polar media that leads to loss of emission from the acceptor unit. Much the same behaviour is observed for the two triads, Figure 4.15 and Figure 4.16, where it appears that the loss of emission occurs over a range of weakly polar solvents but tends towards saturation in more polar media. The underlying trends are obscured to a large extent by the spread in the data, perhaps caused by specific solvent effects or multiple effects. In all cases, the excited-state lifetime and quantum yield respond in the same way to variations in solvent polarity. For **ACC**, there is no obvious reason why the radiative rate constant should depend on solvent polarity since the chromophore is not particularly polar. The loss of fluorescence, therefore, is attributed to increased significance of the non-radiative process. This has nothing to do with the presence of the terminal donor units. Such behaviour has been reported for other systems where light-induced charge transfer is

thermodynamically hindered. Thus, in cases where $\Delta G = 0$ in nonpolar solvent, the process can be promoted by moving towards a polar medium.³¹ With this in mind, we have examined the likelihood for light-induced charge transfer between the chromophores using electrochemical data.

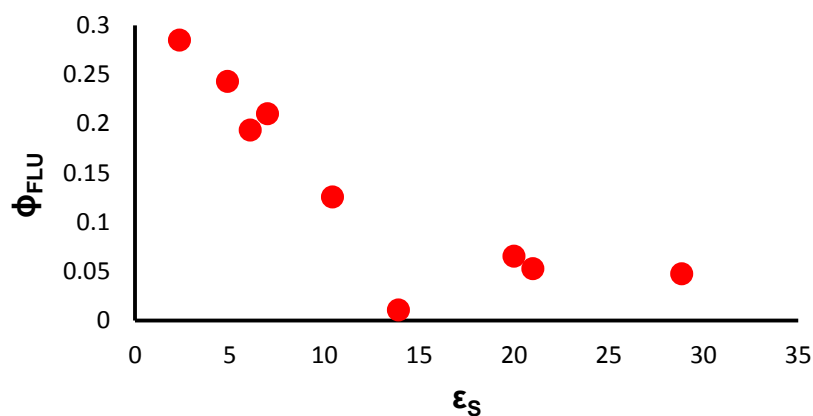


Figure 4.15. Effect of solvent dielectric constant (ϵ_s) on the fluorescence quantum yield (Φ_{FLU}) recorded for **TRI2**.

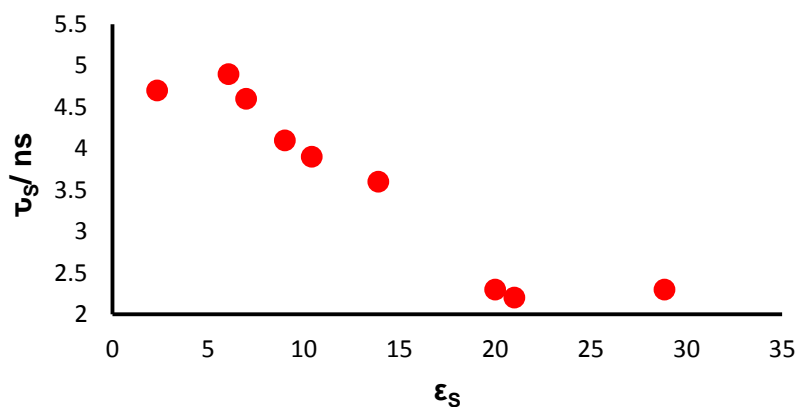


Figure 4.16. Relationship between the singlet-excited state lifetime (τ_s) measured for **TRI1** and the solvent dielectric constant (ϵ_s).

Cyclic voltammograms were recorded by our collaborators in Strasbourg and published as part of the synthetic details in *J. Org. Chem.* **2015**, 80, 6737. The half-wave potentials were measured in deaerated dichloromethane at room temperature; a Pt working electrode was used and the background electrolyte was Bu₄N.PF₆ (0.1 M). The output is presented in Table 4.4. At the time of recording

the electrochemistry, no proper assignments could be made but we were able to complete this task using our computed molecular orbital description for the multi-component molecules and also for the reference compounds.

Table 4.4. Compilation of the electrochemical data collected in deaerated dichloromethane at room temperature. Electrolyte used was $n\text{Bu}_4\text{N}.\text{PF}_6$. Potentials were standardized versus ferrocene (Fc) as internal reference³² and are quoted relative to SCE.

	$E^0(\text{ox, soln}) \text{ (V)},$ $\Delta E \text{ (mV)}$	$E^0(\text{red, soln}) \text{ (V)},$ $\Delta E \text{ (mV)}$
DYA1	+0.67 (60), +1.09 (irr.)	-1.15 (90) -1.25 (60)
TRI1	+0.66 (60), +0.92 (70), +1.16 (60)	-1.20* (irr.)
TRI2	+0.64* (60), +1.19 (irr) , +1.36 (70) +1.50 (irr.)	-1.14 (60), -1.23 (60), -1.75 (irr.)

DYA1 exhibits two oxidation waves, the one at +0.67 V vs SCE is attributed to one-electron oxidation of the BODIPY unit whereas the one at +1.09 V vs SCE is assigned to one-electron oxidation of the DPP dye. Interpretation of the oxidative patterns becomes more complicated for **TRI1** because of the appended TPA unit. This latter fragment has a half-wave potential of +1.16 V vs SCE. Oxidation is further complicated when TPA is replaced with $\text{TPA}(\text{OMe})_2$ in **TRI2**. Here, we observe a two-electron wave centred at +0.64 V vs SCE that is thought to be two overlapping waves corresponding to the successive oxidation of the BODIPY and $\text{TPA}(\text{OMe})_2$ units.

The reduction of **TRI1** consists of an irreversible, two-electron peak centred at -1.20 V vs SCE. This has been assigned to overlapping waves associated with the individual reduction of the BODIPY and DPP units. For **TRI2**, we see two reduction peaks in close proximity, both of which are electrochemically reversible. These waves are accredited to formation of the π -radical anions of the BODIPY and DPP residues. This is also the case for **DYA1**.

Our interest in the electrochemistry of these compounds rests with the concept of light-induced charge transfer along the molecular axis. Our collaborators in Strasbourg had recorded the cyclic voltammograms as part of their work on the synthesis and characterization of the various compounds. We have interpreted the cyclic voltammograms in as much as it is possible to delineate individual processes when separate units are oxidized or reduced at comparable potentials. The electrochemistry results can now be utilized to calculate thermodynamic driving forces for light-induced electron transfer between the various subunits, Equation 4.6.³³⁻³⁵

$$\Delta G_{CT} = e(E_{ox} - E_{red}) - E_{xs} - E_{es} - E_{sol} \quad \text{Equation 4.6}$$

On the basis of all available evidence, it can be concluded that charge transfer between DPP and BODIPY units is unlikely to occur in non-polar solvents, Figure 4.17. However, there is a favourable driving force for charge transfer between the TPA and DPP units; we find ΔG values of -0.029 eV for **TRI1** and -0.49 eV for **TRI2**.

While analyzing the data it also appears that light-induced charge transfer from TPA to BODIPY unit is favourable with $\Delta G = -0.2$ eV but only for **TRI2**.

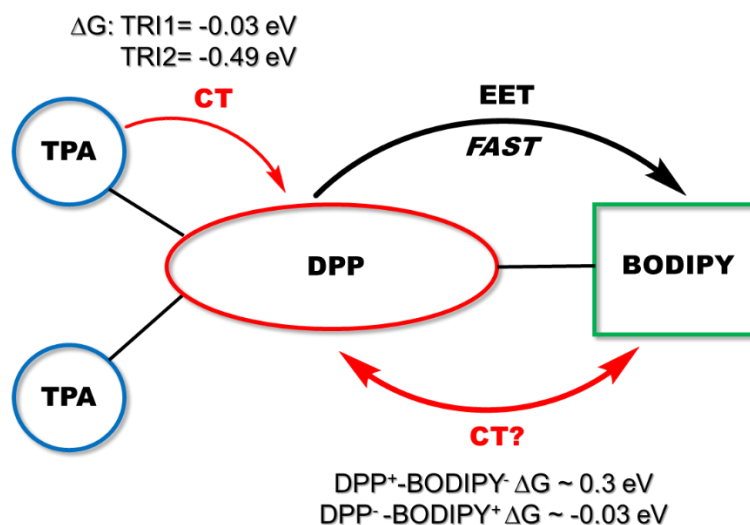


Figure 4.17. Scheme to demonstrate the range of processes occurring in **TRI1** and **TRI2**. The manifestation of charge transfer from BODIPY to DPP unit is strongly solvent dependent.

The key finding to emerge from these studies is that light-induced electron transfer from the excited-singlet state of **ACC** to the nearby DPP is very weakly exergonic in dichloromethane solution. The driving force, calculated in the absence of electrostatic effects, is close to zero (Figure 4.17). None-the-less, because there are no competing processes that shorten the excited-singlet state lifetime of the **ACC** unit, intramolecular charge transfer will contribute towards deactivation of the excited state. Under these conditions where the thermodynamics are so finely balanced, the environmental terms will make a major contribution to the overall driving force for charge transfer. These terms, E_{ES} and E_{SOL} , refer to the electrostatic energy, calculated from Equation 4.7 where R_{CC} is the centre-to-centre separation distance between **ACC** and DPP units, and a correction for the reduction potentials being measured in a different solvent. This latter term can be calculated from Equation 4.8, which was first developed by Weller.³⁶ As with all expressions concerned with electrostatic effects, the energy terms tend to saturate as ϵ_{S} approaches 12. Strongly polar solvents offer no further benefit. This is precisely the effect that we see underlying Figure 4.18 where either the

fluorescence quantum yield or excited-state lifetime decrease with increasing dielectric constant. As such, we attribute the polarity effects noted for the acceptor unit present in the dyad and triads as being due to light-induced charge transfer from **ACC** to DPP. The rate is relatively slow, because of the weak driving force, but accounts for about 50% of the exciton population in polar media.

$$E_{ES} = \frac{e^2}{(4\pi\epsilon_0)\epsilon_s R_{CC}} \quad \text{Equation 4.7}$$

$$E_{SOL} = \frac{e^2}{8\pi\epsilon_0} \left(\frac{1}{R_D} + \frac{1}{R_A} \right) \left(\frac{1}{\epsilon_{ref}} - \frac{1}{\epsilon_s} \right) \quad \text{Equation 4.8}$$

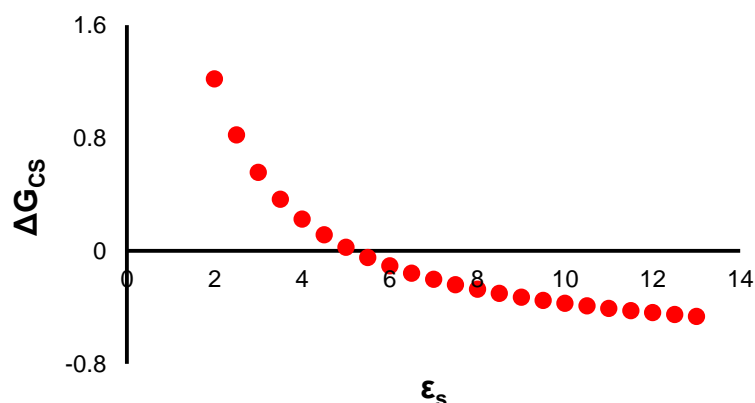


Figure 4.18. A simulation to demonstrate how the driving force for charge separation (ΔG_{cs}) varies with solvent dielectric constant (ϵ_s), simulation performed for a DPP-BODIPY based system, inspired by work by J.W. Verhoeven *et al.* on the interplay between structure and environment of the charge-separated state.³⁷

4.3 Conclusions

In this chapter we have sought to enquire into the possibility of equipping a prototypic molecular-scale rotor with improved optical properties, most notably the capability to absorb over a wide spectral window. Our reasoning is that a cheap, practical sensor would need to avoid the necessity for highly selective excitation wavelengths. The approach taken has involved constructing a molecular dyad comprising two complementary chromophores, in this case DPP and an expanded BODIPY dye, that communicate by way of rapid intramolecular EET. In this way, there is only a single emitter but absorption occurs over much of the visible region. The molecules studied here lack the rotor function but this is easily restored by omitting the blocking groups on the upper rim of the dipyrroin unit. As a final piece of the overall picture, we opted to include a competing light-induced charge-transfer reaction by attaching terminal amine donors to the DPP chromophore (Figure 4.1). The net result is an intricate and elaborate multi-component molecule. The performance of these supermolecules was disappointing to say the least. In fact, the design actually worked as planned with effective EET and competing charge transfer. The problems came about because of restricted solubility, probably caused by the overemphasis on the number of poly(ethylene glycol) residues added to improve solubility, and undesired charge transfer between the chromophores. There is plenty of scope to improve the system by optimizing the DPP chromophore⁵ or by further functionalization of the BODIPY dye.^{28,38,39} One such modification has been described by Zissel *et al.*⁵ where they replaced the phenyl rings attached to the DPP core by thiols in order to improve the photochemical stability of the material.

The limited solubility of the arrays at low temperature could be overcome by further synthesis and this feature might not be insurmountable. More importantly, we observed that a new channel has been opened that favours intramolecular charge transfer between the primary chromophores. The rate of this latter process is slow, because of poor thermodynamics, and does not prevent using emission from the final acceptor for sensing applications. The real problem is that we have introduced a marked sensitivity towards changes in the polarity of the local surroundings. In

effect, the supermolecule could be used only in non-polar media. Undeterred by these difficulties, we introduce a larger molecular edifice in the next chapter and consider in more detail the interplay between the various subunits. This is done in order to gain a better understanding of the intricate processes at play. Obtaining control over these various short-circuits and competing processes is essential if we are to properly design and implement multi-component molecules capable of performing useful tasks under illumination.

4.4 References

- (1) Andrews, D. L. *J. Mater. Res.* **2012**, 27, 627.
- (2) Ziessel, R.; Harriman, A. *Chem. Commun.* **2011**, 47, 611.
- (3) Delphine Hablot, P. R., Raymond Ziessel *Chem. Eur. J.* **2010**, 16.
- (4) Ulrich, G.; Ziessel, R.; Harriman, A. *Angew. Chem. Int. Ed. Engl.* **2008**, 47, 1184.
- (5) Heyer, E.; Ziessel, R. *J. Org. Chem.* **2015**, 80, 6737.
- (6) Wang, B.-C.; Liao, H.-R.; Chang, J.-C.; Chen, L.; Yeh, J.-T. *J. Lumin.* **2007**, 124, 333.
- (7) Wu, J.-H.; Chen, W.-C.; Liou, G.-S. *Polym. Chem.* **2016**, 7, 1569.
- (8) Loudet, A.; Burgess, K. *Chem. Rev.* **2007**, 107, 4891.
- (9) Koziar, J. C.; Cowan, D. O. *Acc. Chem. Res.* **1978**, 11, 334.
- (10) Harriman, A. *J. Chem. Soc. Faraday Trans.* **1981**, 77, 1281.
- (11) Andrews, D. L.; Curutchet, C.; Scholes, G. D. *Laser Photon. Rev.* **2011**, 5, 114.
- (12) Berney, C.; Danuser, G. *Biophys. J.* **2003**, 84, 3992.
- (13) Scholes, G. D.; Fleming, G. R. *J. Phys. Chem. B* **2000**, 104, 1854.
- (14) Scholes, G. D. *Annu. Rev. Phys. Chem.* **2003**, 54, 57.
- (15) Kuhn, H. *J. Chem. Phys.* **1949**, 17, 1198.
- (16) Krueger, B. P.; Scholes, G. D.; Fleming, G. R. *J. Phys. Chem. B* **1998**, 102, 5378.
- (17) Hedley, G. J.; Ruseckas, A.; Benniston, A. C.; Harriman, A.; Samuel, I. D. W. *J. Phys. Chem. A* **2015**, 119, 12665.
- (18) Stryer, L.; Haugland, R. P. *Proc Natl Acad Sci U S A* **1967**, 58, 719.
- (19) Wu, P. G.; Brand, L. *Anal. Biochem.* **1994**, 218, 1.

- (20) Strickler, S. J.; Berg, R. A. *J. Chem. Phys.* **1962**, 37, 814.
- (21) Zoon, P. D.; Brouwer, A. M. *Photochem. Photobiol. Sci.* **2009**, 8, 345.
- (22) da Silva, M. A. T.; Dias, I. F. L.; Duarte, J. L.; Laureto, E.; Silvestre, I.; Cury, L. A.; Guimarães, P. S. S. *J. Chem. Phys.* **2008**, 128, 094902.
- (23) Hemley, R.; Kohler, B. E. *Biophys. J.* **1977**, 20, 377.
- (24) Kasha, M. *Radiat. Res.* **1963**, 20, 55.
- (25) Spano, F. C. *Acc. Chem. Res.* **2009**, 43, 429.
- (26) Hader, K.; May, V.; Lambert, C.; Engel, V. *Phys. Chem. Chem. Phys.* **2016**, 18, 13368.
- (27) Abboud, J. L. M.; Notario, R. *Pure Appl. Chem.* **1999**, 71, 645.
- (28) Harriman, A.; Rostron, J. P.; Cesario, M.; Ulrich, G.; Ziesel, R. *J. Phys. Chem. A* **2006**, 110, 7994.
- (29) Harriman, A.; Ziesel, R. *Photochem. Photobiol. Sci.* **2010**, 9, 960.
- (30) Lakowicz, J. R. *Principles of Fluorescence Spectroscopy*, 3rd ed.; Springer, 2006.
- (31) Grabowski, Z. R.; Rotkiewicz, K.; Rettig, W. *Chem. Rev.* **2003**, 103, 3899.
- (32) Archer, M. D. *J. Appl. Electrochem.* **1975**, 5, 17.
- (33) Miller, S. E.; Lukas, A. S.; Marsh, E.; Bushard, P.; Wasielewski, M. R. *J. Am. Chem. Soc.* **2000**, 122, 7802.
- (34) Kendrow, C.; Baum, J. C.; Marzzacco, C. J. *J. Chem. Educ.* **2009**, 86, 1330.
- (35) Warman, J. M.; Smit, K. J.; Jonker, S. A.; Verhoeven, J. W.; Oevering, H.; Kroon, J.; Paddon-Row, M. N.; Oliver, A. M. *Chem. Phys.* **1993**, 170, 359.
- (36) Gaines, G. L.; O'Neil, M. P.; Svec, W. A.; Niemczyk, M. P.; Wasielewski, M. R. *J. Am. Chem. Soc.* **1991**, 113, 719.

- (37) Kroon, J.; Verhoeven, J. W.; Paddon-Row, M. N.; Oliver, A. M. *Angew. Chem. Int. Ed.* **1991**, 30, 1358.
- (38) Ulrich, G.; Barsella, A.; Boeglin, A.; Niu, S.; Ziesel, R. *Chemphyschem* **2014**, 15, 2693.
- (39) Ziesel, R.; Ulrich, G.; Harriman, A. *New J. Chem.* **2007**, 31, 496.

Chapter 5. A Bifurcated Molecular Pentad Capable of Sequential Electronic Energy Transfer and Intramolecular Charge Transfer

5.1 Introduction

In attempting to mimic certain features of natural photosynthesis, especially with respect to the fundamental processes leading to charge separation, an inordinately wide diversity of molecular systems has been examined. In the main, these materials are intended to exhibit directed electronic energy transfer (EET) along the molecular axis by way of positioning chromophores according to their respective excitation energies, creating a molecular funnel.¹⁻⁴ Other molecular systems have been designed to duplicate the efficient light-induced charge transfer (CT) inherent to the natural reaction centre complex.⁵⁻⁷ In studying such molecules, much fundamental information has been learned about the factors that control the dynamics of EET and/or CT in artificial systems, although many of the subtleties of the living organism have evaded capture in the form of an artificial analogue. Less attention has been given to the study of molecular architectures that successfully combine EET and CT at the same site, even though certain structures are able to achieve this feat. In particular, the vast plethora of molecular dyads, triads, tetrads, etc. known to realise a cascade of EET steps contains few examples where the terminal energy acceptor is linked to a redox centre in such a way that charge-transfer chemistry can take place. We now describe a large molecular pentad (**PEN**) as a prototype of this generic field of hybrid EET/CT molecular multicomponent assemblies. Our specific interest in such molecular systems is to engineer photochemical heat engines that might be suitable for solar heating of domestic water supplies. To be successful, this approach requires serious input

from an engineering viewpoint but here we highlight only the underlying chemistry. Other researchers in our group are developing the appropriate circuitry for coupling the photochemistry to a heat sink. Our biggest concern relates to the stability of multi-component organic molecules under continuous illumination with sunlight. In natural photosynthesis, the elaborate light-harvesting machinery is protected against light-induced damage by repair mechanisms and photo-regulation processes. In the long term, it will be necessary to build such complex features into artificial analogues but we are not yet at that stage of development. Our approach here is to design a system with multiple components but to ensure that rapid electronic energy transfer occurs to generate an excited state resident on the terminal acceptor. This strategy keeps the excited state lifetimes very short for all components except for the final acceptor. In principle, this will be the only component susceptible to photochemical damage. We now enquire if this premise is met.

The target system **(1)** comprises two individual control compounds, Figure 5.1. Specifically, **(1)** consists of two pyrene (**PYR**) residues attached via the boron atom to a conventional boron dipyrromethene (**BODIPY**) dye. The latter unit is well known to serve as an acceptor for excitation energy localised momentarily on one of the pyrene fragments. In contrast, **(2)** is an expanded boron dipyrromethene dye, which will be referred to as **ExBOD** throughout this chapter, intended to function as the final acceptor for excitation energy transferred along the molecular axis. Compound **(2)** differs from BODIPY by way of increased π -conjugation provided by the styryl functions attached at the 3,5-positions to **BODIPY** through the respective pseudo-meso site. This type of connection, when used in conjunction with methyl groups at the 1,7-positions, ensures that each meso-phenylene ring lies essentially orthogonal to the dipyrroin core. The styryl fragments are equipped with a triphenylamine (TPA) residue that is known to be rather easily oxidised in polar solvents. The final piece of the structure consists of a dithiocyclopentane (DTC) unit intended to act as a conduit for charge transfer from TPA to **ExBOD**. The overall molecule, **(3)**, referred to as **PEN** throughout this chapter, adopts a bifurcated geometry because of the nature of the connections and possesses a fully extended length of 47 Å. This molecule is surprisingly soluble in common organic solvents at room temperature and maintains electronic isolation for each

of the five critical components. The three main chromophores, namely **PYR**, **BODIPY** and **ExBOD**, combine to harvest light over the wavelength range from 250 to 800 nm while the DTC fragments provide additional protection against incoming UV photons. The chromophores have been arranged according to their respective excitation energy levels, creating a clear spectroscopic gradient (**PYR**>**BODIPY**>**ExBOD**) to favour a cascade of EET steps following from selective excitation of pyrene.

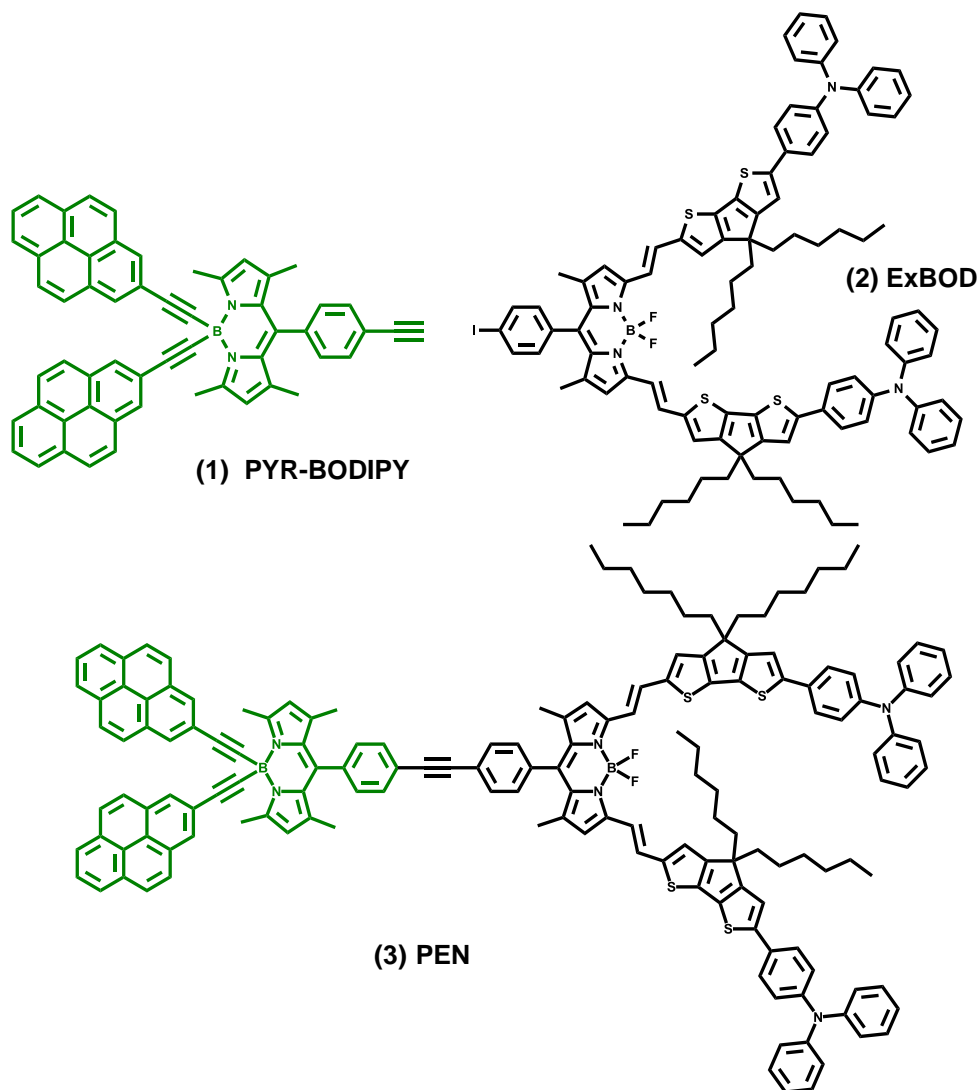


Figure 5.1. Molecular formulae of the two control compounds: donor (**PYR-BODIPY**), acceptor (**ExBOD**) and the combined donor-acceptor molecule (**PEN**).

5.2 Results and Discussion

5.2.1 Photophysical Data

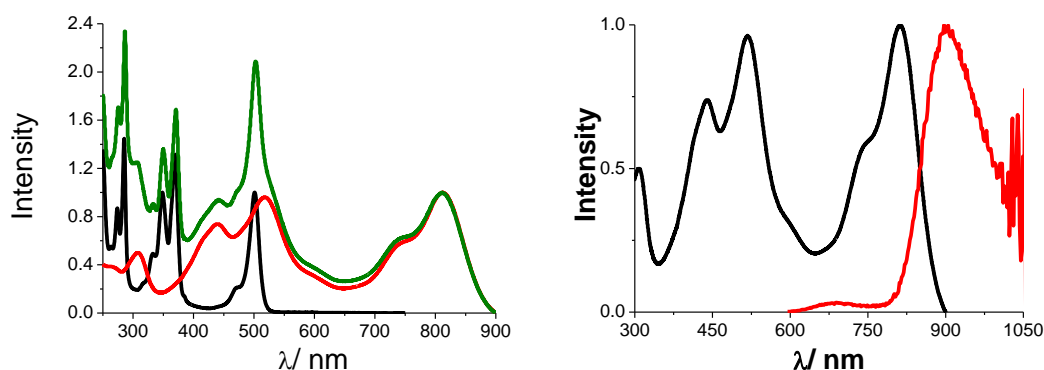


Figure 5.2. Left panel: absorption spectra recorded for (1) in black, (2) in red and (3) in green in dichloromethane. Right panel: Absorption and emission spectra recorded for **ExBod** in DCM solution.

Absorption and emission spectra were recorded in DCM for all three compounds. The spectrum derived for **PEN** is a sum of its individual components and this demonstrates that there is little if any electronic communication between **PYR-BODIPY** (black curve) and **ExBOD** (red curve), Figure 5.2. The strong absorption transitions associated with pyrene at 276, 286, 351 and 371 nm can clearly be observed with **PEN** as well, however they are contaminated with absorption from **ExBOD**. Within the **PYR-BODIPY** there is contamination of pyrene transitions by **BODIPY** itself.⁸ Looking at the absorption spectral profile recorded for **PEN** it is impossible to identify transitions associated with either TPA or DTC fragments. This mutual electronic isolation is most likely achieved because of the orthogonal phenyl rings. The far-red emission spectra and lifetimes of **ExBOD** and the final **PEN** molecule were recorded by Dr Anna Gakamsky, Edinburgh Photonics. A fully-corrected, high radiance integrating sphere was used to determine the fluorescence quantum yield as there is no reliable reference for the far-red region.⁹⁻
¹¹ The **PYR-BODIPY** reference compound has been characterized previously by Harriman *et al.*¹²

Table 5.1 summarizes the photophysical properties of the studied compounds. **PYR-BODIPY** appears to have typical properties expected of a BODIPY-type dye. It is well known that EET from pyrene to BODIPY is very efficient, occurring with a probability close to unity for closely-spaced reagents,^{13,14} while exciting into a pyrene unit no emission associated with it appears, all of the emission appears to come for the S₁ state of the BODIPY core.

The properties of **ExBOD** are more unusual. According to the energy-gap law, we expect the non-radiative rate constant to increase as the energy gap decreases.¹⁵⁻¹⁸ It appears that both **ExBOD** and **PEN** follow this trend, as the rate of non-radiative decay is quite high for both compounds and approximates to $40 \times 10^8 \text{ s}^{-1}$ while the radiative rate constant is rather low at $\approx 0.5 \times 10^8 \text{ s}^{-1}$. The only emission observed for **PEN** is that from **ExBOD** and there is none observed from the donating **PYR-BODIPY** unit. This suggests to us that the probability of EET is close to unity, even though the overlap integral is relatively small. The emission quantum yield and excited-state lifetime recorded for **ExBOD** and **PEN** are closely comparable.

Table 5.1 Summary of photophysical data for **PYR-BODIPY**, **ExBOD** and **PEN** in DCM at room temperature (RT).

	PYR-BODIPY	ExBOD	PEN
$\lambda_{\text{abs}}/\text{nm}$	501	810	502/ 810
$\lambda_{\text{em}}/\text{nm}$	517	908	908
ϕ	0.57	0.013	0.011
τ/s^{-1}	3.3	0.24	0.26
$k_{\text{RAD}}/10^8 \text{ s}^{-1}$	1.7	0.53	0.4
$k_{\text{NR}}/10^8 \text{ s}^{-1}$	1.3	41.1	38.1
SS/cm^{-1}	618	1332	1332
f	0.673	0.57	
J			0.0059

5.2.2 Photolysis

The photochemical stability of **PEN** has been studied in deaerated DCM solution at ambient temperature. The main aim of the experiment was to establish whether it is possible to develop an artificial light-harvesting antenna using this type of molecular architecture.¹⁹ We have opted to use white light illumination, rather than monochromatic light, in order to simulate exposure to sunlight. It is realized that this approach exposes any intermediates generated during early stages of photodegradation to further reaction.

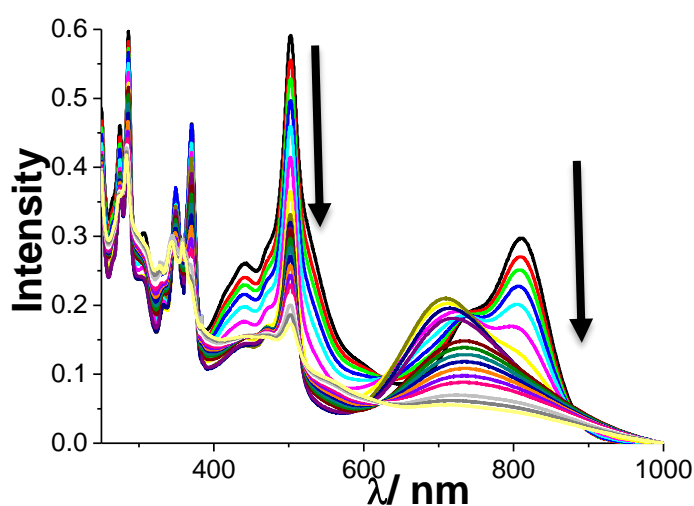


Figure 5.3. Effect of continuous illumination of **PEN** with white light in deaerated DCM recorded at regular intervals over ten hours.

Looking at Figure 5.3, it is apparent that illumination with white light causes bleaching of the **ExBOD** chromophore at 810 nm as well as simultaneously bleaching the peak at 501 nm associated with the BODIPY donor. It has an appearance of an auto-catalytic reaction. Multiple isosbestic points can be observed.

The photolysis was carried out in front of the 450W solar light illuminator. The solution used for photolysis was thoroughly deaerated and the cuvette holding the

sample was sealed. The solvent used was DCM. Figure 5.4 shows that **PEN** can absorb a significant proportion of the solar light emitted by the illuminator.

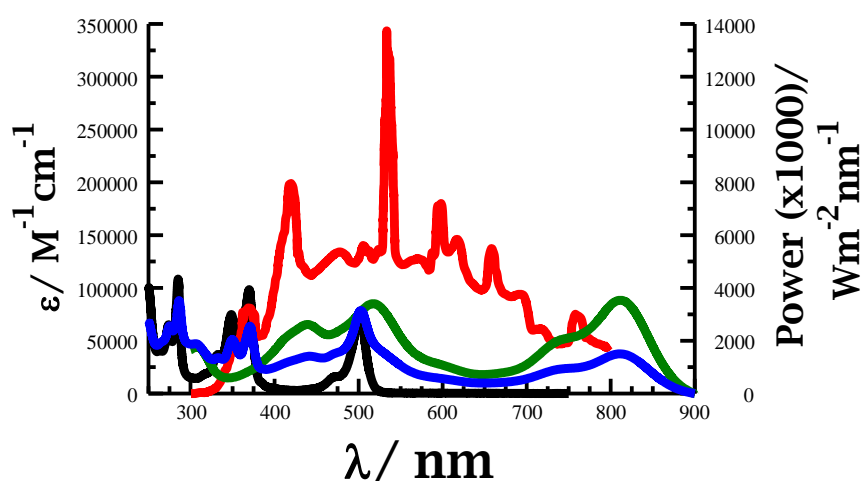


Figure 5.4. Overlap of the absorption spectra recorded for **PEN** (green curve), **ExBOD** (blue curve) and **PYR-BODIPY** (black curve) with the output of the 450W solar illuminator used during the photolysis process (red curve).

Equation 5.1 is used to model the auto-catalytic bleaching process observed with **PEN**.²⁰ Here, rate refers to the rate of photo-bleaching at a certain wavelength in units of $\mu\text{M min}^{-1}$. The actual rate at time, t , was determined as the tangent to a plot of three consecutive time intervals. The terms k_0 and k_c refer, respectively, to the first-order rate constant for bleaching that would be expected in the absence of the auto-catalytic step and to the rate constant for the auto-catalytic process. The concentration of chromophore is designated $[A]$ and has units of μM . Analysis across the entire spectral window allows derivation of k_0 and k_c , respectively, as being 0.0012 min^{-1} and $0.0049 \mu\text{M}^{-1} \text{ min}^{-1}$.

$$\frac{\text{rate}}{[A]} = (k_0 + k_c[A_0]) - k_c[A] \quad \text{Equation 5.1}$$

It can also be seen from the spectral traces that bleaching of **ExBOD** gives rise to a broad charge-transfer absorption band centred at 710 nm. Bleaching of the 710nm absorption band can be approximated to a first-order process with a rate constant of 0.0032 min^{-1} . At 502 nm, both **ExBOD** and **PYR-BODIPY** make

significant contributions to the total absorbance. On longer time scales, the BODIPY chromophores undergoes slow bleaching by approximately first-order kinetics with a rate constant of 0.0019 min^{-1} . It is not practical to monitor bleaching rates for the pyrene chromophore because we determined there was a build-up of a permanent product in the near-UV region. This latter species, which importantly remains fluorescent, bleaches very slowly under white-light illumination.

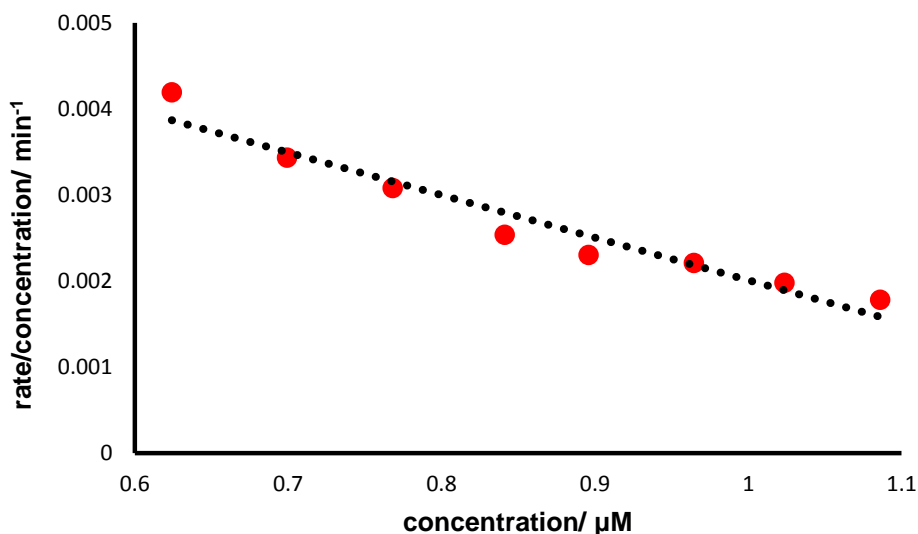


Figure 5.5. Example of a kinetic plot for photo-bleaching of **PEN** in deaerated DCM. It shows a fit to an auto-catalytic process for bleaching of the 811 nm band.

Attempts were made to follow the bleaching process for **PEN** using 700-MHz ^1H -NMR spectroscopy on a dilute solution (ca. 10^{-4} M). In order to make the identification process easier we also recorded the ^1H NMR spectra of the reference compounds; **PYR-BODIPY** and **ExBOD**. From the data, some general conclusions can be drawn however the final product is a complex mixture of compounds. It appears that the pyrene part of the **PEN** chromophore is not damaged at a significant level, according to analysis of the diagnostic signal of the pyrene moiety at 8.63 ppm in deuterated DCM. The most fragile part of the molecule, as might be expected, is the **ExBOD** fragment which undergoes major modifications of the π -pyrrolic protons. This situation most likely reflects attack of the vinylic system. Several new products are formed as can be testified by the presence of at least

three new singlets around 6.0 ppm and new peaks likely assigned, in light of reference compounds, to the DTC fragments. The high intensity of these latter peaks attests to the presence of several products displaying similar molecular frameworks and therefore despite the best efforts we could not identify the final products of the decomposition reaction.

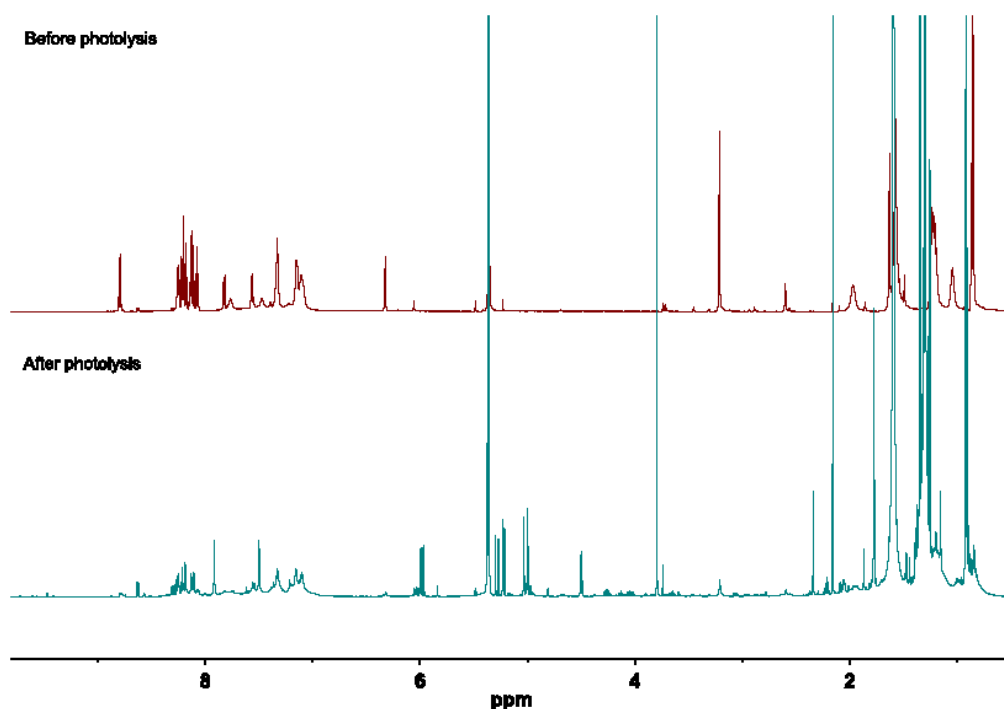


Figure 5.6. Example of ¹H NMR collected in CD₂Cl₂ for **PEN**, the top panel (red) shows spectrum before photolysis, whereas the one on the bottom (green) shows the collected NMR after photolysis.

5.2.3 Charge Transfer

Cyclic voltammetry (CV) data collection was carried out by our collaborators in Strasbourg for **PEN** and both of the control compounds: **ExBOD** and **PYR-BODIPY**. The electrochemistry was performed in deaerated dichloromethane at RT. The background electrolyte used was $n\text{BuN.PF}_6$ (0.1M). The main results are summarized in Table 5.2.

Table 5.2. Electrochemistry was recorded by our collaborators in Strasbourg; Dr. Raymond Ziessel and Dr. Alexandra Sutter. Deoxygenated DCM solution was used to determine potentials by cyclic voltammetry. The electrolyte used was $n\text{BuN.PF}_6$ (0.1M), the solute concentration was ca. 1.5 mM, all spectra were collected at RT. Potentials were standardized versus ferrocene (Fc) as internal reference.²¹

	$E^0(\text{ox, soln})$ (V), ΔE (mV)	$E^0(\text{red, soln})$ (V), ΔE (mV)
PYR-BODIPY	+0.93 (60), +1.39 (irr.)	-1.42 (60)
ExBOD	+0.38 (60), +0.83 (60), +1.00 (60)	-1.00 (70), -1.63 (irr.)
PEN	+0.38 (60), +0.83 (60) , +1.29 (irr.)	-1.02 (70), -1.39 (80), -1.80 (irr.)

The electrochemical data show a rich variety of peaks associated with **ExBod** and **PYR-BODIPY** compounds. For **PYR-BODIPY** we observe two waves. The oxidative wave can be assigned to the reversible formation of the BODIPY π -radical cation, which occurs with $E_{1/2} = 0.93$ V against the SCE. The second wave is associated with the one-electron oxidation of the pyrene units and corresponds to $E_{1/2} = 1.39$ V vs SCE and is electrochemically irreversible. This is consistent with reports in the literature on the electrochemistry of aryl hydrocarbons which form dimer π -radical cations.²² Thus, one-electron oxidation of pyrene forms the

corresponding π -radical cation, which associates with a ground-state pyrene to form the dimer radical cation. It is generally believed that this process is driven by the solvatophobic effect. On reductive scans, there is only a single wave corresponding to formation of the BODIPY π - radical anion. This takes place with a half-wave potential of -1.42 V against the SCE. It might be mentioned that assignment of these various electrochemical steps was made in Newcastle and is based on earlier work with simpler BODIPY-based derivatives.

Oxidative and reductive scans were also carried out for **ExBOD**, under the same experimental conditions. Here, we found two waves on reductive scans. The first reductive wave occurs with a half-wave potential of -1.00 V against SCE. This wave is most likely due to reduction of BODIPY to form the π - radical anion. The second reductive wave is irreversible and has a peak potential located at -1.63 V against SCE. Unfortunately there is insufficient information to assign this irreversible wave with confidence. On the oxidative scans, we observe three successive waves. The first wave is electrochemically reversible and corresponds to a half-wave potential of 0.38 V against SCE. Based on literature precedents and model compounds, we can safely assign this wave to the one-electron oxidation of one of the TPA units. Unfortunately the other two waves cannot be assigned without further information.

Finally, the cyclic voltammetry studies made with **PEN** reveals three oxidative waves with half-wave potentials of 0.38 V, 0.83 V and 1.29 V against SCE. The situation here is similar to that of **ExBOD**. Thus, the wave at 0.38 V is most likely due to oxidation of one or both of the TPA units, however the other two waves cannot be easily distinguished. On the reductive scans, we observe three waves with successive half-wave potentials of -1.02 V, -1.39 V and -1.80 V against SCE. The first two waves are reversible and can be assigned respectively to the one-electron reduction of the BODIPY unit in **PYR-BODIPY** (-1.39 V) and **ExBOD** (-1.02 V). The third irreversible wave is associated with **ExBOD**, however the electrochemistry alone does not indicate exactly where on the **ExBOD** molecule the electron resides.

Analysis of the cyclic voltammetry results, taken together with the optical absorption and fluorescence data, argues against the occurrence of light-induced charge transfer between the two BODIPY-based chromophores following selective excitation into **ExBOD**. This situation is confirmed by the observation that both ϕ_F and τ_S remain insensitive to the presence of the appended BODIPY unit. Thus, although emission from the **ExBOD** fragment in both the control compound and **PEN** appears to be heavily quenched, this is not because of interaction with the nearby BODIPY unit. Instead, quenching of the excited-singlet state of **ExBOD**, in both molecules, is likely to arise from charge transfer from the terminal TPA group, Figure 5.7.

$$\Delta G_{CT} = e(E_{ox} - E_{red}) - E_{xs} - E_{es} - E_{sol} \quad \text{Equation 5.2}$$

There is a modest thermodynamic driving force ($\Delta G = -0.15$ eV) for this process in DCM solution and the interspersed DTC fragment might be expected to function as an effective conduit for intramolecular charge transfer along the molecular axis. This is because the spacer unit is also redox active and could promote through-bond charge transfer by way of super-exchange interactions.²³ It is also important to stress that earlier work²⁴ has described such light-induced charge transfer in somewhat related molecular architectures. The thermodynamic driving force was calculated using Equation 5.2.^{25,26} where the excitation energy for **PEN** is taken to be 1.46 eV.

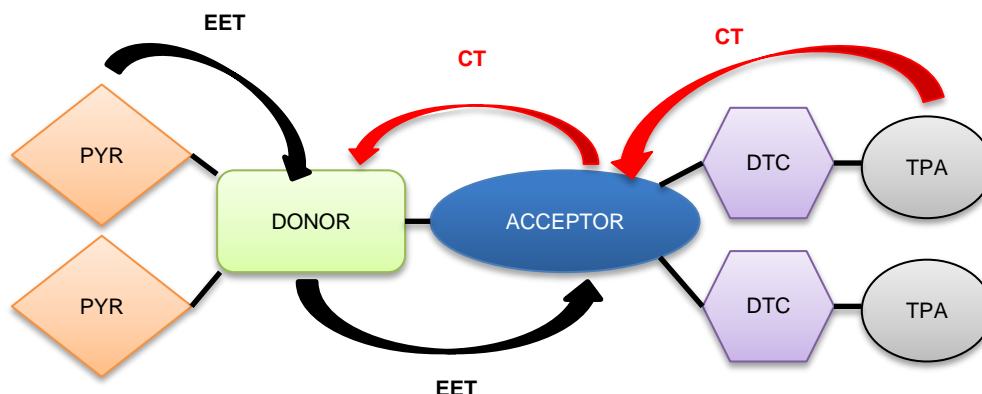


Figure 5.7. A scheme to show the various events that follow from selective excitation into the pyrene units, where: PYR= pyrene, DTC= dithiocyclopentane, TPA= triphenylamine, CT= charge transfer and finally EET= electronic energy transfer.

Pump-probe (FWHM = 120 fs) transient absorption spectroscopy with excitation at 420 nm carried out with **ExBOD** in DCM solution in order to further probe the transient species. It showed the rapid formation of the S_1 state associated with the **ExBOD** chromophore. This assignment can be made on the basis of the pronounced bleaching at 815 nm and the appearance of stimulated emission at 900 nm. Decay of the S_1 state follows first-order kinetics, with a lifetime of 225 ps, to restore the pre-pulse baseline. There is no obvious indication for transient formation of charge- separated species and, in particular, the TPA radical cation cannot be detected in the spectral window around 740 nm where it is known to display a broad but weak absorption band. The indication, therefore, is that charge recombination ($\Delta G = -1.30$ eV) occurs too quickly for significant build-up of any transient species. In fact, charge recombination is likely to be promoted by super-exchange interactions with the bridging DTC unit. Similar results were observed with **PEN** in DCM solution following laser excitation at 420 nm.

5.2.4 Electronic Energy Transfer

The chromophores present in **PEN** have been arranged according to their excitation energy in order to maximize the probability of EET; **PYR** > **BODIPY** > **ExBOD**. The overlap integral, calculated according to Equation 5.3, between **PYR-BODIPY** and **ExBOD** is 0.0059 cm^{-1} . There is no detectable emission from the pyrene units and this is indicative of very efficient EET from BODIPY to PYR under these conditions. In fact, rapid EET between these same reactants has been reported in many other molecular dyads and, in our case, is supported by comparison of the excitation and absorption spectra.^{1,27,28}

$$J_{DA} = AB \int \frac{F_D(v)}{v^3} \times \frac{\epsilon_A(v)}{v} dv \quad \text{Equation 5.3}$$

Indeed, Figure 5.8 demonstrates excellent agreement between absorption and excitation spectra, which we take as a convincing argument for an efficient intramolecular EET. In fact it has been estimated to be at least 85% effective. Since there is no indication for fluorescence from the pyrene subunit present in **PYR-BODIPY** it is possible that an additional non-radiative pathway, such as light-induced electron transfer, competes with intramolecular EET.^{7,29,30}

Our interpretation of the electrochemistry results indicates that there is a small thermodynamic driving force, $\Delta G = -0.19 \text{ eV}$, for light-induced CT from the **ExBOD** to the first-excited state of BODIPY in dichloromethane solution. Unfortunately this cannot be definitely proved by pump-probe transient absorption spectroscopy due to extensive overlap of absorption transitions of the two compounds. This situation prevents identification of a suitable excitation wavelength where selective illumination can be achieved. As such, the rate constant for intramolecular EET has to be estimated from the excitation spectra and this crude approach leads to a value of $k_{\text{EET}} = 3.9 \times 10^{10} \text{ s}^{-1}$. This value seems reasonable in terms of the molecular architecture and overlap integrals.

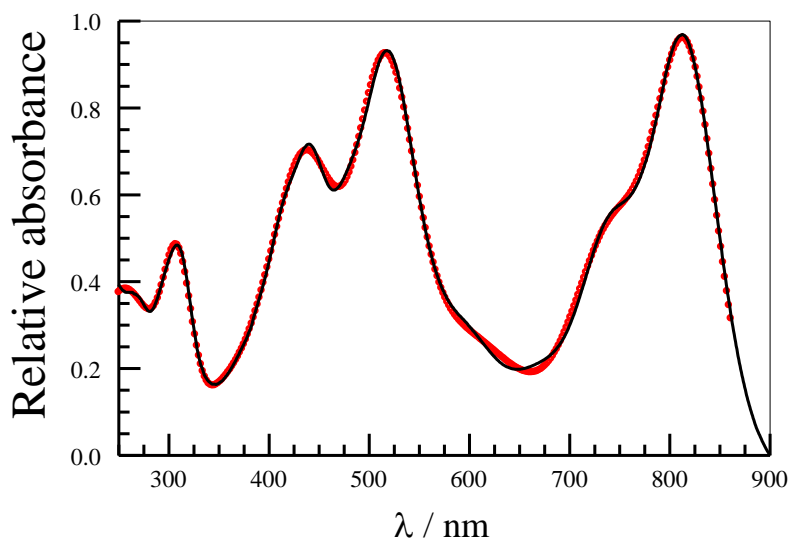


Figure 5.8. Comparison of absorption spectrum of **PEN** (black) and its excitation spectrum (red) in DCM, fluorescence wavelength used was 920 nm.

5.3 Conclusions

This work considers the electrochemical, photophysical and photochemical properties of a large supermolecule assembled by logical positioning of individual subunits. The resultant array absorbs across the entire visible spectral range and into the near-IR. Essentially, more than 99% of the absorbed photonic energy is converted into heat in less than 1 ns. There are many molecular assemblies that degrade excitation energy into heat but an attractive feature of **PEN** is that it absorbs over a very wide spectral range. As such, it possesses the main attributes needed for an organic-based photochemical heat engine, provided the material is sufficiently stable under prolonged exposure to sunlight. A key feature of this molecular array is that photodegradation occurs via a series of steps leading to gradual loss of performance. Each of these bleaching steps decreases the fraction of solar light that can be harvested but does not curtail the solar heating process. The net result is that the array functions for extended periods, especially when dispersed in an inert polymer, Figure 5.9.

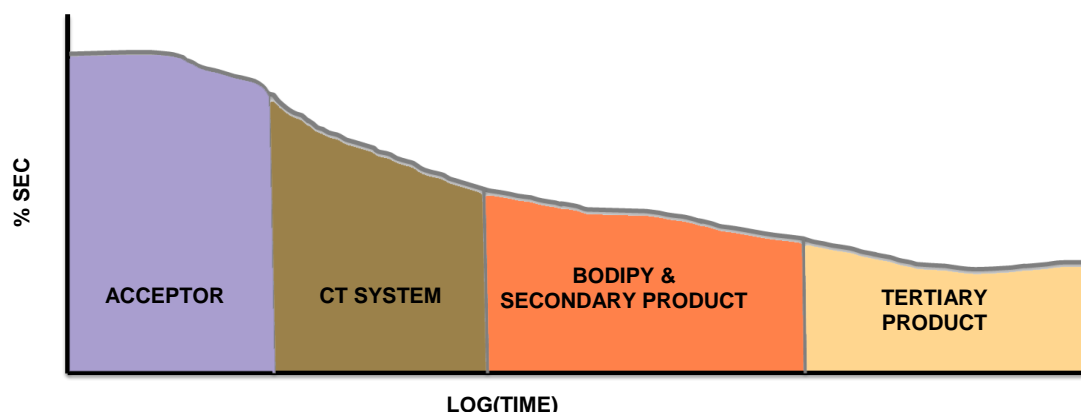


Figure 5.9. Schematic picture used to demonstrate the order of photodegradation events and stability of the final product.

The compound displays a rich variety of electrode-active processes, together with highly efficient intramolecular EET along the molecular axis. The **ExBOD**-based acceptor enters into charge-transfer reactions with the terminal amine units, surely promoted by super-exchange interactions involving the interspersed DTC unit, such that fluorescence is kept to a modest level. On exposure to sunlight, photons can enter the system at any of the principle chromophores but inevitably reach the **ExBOD** site and thereby enter into the CT reaction. The so-formed CT state deactivates quickly, at least relative to its rate of formation, thereby serving the purpose of an effective photochemical molecular heating system. We might mention that the molecule has been used successfully by another member of the group to heat water in a closed flow cell.

5.4 References

- (1) Ziessel, R.; Harriman, A. *Chem. Commun.* **2011**, 47, 611.
- (2) Andrews, D. L.; Rodriguez, J. *J. Chem. Phys.* **2007**, 127, 084509.
- (3) Andrews, D. L.; Bradshaw, D. S.; Jenkins, R. D.; Rodriguez, J. *Dalton Trans.* **2009**, 10006.
- (4) Andrews, D. L.; Curutchet, C.; Scholes, G. D. *Laser Photon. Rev.* **2011**, 5, 114.
- (5) Kosumi, D.; Maruta, S.; Horibe, T.; Fujii, R.; Sugisaki, M.; Cogdell, R. J.; Hashimoto, H. *Angew. Chem. Int. Ed.* **2011**, 50, 1097.
- (6) Harriman, A. *Phil. Trans. R. Soc. A* **2013**, 371.
- (7) Wahadoszamen, M.; Margalit, I.; Ara, A. M.; van Grondelle, R.; Noy, D. *Nat Commun* **2014**, 5.
- (8) Harriman, A.; Stachelek, P.; Sutter, A.; Ziessel, R. *Phys. Chem. Chem. Phys.* **2015**, 17, 26175.
- (9) Porrès, L.; Holland, A.; Pålsson, L.-O.; Monkman, A.; Kemp, C.; Beeby, A. *J Fluoresc* **2006**, 16, 267.
- (10) Suzuki, K.; Kobayashi, A.; Kaneko, S.; Takehira, K.; Yoshihara, T.; Ishida, H.; Shiina, Y.; Oishi, S.; Tobita, S. *Phys. Chem. Chem. Phys.* **2009**, 11, 9850.
- (11) Würth, C.; Pauli, J.; Lochmann, C.; Spieles, M.; Resch-Genger, U. *Anal. Chem.* **2011**, 84, 1345.
- (12) Ziessel, R.; Ulrich, G.; Haefele, A.; Harriman, A. *J. Am. Chem. Soc.* **2013**, 135, 11330.
- (13) Harriman, A.; Hissler, M.; Ziessel, R. *Phys. Chem. Chem. Phys.* **1999**, 1, 4203.
- (14) Benniston, Andrew C.; Harriman, A.; Lawrie, Donald J.; Rostron, Sarah A. *Eur. J. Org. Chem.* **2004**, 2004, 2272.
- (15) Bixon, M.; Jortner, J.; Cortes, J.; Heitele, H.; Michel-Beyerle, M. E. *J. Phys. Chem.* **1994**, 98, 7289.

- (16) Caspar, J. V.; Meyer, T. J. *J. Phys. Chem.* **1983**, 87, 952.
- (17) Englman, R.; Jortner, J. *Mol. Phys.* **1970**, 18, 145.
- (18) Qian, G.; Wang, Z. Y. *Chem. Asian J.* **2010**, 5, 1006.
1. (19) Spillmann, C. M.; Medintz, I. L. *J. Photochem. Photobiol. C* **2015**, 23, 644.
- (20) Mata-Perez, F.; Perez-Benito, J. F. *J. Chem. Educ.* **1987**, 64, 925.
- (21) Archer, M. D. *J. Appl. Electrochem.* **1975**, 5, 17.
- (22) Sessler, J. L.; Kubo, Y.; Harriman, A. *J. Phys. Org. Chem.* **1992**, 5, 644.
- (23) N., P.-R. M. *Aust. J. Chem.* **2014**, 56, 729.
- (24) Roland, T.; Heyer, E.; Liu, L.; Ruff, A.; Ludwigs, S.; Ziessel, R.; Haacke, S. *J. Phys. Chem. C* **2014**, 118, 24290.
- (25) Nano, A.; Ziessel, R.; Stachelek, P.; Alamiry, M. A. H.; Harriman, A. *Chemphyschem* **2014**, 15, 177.
- (26) Gaines, G. L.; O'Neil, M. P.; Svec, W. A.; Niemczyk, M. P.; Wasielewski, M. R. *J. Am. Chem. Soc.* **1991**, 113, 719.
- (27) Harriman, A.; Izzet, G.; Ziessel, R. *J. Am. Chem. Soc.* **2006**, 128, 10868.
- (28) Ziessel, R.; Goze, C.; Ulrich, G.; Cesario, M.; Retailleau, P.; Harriman, A.; Rostron, J. P. *Chem. Eur. J.* **2005**, 11, 7366.
- (29) Berney, C.; Danuser, G. *Biophys. J.* **2003**, 84, 3992.
- (30) Shin, H. K. *Chem. Phys. Lett.* **1967**, 1, 443.

Chapter 6. Stepwise Photoconversion of an Artificial Light-Harvesting Array Built from Extended BODIPY Units

6.1 Introduction

The process of electronic energy transfer (EET) has been used as the underlying methodology by which to engineer numerous analytical protocols, chemical sensors, bio-probes and molecular machines.¹⁻³ Artificial light-harvesting devices, as used to drive solar cells^{4,5} and/or photochemical batteries,⁶ also rely heavily on EET to channel photons to the desired location by creating a spectroscopic gradient.⁷ For these latter systems to be viable, it is necessary that the highly efficient EET process is matched by exceptional stability under prolonged exposure to sunlight. Unfortunately, most organic materials that absorb and emit in the near-IR region,⁸ this being the most interesting window for the sensitization of solar cells, degrade rather quickly under sustained illumination.^{9,10}

We have been interested in trying to stabilize certain classes of highly emissive dyes, most notably the boron dipyrromethene (BODIPY) family that figures prominently in artificial light-harvesting arrays.^{11,12} Here, we concentrate on the photochemistry of one such elaborate multicomponent entity that absorbs across the entire visible region but emits solely in the near-infrared region. The goal of the work is to examine ways to improve the stability of the device under continuous illumination with artificial solar light.

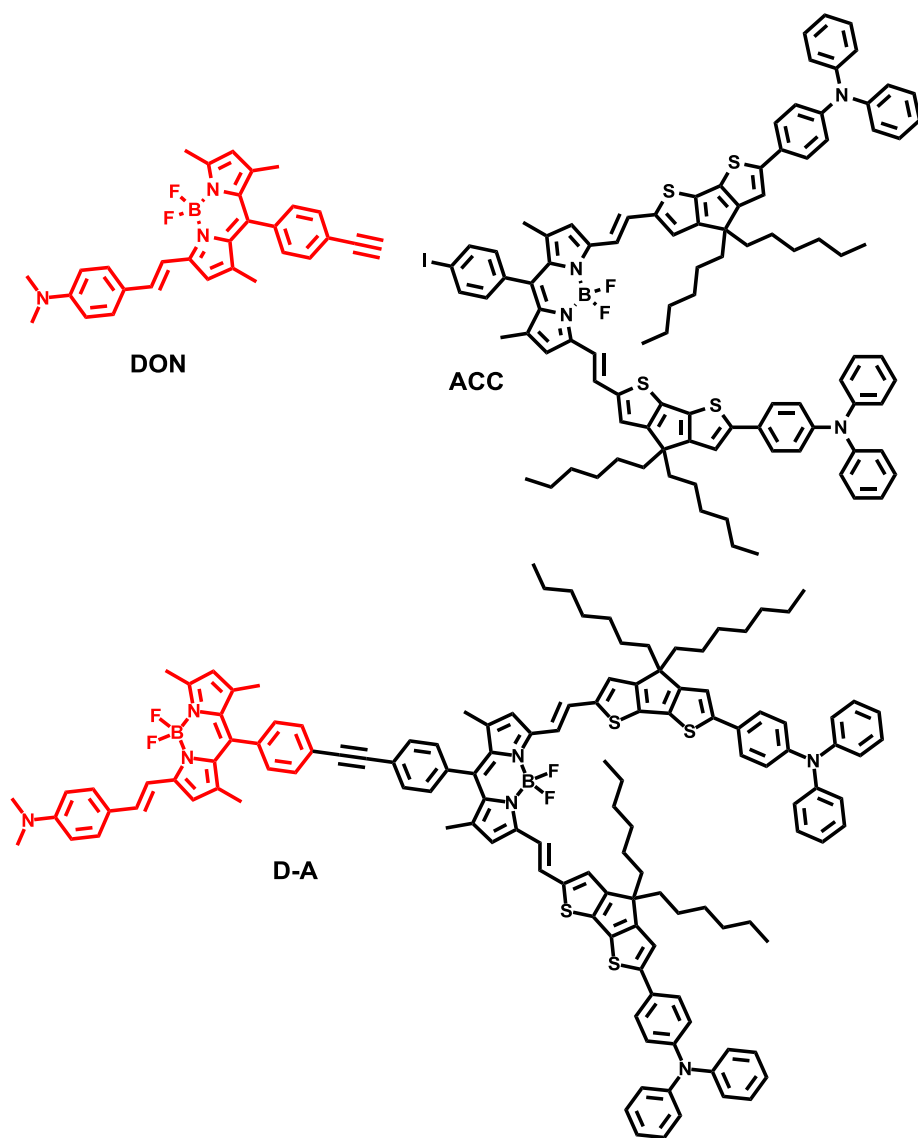


Figure 6.1. Molecular formulae of the energy donor referred to as **DON**, acceptor, **ACC** and covalently bond donor-acceptor system, **D-A**.

6.2 Results and Discussion

6.2.1 Photophysical Properties

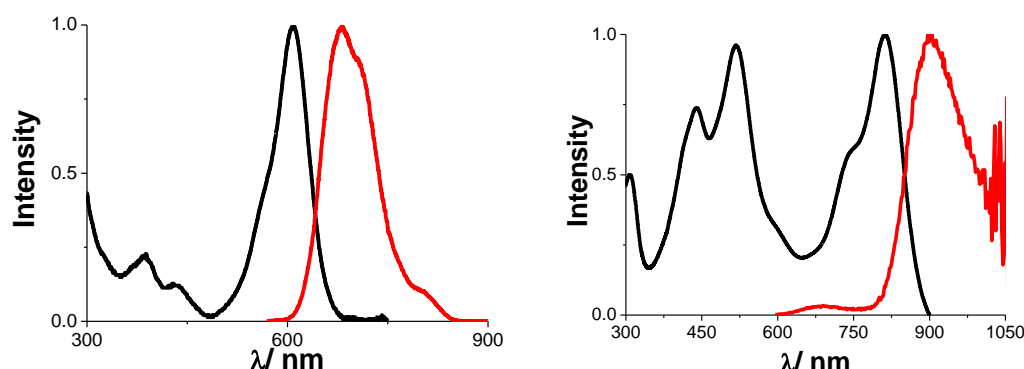


Figure 6.2. On the left absorption and emission spectra of **DON** recorded in DCM at RT, whereas on the right absorption and emission spectra of **ACC** in DCM at RT.

Absorption and emission spectra of the control compounds and the target molecular array, **D-A**, were recorded in DCM at RT. **DON** is known in literature as a pH probe^{13,14} due to a single N,N-dimethylaniline residue. The isolated control compounds are used to better understand the properties of the molecular array.

ACC is significantly larger than the **DON** and has more extensive conjugation pathway that pushes the absorption transition to about 815 nm. This unit bears two fused thiophene fragments attached to BODIPY dye via ethane linkage. Fluorescence from this terminal is relatively weak, with $\phi_F = 0.013$ and $\tau_{\text{FS}} = 0.25$ ns in DCM, and has a maximum at 897 nm. The poor emission properties might reflect the low radiative rate constant, $k_{\text{RAD}} = 5 \times 10^7 \text{ s}^{-1}$, associated with the near-IR spectral profile but also there is the strong likelihood of intramolecular charge-transfer interactions between the appended groups.¹⁵ These latter units are attached to the chromophore to enhance its performance in organic solar cells.^{16,17}

It should be noted that the photophysical properties recorded for the **ACC** unit present in **D-A** are closely comparable to those found for the isolated control compound **ACC** confirming that the restricted fluorescence is not a consequence of interaction with **DON** part of the molecule. The same conclusion cannot be reached for the corresponding **DON** terminal. Thus, fluorescence from **D-A** at

around 700 nm is difficult to resolve from the baseline and corresponds to ϕ_F of $<10^{-4}$. The excited-state lifetime for this emission is reduced to <20 ps. The two most obvious causes of this pronounced intramolecular fluorescence quenching are EET from **DON** to **ACC** and/or light-induced charge transfer along the molecular axis.¹⁸

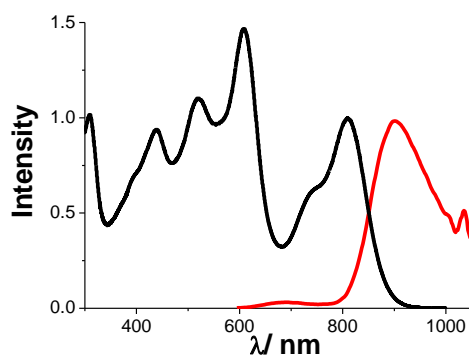


Figure 6.3. Absorption and emission spectra of **D-A** recorded in DCM at RT.

Table 6.1. Summary of photophysical data for **DON**, **ACC** and **D-A** recorded in DCM at RT.

	DON	ACC	D-A
$\lambda_{\text{abs}}/\text{nm}$	608	810	608/ 810
$\lambda_{\text{em}}/\text{nm}$	686	908	908
ϕ	0.38	0.013	0.013
τ/s^{-1}	3.7	0.24	0.23
$k_{\text{RAD}}/10^8 \text{ s}^{-1}$	1.0	0.53	0.57
$k_{\text{NR}}/10^8 \text{ s}^{-1}$	1.68	41.1	42.9
SS/cm^{-1}	1870	1332	1332
f	0.913	0.57	
J			0.0024

6.2.2 Cyclic Voltammetry

In order to assess the significance of light-induced electron transfer within **D-A**, cyclic voltammograms were recorded in DCM containing background electrolyte, $n\text{BuN.PF}_6$ (0.1M). The main findings are summarized in Table 6.2 where the assignments are made on the basis of identical studies performed with the control compounds.

Three peaks are observed on reductive scans. The first two reduction peaks are *quasi*-reversible and correspond to one-electron reduction of **ACC** and **DON** units, respectively, with half-wave potentials of -1.00 and -1.21 V vs SCE. The third reduction peak is irreversible and, by reference to the control compounds, corresponds to addition of a second electron to the **ACC** unit.

A total of four oxidative processes can be identified, each of which corresponds to the *quasi*-reversible removal of one electron from **D-A**. The first two peaks correspond to the generic oxidation of **ACC** and **DON** units, respectively, with half-wave potentials of 0.38 and 0.56 V vs SCE, as identified by comparison with the control compounds. The remaining two oxidation steps are difficult to assign simply by comparison with the reference compounds and further information about the electronic nature of these chromophores was sought from molecular orbital calculations. It is also important to recognize that the acceptor comprises multiple discrete units that might not be in strong electronic communication. There is a need, therefore, to better understand how the redox equivalents introduced during the electrochemical processes are localized within the overall structure.

Table 6.2. Electrochemistry was recorded by our collaborators in Strasbourg; Dr. Raymond Ziessel and Dr. Alexandra Sutter. Deoxygenated DCM solution was used to determine potentials by cyclic voltammetry. The electrolyte used was $n\text{Bu}_4\text{N}^+\text{PF}_6^-$ (0.1M), the solute concentration was ca. 1.5 mM, all spectra were collected at RT. Potentials were standardized versus ferrocene (Fc) as internal reference.¹⁹

	$E^{0'}(\text{ox, soln})$ (V), ΔE (mV)	$E^{0'}(\text{red, soln})$ (V), ΔE (mV)
DON	+0.54 (60), +0.84 (60)	-1.20 (60)
ACC	+0.38 (60), +0.83 (60), +1.00 (60)	-1.00 (70), -1.63 (irr.)
D-A	+0.38 (60), +0.56 (60) , +0.84 (70) +1.00 (60)	-1.00 (80), -1.21 (70), -1.85 (irr.)

6.2.3 Computational Studies

Quantum chemical studies for **DON** have been described previously, together with a few relevant compounds, and the main conclusion is that the entire molecule functions as an extended push-pull electronic system. Charge transfer from the N,N-dimethylanilino unit to the BODIPY nucleus serves to increase the molecular dipole moment (μ) at both ground (DFT/B3LYP/aug-cc-pVTZ: $\mu = 3.0$ D) and excited-state (TD-DFT/CAM-B3LYP: $\mu = 7.2$ D) levels while the wavenumber for the emission maximum decreases with increasing solvent polarity.²⁰ The control compound is highly sensitive to the presence of protons and the resultant protonated species ($\lambda_{\text{ABS}} = 553$ nm; $\lambda_{\text{FLU}} = 561$ nm) is strongly fluorescent ($\phi_F =$

1.0). Related calculations were made for the acceptor component, **D-A**, and indicate that the ground-state dipole moment is 1.6 D with little change on excitation. Interestingly, while the LUMO is essentially localized on the extended dipyrroin nucleus, the HOMO is centred on the terminal amine. Moreover, HOMO(-1) is associated with the thiophene spacer and it is not until we reach HOMO(-2) that electron density is removed from the dipyrroin unit. This finding can be used to imply that the relatively short τ_S and low ϕ_F found for the acceptor unit arise from intramolecular charge transfer with the appended amine.

Combining these orbital descriptions with the above-mentioned electrochemistry, it can be concluded that the only light-induced electron-transfer event able to compete with excited-state deactivation involves charge transfer from the excited-singlet state of **DON** to **ACC**. For this process, the thermodynamic driving force (ΔG_{CT}) is estimated¹⁹ to be ca. 0.5 eV. Our conclusion, therefore, is that intramolecular electron transfer might compete rather ineffectively with EET from **DON** to **ACC** for the target compound in a polar solvent. In non-polar media, we might anticipate a severe reduction in the rate of charge transfer but no real effect on the efficacy of intramolecular EET.

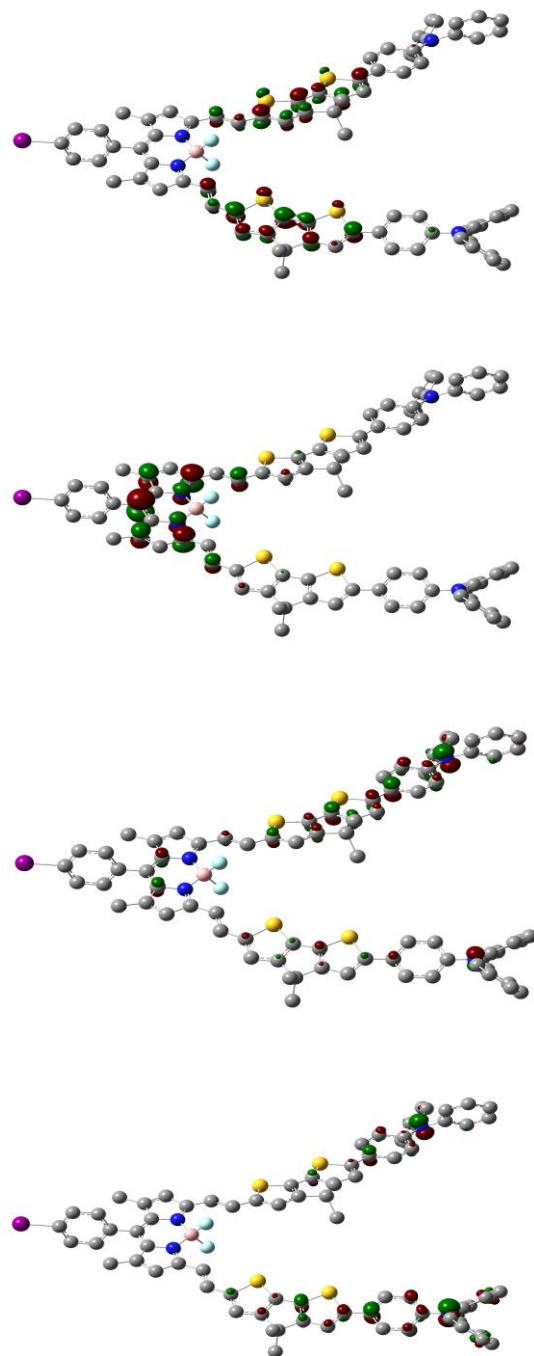


Figure 6.4. Kohn-Sham representations at iso-density of 0.02 for LUMO(1), LUMO, HOMO and HOMO(-1).

6.2.4 Photochemical Degradation

Photochemical bleaching was monitored in anaerobic DCM, Figure 6.5. Output from the lamp was filtered so to remove light $\lambda < 340$ nm but otherwise covering the entire visible region. It was directed to the front surface of the sample cell without focussing, the distance between the lamp and the sample cell was 30 cm. It's important to emphasize that both chromophores absorb incident light under these conditions. Integration of the individual spectral profiles and comparison with output from the lamp allows us to conclude that 32% of incident photons are collected by **DON**, with the remaining 68% being harvested by **ACC**, Figure 6.6.

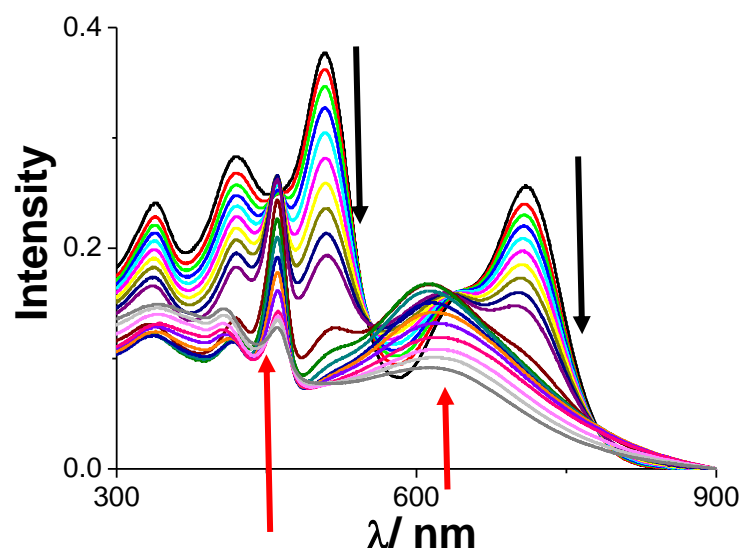


Figure 6.5. Absorption spectra recorded during the irradiation of **D-A** in DCM solution with white light. Individual spectra were recorded at regular time intervals, every 30 minutes.

In qualitative terms, exposure of the sample dissolved at the micromolar level in deoxygenated DCM to white light leads to slow but progressive bleaching of both **DON** ($\lambda_{\text{MAX}} = 612$ nm) and **ACC** ($\lambda_{\text{MAX}} = 815, 525$ and 440 nm) chromophores. Concomitant with bleaching of the primary chromophores, the spectral changes are consistent with the gradual appearance of new absorption bands at 715 and 560 nm. In turn, these intermediary products degrade under further illumination and the final product mixture possesses absorption bands in the near-UV region ($\lambda_{\text{MAX}} = 512$ and 450 nm).

The sharp absorption band centred at 560 nm is highly reminiscent of the protonated form of **DON**, which was studied earlier as a pH probe. Furthermore, the broad absorption profile centred at 715 nm is associated with the **ACC** unit since the same species arises from direct photolysis of **D-A** in deoxygenated DCM.²¹ Interestingly, both intermediary products fluoresce such that the ability to sensitize a solar cell is not lost during the initial bleaching process. Additionally, it was noted that efficient EET occurs from the protonated form of **DON** to the product absorbing at 715 nm. The final, near-UV absorbing species, which does not bleach significantly under our conditions, also retains the ability to sensitize a solar cell. The photochemistry is irreversible, although the overall bleaching efficiency is extremely low.

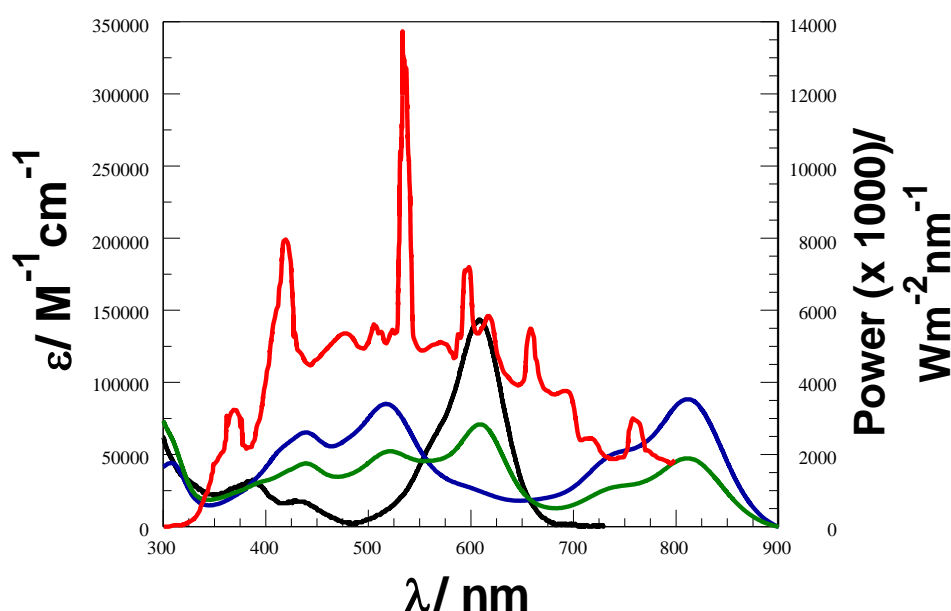


Figure 6.6. Absorption spectra recorded for **DON**, **ACC** and **D-A** in DCM, the red curve is the normalized lamp profile.

The rates of the initial photo-bleaching step, whereby both **DON** and **ACC** units degrade, are very similar, if not identical, for each chromophore despite the unequal photon intake. This behaviour is not to be expected since the excited-state lifetime of the **DON** is extremely short because of intramolecular EET to the proximal **ACC** component. The excited-state of the latter is relatively long lived and should bleach at a much faster rate than found for the donor unit. Bleaching of

ACC is most conveniently followed at 820 nm while that for **DON** can be monitored at 610 nm. For each chromophore, the decrease in absorbance follows a non-linear pattern with respect to illumination time, even at the earliest stages, and the rate of bleaching appears to increase with illumination time. This behaviour indicates some kind of autocatalytic process²⁰ that enhances the rate of photo-bleaching. Leaving the sample overnight in the dark, intended to mimic outdoor conditions, has no effect on the reaction. Further illumination simply continues the bleaching step, for which there are at least 5 isosbestic points across the spectral window for the first stage in the overall bleaching chemistry.

A reaction is deemed to be autocatalytic²²⁻²⁴ when a product-concentration vs time profile is “S-shaped” or when a reaction-rate vs time plot is “bell-shaped” with both an acceleration stage and a decay period. At least two mechanisms must operate, one being responsible for the initial bleaching step and the other making use of a primary product to enhance further bleaching. On the acceptance of *pseudo*-first order conditions being met, this being confirmed by a small concentration dependence study, the overall reaction rate can be expressed in the form of Equation 6.1; where k_0 is a rate constant for the initial reaction and k_1 is the corresponding rate constant for the catalysed reaction.²⁵ Here, the term A refers to absorbance and the subscripts represent the individual reading, i.e. A_0 is the first absorbance reading, A_1 is the second reading, etc. Iterative, least-squares fitting of the photolysis data allows calculation of these two rate constants, as determined by global fitting of the early photolysis stage carried out across a wide wavelength region.²⁶

$$\frac{A_1 - A_3}{\Delta t_{3,1}(\varepsilon_0 - \varepsilon_\infty)[1]_2} = (k_0 + k_1[1]_0) - k_1[1]_2 \quad \text{Equation 6.1}$$

$$k_N = \frac{(A_0 - A_3)}{\Delta t} \frac{1}{(\varepsilon_0 - \varepsilon_\infty)[1]_0} \quad \text{Equation 6.2}$$

The absorption bands associated with the primary products, as seen at 715 and 560 nm, appear at closely comparable rates, indicating that they share a common reaction pathway, before slowly bleaching under continuous illumination, Figure

6.7. The rates of secondary photo-bleaching differ for the two absorption bands. Thus, these two species undergo disparate reaction pathways leading to their slow degradation. Notably, disappearance of the protonated form of **DON**, i.e. **DON-H⁺**, is essentially linear with photolysis time, Equation 6.2 where ϵ refers to the molar absorption coefficient at that wavelength, but loss of the breakdown product from **ACC**, monitored at 690-750 nm, which is abbreviated as **ACC'**, involves a short inhibition period before bleaching sets in. For a typical substrate concentration of 2 μM , the rate of bleaching of **DON-H⁺** is about $12 \text{ nmol dm}^{-3} \text{ min}^{-1}$ while the same analysis shows the decomposition of **ACC'** to occur more slowly with a typical rate of ca. $5 \text{ nmol dm}^{-3} \text{ min}^{-1}$.

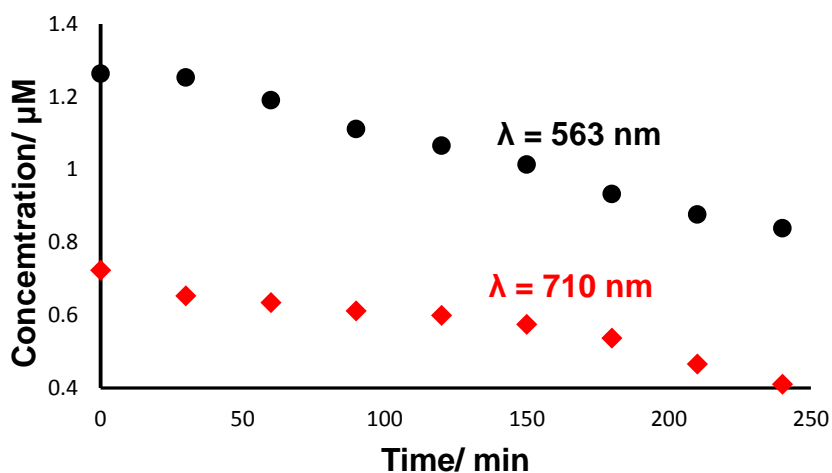


Figure 6.7. Example of a fitting the experimental data to Equation 6.1 a degradation of the intermediary products **DON-H⁺** at 563 nm and **ACC'** at 710 nm.

Table 6.3. Summary of rate constants associated with the stepwise photo-bleaching of the target array in deoxygenated DCM solution.

Process	Direction	k / min ⁻¹	λ /nm ^(b)
DON → DON-H⁺	bleaching	k ₀ = 0.0019 k ₁ = 0.0039	605-615
ACC → ACC'	bleaching	k ₀ = 0.0017 k ₁ = 0.0038	790-830
ACC → ACC'	formation	k ₀ = 0.0016 k ₁ = 0.0038	710-725
DON-H⁺ → DON-H'	bleaching	k ₂ = 0.0058	555-565
ACC' → ACC''	bleaching	k ₃ = 0.0023	690-750
ACC' → ACC''	formation	-k ₃ = 0.0022	425-490

Using the control compound **DON**, after protonation with HCl in DCM solution, it was found that illumination with visible light caused relatively fast bleaching that resulted in a colourless product. In contrast, illumination of **ACC'** leads to a further product that absorbs in the near-UV region. This latter product, **ACC''**, is extremely robust and degrades very slowly under continuous illumination. The rate of formation of **ACC''** agrees remarkably well with the rate of bleaching of **ACC'**. The overall reaction scheme leading to degradation of **DON** under visible light excitation is summarized concisely by way of Figure 6.8.

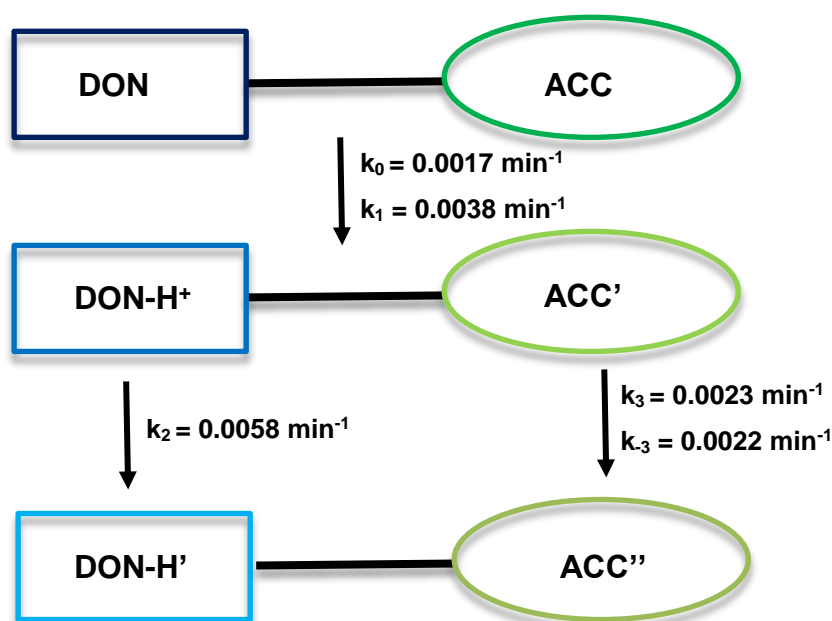


Figure 6.8. Pictorial representation of processes leading to photo-conversion of the **D-A** in DCM solution when exposed to simulated light.

Our understanding of the photo-bleaching of the artificial photon harvester **DON** in DCM can now be summarised as follows: the compound absorbs over a wide spectral range covering the entire visible zone and stretching into the far-red region. Integration of the absorption profile indicates that approximately 68% of absorbed photons are directed to the **ACC**-based acceptor, which shows modest fluorescence centred at around 900 nm. Under visible light illumination, **ACC** undergoes slow bleaching to form the primary product **ACC'** that shows prominent absorption at around 715 nm. During this bleaching process, at least one proton is released into the system and becomes attached to the **DON** terminal, forming **DON-H⁺**. This protonation step is fast such that bleaching of the **ACC** and **DON** chromophores occurs at the same rate. As reaction proceeds, one of the resultant products catalyses bleaching of **ACC** so that the rate increases with time of photolysis. Ultimately, the system reaches the state where **ACC'** and **DON-H⁺** co-exist. Further illumination leads to irreversible bleaching of **DON-H⁺** to form a transparent product and this unit is lost from the system. In contrast, further

bleaching of **ACC'** occurs to form the near-UV absorbing species **ACC''**. This latter product does not bleach under our conditions.

The origin of the proton that attaches itself to **DON** can be traced to breakdown of the DCM solvent²⁷ since **DON-H⁺** does not form when the photochemistry is carried out in either tetrahydrofuran, THF, or poly(methylmethacrylate), PMMA. In aprotic THF, illumination causes slow degradation of **ACC** exactly as described above but there is little loss of **DON** during the early stages of reaction. Instead, this latter chromophore remains intact and able to transfer excitation energy to **ACC'**. Continued illumination, however, leads to very slow degradation of **DON** to form a primary product absorbing at around 500 nm. This latter species possesses an absorption spectral profile consistent with a BODIPY derivative lacking the styryl residue,²⁸ it undergoes extremely slow photo-bleaching, a fact confirmed by separate irradiation of BODIPY in deoxygenated THF solution. Illumination of **D-A** in PMMA, carried out by our collaborators in Strasbourg, follows the same pattern as seen in THF solution but the course of reaction is too slow to monitor meaningful kinetic parameters, even for thin, i.e. 10 μm , films.²⁹

6.3 Conclusions

The use of artificial light-harvesting arrays to sensitize solar cells is at a very early stage of development and it is not yet clear if such devices offer a genuine benefit compared to direct excitation of the semiconductor. Nonetheless, it is an interesting concept that merits proper exploration. One obvious problem relates to the stability of the array under continuous exposure to sunlight and, as such, it is necessary to identify and utilize pigments with exceptional levels of photo-stability. Our approach to this problem has been to introduce a self-protective mechanism whereby photochemical degradation leads to a product that also functions as a useful sensitizer. In this way, the operating timescale is lengthened considerably but there is a certain inevitability that the fraction of solar light harvested by the array decreases at each step. This situation is nicely exemplified by considering the breakdown of **D-A** in aprotic media.

A second lesson learned from this study is the need to select an appropriate medium for the dye; in the case of **D-A** this translates to the avoidance of protic media. This requires systematic engineering of the system to eliminate problems imposed by the environment. Notably, the presence of molecular oxygen has little effect on the course of reaction and cannot be completely eliminated without encasing the array in a protective cover.

The approach used here does not permit identification of the breakdown products; using NMR spectroscopy to monitor the fate of a closely related array showed the process to be highly complicated but confirmed that the BODIPY unit absorbing at lowest energy was the first species to photo-bleach. Indeed it is not necessary to identify the products but there is a need to either repair the damaged sites or improve the overall photochemical stability for the long-wavelength absorbing species. The array described here shows a somewhat comparable turnover number to that of chlorophyll in the natural photosynthetic process but we have no provision for either self-repair or photochemical regulation, features inherent to the natural process.

6.4 References

- (1) Kumar, N.; Bhalla, V.; Kumar, M. *Analyst* **2014**, 139, 543.
- (2) Zhu, H.; Fan, J.; Li, M.; Cao, J.; Wang, J.; Peng, X. *Chem. Eur. J.* **2014**, 20, 4691.
- (3) Chen, Y.; Zhao, J.; Guo, H.; Xie, L. *J. Org. Chem.* **2012**, 77, 2192.
- (4) Feron, K.; Belcher, W.; Fell, C.; Dastoor, P. *Int. J. Mol. Sci.* **2012**, 13, 17019.
- (5) Gratzel, M. *J. Photochem. Photobiol. C* **2003**, 4, 145.
- (6) Yonezawa, Y.; Okai, M.; Ishino, M.; Hada, H. *Bull. Chem. Soc. Jpn.* **1983**, 56, 2873.
- (7) Andrews, D. L.; Rodriguez, J. *J. Chem. Phys.* **2007**, 127, 084509.
- (8) Descalzo, A. B.; Xu, H. J.; Shen, Z.; Rurack, K. In *Fluorescence Methods and Applications: Spectroscopy, Imaging, and Probes*; Wolfbeis, O. S., Ed.; Blackwell Publishing: Oxford, 2008; Vol. 1130, p 164.
- (9) Fabian, J.; Nakazumi, H.; Matsuoka, M. *Chem. Rev.* **1992**, 92, 1197.
- (10) Qian, G.; Wang, Z. Y. *Chem Asian J.* **2010**, 5, 1006.
- (11) Li, F.; Yang, S. I.; Ciringh, Y.; Seth, J.; Martin, C. H.; Singh, D. L.; Kim, D.; Birge, R. R.; Bocian, D. F.; Holten, D.; Lindsey, J. S. *J. Am. Chem. Soc.* **1998**, 120, 10001.
- (12) Ziessel, R.; Ulrich, G.; Haefele, A.; Harriman, A. *J. Am. Chem. Soc.* **2013**, 135, 11330.
- (13) Boens, N.; Leen, V.; Dehaen, W. *Chem. Soc. Rev.* **2012**, 41, 1130.
- (14) Nano, A.; Retailleau, P.; Hagon, J. P.; Harriman, A.; Ziessel, R. *Phys. Chem. Chem. Phys.* **2014**, 16, 10187.
- (15) Bolton, J. R.; Archer, M. D. *J. Phys. Chem.* **1991**, 95, 8453.
- (16) Wood, C. J.; Summers, G. H.; Gibson, E. A. *Chem. Commun.* **2015**, 51, 3915.

- (17) Summers, G. H.; Lefebvre, J.-F.; Black, F. A.; Stephen Davies, E.; Gibson, E. A.; Pullerits, T.; Wood, C. J.; Zidek, K. *Phys. Chem. Chem. Phys.* **2016**, *18*, 1059.
- (18) Benniston, A. C.; Clift, S.; Hagon, J.; Lemmetyinen, H.; Tkachenko, N. V.; Clegg, W.; Harrington, R. W. *Chemphyschem* **2012**, *13*, 3672.
- (19) Archer, M. D. *J. Appl. Electrochem.* **1975**, *5*, 17.
- (20) Rurack, K.; Kollmannsberger, M.; Daub, J. *Angew. Chem. Int. Ed.* **2001**, *40*, 385.
- (21) Harriman, A.; Stachelek, P.; Sutter, A.; Ziessel, R. *Phys. Chem. Chem. Phys.* **2015**, *17*, 26175.
- (22) Mata-Perez, F.; Perez-Benito, J. F. *J. Chem. Educ.* **1987**, *64*, 925.
- (23) Pota, G.; Bazsa, G. *J. Chem. Soc., Faraday Trans. 1* **1988**, *84*, 215.
- (24) Hindson, C. M.; Smith, Z. M.; Barnett, N. W.; Hanson, G. R.; Lim, K. F.; Francis, P. S. *J. Phys. Chem. A* **2013**, *117*, 3918.
- (25) Perez-Benito, J. F. *J. Phys. Chem. C* **2009**, *113*, 15982.
- (26) Mata-Perez, F.; Perez-Benito, J. F. *Can. J. Chem.* **1987**, *65*, 2373.
- (27) Burrows, H. D.; Kemp, T. J.; Welbourn, M. J. *J. Chem. Soc., Perkin Trans. 2* **1973**, 969.
- (28) Ulrich, G.; Ziessel, R.; Harriman, A. *Angew. Chem. Int. Ed. Engl.* **2008**, *47*, 1184.
- (29) Wennmalm, S.; Rigler, R. *J. Phys. Chem. B* **1999**, *103*, 2516.

Chapter 7. Conformational Exchange in Closely-Spaced Dyads and the Effect on Electronic Energy Transfer

7.1 Introduction

Electronic energy transfer (EET) is a crucial process in numerous natural processes (for example, in green-plant and bacterial photosynthesis, DNA repair enzymes and in photo-protection) and is used extensively to direct photonic energy to a site (i.e., an energy funnel) where some type of multi-electron catalysis can take place.^{1,2} In addition, many artificial opto-electronic devices depend critically on EET events.³ Indeed, it can be argued that only by fully understanding these EET processes will it be possible to optimize the device to the point where commercial exploitation can occur. This is certainly the case with organic light-emitting diodes.^{4,5} The EET process can take place without molecular contact and over exceptionally large distances. The rate of EET can be formulated within the “golden rule framework” and has been thoroughly studied by many researchers over many decades.^{6,7} Currently, the key questions in the EET arena are being addressed to: (i) cases where the donor and acceptor are held at unusually short separations and in motion, (ii) biological systems where crystal structures exist, and (iii) practical devices for energy transduction.^{8,9} It can be studied conveniently by way of fluorescence spectroscopy. Using several disparate molecular systems designed with our collaborators in Strasbourg, we have set out to explore how EET proceeds in molecular dyads built from large conjugated subunits and where the reactants can approach each other by way of diffusive motion. The main building blocks for these intricate molecules are BODIPY dyes, chosen because of their exceptional versatility and well-characterized emission.

Molecular dyads have been specifically designed to bring the BODIPY terminals into quite close contact by virtue of attaching two similar dyes to a single scaffold (either 1,10-phenanthroline or 1,2-diaminocyclohexane). The connecting group is an amide; the amide bond plays a special role in biochemistry whereby it provides the key structural features needed to assemble helical peptides and folded proteins.¹⁰ The dyes are in constant motion, sampling many different conformations, and display levels of fluorescence quenching characteristic of the molecular geometry. Our work attempts to relate the experimentally determined photophysical properties with the molecular shape, allowing for internal twisting within the solution. In the 1,10-phenanthroline-bridged dyads, the nature of the surrounding solvent plays a key role in establishing the emissive properties but in the other dyad it is the internal flexibility that controls the rate of intramolecular EET. In the case of 1,2-diaminocyclohexane-bridged dyads we observe unexpectedly high rates of EET, possibly pointing towards a through-space event.

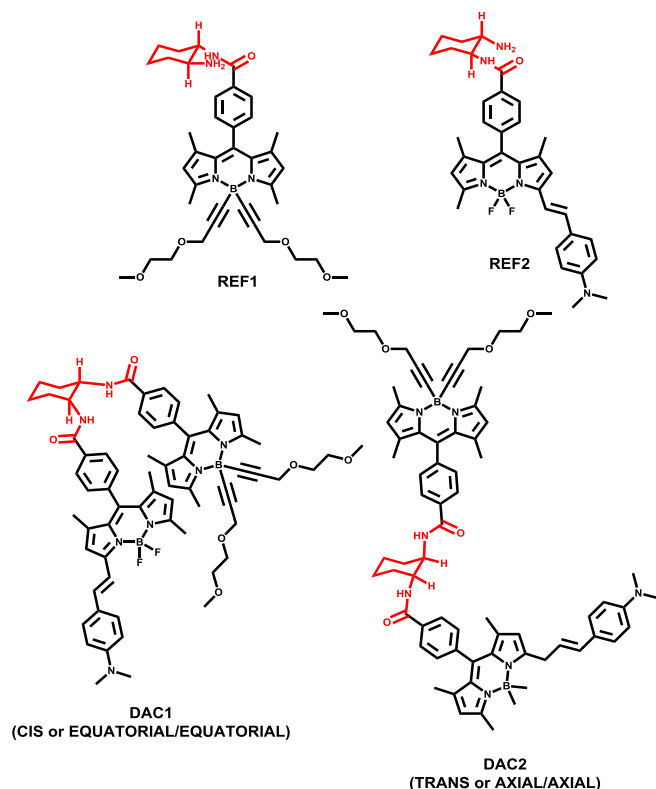


Figure 7.1. Molecular formulae of the 1,2-diaminocyclohexane bridged bichromophores and corresponding control compounds.

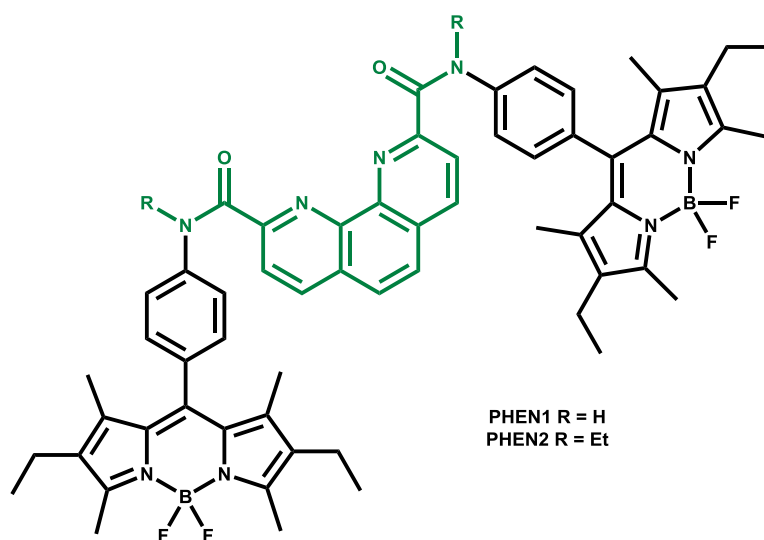


Figure 7.2. Molecular formulae of the 1,10-phenanthroline bridged bichromophores.

Herein, the 1,10-phenanthroline-bridged systems are used as models for dynamic bichromophores in fluid solution; the motion and effect of solvent are discussed in order to gain a deeper understanding of unconstrained motion in a fluid medium. It will be noticed (Figure 7.2) that the BODIPY-based terminals are identical. Attention here lies with the amide connections. In contrast, the 1,2-diaminocyclohexane-bridged dyads are subject to the same kind of dynamics in the solution but we have the added complication of a dynamic bridge. Our interest here is the effect of the conformational exchange on the rate of intramolecular EET. For the former series of the dyads, the only significant difference relates to the type of amide connection. This is varied from secondary to tertiary but all other features remain identical. For the latter series, the difference relates to the connection points since the scaffold permits isolation of axial and equatorial connections that do not interchange in solution.

7.2 Results and Discussion

7.2.1 Spectroscopic Data

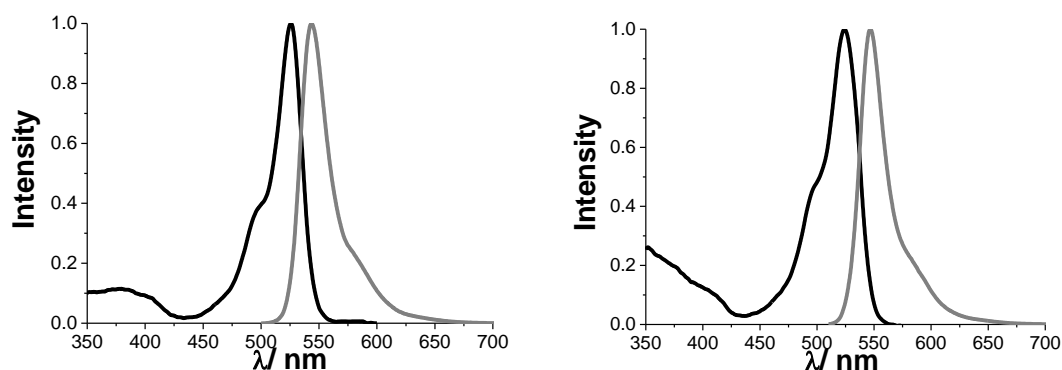


Figure 7.3. The panel on the left shows absorption and emission spectra recorded for **PHEN2** whereas the panel on the right represents **PHEN1** in spectrophotometric grade dichloromethane at room temperature.

The initial spectroscopic data were collected in spectrophotometric grade solvents at room temperature in the presence of molecular oxygen. All compounds appear to be stable under such conditions.

Figure 7.3 illustrates the absorption and emission spectra recorded for **PHEN1** and **PHEN2**; we observe quite good mirror symmetry and relatively narrow optical transitions for both systems under these conditions. The two samples exhibit a certain degree of sensitivity to the solvent type and polarity, which was unexpected.

In MTHF solution, the quantum yields and excited-state lifetimes recorded for **PHEN2** ($\phi_{\text{FLU}} = 75\%$, $\tau_{\text{S}} = 5.5$ ns) and **PHEN1** ($\phi_{\text{FLU}} = 73\%$, $\tau_{\text{S}} = 5.4$ ns) are comparable to those found for the relevant BODIPY reference ($\phi_{\text{FLU}} = 80\%$, $\tau_{\text{S}} = 5.9$ ns) compound, although fluorescence is decreased slightly, especially for **PHEN1**, Table 7.1. For the two bichromophores in MTHF, excitation and absorption spectra are in close agreement and time-resolved decay curves remain mono-exponential over at least three half-lives. The presence of molecular oxygen does not affect the derived properties while changes in solvent polarity have only minimal effect on the absorption and emission spectral profiles.

Table 7.1. Photophysical properties determined for **PHEN1** and **PHEN2** and for the reference BODIPY dye in spectrophotometric grade MTHF at RT. SS is the Stokes' shift whereas k_{SB} is the calculated radiative rate constant using the Strickler-Berg expression.

	$\lambda_{MAX} /$ nm	$\lambda_{FLU} /$ nm	ϕ_{FLU}	$\tau_s /$ ns	SS / cm ⁻¹	$k_{SB} / 10^8$ s ⁻¹
BOD_{REF}	523	536	0.80	5.9	465	1.38
PHEN1	522	540	0.73	5.4	640	1.40
PHEN2	524	538	0.75	5.5	500	1.40

7.2.2 Photophysical Properties of 1,10-Phenanthroline Bridged Bichromophores in a Range of Solvents

Table 7.2 and Table 7.3 illustrate how the photophysical parameters vary with the solvent dielectric constant (ϵ_s) for the two phenanthroline-bridged bichromophores. In the case of **PHEN2**, the variation in ϕ_{FLU} is small across the range of solvents, despite ϵ_s changing from 2 to 47, and there is no noticeable influence of hydrogen-bond donor solvents. On close scrutiny, it seems that there is a gradual decrease in ϕ_{FLU} with increasing solvent polarity but the effect is shallow and certain solvents do not follow the generic pattern, Figure 7.4. The excited-state lifetime measured in the same series of solvents decreases with increasing solvent polarity in much the same manner as found for the quantum yield. However, in polar solvents ($\epsilon_s > 10$) the quality of the statistical fit to a mono-exponential decay falls below the satisfactory level. This fit can be judged best in terms of the randomness of the weighted residuals, but is also evident in an increased chi-squared parameter (χ^2). Inclusion of a short-lived (i.e., <1 ns) or long-lived (i.e., >10 ns) component did not improve the quality of the fit. However, analysis of the decay curves as dual-exponential fits with lifetimes in the range of 5-7 ns and 1-3 ns gave superior (i.e., more random) residuals and χ^2 parameters closer to unity. Although the two lifetimes are too close for unique solutions to be extracted from these fits, the dual-exponential behaviour appears to better represent the situation in polar solution. Even so, certain hydrogen-bond acceptor solvents, specifically N,N-

diethylformamide (DEF), N,N-diethylacetamide (DEA) and dimethylsulfoxide (DMSO), appear to behave anomalously.

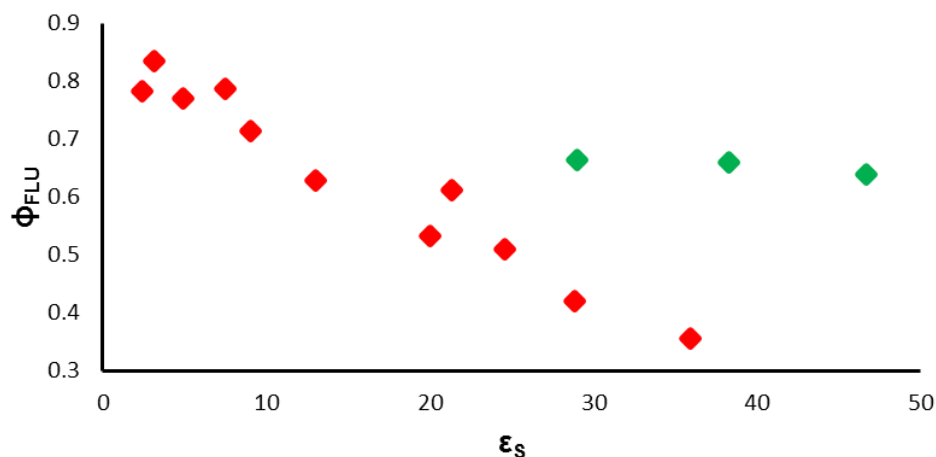


Figure 7.4. Relationship between the dielectric constant (ϵ_s) and emission quantum yield (ϕ_{FLU}) for **PHEN2**. Markers in green correspond to N,N-diethylformamide ($\epsilon_s = 29$), N,N-diethyl-acetamide ($\epsilon_s = 38.3$) and dimethylsulfoxide ($\epsilon_s = 46.7$).

An increased level of solvent sensitivity is displayed by **PHEN1** across the same series of solvents, Table 7.3. In general, increasing ϵ_s leads to a decrease in ϕ_{FLU} , although the overall behaviour is non-linear and again there are a few anomalous solvents. These latter solvents are identified as being acetone ($\epsilon_s = 21.4$), DEF ($\epsilon_s = 29$), DEA ($\epsilon_s = 38.3$) and DMSO ($\epsilon_s = 46.7$) and are hydrogen-bond acceptors. As such, these solvents might be expected to form a hydrogen bond with the amide proton and thereby perturb the molecular conformation. Otherwise, protic and aprotic solvents follow a common trend and there is no indication that solvent attachment to the aza-N atoms is important in the fluorescence quenching process. In mixtures of THF ($\epsilon_s = 7.6$) and acetonitrile ($\epsilon_s = 37.5$), ϕ_{FLU} decreases progressively with increasing mole fraction of acetonitrile while that for the control compound shows no such effect.

Table 7.2. Effect of solvent dielectric constant on the photophysical properties derived for **PHEN2** at RT. χ^2 is the reduced chi-squared parameter associated with the single-exponential fit, DEF = N,N-Diethylformamide, DEA = N,N-Diethylacetamide, and DMSO = Dimethylsulfoxide.

Solvent	ϵ_s	ϕ_{FLU}	$\tau_s / \text{ns}^{[a]}$	$k_{\text{RAD}} / 10^8 \text{ s}^{-1}$	χ^2 (a)
Toluene	2.43	0.78	5.74	1.36	0.95
Dibutyl ether	3.18	0.83	6.85	1.21	0.92
Diethyl ether	4.33	0.86	6.35	1.35	1.05
CHCl_3	4.89	0.85	6.45	1.32	1.07
Ethyl acetate	6.02	0.82	6.60	1.24	1.06
MTHF	7.47	0.79	6.60	1.20	0.99
THF	7.58	0.75	5.85	1.28	0.96
DCM	9.02	0.78	6.17	1.26	1.12
Heptyl cyanide	13.0	0.68	6.10	1.12	1.30
Valeronitrile	20.0	0.58	6.00	0.97	1.43
Acetone	21.4	0.67	6.00	1.12	1.12
Ethanol	24.3	0.48	5.60	0.86	1.39
Butyronitrile	24.6	0.55	5.90	0.93	1.52
Nitropropane	27.3	0.46	5.55	0.83	1.87
Propionitrile	28.9	0.44	5.60	0.79	1.51
DEF	29.0	0.66	6.05	1.09	1.09
Chloroacetonitrile	30.0	0.51	4.85	1.05	1.73
Methanol	33.6	0.43	4.15	1.04	1.87
Acetonitrile	37.5	0.35	3.35	1.05	2.20
DEA	38.3	0.66	5.65	1.17	1.32
DMSO	46.7	0.64	5.74	1.11	1.28

(a) The quality of the fit is improved in polar solvent by replacing the single-exponential fit with a dual-exponential model but, for the discussion here, the single-exponential behaviour suffices.

Table 7.3. Effect of solvent dielectric constant on the photophysical properties determined for **PHEN1** at RT. χ^2 is the reduced chi-squared parameter associated with the single-exponential fit, DEF = N,N-Diethylformamide, DEA = N,N-Diethylacetamide, and DMSO = Dimethylsulfoxide.

Solvent	ϵ_s	ϕ_{FLU}	$\tau_s / \text{ns}^{[a]}$	$k_{\text{RAD}} /$	$\chi^2 \text{ (a)}$
				10^8 s^{-1}	
Toluene	2.43	0.60	4.19	1.43	1.02
Dibutyl ether	3.18	0.65	4.50	1.44	0.96
Diethyl ether	4.33	0.71	5.15	1.38	0.97
CHCl_3	4.89	0.73	5.52	1.32	1.10
Ethyl acetate	6.02	0.74	5.23	1.41	1.08
MTHF	7.47	0.73	4.88	1.50	1.18
THF	7.58	0.73	5.36	1.36	1.14
DCM	9.02	0.63	5.40	1.17	1.38
Heptyl cyanide	13.0	0.66	5.20	1.27	1.53
Valeronitrile	20.0	0.56	5.14	1.10	1.82
Acetone	21.4	0.50	5.18	0.97	1.48
Ethanol	24.3	0.46	4.60	1.00	1.94
Butyronitrile	24.6	0.44	4.55	0.97	2.11
Nitropropane	27.3	0.39	3.57	1.11	1.82
Propionitrile	28.9	0.23	1.96	1.12	2.35
DEF	29.0	0.48	4.85	1.00	1.60
Chloroacetonitrile	30.0	0.21	1.91	1.10	2.28
Methanol	33.6	0.19	1.00	1.90	2.35
Acetonitrile	37.5	0.07	0.74	0.95	3.10
DEA	38.3	0.42	3.92	1.07	2.23
DMSO	46.7	0.12	0.90	1.33	1.93

(a) Note the quality of the fit is unsatisfactory in most polar solvents. See later.

For **PHEN1**, the time-resolved emission decay profiles could be analysed with reasonable confidence in terms of single-exponential fits. The fit was less satisfactory in certain polar solvents, where a two-exponential fit was clearly superior. This situation was exacerbated for **PHEN1** where the single-exponential fit was unacceptable in many polar solvents (Table 7.3). In these cases, it was found that the quality of the fit could be much improved by adding a short-lived component. The revised fitting parameters are provided in Table 7.4. In summary, the fractional contribution (A_1) of the shorter-lived component was seen to increase with increasing solvent dielectric constant. Across all the polar solvents, the shorter-lived lifetime (τ_1) had a mean lifetime of ca. 0.5 ns while the longer-lived component (τ_2) retained a mean lifetime of ca. 3 ns (Table 7.4). The total contribution of the shorter component increased in more polar solvents but the mean lifetime did not correlate with ϵ_s . We are led to the conclusion that the reduced quantum yield found in most polar solvents arises from increased population of a family of bichromophores more susceptible to intramolecular fluorescence quenching. The nature of the solvent determines the extent of this population but there is no relationship between the level of quenching inherent to that family and the solvent polarity.

Table 7.4. Effect of solvent dielectric constant on the photophysical properties determined for **PHEN1** at RT. χ^2 is the reduced chi-squared parameter associated with the single-exponential fit, DMSO = Dimethylsulfoxide. A_1 is the fractional contribution of the shorter-lived component.

	ϵ_s	τ_1 / ns	τ_2 / ns	χ^2	A_1 %
DCM	9.02	1.45	5.3	1.72	19
Heptyl cyanide	13.0	0.77	5.6	1.39	12
Valeronitrile	20.0	0.66	4.9	1.29	14
Acetone	21.4	1.62	4.9	1.42	7
Ethanol	24.3	0.92	4.2	1.63	8
Butyronitrile	24.6	0.48	4.6	1.22	31
Nitropropane	27.3	0.33	4.1	1.47	16
Propionitrile	28.9	0.27	4.05	1.55	40
Chloroacetonitrile	30.0	0.36	3.7	1.4	38
Methanol	33.6	0.96	2.2	1.75	60
Acetonitrile	37.5	0.38	2.4	1.18	74
DMSO	46.7	0.7	3.6	1.4	88

It might be important to stress that ϵ_s is not the only means for expressing solvent polarity¹¹ and, in fact, several alternatives are available. These include Reichardt's empirical ET(30) parameter,¹² the Kirkwood factor¹³ and the Catalan SPP¹⁴ and SB¹⁵ factors. It is not the purpose of the present investigation to critically compare these solvent descriptors but it should be emphasized that similar behaviour is noted in all cases with regards to the polarity effect on fluorescence probability. Likewise, there are other ways to analyse the time-resolved fluorescence decay curves rather than rely on a sum of exponentials. We have noted that reliance on a single-exponential component fails to explain the data in polar media and introduces a radiative decay rate constant that is strangely sensitive to the nature of the solvent. The main problem with a sum of exponential terms is that it does not properly represent the situation where families of conformers abound. This is almost certainly the case with these bichromophores.

There are many available theories on how the choice of solvent might affect the dynamics of solute motion; one of these argues that *cis/trans* photoisomerization is dependent on the class of solvent used and its molecular weight.¹⁶ It has also been shown that the symmetry of multi-component assemblies can play a significant role in solvation dynamics.¹⁷ We now consider the most plausible reason for the observed solvent dependence identified above.

7.2.3 Fluorescence Quenching of 1,10-Phenanthroline-Bridged Bichromophores

In consideration of the fluorescence quenching mechanism, we draw attention to the similar qualitative behaviour of the two compounds but note that fluorescence quenching is much more pronounced for **PHEN1** than for **PHEN2**. The two bichromophores exhibit comparable optical spectroscopy and electrochemistry such that the disparate quenching level displayed in any given solvent cannot be ascribed to thermodynamic effects; electrochemical studies for these compounds were carried out by our collaborators in Strasbourg, Table 7.5.

Table 7.5. Electrochemical data recorded by our collaborators in Strasbourg. Cyclic voltammetry was carried out in deoxygenated DCM, containing 0.1M NBu₄PF₆ at RT Potentials quoted vs SCE.

	$E^0_{\text{ox}}, \text{V } (\Delta E, \text{mV})$	$E^0_{\text{red}}, \text{V } (\Delta E, \text{mV})$
BOD_{REF}	+0.95 (32)	-1.39 (74)
PHEN1	+0.98 (82)	-1.31 (62); -1.60 (78)
PHEN2	+0.99 (66)	-1.31 (70)

The only chemical difference between these compounds relates to the substitution pattern around the amide linker. This latter group is not in electronic communication with the excited state localized on the BODIPY chromophore, suggesting that its role in the quenching event is to perturb the molecular conformation. We can also eliminate light-induced charge transfer between BODIPY and 1,10-phenanthroline

as playing an important role since such processes are thermodynamically unfavourable, unless the latter unit is protonated.

Consideration of the cyclic voltammograms and taking due allowance for the excitation energy of the BODIPY chromophore, as derived from the intersection of normalized absorption and fluorescence spectra, indicates that light-induced charge transfer between the two BODIPY units is weakly exergonic in dichloromethane solution. Indeed, the thermodynamic driving force ($-\Delta G_{cs}$) is 0.05 eV in the absence of electrostatic effects. This mechanism remains the most likely cause of the observed emission quenching in the target bichromophores and it is well established¹⁸ that the thermodynamics for light-induced charge transfer are sensitive to the nature of the solvent. It might be mentioned that other molecules containing two BODIPY-based chromophores have reported excimer emission,^{19,20} dimerization²¹ and light-induced charge transfer²² in fluid solution.

The details of computational simulations made for both **PHEN1** and **PHEN2** can be found in *Chem. Eur. J.* **2016**, DOI: 10.1002/chem.201602354, herein we will concentrate on discussing the conclusions we can draw from these experiments. We raise the hypothesis that the only viable mechanism able to account for the observed solvent effect on the emission properties of the BODIPY unit in these bichromophores is light-induced charge transfer^{22,23} between the terminal dyes. As such, it is instructive to enquire if changes in molecular conformation can explain the experimental observations.

For **PHEN2**, the two BODIPY units are held apart under all reasonable conditions to such an extent that through-space charge transfer²⁴ is unlikely to compete effectively with the inherent radiative and non-radiative decay routes. Fluorescence quenching is ineffectual for this compound, except in strongly polar media. Polar solvent promotes conversion of the *cis*-species to the corresponding *trans*-tautomer. Our modelling studies would suggest that, in strongly polar media, the bichromophore should persist as a mixture of all-*trans* and *cis/trans* isomers. In non-polar media we expect to observe only the all-*cis* species.

Combining this result with the fluorescence behaviour, we can speculate that the *trans*-geometry provides a better conduit²⁵ for through-bond charge transfer. The long pathway so involved,²⁶ together with the modest thermodynamic driving force,

means emission quenching will be kept at a minimum, as is observed. It might be emphasized that the quality of the fit for the time-resolved emission decay profiles recorded in certain polar solvents could be improved by adding a shorter-lived component. For example, in acetonitrile the best fit involved equal components with lifetimes of 1.1 and 4.1 ns. Likewise, in propionitrile about 30% of the signal decayed with a lifetime of 1.15 ns while the remainder possessed a lifetime of 4.2 ns. The fractional contribution of the shorter-lived component increased with increased ϵ_s but there was no such correlation with the magnitude of the lifetime. We attribute the short lifetime to the *trans*-species and the longer lifetime to the corresponding *cis*-isomer. The mean difference between the two sets of emission lifetimes, taken together with the lifetime of the control compound, translates to a ratio of rate constants for charge-separation of 2-fold in favour of the *trans*-amide.

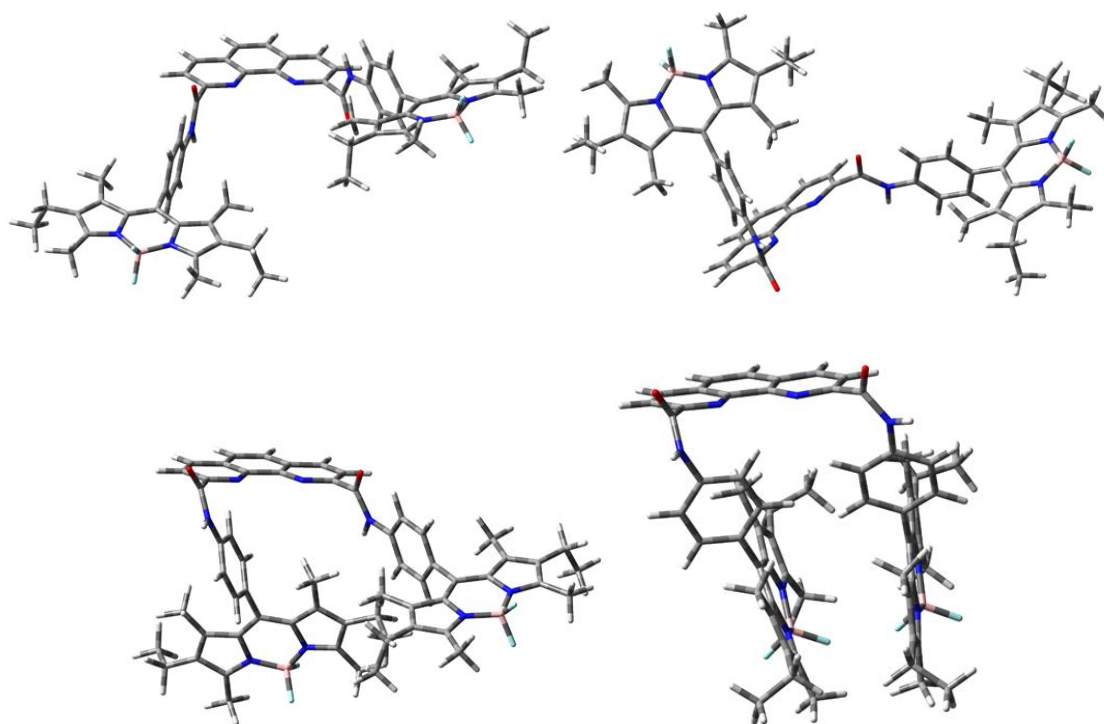


Figure 7.5. Snapshots of molecular conformations representing the important distributions for all-*trans* (uppermost left), mixed-*cis/trans* (upper right and lower left), and all-*cis* (lower right) geometries for **PHEN1** in solution.

There is, in fact, ample evidence to indicate that the *trans*-geometry provides a better pathway for super-exchange interactions in many different types of molecular dyads built around a spacer unit.^{27,28} This is attributed to the improved electronic coupling between the reactants and helps to explain the observations made with **PHEN2**. The computational studies suggest that the all-*cis* species will predominate in non-polar solvents and also in weakly polar media. Strongly polar solvents, however, trigger the switch to the *trans*-geometry and we would expect to see increased population of the *trans/cis* species in the more polar solvents. Isomerization is unlikely to be competitive with inherent deactivation of the excited-state. Instead, illumination of the ground-state equilibrium will produce a distribution of geometries that do not interconvert on the relevant time scale. This situation would equate to two families of conformers, each displaying a range of non-radiative rate constants representing the mean geometry at the moment of excitation (Figure 7.6).

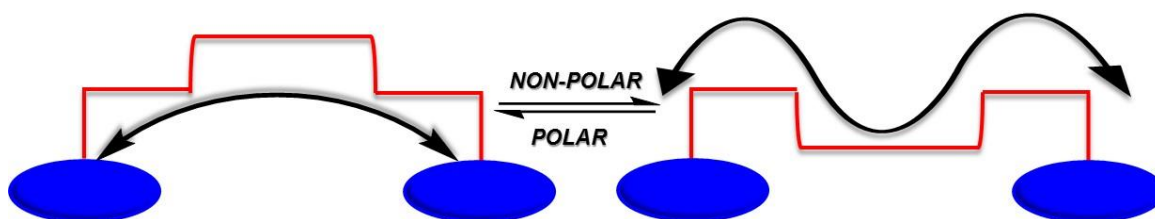


Figure 7.6. Cartoon demonstrating a solvent-driven exchange for the amide linked bichromophoric **PHEN2** in solution.

Unexpectedly, there are major structural differences between **PHEN2** and **PHEN1** caused by internal steric crowding and/or electronic effects. Fluorescence quenching is more effective for **PHEN1** although the thermodynamic driving force is the same as that for **PHEN2** and there is a similar sensitivity towards solvent polarity. Calculations made for **PHEN1** predict that the *trans*-geometry is favoured in all solvents, this being the opposite situation to that found for **PHEN2**, but polar solvent promotes transformation to the *cis*-isomer. In non-polar solvents, we would expect to see only the all-*trans* species. Increasing the solvent polarity raises the possibility for finding the *trans/cis* species. This is a remarkable difference between

secondary and tertiary amide connections that was unexpected at the onset of the investigation.

By analogy to **PHEN2**, increasing the contribution of the *cis*-species might be expected to extinguish through-bond charge separation. This would restore fluorescence. However, for **PHEN1** the *cis/trans* species has the two BODIPY units close together, contact being possible in the extreme case, while rotation around one of the carbonyl groups further reduces the edge-to-edge separation, Figure 7.5. As such, the *cis*-isomer can be expected to promote through-space, light-induced charge separation²⁹ between the two BODIPY units. This situation would introduce a short-lived component into the decay records in polar solvents.

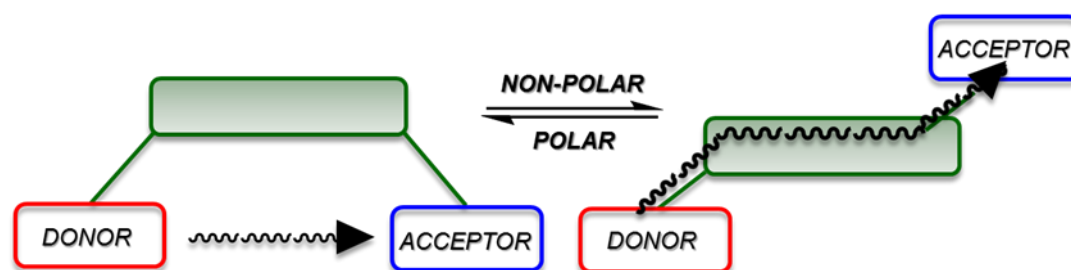


Figure 7.7. Cartoon to illustrate the two main families of conformers relevant for **PHEN1** in solution. On the left hand side, we have the *cis*-isomer that brings the reactants into quite close proximity. On the right-hand side, we have the *trans*-geometry that forces the reactants to wider separation.

This work has shown that the amide linkage provides for multiple molecular conformations that differ in terms of their propensity to promote either through-bond or through-space charge transfer. In addition to isomerization around the central C-N amide bond, structural complications arise from electronic interactions between the carbonyl O atom and the aza-N atom of the 1,10-phenanthroline unit. Indeed, the BODIPY-based arms attached to the heterocyclic linker provide a crude cavity wherein hydrogen-bonding and steric interactions further restrict conformational freedom to such an extent that the two target compounds appear structurally distinct. This situation is exemplified by the realization that **PHEN2** adopts the *cis*-geometry while **PHEN1** takes up the *trans*-geometry. These various

conformations influence the quantum yield for fluorescence from the BODIPY appendages, but quenching is kept to a minimum by limited thermodynamics. It seems likely that these effects could be greatly amplified by appropriate choice of the terminals. Thus, the amide linkage might offer some unusual opportunities to switch between emissive and dark states under suitable stimulation. This situation is made possible because the absolute energies of the various tautomers are quite comparable while rotational barriers will impose kinetic limitations at the excited-state level.

7.2.4 Energy Transfer in 1,2-Diaminocyclohexane-Bridged Dyads

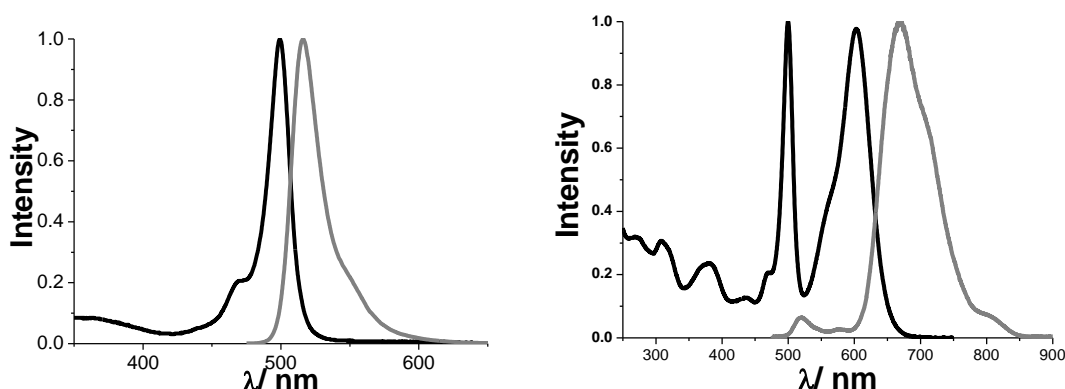


Figure 7.8. Absorption and emission spectra recorded for **REF1** (left-hand panel) and **DAC2** (right-hand panel) in spectrophotometric grade MTHF at room temperature.

Here, we examine an interesting case of EET in two 1,2-diaminocyclohexane-bridged molecular dyads. **DAC1** and **DAC2**. The dyads comprise **REF1** and **REF2** linked by a non-conjugated spacer unit so as to provide two different orientations. In the case of **DAC1**, the donor and acceptor are in one plane, spatially isolated, whereas in the case of **DAC2** the donor and acceptor are essentially parallel. Figure 7.8 illustrates how the absorption spectrum recorded for **DAC2** differs from those measured for **REF1**. In Figure 7.9, we compare spectra recorded for **REF1**

and **REF2** with that of **DAC1** recorded under identical conditions. We can observe that the spectra match relatively well with the only significant difference being a small bathochromic shift to the absorption maximum of the acceptor segment of **DAC1**. Even here the shift amounts to only 140 cm^{-1} ; the same red shift is observed for **DAC2**. Both donor and acceptor emission spectra are red-shifted compared to the corresponding reference compounds, although once again the shifts are small. Emission for the donor entity in **DAC1** is red-shifted by 295 cm^{-1} , whereas emission of the acceptor entity in both bichromophores is red-shifted by 365 cm^{-1} . These shifts are most likely caused by excluding solvent from the chromophore for the dyads relative to the mono-chromophoric species. Both donor and acceptor can be excited with a good level of selectivity.

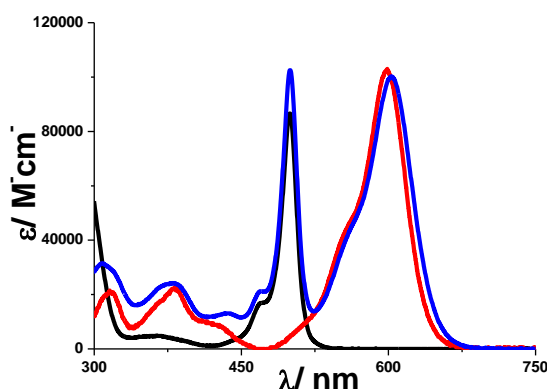


Figure 7.9. Absorption spectra recorded for the individual components of **DAC1** as well as that of the dyad itself, measured in MTHF at room temperature. **REF1** is shown as a black curve, **REF2** is presented in red and finally **DAC1** is given as a blue curve.

The molecular formulae for **DAC1** and **DAC2** are given as part of Figure 7.1, together with those of the control compounds. The 1,2-diaminocyclohexane-based spacer is an unusually small scaffold for use with donor-acceptor dyads and was specifically designed to address the problem of EET across short separations. An obvious problem with cyclohexane-derived structures is that they are subject to fast axial-equatorial conformational exchange. We can illustrate this process by way of Figure 7.10. Here, the dyads are believed to exist in two forms, each of which is in fast equilibrium as two limiting species. The two forms do not interconvert – this is the key point. To provide an easy recognition pattern, we will

refer to the two forms as being *cis* or *trans* – this refers to the basic arrangement of the donor (D) and acceptor (A) appended to the ring. The *cis*-form (**DAC1**) can arrange the D and A species as axial/equatorial (a,e) or as equatorial/axial (e,a). These two arrangements are considered to be in rapid equilibration at room temperature. The *trans*-form (**DAC2**) can position the reactants as axial/axial (a,a) or as equatorial/equatorial (e,e). Again, these species are in fast equilibration but there is no interconversion between *cis* and *trans*. Thus, we have two sets of pairs of conformers.

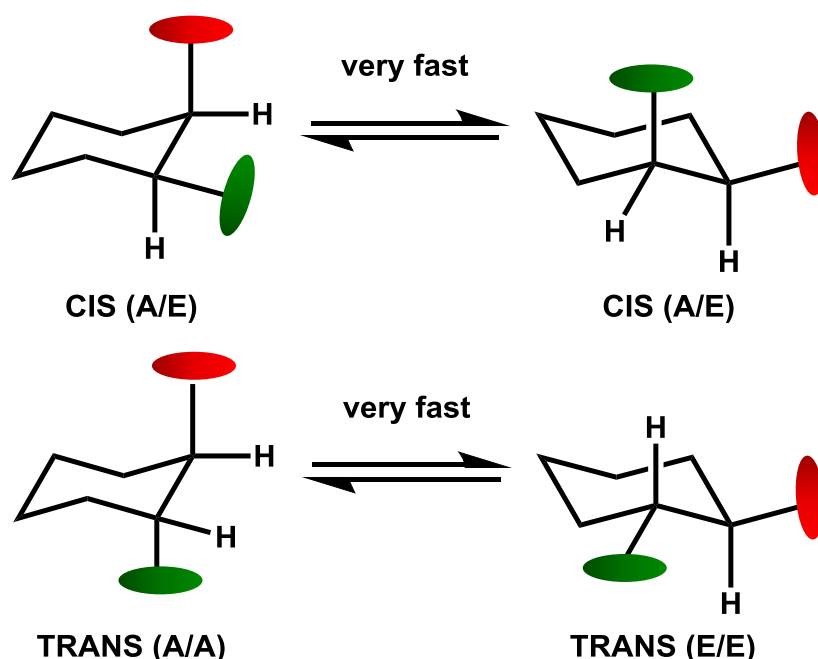


Figure 7.10. Representation of two rapidly interconverting cyclohexane chair conformations. The energy donor is represented by the red oval, whereas the energy acceptor is represented by the green oval. A stands for axial, while E refers to equatorial.

The compounds were synthesized by our collaborators in Strasbourg. We carried out detailed 700 MHz NMR spectroscopy here in Newcastle, courtesy of Dr. Corrine Wills, to aid interpretation. The NMR spectra are provided here (Figure 7.11) but their interpretation is well outside our ability. We accept the conclusions drawn by the experts and resort to the structures, and their labelling, inherent to Figure 7.10.

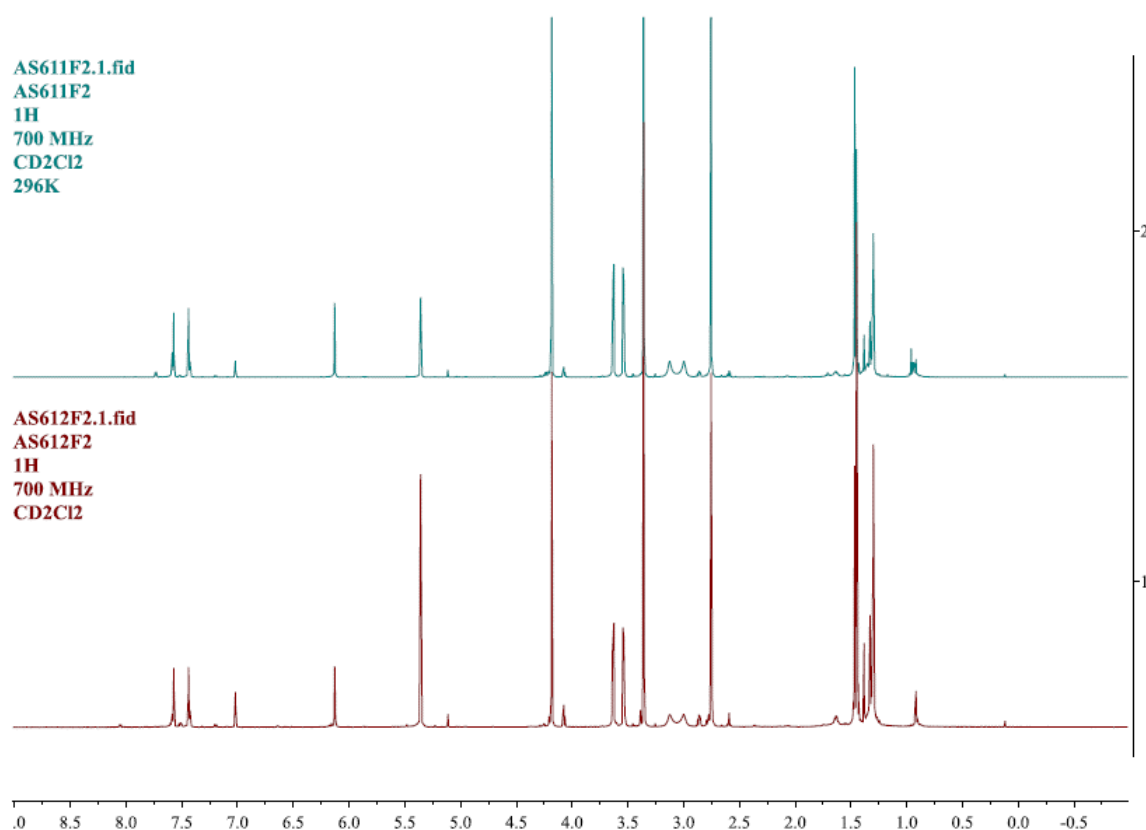


Figure 7.11. An example of 700 MHz, ^1H NMR spectrum collected for a control bichromophore studied. The spectrum was recorded by Dr. Corrine Wills. AS611F2 refers to the *trans*-geometry (equivalent to **DAC2**), whereas AS612F2 refers to the *cis*-geometry (equivalent to **DAC1**).

The new molecular dyads comprise two disparate BODIPY dyes that differ in terms of their respective conjugation lengths. The donor function is a conventional BODIPY dye that absorbs and emits in the blue region. The acceptor function is an expanded BODIPY-based dye that absorbs and emits in the red region. The compounds, both dyads and control compounds, dissolve easily in MTHF and were studied in this solvent. As a starting point, we measured the fluorescence quantum yields and excited-state lifetimes for the acceptor component and compared the derived values to those found for **REF2** under the same conditions. The various values are similar but there might be a small degree of quenching of the acceptor S_1 state in the dyads. This is the same situation as found with the multi-component array used for photobleaching studies where light-induced electron transfer was invoked to explain the small decrease in fluorescence from the terminal acceptor. The same behaviour might be involved here. Even so, the radiative rate constants

remain in quite good agreement with those calculated from the Strickler-Berg expression (Table 7.6).³⁰ There is no obvious sensitivity towards solvent polarity or the presence of dissolved oxygen.³¹

Table 7.6. Photophysical properties recorded for the 1,2-diaminocyclohexane-linked dyads, measured in spectrophotometric grade MTHF at room temperature. N.B. k_{SB} refers to the radiative rate constant calculated from the Strickler-Berg expression.

	λ_{ABS}	λ_{EM}	ϕ_{FLU}	τ_s / ns	$k_{RAD}/s^{-1} \times 10^8$	$k_{NR}/s^{-1} \times 10^8$	$k_{SB}/s^{-1} \times 10^8$
REF1	499	516	0.61	3.9	1.56	1	1.89
REF2	598	653	0.76	4.1	1.85	0.59	2.3
DAC1	499/ 603	524/ 669	0.003/ 0.2	3.5	0.57	2.29	N/A
DAC2	499/ 602	516/ 664	0.008/ 0.2	3.6	0.55	2.22	N/A

In contrast, it proved difficult to resolve fluorescence from the donor component from the baseline and the apparent quantum yield for emission in the blue region is less than 0.1% for each of the two dyads. This can be compared with a value of 61% found for **REF1** under the same conditions (Figure 7.6). Also, excitation spectra were found to agree remarkably well with absorption spectra recorded across the entire visible spectral window. These findings are consistent with highly efficient EET along the molecular axis (Figure 7.12). It might be stressed that, at the very low concentrations used for this work, there is no likelihood for intermolecular EET.

The various parameters associated with EET were determined from spectroscopic measurements made in MTHF at ambient temperature. These include the spectral overlap integral, the mutual orientation factor and the Coulombic electronic exchange matrix element. These terms are collected in Table 7.7 and were used to compute the likely rate constants for dipole-dipole EET across the two dyads. The derived rates are extremely fast, no doubt aided by the very short separation distances. Molecular models were used to generate the required structural data. The high EET probabilities are in line with those estimated from the excitation spectra and from the residual donor emission. They should be regarded as rather crude estimates, however, because of shortcomings in the structural data.^{32,33}

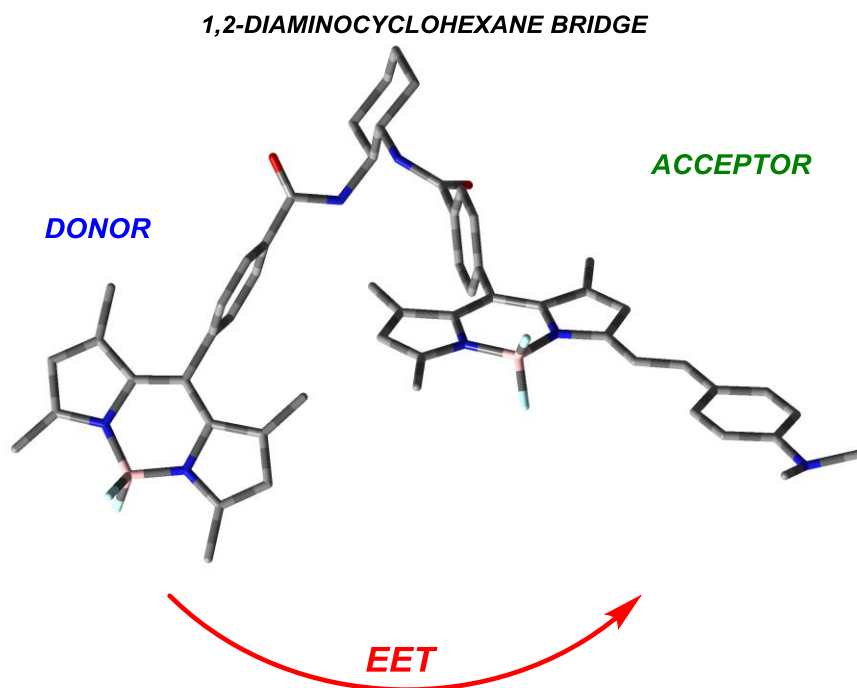


Figure 7.12. Pictorial representation of the proposed electronic energy transfer (EET) in one of the diaminocyclohexane-bridged dyads. The arrow represents through-space EET.

Our studies using steady-state spectroscopy were followed by time-resolved emission spectroscopy in an attempt to determine the rate of EET in these dyads. Unfortunately, the excited state lifetimes for the donor components were too short ($\tau_s < 60$ ps) for us to resolve by single-photon counting methodology. To improve this situation, ultrafast energy transfer measurements were carried out by our collaborators at St. Andrews University where it proved possible to resolve the excited-state dynamics for the donor. An excitation wavelength of 515 nm was used for this work. This is not ideal because some 40% of the excitation energy is directed straight into the acceptor unit. None-the-less, for **DAC1** it was possible with their vastly improved temporal resolution to fit the experimental data to two rise-time constants of 250 fs and 970 fs. Similar values were found for the decay of the donor fluorescence. These rate constants represent the time taken for EET from the donor to the acceptor BODIPY and appear to suggest that two distinct conformations are present in solution. Both conformers undergo very fast EET. Under the same conditions, only a single lifetime of 320 fs was recorded for **DAC2**,

suggesting the presence of one dominant conformer, Figure 7.13. Again, the rate of EET is extremely fast and consistent with our measurements

Table 7.7. Energy transfer data collected for the dyads in MTHF solution.

	P_{EET}	J_{DA}	κ^2	$V_{\text{DA}}/\text{cm}^{-1}$	$R_{\text{DA}}/\text{\AA}$	$k_{\text{EET}}/\text{s}^{-1} \times 10^{12}$
DAC1	99.20%	0.00413	2.88	27.9	11.14	4.18
DAC2	99.80%	0.00344	1.53	21.3	13.09	1.18

The rates of EET measured for these two dyads are not too far removed with those calculated from the spectroscopic data according to the ideal dipole approximation. We are aware that there are doubts about the validity of this theory at very short separations and we hope that our work will help in this evaluation. The bridge is unlikely to favour through-bond EET and so we consider that the major mechanism for the EET event involves a through-space interactive process. To gain further insight into the possible geometries available to these dyads, a series of molecular dynamics simulations were run. For **DAC2**, the calculations indicate two families of conformations where the reactants are held at short separations. The two families do not exchange on short time scales but there is exchange on much longer time scales. Since the reactants are close together, EET is expected to be rapid. For **DAC1**, there are also two families of conformations (Figure 7.14) but here one group has a rather extended geometry. We can suppose that the rate of EET will depend upon the separation distance and, if this is so, the observed lifetimes can be assigned to the EET within each family of conformers. Again, the molecular dynamics indicate diffusive motion around a mean geometry but no exchange on short time scales.

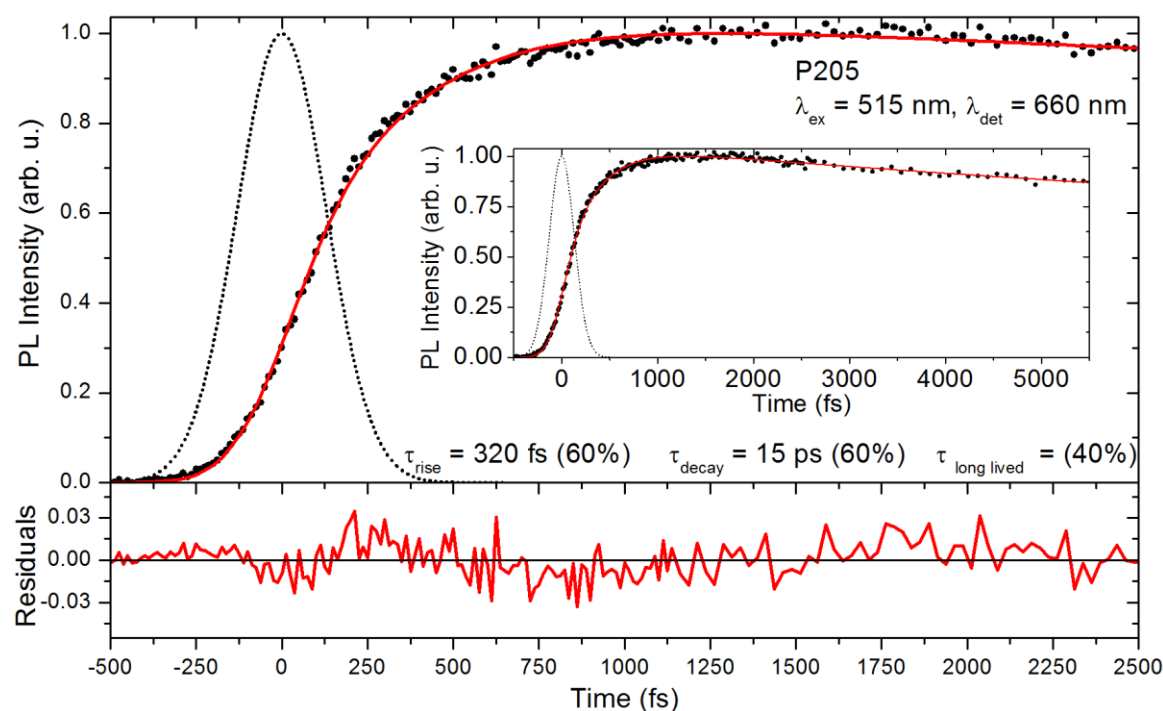


Figure 7.13. Ultrafast PL from **DAC2**, the rise of the PL can be fitted with a time constant of 320 fs. A decay is fitted to ~ 15 ps, with a further long-lived offset. The dotted line is the instrument response function. Measurements and analysis were carried out by Dr. Gordon Hedley at St. Andrew's University.

It has been shown that the nature of the bridging group has great significance for the rates of EET in many molecular systems.^{5,34-36} Such bridges are typically based on fluorene, diphenyl acetylene and p-phenylene vinylene.^{33,37-39} In such cases, through-bond EET is a strong possibility but this is not the case for the dyads investigated here. Specifically, in the case of **DAC1** we hypothesise that the rate of EET is set by the average geometry of the molecule at the moment of excitation. In fact, EET is so fast that there is no time for the geometry to change significantly and no time for exchange to occur. As a result, we find two lifetimes. The same situation is likely to hold for **DAC2** but the geometries of the two groups of conformers are comparable and so similar rates of EET are to be expected. We can improve on this situation by using the molecular dynamics to compute average rates of EET within each family, as has been done by DL Andrews for various types of fluctuating structures, and a collaboration has been started with Dr. TJ Penfold of Newcastle University to explore this possibility. For the moment, we consider

that the various rates of fast EET in these dyads can be explained crudely in terms of the respective molecular geometries⁴⁰ (Figure 7.14). Although we have focussed on the continuously interconverting steps between the two chair conformations, it might be recalled that additional flexibility is provided by the amide bond. This adds to the complexity of the system.

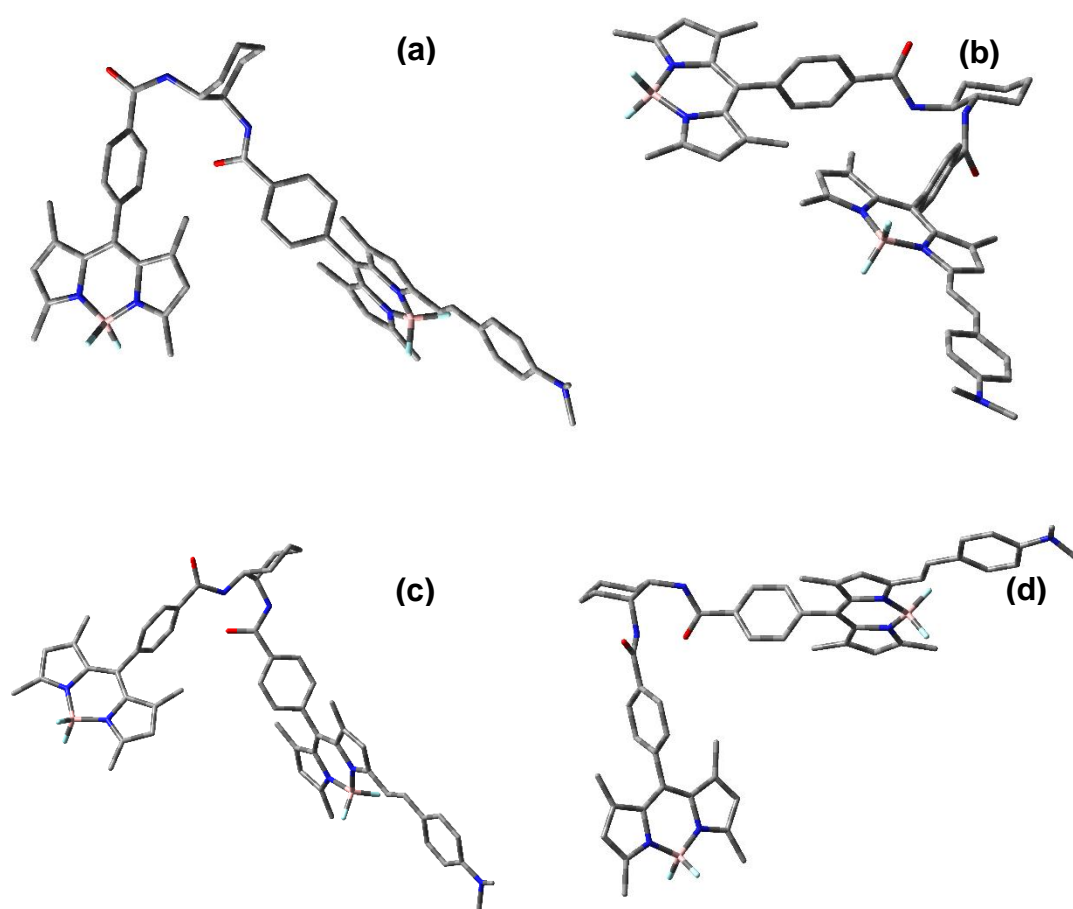


Figure 7.14. Snapshots of molecular conformations representing the important distributions for trans ((a) and (b)) for **DAC2**, and cis ((c) and (d)) geometries for **DAC1**.

7.3 Conclusions

Molecules are in motion when dissolved in a fluid solution at ambient temperature. The largescale rotations can be monitored by fluorescence anisotropy or by FRAP (i.e., fluorescence recovery and photolysis).⁴¹ It is well known from polymer physics, that flexible molecules undergo structural changes that reduce the end-to-end distances and, in many cases, minimize contact with the solvent. In fact, there are many interesting examples of the solvatophobic effect in respect to massive changes in molecular topology. With small semi-flexible molecules it is also reasonable to expect important rotations that have a serious effect on the overall geometry but these can be obscured or hidden from view. In this chapter, we have examined two such examples; the first case relates to a solvent-induced molecular change that involves an unexpected isomerization of an amide linkage. The second example relies on inversion of a cyclohexane ring to modulate the mean geometry of molecular dyad. Unlike many spectroscopic tools, such as NMR spectroscopy, fluorescence can be used to study molecular topologies on timescales faster than the internal rotation. As such, information might be gathered on the individual conformational families.

The first system studied proved very challenging in as much as the differences between secondary and tertiary amides was completely unexpected. The two dyads studied adopted opposite structures with respect to the geometry of the amide linkage in non-polar solvents. Both compounds altered structure in polar solvents but again the opposite isomers were found. This finding testifies to the fantastic opportunities to assemble complex molecular architectures that are provided by an amide linkage. Such connection points are very common in biology but are not so popular in artificial systems. Our work has shown that the geometry of the supermolecule cannot be predicted in advance. We believe that the structure taken up by the assembled entity is set by the entire molecule and not by particular sections. This is because the energies of the various conformers are comparable and subject to varying solvent and/or temperature effects.

The second system investigated was more predictable in terms of the adopted geometry. We were anticipating dynamic exchange interactions but it was impossible to predict the outcome of the EET studies. In fact, EET is one of the few experimental techniques that might be applied to such systems. We were able to resolve two families of conformers in one case but not in the other. This particular study was intended to challenge the idea that the ideal dipole approximation could be applied to molecular dyads where the reactants are in very close proximity. In our case, the separation distance is comparable to the sum of the transition dipole moment vectors. There have been very few attempts to measure rates of EET under such conditions. A final conclusion on this work awaits the results of a detailed molecular dynamics simulation study.

7.4 References

- (1) Forster, T. *Farad. Discuss.* **1959**, 27, 7.
- (2) Harriman, A.; Izzet, G.; Ziesel, R. *J. Am. Chem. Soc.* **2006**, 128, 10868.
- (3) Zhu, L.; Zhao, Y. *J. Mater. Chem. C* **2013**, 1, 1059.
- (4) Seino, Y.; Sasabe, H.; Pu, Y.-J.; Kido, J. *Adv. Mater.* **2014**, 26, 1612.
- (5) Toledano, E.; Rubin, M. B.; Speiser, S. *J. Photochem. Photobiol., A Chem.* **1996**, 94, 93.
- (6) Stryer, L.; Haugland, R. P. *Proc Natl Acad Sci U S A* **1967**, 58, 719.
- (7) Stein, I. H.; Schuller, V.; Bohm, P.; Tinnefeld, P.; Liedl, T. *Chem. Phys. Chem.* **2011**, 12, 689.
- (8) Andrews, D. L.; Curutchet, C.; Scholes, G. D. *Laser Photon. Rev.* **2011**, 5, 114.
- (9) Andrews, D. L.; Rodriguez, J. *J. Chem. Phys.* **2007**, 127, 084509.
- (10) Bencini, A.; Lippolis, V. *Coord. Chem. Rev.* **2010**, 254, 2096.
- (11) Katritzky, A. R.; Fara, D. C.; Yang, H.; Tamm, K.; Tamm, T.; Karelson, M. *Chem. Rev.* **2004**, 104, 175.
- (12) Reichardt, C. *Chem. Rev.* **1994**, 94, 2319.
- (13) Zhou, Y.; Stell, G. *J. Chem. Phys.* **1992**, 96, 1507.
- (14) Catalán, J.; López, V.; Pérez, P.; Martin-Villamil, R.; Rodríguez, J.-G. *Liebigs Annalen* **1995**, 1995, 241.
- (15) Catalán, J.; Díaz, C.; López, V.; Pérez, P.; De Paz, J.-L. G.; Rodríguez, J. G. *Liebigs Annalen* **1996**, 1996, 1785.
- (16) Sauerwein, B.; Murphy, S.; Schuster, G. B. *J. Am. Chem. Soc.* **1992**, 114, 7920.
- (17) Megerle, U.; Selmaier, F.; Lambert, C.; Riedle, E.; Lochbrunner, S. *Phys. Chem. Chem. Phys.* **2008**, 10, 6245.

- (18) Benniston, A. C.; Copley, G.; Harriman, A.; Howgego, D.; Harrington, R. W.; Clegg, W. *J. Org. Chem* **2010**, 75, 2018.
- (19) Barbara, P. F.; Meyer, T. J.; Ratner, M. A. *J. Phys. Chem.* **1996**, 100, 13148.
- (20) Spies, C.; Gehrke, R. *J. Lumin.* **1999**, 82, 333.
- (21) King, G.; Warshel, A. *J. Chem. Phys.* **1990**, 93, 8682.
- (22) Harriman, A.; Rostron, J. P.; Cesario, M.; Ulrich, G.; Ziessel, R. *J. Phys. Chem. A* **2006**, 110, 7994.
- (23) Giaimo, J. M.; Gusev, A. V.; Wasielewski, M. R. *J. Am. Chem. Soc.* **2002**, 124, 8530.
- (24) Bandi, V.; El-Khouly, M. E.; Ohkubo, K.; Nesterov, V. N.; Zandler, M. E.; Fukuzumi, S.; D'Souza, F. *J. Phys. Chem. C* **2014**, 118, 2321.
- (25) Oliver, A. M.; Craig, D. C.; Paddon-Row, M. N.; Kroon, J.; Verhoeven, J. W. *Chem. Phys. Lett.* **1988**, 150, 366.
- (26) Brun, A. M.; Harriman, A.; Heitz, V.; Sauvage, J. P. *J. Am. Chem. Soc.* **1991**, 113, 8657.
- (27) Benniston, A. C.; Harriman, A. *Chem. Soc. Rev.* **2006**, 35, 169.
- (28) Pettersson, K.; Kyrychenko, A.; Rönnow, E.; Ljungdahl, T.; Mårtensson, J.; Albinsson, B. *J. Phys. Chem. A* **2006**, 110, 310.
- (29) Harriman, A.; Heitz, V.; Sauvage, J. P. *J. Phys. Chem.* **1993**, 97, 5940.
- (30) Ziessel, R.; Ulrich, G.; Harriman, A. *New J. Chem.* **2007**, 31, 496.
- (31) Strickler, S. J.; Berg, R. A. *J. Chem. Phys.* **1962**, 37, 814.
- (32) Harriman, A.; Ziessel, R. *Photochem. Photobiol. Sci.* **2010**, 9, 960.
- (33) Gilbert, M.; Albinsson, B. *Chem. Soc. Rev.* **2015**, 44, 845.
- (34) Benniston, A. C.; Clift, S.; Hagon, J.; Lemmetyinen, H.; Tkachenko, N. V.; Clegg, W.; Harrington, R. W. *Chemphyschem* **2012**, 13, 3672.
- (35) Eng, M. P.; Albinsson, B. *Chem. Phys.* **2009**, 357, 132.

- (36) Schanze, K. S.; Neyhart, G. A.; Meyer, T. J. *J. Phys. Chem.* **1986**, *90*, 2182.
- (37) Davis, W. B.; Svec, W. A.; Ratner, M. A.; Wasielewski, M. R. *Nature* **1998**, *396*, 60.
- (38) de la Torre, G.; Giacalone, F.; Segura, J. L.; Martín, N.; Guldi, D. M. *Chem. Eur. J.* **2005**, *11*, 1267.
- (39) Miura, T.; Carmieli, R.; Wasielewski, M. R. *J. Phys. Chem. A* **2010**, *114*, 5769.
- (40) Kasha, M. *Radiat. Res.* **1963**, *20*, 55.
- (41) Cardarelli, F.; Tosti, L.; Serresi, M.; Beltram, F.; Bizzarri, R. *J. Biol. Chem.* **2012**, *287*, 5554.

Chapter 8. Experimental Methods

8.1 Materials

All solvents used throughout this research project were of the highest available purity, usually spectrophotometric grade, with the exception of solvents used for electrochemical studies. The spectrophotometric grade solvents were purchased from Sigma-Aldrich and used without further purification after checking for the presence of fluorescent impurities. The purity and properties of solvents used are important here. Factors such as dielectric constant and polarity can affect the spectroscopic behaviour of dyes, for example peak maxima, Stokes' shifts, the fluorescence quantum yields, and so on. In order to be consistent, a single literature source was used to identify these properties as much as is possible.¹ Solvents used for electrochemical investigations were refluxed over appropriate drying reagents, distilled and used immediately. Tetrabutylammonium hexafluorophosphate (NBu_4PF_6) and ammonium hexafluorophosphate (NH_4PF_6) were used as electrolytes, both purchased from Sigma-Aldrich and used after repeated recrystallisation. These materials were kept dry. Special materials, such as sucrose octaacetate, were purified by standard protocols before use and certain solvents, such as butyronitrile, were redistilled by other members of the group immediately before use. Anhydrous solvents were purchased from Sigma-Aldrich and used by way of syringe injection techniques. Ethers, most notably 2-methyltetrahydrofuran— used extensively for low-temperature emission spectroscopy – was used fresh and kept away from air. Samples were replaced at very regular intervals in order to avoid contamination by peroxides.

The vast majority of the compounds studied here were synthesised in the research laboratory of Dr Raymond Ziessel at the Université Louis Pasteur de Strasbourg. The samples were subjected to comprehensive purification procedures before shipping to Newcastle. The compounds were fully characterised by a wide battery

of analytical techniques. Some samples were further analysed by 700 MHz NMR spectroscopy by Dr. Corrine Wills at Newcastle University. We are grateful to both Dr. Ziesel and Dr. Wills for their collaboration and for many fruitful discussions during the course of this work. The team in Strasbourg also recorded some of the electrochemical measurements but, wherever possible, these were repeated in Newcastle. Sometimes, the amount of sample provided – the emphasis being placed on purity not quantity – was insufficient for electrochemistry or for determination of the molar absorption coefficient. The latter measurements were made at the end of the series of experiments, often consuming all the remaining material. Usually, samples were part of a small series, with control compounds being available for comparative studies.

Additional compounds were synthesised in Newcastle by the research group supervised by Dr. Julian Knight. These compounds were returned to the group for further purification after initial trial studies. Several iterations were needed before complete satisfaction about their purity was reached. Fresh samples were synthesised for comparative purposes. These particular compounds were essentially non-fluorescent at room temperature and therefore especially vulnerable to the presence of trace impurities at levels far below what can be detected by NMR spectroscopy. All samples were stored as solids in the dark and usually in the fridge.

In order to measure fluorescence quantum yields (ϕ_F), some well-known and thoroughly established reference compounds were used. These include magnesium *meso*-tetraphenylporphyrin (Mg[TPP]),² Cresyl Violet,³ Rhodamine 6G,⁴ Rhodamine B,⁴ and Nile Red.⁵ The emission quantum yields of these standards are available from peer-reviewed literature citations. In addition, many secondary standards were employed for quantum yield measurements. Without exception, these were BODIPY-based dyes studied by other members of the MPL. Appropriate solvents were used for these studies and great care was taken to ensure that the solution was free from undissolved solid. Some fluorescence measurements, notably those with solid samples, were undertaken with an integrating sphere.

8.2 UV-Visible Absorption Spectroscopy

All the solutions used for absorption spectroscopy were prepared using spectrophotometric grade solvents. Most spectra were recorded using a Hitachi U3310 dual-beam spectrophotometer. Cuvettes used in these experiments were fabricated from optical quality quartz. The scan rate used for routine spectra was usually set at 60 nm/ min, slit width at 1 nm and the resolution was set at 0.2 nm unless specified otherwise. The possible error in wavelength position is estimated to be less than 1 nm. The concentration of solutions was kept between 10^{-7} M, for samples with very high molar absorption coefficient (i.e., in excess of $100\,000\text{ M}^{-1}\text{ cm}^{-1}$), and 10^{-6} M to prepare the solution of interest. In some cases, when the absorption maximum of the target dye was above 700 nm, a Perkin-Elmer Lambda 35 spectrophotometer was used due to its improved stability at lower energies. Essentially, this translates to less noise at longer wavelengths. All of the settings and procedures were kept the same as for the Hitachi U3310 spectrophotometer mentioned above. In order to determine the molar absorption coefficient (ϵ) of the dyes described here, the Beer-Lambert law was used, Equation 8.1.

$$\epsilon = A/cl \qquad \text{Equation 8.1}$$

The molar absorption coefficient in units of $\text{M}^{-1}\text{ cm}^{-1}$ is determined by dividing absorbance (dimensionless) by concentration (M) multiplied by the path length in centimetres. As necessary, a series of cuvettes of different path lengths was used for improved precision and a range of concentrations was employed. The limit to the accuracy of these measurements was set by the amount of material available. Solutions were filtered with a sub-micron membrane filter prior to recording the absorption spectrum. Temperature variations were achieved with either a circulating fluid bath or a high-temperature Harrick's demountable cell. For some studies, the absorption spectrum was recorded at low temperature using an optical Dewar.

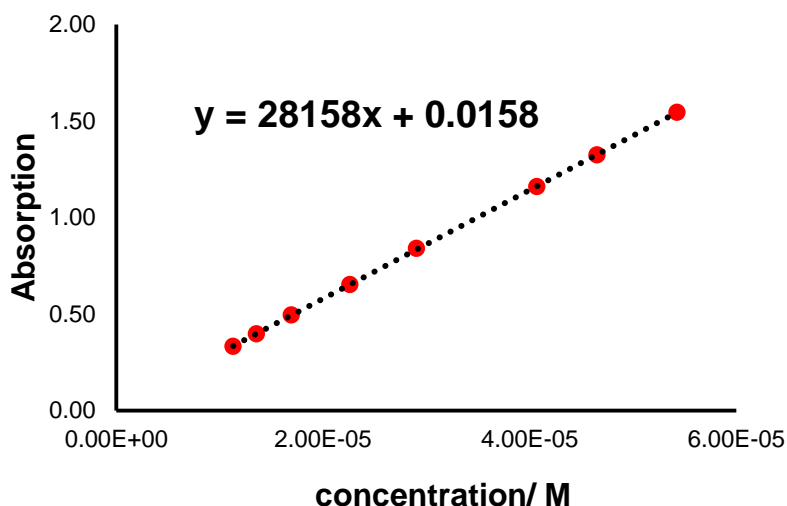


Figure 8.1. An example of a Beer-Lambert plot determined for a constrained BODIPY dye.

8.3 Fluorescence Spectroscopy

Fluorescence spectra were recorded using a Hitachi F-4500 fluorescence spectrophotometer, for most measurements the scan rate was kept at 60 nm/ min. The excitation and emission slit widths were kept at 2.5 for most solutions. They were usually increased for solid samples as well as for quartz slides and for low-temperature measurements carried out using an optical cryostat (Oxford Instruments). The response rate was kept at the auto setting but was varied for weak samples. Dilute solutions were used, the absorbance at the excitation wavelength was kept between 0.05 and 0.1. This was done in order to avoid re-absorption and inner-filter effects. The solutions used were always prepared using spectrophotometric grade solvents and recorded using quartz cuvettes. Solutions were prepared freshly and passed through a sub-micron membrane filter before making the measurement. Optical filters were always used to isolate fluorescence from scattered light coming from the excitation source. As for the absorption spectral measurements, the resolution of all spectra recorded was 0.2 nm. This guarantees small experimental error for the emission wavelength, this being less than 1 nm. Without exception, fluorescence excitation spectra were recorded for the dyes of interest and compared with the corresponding absorption spectrum.

Spectra were corrected for spectral imperfections using a calibration curve supplied by the instrument maintenance staff. At regular intervals, calibration curves were recorded using Rhodamine B solutions supplied by the instrument maker. The instrument was maintained by LAT Inc. and serviced at six-monthly intervals to ensure proper calibration of wavelength and intensity linearity. All spectral data were removed from the controlling PC and analysed separately, usually after conversion from wavelength to wavenumber. All fluorescence measurements were repeated several times to ensure self-consistency.

8.4 Lifetime Measurements

Time-resolved fluorescence spectroscopy is an essential technique needed in order to investigate the excited state of a luminescent chromophore. Factors contributing to the overall emission lifetime are solvent relaxation, interactions with surrounding molecules, and changes in macromolecular conformation.⁶ Lifetime measurements were carried out at room temperature using optically dilute samples. The absorbance at the excitation wavelength was about 0.1. For most compounds studied here, 600 channels were used and 150 runs were signal averaged. The method used for recording fluorescent lifetimes was time-correlated, single photon counting (TCSPC). Here, results are presented as a graph of time (ns) against voltage (V). It is a highly sensitive method with good resolution.^{7,8} TCSPC determines the statistical distribution of the intensity decay by recording the arrival times of individual photons after the incident pulse of light.^{9,10} A high-resolution PTI EasyLife set-up was used to collect data; pulsed laser diodes were used as excitation source with output at 310, 440, 505, 525 or 635 nm. The scattered laser light was measured using a solution of Ludox in distilled water in order to generate the instrument response (IRF).

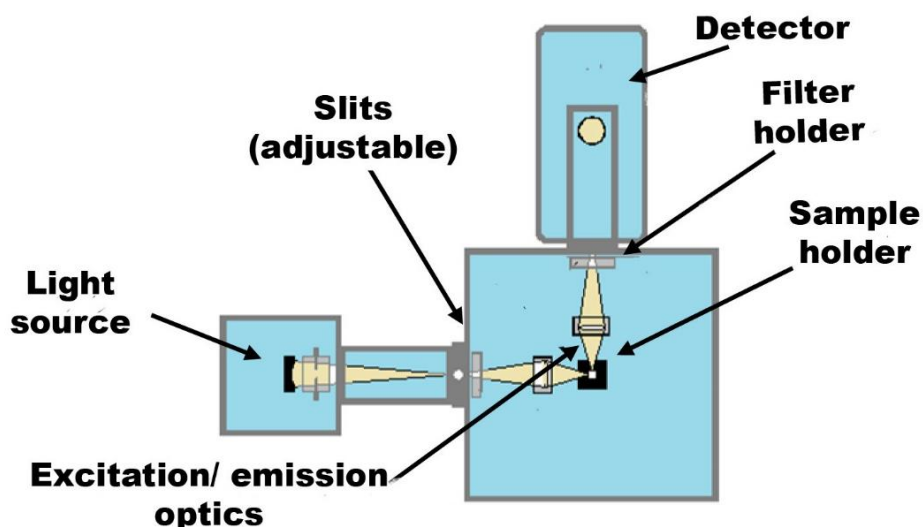


Figure 8.2. A schematic representation of the lifetime measurement set up.

Data analysis was carried out using Felix 32 software. In order to perform the analysis, the decay curve needs to be selected, the range of interest is identified and highlighted. The method used was non-linear, least-squares iteration. This approach requires an initial estimate of the lifetime and the preferred method of analysis. A mono-exponential fit was usually the approach of choice, at least at the beginning of the analysis, unless there was a strong possibility for a second component. A range of time bases is needed and a small variation of count rates should be used to increase reliability of the output. Emission can be isolated from scattered laser light using optical filters in conjunction with a high-radiance monochromator. Wherever possible, different excitation wavelengths should be used. After analysis, it is necessary to judge the quality of the weighted residuals, the auto-correlation function and the deconvoluted decay.

Data analysis was made at the instrument using software provided by the manufacturer. Protocols for assessing the quality of the fit were taken from the literature; established by Eaton¹¹ as well as by O'Connor and Phillips.¹² These analytical tests included minimization of chi squared and visual inspection of weighted residuals. Curve fitting was carried out by means of non-linear, least squares method; it is a statistical fitting approach, therefore substantial data sets are required to ensure validity. The use of this method however is discouraged

when more than three components are present. In complex cases, analytical methods like global analysis and maximum entropy methods are recommended.^{11,13}

8.5 Temperature- Dependent Spectroscopic Studies

8.5.1 Low-Temperature

Low- temperature studies were performed using an Oxford Instruments Optistat DN cryostat, connected to an ITC temperature controller. The cryostat used here is a nitrogen cryostat, i.e. it uses liquid nitrogen to cool a sample by conduction via a stream of nitrogen gas. The nitrogen reservoir and heat exchanger are surrounded by a high vacuum. The temperature is regulated using a precision controller and can be adjusted by manual nitrogen flow control. Solutions were prepared in a solvent known to form an optical glass at low temperature. The optical absorbance at the excitation wavelength was kept low, between 0.05 and 0.1. The prepared solution was purged with nitrogen for 5 minutes before being sealed into a glass cuvette and placed in the sample holder of the cryostat. Using this set up, it is possible to record absorption, emission and excitation spectra over a range from 80 to 340K.

8.5.2 High-Temperature

High-temperature spectroscopy was carried out on solid-state samples in the form of KBr discs. The measurements were carried out using a temperature-controlled, demountable liquid cell purchased from Harrick Scientific Products. This cell was used for measurements over the range from 298 to 513K (although according to the manufacturer the lowest temperature it can go to is 223K). High-temperature measurements were also carried out on liquid samples, this was done using either the demountable cell or a circulating fluid bath. Using this latter technique, the available temperature range is from 273K to about 333K. At the lower

temperatures, the cell windows were purged constantly with a strong flow of N₂ to avoid misting, especially on humid days.

8.6 Electrochemistry

Cyclic voltammetry was carried out using dry solvents, usually anhydrous dichloromethane or acetonitrile. The solvent was used to prepare a 0.1M electrolyte background solution. The background solution was purged with dried nitrogen in order to eliminate any oxygen, great care was taken to make sure the cell was kept dry and no water was present in the system before addition of 1×10^{-3} M compound of interest. This was done by recording a background CV, once satisfied there is neither water nor oxygen present in the system, the appropriate amount of the solid compound of interest was added. Electrodes most often used were glassy carbon or platinum as working electrodes, and wither silver or platinum wire as counter electrodes. The reference electrode was an Ag/ Ag⁺ electrode. The working and counter electrodes were polished using an alumina slurry before use. Ferrocene was used as an internal reference. The measurements were also done over a range of scan rates as this provides valuable information on the degree of reversibility of the oxidation / reduction reactions. The software used to record and extract information was Chi600.

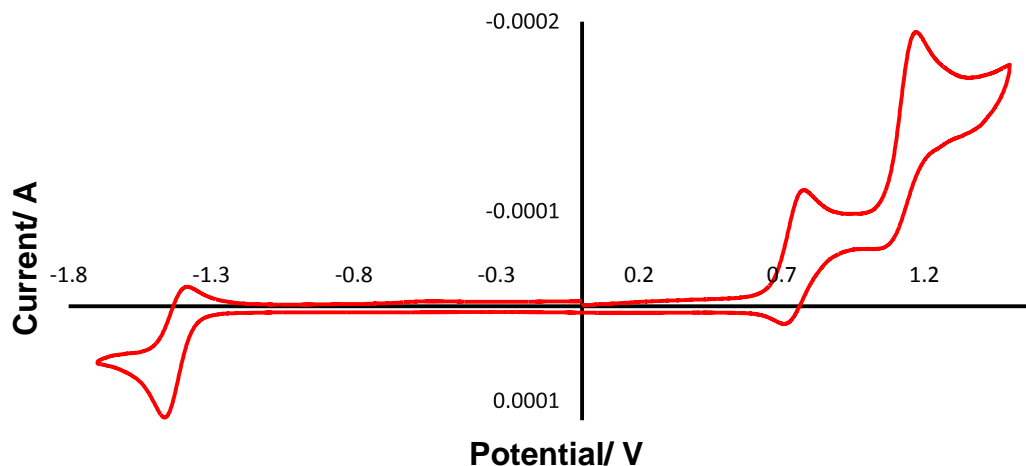


Figure 8.3. Above is an example of a CV of one of the compounds presented within this thesis.

Spectroelectrochemistry was carried out using a CHI potentiostat and employing a honeycomb spectro-electrochemical cell from Pine-Research Instruments Inc.. The working electrode was of the honeycomb design, which means there are holes in the electrode that allow the light to pass directly through the solution.

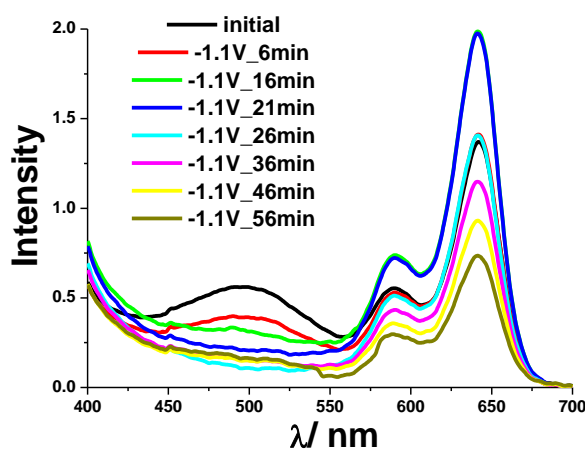


Figure 8.4. An example of a spectro-electrochemical study on a TPA-DPP-BODIPY system.

8.7 Sample Preparation

All solvents used here were of spectrophotometric grade, they were checked for absorbing or emitting impurities before being used. While working with fluorescent materials, the cleanliness of glassware, as well as the work station, is of great importance. Fluorescence spectroscopy is a very sensitive technique; any impurity can be picked up while running an emission spectrum. Excitation spectra were always collected and compared to the absorption spectrum, this was done to confirm the authenticity of the recorded fluorescence.

Solutions for spectroscopic examinations were prepared by dissolving a small amount of compound in the solvent of interest. Most of the dyes encountered here were readily soluble in organic solvents, however in order to make sure the sample is fully dissolved in a chosen solvent the solutions were placed in an ultra-sonic bath for a minute. The solutions were passed through micro-porous discs to ensure the sample was fully uniform. KBr discs for high-temperature fluorescence experiments were prepared by grinding together oven-dried KBr salt with a small amount of a chosen compound, about 1% w/w concentration. This was followed by compressing the powder into a small disc under vacuum using a stainless steel die press.

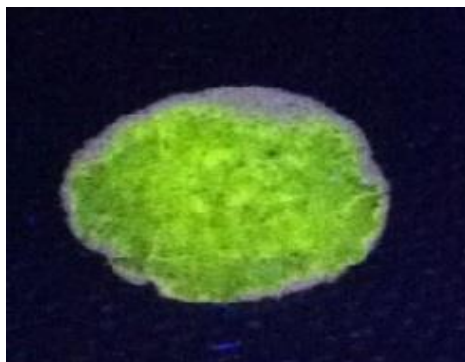


Figure 8.5. An example of a fluorescent KBr disc.

8.8 Data Analysis

8.8.1 Fluorescence Quantum Yield

Fluorescence quantum yield measurements were carried out with great care, usually at room temperature. The samples were prepared as described in Section 8.7. In principle, the number of absorbed and emitted photons need to be measured in order to determine the emission quantum yield. Equation 8.2¹⁴ is used to calculate the quantum yield of fluorescence. Here, F_s is the area under the emission curve of the sample, whereas F_R is the area under the emission curve of the reference compound recorded over the same spectral range. The term A_R refers to the effective absorbance at the respective excitation wavelength for the reference compound (A_S is the corresponding value for the sample) and finally n_s and n_R are refractive indices for the solvent used to dissolve the sample and for the reference, respectively. Wherever possible, the same solvent was used for sample and reference. The spectral correction factor supplied with the instrument was used and all data manipulations were made after conversion from wavelength to wavenumber. As appropriate, reduced emission spectra were used.

$$\Phi = \frac{F_s \times (1 - \exp(-A_R \times \ln(10))) \times n_s^2}{F_R \times (1 - \exp(-A_S \times \ln(10))) \times n_R^2} \Phi_R \quad \text{Equation 8.2}$$

When measuring a fluorescence quantum yield, great care needs to be taken as there are many possibilities for experimental error: These include inner filter effects, temperature perturbations, and impurity effects amongst others.¹¹ The use of a reference standard is a further source of error. There are very few reference compounds with a well-established fluorescence quantum yield that is free of potential problems. Often, finding a reference with similar absorption and emission profiles to those of the sample is a great challenge, however this is crucial for the measurement to be successful. Cresyl Violet³ is a good example of the sort of difficulties that might be encountered. This reference is useful for the red region but the reported quantum yield is sensitive to concentration and solvent, varying

enormously over a modest range. A member of the MPL has studied this compound in detail and found quantum yields ranging from unity to less than 20% according to the experimental conditions.

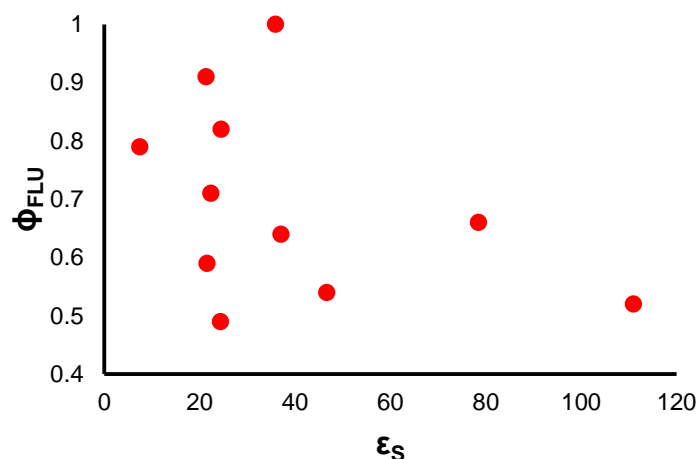


Figure 8.6 A plot of fluorescence quantum yield for Cresyl Violet (ϕ_{FLU}) against solvent dielectric constant (ϵ_S). It demonstrates how Cresyl Violet is very sensitive to solvent. This data was collected by Roza Al-Aqar. ϵ_S is used for convenience, however the specific interaction between solvent and Cresyl Violet depends on the nature of the solvent.

Standard quartz cuvettes were used throughout, and the absorbance at the excitation wavelength was never higher than 0.1; this is crucial if one wants to avoid the inner-filter effect. Often, ϕ is dependent on temperature, this is especially so for the molecular-scale rotors. Therefore, all experiments were carried out at 20°C unless stated otherwise. The rate of radiative decay is also dependent on solvent refractive index and therefore one will encounter studies on the effect of solvent on the rate of radiative decay (and by extension the fluorescence quantum yield). Experimentally, it is crucial to establish that the spectrophotometer is properly calibrated and we regularly employed a concentrated solution of Rhodamine 6G in ethanol to confirm the correction factor. In all cases, the absorbance at the excitation wavelength was checked before and after recording the emission spectrum. This was done to confirm that the solution was stable and free from particulate material.

8.8.2 Radiative Rate Constant (k_{rad})

The radiative rate constant describes the rate at which the excited state of the fluorophore relaxes by a process accompanied by photon emission. This is in competition with a non-radiative process that ultimately returns the molecule to the ground state. The radiative rate constant is determined experimentally from Equation 8.3:

$$k_{rad} = \frac{\phi}{\tau} \quad \text{Equation 8.3}$$

Here, ϕ is the experimentally determined emission quantum yield, τ is the corresponding excited-state lifetime (in seconds). This experimental estimate of the radiative rate constant can be compared to the theoretical value determined from the Strickler-Berg expression¹⁵, Equation 8.4:

$$k_{rad} = 2.88 \times 10^{-9} n^2 < \nu^{-3} >_{av} \frac{g_l}{g_u} \int \epsilon d \ln \tilde{\nu} \quad \text{Equation 8.4}$$

Here, n is the solvent refractive index, ν is the fluorescence maximum in cm^{-1} , $\int \epsilon d \ln \tilde{\nu}$ represents the area under the spectral curve (only takes into consideration the lowest-energy transition), and finally $\frac{g_l}{g_u}$ refers to degeneracy of the respective upper and lower states. The Strickler-Berg expression is very useful, however it does have limitations. Firstly, it needs to be taken into account that it works only for compounds with a small Stokes' shift. A second important requirement is the mirror symmetry of lowest-energy transition in the absorption spectrum and the emission curve. It is also worth noting that it can only be applied safely when the quantum yield is relatively high, i.e. in excess of 10%. Nevertheless this is a very useful expression, it works very well with molecules that meet the conditions mentioned earlier but it is often applied to cases outside these limits. It might also be mentioned that some authors, notably Birks,¹⁶ Knox^{17,18} and Phillips,¹⁹ have questioned the exact formulation of the refractive index factor. Knox, in particular, has questioned the squared dependence.

8.8.3 Electronic Energy Transfer Rate Constant

Electronic energy transfer plays a crucial role throughout this work. The Fermi golden rule has been applied to calculate the rate constant for electronic energy transfer (EET).²⁰

$$k_{EET} = \frac{2\pi}{\hbar} \times |v_{DA}|^2 \times |\kappa^2| \times s^2 \times J_{DA} \quad \text{Equation 8.5}$$

Here, k_{EET} is the rate constant for the EET event in s^{-1} , κ is the orientation factor, J_{DA} is the overlap integral between the donor emission and the corresponding acceptor absorption spectra (Equation 8.5). Absorption and emission spectra for J_{DA} are always recorded in the same solvent under the same conditions; the wavelength (in nm) is converted to wavenumber (in cm^{-1}) and reduced (Equation 8.6). The term v_{DA} refers to the electronic coupling matrix element between donor and acceptor (Equation 8.7),²¹ and finally s is the Onsager cavity screening factor (Equation 8.8). It is worth mentioning that for random orientations the value of κ is equal to approximately 0.67 (or $2/3$). The body of this work is concerned with molecular dyads and related species and therefore complicated computational operations have to be carried out in order to determine an appropriate value for κ .

$$J_{DA} = AB \int \frac{F_D(v)}{v^3} \times \frac{\epsilon_A(v)}{v} dv \quad \text{Equation 8.6}$$

$$v_{DA} = \frac{\mu_D \times \mu_A}{R_{DA}^3 \times (4\pi\epsilon_0)} \quad \text{Equation 8.7}$$

$$s = \frac{3}{2n^2 + 1} \quad \text{Equation 8.8}$$

$$\mu^2 = 9.186 \times 10^{-3} \times n \times \int \frac{\epsilon}{v} dv \quad \text{Equation 8.9}$$

Crucial terms above are: R_{DA} is the centre-to-centre distance between donor and acceptor, n is the refractive index of the surrounding medium, ε_A is the molar absorption coefficient of the acceptor, F_D is the emission profile of the donor, while μ_D and μ_A are the transition dipole moments for the donor and acceptor, respectively. In order

to calculate a transition dipole moment of either donor or acceptor Equation 8.9 is applied. However, it is important to remember that Equation 8.10 is in fact the original equation derived by Förster.²²

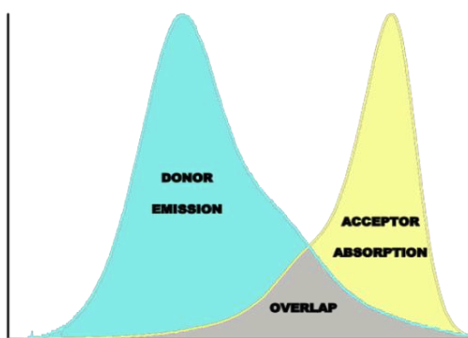


Figure 8.7. Reduced spectra of two Bodipy compounds. Highlighted in grey is the spectral overlap.

$$|\mu_A^2| = \frac{3000 \ln 10 \hbar c n}{8 N_A \pi^3 f^2} \int \left(\frac{\varepsilon_A}{\nu} \right) d\nu$$

Equation 8.10

8.8.4 Energy Transfer Probability

There are many different equations used to calculate the probability of electronic energy transfer (P_{EET}) from donor to acceptor. The choice of applicable equation is dependent on available information. Equation 8.11 and Equation 8.12 show the most widely applied method used in this thesis. This method establishes the probability of energy transfer by taking a ratio of fluorescence quantum yields (or lifetimes) of the D-A system and of the isolated donor.^{23,24}

$$P_{EET} = 1 - \frac{\phi_{DA}}{\phi_A} \quad \text{Equation 8.11}$$

$$P_{EET} = 1 - \frac{\tau_{DA}}{\tau_A} \quad \text{Equation 8.12}$$

$$P_{EET} = \frac{k_{EET}}{(k_{EET} + \tau_s^{-1})} \quad \text{Equation 8.13}$$

$$P_{EET} = \frac{R_0^6}{(R_0^6 + R_{DA}^6)} \quad \text{Equation 8.14}$$

Equation 8.14 is similar to Equation 8.13, however it uses the critical distance for the EET event rather than the rate of energy transfer.²⁵⁻²⁷

8.8.5 Englman-Jortner Energy-Gap Law

The Englman-Jortner energy-gap law has been proven to be hugely appropriate as a tool by which to study non-radiative processes for a wide range of excited states.^{28,29} Equation 8.15 demonstrates that the rate of the radiationless transition decreases as the energy gap between the two states increases.³⁰

$$k_{NR} = \frac{\sqrt{2\pi}}{\hbar} \times \frac{C^2}{\sqrt{k_B T \hbar \omega}} \times \exp(-S) \times$$

Equation 8.15

$$\exp\left(\frac{-\Upsilon \Delta E}{\hbar \omega}\right)$$

Here, k_{NR} is the non-radiative rate constant, C is the electron-vibrational coupling matrix element, ΔE is the energy gap between electronic levels, $\hbar \omega$ is the coupling vibrational mode, λ is the nuclear distortion, S is the Huang-Rhys factor, Equation 8.16, and finally Υ is a coefficient, Equation 8.17.

$$S = \lambda / \hbar \omega$$

Equation 8.16

$$\Upsilon = \ln(|\Delta E| / S \hbar \omega) - 1$$

Equation 8.17

The Englman-Jortner expression is based on a number of assumptions; it is assumed that the normal modes and their frequencies are equivalent in the two electronic states with the noted exceptions of their mutual displacement in the origins of the normal coordinates. In the original publication, only a two-electronic level system is considered and anharmonicity effects are disregarded.^{30,31}

8.8.6 Electron Transfer

Electron transfer is of crucial importance in Nature; Marcus³²⁻³⁴ was first to formulate the expression for the rate of electron transfer in the 1950's. There is an excellent review on charge-transfer processes written by Wasielewski.³⁵ The activation energy for electron transfer (Equation 8.21) is reliant on the total reorganization energy (λ) and the thermodynamic driving force (ΔG_{CT}), the electronic coupling matrix element (V_{DA}) and the thermally averaged Franck-Condon factor (FC).³⁶ In turn, the reorganization energy (Equation 8.22) involves both the nuclear reorganization (λ_N) and corresponding solvent rearrangement (λ_S) terms.

$$k_{ET} = \left(\frac{2\pi}{\hbar}\right) V_{DA}^2 (FC) \quad \text{Equation 8.18}$$

$$V_{DA} = V_{DA}^0 \exp(-\beta R) \quad \text{Equation 8.19}$$

$$[FC] = \left(\frac{1}{\sqrt{4\pi k_B T \lambda}}\right) \exp\left(\frac{-\Delta G^*}{T k_B}\right) \quad \text{Equation 8.20}$$

$$\Delta G^* = (\lambda + \Delta G_{CT})^2 / 4\lambda \quad \text{Equation 8.21}$$

$$\lambda = \lambda_N + \lambda_S \quad \text{Equation 8.22}$$

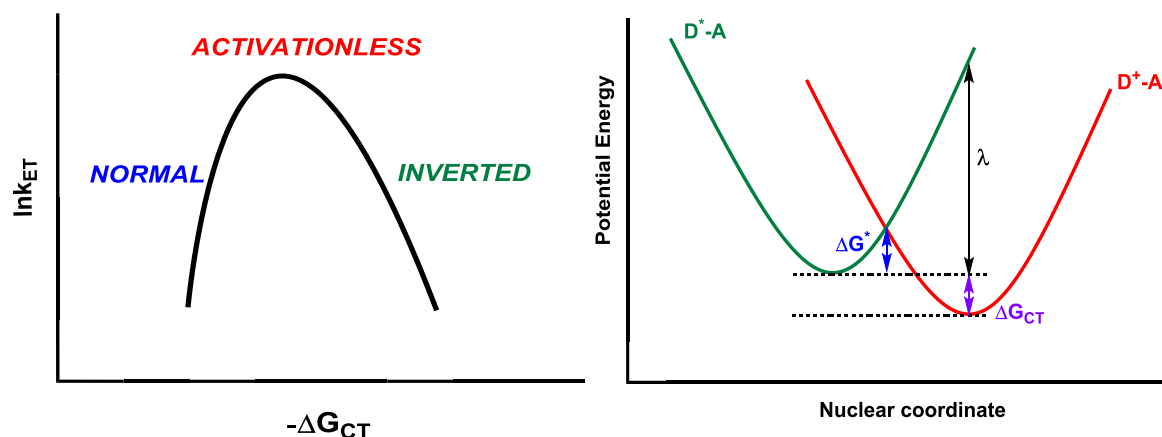


Figure 8.8. Panel on the left demonstrates the dependence of the rate of electron transfer on the thermodynamic driving force; whereas the panel on the right shows the potential energy curves for electron transfer in the Marcus normal regime.

The rate of electron transfer is dependent on the scale of the driving force (Equation 8.23), critically it is a quadratic dependence. This gives rise to three distinct regions: identified as normal, activationless and inverted. In the case of the normal region, the magnitude of the driving force is less than that of the reorganisation energy, for the activationless process the reorganisation energy and the driving force are equal. Finally in the case of the inverted region, the driving force is greater than the reorganisation energy.³⁷

$$\Delta G_{CT} = e[E_{OX} - E_{RED}] - E_{00} - E_{ES} - E_{SOL} \quad \text{Equation 8.23}$$

$$E_{ES} = \frac{e^2}{(4\pi\epsilon_0)\epsilon_S R_{CC}} \quad \text{Equation 8.24}$$

$$E_{SOL} = \frac{e^2}{8\pi\epsilon_0} \left(\frac{1}{R_D} + \frac{1}{R_A} \right) \left(\frac{1}{\epsilon_{Ref}} - \frac{1}{\epsilon_{Sol}} \right) \quad \text{Equation 8.25}$$

The thermodynamic driving force (Equation 8.23) is calculated with the help of cyclic voltammograms obtained experimentally. Here, E_{ES} refers to the electrostatic energy, calculated from Equation 8.24 where R_{CC} is the centre-to-centre separation distance between an acceptor and donor units, whereas E_{SOL} refers to a correction for the reduction potentials being measured in a different solvent (Equation 8.25).

8.9 Computational Methods

8.9.1 PeakFit- Spectral Analysis

The commercially available PeakFit software is used to deconstruct broad absorption and emission spectral traces into a series of components. We aimed to fit each spectrum into a minimum number of Gaussian-shaped bands.³⁸ The software estimates the number of components needed, however the operator is able to adjust that estimate (add or remove components) in order to improve the fit and decides whether the estimates need to be of the same half-width. This is an important step as the spectral analysis needs to be scientifically plausible as well as being mathematically accurate. In order to perform a PeakFit analysis, a spectral region of interest is selected (usually the lowest-energy transition). Secondly, the spectrum needs to be converted from wavelength (nm) to wavenumber (cm^{-1}) and reduced. While performing a spectral analysis using PeakFit it is important to determine whether the baseline needs correcting. If so, the software offers a range of different baseline corrections procedures. The best procedure, however, is to make all necessary corrections prior to importing a spectrum into the software.

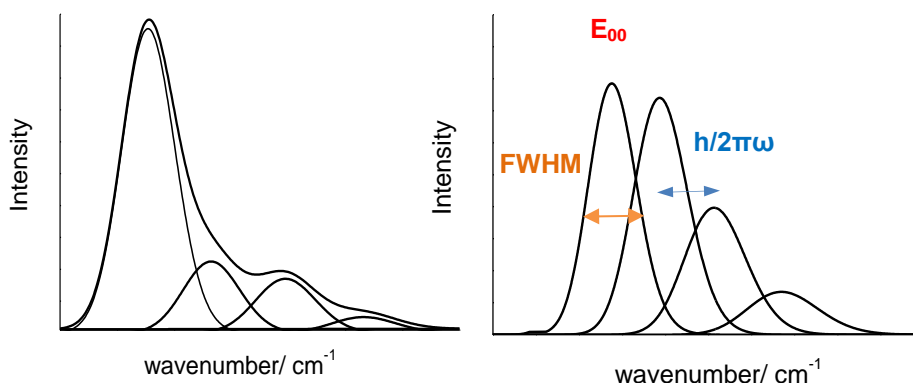


Figure 8.9. Panel on the left hand side shows an example of spectral fit carried out using PeakFit whereas panel on the right demonstrates parameters extracted from spectral fitting.

In the case of very weakly fluorescent compounds, spectra often needed smoothing. However, one needs to be very careful when selecting the degree of smoothing as this can severely alter the spectral profile as well as obscure subtle details present in the spectra. Figure 8.9 is an example of a PeakFit analysis. On the left-hand side, the experimentally obtained absorption spectrum is deconstructed into individual Gaussian bands; on the right-hand side the parameters obtained from the spectral fitting are highlighted. Each Gaussian band corresponds to an individual transition.

There are several crucial pieces of numerical data that can be obtained by carrying out a PeakFit analysis, such as the peak position (E_{00}), the full width at half maximum (FWHM), the accompanying vibrational frequencies ($h\omega$) and the peak intensities. These data can, in turn, be used to carry out more detailed spectral analyses. For example, the nuclear reorganization energy is one such parameter, Equation 8.26.

$$\lambda = \frac{(\Delta v_{1/2})^2}{16 \ln 2 k_B T} \quad \text{Equation 8.26}$$

PeakFit can also be used to obtain the important Huang-Rhys factor (S), which is dimensionless and is often related to the Stokes' shift (SS) by means of Equation 8.27. The Huang-Rhys factor is directly related to changes in chemical geometry upon electronic excitation (Figure 8.10).^{39,40}

$$SS = (2S - 1)\hbar\omega \quad \text{Equation 8.27}$$

The success of the spectral fit is determined by evaluating the r^2 value and the standard error value. The r^2 value quantifies the goodness of fit, it is usually a fraction between 0 and 1.^{41,42} The higher the r^2 and lower the standard error the more successful the fit. These two values, as well as the 95% confidence error, standard deviation, and t-values are compared in the final output file produced by the software.

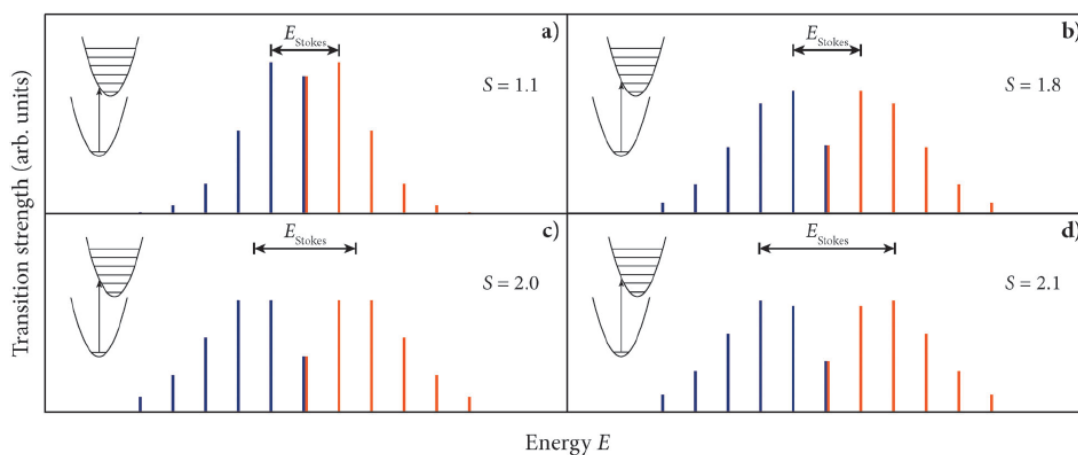


Figure 8.10. Image adapted from *Phys. Chem. Chem. Phys.*, **2015**, 17, 16959. It demonstrates how the Stokes' shift (E_{Stokes}) changes with the Huang-Rhys factor (S); panels (a) to (d). Blue lines represent calculated emission, whereas orange lines represent calculated absorption.

8.9.2 Spartan'06

The Spartan'06 software can be used to gain insight into ground-state structures, molecular orbital descriptions, relative stability, and so on. It is capable of carrying out molecular mechanics as well as quantum mechanical calculations, including DFT at various levels. This software package was also used to calculate IR spectra. It was often employed to calculate energy-minimized geometries which in turn were used to measure center-to-center distances in large dyads investigated throughout this report. Many of the geometrical parameters used in the EET calculations were obtained in this way.

8.9.3 GAMESS

General Atomic and Molecular Electronic Structure System^{43,44} or GAMESS is the molecular simulation software most commonly used throughout this investigation due to its versatility. It is able to perform a wide range of essential calculations like geometry optimization, prediction of excited spectra as well as more advanced operations. GAMESS is able to perform calculations on the entire periodic table.⁴⁴ It is able to do the same calculations as Spartan'06 and more. Here it's most commonly used for large dyads to calculate energy-minimised geometries. These structures were then used to obtain values necessary for calculations described in section like the orientation factor (κ), D-A centre to centre distance (R_{cc}).

Energy-minimized structures of large donor-acceptor molecules were usually obtained in two stages. Stage 1 involved obtaining optimised structures at a very basic level like AM1. Stage 2 involved using the data from stage 1 as a starting point for more sophisticated calculations like DFT B3LYP/6-31G. We found that this approach worked very well for large molecules as it provided a good initial guess of wave function for the more sophisticated calculation. Without a good initial guess, calculations of large complicated dyads tend to fail almost instantly.⁴⁵

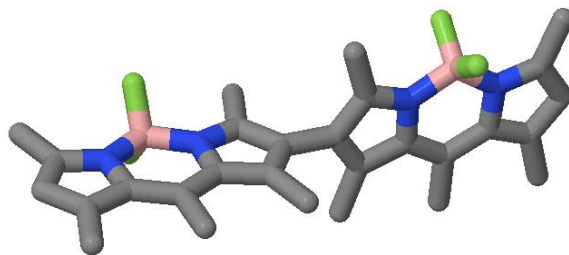


Figure 8.11. Example of a computed structure for a BODIPY bichromophore. Geometry was optimized by the means of DFT B3LYP/6-31G calculation.

8.10 References

- (1) Abboud, J. L. M.; Notario, R. *Pure Appl. Chem.* **1999**, 71, 645.
- (2) Harriman, A. *J. Chem. Soc. Faraday Trans.* **1981**, 77, 1281.
- (3) Magde, D.; Brannon, J. H.; Cremers, T. L.; Olmsted, J. J. *Phys. Chem.* **1979**, 83, 696.
- (4) Kubin, R. F.; Fletcher, A. N. *J. Lumin.* **1982**, 27, 455.
- (5) Davis, M. M.; Helzer, H. B. *Anal. Chem.* **1966**, 38, 451.
- (6) Millar, D. P. *Curr. Opin. Struct. Biol.* **1996**, 6, 637.
- (7) Phillips, D. *Analyst* **1994**, 119, 543.
- (8) Spies, C.; Gehrke, R. *J. Lumin.* **1999**, 82, 333.
- (9) Fleming, C. N.; Maxwell, K. A.; DeSimone, J. M.; Meyer, T. J.; Papanikolas, J. M. *J. Am. Chem. Soc.* **2001**, 123, 10336.
- (10) Lakowicz, J. R.; Szmajnski, H.; Nowaczyk, K.; Berndt, K. W.; Johnson, M. *Anal. Biochem.* **1992**, 202, 316.
- (11) Eaton, D. F. In *Pure Appl. Chem.* 1988; Vol. 60, p 1107.
- (12) Desmond V. O'Connor, D. P.; *Time-Correlated Single Photon Counting*, Academic Press, 1984, p 300.
- (13) Esposito, R.; Mensitieri, G.; de Nicola, S. *Analyst* **2015**, 140, 8138.
- (14) Brouwer Albert, M. In *Pure Appl. Chem.* 2011; Vol. 83, p 2213.
- (15) Strickler, S. J.; Berg, R. A. *J. Chem. Phys.* **1962**, 37, 814.
- (16) Birks, J. B.; Dyson, D. J. *Proc. R. Soc. A.* **1963**, 275, 135.
- (17) Knox, R. S. *Photochem. Photobiol.* **2003**, 77, 492.
- (18) Knox, R. S.; van Amerongen, H. *J. Phys. Chem. B* **2002**, 106, 5289.
- (19) Hirayama, S.; Phillips, D. *Journal of Photochemistry* **1980**, 12, 139.

- (20) Ziessel, R.; Goze, C.; Ulrich, G.; Cesario, M.; Retailleau, P.; Harriman, A.; Rostron, J. P. *Chem. Eur. J.* **2005**, *11*, 7366.
- (21) Scholes, G. D. *Annu. Rev. Phys. Chem.* **2003**, *54*, 57.
- (22) Alamiry, M. A. H.; Hagon, J. P.; Harriman, A.; Bura, T.; Ziessel, R. *Chem. Sci.* **2012**, *3*, 1041.
- (23) Lakowicz, J. R. *Principles of Fluorescence Spectroscopy*; 3rd ed.; Springer, 2006.
- (24) Toledano, E.; Rubin, M. B.; Speiser, S. J. *Photochem. Photobiol., A Chem.* **1996**, *94*, 93.
- (25) Berney, C.; Danuser, G. *Biophys. J.* **2003**, *84*, 3992.
- (26) Stryer, L.; Haugland, R. P. *Proc Natl Acad Sci U S A* **1967**, *58*, 719.
- (27) Mondal, J. A.; Ramakrishna, G.; Singh, A. K.; Ghosh, H. N.; Mariappan, M.; Maiya, B. G.; Mukherjee, T.; Palit, D. K. *J. Phys. Chem. A* **2004**, *108*, 7843.
- (28) Caspar, J. V.; Meyer, T. J. *J. Phys. Chem.* **1983**, *87*, 952.
- (29) Kober, E. M.; Caspar, J. V.; Lumpkin, R. S.; Meyer, T. J. *J. Phys. Chem.* **1986**, *90*, 3722.
- (30) Bixon, M.; Jortner, J.; Cortes, J.; Heitele, H.; Michel-Beyerle, M. E. *J. Phys. Chem.* **1994**, *98*, 7289.
- (31) Englman, R.; Jortner, J. *Mol. Phys.* **1970**, *18*, 145.
- (32) Marcus, R. A. *Rev. Mod. Phys.* **1993**, *65*, 599.
- (33) Marcus, R. A. *Annu. Rev. Phys. Chem.* **1964**, *15*, 155.
- (34) Marcus, R. A.; Sutin, N. *Biochim. Biophys. Acta* **1985**, *811*, 265.
- (35) Wasielewski, M. R. *Chem. Rev.* **1992**, *92*, 435.
- (36) Bixon, M.; Jortner, J.; Verhoeven, J. W. *J. Am. Chem. Soc.* **1994**, *116*, 7349.

- (37) Harriman, A.; Heitz, V.; Ebersole, M.; van Willigen, H. *J. Phys. Chem.* **1994**, *98*, 4982.
- (38) Harriman, A.; Hissler, M.; Ziessel, R. *Phys. Chem. Chem. Phys.* **1999**, *1*, 4203.
- (39) de Jong, M.; Seijo, L.; Meijerink, A.; Rabouw, F. T. *Phys. Chem. Chem. Phys.* **2015**, *17*, 16959.
- (40) Oliveira, F. A. C.; Cury, L. A.; Righi, A.; Moreira, R. L.; Guimarães, P. S. S.; Matinaga, F. M.; Pimenta, M. A.; Nogueira, R. A. *J. Chem. Phys.* **2003**, *119*, 9777.
- (41) Colin Cameron, A.; Windmeijer, F. A. G. *Journal of Econometrics* **1997**, *77*, 329.
- (42) Nagelkerke, N. J. D. *Biometrika* **1991**, *78*, 691.
- (43) Schmidt, M. W.; Baldridge, K. K.; Boatz, J. A.; Elbert, S. T.; Gordon, M. S.; Jensen, J. H.; Koseki, S.; Matsunaga, N.; Nguyen, K. A.; Su, S.; Windus, T. L.; Dupuis, M.; Montgomery, J. A. *J. Comput. Chem.* **1993**, *14*, 1347.
- (44) Guest, M. F.; Bush, I. J.; Van Dam, H. J. J.; Sherwood, P.; Thomas, J. M. H.; Van Lenthe, J. H.; Havenith, R. W. A.; Kendrick, J. *Mol. Phys.* **2005**, *103*, 719.
- (45) James B. Foresman, A. F. *Exploring Chemistry With Electronic Structure Methods: A Guide to Using Gaussian*; Gaussian, 1996.

Appendix

List of Publications

- i. Nano, A.; Ziessel, R.; Stachelek, P.; Harriman, A. *Chem. Eur. J.*, **2013**, 19, 13528.
- ii. Nano, A.; Ziessel, R.; Stachelek, P.; Alamiry, M. A. H.; Harriman, A. *Chemphyschem*, **2014**, 15, 177.
- iii. Bahaidarah, E.; Harriman, A.; Stachelek, P.; Rihn, S.; Heyer, E.; Ziessel, R. *Photochem. Photobiol. Sci.*, **2014**, 13, 1397.
- iv. Harriman, A.; Stachelek, P.; Sutter, A.; Ziessel, R. *Photochem. Photobiol. Sci.*, **2015**, 14, 1100.
- v. Harriman, A.; Stachelek, P.; Sutter, A.; Ziessel, R. *Phys. Chem. Chem. Phys.*, **2015**, 17, 26175.
- vi. Thakare, S.; Stachelek, P.; Mula, S.; More, A. B.; Chattopadhyay, S.; Ray, A. K.; Sekar, N.; Ziessel, R.; Harriman, A. *Chem. Eur. J.* **2016**, 22, 14356.
- vii. Stachelek P.; Harriman A., *J. Phys. Chem. A.*, Just Accepted,

DOI: 10.1021/acs.jpca.6b08284

Charge-Recombination Fluorescence from Push-Pull Electronic Systems Constructed around Amino-Substituted Styryl-BODIPY Dyes

CHEMISTRY
A EUROPEAN JOURNAL

ChemPubSoc
Europe

DOI: 10.1002/chem.201301045

Charge-Recombination Fluorescence from Push-Pull Electronic Systems Constructed around Amino-Substituted Styryl-BODIPY Dyes**

Adela Nano,^[a] Raymond Ziessel,^{*,[a]} Patrycja Stachelek,^[b] and Anthony Harriman^{*,[b]}

Abstract: A small series of donor-acceptor molecular dyads has been synthesized and fully characterized. In each case, the acceptor is a dicyanovinyl unit and the donor is a boron dipyrromethene (BODIPY) dye equipped with a single styryl arm bearing a terminal amino group. In the absence of the acceptor, the BODIPY-based dyes are strongly fluorescent in the far-red region and the relaxed excited-singlet states possess significant charge-trans-

fer character. As such, the emission maxima depend on both the solvent polarity and temperature. With the corresponding push-pull molecules, there is a low-energy charge-transfer state that can be observed by both absorp-

Keywords: donor-acceptor systems • electrochemistry • electron transfer • fluorescence • photophysics

tion and emission spectroscopy. Here, charge-recombination fluorescence is weak and decays over a few hundred picoseconds or so to recover the ground state. Overall, these results permit evaluation of the factors affecting the probability of charge-recombination fluorescence in push-pull dyes. The photophysical studies are supported by cyclic voltammetry and DFT calculations.

Introduction

Push-pull π -conjugated chromophores are of great topical interest because of their putative applications in optoelectronics,^[1] organic light-emitting diodes,^[2] and information-storage devices.^[3] Such compounds comprise an electron donor (D) fitted with one or more electron-withdrawing (A) groups connected through a π -conjugated spacer so as to generate a substantive dipole moment across the molecule. In addition, push-pull D- π -A chromophores have been investigated extensively for their nonlinear optical properties^[4-6] and have proved to be useful materials for exploring the intricacies of electron-transfer processes.^[7] The field benefits from the almost limitless variety of D- π -A systems that can be isolated by combining different donor/acceptor modules with known π -bridging spacer units. Many of the

original series of D- π -A compounds were based on a 4-nitrophenyl moiety as the electron acceptor with an *N,N*-dimethylanilino group as the complementary electron donor.^[8] More recently, attention has turned to the use of stronger organic donor and acceptor functions, including julolidine^[9] derivatives, pyran-containing compounds such as 2-(2-*tert*-butyl-6-methyl-4*H*-pyran-4-ylidene)malonitrile,^[10] 4,5-dicyanoimidazole derivatives,^[11] and the so-called “super-acceptor” 7,7,8,8-tetracyanoquinodimethene.^[12] The nature of the terminals affects the optical and electronic properties of the resultant materials, but so does the composition and length of the π -conjugated backbone. Various conjugated spacers, such as fluorene, stilbene, thiophene, polyenes, polyynes, porphyrins, phthalocyanines, and merocyanine dyes, have been incorporated into push-pull electronic systems.^[13,14]

Along somewhat related lines, it is recognized that photo-induced electron transfer remains one of the most intensive-studied subjects in contemporary science and has particular relevance for understanding the workings of both natural and artificial photosynthesis.^[15] Innumerable studies have addressed the various factors that promote light-induced electron transfer in molecular dyads, triads, tetrads, and higher-order analogues. The information gathered from such studies, used in conjunction with our ever-growing awareness of the natural process,^[16] has led to new ideas about how to achieve sustainable solar-fuel production.^[17] It has become clear that the efficacy of a light-induced electron-transfer reaction depends critically on a range of parameters that must be controlled to a supreme level of precision to achieve the optimum output. The main variables include both thermodynamic properties (excitation energy and electrode potentials) and structural elements (separation distance, mutual orientation, and nature of the bridge).^[18] The

[a] A. Nano, Dr. R. Ziessel
LCOSA, ICPEES, UMR7515
CNRS/Université de Strasbourg/ECPM
25 rue Becquerel, 67087 Strasbourg
Cedex 02 (France)
Fax: (+33)3-68-85-27-61
E-mail: ziessel@unistra.fr

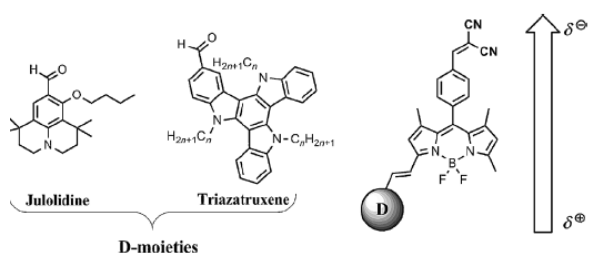
[b] P. Stachelek, Prof. Dr. A. Harriman
Molecular Photonics Laboratory
School of Chemistry, Bedson Building
Newcastle University
Newcastle upon Tyne, NE1 7RU (UK)
Fax: (+44) 191-222-8660
E-mail: anthony.harriman@ncl.ac.uk

[**] BODIPY: boron dipyrromethene (4,4-difluoro-8-(4-iodo)phenyl-1,3,5,7-tetramethyl-4-bora-3a,4a-diaza-s-indacene).

Supporting information for this article is available on the WWW under <http://dx.doi.org/10.1002/chem.201301045>.

range of systems that has been developed to advance this subject is incredibly far-flung and includes covalently linked donor-acceptor pairs,^[17,19] supramolecular assemblies based on coordinative interactions^[20] or hydrogen-bonding strategies,^[21] and self-associated donor-acceptor systems.^[22] Along these lines, boron dipyrromethene (BODIPY) derivatives, featuring invaluable optical and electrochemical^[23] properties, have been less exploited as photoactive bridges in D- π -A scaffolds and photoinduced electron transfer involving BODIPY dyes is not so common.^[24] The most popular reactants for such materials are bioinspired, such as porphyrins, carotenes, and quinones.

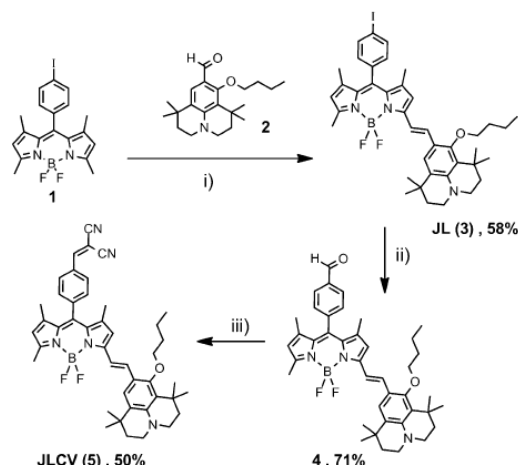
Our current interest in this field includes developing new artificial systems for light-induced electron-transfer processes that incorporate BODIPY chromophores. Such dyes have been used successfully in photovoltaic devices,^[25] as ion sensors,^[26] and as fluorescent probes in biological analyses.^[27] Surprisingly, given the great popularity of these highly emissive dyes, there have been few attempts to incorporate BODIPY dyes into push-pull molecular architectures.^[28] Notably, D- π -A chromophores have been built from a BODIPY-based core with electron-donor and electron-acceptor units attached at the 2- and 6-positions.^[29] Such compounds, although enabling facile tuning of the optical properties, do not promote light-induced charge separation. In the present work, we report the synthesis of dipolar push-pull chromophores having unusually strong donating (i.e., julolidine or triazatruxene) and withdrawing (i.e., dicyanovinyl) substituents attached to the central π -conjugated backbone (Scheme 1). The photophysical properties of the target molecules become understandable by virtue of systematic examination of model compounds lacking the dicyanovinyl terminal.



Scheme 1. Schematic representation of putative dipolar push-pull chromophores built around a central BODIPY unit.

Results and Discussion

Synthetic strategy: The prototypic push-pull chromophore JLCV (compound 5 in the synthetic schemes) was prepared in three steps from the tetramethyl-BODIPY derivative 1 as depicted in Scheme 2. Condensation of 1 with 9-formyl-10-butoxy-1,1,7,7-tetramethyl-2,3,6,7-tetrahydro-1*H*,5*H*-pyrido[3,2,1-*ij*]quinoline^[30] gave rise to the monostyryl derivative JL (compound 3 in the synthetic schemes) despite the pres-

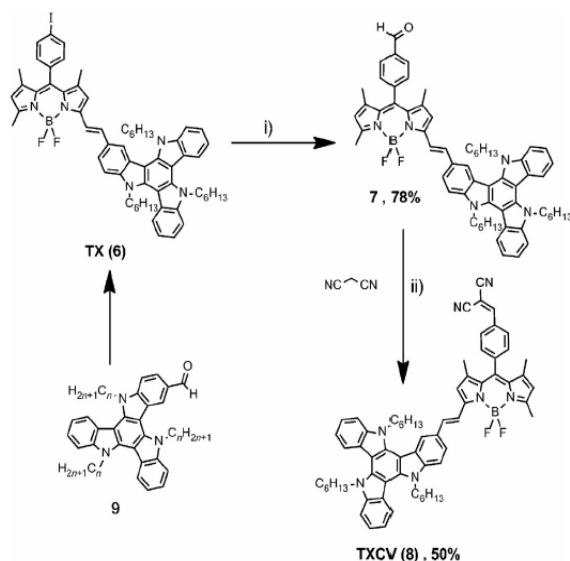


Scheme 2. Synthesis of compound 5 and its precursors: i) *p*-TsOH cat., piperidine, toluene, 140 °C; ii) [Pd(PPh₃)₂Cl₂] (10 mol %), HCOONa, DMF under a flow of CO, 100 °C; iii) AcOH/piperidine cat., methanol, 85 °C, 1 h.

ence of an excess amount of aldehyde. Formation of the mono-functionalized analogue might be explained in terms of julolidine being a strong electron donor that influences the acidity of the methyl group located at the 5-position on the BODIPY core. In any event, the result is the second known example of selective mono-condensation of a BODIPY dye with an electrophilic aldehyde.^[31] Transformation of JL into the carbaldehyde derivative 4 was realized using a carboformylation reaction catalyzed by a palladium(II) precursor and with sodium formate as the reducing reagent under a flow of CO at atmospheric pressure. The target compound JLCV was synthesized in 50% yield by condensation of 4 with malonitrile, using a Knoevenagel-type reaction carried out according to a literature procedure.^[32,33] All compounds were fully characterized by modern spectroscopic protocols, as outlined in the Experimental Section and Supporting Information.

By way of analogy with the julolidine-based system, related dyes were synthesized from the triazatruxene platform as sketched in Scheme 3. This slightly ruffled scaffold has three interconnecting amino groups and an anchor by which to append secondary units. The iodo group on TX (compound 6 in the synthetic schemes) was converted to the corresponding formyl derivative using a carboformylation reaction, before the latter was transformed to the dicyanovinyl derivative TXCV (compound 8 in the synthetic schemes) using malonitrile as the reagent. It might be stressed that some of these dipolar BODIPY-based chromophores are difficult to isolate in high yield owing to their inherent instability during the purification procedures.

Electrochemistry: The redox behavior of the new BODIPY dyes was investigated by cyclic voltammetry in CH₂Cl₂ containing 0.1 M tetra-*N*-butylammonium hexafluorophosphate



Scheme 3. i) $[\text{Pd}(\text{PPh}_3)_4\text{Cl}_2]$ (10 mol %), HCOONa , DMF under a flow of CO , 100 °C; ii) NC-CN , $\text{AcOH/piperidine cat.}$, THF, 95 °C, 20–30 min.

(TBAPF_6) as supporting electrolyte and the results are gathered in Table 1. The starting material lacking the styryl arm, **1**, displays a single reversible wave on both oxidative and reductive scans owing to the formation of the π -radical cation and π -radical anion, respectively, as has been observed previously for related compounds.^[34] These waves are highly reversible ($i_p/i_{pc} \approx 1$) and exhibit the characteristic shape ($\Delta E_p = 60\text{--}70\text{ mV}$) of a Nernstian, one-electron process. The monostyryl BODIPY dyes **JL** and **4** display two distinct waves under oxidative scans, each of which is fully reversible and corresponds to transfer of a single electron. The first wave occurs with a half-wave potential of 0.38 V versus SCE and this oxidation is considerably easier (about 480 mV)

Table 1. Electrochemical data for the BODIPY, julolidine, and triazatruxene derivatives and relevant control compounds.^[a]

Compound	$E^0(\text{ox, soln})$ [V] (ΔE [mV])	$E^0(\text{red, soln})$ [V] (ΔE [mV])
1	+1.15 (70)	−1.24 (60)
2	+0.86 (60)	—
JL (3)	+0.38 (70), +0.79 (60)	−1.17 (70)
4	+0.38 (60), +0.81 (60)	−1.16 (70)
JLCV (5)	+0.38 (70), +0.80 (60)	−1.04 (irr.), −1.24 (70)
TX (6)	+0.67 (70), +0.90 (70)	−1.09 (70)
7	+0.66 (70), +0.92 (70)	−1.06 (70)
TXCV (8)	+0.72 (60), +0.97 (70)	−0.98 (irr.), −1.10 (60)
9	+0.86 (70), +1.45 (70)	—

[a] Potentials determined by cyclic voltammetry in deoxygenated dichloromethane, containing 0.1 M TBAPF_6 [electrochemical window from +1.6 to −2.2 V], at a solute concentration of approximately 1.5 mM and at RT. Potentials were standardized versus ferrocene (Fc) as internal reference and converted to the SCE scale assuming that $E_{1/2}(\text{Fc}/\text{Fc}^+) = +0.38\text{ V}$ ($\Delta E_p = 60\text{ mV}$) versus SCE. The error in half-wave potentials is $\pm 10\text{ mV}$. For irreversible processes the peak potentials (E_{ap}) are quoted. All reversible redox steps result from one-electron processes.

than for the isolated fragments. These potential shifts are a clear consequence of the increased conjugation provided by the connecting styryl linkage and to the occurrence of electronic coupling between the two units.

Turning attention to the triazatruxene-based scaffold, it is notable that the parent compound, **9**, exhibits two reversible waves on oxidative scans but no observable peaks on reduction. These oxidative waves, which correspond to half-wave potentials of 0.86 and 1.45 V versus SCE, respectively (Table 1), are assigned to successive one-electron oxidation of the aminocarbazole units. The difference between the observed half-wave potentials is ascribed to electrostatic effects but the anticipated third oxidation step is not seen within the available anodic window. Appending a monostyryl BODIPY dye to the scaffold, thereby forming compounds **TX** or **7**, lowers the half-wave potential for one-electron oxidation by approximately 200 mV owing to the increased conjugation provided by the styryl arm. Comparing this latter value with that derived for the analogous julolidine-based dye, **4**, indicates that oxidation is more difficult for **7** by approximately 280 mV. It is also notable that, although the parent julolidine, **2**, and triazatruxene, **9**, compounds have the same half-wave potential when isolated, these units display quite disparate half-wave potentials when attached to the BODIPY unit. This is an important point that illustrates the differing degrees to which the principal donor couples to the extended BODIPY unit.

For **JL**, DFT calculations indicate that both HOMO and HOMO(−1) are spread over much of the molecule and include contributions from the BODIPY and julolidine residues (see the Supporting Information). As such, it is inaccurate to ascribe the first oxidation step as being localized on the julolidine unit. Identical calculations made with **TX** show that the HOMO is also spread over much of the molecule but incorporates only the amino group closest to the styryl arm. A similar distribution is observed for HOMO(−1) but the second amino group (this being separated from the styryl unit by 3 bonds compared with only 1 bond for the proximal amino group) makes an important contribution to HOMO(−2). The distal amino group (which is removed by 5 bonds from the styryl unit) is the major contributor to HOMO(−3) (see the Supporting Information). The energy-minimized structures indicate that the julolidine-based N atom present in **JL** is out of alignment with the styryl unit by only 2.5° but the proximal N atom on the triazatruxene unit present in **TX** is twisted out of alignment by approximately 10°. Such structural facets must contribute significantly towards the differing extents of electronic coupling found for these two electronic systems.

Further confirmation for the disparate electronic character of **JL** and **TX** comes from comparison of their absorption spectra recorded in 2-methyltetrahydrofuran (MTHF). Thus, the spectrum recorded for **TX** ($\lambda_{\text{MAX}} = 607\text{ nm}$, $\epsilon_{\text{MAX}} = 103\,055\text{ M}^{-1}\text{ cm}^{-1}$) resembles those reported for related styryl-based BODIPY dyes, although the half-width for the lowest-energy transition is somewhat elevated, and the total oscillator strength^[35] (f) is 0.86. This latter transition can be

accounted for in terms of three vibrational modes of 1200 cm^{-1} , each with a half-width of 1135 cm^{-1} . For **JL** under the same conditions, the corresponding absorption transition ($\lambda_{\text{MAX}}=631\text{ nm}$, $\epsilon_{\text{MAX}}=89\,630\text{ M}^{-1}\text{ cm}^{-1}$) is considerably broader, with $f=0.94$, and redshifted. Spectral deconvolution into Gaussian-shaped bands requires three vibrational modes of 1200 cm^{-1} with half-widths of 1500 cm^{-1} .

One-electron reduction of the BODIPY core is easier by approximately 80 mV in both **JL** and **4** relative to the original dye, **1**. In fact, this observation is consistent with the optical properties of the monostyryl BODIPY dyes, as discussed later, and is a consequence of the extended π -delocalization pathway. In each case, the one-electron reduction step is quasireversible. Similar behavior is found for the triazatruxene-based dyes, **TX** and **7**, although the latter are somewhat easier to reduce (Table 1). This generic behavior follows from the situation outlined above for the corresponding oxidative processes. Quantum chemical calculations performed at the DFT level (B3LYP 6-31G*) are suggestive of the LUMO being distributed over the styryl-BODIPY without significant penetration onto the amino-based donor (see the Supporting Information).

In the case of the prototypic push-pull dye, **JLCV**, reductive scans point to an irreversible wave attributable to one-electron reduction of the dicyanovinyl unit and a reversible wave due to reduction of the BODIPY core. Again, electrostatic repulsion perturbs the latter value. Similar properties are apparent for **TXCV**, although there are important disparities in the derived half-wave potentials for reduction of both units (Table 1), as might be anticipated in light of the above discussion comparing the electronic properties of the two sets of donors. It is interesting to note that this electronic effect carries over to reduction of the dicyanovinyl unit.

Photophysics of the BODIPY-julolidine and BODIPY-triazatruxene dyes: The absorption spectral features of the two amino-substituted styryl-based BODIPY dyes were outlined

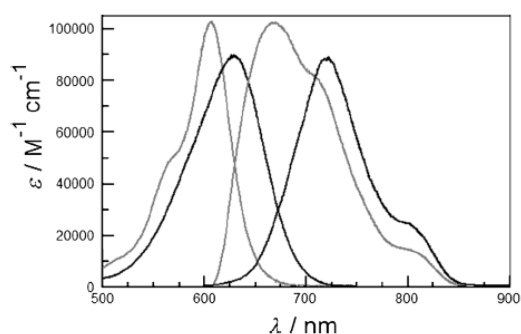


Figure 1. Absorption and fluorescence spectra recorded for compounds **JL** (black curves) and **TX** (grey curves) in MTHF at room temperature.

above and are reproduced in Figure 1. Fluorescence is readily apparent from both compounds in MTHF at room temperature and occurs in the far-red region (Figure 1). For **TX**, the emission spectrum is broad, but partially resolved, and has a maximum at 672 nm in MTHF. The entire spectral envelope can be deconstructed into Gaussian-shaped components with a common half-width of 1050 cm^{-1} . The accompanying vibronic modes coupled with nonradiative decay are estimated from spectral curve fitting to correspond to a mixture of torsional modes ($\nu=750\text{ cm}^{-1}$, $S=0.96$, in which S refers to the Huang–Rhys factor) and skeletal bending modes ($\nu=1400\text{ cm}^{-1}$, $S=0.79$).^[36] There is good agreement between the excitation and absorption spectra across the entire visible and near-UV regions. In MTHF, the fluorescence quantum yield is 0.56, and the excited-singlet-state lifetime, obtained from monoexponential decay curves, is 3.5 ns (Table 2). The spectrum has the appearance of a

Table 2. Summary of the photophysical properties recorded for the various amino-substituted styryl-BODIPY compounds in MTHF at room temperature.

Property	JL	TX	JLCV	TXCV
λ_{ABS} [nm]	631	607	638	619
ϵ_{MAX} [$\text{M}^{-1}\text{ cm}^{-1}$]	103055	89630	88900	114720
$f^{\text{[a]}}$	0.94	0.86	1.01	1.02
d_{GS} [D] ^[b]	2.5	3.0	9.3	8.0
λ_{FLU} [nm]	720	672	725	685
$S^{\text{[c]}}$	1.7:1.15	0.96:0.79	1.05:0.70	0.82:0.65
Φ_{F}	0.30	0.56	0.0020	0.0023
τ_{S} [ns]	2.8	3.5	0.13	0.26
k_{RAD} [10^7 s^{-1}]	10.7	15.6	1.5	0.9
λ_{CR} [eV] ^[d]	0.10	0.06	0.075	0.068

[a] Oscillator strength calculated from the integrated absorption spectrum. [b] Computed dipole moment for the ground state. [c] Huang–Rhys factor calculated from the deconstructed emission spectrum, with the values referring to the medium- and low-frequency modes, respectively. [d] Reorganisation energy accompanying charge-recombination emission extracted from spectral curve fitting.

single component. On cooling the solution, the emission maximum undergoes a substantive redshift until reaching 727 nm at 160 K from whence further lowering of the temperature causes the maximum to revert to higher energy. The emission intensity and lifetime decrease slightly during the redshift, in line with the Englman–Jortner energy-gap law,^[37] but recover during the subsequent blueshift (see the Supporting Information). These changes are modest but there is a larger effect as the solvent starts to freeze at around 140 K. Here, the emission maximum shifts rapidly with falling temperature until settling at 640 nm at approximately 115 K.

At $<110\text{ K}$, at which temperatures MTHF forms a glassy matrix,^[38] the emission profile resembles that expected for a monostyryl BODIPY dye lacking significant charge-transfer interactions (Figure 2).^[39] The emission peak lies at 640 nm (i.e., $15\,635\text{ cm}^{-1}$) and the profile can be deconstructed into Gaussian-shaped bands with a common half-width of 680 cm^{-1} and accompanying vibronic components of 1300 and 580 cm^{-1} . The Huang–Rhys factors (S), which are 0.96 ($\nu=750\text{ cm}^{-1}$) and 0.79 ($\nu=1600\text{ cm}^{-1}$) at room temperature,

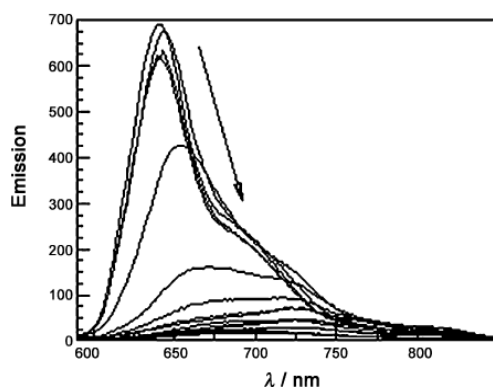


Figure 2. Effect of temperature on the fluorescence spectral profile recorded for **TX** in MTHF. The arrow indicates the effect of warming the solution from 80 to 290 K in equal increments.

have values of 0.30 ($\nu=735\text{ cm}^{-1}$) and 0.11 ($\nu=1570\text{ cm}^{-1}$) in the glassy matrix and are in better accord with those expected^[40] for a $\pi\text{--}\pi^*$ transition. The implication, therefore, is that the glassy matrix restricts internal charge transfer by virtue of its rigid nature; it might be noted that the polarity of glassy MTHF has been likened to that of *N,N*-dimethylformamide at room temperature.^[41] In other solvents at room temperature, the fluorescence maximum recorded for **TX** shows a marked dependence on the static dielectric constant (ϵ_s) and undergoes a redshift as the polarity increases. Thus, the emission maximum transforms from 650 nm in di-*n*-butyl ether ($\epsilon_s=3.1$), to 668 nm in ethyl acetate ($\epsilon_s=6.02$), to 720 nm in dichloromethane ($\epsilon_s=8.93$), and to approximately 740 nm in acetonitrile ($\epsilon_s=37.5$). The quantum yield and lifetime fall steadily as the emission peak moves to lower energy and fluorescence is difficult to resolve in strongly polar solvents; for details see the Supporting Information.

For the corresponding julolidine-based fluorophore, **JL**, fluorescence is redshifted relative to that of **TX** and has a maximum at 720 nm in MTHF at room temperature (Figure 1). Spectral curve fitting again requires the involvement of three Gaussian-shaped components with a common half-width of 950 cm^{-1} , and with underlying vibronic components of 755 and 1310 cm^{-1} . Excitation and absorption spectra are in accord across the relevant spectral window. At room temperature in MTHF solution, Φ_F has a value of 0.30 and τ_s is 2.8 ns; again, decay curves are well explained in terms of monoexponential fits. Cooling the solution results in a redshift, the maximum reaching 755 nm at 160 K and with an accompanying decrease in emission yield, until approaching the freezing point of the solvent (see the Supporting Information). On lowering the temperature further, there is a substantial blueshift and a marked escalation in emission. At 80 K in glassy MTHF, Φ_F reaches a limiting value of 0.58, and the emission maximum is found at 685 nm. The spectral profile remains fairly broad even in the glassy matrix but can be analyzed in terms of medium-

(i.e., $\nu=1300\text{ cm}^{-1}$, $S=0.21$) and low-frequency (i.e., $\nu=600\text{ cm}^{-1}$, $S=0.53$) vibronic peaks with a half-width of 815 cm^{-1} . The Huang–Rhys factors^[36] derived at 80 K, although much smaller than those found at room temperature, are still somewhat too high for a pure $\pi\text{--}\pi^*$ transition. These spectral shifts can be explained in terms of solvation of a polar species, taking into account that the dielectric constant of fluid MTHF increases with decreasing temperature.^[41] Again, it is proposed that freezing of the solvent hinders some important structural change that is essential for effective charge transfer along the molecular axis.

Aided by the quantum chemical studies outlined above, our understanding of the photophysical properties of **TX** can be summarized as follows (Table 2): Illumination creates an excited-singlet state possessing significant charge-transfer character, with the resultant transition dipole moment being spread over most of the molecule. The radiative rate constant (k_{RAD}) decreases with increasing polarity of the solvent, due to a corresponding change in geometry,^[42] while the competing nonradiative rate constant (k_{nr}) increases under the same conditions, due to the energy-gap law.^[37] The net result is that fluorescence is reasonably pronounced in nonpolar media but is extinguished in strongly polar environments. It appears that formation of the excited state demands a change in geometry, as is evident by the unusually large Stokes' shift of 1550 cm^{-1} in MTHF. This structural change, presumed to involve mutual alignment of the π cloud and the N lone pair, is restricted in rigid media in which the excited state more closely resembles a locally excited $\pi\text{--}\pi^*$ species. The ground state does not appear to be a polar species, in agreement with the DFT calculations ($\mu_{\text{GS}}=3.0\text{ D}$), since the position of the absorption maximum varies with the polarizability (P_{ONS}) of the solvent^[43] but not with the dielectric constant. Indeed, there is a linear relationship between the wavenumber (ν_{ABS}) at the maximum of the lowest-energy absorption transition and P_{ONS} (Figure 3), as has been reported for many classes of nonpolar chromophores,^[44] including BODIPY dyes.^[45] This linearity permits estimation of the radius of the solvent cavity housing the dye as being 4.3 \AA and predicts the absorption maximum under vacuum to be at 560 nm, similar to that of the monostyryl dye lacking the amino group.^[39] Now the change in dipole moment accompanying excitation can be estimated from the Lippert–Mataga relationship^[46] as being 15.7 D for **TX** (Figure 2). Similar behavior is observed for **JL** (Table 2), where the change in dipole moment on excitation is calculated as approximately 17 D and the Stokes' shift in MTHF is 1960 cm^{-1} .

In glassy MTHF at 80 K, emission spectra recorded for the two compounds do not coincide and the julolidine-based system **JL** is subjected to a redshift of approximately 45 nm relative to **TX**. The same is true for excitation spectra. The parent monostyryl BODIPY dye^[39] that lacks charge-transfer interactions shows absorption and emission maxima at 573 and 583 nm, respectively, thereby giving a Stokes' shift of approximately 300 cm^{-1} . Extrapolation of the Lippert–Mataga plot recorded for **TX** also indicates that the Stokes'

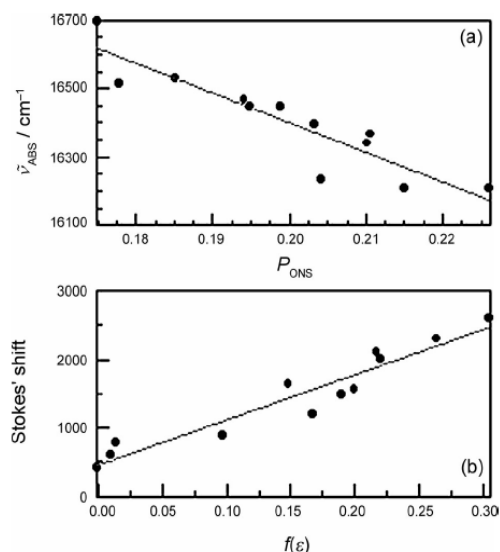


Figure 3. Effect of solvent on a) absorption and b) fluorescence spectral properties recorded for TX at room temperature: panel (a) represents the effect of solvent polarizability on the absorption maximum for the lowest-energy transition whereas panel (b) refers to a Lippert–Mataga plot for the Stokes' shift versus the solvent Pekkar function ($f(\epsilon)$). The points are experimental values and the solid lines refer to fits to the corresponding theoretical model.

shift is 300 cm^{-1} under vacuum, where charge-transfer interactions are likely to be minimal. As such, the amino-substituted derivatives can be considered to possess increased conjugation lengths because of the N lone pair, which accounts for the redshifted absorption maximum, in addition to their inherent charge-transfer character. An important point to bear in mind is that this charge-transfer effect does not lead to light-induced charge separation.

Overall, the photophysical properties recorded in fluid solution appear consistent with those reported by Rurack^[47] and Baruah^[48] and their co-workers for the corresponding monostyryl BODIPY dye bearing a terminal *N,N*-dimethyl-anilino unit. Here, the absorption spectrum is hardly affected by changes in solvent but the emission maximum moves to lower energy as the solvent polarity increases. A particular emphasis in the work outlined by Baruah et al.^[48] is placed on establishing the most appropriate descriptor for solvent polarity. We are less concerned with this point since our main interest lies with the push-pull dyes. Nonetheless, it is important to highlight the fact that k_{RAD} for the *N,N*-dimethylanilino-based dye^[47,48] is approximately $1.9 \times 10^8\text{ s}^{-1}$, which is slightly higher than that found in this work, but consistent with the general observation that k_{RAD} decreases with increasing charge-transfer character. As reported by others for related compounds,^[47–49] the amino N atom is readily protonated in acidic solution and this causes a marked spectral shift for both absorption and emission maxima. In the case of **JL**, for example, protonation in

MTHF shifts the absorption and fluorescence peaks to 575 and 585 nm, respectively, and Φ_F increases to 0.95.

Photophysics of the push-pull compounds JLCV and TXCV: The push-pull compounds differ from the parent amino-substituted styryl-BODIPY dyes by virtue of having an electron-affinic dicyanovinyl unit appended through the *meso* position. It might be noted that this type of electron acceptor has a long history in the generic field of molecular photophysics.^[50] Absorption spectra recorded for these new push-pull molecules, **JLCV** and **TXCV**, in MTHF at room temperature are similar to those described for the corresponding BODIPY-amine compounds, **JL** and **TX**, but are redshifted by approximately 10 nm and slightly broadened (Figure 4). Oscillator strengths, which are 1.02 for both com-

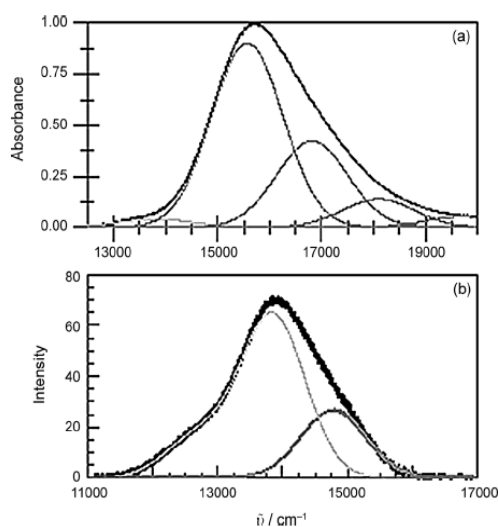


Figure 4. a) Absorption and b) fluorescence spectra recorded for **JLCV** in MTHF at room temperature (see the Supporting Information for corresponding plots for **TXCV**). In part (a), the solid black curve is the experimental spectrum, the light grey curve is the deconstructed charge-transfer transition, and the dark grey curves are Gaussian components for the normal π - π^* transition. In part (b), the solid black curve is the experimental spectrum, the light grey curve is the deconstructed spectrum for the emissive state and the dark grey curve is the proposed impurity.

pounds, are increased relative to the parent compounds and, most importantly, there are indications for the presence of a charge-transfer transition lying under the lowest-energy π - π^* absorption band. The latter situation is most evident for **JLCV** but spectral curve fitting confirms the presence of a charge-transfer contribution to the total absorption spectral profile of **TXCV**. The maxima of these transitions are found at 660 and 724 nm for **TXCV** and **JLCV** in MTHF, respectively. The origin of both transitions is considered to involve charge transfer from the styryl-BODIPY to the dicyanovinyl unit since DFT calculations show the HOMO and LUMO(1) to be localized on the styryl-based BODIPY resi-

due whereas the LUMO is centered on the dicyanovinyl appendage. Interestingly, the DFT calculations indicate substantially increased dipole moments for both push–pull compounds relative to the original amino derivative. Thus, the computed ground-state dipole moments are 9.3 and 8.0 D for **JLCV** and **TXCV**, respectively.

Fluorescence from the target push–pull systems is difficult to resolve in liquid MTHF and it is clear that the emission is extensively quenched relative to the analogues lacking the dicyanovinyl unit. For **TXCV**, fluorescence is decreased by a factor of approximately 300-fold relative to **TX** while the emission maximum is shifted to 695 nm (Table 2). In glassy MTHF at temperatures <115 K, the emission spectrum resembles that recorded for the control compound **TX**, and at 80 K Φ_F has a value of 0.32, which remains less than that measured for **TX** ($\Phi_F=0.85$) under the same conditions (Figure 5). As the glass melts, there is a dramatic fall in Φ_F

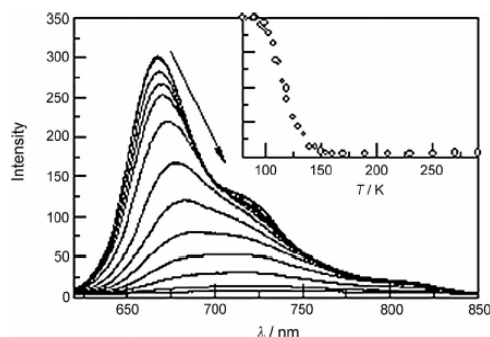


Figure 5. Effect of temperature on the fluorescence spectral profile recorded for **TXCV** in MTHF. The arrow indicates the effect of warming the solution from 80 to 290 K in equal increments. The inset shows the effect of temperature on the relative emission quantum yield.

and a significant redshift, which reaches a maximum at 170 K where the fluorescence peak lies at 740 nm. Under critical examination of the emission spectral profiles it becomes clear that there are important differences between room-temperature spectra recorded for the push–pull system and the simpler amino derivative. Indeed, the total emission spectrum recorded for **TXCV** appears as a mixture of a fluorescence profile somewhat similar to that of **TX** and a new band lying at lower energy (Figure 5). This second component is broad and essentially featureless, with the maximum being strongly temperature dependent.

Time-resolved emission studies carried out for **TXCV** in MTHF show that decay profiles require analysis in terms of dual-exponential kinetics (Figure 6). One component, with a lifetime of 2.4 ns, is a minor species and is tentatively assigned to a trace impurity on account of its spectral profile being similar to that of **TX**. The second component, which has a lifetime of 260 ps, is the dominant species and corresponds to the redshifted species (Figure 7). From the spectral curve fitting analysis, Φ_F for this latter component is estimated to be approximately 0.002, hence k_{RAD} must be ap-

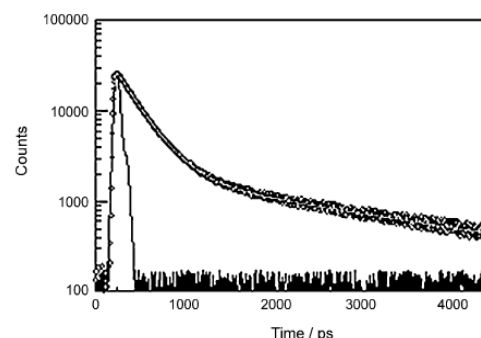


Figure 6. Time-resolved fluorescence decay profile recorded for **TXCV** in MTHF following excitation at 635 nm and with detection at 710 nm. The instrument response function is shown as a black solid curve and the experimental data points appear as open circles. The analytical fit is shown as a red curve superimposed over the data points. For this analysis, $\chi^2=1.09$.

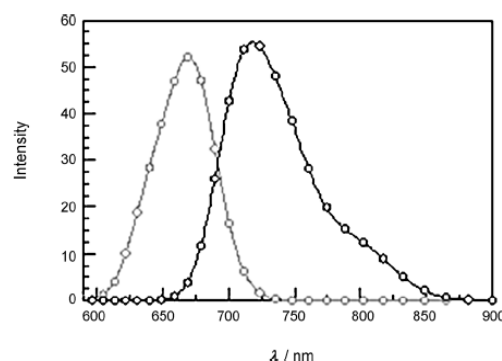


Figure 7. Decay-associated emission spectra derived from analysis of the time-resolved fluorescence spectra recorded for **TXCV** in MTHF following excitation at 590 nm. The grey curve corresponds to the longer-lived species and the black curve is for the shorter-lived component. See the Supporting Information for the analogous spectra derived for **JLCV**.

proximately 10^7 s^{-1} at room temperature. The same analysis can be made for **JLCV**, where the shorter lifetime is 130 ps and the residual impurity has a lifetime of 2.8 ns. In this case, the emission spectrum shows only a minor contribution from the “impurity” whilst the shorter-lived species has an emission maximum at 725 nm. The emission quantum yield for this latter species is very low in MTHF at room temperature, where k_{RAD} is estimated to be approximately $2 \times 10^7 \text{ s}^{-1}$. Temperature-dependent emission studies again show that the blueshifted emission characteristic of **JL** is apparent in the glassy matrix at <110 K but disappears on melting. As for **TXCV**, the peak position for the redshifted species is strongly temperature dependent. On the basis that this emission arises from a charge-transfer state, the reorganization energy for charge recombination is approximately 0.1 eV (Table 2).

The photophysical properties of these push–pull dyes can be interpreted as follows: The lowest-lying singlet-excited

state in both compounds is accessed through direct excitation into the charge-transfer transition identified on the red edge of the strong absorption band associated with the amino-substituted styryl-BODIPY dye. This state is weakly emissive. The excited-state lifetimes are fairly short, owing to the energy-gap law,^[37] the corresponding radiative rate constants are relatively small because of the low oscillator strengths for the charge-transfer absorption transition.^[42] Illumination into the BODIPY dye forms the corresponding localized state possessing considerable charge-transfer character but this species undergoes rapid internal conversion to populate the lower-energy state. The polar solvent stabilizes this latter state and thereby gives rise to the observed redshift as the temperature falls. In the glassy matrix, such stabilization is not possible,^[51] because the solvent cannot reorient around the emergent dipole, and the energy of the charge-transfer state increases dramatically. At <115 K, this state lies at higher energy than the singlet-excited state associated with the amino-substituted styryl-BODIPY dye. The net result is complete recovery of blueshifted fluorescence in the glass. In fact, the fluorescence properties (both integrated area and peak position) provide a convenient means by which to monitor global changes in the nature of the solvent as a function of temperature. Although other dyes have been used^[41,52] as optical probes for the temperature-induced change in the dielectric constant of MTHF, these push-pull molecules are especially useful for following vitrification.

Conclusion

The two amino-substituted monostyryl BODIPY dyes undergo a significant increase in dipole moment on promotion to the first-allowed excited state. Both dyes are strongly fluorescent, without the anticipated quenching by the amino group, with the emission maximum depending on the local polarity. The relevant excited states, which possess strong charge-transfer character, are accessed by means of a key geometry change that is inhibited in a frozen glass at low temperature. Consequently, in the case of **TX** in MTHF, vitrification of the solvent is accompanied by a 90 nm blueshift, which occurs over a temperature range of approximately 30 K. These compounds are characterized by relatively high radiative rates and it is interesting to note how k_{RAD} depends on the strength of the donor. In fact, it can be argued that k_{RAD} provides an indirect measure of the internal charge-transfer characteristics for this class of styryl-BODIPY dyes. Data collected in different solvents for **JL**, **TX**, and the *N,N*-dimethylanilino^[47,48] derivative show reasonable linearity between k_{RAD} and the emission peak maximum, which suggests comparable coupling elements for all three dyes. In the same solvent, the measured Stokes' shifts are 1960, 1550, and 1420 cm⁻¹ for **JL**, **TX**, and the *N,N*-dimethylanilino compound, respectively, which could be taken as a relative measure of the donor ability.

Adding the dicyanovinyl acceptor, by means of an orthogonal phenylene ring, provides a route for increasing the molecular dipole moment and is accompanied by a large decrease in fluorescence. Electronic coupling is so strong, despite the bridge, that the absorption spectrum shows evidence of a low-lying charge-transfer state. On vitrification, the emission spectrum moves towards that of the amino-BODIPY derivative. This effect is explained in terms of the glass being unable to adequately solvate the charge-transfer state and preventing the essential geometry change. There is considerable interest in monitoring the properties of optical glasses formed by freezing an organic solvent, especially with regard to the local polarity.^[41] In this respect we note that compounds **JLCV** and **TXCV** function as exquisite mirrors for the vitrification of the solvent and clearly distinguish between a rigid glass and an amorphous glassy regime. These effects are due to changes in viscosity, rather than polarity, but could be adapted to develop improved optical sensors for glass transition temperatures.

Experimental Section

Synthesis and characterization

General procedure A: In a round-bottomed flask, piperidine and a crystal of *p*-toluenesulfonic acid (*p*-TsOH) were added to a solution of compound **1** (1 equiv) and 9-formyl-10-butoxy-1,1,7,7-tetramethyl-2,3,6,7-tetrahydro-1*H*,5*SH*-pyrido[3,2,1-*ij*]quinoline (1.5 equiv) in toluene. The solution was heated at 140 °C until it had evaporated to dryness. The colored solids were purified by silica gel chromatography before being recrystallized.

General procedure B: [Pd(PPh₃)₂Cl₂] (10 mmol %) and sodium formate (1.2 equiv) were added to a solution of **3** (1 equiv) in anhydrous DMF (8 mL) in a two-necked flask equipped with a reflux condenser, a gas bubbler, and a magnetic stirring bar. The reaction mixture was degassed under a continuous flow of CO at atmospheric pressure and stirred at 90 °C for 3 h. After cooling to room temperature, the mixture was extracted with dichloromethane and washed several times with water. The organic phase was dried over hygroscopic cotton wool and evaporated. The crude residue was then purified by flash chromatography.

General procedure C: In a Schlenk tube equipped with a magnetic stirring bar, malonitrile (1.2 equiv) and several drops of piperidine/acetic acid were added to a suspension of the aldehyde precursor (1 equiv) in methanol (2.5 mL). The mixture was stirred at 85–95 °C for 1 h.

Details regarding the spectroscopic investigations are also provided in the Supporting Information.

Compound JL (3): Compound **3** was synthesized according to general procedure A, starting from 4,4-difluoro-8-(4-iodophenyl)-1,3,5,7-tetramethyl-4-bora-3a,4a-diaza-*s*-indacene (BODIPY; 226 mg, 0.50 mmol). Column chromatography (silica gel, CH₂Cl₂/petroleum ether 4:6, v/v) and recrystallization from ethanol/CH₂Cl₂ gave **3** (220 mg, 58%) as a dark blue solid. R_f = 0.30 (CH₂Cl₂/petroleum ether 4:6); ¹H NMR (CDCl₃, 300 MHz): δ = 0.99 (t, ³*J* = 7.3 Hz, 3H), 1.33 (s, 6H), 1.41–1.42 (m, 9H), 1.46 (s, 3H), 1.52–1.57 (m, 2H), 1.70–1.74 (m, 4H), 1.80–1.90 (m, 2H), 2.58 (s, 3H), 3.16 (t, ³*J* = 5.7 Hz, 2H), 3.23 (t, ³*J* = 5.7 Hz, 2H), 3.83 (t, ³*J* = 6.6 Hz, 2H), 5.95 (s, 1H), 6.58 (s, 1H), 7.08 (d, ³*J* = 8.2 Hz, 2H), 7.32 (d, ³*J* = 16.2 Hz, 1H), 7.37 (s, 1H), 7.42 (d, ³*J* = 16.2 Hz, 1H), 7.83 ppm (d, ³*J* = 8.2 Hz, 2H); ¹³C NMR (CDCl₃, 50 MHz): δ = 14.3, 14.1, 14.7, 14.7, 15.2, 19.6, 30.2, 31.0, 32.4, 32.4, 32.8, 36.6, 40.1, 47.0, 47.6, 94.6, 113.2, 113.3, 113.3, 117.4, 118.3, 120.3, 120.3, 122.0, 123.6, 126.9, 130.7, 135.3, 136.4, 138.3, 139.5, 142.7, 144.7, 152.2, 156.6, 157.6 ppm; ¹⁵B NMR (CDCl₃, 128 MHz): δ = 1.07 ppm (t, *J*(B,F) = 32.6 Hz); EIMS (neat matter): *m/z* calcd for C₄₀H₄₀BF₂IN₃O: 761.2; found: 761.1 (100) [*M*⁺].

688.2 (30) $[M-(OC_4H_9)]^+$; elemental analysis calcd (%) for $C_{40}H_{47}BF_2N_3O$: C 63.09, H 6.22, N 5.52; found: C 62.76, H 6.04, N 5.38.

Compound 4: Compound 4 was synthesized according to general procedure B, starting from compound 3 (155 mg, 0.203 mmol). The crude residue so obtained was purified by column chromatography (silica gel), eluting with toluene/ CH_2Cl_2 (8:2, v/v) to give the desired compound as a dark blue solid (95 mg, 71%). $R_f=0.46$ (toluene/ CH_2Cl_2 8:2); 1H NMR ($CDCl_3$, 300 MHz): $\delta=0.98$ (t, $^3J=7.2$ Hz, 3H), 1.33–1.42 (m, 18H), 1.51–1.57 (m, 2H), 1.73 (t, $^3J=6.0$ Hz, 4H), 1.81–1.88 (m, 2H), 2.59 (s, 3H), 3.16–3.24 (m, 4H), 3.83 (t, $^3J=6.7$ Hz, 2H), 5.96 (s, 1H), 6.59 (s, 1H), 7.46–7.48 (m, 3H), 7.54 (d, $^3J=8.1$ Hz, 2H), 8.02 (d, $^3J=8.1$ Hz, 2H), 10.12 ppm (s, 1H); ^{13}C NMR ($CDCl_3$, 50 MHz): $\delta=14.2$, 14.4, 14.6, 15.0, 19.5, 29.74, 30.1, 30.8, 30.9, 32.3, 32.7, 36.4, 40.0, 46.9, 47.5, 113.1, 117.3, 118.4, 120.3, 121.9, 123.5, 125.3, 126.9, 128.3, 129.1, 129.8, 130.2, 132.8, 135.6, 135.8, 136.5, 137.9, 139.1, 142.2, 142.3, 142.4, 144.7, 152.3, 156.8, 157.6, 191.7 ppm; ^{11}B NMR ($CDCl_3$, 128 MHz): $\delta=1.07$ ppm (t, $J(B,F)=33.2$ Hz); IR: $\tilde{\nu}=701$, 763, 976, 1061, 1116, 1156, 1194, 1290, 1317, 1464, 1497, 1532, 1581, 1702 (CHO), 2869, 2927, 2957 cm^{-1} ; EIMS (neat matter): m/z calcd for $C_{41}H_{48}BF_2N_3O_2$: 663.3; found: 663.2 (100) $[M]^+$, 590.2 (35) $[M-(OC_4H_9)]^+$; elemental analysis calcd (%) for $C_{41}H_{48}BF_2N_3O_2$: C 74.20, H 7.29, N 6.33; found: C 73.92, H 6.98, N 6.12.

Compound JLCV (5): Compound 5 was synthesized according to general procedure C, starting from compound 4 (39 mg, 0.056 mmol). After cooling the reaction to room temperature, the precipitate formed was isolated by centrifugation and washed several times with methanol, giving the product as a dark blue powder (20 mg, 50%). 1H NMR ($CDCl_3$, 300 MHz): $\delta=0.98$ (t, $^3J=7.3$ Hz, 3H), 1.33–1.42 (s, 18H), 1.50–1.55 (m, 2H), 1.71–1.75 (m, 4H), 1.80–1.90 (m, 2H), 2.59 (s, 3H), 3.17 (t, $^3J=5.8$ Hz, 2H), 3.25 (t, $^3J=5.8$ Hz, 2H), 3.82 (t, $^3J=6.7$ Hz, 2H), 5.96 (s, 1H), 6.60 (s, 1H), 7.73–7.48 (m, 3H), 7.55 (d, $^3J=8.2$ Hz, 2H), 7.84 (s, 1H), 8.05 ppm (d, $^3J=8.3$ Hz, 2H); ^{13}C NMR ($CDCl_3$, 100 MHz): $\delta=14.3$, 14.5, 14.6, 15.1, 19.5, 29.4, 29.7, 30.0, 30.8, 32.3, 32.3, 32.7, 36.4, 39.9, 46.9, 47.5, 75.9, 83.9, 112.5, 112.9, 113.5, 117.2, 118.7, 120.4, 121.9, 123.5, 126.9, 129.8, 130.0, 130.5, 131.1, 131.2, 132.7, 134.7, 135.9, 138.7, 142.2, 142.6, 144.8, 152.3, 157.1, 157.7, 158.9, 165.5 ppm; ^{11}B NMR ($CDCl_3$, 128 MHz): $\delta=1.04$ (t, $J(B,F)=32.9$ Hz); IR: $\tilde{\nu}=702$, 795, 854, 984, 1014, 1156, 1196, 1257, 1294, 1320, 1465, 1496, 1533, 1583, 2228 (–CN), 2963, 2961, 2926 cm^{-1} ; EIMS (neat matter): m/z calcd for $C_{44}H_{48}BF_2N_3O$: 711.4; found: 711.2 (100) $[M]^+$, 692.2 (30) $[M-F]^+$; elemental analysis calcd (%) for $C_{44}H_{48}BF_2N_3O$: C 74.26, H 6.80, N 9.84; found: C 73.94, H 6.62, N 9.62.

Compound 7: Compound 7 was synthesized according to general procedure B, starting from compound 6a (101 mg, 0.077 mmol). Flash chromatography from silica gel (toluene/petroleum ether 7:3, v/v) gave the product as a dark blue solid (78%, 73 mg). $R_f=0.48$ (toluene/petroleum ether 7:3); 1H NMR ($CDCl_3$, 300 MHz): $\delta=0.78$ –0.85 (m, 9H), 1.19–1.43 (m, 25H), 1.93–2.04 (m, 6H), 2.66 (s, 3H), 4.88–4.96 (m, 6H), 6.04 (s, 1H), 6.73 (s, 1H), 7.35 (t, $^3J=7.4$ Hz, 2H), 7.43–7.50 (m, 3H), 7.55 (d, $^3J=8.0$ Hz, 2H), 7.62–7.70 (m, 3H), 7.71 (s, 1H), 7.85 (d, $^3J=16.0$ Hz, 1H), 8.04 (d, $^3J=8.0$ Hz, 2H), 8.22–8.29 (m, 3H), 10.12 ppm (s, 1H); ^{11}B NMR ($CDCl_3$, 128 MHz): $\delta=1.10$ ppm (t, $J(B,F)=32.6$ Hz); IR: $\tilde{\nu}=706$, 727, 794, 984, 1015, 1075, 1157, 1193, 1260, 1298, 1372, 1464, 1499, 1538, 1705 (–CHO), 2852, 2923, 2958 cm^{-1} ; EIMS (neat matter): m/z calcd for $C_{40}H_{48}BF_2N_3O$: 959.5; found: 959.3 (100) $[M]^+$, 940.3 (35) $[M-F]^+$; elemental analysis calcd (%) for $C_{40}H_{48}BF_2N_3O$: C 78.82, H 7.14, N 7.29; found: C 78.54, H 6.72, N 6.82.

Compound TXCV (8): Malonitrile (7 mg, 0.112 mmol) and several drops of piperidine/acetic acid were added to a Schlenk tube equipped with a stirrer bar and containing a solution of aldehyde precursor 7 (68 mg, 0.056 mmol) in THF (3 mL). The mixture was stirred at 95°C for 20–30 min. After purification by column chromatography (silica gel, toluene/ CH_2Cl_2 8:2, v/v), the product was obtained as a dark blue solid (22 mg, 50%). $R_f=0.64$ (toluene/ CH_2Cl_2 8:2); 1H NMR ($CDCl_3$, 400 MHz): $\delta=0.78$ –0.85 (m, 9H), 1.21–1.33 (m, 18H), 1.41 (s, 3H), 1.47 (s, 3H), 1.94–2.03 (m, 6H), 2.65 (s, 3H), 4.91–4.98 (m, 6H), 6.05 (s, 1H), 6.76 (s, 1H), 7.36 (t, $^3J=7.4$ Hz, 2H), 7.46 (t, $^3J=8.1$ Hz, 2H), 7.54 (d, $^3J=7.6$ Hz, 1H), 7.58 (d, $^3J=8.3$ Hz, 2H), 7.36–7.66 (m, 2H), 7.69 (d, $^3J=8.5$ Hz, 1H), 7.75 (s, 1H), 7.85 (d, $^3J=16.2$ Hz, 1H), 7.86 (s, 1H), 8.08 (d, $^3J=$

8.3 Hz, 2H), 8.26 (d, $^3J=8.5$, 1H), 8.29 ppm (d, $^3J=7.9$ Hz, 2H); ^{13}C NMR ($CDCl_3$, 50 MHz): $\delta=13.9$, 13.9, 14.1, 14.6, 14.9, 22.4, 22.5, 22.7, 26.3, 26.4, 29.3, 29.7, 31.4, 31.4, 31.4, 31.9, 47.1, 84.2, 110.3, 110.6, 119.3, 119.8, 119.8, 121.4, 121.5, 121.6, 122.7, 123.3, 123.4, 124.6, 129.7, 130.2, 130.9, 131.3, 138.5, 138.8, 139.4, 140.9, 141.0, 141.2, 142.0, 154.5, 155.1, 158.7 ppm; ^{11}B NMR ($CDCl_3$, 128 MHz): $\delta=1.07$ ppm (t, $J(B,F)=32.0$ Hz); IR: $\tilde{\nu}=710$, 727, 800, 984, 1018, 1039, 1077, 1158, 1194, 1299, 1373, 1409, 1463, 1500, 1540, 1589, 2229 (–CN), 2853, 2923, 2954 cm^{-1} ; EIMS (neat matter): m/z calcd for $C_{66}H_{68}BF_2N_7$: 1007.5; found: 1007.3 (100) $[M]^+$, 988.3 (20) $[M-F]^+$; elemental analysis calcd (%) for $C_{66}H_{68}BF_2N_7$: C 78.63, H 6.80, N 9.73; found: C 78.42, H 6.62, N 9.42.

Acknowledgements

We thank the CNRS, EPSRC (EP/G04094X/1), ECPM-Strasbourg, and Newcastle University for financial support of this work. We gratefully acknowledge IMRA Europe S.A.S. (Sophia Antipolis, France) for awarding a PhD fellowship to A.N. Drs. Stéphane Jacob and Gilles Dennler (IMRA Europe) are thanked for many helpful and fruitful discussions. Dr. Takashi Mitsumoto and Dr. Hiroyuki Katsuda are also acknowledged for their continuous encouragement.

- [1] M. C. Ruiz Delgado, J. Casado, V. Hernández, J. T. López Navarrete, J. Orduna, B. Villacampa, R. Alicante, J.-M. Raimundo, P. Blanchard, J. Roncali, *J. Phys. Chem. C* **2008**, *112*, 3109–3120.
- [2] J. Li, D. Liu, Z. Hong, S. Tong, P. Wang, C. Ma, O. Lengyel, C.-S. Lee, H.-L. Kwong, S. Lee, *Chem. Mater.* **2003**, *15*, 1486–1490.
- [3] B. A. Reinhardt, L. L. Brott, S. J. Clarson, A. G. Dillard, J. C. Bhatt, R. Kannan, L. Yuan, G. S. He, P. N. Prasad, *Chem. Mater.* **1998**, *10*, 1863–1874.
- [4] D. R. Kanis, M. A. Ratner, T. J. Marks, *Chem. Rev.* **1994**, *94*, 195–242.
- [5] M. Blanchard-Desce, V. Alain, P. V. Bedworth, S. R. Marder, A. Fort, C. Runser, M. Barzoukas, S. Lebus, R. Wortmann, *Chem. Eur. J.* **1997**, *3*, 1091–1104.
- [6] a) F. Tancini, Y.-L. Wu, B. Schweizer, J.-P. Gisselbrecht, C. Boudon, P. D. Jarowski, M. T. Beels, I. Biaggio, F. Diederich, *Eur. J. Org. Chem.* **2012**, 2756–2771; b) M. Kivala, F. Diederich, *Acc. Chem. Res.* **2009**, *42*, 235–248.
- [7] A. Myers Kelley, *J. Phys. Chem. A* **1999**, *103*, 6891–6903.
- [8] a) S. Priyadarshy, M. J. Terien, D. N. Beratan, *J. Am. Chem. Soc.* **1996**, *118*, 1504–1510; b) R. A. Rijkenberg, D. Bebelar, W. J. Buma, J. W. Hofstra, *J. Phys. Chem. A* **2002**, *106*, 2446–2456; c) B. Schmidt, C. Sobotta, S. Malkmus, S. Laimgruber, M. Braun, W. Zinth, P. Gilch, *J. Phys. Chem. A* **2004**, *108*, 4399.
- [9] C.-C. Lee, A. T. Hu, *Dyes Pigm.* **2003**, *59*, 63–69.
- [10] Y. J. Chang, T. J. Chow, *J. Mater. Chem.* **2011**, *21*, 3091–3099.
- [11] J. Kulhanek, F. Bures, A. Wojciechowski, M. Makowska-Janusik, E. Gondek, I. V. Kityk, *J. Phys. Chem. A* **2010**, *114*, 9440–9446.
- [12] S. H.-I. Kato, F. Diederich, *Chem. Commun.* **2010**, 46, 1994–2006.
- [13] a) K. D. Belfield, D. J. Hagan, E. W. Van Stryland, K. J. Schafer, R. A. Negres, *Org. Lett.* **1999**, *1*, 1575–1578; b) E. Ortí, P. M. Viruela, R. Viruela, F. Effenberger, V. Hernández, J. T. López Navarrete, *J. Phys. Chem. A* **2005**, *109*, 8724–8731.
- [14] a) M. Yeung, A. C. H. Ng, M. G. B. Drew, E. Vorpagel, E. M. Breitung, R. J. McMahan, D. K. P. Ng, *J. Org. Chem.* **1998**, *63*, 7143–7150; b) S. M. LeCours, H.-W. Guan, S. G. DiMaggio, C. H. Wang, M. J. Therien, *J. Am. Chem. Soc.* **1996**, *118*, 1497–1503; c) N. Jiang, G. Zuber, S. Keinan, A. Nayak, W. Yang, M. J. Therien, D. N. Beratan, *J. Phys. Chem. C* **2012**, *116*, 9724–9733.
- [15] a) N. S. Lewis, D. G. Nocera, *Proc. Natl. Acad. Sci. USA* **2006**, *103*, 15729–15735; b) N. Ammaroli, V. Balzani, *Angew. Chem.* **2007**, *119*, 52–67; *Angew. Chem. Int. Ed.* **2007**, *46*, 52–66; c) J. Liu, G. Cao, Z. Yang, D. Wang, D. Dubois, X. Zhou, G. L. Graff, L. R. Pederson, J.-G. Zhang, *ChemSusChem* **2008**, *1*, 676–697.

- [16] a) J. Jortner, *J. Chem. Phys.* **1976**, *64*, 4860–4867; b) J. Jortner, *J. Am. Chem. Soc.* **1980**, *102*, 6676–6686; c) S. Franzen, R. F. Goldstein, S. G. Boxer, *J. Phys. Chem.* **1993**, *97*, 3040–3053; d) C. C. Page, P. Moser, X. Chen, P. L. Dutton, *Nature* **1999**, *402*, 47–52.
- [17] a) M. R. Wasielewski, *Chem. Rev.* **1992**, *92*, 435–461; b) D. Gust, T. A. Moore, A. L. Moore, *Acc. Chem. Res.* **1993**, *26*, 198–205; c) H. B. Gray, J. R. Winkler, *Ann. Rev. Biochem.* **1996**, *65*, 537–561.
- [18] R. A. Marcus, *J. Chem. Phys.* **1956**, *24*, 966–978.
- [19] D. Holten, D. F. Bocian, J. S. Lindsey, *Acc. Chem. Res.* **2002**, *35*, 57–69.
- [20] a) N. Armaroli, *Photochem. Photobiol. Sci.* **2003**, *2*, 73–87; b) T. S. Balaban, *Acc. Chem. Res.* **2005**, *38*, 612–623.
- [21] L. Sánchez, N. Martín, D. Guldí, *Angew. Chem.* **2005**, *117*, 5508–5516; *Angew. Chem. Int. Ed.* **2005**, *44*, 5374–5382.
- [22] F. J. M. Hoeben, P. Jonkhøj, E. W. Meijer, A. P. H. J. Schenning, *Chem. Rev.* **2005**, *105*, 1491–1556.
- [23] N. Saki, T. Dinc, E. U. Akkaya, *Tetrahedron* **2006**, *62*, 2721–2725.
- [24] a) R. Ziessel, G. Ulrich, A. Harriman, *New J. Chem.* **2007**, *31*, 496–501; b) R. Ziessel, *Compt. Rendus Acad. Sciences Chimie* **2007**, *10*, 622–629; c) A. Loudet, K. Burgess, *Chem. Rev.* **2007**, *107*, 4891–4932; d) G. Ulrich, R. Ziessel, A. Harriman, *Angew. Chem.* **2008**, *120*, 1202–1219; *Angew. Chem. Int. Ed.* **2008**, *47*, 1184–1201.
- [25] a) S. Kolemen, Y. Cakmak, S. Erten-Ela, Y. Altay, J. Brendel, M. Thelakkat, E. U. Akkaya, *Org. Lett.* **2010**, *12*, 3812–3815; b) T. Rousseau, A. Cravino, J. Roncali, T. Bura, G. Ulrich, R. Ziessel, *Chem. Commun.* **2009**, 1673–1675; c) T. Rousseau, A. Cravino, J. Roncali, T. Bura, G. Ulrich, R. Ziessel, *J. Mater. Chem.* **2009**, *19*, 2298–2300; d) T. Rousseau, A. Cravino, E. Ripaud, P. Leriche, S. Rhin, A. De Nicola, R. Ziessel, J. Roncali, *Chem. Commun.* **2010**, 46, 5082–5084; e) B. Kim, B. Ma, V. R. Donuru, H. Liu, J. M. J. Frechet, *Chem. Commun.* **2010**, 46, 4148–4150.
- [26] a) G. Ulrich, C. Goze, L. Charbonnière, R. Ziessel, *Chem. Eur. J.* **2003**, *9*, 3748–3755; b) S. Atilgan, T. Ozdemir, E. U. Akkaya, *Org. Lett.* **2008**, *10*, 4065–4067; c) S. Atilgan, T. Ozdemir, E. U. Akkaya, *Org. Lett.* **2010**, *12*, 4792–4795.
- [27] S. L. Niu, C. Massif, G. Ullrich, R. Ziessel, P.-Y. Renard, A. Romieu, *Org. Biomol. Chem.* **2010**, *8*, 66–69.
- [28] a) R. Ziessel, P. Retailleau, K. J. Elliott, A. Harriman, *Chem. Eur. J.* **2009**, *15*, 10369–10376; b) X. Yin, Y. Li, Y. Zhu, X. Tang, H. Zheng, D. Zhu, *Tetrahedron* **2009**, *65*, 8373–8377; c) X. Yin, Y. Li, Y. Zhu, X. Jing, Y. Li, D. Zhu, *Dalton Trans.* **2010**, 39, 9929–9935; d) W.-J. Shi, P.-C. Lo, A. Singh, I. K. P. Ledoux-Rak, D. Ng, *Tetrahedron* **2012**, *68*, 8712–8718.
- [29] a) S. Niu, G. Ullrich, P. Retailleau, R. Ziessel, *Org. Lett.* **2011**, *13*, 4996–4999; b) S. L. Niu, G. Ullrich, P. Retailleau, R. Ziessel, *Tetrahedron Lett.* **2011**, *52*, 4848–4853.
- [30] a) J. J. Holt, B. D. Caltree, J. Vincek, M. K. Gannon, M. R. Detty, *J. Org. Chem.* **2007**, *72*, 2690–2693; b) A. R. Katritzky, B. Rachwal, S. Rachwal, *J. Org. Chem.* **1996**, *61*, 3117–3125; c) K. H. Lee, M. H. Park, S. M. Kim, Y. K. Kim, S. S. Yoon, *Jpn. J. Appl. Phys.* **2010**, *49*, 08JG02–08JG04.
- [31] T. Bura, N. Leclerc, S. Fall, P. Lévêque, T. Heiser, R. Ziessel, *Org. Lett.* **2011**, *13*, 6030–6033.
- [32] A. Zhu, B. Wang, J. O. White, H. G. Drickamer, *J. Phys. Chem. A* **2003**, *107*, 6932–6935.
- [33] C.-H. Lee, H.-J. Yoon, J.-S. Shim, W.-D. Jang, *Chem. Eur. J.* **2012**, *18*, 4513–4516.
- [34] a) R. Ziessel, L. Bonardi, P. Retailleau, G. Ulrich, *J. Org. Chem.* **2006**, *71*, 3093; b) T. Bura, R. Ziessel, *Tetrahedron Lett.* **2010**, *51*, 2875–2879.
- [35] A. Harriman, M. Hissler, R. Ziessel, *Phys. Chem. Chem. Phys.* **1999**, *1*, 4203–4211.
- [36] Z. Shuai, J. L. Brédas, W. P. Su, *Chem. Phys. Lett.* **1994**, *228*, 301–306.
- [37] R. Englman, J. Jortner, *Mol. Phys.* **1970**, *18*, 145–170.
- [38] a) R. Richert, *Chem. Phys. Lett.* **1992**, *199*, 355–359; b) C. Reichardt, *Chem. Rev.* **1994**, *94*, 2319–2358.
- [39] W. W. Qin, T. F. Rohand, W. Dehaen, J. N. Clifford, K. Driessen, D. Beljonne, B. Van Averbek, M. Van der Auweraer, N. Boens, *J. Phys. Chem. A* **2007**, *111*, 8588–8597.
- [40] R. Ziessel, S. Rihn, A. Harriman, *Chem. Eur. J.* **2010**, *16*, 11942–11953.
- [41] G. U. Bublitz, S. G. Boxer, *J. Am. Chem. Soc.* **1998**, *120*, 3988–3992.
- [42] a) M. Bixon, J. Jortner, J. W. Verhoeven, *J. Am. Chem. Soc.* **1994**, *116*, 7349–7355; b) J. W. Verhoeven, T. Scherer, B. Wegewijs, R. M. Hermant, J. Jortner, M. Bixon, S. Depaemelaere, F. C. De Schryver, *Rec. Trav. Chim. Pays-Bas* **1995**, *114*, 443–449.
- [43] F. A. Bovey, S. S. Yanari, *Nature* **1960**, *186*, 1042–1044.
- [44] a) I. Renge, *J. Phys. Chem.* **1995**, *99*, 15955–15962; b) T. Renger, B. Grundkötter, M. E. A. Madjet, F. Müh, *Proc. Natl. Acad. Sci. USA* **2008**, *105*, 13235–13240.
- [45] A. Filarowski, M. Kluba, K. Cieslik-Boczuła, A. Koll, A. Kochel, L. Pandey, W. M. de Borggraeve, M. Van der Auweraer, J. Catalan, N. Boens, *Photochem. Photobiol. Sci.* **2010**, *9*, 996–1008.
- [46] a) E. Lippert, *Z. Naturforsch. A: Phys. Sci.* **1955**, *10*, 541–545; b) N. Mataga, Y. Kaifu, M. Koizumi, *Bull. Chem. Soc. Jpn.* **1955**, *28*, 690–691; c) N. Mataga, Y. Kaifu, M. Koizumi, *Bull. Chem. Soc. Jpn.* **1956**, *29*, 465–470.
- [47] a) K. Rurack, M. Kollmannsberger, J. Daub, *New J. Chem.* **2001**, *25*, 289–292; b) Y. H. Yu, A. B. Descalzo, Z. Shen, H. Rohr, Q. Liu, Y. W. Wang, M. Spieles, L. Z. Li, K. Rurack, X. Z. You, *Chem. Asian J.* **2006**, *1*, 176–187.
- [48] M. Baruah, W. W. Qin, C. Flors, J. Hofkens, R. A. L. Vallee, D. Beljonne, M. Van der Auweraer, W. M. De Borggraeve, N. Boens, *J. Phys. Chem. A* **2006**, *110*, 5998–6009.
- [49] R. Ziessel, G. Ulrich, A. Harriman, M. A. H. Alamiry, B. Stewart, P. Retailleau, *Chem. Eur. J.* **2009**, *15*, 1359–1369.
- [50] a) J. A. Levitt, P. H. Chung, M. K. Kuimova, G. Yahioglu, Y. Wang, J. L. Qu, K. Suhling, *ChemPhysChem* **2011**, *12*, 662–672; b) E. Ishow, R. Guillot, G. Buntinx, O. Poizat, *J. Photochem. Photobiol. A* **2012**, *234*, 27–36; c) F. J. Hoogesteger, C. A. van Walree, L. W. Jenneskens, M. R. Roest, J. W. Verhoeven, W. Schuddeboom, J. J. Piet, J. M. Warman, *Chem. Eur. J.* **2000**, *6*, 2948–2959; d) D. L. Phillips, I. R. Gould, J. W. Verhoeven, D. Tittelbach-Helmrich, A. B. Meyers, *Chem. Phys. Lett.* **1996**, *258*, 87–93; e) J. M. Lawson, M. N. Paddon-Row, W. Schuddeboom, J. M. Warman, A. H. A. Clayton, K. P. Ghiggino, *J. Phys. Chem.* **1993**, *97*, 13099–13106; f) M. Koeberg, M. de Groot, J. W. Verhoeven, N. R. Lokan, M. J. Shephard, M. N. Paddon-Row, *J. Phys. Chem. A* **2001**, *105*, 3417–3424.
- [51] F. B. Dias, S. Pollock, G. Hedley, L. O. Palsson, A. R. Monkman, I. I. Perepichka, I. F. Perepichka, M. Tavasli, M. R. Bryce, *J. Phys. Chem. B* **2006**, *110*, 19329–19339.
- [52] C. Streck, R. Richert, *Ber. Bunsen.-Gesell. Phys. Chem. Chem. Phys.* **1994**, *98*, 619–625.

Received: March 18, 2013

Revised: June 14, 2013

Published online: August 14, 2013

Exciplex Emission From a Boron Dipyrromethene Bodipy Dye Equipped with a Dicyanovinyl Appendage

CHEMPHYSICHEM
ARTICLES

ChemPubSoc
Europe

DOI: 10.1002/cphc.201300805

Exciplex Emission from a Boron Dipyrromethene (Bodipy) Dye Equipped with a Dicyanovinyl Appendage

Adela Nano,^[a] Raymond Ziessel,^{*,[a]} Patrycja Stachelek,^[b] Mohammed A. H. Alamiry,^[b] and Anthony Harriman^{*,[b]}

The photophysical properties of a prototypic donor–acceptor dyad, featuring a conventional boron dipyrromethene (Bodipy) dye linked to a dicyanovinyl unit through a *meso*-phenylene ring, have been recorded in weakly polar solvents. The absorption spectrum remains unperturbed relative to that of the parent Bodipy dye but the fluorescence is extensively quenched. At room temperature, the emission spectrum comprises roughly equal contributions from the regular π, π^* excited-singlet state and from an exciplex formed by partial charge transfer from Bodipy to the dicyanovinyl residue. This mixture moves progressively in favor of the locally excited π, π^* state on cooling and the exciplex is no longer seen in frozen media; the overall emission quantum yield changes dramatically near the freezing point of the solvent. The exciplex, which has a life-

time of approximately 1 ns at room temperature, can also be seen by transient absorption spectroscopy, in which it decays to form the locally excited triplet state. Under applied pressure ($P < 170$ MPa), formation of the exciplex is somewhat hindered by restricted rotation around the semirigid linkage and again the emission profile shifts in favor of the π, π^* excited state. At higher pressure ($170 < P < 550$ MPa), the molecule undergoes reversible distortion that has a small effect on the yield of π, π^* emission but severely quenches exciplex fluorescence. In the limiting case, this high-pressure effect decreases the molar volume of the solute by approximately 25 cm³ and opens a new channel for nonradiative deactivation of the excited-state manifold.

1. Introduction

Fluorescent exciplexes are often formed in weakly polar solvents under conditions in which the driving force for excited-state electron transfer from donor to acceptor is close to zero.^[1] An important feature of all exciplexes concerns the extent of charge transfer that occurs under illumination,^[2] a factor that depends on many parameters including structure, temperature, and environment.^[3] It is common practice to consider the exciplex wave function in terms of contributions from extreme forms associated with a nonpolar (i.e. π, π^* or locally excited) state and a polar (i.e. charge-transfer) state.^[4] Because there is no ground-state counterpart, the exciplex can retain a relatively long lifetime but fluorescence is kept to a modest level by the low radiative rate constant. A further point of in-

terest relating to exciplex formation is that a significant decay route can involve intersystem crossing to the triplet manifold.^[5] Indeed, exciplex formation provides a convenient means by which to access the triplet state for dyes that possess very slow rates of inherent intersystem crossing. Such behavior has already been reported^[6] for a few boron dipyrromethene (Bodipy) dyes fitted with appropriate electrode-active subunits. Notably, subtle geometry changes often accompany the charge-transfer step.^[7] This type of geometry alteration is especially important in closely spaced, donor–acceptor systems built around semirigid spacers. Of course, many organic moieties (e.g. aryl hydrocarbons,^[8] heterocycles,^[9] porphyrins,^[10] oligomers,^[11] polymers,^[12] dendrimers,^[13] cholesteric liquid crystals,^[14] and so forth) are known to form emissive exciplexes under certain conditions. Recent work has implicated^[15] an exciplex as a key intermediate during intramolecular electronic energy transfer, and several interesting applications have been found for exciplexes.^[16] Many of these revolve around analytical protocols such as temperature, viscosity, or polarity sensors.

In the present work we are concerned with extending the range of Bodipy-based fluorescent exciplexes that undergo intersystem crossing to the corresponding triplet state.^[5,6] Of particular importance is the effect of local environment on both exciplex formation and its subsequent decay. We restrict our attention to a single intramolecular exciplex in which a strong electron acceptor (i.e. dicyanovinyl) is attached to a conventional Bodipy dye through a bridging phenylene ring. The terminal acceptor is free to rotate around the connection to the bridge,

[a] A. Nano, Dr. R. Ziessel
LCOSA, ICPEES, UMR7515
CNRS/Université de Strasbourg/ECPM
25 rue Becquerel, 67087 Strasbourg, Cedex 02 (France)
Fax: (+33) 3-68-85-27-61
E-mail: ziessel@unistra.fr
Homepage: <http://icpees.unistra.fr/lcosa/>

[b] P. Stachelek, Dr. M. A. H. Alamiry, Prof. Dr. A. Harriman
Molecular Photonics Laboratory
School of Chemistry, Bedson Bldg.
Newcastle University
Newcastle upon Tyne, NE1 7RU (UK)
Fax: (+44) 191 222 8660
E-mail: anthony.harriman@ncl.ac.uk
Homepage: <http://ncl.ac.uk/mp/>

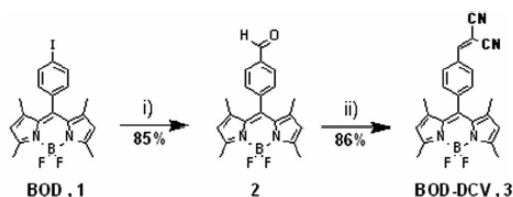
Supporting Information for this article is available on the WWW under <http://dx.doi.org/10.1002/cphc.201300805>.

thereby providing access to a wide range of possible geometries in terms of the mutual alignment of the two electrode-active partners. The phenylene ring serves to decouple the two electronic systems in the ground state. It might be mentioned that the dicyanovinyl residue has been used extensively as an electron acceptor in the generic field of molecular photo-physics^[17] and is a common participant in exciplex chemistry.^[18] It has also found prominent use in fluorescent sensors for monitoring changes in rheology.^[19] More importantly, the dicyanovinyl residue is a popular constituent of materials used in the emerging field of molecular organic photovoltaics,^[20] especially when combined with poly(thiophene) units.^[21] As Bodipy dyes are also showing promise as reagents in organic light-emitting diodes and organic solar cells,^[22] it seems opportune to combine these features into a single entity.

2. Results and Discussion

Synthesis and Energetics

The target compound, BOD-DCV, was prepared from the parent compound **1**^[23] by an original formylation reaction,^[24] first leading to **2** and then undergoing reaction with malononitrile^[25] to afford the required material **3** in good yield (Scheme 1). The final compound was purified by flash chroma-



Scheme 1. Reaction conditions: i) $[\text{Pd}(\text{PPh}_3)_2\text{Cl}_2]$ (10 mol%), HCOONa , N,N -dimethylformamide (DMF) under a flow of CO at atmospheric pressure, 100 °C; ii) malononitrile, AcOH/piperidine cat., THF, 95 °C, 20–30 min.

tography on a silica column and analyzed by NMR spectroscopy. Diagnostic signals include the chemical shift of the malononitrile proton at 7.84 ppm in **3** that is formed at the expense of the formyl peak at 10.11 ppm in **2**. The stretching vibrations of the formyl and dicyano groups were observed, respectively, at 1704 and 2229 cm^{-1} in the IR spectra. Full synthetic details are provided in the Experimental Section.

Quantum chemical calculations were used to model the geometry of the lowest-energy conformation of BOD-DCV in solution (Figure 1). It is seen that the ancillary methyl groups force the *meso*-phenylene ring into an orthogonal geometry but this subunit can gyrate around its mean position at ambient temperature. The dicyanovinyl subunit prefers to align with the π cloud resident on the Bodipy unit. This has the effect of bringing one of the cyano groups into close proximity with the Bodipy residue. For the energy-minimized geometry, the computed dipole moment is 3.5 D compared to a value of 2.0 D for the corresponding *meso*-phenylene derivative lacking the dicyanovinyl unit (i.e. BOD). These calculations predicted

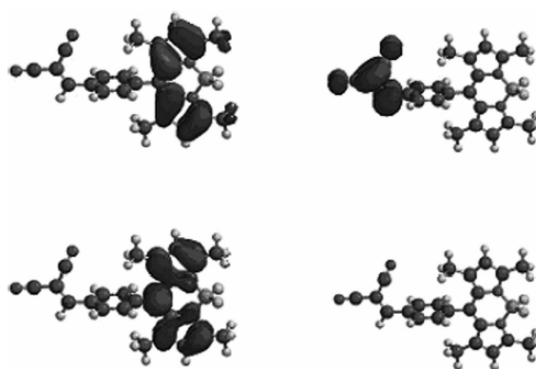


Figure 1. Compound BOD-DCV: Pictorial representations of the HOMO (upper left-hand side), LUMO (upper right-hand side), and LUMO(1) (lower left-hand side). Also shown is the energy-minimized geometry for the ground state.

the absorption maximum to be at 519 nm and the cyano stretching vibration to be at 2190 cm^{-1} .

The redox behavior of these Bodipy dyes was investigated by cyclic voltammetry in CH_2Cl_2 solution containing 0.1 M tetra-*N*-butylammonium hexafluorophosphate (TBAPF₆) as supporting electrolyte and the results are gathered in Table 1. The starting material BOD (compound **1** in Scheme 1) displays

Table 1. Electrochemical data for the target Bodipy dyes.^[a]

Compound	$E^{\text{ox}}(\text{ox.}, \text{soln.}) [\text{V}]$ $\Delta E [\text{mV}]$	$E^{\text{red}}(\text{red.}, \text{soln.}) [\text{V}]$ $\Delta E [\text{mV}]$
BOD, 1	+1.15 (70)	−1.24 (60)
2	+1.17 (70)	−1.22 (60)
BOD-DCV, 3	+1.19 (70)	−1.03 (irr.); −1.32 (70)

[a] Potentials determined by cyclic voltammetry in deoxygenated dichloromethane solution containing 0.1 M TBAPF₆ (electrochemical window from +1.6 to −2.2 V), at a solute concentration of approximately 1.5 mM and at room temperature. Potentials were standardized versus ferrocene (Fc) as internal reference and converted to the SCE scale assuming $E_{1/2}(\text{Fc}/\text{Fc}^+) = +0.38 \text{ V}$ (vs. SCE) and $\Delta E_p = 60 \text{ mV}$. Error in half-wave potentials is $\pm 10 \text{ mV}$. For irreversible processes, the peak potentials (E_{ap}) are quoted. All reversible redox steps result from one-electron processes.

a single reversible wave on both oxidative [$E_{\text{ox}} = 1.15 \text{ V}$ vs. saturated calomel electrode (SCE)] and reductive ($E_{\text{red}} = -1.24 \text{ V}$ vs. SCE) scans due to the formation of the π -radical cation and π -radical anion, respectively, as has been observed previously for related compounds.^[26] These waves are highly reversible ($I_{\text{pa}}/I_{\text{pc}} \approx 1$) and exhibit the characteristic shape ($\Delta E_p = 60$ –70 mV) of a Nernstian, one-electron process. Closely comparable behavior is found with BOD-DCV. Here, the characteristic half-wave potential for one-electron oxidation of the Bodipy nucleus is 1.19 V (vs. SCE) in CH_2Cl_2 solution.

On reductive scans, BOD-DCV displays an additional but irreversible wave at −1.03 V (vs. SCE). By reference to other deriva-

tives bearing the dicyanovinyl residue,^[27] this new wave is attributable to one-electron reduction of the latter unit. The half-wave potential ($E^0 = -1.32$ V vs. SCE) for reduction of the Bodipy nucleus is now displaced to a slightly more negative value due to electrostatic repulsion. Such behavior seems consistent with DFT calculations made for BOD-DCV that place the HOMO and LUMO(1) on the Bodipy core but identify the LUMO as being localized on the dicyanovinyl unit (Figure 1). The orthogonal phenylene ring will minimize electronic coupling between the electrode-active units, but the short center-to-center separation (i.e. ca. 8.8 Å) remains in line with the observed through-space electrostatic perturbation.

The cyclic voltammetry data can be used in conjunction with basic spectroscopic information (see later) to determine^[28] the thermodynamic driving force (ΔG_{CT}) for light-induced charge transfer in BOD-DCV. Thus, on the basis of Equation (1) it can be concluded that in 2-methyltetrahydrofuran (MTHF) at 20 °C there is a modest driving force for charge transfer ($\Delta G_{CT} = -0.17$ eV).

$$\begin{aligned}\Delta G_{CT} &= e[E_{OX} - E_{RED}] - E_{XS} - E_{ES} - E_{SOL} \\ E_{ES} &= \frac{e^2}{(4\pi\epsilon_0)\epsilon_S R_{CC}} \\ E_{SOL} &= \frac{e^2}{8\pi\epsilon_0} \left(\frac{1}{R_D} + \frac{1}{R_A} \right) \left(\frac{1}{\epsilon_{REF}} - \frac{1}{\epsilon_S} \right)\end{aligned}\quad (1)$$

The parameters used in Equation (1) include the excited-state energy ($E_{XS} = 2.43$ eV) as derived from the intersection between normalized absorption and fluorescence spectra. Correction^[29] is made for the difference in solvent dielectric constant between MTHF ($\epsilon_S = 6.24$) and CH_2Cl_2 ($\epsilon_{REF} = 9.08$) and all molecular dimensions of donor ($R_D = 3.5$ Å) and acceptor ($R_A = 1.8$ Å) are available from the computer models (Figure 1). A further correction is applied for the electrostatic attractive forces pertinent to the resultant charge-transfer state on the basis of full electron transfer. This latter point is a matter of some conjecture and introduces an error of approximately 0.05 eV into the final ΔG_{CT} value. The same error is introduced into the thermodynamic driving force (ΔG_{CR}) for charge recombination to reform the ground state. In this case, however, the error is insignificant since the overall ΔG_{CR} is approximately -2.2 eV. A more important error relates to the fact that reduction of the dicyanovinyl unit is electrochemically irreversible.

The triplet-excited state of BOD lies at an energy of approximately 1.60 eV above the ground state.^[30] Taking the same value for BOD-DCV, it appears that the triplet state lies below the charge-transfer state by approximately 0.6 eV. Even allowing for the anticipated error in the electrostatic correction term, it seems reasonable to suppose that decay of any charge-transfer state might populate the triplet-excited state resident on the Bodipy unit. This spin-forbidden process has been the subject of much debate over the years^[31] and is favored by the energy-gap law^[32] when compared to formation of the ground state. In the absence of an external heavy-atom perturber,^[33] it was not possible to detect phosphorescence from BOD-DCV in MTHF at 77 K. Even in the presence of 20 %

(v/v) iodoethane it was difficult to resolve triplet emission from the tail of the fluorescence peak following. The phosphorescence peak occurs at 780 nm at 77 K.^[34]

Fluorescence Spectroscopy with BOD-DCV

In MTHF, the absorption spectrum of BOD-DCV ($\lambda_{MAX} = 503$ nm, $\epsilon_{MAX} = 79300$ M⁻¹ cm⁻¹) closely resembles that recorded for the parent dye, BOD, and there is no indication of significant electronic perturbation of the Bodipy π system by the electron-afinic appendage (Figure 2). In contrast, the fluorescence spec-

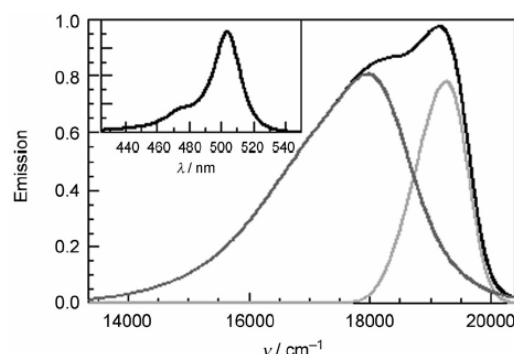


Figure 2. Fluorescence spectrum (black curve) recorded for BOD-DCV in MTHF at room temperature; the spectrum has been subjected to deconstruction to show contributions from the local (light gray curve) and exciplex (dark gray curve) emission. The inset shows the lowest-energy absorption transition recorded under the same conditions.

trum recorded for BOD-DCV in MTHF at room temperature is weak, relatively broad, and has the appearance of two overlapping sets of bands. Indeed, the spectrum sharpens on cooling and, at temperatures below the freezing point^[35] of MTHF (ca. 140 K), takes on the expected features^[36] of the π, π^* emission observed for the parent dye (Figure 3). The total fluorescence quantum yield (Φ_f), which is 0.008 at room temperature compared to a value of 0.72 for BOD, increases to 0.30 at 80 K.

Deconstruction^[37] of the room-temperature emission spectrum shows that there is a broad, featureless profile superimposed on the normal π, π^* fluorescence that has a maximum at approximately 558 nm (Figure 2, also see the Supporting Information); fluorescence from the locally excited π, π^* excited-singlet state has a maximum at 516 nm, which corresponds to a Stokes shift of 500 cm⁻¹ compared to 380 cm⁻¹ for BOD. The broad spectral profile accounts for about 70 % of the total spectrum at room temperature. Excitation spectra confirm that both emission bands arise from direct excitation into the Bodipy-based absorption transition. Notably, the band maximum for the locally excited fluorescence remains fixed whereas that for the broad profile moves steadily to the red as the fluid solution is cooled. This redshift is quite significant (e.g. the maximum moves from 558 nm at room temperature to 610 nm at 230 K) and is fully reversible.

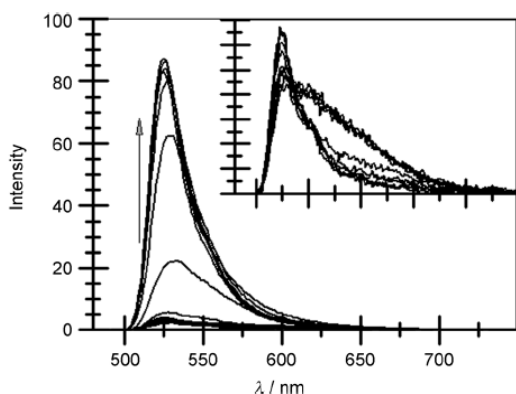


Figure 3. Effect of temperature on the emission spectrum recorded for BOD-DCV in MTHF; the arrow indicates the spectral changes occurring on warming the solution from 80 to 290 K. The inset shows an expansion of spectral changes occurring from 180 to 290 K.

In diethyl ether, the emission spectrum recorded for BOD-DCV is similar to that observed in MTHF but the broad component overlaps more strongly with the π, π^* fluorescence and contributes less to the total signal; here, $\Phi_F = 0.012$ and $\tau_S = 0.85$ ns. Spectral curve fitting indicates that the emission maximum for the second component, which is the longer-lived species, lies at approximately 545 nm. This emission maximum moves progressively towards the red on cooling the solution, while the intensity increases steadily, and there is a progressive separation of fluorescence profiles attributable to the π, π^* excited state and the second component (see the Supporting Information). Limited solubility prevents the use of less polar solvents and almost no fluorescence is apparent in polar media, such as acetonitrile. Overall, such behavior is typical of that expected for a two-state model in which the locally excited π, π^* state collapses to an emissive exciplex.^[38]

On the basis of the electrochemistry, the broad, featureless fluorescence spectral profile appears consistent with formation of an emissive exciplex by way of partial charge transfer from the Bodipy excited state to the appended dicyanovinyl unit. It is known^[39] that the emission peak for many exciplexes, including Bodipy-derived species,^[40] moves to lower energy as the solvent polarity, usually expressed^[41] in terms of the static dielectric constant (ϵ_s), increases. Such behavior explains the temperature dependence observed for BOD-DCV in fluid MTHF ($\epsilon_s = 6.24$) and in diethyl ether ($\epsilon_s = 4.34$). In frozen MTHF, formation of the exciplex becomes highly restricted and does not compete with fluorescence from the π, π^* excited-singlet state. This finding indicates that an important structural change accompanies exciplex formation. In polar media, the exciplex decays rapidly such that fluorescence becomes difficult to resolve from the baseline. In both MTHF and diethyl ether, the spectral profile can be analyzed in terms of charge-transfer interactions (see the Supporting Information). This type of spectral reconstruction allows estimation of the accompanying reorganization energy ($\lambda_{CR} = 1010$ cm⁻¹) and identification of the principal medium-frequency vibronic modes ($\nu_M =$

1275 and 2225 cm⁻¹) coupled to nonradiative decay. The DFT calculations predict important bending vibrations at around 1230 cm⁻¹ that are associated with the Bodipy nucleus, including distortions around the N-B-N axis.

Time-resolved fluorescence studies carried out using time-correlated, single-photon counting methodology with temporal resolution of approximately 30 ps indicate that the decay curves can be well explained in terms of single-exponential fits with an average lifetime (τ_S) of 0.95 ns in MTHF. Interrogation at different detection wavelengths supports the idea that this lifetime is associated with the broad spectral profile, thus leading to the conclusion that the lifetime of the π, π^* excited-singlet state is less than 30 ps (Figure 4). In MTHF at room temperature, the radiative rate constant for exciplex emission is 8×10^6 s⁻¹. The temperature dependence noted above for the

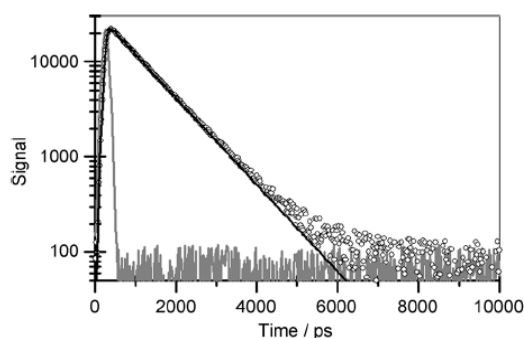


Figure 4. Typical time-resolved fluorescence decay curve recorded for BOD-DCV in MTHF at room temperature; the excitation wavelength was 420 nm. The instrumental response function is shown as a gray curve with the averaged data points appearing as open circles. The nonlinear, least-squares fit to the deconvoluted data is shown as a solid black line.

π, π^* excited-singlet state points towards a strongly activated decay process, in contrast to BOD for which the emission quantum yield is essentially temperature independent. For BOD-DCV, Φ_F reaches a plateau value of around 0.3 in the glassy region below 110 K but falls dramatically as the solid matrix melts at approximately 140 K (Figure 5). This type of behavior points clearly to exciplex formation demanding a large structural change, which is curtailed in the solid medium. Notably, the polarity of glassy MTHF has been reported^[35a] to be akin to that of liquid *N,N*-dimethylformamide such that the observed temperature dependence is not a consequence of decreasing the local polarity.

In fluid solution, Φ_F decreases steadily with increasing temperature and follows Arrhenius-type behavior (Figure 5). On the basis that the radiative rate constant ($k_{RAD} = 1.2 \times 10^8$ s⁻¹), as calculated for the π, π^* excited-singlet state using the Strickler-Berg expression^[42] (for BOD, $k_{RAD} = 1.15 \times 10^8$ s⁻¹), is not affected by temperature, the activation barrier for exciplex formation is approximately 7 kJ mol⁻¹. This is a modest barrier that must be associated with some type of internal structural reorganization. Presumably, this involves rotation around the connecting linkage but its precise nature cannot

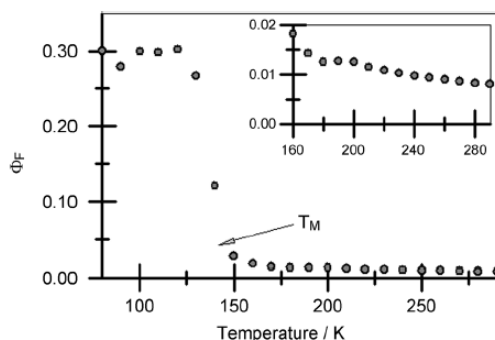


Figure 5. Effect of temperature on the fluorescence quantum yield determined for BOD-DCV in MTHF. The melting point T_M of the solvent is indicated. The inset shows an expansion of the region corresponding to the fluid solvent.

be better defined at this stage. Adding together the two temperature-dependent steps, it becomes clear that exciplex formation is subjected to a serious change in molecular conformation. Incidentally, the charge-transfer event itself is almost activationless in fluid solution, since the driving force is essentially balanced by the reorganization energy.

Laser Spectroscopy

Laser flash photolysis studies of BOD-DCV in MTHF at room temperature show that the π, π^* excited-singlet state is produced during the excitation pulse (Figure 6). This species is easily recognized by strong bleaching of the ground-state absorption transition centered at 505 nm, stimulated emission in the 510–540 nm region, and weak absorption towards the blue. This locally excited π, π^* state decays with a time constant of approximately 12 ps to form a transient species displaying a weak, broad absorption band centered at around 580 nm in addition to strong ground-state bleaching. The

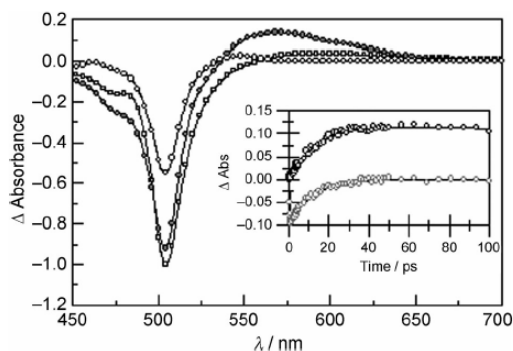


Figure 6. Decay-associated differential absorption spectra derived for the locally excited singlet state (squares), exciplex (gray dots), and triplet-excited state (open circles) following laser excitation of BOD-DCV in MTHF. The inset shows decay profiles recorded at 557 nm (upper plot, growth of the exciplex) and 536 nm (lower plot, formation and decay of the locally excited singlet state).

580 nm signal grows as the locally excited state decays. Similar spectral features are observed in diethyl ether solution, in which the locally excited singlet state has a lifetime of approximately 45 ps, and are attributed to the exciplex. Decay of this species occurs with a time constant of approximately 1 ns to form a mixture of the triplet-excited state and the ground state but without clear population of a charge-separated species. Such behavior has been reported previously for Bodipy-related exciplexes^[43] in solvents of medium polarity, and intersystem crossing within exciplexes is well known.^[44]

The triplet-excited state can be seen after excitation of BOD-DCV with a 4 ns laser pulse at 470 nm (Figure 7), for which the decay profile is monoexponential with a lifetime of approximately 90 μ s in the absence of dissolved oxygen. Aeration of the solution causes the triplet lifetime to decrease to around 200 ns. Application of a magnetic field (< 200 G) has no clear effect on the yield or lifetime of the excited-triplet state in de-aerated MTHF solution. The triplet yield does increase, albeit only by about 15 %, in the presence of iodoethane (20 % v/v), and the triplet lifetime falls to 5 μ s. The heavy-atom perturber does not modify the differential absorption spectrum of the triplet-excited state.

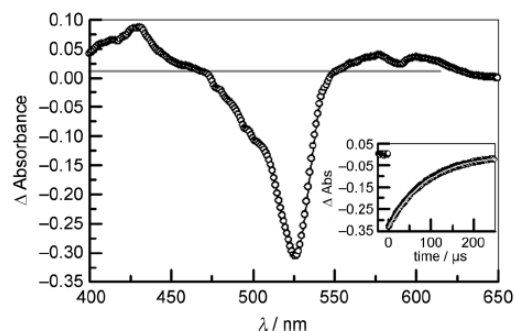


Figure 7. Differential absorption spectrum recorded for the locally excited triplet state following excitation of BOD-DCV in MTHF with a 4 ns laser pulse at 470 nm. The inset shows a decay profile recorded at 530 nm and a nonlinear, least-squares fit to a lifetime of 90 μ s.

High-Pressure Studies Made with BOD-DCV

In an attempt to isolate geometry changes from any variations in the thermodynamic parameters introduced by altering the temperature, the emission properties of BOD-DCV were studied as a function of applied pressure. For this work, the preferred solvent was MTHF because it is known^[45] that this solvent does not freeze at pressures less than 600 MPa. In line with previous studies made with Bodipy derivatives,^[46] the absorption maximum shifts slightly (i.e. < 5 nm) towards the red due to the pressure-induced change in polarizability^[47] of MTHF but this is a small effect. There is also an increase in absorbance of around 20% on application of 550 MPa due to compression of the solvent (see the Supporting Information). The more interesting experiment is how applied pressure perturbs the emission spectrum and this was followed after exci-

tation of BOD-DCV at 408 nm with a stabilized laser diode at 20 °C. This high-energy absorption band does not shift significantly under applied pressure and, therefore, serves as a better excitation wavelength than does the high-energy tail of the S_0 - S_1 transition.

The effect of applied pressure on exciplex formation has not been studied much, although high pressures have been shown to affect the fluorescence properties of both inter- and intramolecular exciplexes from pyrene/*N*-methyl-4-methoxyaniline in powdered form.^[48] In this particular study, pressure causes changes in the molecular conformation and in close packing between molecules in the solid sample. This effect is especially important for intermolecular exciplexes. There is no comparable concentration effect for BOD-DCV in MTHF solution and no spectroscopic evidence to suggest intermolecular association at any pressure or temperature available to us. Under applied pressure, the fluorescence maximum undergoes a slight redshift due to changes in the polarizability and polarity of the solvent. The maximum shift is approximately 4 nm at an applied pressure of 550 MPa and is fully reversible on release of the pressure. This effect, which has been reported previously for somewhat related Bodipy derivatives,^[46] is the counterpart of the absorption spectral shifts seen for the π, π^* excited state. A closely comparable shift is observed for BOD in MTHF.^[45]

To isolate the pressure effects on the π, π^* emission and exciplex, it was necessary to conduct spectral deconstruction patterns as outlined in Figure 2 as a function of applied pressure. Now it becomes apparent that the exciplex emission maximum shifts towards the red as the pressure increases. This is a smooth transition (Figure 8) and is considerably more noticeable than the polarizability-induced effect on the corresponding π, π^* emission. The same spectral shift can be obtained by replacing MTHF with solvents of slightly higher dielectric constant. Thus, the observed effect on the spectral maximum is attributed to a pressure-induced increase in dielectric constant,

as has been reported for many other solvents.^[41] The magnitude of the pressure effect on the exciplex emission band amounts to approximately 35 nm at 550 MPa. Over the same pressure range, ϵ_s increases from 6.96 to approximately 8.28.

At modest pressure (<175 MPa), there is a steady increase in the fluorescence intensity recorded for BOD-DCV in MTHF solution. This is to be expected on the basis of the fact that pressure raises the density of MTHF and this causes an increase in the effective concentration of the solute,^[46] although not sufficient to induce self-association. This effect is easily corrected using the pressure-induced increase in absorbance at the peak maximum. Exactly the same absorbance changes are found for BOD. It is also necessary to allow for pressure-induced changes in refractive index, which are a further consequence of the higher density of the solvent. After making this additional correction, it is clear that Φ_F for BOD shows only a slight dependence on applied pressure whereas that for BOD-DCV is more substantive (Figure 8). Furthermore, on restricting attention to the lower-pressure region (i.e. <170 MPa) and carrying out spectral deconstruction, it appears that Φ_F for the π, π^* excited-singlet state increases with increasing pressure but that for the exciplex decreases under the same conditions. In part, this latter effect arises from the increased ϵ_s for MTHF but this is a minor effect. In any case, it would not increase Φ_F for the π, π^* excited-singlet state. As there is no clear distortion of the emission spectra over this limited pressure range, the total fluorescence yield can be considered as a linear combination of the π, π^* excited-singlet state (Φ_{LESS}) and exciplex (Φ_{EXC}) quantum yields [Eq. (2)].

$$\Phi_F = \alpha \Phi_{\text{LESS}} + (1 - \alpha) \Phi_{\text{EXC}} \quad (2)$$

On this basis, the fractional contribution (α) of the π, π^* excited-singlet state to the total excited-state manifold doubles from 0.003 at atmospheric pressure to 0.006 at an applied pressure of 165 MPa. This, we believe, is a consequence of restricted rotation around the connecting bridge.

Our understanding of the restricted pressure region is that, in addition to the anticipated alteration of the solvent properties, applied pressure hinders internal rotation of the subunits. This situation might arise from the increased viscosity, as is believed to happen with fluorescent rotors,^[49] or because of minor structural distortions around connecting linkages.^[46] Exciplex formation invariably involves some kind of internal reorganization to optimize electronic factors,^[50] and the low-temperature fluorescence results seem consistent with a key geometry change accompanying exciplex formation. Molecular dynamics simulations carried out in a reservoir of water molecules indicate that BOD-DCV undergoes facile rotation around the vinyl linkage. This same rotational barrier^[51] has been invoked to explain the ability of certain dicyanovinyl derivatives to function as molecular probes for viscosity. A likely situation, therefore, is that pressure restricts rotation around the vinyl connection and thereby limits access to the more favorable exciplex geometries.

At higher pressure, the total Φ_F starts to decrease and falls steeply over the range 190 to 550 MPa (Figure 9). This effect,

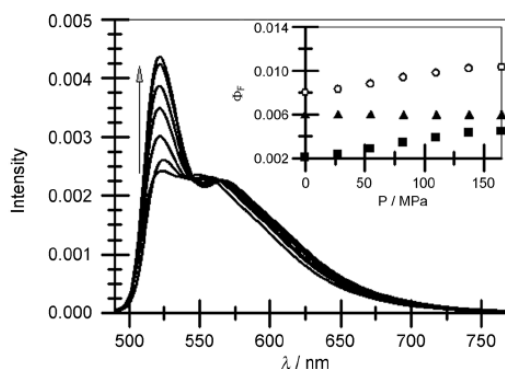


Figure 8. Effect of applied pressure on the fluorescence spectrum recorded for BOD-DCV in MTHF at room temperature. The pressure increases from atmospheric pressure to 165 MPa in equal increments; the arrow shows the effect of increasing pressure. The inset shows how pressure affects the fluorescence quantum yield for total emission (○), the π, π^* excited state (■), and the exciplex (▲).

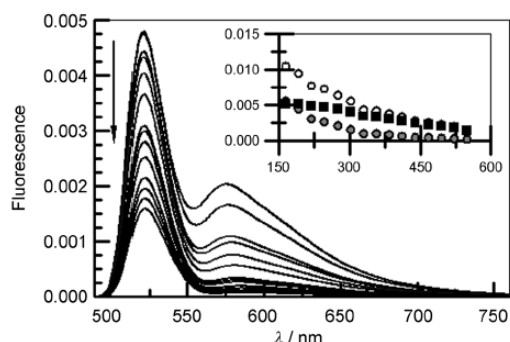


Figure 9. Effect of applied pressure on the fluorescence spectrum recorded for BOD-DCV in MTHF at room temperature. The pressure increases from 165 to 550 MPa in equal increments; the arrow shows the effect of increasing pressure. The inset shows how pressure affects the fluorescence quantum yield for the total emission (\circ), the π,π^* excited state (\blacksquare), and the exciplex (\bullet).

which is not replicated in absorption spectra, is fully reversible on release of the applied pressure. Close examination of the fluorescence spectra indicates that the drop in exciplex emission is more serious than predicted on the basis of the pressure effect for ϵ_S . As a general rule, semirigid molecules attempt to reduce their molar volume under applied pressure,^[7,52] so we can consider this secondary pressure effect in terms of a large-scale change in molecular conformation. No such structural distortion^[45] is evident for BOD over the same pressure range.

This high-pressure effect can be considered in terms of Equation (3)

$$\frac{d \ln k_{NR}}{dP} = -\frac{\Delta V_M}{RT} \quad (3)$$
$$k_{NR} \approx \left(\frac{\phi_F^0}{\phi_F^P} \right) \left(\frac{1}{\tau_S} \right)$$

in which ΔV_M is the change in molar volume of the solute, P is the applied pressure, and k_{NR} is the corresponding rate constant for nonradiative decay of the excited state. In turn, k_{NR} can be estimated from data collected under ambient conditions assuming the radiative rate constant is independent of applied pressure. For the exciplex, we see a linear fit to Equation (3) with ΔV_M of approximately 25 cm^3 (the molar volume for BOD-DCV is calculated as 357 cm^3). The same plot made for the corresponding π,π^* excited state is nonlinear but looks to be much more shallow (see the Supporting Information). This situation might be indicative of pressure enhancing deactivation of the exciplex rather than limiting its formation from the π,π^* state. As we are relying on quantum yields rather than lifetimes, the above point takes on extra significance. Nonetheless, we can propose a set of potential energy diagrams to explain the observed pressure effect (Figure 10).

Under ambient conditions (Figure 10a), excitation of BOD-DCV leads to population of the π,π^* excited-singlet state (S_1),

which returns to the ground state (S_0) through fluorescence, intersystem crossing to the first excited-triplet state (T_1), or charge transfer to form the exciplex (EX). The exciplex displays weak fluorescence but enhances population of T_1 . Application of modest pressure raises the barrier to exciplex formation by imposing structural rigidity such that the emission spectral profile moves in favor of the π,π^* state (Figure 10b). The model implies that pressure will restrict formation of the T_1 state but our experimental setup does not allow this point to be confirmed. Note that fluorescence from the parent compound BOD is insensitive to changes in pressure over this range.

A new molecular conformation (S_0) can be accessed at high pressure (Figure 10c) but there is a substantial barrier to reach this state from S_0 . Surface crossing from S_1 is more allowed because of the higher potential energy available to this state, but this process does not compete effectively with exciplex formation. The exciplex, however, is longer lived than S_1 and can utilize this new decay channel. Thus, as the pressure increases, there is a corresponding drop in exciplex emission due to population of the distorted geometry. The latter resides in equilibrium with the ground state.

3. Conclusions

This work has confirmed^[6] the formation of weakly emissive exciplexes from Bodipy-based donor–acceptor dyads under appropriate conditions. The presence of an orthogonally sited phenylene ring as the connecting moiety is probably a key constituent^[53] in modulating the degree of electronic coupling between the reagents. In fact, the conditions necessary for exciplex emission from BOD-DCV are rather demanding in terms of polarity, temperature, and pressure. The temperature effect has been analyzed in terms of an important geometry change accompanying exciplex formation, and in the absence of structural information we tentatively attribute this effect to internal rearrangement around the dicyanovinyl group. Application of a modest pressure, which will hinder internal rotation, leads to partial restoration of π,π^* fluorescence at the expense of exciplex formation. In this respect, temperature and pressure perform the same task. As far as we can see, this is the first such report of using pressure to limit exciplex emission. The behavior is complicated, however, by the realization that applied pressure affects the viscosity, density, polarity, and refractive index of the surrounding solvent. The same can be said of temperature so it becomes difficult to clarify the precise factors that control exciplex emission in these systems.

At higher pressure, a significant structural change occurs as the molecule seeks to minimize its volume. This effect opens a new channel for nonradiative deactivation of the π,π^* excited-singlet state and essentially extinguishes exciplex emission. In this way, BOD-DCV functions as a sensor for the high-pressure region.

There are many important applications for novel pressure sensors but the relatively weak emission signals inherent to BOD-DCV limit its applicability in practical systems. Improvements might be anticipated by extending the Bodipy π -conju-

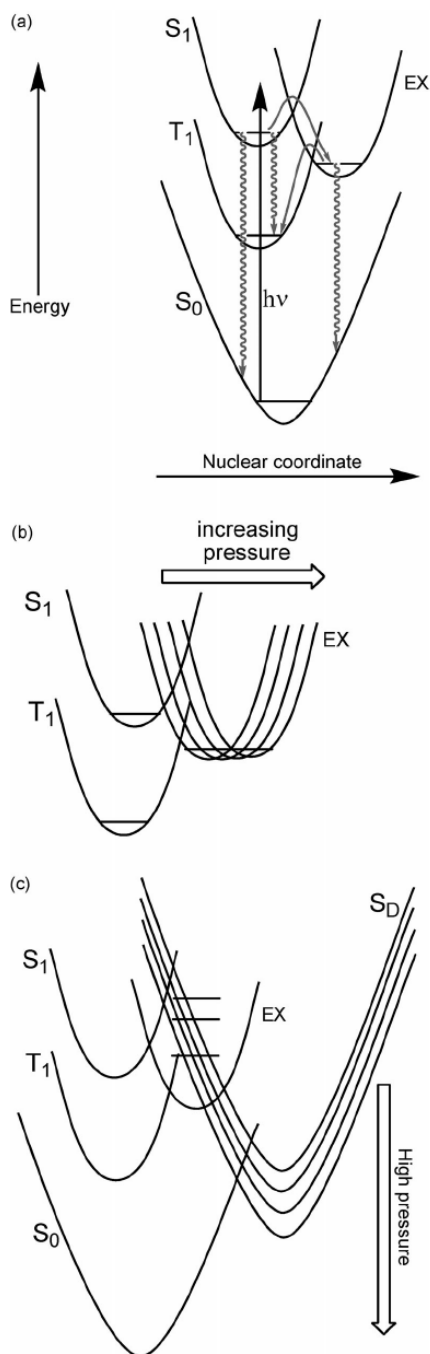


Figure 10. Potential energy level diagrams proposed for BOD-DCV: a) under ambient conditions, b) under modest pressure, and c) under high pressure.

gation length with groups, such as styryl, that are susceptible to large-scale structural modification. Combining these effects

might help amplify the scale of pressure-induced spectral changes. In this respect, comparing the relative yields of the π, π^* state and exciplex is recognized as being beneficial relative to relying on changes in emission intensity of a single band.

Experimental Section

Routine absorption spectral measurements were made with a Hitachi U3310 spectrophotometer and fluorescence spectra were recorded with a Hitachi F4500 spectrophotometer. Solvents for spectroscopic studies were purchased at the highest possible grade and checked for fluorescent impurities before use. Emission quantum yields were measured by standard protocols, using optically dilute solutions, and referenced to appropriate standards. Fluorescence lifetimes were measured at room temperature using several complementary experimental protocols. Routine measurements were made with a PTI EasyLife setup using pulsed laser diodes (310, 440, or 505 nm output) as excitation source. Samples were optically dilute, having an absorbance less than 0.10 at the excitation wavelength, and 150 runs were signal averaged before data analysis. Fluorescence was isolated using a series of narrow-band-pass filters. This instrument gave highly reproducible lifetimes for the control compounds. In most cases, after iterative reconvolution of the instrument response function (IRF) and standard Marquadt analysis, single exponential fits were recovered as judged by the goodness-of-fit criteria established by Eaton^[54] and by O'Connor and Phillips.^[55] These analytical tests included minimization of chi-squared, visual inspection of weighted residuals, the Demas method of moments, and the phase plane method. Improvements in performance were obtained using time-correlated, single-photon counting with a picosecond laser diode (FWHM < 70 ps) as excitation source at 420 nm and with a cooled microchannel-plate photomultiplier tube as detector interfaced to a high-radiance monochromator. With iterative reconvolution of the IRF, the temporal resolution of this setup was approximately 30 ps.

Conventional laser flash photolysis studies were made with an Applied Photophysics Ltd. LK550 instrument fitted with an optical parametric amplifier. The sample was dissolved in deoxygenated solvent and exposed to 4 ns pulses delivered from a frequency-tripled, Q-switched Nd:YAG laser and converted to 470 nm. A pulsed, high-intensity Xe arc lamp was used as monitoring beam and transient differential absorption spectra were compiled point by point. At least five individual records were averaged at each wavelength. Kinetic measurements were made at fixed wavelength, with about 100 individual traces being averaged.

Fast transient spectroscopy was made by pump-probe techniques using femtosecond pulses delivered from a Ti:sapphire generator amplified with a multipass amplifier pumped through the second harmonic of a Q-switched Nd:YAG laser. The amplified pulse energies varied from 0.3 to 0.5 mJ, and the repetition rate was kept at 10 Hz. Part of the beam (ca. 20%) was focused onto a second-harmonic generator to produce the excitation pulse. The residual output was directed onto a 4 mm sapphire plate to create a white-light continuum for detection purposes. The continuum was collimated and split into two equal beams. The first beam was used as reference, whereas the second beam was combined with the excitation pulse and used as the diagnostic beam. The two beams were directed to different parts of the entrance slit of a cooled charge-coupled device (CCD) detector and used to calculate differential absorbance values. The CCD shutter was kept open for 1 s, and the accumulated spectra were averaged. This procedure was

repeated until about 100 individual spectra had been averaged. Time-resolved spectra were recorded with a delay line stepped in increments of 100 fs for short time measurements. This step length was increased for longer time measurements. The decay profiles were fitted globally as the sum of exponentials and deconvoluted with a Gaussian excitation pulse. The group velocity dispersion across one spectrum (ca. 220 nm) was approximately 1 ps, and the overall temporal resolution of this setup was approximately 0.8 ps. The sample, which possessed an absorbance of approximately 0.5 at 420 nm, was flowed through a quartz cuvette (optical path length = 1 mm) and maintained under an atmosphere of N₂. Laser intensities were measured with a Coherent power meter operating in the optical-energy mode.

The high-pressure rig was purchased from Stansted Fluid Power Ltd. The general layout comprises a hydraulic compressor constructed from stainless steel. Ethanol is used as the hydraulic medium. The two-stage pump is fitted with an intensifier and diaphragm compressor capable of reaching about 700 MPa. The sample chamber is machined from a block of stainless steel and is equipped with three optical windows and a Bourdon pressure gauge. The windows show good transmission at wavelengths longer than 370 nm. For absorption measurements, the sample chamber is connected to a Perkin-Elmer lambda-5 spectrophotometer using input and output optical-fiber bundles. The absorbance signal is calibrated by reference to the sample solution being recorded in conventional cuvettes with background subtraction. For emission studies, an appropriate laser diode is used as excitation source and output, collected at 90° to excitation, is directed to the spectrofluorimeter with an optical-fiber bundle. Purpose-made cells are used to accommodate liquid samples of appropriate concentration. For fluorescence studies, the sample cell is a glass tube, diameter approximately 4 mm, having a narrow mouth that can be capped with a polyethylene seal. The latter takes the form of a short tube that is heat-sealed at one end. For absorption measurements, a hollow glass disk fitted with a narrow inlet tube is used to hold the sample. This disk has a diameter of approximately 1 cm and a path length of 2 mm. Again, a polyethylene tube is used as stopper for the cell and the actual path length can be calibrated by absorption spectroscopy. Sample cells and polyethylene seals are used once and then discarded.

In a typical experiment, a solution of the compound was prepared in MTHF and the concentration adjusted appropriately; absorption spectral measurements were made with an absorbance of approximately 0.50 at the peak maximum and fluorescence studies were carried out with an absorbance of approximately 0.10 at the excitation wavelength. Spectra were recorded at atmospheric pressure and compared with those obtained under conventional conditions using optical cuvettes. The pressure was increased in small jumps, the sample equilibrated at each pressure, and the spectrum recorded. Having reached the maximum pressure, which was restricted to 550 MPa for safety reasons, the pressure was released and spectra recorded to ensure full reversibility of any effects. In other experiments, the pressure was raised to 550 MPa and released slowly with spectra recorded at each stage. To check for self-consistency, spectra were recorded at certain pressures after leaving the sample for prolonged periods at that pressure. All measurements were repeated using fresh solutions and, for emission studies, different excitation wavelengths. Data analysis included making background corrections, especially for absorption measurements, and averaging several spectra recorded under the same conditions.

Compound 2: In a two-neck flask equipped with a reflux condenser, a gas bubbler, and a magnetic stirring bar, [Pd(PPh₃)₂Cl₂]

(10 mmol%) and sodium formate (1.2 equiv) were added to a solution of BOD (112 mg, 0.248 mmol) in anhydrous DMF (8 mL). The reaction mixture was degassed under a continuous flow of CO at atmospheric pressure and stirred at 90 °C for 3 h. After cooling to room temperature, the mixture was extracted with dichloromethane and washed several times with water. The organic phase was dried over hygroscopic cotton wool and evaporated. The crude residue was then purified by flash chromatography using toluene/CH₂Cl₂ (8:2, v/v) as mobile phase, which afforded the desired compound 2 as an orange solid (75 mg, 85%). *R*_f = 0.30 (toluene/CH₂Cl₂, 8:2); ¹H NMR (CDCl₃, 400 MHz): δ = 1.35 (s, 6H), 2.56 (s, 6H), 6.00 (s, 2H), 7.51 (d, ³*J* = 8.1 Hz, 2H), 8.03 (d, ³*J* = 8.0 Hz, 2H), 10.11 ppm (s, 1H); ¹³C NMR (CDCl₃, 100 MHz): δ = 14.6, 14.7, 121.6, 129.2, 130.4, 130.8, 136.7, 139.7, 141.4, 142.8, 156.3, 191.5 ppm; ¹¹B NMR (CDCl₃, 128 MHz): δ = 0.77 ppm (t, *J*_{B-F} = 33.0 Hz); IR: $\tilde{\nu}$ = 702, 760, 800, 971, 1043, 1152, 1189, 1259, 1303, 1407, 1464, 1505, 1541, 1606, 1704 (–CHO), 2849, 2920, 2961 cm^{–1}; MS (EI neat matter): *m/z* (intensity, %): calcd for [M]: 352.2; found: 352.1 (100); 333.1 (20), [M–F]; elemental analysis calcd (%) for C₂₀H₁₉BF₂N₂O: C 68.21, H 5.44, N 7.95; found: C 67.91, H 5.24, N 7.72.

Compound BOD-DCV: In a Schlenk tube equipped with a stir bar, malononitrile (1.2 equiv) and several drops of piperidine/acetic acid were added to a suspension of the aldehyde 2 (40 mg, 0.113 mmol) in methanol (2.5 mL). The mixture was stirred at 85–95 °C for 1 h. The residue was purified by flash chromatography (SiO₂, CH₂Cl₂/petroleum ether, 7:3, v/v) and recrystallization from CH₂Cl₂/ethanol mixture yielded BOD-DCV as an orange solid (39 mg, 86%). *R*_f = 0.26 (CH₂Cl₂/petroleum ether, 7:3); ¹H NMR (CDCl₃, 300 MHz): δ = 1.38 (s, 6H), 2.56 (s, 6H), 6.01 (s, 2H), 7.52 (d, ³*J* = 8.2 Hz, 2H), 7.84 (s, 1H), 8.06 ppm (d, ³*J* = 8.2 Hz, 2H); ¹³C NMR (CDCl₃, 50 MHz): δ = 14.8, 14.8, 29.8, 84.5, 112.5, 113.5, 121.9, 121.9, 129.9, 131.4, 131.5, 138.9, 141.8, 142.7, 156.7, 158.8 ppm; ¹¹B NMR (CDCl₃, 128 MHz): δ = 0.74 ppm (t, *J*_{B-F} = 33.0 Hz); IR: $\tilde{\nu}$ = 705, 759, 804, 833, 913, 967, 1047, 1153, 1183, 1263, 1306, 1362, 1407, 1463, 1508, 1540, 1593, 2229 (–CN), 2864, 2926, 2964 cm^{–1}; MS (EI neat matter): *m/z* (intensity, %): calcd for [M]: 400.2; found: 400.1 (100); 381.1 (15), [M–F]; elemental analysis calcd (%) for C₂₃H₁₉BF₂N₄: C 69.02, H 4.78, N 14.00; found: C 68.74, H 4.56, N 13.69.

Acknowledgements

We thank the Centre National de la Recherche Scientifique (CNRS), the Engineering and Physical Sciences Research Council (EPSRC, EP/G04094X/1), the Ecole de Chimie, Polymères et Matériaux de Strasbourg (ECPM-Strasbourg), and Newcastle University for financial support of this work. We gratefully acknowledge IMRA Europe S.A.S. (Sophia Antipolis, France) for awarding a PhD fellowship to A.N. Drs Stéphane Jacob and Gilles Dennler (IMRA Europe) are thanked for many helpful discussions.

Keywords: donor–acceptor systems · dyes/pigments · exciplexes · fluorescence · photophysics

- [1] W. Schuddeboom, S. A. Jonker, J. M. Warman, U. Leinhos, W. Kuhnle, K. A. Zachariasse, *J. Phys. Chem.* **1992**, *96*, 10809–10819.
- [2] I. R. Gould, R. H. Young, L. J. Mueller, A. C. Albrecht, S. Farid, *J. Am. Chem. Soc.* **1994**, *116*, 8188–8199.
- [3] A. Kapturkiewicz, J. Herbich, J. Karpiuk, J. Nowacki, *J. Phys. Chem. A* **1997**, *101*, 2332–2344.
- [4] N. Mataga, *Pure Appl. Chem.* **1997**, *69*, 729–734.

- [5] N. Mataga, H. Chosrowjan, S. Taniguchi, *J. Photochem. Photobiol. C* **2005**, *6*, 37–97.
- [6] a) A. Harriman, L. J. Mallon, G. Ulrich, R. Ziessel, *ChemPhysChem* **2007**, *8*, 1207–1214; b) R. Ziessel, B. D. Allen, D. B. Rewinska, A. Harriman, *Chem. Eur. J.* **2009**, *15*, 7382–7393; c) A. C. Benniston, A. Harriman, V. L. Whittle, M. Zelzer, R. W. Harrington, W. Clegg, *Photochem. Photobiol. Sci.* **2010**, *9*, 1009–1017; d) A. C. Benniston, G. Copley, H. Lemmetyinen, N. V. Tkachenko, *ChemPhysChem* **2010**, *11*, 1685–1692.
- [7] S. Schneider, W. Jager, X. Y. Lauteslager, J. W. Verhoeven, *J. Phys. Chem.* **1996**, *100*, 8118–8124.
- [8] A. Morandeira, A. Furstenberg, E. Vauthey, *J. Phys. Chem. A* **2004**, *108*, 8190–8200.
- [9] K. Takagi, T. Nakagawa, H. Takao, *J. Polym. Sci. Part A* **2010**, *48*, 91–98.
- [10] T. J. Kesti, N. V. Tkachenko, V. Vehmanen, H. Yamada, H. Imahori, S. Fukuzumi, H. Lemmetyinen, *J. Am. Chem. Soc.* **2002**, *124*, 8067–8077.
- [11] W. M. Kwok, C. Ma, D. L. Phillips, *J. Phys. Chem. B* **2009**, *113*, 11527–11534.
- [12] S. A. Jenekhe, J. A. Osaheni, *Science* **1994**, *265*, 765–768.
- [13] M. Lor, J. Thielemans, L. Viane, M. Cotlet, J. Hofkens, T. Weil, C. Hampel, K. Mullen, J. W. Verhoeven, M. Van der Auweraer, F. C. De Schryver, *J. Am. Chem. Soc.* **2002**, *124*, 9918–9925.
- [14] a) M. Shishido, X. F. Wang, K. Kawaguchi, Y. Manishi, *J. Phys. Chem.* **1988**, *92*, 4801–4806; b) S. Fukuma, K. Irie, T. Ikegami, S. Masuo, S. Machida, N. Tanaka, A. Itaya, *J. Photochem. Photobiol. A* **2007**, *189*, 55–64.
- [15] S. Mula, K. J. Elliott, A. Harriman, R. Ziessel, *J. Phys. Chem. A* **2010**, *114*, 10515–10522.
- [16] a) R. A. Bissell, A. P. de Silva, H. Q. W. Gunaratne, P. L. M. Lynch, G. E. M. Maguire, C. P. McCoy, K. Sandanayake, *Top. Curr. Chem.* **1993**, *168*, 223–264; b) J. S. Wu, W. M. Liu, J. C. Ge, H. Y. Zhang, P. F. Wang, *Chem. Soc. Rev.* **2011**, *40*, 3483–3495; c) N. Chandrasekharan, L. A. Kelly, *J. Am. Chem. Soc.* **2001**, *123*, 9898–9899.
- [17] a) Q. Wang, S. Li, L. He, Y. Qian, X. P. Li, W. H. Sun, M. Liu, J. Li, Y. Li, G. Q. Yang, *ChemPhysChem* **2008**, *9*, 1146–1152; b) M. Seischab, T. Lodenkemper, A. Stockmann, S. Schneider, M. Koeberg, M. R. Roest, J. W. Verhoeven, J. M. Lawson, M. N. Paddon-Row, *Phys. Chem. Chem. Phys.* **2000**, *2*, 1889–1897; c) M. Lilichenko, D. Tittelbach-Helmrich, J. W. Verhoeven, I. R. Gould, A. B. Myers, *J. Chem. Phys.* **1998**, *109*, 10958–10969; d) H. Meier, B. Muehling, J. Gerold, D. Jacob, A. Oehlhof, *Eur. J. Org. Chem.* **2007**, 625–631.
- [18] a) M. R. Roest, J. W. Verhoeven, W. Schuddeboom, J. M. Warman, J. M. Lawson, M. N. Paddon-Row, *J. Am. Chem. Soc.* **1996**, *118*, 1762–1768; b) W. D. Oosterbaan, C. Koper, T. W. Braam, F. J. Hoogesteger, J. J. Piet, B. A. J. Jansen, C. A. van Walree, H. J. van Ramesdonk, M. Goes, J. W. Verhoeven, W. Schuddeboom, J. M. Warman, L. W. Jenneskens, *J. Phys. Chem. A* **2003**, *107*, 3612–3624; c) J. Kurazawa, S. Schneider, J. Buber, R. Gleiter, T. Clark, *Phys. Chem. Chem. Phys.* **2004**, *6*, 3811–3823; d) W. D. Oosterbaan, V. E. M. Kaats-Richters, L. W. Jenneskens, C. A. Van Walree, *J. Polym. Sci. Part A* **2004**, *42*, 4775–4784.
- [19] C. Rumble, K. Rich, G. He, M. Maroncelli, *J. Phys. Chem. A* **2012**, *116*, 10786–10792.
- [20] a) A. Yassin, T. Rousseau, P. Leriche, A. Cravino, J. Roncali, *Sol. Energy Mater. Sol. Cells* **2011**, *95*, 462–468; b) M. S. Wrackmeyer, M. Hein, A. Petrich, J. Meiss, M. Hummert, M. K. Riede, K. Leo, *Sol. Energy Mater. Sol. Cells* **2011**, *95*, 3171–3175; c) W. F. Zhang, S. C. Tse, J. Lu, Y. Tao, M. S. Wong, *J. Mater. Chem.* **2010**, *20*, 2182–2189.
- [21] a) J. Y. Shao, S. M. Li, X. L. Li, J. Z. Zhao, F. K. Zhou, H. M. Guo, *Eur. J. Org. Chem.* **2011**, 6100–6109; b) H. Ziehlke, L. Burtone, C. Koerner, R. Fitzner, E. Reinold, P. Baeuerle, K. Leo, M. Riede, *Org. Electron.* **2011**, *12*, 2258–2267; c) R. Fitzner, E. Reinold, A. Mishra, E. Mena-Osteritz, H. Ziehlke, C. Koerner, K. Leo, M. Riede, M. Weil, O. Tsaryova, A. Weiss, C. Uhrich, M. Pfeiffer, P. Baeuerle, *Adv. Funct. Mater.* **2011**, *21*, 897–910.
- [22] a) T. Rousseau, A. Cravino, E. Ripaud, P. Leriche, S. Rihn, A. de Nicola, R. Ziessel, J. Roncali, *Chem. Commun.* **2010**, 46, 5082–5084; b) T. Rousseau, A. Cravino, T. Bura, G. Ulrich, R. Ziessel, J. Roncali, *Chem. Commun.* **2009**, 1673–1675.
- [23] T. Bura, R. Ziessel, *Org. Lett.* **2011**, *13*, 3072–3075.
- [24] T. Bura, P. Retailleau, R. Ziessel, *Angew. Chem.* **2010**, *122*, 6809–6813; *Angew. Chem. Int. Ed.* **2010**, *49*, 6659–6663.
- [25] T. Qi, Y. Liu, W. Qiu, H. Zhang, X. Gao, Y. Liu, K. Lu, C. Du, G. Yu, D. Zhu, *J. Mater. Chem.* **2008**, *18*, 1131–1138, and references therein.
- [26] a) R. Ziessel, L. Bonardi, P. Retailleau, G. Ulrich, *J. Org. Chem.* **2006**, *71*, 3093; b) T. Bura, R. Ziessel, *Tetrahedron Lett.* **2010**, *51*, 2875–2879.
- [27] J. Daub, J. Salbeck, T. Knöchel, C. Fischer, H. Kunkely, K. M. Rapp, *Angew. Chem.* **1989**, *101*, 1541–1542; *Angew. Chem. Int. Ed. Engl.* **1989**, *28*, 1494–1496.
- [28] M. R. Wasielewski, M. P. Niemczyk, W. A. Svec, E. B. Pewitt, *J. Am. Chem. Soc.* **1985**, *107*, 1080–1082.
- [29] A. Weller, *Z. Phys. Chem.* **1982**, *133*, 93–98.
- [30] A. A. Rachford, R. Ziessel, T. Bura, P. Retailleau, F. N. Castellano, *Inorg. Chem.* **2010**, *49*, 3730–3736.
- [31] a) J. W. Verhoeven, H. J. van Ramesdonk, M. M. Groeneveld, A. C. Benniston, A. Harriman, *ChemPhysChem* **2005**, *6*, 2251–2260; b) J. W. Verhoeven, H. J. van Ramesdonk, H. Zhang, M. M. Groeneveld, A. C. Benniston, A. Harriman, *Int. J. Photoenergy* **2005**, *7*, 103–108.
- [32] R. Englman, J. Jortner, *Mol. Phys.* **1970**, *18*, 145–176.
- [33] D. Beljonne, Z. Shuai, G. Pourtois, J. L. Brédas, *J. Phys. Chem. A* **2001**, *105*, 3899–3907.
- [34] a) M. Galletta, F. Puntoriero, S. Campagna, C. Chiorboli, M. Quesada, S. Goeb, R. Ziessel, *J. Phys. Chem. A* **2006**, *110*, 4348–4358; b) A. Harriman, J. P. Rostron, M. Cesario, G. Ulrich, R. Ziessel, *J. Phys. Chem. A* **2006**, *110*, 7994–8002.
- [35] a) G. U. Bublitz, S. G. Boxer, *J. Am. Chem. Soc.* **1998**, *120*, 3988–3992; b) Q.-H. Xu, M. D. Fayer, *J. Chem. Phys.* **2002**, *117*, 2732–2740.
- [36] G. Ulrich, R. Ziessel, A. Harriman, *Angew. Chem.* **2008**, *120*, 1202–1219; *Angew. Chem. Int. Ed.* **2008**, *47*, 1184–1201.
- [37] K. Okamoto, M. Terazima, *J. Phys. Chem. B* **2008**, *112*, 7308–7314.
- [38] T. Ganguly, L. Farmer, D. Gravel, G. Durocher, *J. Photochem. Photobiol. A* **1991**, *60*, 63–82.
- [39] a) F. D. Lewis, G. D. Reddy, S. Schneider, M. Gahr, *J. Am. Chem. Soc.* **1991**, *113*, 3498–3506; b) F. D. Lewis, J. L. Hougland, S. A. Markarian, *J. Phys. Chem. A* **2000**, *104*, 3261–3268; c) J. W. Verhoeven, T. Scherer, R. J. Willemse, *Pure Appl. Chem.* **1993**, *65*, 1717–1722.
- [40] A. C. Benniston, S. Clift, A. Harriman, *J. Mol. Struct.* **2011**, *985*, 346–354.
- [41] F. D. Lewis, B. E. Cohen, *J. Phys. Chem.* **1994**, *98*, 10591–10597.
- [42] S. J. Strickler, R. A. Berg, *J. Chem. Phys.* **1962**, *37*, 814–822.
- [43] A. C. Benniston, S. Clift, J. Hagon, H. Lemmetyinen, N. V. Tkachenko, W. Clegg, R. W. Harrington, *ChemPhysChem* **2012**, *13*, 3672–3681.
- [44] P. Van Haver, N. Helsen, S. De Paemelaere, M. Van der Auweraer, F. C. De Schryver, *J. Am. Chem. Soc.* **1991**, *113*, 6849–6857.
- [45] M. A. H. Alamiry, E. Bahaidarah, A. Harriman, J. H. Olivier, R. Ziessel, *Pure Appl. Chem.* **2013**, *85*, 1349–1365.
- [46] D. Hablot, R. Ziessel, M. A. H. Alamiry, E. Bahaidarah, A. Harriman, *Chem. Sci.* **2013**, *4*, 444–453.
- [47] A. Filarowski, M. Kluba, K. Cieslik-Boczula, A. Koll, A. Kochel, L. Pandey, W. M. De Borggraeve, M. Van der Auweraer, J. Catalan, N. Boens, *Photochem. Photobiol. Sci.* **2010**, *9*, 996–1008.
- [48] L. M. He, F. Xiong, S. Y. Li, Q. Gan, G. C. Zhang, Y. Li, B. W. Zhang, B. Chen, G. C. Yang, *J. Phys. Chem. B* **2004**, *108*, 7092–7097.
- [49] M. A. H. Alamiry, A. C. Benniston, G. Copley, K. J. Elliott, A. Harriman, B. Stewart, Y.-G. Zhi, *Chem. Mater.* **2008**, *20*, 4024–4032.
- [50] A. M. Brun, A. Harriman, Y. Tsuboi, T. Okada, N. Mataga, *J. Chem. Soc. Faraday Trans.* **1995**, *91*, 4047–4057.
- [51] B. D. Allen, A. C. Benniston, A. Harriman, S. A. Rostron, *Phys. Chem. Chem. Phys.* **2005**, *7*, 3035–3040.
- [52] B. Wegewijs, J. W. Verhoeven, S. E. Braslavsky, *J. Phys. Chem.* **1996**, *100*, 8890–8894.
- [53] B. D. Allen, A. C. Benniston, A. Harriman, I. Llerena, C. A. Sams, *J. Phys. Chem. A* **2007**, *111*, 2641–2649.
- [54] D. F. Eaton, *Pure Appl. Chem.* **1990**, *62*, 1631–1648.
- [55] D. V. O'Connor, D. Phillips, *Time-Correlated, Single Photon Counting*, Academic Press, London, **1984**, pp. 158–211.

Received: September 2, 2013

Published online on December 20, 2013

Photochemical & Photobiological Sciences

An international journal
www.rsc.org/pps



ISSN 1474-905X





Cite this: *Photochem. Photobiol. Sci.*, 2014, **13**, 1397

Fluorescent molecular rotors based on the BODIPY motif: effect of remote substituents†

Effat Bahaidarah,^a Anthony Harriman,^{*a} Patrycja Stachelek,^a Sandra Rihn,^{‡b} Elodie Heyer^b and Raymond Ziessel^b

The ability of an unconstrained boron dipyrromethene dye to report on changes in local viscosity is improved by appending a single aryl ring at the lower rim of the dipyrin core. Recovering the symmetry by attaching an identical aryl ring on the opposite side of the lower rim greatly diminishes the sensory activity, as does blocking rotation of the *meso*-aryl group. On the basis of viscosity- and temperature-dependence studies, together with quantum chemical calculations, it is proposed that a single aryl ring at the 3-position extends the molecular surface area that undergoes structural distortion during internal rotation. The substitution pattern at the lower rim also affects the harmonic frequencies at the bottom of the potential well and at the top of the barrier. These effects can be correlated with the separation of the H₁, H₇ hydrogen atoms.

Received 8th June 2014,
Accepted 28th July 2014
DOI: 10.1039/c4pp00204k
www.rsc.org/pps

Introduction

A substantial body of information has accumulated regarding small molecules whose fluorescence properties are controlled, at least to some degree, by the extent of frictional forces between the molecule (*i.e.*, the rotor) and the surrounding environment. Such systems, which should be distinguished from cases where intramolecular charge transfer causes minor structural change, can be used to probe the local rheology and to operate as crude temperature or pressure indicators.¹ Related systems form the basis of molecular machines,² switches,³ sensors,⁴ *etc.* and there is a steadily growing interest in applying molecular rotors to monitor changes in viscosity within biological media⁵ or nano-cavities.^{6,7} Of the known molecular systems that function as fluorescent rotors, the boron dipyrromethene (BODIPY) family of dyes⁸ has many important advantages and has been used as the starting point for the design of several different types of rheology probes.^{9–16}

As reported first by Holten *et al.*¹⁷ these BODIPY-based rotors operate by partial restriction of the rotation of a *meso*-phenylene ring around a relatively unconstrained dipyrin backbone. Such rotation by itself will not affect the emissive properties of the BODIPY nucleus but, in order for the phenylene ring to complete a full turn, it is necessary for the dipyrin backbone to buckle slightly. It is this latter process that leads^{10,17} to enhanced nonradiative decay. The underlying structural change creates the possibility to correlate fluorescence intensity with key properties of the local environment. Attaching bulky substituents to either the phenylene ring¹¹ or the 1,7-positions of the dipyrin backbone^{10,17} affects the rotary action, in many cases curtailing the sensory capability. We now show that gross modulation of the rotor-like behaviour can be realized by attaching aryl groups at the lower rim of the BODIPY unit, well away from the buckling dipyrin core.

Results and discussion

Molecular structures for the target compounds are shown by way of Fig. 1 and are based on the unconstrained¹⁷ BODIPY nucleus. The prototypic fluorescent rotor, ROBOD, has been studied previously^{10,13} and is used here as a reference compound. Likewise, the constrained analogue, BOD, bearing methyl groups at the 1,7-positions, has received extensive study in the literature.⁸ This highly fluorescent dye cannot be applied to monitor changes in the local environment. Simple derivatives of ROBOD are PHEN1 and PHEN2, which are equipped with one or two tolyl groups at positions where they

^aMolecular Photonics Laboratory, School of Chemistry, Bedson Building, Newcastle University, Newcastle upon Tyne, NE1 7RU, UK.

E-mail: anthony.harriman@ncl.ac.uk; Fax: +44 (0)191 208 8660;

Tel: +44 (0)191 208 8660

^bLaboratoire de Chimie Organique et de Spectroscopies Avancées (ICPEES-LCOSA),

UMR 7515 CNRS, 25 rue Becquerel, 67087 Strasbourg Cedex 2, France

†Electronic supplementary information (ESI) available: Synthesis and characterization of PHEN1, PHEN2 and CORE, experimental and computational details, additional spectroscopic data, effect of temperature on Φ_f and output from the quantum chemical calculations. See DOI: 10.1039/c4pp00204k

‡Present address: School of Chemistry, Bedson Building, Newcastle University, Newcastle upon Tyne, NE1 7RU, UK.

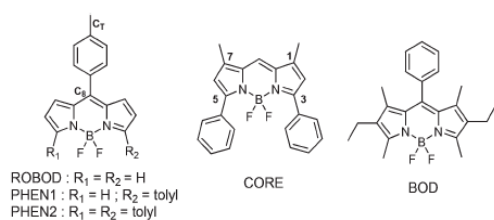


Fig. 1 Molecular formulae of the compounds investigated herein.

Table 1 Summary of the photophysical properties recorded for the target compounds in MTHF at 20 °C

Property	ROBOD	BOD	PHEN1	PHEN2	CORE
$\lambda_{\text{MAX}}/\text{nm}^a$	502	525	531	559	547
$\epsilon_{\text{MAX}}/\text{M}^{-1}\text{cm}^{-1}\text{ }^b$	71 000	74 000	59 100	62 235	62 100
$\lambda_{\text{FLU}}/\text{nm}^c$	530	547	564	602	588
$\text{SS}/\text{cm}^{-1}\text{ }^d$	1050	765	1105	1280	1280
Φ_{F}^e	0.023	0.78	0.013	0.28	0.92
$\tau_{\text{S}}/\text{ns}^f$	0.15	5.4	0.092	2.1	6.6
$k_{\text{RAD}}/10^8\text{ s}^{-1}\text{ }^g$	1.50	1.45	1.42	1.30	1.40
$k_{\text{NR}}/10^8\text{ s}^{-1}\text{ }^h$	65	0.40	110	3.5	0.12

^a Absorption maximum. ^b Molar absorption coefficient. ^c Emission maximum. ^d Stokes' shift. ^e Fluorescence quantum yield. ^f Excited-singlet state lifetime. ^g Radiative rate constant. ^h Non-radiative rate constant for decay of the S₁ state.

will not block rotation of the *meso*-substituent by steric factors. The series is augmented by a control compound, CORE, which has the ancillary tolyl groups at the 3,5-positions but lacks the *meso*-phenyl group. It might be noted that the alkyl groups present in certain derivatives affect the absorption and emission spectral properties by way of inductive effects.⁸ The synthesis of the new dyes was inspired by previously described^{18,19} protocols as outlined in the ESI†

The photophysical properties of ROBOD were recorded in 2-methyltetrahydrofuran (MTHF) at room temperature and the main findings are collected in Table 1; NB the same properties recorded in dichloromethane at room temperature are reported in Table S1 (see ESI†). The absorption maximum (λ_{MAX}) occurs at 502 nm, with a molar absorption coefficient (ϵ_{MAX}) of 71 000 M⁻¹ cm⁻¹. There is a modest Stokes' shift (SS = 1050 cm⁻¹), with the fluorescence maximum (λ_{FLU}) lying at 530 nm. The emission profile shows reasonable mirror symmetry with the absorption spectrum and there is excellent correspondence between absorption and excitation spectra (Fig. S1†). Similar behaviour is found for the constrained analogue BOD, allowing for a 20 nm red shift induced by the alkyl substituents (Table 1). The two compounds exhibit rather disparate fluorescence quantum yields (Φ_{F}) and excited-state lifetimes (τ_{S}) under these conditions, with ROBOD being weakly emissive. Radiative rate constants (k_{RAD}), which remain in good agreement with those calculated from the Strickler-Berg expression,²⁰ are comparable while the corresponding non-radiative rate constants (k_{NR}) reflect the difference in emission yields (Table 1). We attribute the fast deactivation of the

excited-singlet state of ROBOD to the internal rotor effect, as has been done previously^{10,17} and which for BOD is inhibited by the presence of the 1,7-methyl groups. We return later to the exact meaning of this phenomenon: Firstly, we consider the effects of substitution at the lower rim of the BODIPY nucleus.

Insertion of a tolyl group at the 3-position introduces a 30 nm red shift for both absorption and emission spectra relative to ROBOD (Fig. S2†), while there is a small (*i.e.*, 10%) increase in the magnitude of the Stokes' shift. Also, the absorption band is somewhat broader for PHEN1 compared to ROBOD, reflecting a certain degree of heterogeneity for the ground-state geometry that largely disappears on excitation. More importantly, there is a significant fall in both Φ_{F} and τ_{S} without perturbing k_{RAD} . The decreased fluorescence, therefore, is a consequence of an enhancement in k_{NR} . Appending a second tolyl ring at the 5-position, forming PHEN2, leads to a dramatic increase in both Φ_{F} and τ_{S} . At the same time, such substitution increases the Stokes' shift, further broadens the absorption spectral profile, amplifies the red shifts to >60 nm and partially assuages k_{NR} . Moving to the control molecule lacking the *meso*-substituent, CORE, we find that Φ_{F} and τ_{S} exceed those found for BOD, although there is an exacerbated red shift and broadening of the absorption profile. Throughout this series there is a progressive decrease in k_{RAD} as the emission peak moves towards lower energy, as is to be expected from the Strickler-Berg expression.²⁰ The red shifts are probably due to increased π -conjugation caused by partial orbital mixing between dipyrin and tolyl substituent. Indeed, this assertion is supported by the results of DFT (B3LYP/6-31+G(d)/PCM) calculations that indicate orbital mixing for the LUMO but not for the corresponding HOMO (see ESI†). Comparison of the photophysical properties recorded for the unconstrained dyes with those found for the control compounds indicates that nonradiative decay is promoted by the presence of a *meso*-aryl ring.

$$k_{\text{NR}} = \frac{\nu}{\eta^{\alpha}} \exp\left(-\frac{E_{\text{A}}}{RT}\right) \quad (1)$$

Increasing solvent viscosity (η), by using a homologous series of *n*-alcohols at 20 °C, leads to a progressive increase in τ_{S} for ROBOD, PHEN1 and PHEN2 but not for CORE, thereby confirming that each of these unconstrained molecules operates as a fluorescent rotor. Across this series of solvents, there is a reasonably linear relationship between k_{NR} and shear viscosity, as considered in the form of log-log plots (Fig. 2), but with differing gradients and intercepts. Indeed, the experimental data collected at 20 °C can be considered in terms of eqn (1),²¹ where ν corresponds to a limiting pressure exerted by the rotor, α is a coefficient that effectively describes the sensitivity towards viscosity, and E_{A} is a barrier for internal rotation (Table 2). For the prototypic rotor ROBOD, α has a value of 0.41, which is similar to that determined earlier for a closely related dye,¹⁰ and this falls to 0.31 for PHEN2. In contrast, α determined for PHEN1 is 0.62, which is the highest

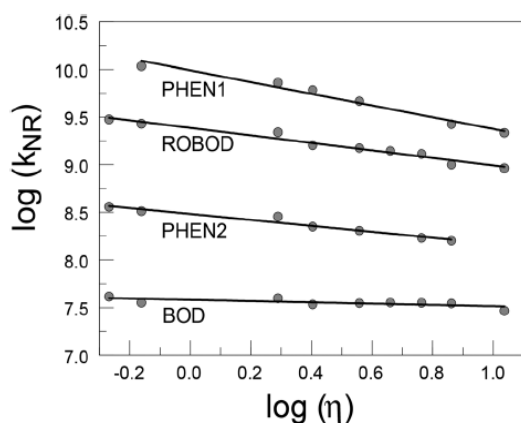


Fig. 2 Effect of solvent viscosity on the rate constant for nonradiative decay measured in a series of linear alcohols at 20 °C.

Table 2 Compilation of the various parameters associated with rotation of the meso-aryl ring

Property	ROBOD	BOD	PHEN1	PHEN2	CORE
$k_0/10^7 \text{ s}^{-1}^a$	17	1.8	12	1.9	1.2
$k_{\text{ACT}}/10^9 \text{ s}^{-1}^b$	36.5	5.9	51.0	0.8	NA
$E_B/\text{kJ mol}^{-1}^c$	2.6	7.7	2.3	1.4	NA
α^d	0.41	0.07	0.62	0.31	NA
B–C ₈ –C _T /° ^e	179.8	180.0	178.8	177.9	NA
B–C ₈ –C _T /° ^f	177.8	179.8	176.3	175.2	NA
B–C ₈ –C _T /° ^g	163.5	146.6	163.4	162.1	NA
$A_{\text{FF}}/\text{°}^e$	0.12	0.04	4.4	6.9	5.1
$A_{\text{FF}}/\text{°}^f$	1.2	0.27	5.4	9.5	5.5
$A_{\text{FF}}/\text{°}^g$	28.5	30.0	30.4	32.0	NA
H ₁ H ₂ /Å ^f	5.670	5.279	5.717	5.518	5.700

^a Activationless rate constant according to eqn (2). ^b Activated rate constant according to eqn (2). ^c Activation energy according to eqn (2). ^d Viscosity sensitive parameter according to eqn (1). ^e Refers to the ground state. For atom labeling see Fig. 1. ^f Refers to the first-allowed excited state. ^g Refers to the transition state for full rotation of the meso-aryl ring.

such value found for any BODIPY-based rotor and is far superior to that measured for the industry standard²² under the same conditions. Thus, PHEN1 performs remarkably well as a fluorescent rotor, in marked contrast to PHEN2. Of the two control compounds, CORE shows no viscosity dependence while BOD exhibits a shallow ($\alpha \approx 0.07$), but definite, sensitivity towards shear viscosity (Fig. 2).

In separate experiments, Φ_F was examined as a function of temperature in MTHF. After correction²³ for solvent contraction on cooling, Φ_F for CORE is barely affected by changes in temperature whereas that for BOD is constant at temperatures below 200 K but decreases steadily, albeit marginally, as the temperature is raised further (Fig. S3†). Neither of these compounds functions as a viable molecular rotor. In marked contrast, Φ_F for ROBOD increases progressively with decreasing temperature until approaching the freezing point ($T_F = 137$ K) of the solvent. As the solvent solidifies, Φ_F increases dramati-

cally before remaining essentially constant in both amorphous ($\Phi_F = 0.93$) and glassy ($\Phi_F = 0.99$) regions; note that the limiting Φ_F measured in the glassy matrix is comparable to that of CORE under these conditions. This behaviour, which amounts to a 45-fold variation in Φ_F over the full temperature range, is considered typical for a fluorescent rotor. Both PHEN1 and PHEN2 show similar temperature-dependent Φ_F to that observed for ROBOD (Fig. S3†), confirming that these compounds operate as fluorescent rotors. The total variation in Φ_F found for PHEN2 is only *ca.* 3-fold, but that for PHEN1 varies by a factor of *ca.* 75-fold and is far greater than that recorded for ROBOD. For each compound, Φ_F approaches unity in the glassy matrix.

Small spectral shifts accompany the freezing and vitrification processes, as is exemplified for PHEN2 in Fig. S4† although the absorption and emission maxima do not correlate with changes in solvent polarisability. Here, the emission maximum moves towards lower energy as the temperature falls throughout the liquid phase, amounting to a red shift of *ca.* 200 cm⁻¹ between 290 and 150 K, before shifting slightly to higher energy as the solvent freezes. The initial red shift can be explained in terms of increased π -electron delocalization between dipyrin and the 3,5-tolyl rings; identical behaviour is found with both CORE and PHEN1 but not for either BOD or ROBOD. The core aryl ring(s) has a dihedral angle of *ca.* 50° (B3LYP/6-31+G(d)/PCM) for all three derivatives but rotation at the connecting C–C linkage is facile except at around 20° where some instability is caused by close proximity (*i.e.*, 1.6 Å) between a fluorine atom and the *ortho*-hydrogen atom on the tolyl ring. This steric clash introduces a barrier (*i.e.*, 50 kJ mol⁻¹) for complete rotation of the core-tolyl ring but there are wide ranges over which oscillation is essentially barrierless. Each of these compounds can attain the geometry having the core-tolyl ring aligned with the dipyrin unit (Fig. S5†). This alignment will maximize π -conjugation, leading to the observed red-shifted absorption and emission spectra, as confirmed by molecular orbital calculations (Fig. S6†). A significant feature of these calculations is that planarization of the core tolyl rings causes the dipyrin unit to display slight curvature. It is also apparent that excitation favours adoption of a conformation where the core aryl rings are more aligned with the dipyrin unit and with the latter being somewhat more curved (see ESI†).

$$k_{\text{NR}} = k_0 + k_{\text{ACT}} \exp\left(-\frac{E_B}{R(T - T_G)}\right) \quad (2)$$

For CORE, the nonradiative decay rate constant, k_{NR} , is independent of temperature throughout the range where the solvent is fluid ($T > 140$ K). For each of the other compounds, the effect of temperature on k_{NR} can be satisfactorily explained in terms of eqn (2) (Fig. 3) where k_0 refers to an activationless rate constant, k_{ACT} is the corresponding activated term and T_G (≈ 110 K) is the glass transition temperature of MTHF (Table 2). The activation barrier, E_B , contains contributions from both changes in viscosity and internal rotation. The activationless rates are relatively slow and fall into two distinct

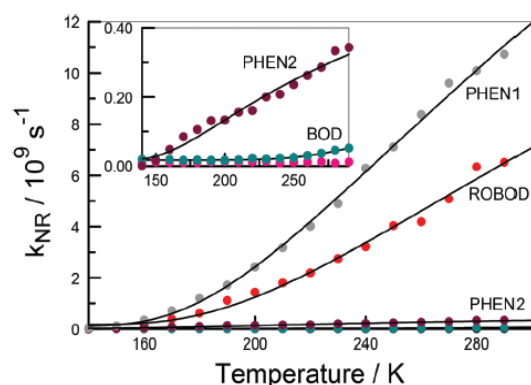


Fig. 3 Effect of temperature on the derived rate constants for non-radiative decay as recorded in MTHF: PHEN1 (grey points), ROBOD (red points), PHEN2 (plum points), BOD (blue points) and CORE (crimson points). Solid lines refer to nonlinear-least square fits to eqn (2). The insert shows an expansion of the low-temperature region. For convenience, the experimental data are given in the ESI.†

groups; those pertaining to the effective rotors ($k_0 > 10^8 \text{ s}^{-1}$) and those associated with poor rotors ($k_0 = 10^7 \text{ s}^{-1}$). The activated terms are sensitive towards the substitution pattern and vary dramatically among the various compounds.

There is a comparatively large barrier for BOD that can only be crossed at elevated temperature. For the remaining compounds, the magnitude of the barrier decreases with increasing effective mass of the dipyrin unit. As mentioned above, the core tolyl groups cause slight curvature of this latter unit, which escalates as the two groups become co-planar. Double substitution, and also electronic excitation, increases this curvature and forces the *meso*-aryl ring out of the plane of symmetry, as is evident by the B-C₈-C_T angle²⁴ (Table 2). Forced curvature of the dipyrin backbone also introduces asymmetry for the two fluorine atoms and this is a convenient tool by which to represent geometric perturbation (Table 2). At the excited-state level, this structural distortion will rupture the S_1 surface so as to create pinholes²⁵ (or conical intersections²⁶) through which the wave-packet can escape back to the ground state. Within this model, it is entirely intuitive that E_B is controlled, in part, by the difference in initial geometry of the reactant and that at the pinhole. This pinhole is not the transition state for full rotation of the *meso*-aryl ring and, as a consequence, is rather difficult to characterise.

Several parameters combine to define the performance of the dye in terms of its ability to function as a fluorescent rotor, including α , k_{ACT} and k_0 . The relative values determined for α can be considered as a crude measure of the volume of solvent affected by the geometry change undertaken by the solute. For BOD, few solvent molecules are affected and the geometry change is considered to be either minor or highly localised. Symmetrical dyes, such as ROBOD and PHEN2, are susceptible to buckling of the dipyrin core, but according to semi-empirical (PM6, RHF, COSMO) quantum chemical calculations this is mostly restricted to the upper rim. Asymmetrical dyes, such as

PHEN1, undergo more substantive structural distortion during rotation and this will engage more solvent molecules. We now see a clear correlation between α and the asymmetry factor $A_{F,B}$,²⁷ the latter being a convenient monitor of the extent of structural change needed to effect full rotation. Since the computed rotational barriers are much less than those derived experimentally for the excited-singlet state, it should be considered that full rotation is not a pre-requisite for sensing activity.

The derived k_0 values are thought to describe the harmonic frequency at the bottom of the potential well²⁸ where the friction coefficient might be large. The results indicate a substantial increase in this frequency for ROBOD and PHEN1 relative to the more constrained analogues. This constraint is imposed by the blocking methyl groups present in BOD and by the pincher effect of the core-phenylene rings for PHEN2 that force the H₁,H₇ atoms into closer proximity. In fact, there is a crude correlation between k_0 and the H₁,H₇ distance computed for the excited-singlet state. Likewise, the derived k_{ACT} values can be considered to represent, at least in part, the harmonic frequency at the top of the barrier²⁸ and, as such, are associated with the corresponding escape rates at the pinhole. It appears that k_0 and k_{ACT} are correlated and, on this basis, we can infer that the same structural facets, most notably the extent of H₁,H₇ separation, control both frequencies. Clearly, retaining high symmetry does not facilitate development of improved molecular rotors.

Conclusions

The development of fluorescent probes for *in situ* monitoring of changes in rheology is an active research field with important applications in medicine, chemical engineering, environmental preservation and personal security. Advanced molecular sensors are required that display highly selective properties and this need creates the stimulus for the design of novel reagents that advance the state-of-the-art. Probes based on the BODIPY fluorophore are attractive reagents because of their robustness, high radiative rate constants and facile modification by synthetic procedures. The results outlined above indicate that improved performance might be achieved by incorporating substituents at remote sites on the BODIPY fluorophore. Aryl substituents attached at the lower rim of the dipyrin unit serve to push the absorption and emission maxima towards the red region, *via* increased π -conjugation, and to squeeze the upper rim by what might be termed "a scissor-like effect". The latter situation affects the space available for the *meso*-aryl rotor and modulates the rate of non-radiative decay of the fluorescent state. The disparity between symmetrical and asymmetrical derivatives is most unexpected and clearly opens the way to design new and improved sensors.

Acknowledgements

We thank Newcastle University, ECPM-Strasbourg, King Abdulaziz University of Saudi Arabia, CNRS and EPSRC for financial support of this work.

References

- 1 M. A. Haidekker and E. A. Theodorakis, Environment-sensitive Behavior of Fluorescent Molecular Rotors, *J. Biol. Eng.*, 2010, **4**, 11–25.
- 2 W. R. Browne and B. L. Feringa, Making Molecular Machines Work, *Nat. Technol.*, 2006, **1**, 25–35.
- 3 N. Koumura, R. W. J. Nijlstra, R. A. van Delden, N. Harada and B. L. Feringa, Light-driven Monodirectional Molecular Rotors, *Nature*, 1999, **401**, 152–155.
- 4 M. A. Haidekker, W. Akers, D. Lichlyter, T. P. Brady and E. A. Theodorakis, Sensing of Flow and Shear Stress using Fluorescent Molecular Rotors, *Sensor Lett.*, 2005, **3**, 42–48.
- 5 R. M. Yusop, A. Unciti-Broceta and M. Bradley, A Highly Sensitive Fluorescent Viscosity Sensor, *Bioorg. Med. Chem. Lett.*, 2012, **22**, 5780–5783.
- 6 K. Gawala, W. D. Sasikala, A. Sengupta, S. A. Dalvi, A. Mukherjee and P. Hazra, Modulation of Excimer Formation of 9-(Dicyanovinyl)-Julolidene by the Macroscopic Host, *Phys. Chem. Chem. Phys.*, 2013, **15**, 330–340.
- 7 M. D'Amico, G. Schiro, A. Cupane, L. D'Alfonso, M. Leone, V. Militello and V. Vetri, High Fluorescence of Thioflavin T Confined in Mesoporous Silica Xerogels, *Langmuir*, 2013, **29**, 10238–10246.
- 8 G. Ulrich, R. Ziessel and A. Harriman, The Chemistry of Fluorescent BODIPY Dyes: Versatility Unsurpassed, *Angew. Chem., Int. Ed.*, 2008, **47**, 1184–1201.
- 9 M. K. Kuimova, G. Yahiloglu, J. A. Levitt and K. Suhling, Molecular Rotor Measures Viscosity of Live Cells via Fluorescence Lifetime Imaging, *J. Am. Chem. Soc.*, 2008, **130**, 6672–6673.
- 10 M. A. H. Alamiry, A. C. Benniston, G. Copley, K. J. Elliott, A. Harriman, B. Stewart and Y.-G. Zhi, A Molecular Rotor Based on an Unhindered Boron Dipyrromethene (Bodipy) Dye, *Chem. Mater.*, 2008, **20**, 4024–4032.
- 11 J. A. Levitt, M. K. Kuimova, G. Yahiloglu, P.-H. Chung, K. Suhling and D. Phillips, Membrane-bound Molecular Rotors Measure Viscosity in Live Cells via Fluorescence Lifetime Imaging, *J. Phys. Chem. C*, 2009, **113**, 11634–11642.
- 12 A. C. Benniston, A. Harriman, V. L. Whittle and M. Zelzer, Molecular Rotors Based on the Boron Dipyrromethene Fluorophore, *Eur. J. Org. Chem.*, 2010, 523–530.
- 13 M. A. H. Alamiry, E. Bahaidarah, A. Harriman, T. Bura and R. Ziessel, Fluorescent Molecular Rotors under Pressure: Synergistic Effects of an Inert Polymer, *RSC Adv.*, 2012, **2**, 9851–9859.
- 14 N. A. Hosny, G. Mohamedi, P. Rademeyer, J. Owen, Y. Wu, M.-X. Tang, R. J. Eckersley, E. Stride and M. K. Kuimova, Mapping Microbubble Viscosity using Fluorescence Lifetime Imaging of Molecular Rotors, *Proc. Natl. Acad. Sci. U. S. A.*, 2013, **110**, 9225–9230.
- 15 P. Loison, N. A. Hosny, P. Gervais, D. Champion, M. K. Kuimova and J.-M. Perrier-Cornet, Direct Investigation of Viscosity of an Atypical Inner Membrane of Bacillus Spores: A molecular Rotor/FLIM Study, *Biochim. Biophys. Acta*, 2013, **1828**, 2436–2443.
- 16 H. Zhu, J. Fan, M. Li, J. Cao, J. Wang and X. Peng, A “Distorted-BODIPY”-based Fluorescent Probe for Imaging of Cellular Viscosity in Live Cells, *Chem. – Eur. J.*, 2014, **20**, 4691–4696.
- 17 H. L. Kee, C. Kirmaier, L. Yu, P. Thamyongkit, W. J. Youngblood, M. E. Calder, L. Ramos, B. C. Noll, D. F. Bocian, W. R. Scheidt, R. R. Birge, J. S. Lindsey and D. Holten, Structural Control of the Photodynamics of Boron-Dipyrin Complexes, *J. Phys. Chem. B*, 2005, **109**, 20433–20443.
- 18 S. Rihn, P. Retailleau, N. Bugsaliewicz, A. De Nicola and R. Ziessel, Versatile Synthetic Methods for the Engineering of Thiophene-Substituted BODIPY Dyes, *Tetrahedron Lett.*, 2009, **50**, 7008–7013.
- 19 A. Poirel, A. De Nicola, P. Retailleau and R. Ziessel, Oxidative Coupling of 1,7,8-Unsubstituted BODIPYs: Synthesis and Electrochemical and Spectroscopic Properties, *J. Org. Chem.*, 2012, **77**, 7512–7525.
- 20 S. J. Strickler and R. A. Berg, Relationship between Absorption Intensity and Fluorescence Lifetime of Molecules, *J. Chem. Phys.*, 1962, **37**, 814–822.
- 21 S. P. Velsko and G. R. Fleming, Solvent Influence on Photochemical Isomerizations – Photophysics of DODCI, *Chem. Phys.*, 1982, **65**, 59–70.
- 22 B. D. Allen, A. C. Benniston, A. Harriman, S. A. Rostron and C. F. Yu, The Photophysical Properties of a Julolidene-based Molecular Rotor, *Phys. Chem. Chem. Phys.*, 2005, **7**, 3035–3040.
- 23 P. D. Zoon and A. M. Brouwer, A Push-Pull Aromatic Chromophore with a Touch of Merocyanine, *Photochem. Photobiol. Sci.*, 2009, **8**, 345–353.
- 24 The term B-C₈-C_T refers to the angle tended by the boron atom, the meso-carbon atom and the carbon atom of the para-methyl group on the tolyl group (for BOD this latter atom is replaced with the para-hydrogen atom).
- 25 D. Ben-Motz and C. B. Harris, Torsional Dynamics of Molecules on Barrierless Potentials in Liquids. II. Test of Theoretical Models, *J. Chem. Phys.*, 1987, **86**, 5433–5440.
- 26 B. G. Levine and T. J. Martinez, Isomerization Through Conical Intersections, *Annu. Rev. Phys. Chem.*, 2007, **58**, 613–634.
- 27 Calculated as the difference between the two C₈-B-F bond angles.
- 28 S. P. Velsko, D. H. Waldeck and G. R. Fleming, Breakdown of Kramers Theory Description of Photochemical Isomerization and the Possible Involvement of Frequency Dependent Friction, *J. Chem. Phys.*, 1983, **78**, 249–258.

Stepwise Photoconversion of an Artificial Light Harvesting Array Built from Extended BODIPY Units

Photochemical & Photobiological Sciences



PAPER

View Article Online

View Journal | View Issue



Cite this: *Photochem. Photobiol. Sci.*, 2015, **14**, 1100

Stepwise photoconversion of an artificial light-harvesting array built from extended BODIPY units†

Anthony Harriman,^{*a} Patrycja Stachelek,^a Alexandra Sutter^b and Raymond Ziessel^{*b}

A molecular dyad, comprising two disparate extended boron dipyrromethene (BODIPY) units, has been identified as a potential component of artificial light-harvesting arrays. Highly efficient, intramolecular electronic energy transfer takes place under illumination but there is some competition from light-induced electron transfer along the molecular axis. The primary energy acceptor has a somewhat shortened excited-state lifetime and reduced emission quantum yield due to charge transfer from a terminal amine residue, the latter being required for the molecular system to operate in organic solar cells. Under continuous illumination with simulated solar light, the dyad undergoes very slow decomposition. In a protic solvent, both BODIPY units degrade at the same rate via an autocatalytic process. The products, one of which is a protonated analogue of the donor, degrade further by independent routes. In aprotic solvents or thin plastic films, the acceptor BODIPY dye absorbing at lowest energy undergoes photochemical degradation as above but the donor is much more stable under these conditions. At each stage of degradation, the molecule retains the ability to sensitize an amorphous silicon solar cell and the overall turnover number with respect to absorbed photons exceeds 10 million. The optical properties of the target compound nicely complement those of the solar cell and sensitization helps to avoid Staebler–Wronski photo-degradation.

Received 15th January 2015,
Accepted 2nd April 2015

DOI: 10.1039/c5pp00021a

www.rsc.org/paps

Introduction

The process of electronic energy transfer (EET) has been used as the underlying methodology by which to engineer numerous analytical protocols,¹ chemical sensors,² bio-probes³ and molecular machines.⁴ Artificial light-harvesting devices,⁵ as used to drive solar cells⁶ and/or photochemical batteries,⁷ also rely heavily on EET to channel photons to the desired location. For these latter systems to be viable, it is necessary that the highly efficient EET process is matched by exceptional stability under prolonged exposure to sunlight. Unfortunately, most organic materials that absorb and emit in the near-IR region, this being the most interesting window for the sensitization of solar cells,⁸ degrade rather quickly under sustained illumina-

tion. We have, of late, become interested in seeking ways to stabilize certain classes of highly emissive dyes, most notably the boron dipyrromethene⁹ (BODIPY) family that figures prominently in artificial light-harvesting arrays.⁵ Here, we provide a preliminary account of the photochemistry of one such elaborate molecular entity that absorbs across the entire visible region but emits solely in the near-infrared region. The goal of the work is to examine ways to improve the stability of the device under continuous illumination with artificial solar light.

To test the system, we have developed a simple experimental set-up whereby the target compound is dispersed in a plastic block and used to sensitize an amorphous silicon (a-Si:H) cell. It is noted that thin film a-Si:H solar cells appear as promising alternatives to similar cells constructed from highly crystalline silicon wafers for photovoltaic power generation. In part, this is because of their low cost and facile fabrication but a serious disadvantage relates to their low solar-to-electricity conversion efficiency. Because of the disordered nature of amorphous silicon, such solar cells are subject to the Staebler–Wronski effect,¹⁰ which concerns recombination of charge not extracted from the cell, that causes structural damage and reduces efficiency during the first 100 hours or so of operation. This distortion arises, at least to a large degree, by illumination with blue light and therefore might be avoided by sensitization with a far-red emitting dye.

^aMolecular Photonics Laboratory, School of Chemistry, Bedson Building, Newcastle University, Newcastle upon Tyne, NE1 7RU, UK

E-mail: anthony.harriman@ncl.ac.uk; Tel: +44 (0)191 208 8660

^bLaboratoire de Chimie Organique et Spectroscopies Avancées, ICPEES-LCOSA, UMR7515, CNRS/ECPM, 25 rue Becquerel, 67087 Strasbourg, Cedex 02, France

E-mail: ziessel@unistra.fr

†Electronic supplementary information (ESI) available: Spectroscopic characterization of new compounds, energy-minimized structures for A1, D1 and 1, details for estimation of ΔG_{CT} , version of Fig. 5 showing reaction times, spectra showing photo-conversion of A1. See DOI: 10.1039/c5pp00021a

Results and discussion

Characterization and background studies

The target molecular array, **1**, which is unusually large (molar mass equals 1721 g mol^{-1} ; solvent accessible surface area equals $910 \text{ cm}^2 \text{ mol}^{-1}$), comprises two BODIPY-based components interconnected *via* a tolane linker (Fig. 1). Both chromophores are built from styryl-BODIPY dyes⁹ but differ in terms of their respective conjugation lengths, and hence their optical properties. The smaller terminal, BDMA, has a styryl-BODIPY unit equipped with a single *N,N*-dimethylaniline residue that is known¹¹ to function as a pH probe. The reference compound, D1 (Fig. 2), for this component absorbs intensely at about 600 nm and fluoresces with a maximum at about 710 nm in CH_2Cl_2 . The fluorescence quantum yield (Φ_F) for D1 in CH_2Cl_2 at room temperature is 0.38 while the corresponding excited-singlet state lifetime (τ_S) is 3.7 ns. It might be noted that the emission properties, including the radiative rate constant ($k_{\text{RAD}} = 1 \times 10^8 \text{ s}^{-1}$ in CH_2Cl_2), are sensitive to the dielectric constant of the surrounding solvent, due to the inherent charge-transfer character of this molecule, and also to the presence of adventitious protons.¹¹

The complementary terminal is significantly larger with a more expansive conjugation pathway that pushes the lowest-energy absorption transition to about 815 nm. This unit, BTH, bears two fused thiophene fragments attached to the BODIPY dye *via* an ethene linkage. Fluorescence from this terminal is

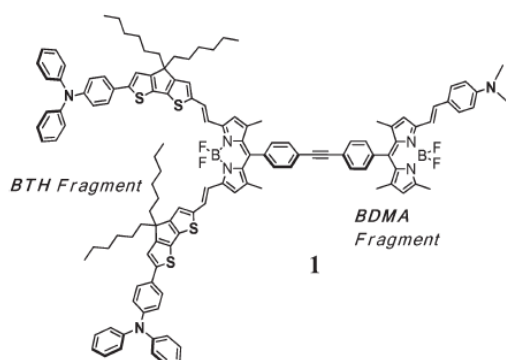


Fig. 1 Molecular formula of the artificial light harvester, **1**, examined in this work. See ESI† for the energy-minimized geometry.

† Compound **1** was prepared under standard conditions, previously elaborated in the literature,³¹ by cross coupling the preformed derivatives A1 and D1³² in the presence of catalytic amounts of $[\text{Pd}(\text{PPh}_3)_4]$ under mild reaction conditions. Purification by column chromatography on flash silica was straightforward and additional purification was assured by crystallization from suitable solvents. The highly soluble compound **1** was isolated in 71%. The analytically pure deep-brown compound was analyzed by NMR spectroscopy, mass spectrometry and elemental analysis, thereby unambiguously confirming the molecular structure (see ESI). In particular, the mass spectral analysis revealed a molecular peak at 2000.1 amu with successive fragments assigned to the release of fluorine atoms [at 1981.1 (35%), 1962.2 (15%)] amu.

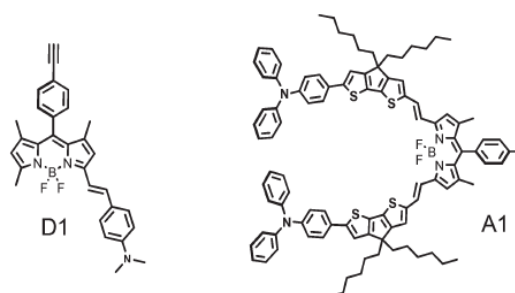


Fig. 2 Molecular formulae for the isolated control compounds used to better understand the properties of the molecular array. See ESI† for the energy-minimized structures.

relatively weak, with $\Phi_F = 0.013$ and $\tau_S = 0.25 \text{ ns}$ in CH_2Cl_2 , and has a maximum at 897 nm. The poor emission properties might reflect the low radiative rate constant ($k_{\text{RAD}} = 5 \times 10^7 \text{ s}^{-1}$) associated with the near-IR spectral profile¹² but also there is the strong likelihood of intramolecular charge-transfer interactions between the appended groups. These latter units are attached to the chromophore to enhance its performance in organic solar cells.¹³ It should be noted that the photophysical properties recorded for the BTH unit present in **1** are closely comparable to those found for the isolated control compound A1 (Fig. 2), confirming that the restricted fluorescence is not a consequence of interaction with BDMA. The same conclusion cannot be reached for the corresponding BDMA terminal. Thus, fluorescence from **1** at around 700 nm is difficult to resolve from the baseline and corresponds to Φ_F of $<10^{-4}$. The excited-state lifetime for this emission is reduced to $<20 \text{ ps}$. The two most obvious causes of this pronounced intramolecular fluorescence quenching are EET from BDMA to BTH and/or light-induced charge transfer along the molecular axis.

In consideration of intramolecular EET, it is noted that the relative positioning of excited-state energy levels, the close proximity of the chromophores, the centre-to-centre separation being 19.7 \AA , and high spectral overlap integral¹⁴ ($J_{\text{DA}} = 0.0024 \text{ cm}$) calculated for **1** are somewhat offset by the modest orientation factor¹⁵ ($\kappa^2 = 0.15$). A conventional Förster-type calculation,¹⁶ based on the ideal-dipole approximation, predicts a rate constant for intramolecular EET from BDMA to BTH of *ca.* $1.5 \times 10^{11} \text{ s}^{-1}$, while this value falls very slightly to $1.4 \times 10^{11} \text{ s}^{-1}$ when the Kuhn extended dipole approach is used.¹⁷ Furthermore, the excitation spectrum indicates that at least 80% of photons collected by the BDMA chromophore are transferred to the appended BTH unit. Thus, intramolecular EET from BDMA to BTH is likely to be highly efficacious.

In order to assess the significance of light-induced electron transfer within **1**, cyclic voltammograms were recorded in CH_2Cl_2 containing background electrolyte. The main findings are summarized in Table 1 where the assignments are made on the basis of identical studies performed with the control compounds. Now, three peaks are observed on reductive scans. The first two reduction peaks are *quasi-reversible* and

Table 1 Summary of the electrochemical properties recorded for **1** and the control compounds as recorded in CH₂Cl₂ containing TBAP (0.1 M) as background electrolyte

Cmpd.	E^{ox} (ox, soln) (V), ΔE^{a} (mV)	E^{red} (red, soln) (V), ΔE^{b} (mV)
D1	+0.54 (60), +0.87 (60)	−1.20 (60)
A1	+0.38 (60), +0.83 (60), +1.00 (60)	−1.00 (70), −1.63 ^c (irr.)
1	+0.38 (60), +0.56 (60), +0.84 (70), +1.00 (60)	−1.00 (80), −1.21 (70), −1.85 ^c (irr.)

^a Refers to oxidative processes. ^b Refers to reductive processes. ^c N.B. irr means irreversible electrochemical step.

correspond to one-electron reduction of BTH and BDMA units, respectively, with half-wave potentials of −1.00 and −1.21 V vs. SCE. The third reduction peak is irreversible and, by reference to the control compounds, corresponds to addition of a second electron to the BTH unit. A total of four oxidative processes can be identified, each of which corresponds to the *quasi*-reversible removal of one electron from **1**. The first two peaks correspond to the generic oxidation of BTH and BDMA units, respectively, with half-wave potentials of 0.38 and 0.56 V vs. SCE, as identified by comparison with the control compounds. The remaining two oxidation steps are difficult to assign simply by comparison with these same reference compounds and further information about the electronic nature of these chromophores was sought from molecular orbital calculations. It is also important to recognize that the acceptor comprises multiple discrete units that might not be in strong electronic communication. There is a need, therefore, to better understand how the redox equivalents introduced during the electrochemical processes are localized within the overall structure.

Quantum chemical studies for BDMA have been described previously,¹¹ together with a few relevant compounds, and the main conclusion is that the entire molecule functions as an extended push-pull¹⁸ electronic system. Charge transfer from the *N,N*-dimethylanilino unit to the BODIPY nucleus serves to increase the molecular dipole moment (μ) at both ground (DFT/B3LYP/aug-cc-pVTZ: $\mu = 3.0$ D) and excited-state (TD-DFT/CAM-B3LYP: $\mu = 7.2$ D) levels while the wavenumber for the emission maximum decreases with increasing solvent polarity.¹¹ The control compound is highly sensitive to the presence of protons¹¹ and the resultant protonated species ($\lambda_{\text{ABS}} = 553$ nm; $\lambda_{\text{FLU}} = 561$ nm) is strongly fluorescent ($\Phi_{\text{F}} = 1.0$). Related calculations were made for the acceptor component, A1, and indicate that the ground-state dipole moment is 1.6 D with little change on excitation. Interestingly, while the LUMO is essentially localized on the extended dipyrin nucleus, the HOMO is centred on the terminal amine (see ESI†). Moreover, HOMO(−1) is associated with the thiophene spacer and it is not until we reach HOMO(−2) that electron density is removed from the dipyrin unit (see ESI†). The same type of molecular orbital description is found for the full molecule **1** and partial MO pictures are shown below (Fig. 3); see ESI† for the full molecule. This finding can be used to imply

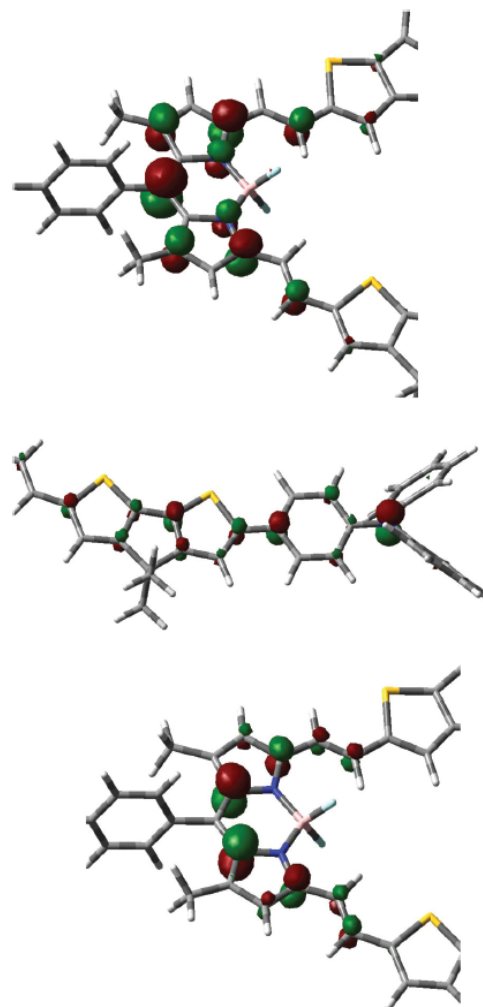


Fig. 3 Kohn-Sham representations for **1** at isodensity of 0.015 for LUMO (upper), HOMO (centre) and HOMO(−2) (lower). NB the hexyl chains have been replaced with methyl groups.

that the relatively short τ_{S} and low Φ_{F} found for the acceptor unit arise from intramolecular charge transfer with the appended amine.

Combining these orbital descriptions with the above-mentioned electrochemistry, it can be concluded that the only light-induced electron-transfer event able to compete with excited-state deactivation involves charge transfer from the excited-singlet state of BDMA to BTH. For this process, the thermodynamic driving force (ΔG_{CT}) is estimated¹⁹ to be *ca.* 0.5 eV (see ESI†) and it is possible that this route contributes towards the missing 20% or so from the comparative excitation and absorption spectra. Our conclusion, therefore, is that intramolecular electron transfer might compete rather ineffec-

tively with EET from BDMA to BTH for the target compound in a polar solvent. In nonpolar media, we might anticipate a severe reduction in the rate of charge transfer but no real effect on the efficacy of intramolecular EET.

Photochemical degradation

We now turn our attention to the main focus of this work, namely the effect of illumination with simulated sunlight on the target compound. Preliminary studies carried out with **1** dispersed in plastic films, such media being relevant for the sensitization of solar cells, indicated that the course of reaction was too slow to be followed in a meaningful manner. Photochemical bleaching in anaerobic organic solvents is slow but can be monitored by absorption spectroscopy. Of the available solvents, CH_2Cl_2 is the most suitable in terms of solubility. Output from the lamp, filtered to remove $\lambda < 340$ nm but otherwise covering the entire visible region (Fig. 4), was directed to the front surface of the sample cell without focussing. It should be emphasized that both chromophores absorb incident light under these conditions. Integration of the individual spectral profiles and comparison with output from the lamp allows us to conclude that 32% of incident photons are collected by BDMA, with the remaining 68% being harvested by BTH.

In qualitative terms, exposure of the sample dissolved at the micromolar level in deoxygenated CH_2Cl_2 to white light leads to slow but progressive bleaching of both BDMA ($\lambda_{\text{MAX}} = 612$ nm) and BTH ($\lambda_{\text{MAX}} = 815$, 525 and 440 nm) chromophores (Fig. 5). Concomitant with bleaching of the primary chromophores, the spectral changes are consistent with the gradual appearance of new absorption bands at 715 and 560 nm. In turn, these intermediary products degrade under further illumination and the final product mixture possesses absorption bands in the near-UV region ($\lambda_{\text{MAX}} = 512$ and 450 nm). The sharp absorption band centred at 560 nm is highly reminiscent of the protonated form of BDMA, which was studied earlier as a putative pH probe.¹¹ Furthermore, the broad

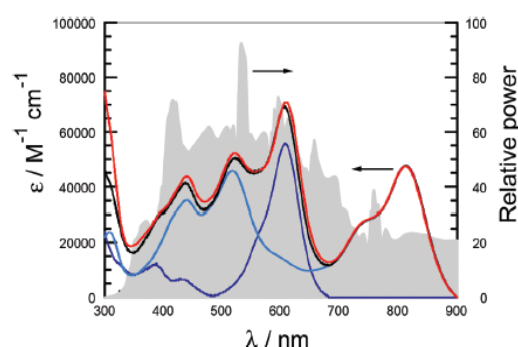


Fig. 4 Absorption spectra recorded for D1 (dark blue curve), A1 (light blue curve, an equimolar mixture of D1 and A1 (black curve) and **1** (red curve) in CH_2Cl_2 solution: the normalized lamp profile is shown as the shaded grey curve.

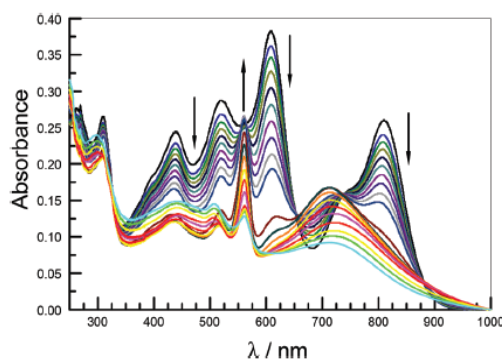


Fig. 5 Selection of absorption spectra recorded during the irradiation of **1** in CH_2Cl_2 solution with white light. Individual spectra were recorded at regular time intervals covering 450 min; see ESI† for actual times.

absorption profile centred at 715 nm is associated with the BTH unit since the same species arises from direct photolysis of A1 in deoxygenated CH_2Cl_2 (see ESI†). Interestingly, both intermediary products fluoresce such that the ability to sensitize a solar cell is not lost during the initial bleaching process. Furthermore, it was noted that efficient EET occurs from the protonated form of BDMA to the product absorbing at 715 nm. The final, near-UV absorbing species, which does not bleach significantly under our conditions, also retains the ability to sensitize a solar cell. The photochemistry is irreversible, although the overall bleaching efficiency is extremely low (see later). We now consider the three stages of reaction as identified above.

The rates of the initial photo-bleaching step, whereby both BDMA and BTH units degrade, are very similar, if not identical, for each chromophore despite the imbalanced photon intake. This behaviour is not to be expected since the excited-state lifetime of the BDMA donor is extremely short because of intramolecular EET to the proximal BTH component. The excited-state of the latter is relatively long lived and should bleach at a much faster rate than found for the donor unit. Bleaching of BTH is most conveniently followed at 820 nm while that for BDMA can be monitored at 610 nm. For each chromophore, the decrease in absorbance follows a non-linear pattern with respect to illumination time, even at the earliest stages and the rate of bleaching appears to increase with illumination time (Fig. 6). This behaviour indicates some kind of autocatalytic process²⁰ that enhances the rate of photo-bleaching. Leaving the sample overnight in the dark, intended to mimic outdoor conditions, has no effect on the reaction. Further illumination simply continues the bleaching step, for which there are at least 5 isosbestic points across the spectral window (Fig. 6 and S5†) for the first stage in the overall bleaching chemistry (Scheme 1).

A reaction is deemed to be autocatalytic²⁰ when a product-concentration vs. time profile is “S-shaped” or when a reaction-rate vs. time plot is “bell-shaped” with both an accelera-

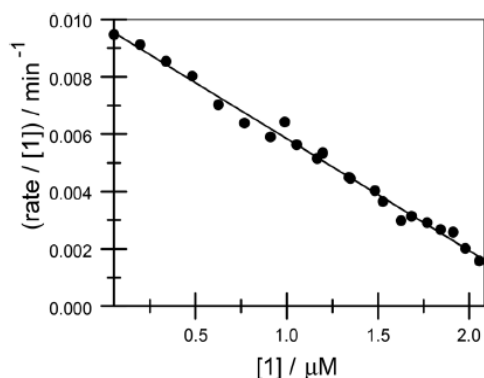
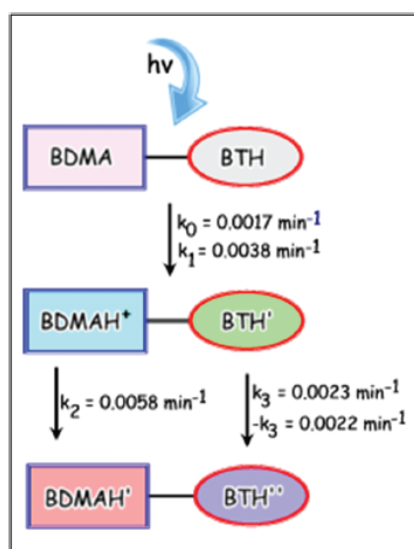


Fig. 6 Example of the fitting of experimental data ($\lambda = 812$ nm) to an autocatalytic process (i.e., eqn (1)). The points are experimental measurements and the solid line is a non-linear, least-squares fit to eqn (1).



Scheme 1 Pictorial representation of the processes leading to photo-conversion of the target compound 1 in CH_2Cl_2 solution when exposed to simulated sunlight.

tion stage and a decay period. At least two mechanisms must operate, one being responsible for the initial bleaching step and the other making use of a primary product to enhance further bleaching. On the acceptance of *pseudo*-first order conditions being met, this being confirmed by a small concentration dependence study, the overall reaction rate can be expressed in the form of eqn (1) where k_0 is a rate constant for the initial reaction and k_1 is the corresponding rate constant for the catalysed reaction. Here, the term A refers to absorbance and the subscripts represent the individual reading (i.e., A_0 is the first absorbance reading, A_1 is the second reading, etc.). Iterative, least-squares fitting of the photolysis data allows calculation of these two rate constants (Table 2), as determined by global fitting of the early photolysis stage carried out across a wide wavelength region.

$$\frac{A_1 - A_3}{\Delta t_{3,1}(\epsilon_0 - \epsilon_\infty)[1]_2} = (k_0 - k_1[1]_0) - k_1[1]_2 \quad (1)$$

$$k_N = \frac{(A_0 - A_t)}{\Delta t} \frac{1}{(\epsilon_0 - \epsilon_\infty)[1]_0} \quad (2)$$

The absorption bands associated with the primary products, as seen at 715 and 560 nm, appear at closely comparable rates, indicating that they share a common reaction pathway, before slowly bleaching under continuous illumination. The rates of secondary photo-bleaching differ for the two absorption bands (Fig. 7). Thus, these two species undergo disparate reaction pathways leading to their slow degradation. Notably, disappearance of the protonated form of BDMA (i.e., BDMAH^+) is essentially linear with photolysis time (eqn (2) where ϵ refers to the molar absorption coefficient at that wavelength) but loss of the breakdown product from BTH (monitored at 690–750 nm), which is abbreviated as BTH' , involves a short inhibition period before bleaching sets in. For a typical substrate concentration of $2 \mu\text{M}$, the rate of bleaching of BDMAH^+ is about $12 \text{ nmol dm}^{-3} \text{ min}^{-1}$ (Table 2) while the same analysis shows the decomposition of BTH' to occur more slowly with a typical rate of ca. $5 \text{ nmol dm}^{-3} \text{ min}^{-1}$.

Using the control compound D1, after protonation with HCl in CH_2Cl_2 solution, it was found that illumination with visible light caused relatively fast bleaching that resulted in a colourless product. In contrast, illumination of BTH' leads to a further product that absorbs in the near-UV region. This latter

Table 2 Summary of rate constants associated with the stepwise photo-bleaching of the target array in deoxygenated CH_2Cl_2 solution

Process	Direction	k/min^{-1} ^a	λ/nm ^b	Statistics ^c
$\text{BDMA} \rightarrow \text{BDMAH}^+$	Bleaching	$k_0 = 0.0019$; $k_1 = 0.0039$	605–615	SD = 0.0005; GF = 0.9923
$\text{BTH} \rightarrow \text{BTH}'$	Bleaching	$k_0 = 0.0017$; $k_1 = 0.0038$	790–830	SD = 0.0002; GF = 0.9954
$\text{BTH} \rightarrow \text{BTH}'$	Formation	$k_0 = 0.0016$; $k_1 = 0.0038$	710–725	SD = 0.0003; GF = 0.9967
$\text{BDMAH}^+ \rightarrow \text{BDMAH}'$	Bleaching	$k_2 = 0.0058$	555–565	SD = 0.0854; GF = 0.9960
$\text{BTH}' \rightarrow \text{BTH}''$	Bleaching	$k_3 = 0.0023$	690–750	SD = 0.0229; GF = 0.9986
$\text{BTH}' \rightarrow \text{BTH}''$	Formation	$-k_3 = 0.0022$	425–490	SD = 0.0444; GF = 0.9916

^a Refer to Scheme 1 for definition of individual rate constants. ^b Wavelength range for global data analysis. ^c SD refers to standard deviation for the fit and GF refers to the goodness-of-fit correlation term.

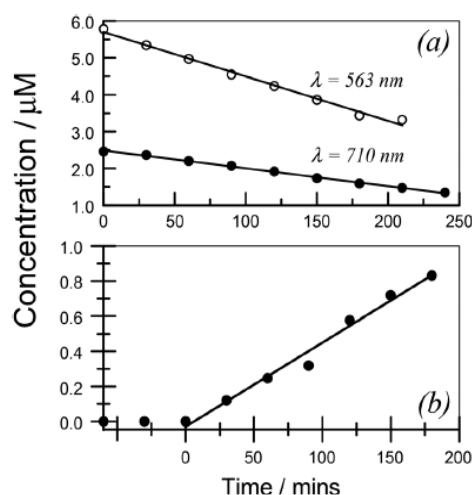


Fig. 7 Examples of fitting the experimental data to eqn (2) for (a) degradation of the intermediary products BDMAH⁺ ($\lambda = 563 \text{ nm}$) and BTH' ($\lambda = 710 \text{ nm}$) and (b) formation of the final product, BTH''.

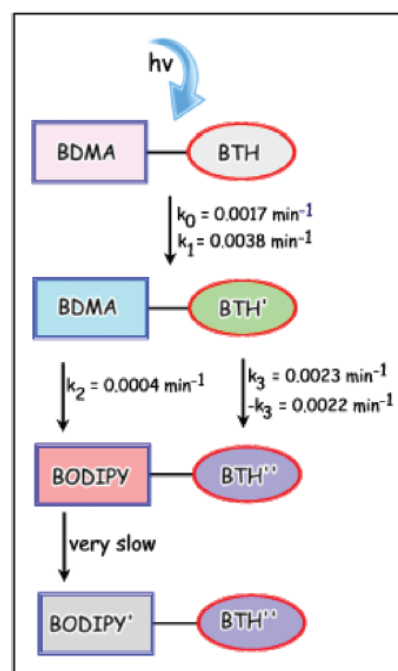
product, BTH'', is extremely robust and degrades very slowly under continuous illumination. The rate of formation of BTH'' agrees remarkably well with the rate of bleaching of BTH' (Table 2). The overall reaction scheme leading to degradation of 1 under visible light excitation is summarized concisely by way of Scheme 1.

Our understanding of the photo-bleaching of the artificial photon harvester 1 in CH_2Cl_2 can now be summarised as follows: The compound absorbs over a wide spectral range covering the entire visible zone and stretching into the far-red region. Integration of the absorption profile indicates that approximately 70% of absorbed photons are directed to the BTH-based acceptor, which shows modest fluorescence centred at around 900 nm. Under visible light illumination, BTH undergoes slow bleaching to form the primary product BTH' that shows prominent absorption at around 715 nm. During this bleaching process, at least one proton is released into the system and becomes attached to the BDMA terminal, forming BDMAH⁺. This protonation step is fast such that bleaching of the BTH and BDMA chromophores occurs at the same rate. As reaction proceeds, one of the resultant products catalyses bleaching of BTH so that the rate increases with time of photolysis. Ultimately, the system reaches the state where BTH' and BDMAH⁺ co-exist. Further illumination leads to irreversible bleaching of BDMAH⁺ to form a transparent product and this unit is lost from the system. In contrast, further bleaching of BTH' occurs to form the near-UV absorbing species BTH''. This latter product does not bleach under our conditions.

The origin of the proton that attaches itself to BDMA can be traced to breakdown of the CH_2Cl_2 solvent since BDMAH⁺ does not form when the photochemistry is carried out in either tetrahydrofuran (THF) or poly(methylmethacrylate)

(PMMA). In fact, it is known that certain aryl amines undergo auto-catalytic breakdown under photolysis in the presence of carbon tetrachloride.²¹ Here, the degradation mechanism might be considered to involve light-induced electron transfer from chromophore to solvent, with subsequent loss of a chloride anion from the CCl_4 radical anion and addition of a molecule of O_2 to form a peroxy ($\text{CCl}_3\text{OO}^\bullet$) radical. This latter species is well known in radiation chemistry²² and is capable of causing further oxidative damage.²³ The peroxy radical can also undergo hydrogen abstraction to form a solvent-derived hydroperoxide and this could be the source of the acidic proton.

Photolysis in aprotic THF, causes slow degradation of BTH exactly as described above but there is little loss of BDMA during the early stages of reaction. Instead, this latter chromophore remains intact and able to transfer excitation energy to BTH'. Continued illumination, however, leads to very slow degradation of BDMA to form a primary product absorbing at around 500 nm (Scheme 2). This latter species possesses an absorption spectral profile consistent with a BODIPY derivative lacking the styryl residue.⁹ This latter species undergoes extremely slow photo-bleaching, a fact confirmed by separate irradiation of BODIPY in deoxygenated THF solution. Illumination of 1 in PMMA follows the same pattern as seen in THF solution but the course of reaction is too slow to monitor meaningful kinetic parameters, even for thin (*i.e.*, 10 μm) films.



Scheme 2 Pictorial representation of the events leading to photo-conversion of 1 in non-protic media when exposed to simulated sunlight.

Sensitization of amorphous silicon solar cells

Prior to photo-bleaching, **1** emits weakly at 900 nm and, in principle, should be capable of sensitizing a silicon or gallium arsenide solar cell. The fluorescence quantum yield ($\Phi_F = 0.013$) is kept low by partial charge transfer with the terminal amine but could be improved by eliminating this latter component. The product allows for EET from BDMAH^+ to BTH' and for continued sensitization of the solar cell by way of emission from BTH' . This intermediary product absorbs strongly in the visible region but lacks the ability to harvest photons in the far-red region. Further degradation to form BTH'' is slow and the product is a relatively poor photon collector since it absorbs only at wavelengths below about 600 nm. Nonetheless, it should continue to direct photons to the solar cell. The overall turnover number for one molecule of **1** under continuous illumination with white light exceeds ten million, allowing for all stages of photo-bleaching.

It might be noted that the absorption spectrum of **1** overlaps strongly with that of a thin film of hydrogenated amorphous silicon, a-Si:H, as indicated by way of Fig. 8. The organic dye protects the solar cell from exposure to UV-light and strongly amplifies light harvesting in the far-red region where a-Si:H absorbs weakly. Spectral overlap between emission from **1** and absorption by a-Si:H is weak but nonetheless sensitization of the solar cell is possible. This latter point was confirmed by recording action spectra for a thin-film of a-Si:H deposited onto a flexible plastic sheet. The action spectrum (Fig. 9), recorded for open-circuit photocurrent measurements, resembles the absorption spectrum recorded for the solar panel (Fig. 8). In order to sensitize the solar panel, a rod (diameter 1.2 cm and length 2.5 cm) of PMMA doped with **1** was prepared by slow polymerisation and polished along all surfaces. The solar panel was wrapped around the rod, leaving the ends exposed. A collimated beam of white light was passed through the rod and the resultant photocurrent from the solar panel was recorded (Fig. 9). Comparison of the two action

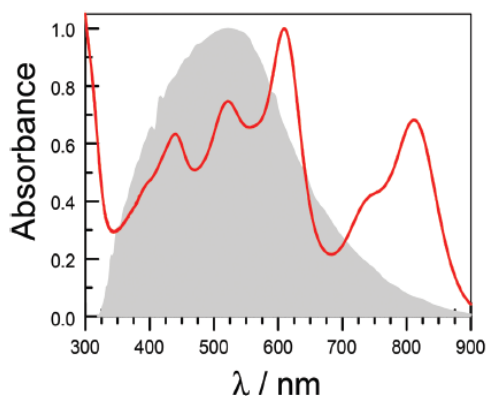


Fig. 8 The absorption spectrum recorded for **1** (red curve) in CH_2Cl_2 superimposed over that of a thin-film of amorphous silicon deposited onto a flexible plastic substrate.

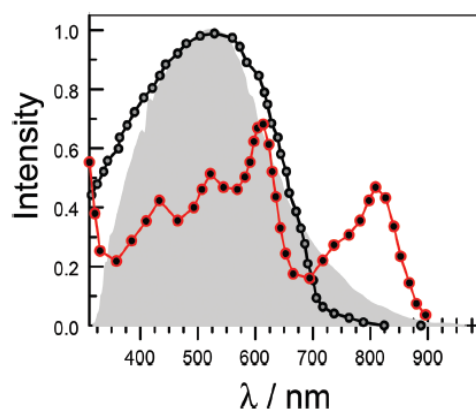


Fig. 9 Action spectra recorded for a thin-film a-Si:H flexible solar cell (black points) compared to the absorption spectrum of the panel (grey shadow). The action spectrum recorded for sensitization of a-Si:H by **1** dispersed in PMMA is shown as the red curve.

spectra clearly shows that the solar cell is sensitized by emission from **1** under these conditions. It should be noted that the set-up was far from being optimal but serves the purpose for proof-of-concept. In particular, the a-Si:H solar panels perform better in terms of current generation when flat so our experimental arrangement is far from ideal.

The most notable feature of the sensitization experiment concerns the enhanced sensitivity towards far-red light (Fig. 9). This provides a simple means to protect the solar cell from undue exposure to blue light, this being a major cause of Staebler-Wronski degradation. Thus, indirect sensitization of the type discussed here could provide an effective means for stabilizing a-Si:H solar cells. It was not possible to confirm this possibility because of the experimental set-up employed, most notably the geometry of the sensitization experiments precludes direct illumination of the solar panel. Instead, we will address this point in a forthcoming article, where we will also explore the underlying mechanism leading to EET from dye to semiconductor.

Conclusion

The use of artificial light-harvesting arrays to sensitize solar cells is at a very early stage of development^{5–7} and it is not yet clear if such devices offer a genuine benefit compared to direct excitation of the semiconductor. Nonetheless, it is an interesting concept that merits proper exploration. One obvious problem relates to the stability of the array under continuous exposure to sunlight²⁴ and, as such, it is necessary to identify and utilize pigments with exceptional levels of photo-stability. Our approach to this problem has been to introduce a self-protective mechanism whereby photochemical degradation leads to a product that also functions as a useful sensitizer. In this way, the operating timescale is lengthened considerably but there is a certain inevitability that the fraction of solar light

harvested by the array decreases at each step. This situation is nicely exemplified by considering the breakdown of **1** in aprotic media. Thus, integration of the absorption spectral profile with respect to a thin-film a-Si:H solar panel indicates about 71% of the spectral distribution is covered by the array. On conversion of BTH to BTH', this value falls to 63% while further reaction to convert BTH' to BTH'' causes a drop to 42%. Conversion of the BDMA unit to BODIPY' is accompanied by a further fall to 31%. The severely damaged array still fulfils its duty as a sensitizer but no longer collects far-red photons. It might be noted that it proved impossible to determine a meaningful quantum yield for photochemical degradation using monochromatic light, even when using a red-emitting laser diode. This is because the rate of decomposition, especially at the onset of the experiment, is too slow to allow accurate monitoring of the course of reaction.

A second lesson learned from this study is the need to select an appropriate medium for the dye; in the case of **1** this translates to the avoidance of protic media. This requires systematic engineering of the system to eliminate problems imposed by the environment. Notably, the presence of molecular oxygen has little effect on the course of reaction and cannot be completely eliminated without encasing the array in a protective cover.²⁵ It is also important to carefully match the sensitizer with the semiconductor in order to obtain the optimal effect. There are, in fact, clear synergistic effects to be gained by combining a-Si:H with dyes such as **1**. Not only does the dye remove near-UV light, which is harmful to the solar cell, but it also protects the cell from Staebler-Wronski¹⁰ degradation by avoiding direct excitation with blue light.

The approach used here does not permit identification of the breakdown products; using NMR spectroscopy to monitor the fate of a closely related array showed the process to be highly complicated but confirmed that the BODIPY unit absorbing at lowest energy was the first species to photobleach. Indeed it is not necessary to identify the products but there is a need to either repair the damaged sites or improve the overall photochemical stability for the long-wavelength absorbing species. The array described here shows a somewhat comparable turnover number to that of chlorophyll in the natural photosynthetic process²⁶ but we have no provision for either self-repair²⁷ or photochemical regulation.²⁸ Such features, which are inherent to the natural process,²⁶ will be addressed in a forthcoming publication.

Experimental details

Solvents were purchased from Sigma-Aldrich as spectroscopic grade and were used as received. Absorption spectra were recorded with a Perkin-Elmer Lambda-35 spectrophotometer while emission spectra were recorded with an Hitachi F-4500 spectrofluorimeter. For the far-red emitting samples, specialised facilities were provided by Edinburgh Photonics (a division of Edinburgh Instruments). Fluorescence quantum yields were determined with a fully-corrected, high radiance integrat-

ing sphere. Fluorescence lifetimes were determined by time correlated, single-photon counting methods following excitation with an ultra-short laser diode. For steady-state irradiation experiments, the solution was deoxygenated by purging with dry N₂ and sealed into a glass cuvette. The sample was exposed to the white light source (JCC Model IP66, 450W E40) for varying time intervals. The light intensity at the front surface of the cuvette was determined with a PM100 power meter fitted with a Si-photodiode sensor head. Electrochemical measurements were made by cyclic voltammetry using a Pt working electrode, a Ag wire counter electrode and a standard SCE reference electrode. Ferrocene was used as internal standard. The CH₂Cl₂ solvent was dried and freshly distilled immediately before use while tetra-*N*-butylammonium perchlorate used as the background electrolyte at a concentration of 0.1 M was recrystallised several times from ethanol and dried under vacuum. A variety of scan rates was used but the quoted data refer to a fixed scan rate of 60 mV per second. All measurements were made under an atmosphere of dry N₂ at room temperature.

Thin films of the dye incorporated into PMMA were prepared by spin coating (Laurell WS-650SZ-6NPP) while thicker films were prepared by simple casting from concentrated solution in CH₂Cl₂. The PMMA rod was prepared by *in situ* polymerization of methyl methacrylate, after removal of the inhibitor by vacuum distillation, using 1,1'-azobis(cyclohexanecarbonitrile) (0.02% w/w) at 10 °C under modest vacuum. The rod was cut to size and polished using very fine 600 grit emery paper.

The amorphous silicon solar panel, presented in the form of a flexible sheet, was provided by Sanyo. Action spectra were recorded under open circuit conditions using a Sinclair digital current meter and a high-radiance monochromator. The light source was a calibrated 250 W Xe-arc lamp.

Quantum chemical calculations were made with TURBO-MOLE²⁹ running on a multiple processor workstation. Calculations were made at both ground- (DFT/B3LYP/aug-cc-pVTZ) and excited-state (TD-DFT/CAM-B3LYP) levels with the target compound embedded in a solvent continuum using the CPCM model.³⁰

Acknowledgements

We thank the Douglas Bomford Trust, EPSRC-IAA, Newcastle University, CNRS and ECMP-Strasbourg for financial support of this work. We also thank Dr Anna Gakamsky (Edinburgh Photonics Ltd) for help with recording the photophysical properties of the far-red emitting dyes.

Notes and references

- 1 D. Beljonne, C. Curutchet, G. D. Scholes and R. J. Silbey, Beyond Förster resonance energy transfer in biological

- and nanoscale systems, *J. Phys. Chem. B*, 2009, 113, 6583–6599.
- 2 J. S. Wu, W. M. Liu, J. C. Ge, H. Y. Zhang and P. F. Wang, New sensing mechanisms for design of fluorescent chemosensors emerging in recent years, *Chem. Soc. Rev.*, 2011, 40, 3483–3495.
- 3 C. H. Fan, K. W. Plaxco and A. J. Heeger, Biosensors based on binding-modulated donor-acceptor distances, *Trends Biotechnol.*, 2005, 23, 186–192.
- 4 V. Balzani, Photochemical molecular devices, *Photochem. Photobiol. Sci.*, 2003, 2, 459–476.
- 5 R. Ziessel and A. Harriman, Artificial light-harvesting antennae: Electronic energy transfer by way of molecular funnels, *Chem. Commun.*, 2011, 47, 611–631.
- 6 A. C. Benniston, A. Harriman and S. Yang, Providing power for miniaturized medical implants: Triplet sensitization of semiconductor surfaces, *Philos. Trans. R. Soc. London, A*, 2013, 371, 20120334.
- 7 R. Ziessel, G. Ulrich, A. Haefele and A. Harriman, An artificial light-harvesting array constructed from multiple Bodipy dyes, *J. Am. Chem. Soc.*, 2013, 135, 11330–11344.
- 8 B. A. Gregg, Excitonic solar cells, *J. Phys. Chem. B*, 2003, 107, 4688–4698.
- 9 G. Ulrich, R. Ziessel and A. Harriman, The chemistry of fluorescent Bodipy dyes: Versatility unsurpassed, *Angew. Chem., Int. Ed.*, 2008, 47, 1184–1201.
- 10 A. Klaver and R. A. van Swaaij, Modelling of light-induced degradation of amorphous silicon solar cells, *Sol. Energy Mater. Sol. Cells*, 2008, 92, 50–60.
- 11 (a) N. Boens, V. Leen and W. Dehaen, Fluorescent indicators based on BODIPY, *Chem. Soc. Rev.*, 2012, 41, 130–1172; (b) A. Nano, P. Retailleau, J. P. Hagon, A. Harriman and R. Ziessel, A hybrid bis(amino-styryl) substituted Bodipy dye and its conjugate diacid: Synthesis, structure, spectroscopy and quantum chemical calculations, *Phys. Chem. Chem. Phys.*, 2014, 16, 10187–10198.
- 12 J. R. Bolton and M. D. Archer, Calculation of natural radiative lifetimes from absorption and fluorescence properties of semiconductors and molecules, *J. Phys. Chem.*, 1991, 95, 8453–8461.
- 13 T. Bura, N. Leclerc, S. Fall, P. Leveque, T. Heiser, P. Retailleau, S. Rihn, A. Mirloup and R. Ziessel, High-performance solution-processed solar cells and ambipolar behavior in organic field effect transistors with thienyl-BODIPY scaffolding, *J. Am. Chem. Soc.*, 2012, 134, 17404–17407.
- 14 A. Harriman, G. Izzet and R. Ziessel, Rapid energy transfer in cascade-type Bodipy dyes, *J. Am. Chem. Soc.*, 2006, 128, 10868–10875.
- 15 R. E. Dale, J. Eisinger and W. E. Blumberg, Orientational freedom of molecular probes - orientation factor in intramolecular energy transfer, *Biophys. J.*, 1979, 26, 161–193.
- 16 P. G. Wu and L. Brand, Resonance energy transfer – methods and applications, *Anal. Biochem.*, 1994, 218, 1–13.
- 17 V. Czikkely, H. D. Forsterling and H. Kuhn, Extended dipole model for aggregates of dye molecules, *Chem. Phys. Lett.*, 1970, 6, 207–210.
- 18 R. Ziessel, P. Retailleau, K. J. Elliott and A. Harriman, Boron dipyrin dyes exhibiting push-pull-push electronic signatures, *Chem. – Eur. J.*, 2009, 15, 10369–10374.
- 19 M. R. Wasielewski, Photoinduced electron-transfer in supramolecular systems for artificial photosynthesis, *Chem. Rev.*, 1992, 92, 435–461.
- 20 F. Mata-Perez and J. F. Perez-Benito, The kinetic rate law for autocatalytic reactions, *J. Chem. Educ.*, 1987, 64, 925–927.
- 21 (a) O. M. Usov, M. I. Bardamova and I. L. Kotlyarevskii, Photochemistry of acetylenic derivatives of aromatic amines. 1. Photolysis products of paraethynyl-N,N-dimethylaniline in carbon tetrachloride, *Bull. Acad. Sci. USSR Div. Chem. Sci.*, 1986, 35, 1055–1057; (b) M. I. Bardamova and O. M. Usov, Photochemistry of acetylenic derivatives of aromatic amines. 2. Photolysis of para-ethynyl-N,N-dibenzylaniline and para-butadiynyl-N,N-dibenzylaniline in the presence of carbon tetrachloride and oxygen, *Bull. Acad. Sci. USSR Div. Chem. Sci.*, 1986, 35, 1055–1057.
- 22 Z. B. Alfassi, A. Harriman, S. Mosseri and P. Neta, Rates and mechanisms of oxidation of ZnTPP by CCl_3O_2 radicals in various solvents, *Int. J. Chem. Kinet.*, 1986, 18, 1315–1321.
- 23 (a) H. D. Burrows, T. J. Kemp and D. Greatore, Solute radical cation yields in pulse radiolysis of solutions of aromatic amines in chlorinated hydrocarbons, *J. Phys. Chem.*, 1972, 76, 20–27; (b) H. D. Burrows, T. J. Kemp and M. J. Welbourn, Intermediates in the pulse radiolysis of solutions of phenothiazine and its derivatives - Reactions of cycloalkylperoxyl radicals with phenothiazines, *J. Chem. Soc., Perkin Trans. 2*, 1973, 969–974.
- 24 S. Wennmalm and R. Rigler, On death numbers and survival times of single dye molecules, *J. Phys. Chem. B*, 1999, 103, 2516–2519.
- 25 H. S. Weerasinghe, S. E. Watkins, N. Duffy, D. J. Jones and A. D. Scully, Influence of moisture out-gassing from encapsulant materials on the lifetime of organic solar cells, *Sol. Energy Mater. Sol. Cells*, 2015, 132, 485–491.
- 26 (a) A. A. Pascal, Z. F. Liu, K. Broess, B. van Oort, H. van Amerongen, C. Wang, P. Horton, B. Robert, W. R. Chang and A. Ruban, Molecular basis of photoprotection and control of photosynthetic light-harvesting, *Nature*, 2005, 436, 134–137; (b) G. Peers, T. B. Truong, E. Ostendorf, A. Busch, D. Elrad, A. R. Grossman, M. Hippler and K. K. Niyogi, An ancient light-harvesting protein is critical for the regulation of algal photosynthesis, *Nature*, 2009, 462, 518–522.
- 27 H. R. Bolharnordenkamp, M. Hofer and E. G. Lechner, Analysis of light-induced reduction of the photochemical capacity in field-grown plants – evidence for photoinhibition, *Photosynth. Res.*, 1991, 27, 31–39.
- 28 P. Horton, A. V. Ruban and M. Wentworth, Allosteric regulation of the light-harvesting system of photosystem II, *Philos. Trans. R. Soc. London, Ser. B*, 2000, 355, 1361–1370.

- 29 R. Ahlrichs, M. Bär, M. Häser, H. Horn and C. Kölmel, Electronic structure calculations on workstation computers: The program system Turbomole, *Chem. Phys. Lett.*, 1989, **162**, 165–169.
- 30 (a) V. Barone and M. Cossi, *J. Phys. Chem. A*, 1998, **102**, 1995–2001; (b) H. Li and J. H. Jensen, *J. Comput. Chem.*, 2004, **25**, 1449–1456.
- 31 R. Ziesse, S. Rihn and A. Harriman, Quasi-one-dimensional electronic systems formed from boron dipyrromethene (BODIPY) dyes, *Chem. – Eur. J.*, 2010, **16**, 11942–11953.
- 32 A. Sutter and R. Ziesse, A versatile synthesis of long-wavelength-excitable BODIPY dyes from readily modifiable cyclopenta[2,1-b:3.4-b]dithiophenes, *Synlett*, 2014, 1466–1472.

A Bifurcated Molecular Pentad Capable of Sequential Electronic Energy Transfer and Intramolecular Charge Transfer



PCCP

PAPER

View Article Online

View Journal | View Issue



Cite this: *Phys. Chem. Chem. Phys.*, 2015, 17, 26175

A bifurcated molecular pentad capable of sequential electronic energy transfer and intramolecular charge transfer†

Anthony Harriman,^a Patrycja Stachelek,^a Alexandra Sutter^b and Raymond Ziessel^{*b}

An extended molecular array, comprising three distinct types of chromophores and two additional redox-active subunits, that harvests photons over most of the visible spectral range has been synthesized and characterised. The array exhibits a rich variety of electrochemical waves when examined by cyclic voltammetry but assignment can be made on the basis of control compounds and molecular orbital calculations. Stepwise electronic energy transfer occurs along the molecular axis, corresponding to a gradient of excitation energies, to populate the lowest-energy excited state of the ultimate acceptor. The latter species, which absorbs and emits in the far-red region, enters into light-induced charge transfer with a terminal amine group. The array is relatively stable under illumination with white light but degrades slowly via a series of well-defined steps, the first of which is autocatalytic. One of the main attributes of this system is the capability to harvest an unusually high fraction of sunlight while providing protection against exposure to UV light.

Received 7th July 2015,
Accepted 27th August 2015

DOI: 10.1039/c5cp03932k

www.rsc.org/pccp

Introduction

In attempting to mimic certain features of natural photosynthesis,¹ especially with respect to the fundamental processes leading to charge separation,² an inordinately wide diversity of molecular systems has been examined.^{3–8} In the main, these materials are intended to exhibit directed electronic energy transfer (EET) along the molecular axis by way of positioning chromophores according to their respective excitation energies.⁹ Other molecular systems^{10–15} have been designed to duplicate the efficient light-induced charge transfer (CT) inherent to the natural reaction centre complex. In studying such molecules, much fundamental information has been learned about the factors that control the dynamics of EET and/or CT in artificial systems, although many of the subtleties of the living organism have evaded capture in the form of an artificial analogue. Less attention has been given to the study of molecular architectures that successfully combine EET and CT at the same site, even though certain structures are able to achieve this feat.^{16–18} In particular, the vast plethora of molecular dyads, triads, tetrads, *etc.* known to realise a cascade of EET steps contain few examples where the

terminal energy acceptor is linked to a redox centre in such a way that charge-transfer chemistry can take place. We now describe a giant molecular pentad as a prototype of this generic field of hybrid EET/CT molecular edifices. Our specific interest in such molecular systems is to engineer photochemical heat engines that might be suitable for solar heating of domestic water supplies.

The target system comprises two pyrene (PYR) residues attached via the boron atom to a conventional boron dipyrromethene (BODIPY) dye. The latter unit is well known¹⁹ to serve as an acceptor for excitation energy localised momentarily on one of the pyrene fragments. An expanded boron dipyrromethene (ExBOD) dye, differing from BODIPY by way of increased π -conjugation²⁰ provided by the styryl functions attached at the 3,5-positions, is attached to BODIPY through the respective pseudo-*meso* site. This type of connection, when used in conjunction with methyl groups at the 1,7-positions, ensures that each *meso*-phenylene ring lies essentially orthogonal to the dipyrromethene core. The styryl fragments are equipped with a triphenylamine (TPA) residue that is known to be rather easily oxidised²¹ in polar solvents. The final piece of the structure consists of a dithiocyclopentane (DTC) unit intended to act as a conduit for CT between TPA and ExBOD. The overall molecule, which adopts a bifurcated geometry because of the nature of the connections, has a fully extended length of 46.7 Å. This molecule is surprisingly soluble in common organic solvents at room temperature and maintains electronic isolation for each of the five critical components, at least according to the computed molecular orbital description to

^a Molecular Photonics Laboratory, School of Chemistry, Bedson Building, Newcastle University, Newcastle upon Tyne, NE1 7RU, UK.
E-mail: Anthony.harriman@ncl.ac.uk

^b Ecole de Chimie, Polymères et Matériaux, 25, rue Becquerel, 67087 Strasbourg, France

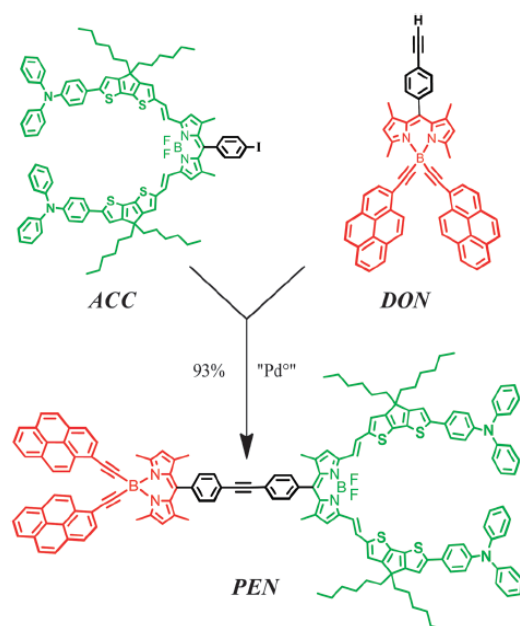
† Electronic supplementary information (ESI) available: Full experimental details, molecular orbital descriptions of control compounds, kinetic plots and additional spectroscopic output to support the text. See DOI: 10.1039/c5cp03932k

be discussed later. Three main chromophores, namely PYR, BODIPY and ExBOD, combine to harvest light over the wavelength range from 250 to 800 nm while the DTC fragments provide additional protection against UV photons. It will be appreciated that these chromophores have been arranged according to their respective excitation energy levels (PYR > BODIPY > ExBOD) so as to favour a cascade of EET steps following from selective excitation of pyrene.

Results and discussion

Synthesis and characterisation

The target multi-chromophoric light harvester PEN was prepared according to Scheme 1.† The red (DON) and green (ACC) modules were prepared and purified as described previously²² and their molecular structures were established unambiguously by NMR spectroscopy. The key cross-coupling reaction between DON and ACC is realized in the presence of catalytic amounts of $[Pd(PPh_3)_4]$ under anaerobic conditions.²³ Purification by column chromatography on flash silica was straightforward and additional purification was ensured by crystallization from appropriate solvents. The highly soluble PEN compound was isolated in 93% yield. The analytically pure compound was analysed by NMR and mass spectroscopy and by elemental composition, unambiguously confirming the molecular structure of the target compound. In particular, the mass analysis revealed a molecular peak at 2281.1 ($[M]$, 100% intensity) with successive fragments



Scheme 1 Synthetic strategy used for the preparation of the artificial light harvester PEN as examined in this account.

† Full experimental details are provided as part of the ESI.†

assigned to the release of fluorine atoms at 2262.1 ($[M - F]$, 30%) and 2243.1 ($[M - 2 F]$, 15%). No additional significant fragmentation peaks are observed. A representation of the computed energy-minimised structure is provided as part of the ESI.†

Cyclic voltammetry

Cyclic voltammetry studies were conducted with the target compound, PEN, dissolved in deaerated CH_2Cl_2 containing background electrolyte at room temperature. To aid the assignment of the various peaks, comparable studies were carried out with the isolated molecular fragments DON and ACC. It was also necessary to consult literature reports for somewhat related BODIPY-based compounds. The main results are summarized in Table 1 and indicate the following principal points: firstly, a single quasi-reversible wave is seen for DON on reductive scans and attributed to the formation of the BODIPY-based π -radical anion. The corresponding half-wave potential ($E_{1/2}$) is -1.42 V vs. SCE. For ACC, two waves are seen on reductive scans. The first wave has an $E_{1/2}$ value of -1.00 V vs. SCE but the second wave is electrochemically irreversible and exhibits a cathodic peak potential of -1.63 V vs. SCE. It is possible to assign²⁴ the first reduction wave to the formation of the π -radical anion associated with the ExBOD fragment but it is not obvious as to exactly which part of the extended conjugation path is included in the respective molecular orbitals. Likewise, the second wave is not easily attributable to reduction of a particular molecular fragment without further information. The target compound, PEN, exhibits three reductive waves with successive $E_{1/2}$ values of -1.02 , -1.39 and ca. -1.80 V vs. SCE. The first two waves are quasi-reversible and can be attributed to one-electron reduction of ExBOD and BODIPY units, respectively. The third wave, being electrochemically irreversible, occurs at strongly cathodic potentials and appears to be associated with the ExBOD unit. Again, more precise identification demands a proper understanding of the nature of the molecular orbitals involved.

On oxidative scans, DON exhibits two waves. The first wave corresponds to the formation of the BODIPY-based π -radical cation, which being quasi-reversible has an $E_{1/2}$ value of $+0.93$ V vs. SCE. The second oxidative step is irreversible and appears to be associated with the pyrene unit. In fact, it is well known²⁵ that one-electron oxidation of aryl hydrocarbons is often followed by rapid association of the π -radical cation with a neutral molecule, thus forming a dimer π -radical cation. Three quasi-reversible waves are observed for ACC under anodic scans. The first wave, having an $E_{1/2}$ of $+0.38$ V vs. SCE, is most likely associated with the one-electron oxidation of one or both of the TPA units but the remaining two waves cannot be assigned without further information. The same is true for the three oxidative waves associated with PEN. Here, the first wave is quasi-reversible and corresponds to the removal of one electron. The second wave has the appearance of two overlapping peaks and is also quasi-reversible while the third wave is electrochemically irreversible.

In fact, quantum chemical calculations suggest that both the LUMO and the HOMO associated with DON are localized on the BODIPY unit (Fig. S4, ESI†). Furthermore, HOMO(−1) lies

Table 1 Summary of the electrochemical properties recorded for **PEN** and the two isolated compounds **ACC** and **DON** in CH_2Cl_2 containing $n\text{Bu}_4\text{NPF}_6$ as a supporting electrolyte

Compound	$E^{\text{ox}}(\text{ox, soln})$ (V), ΔE^{a} (mV)	$E^{\text{red}}(\text{red, soln})$ (V), ΔE^{b} (mV)
ACC	+0.38 (60), +0.83 (60), +1.00 (60)	−1.00 (70), −1.63 (irr.) ^c
DON	+0.93 (60), +1.39 (irr.)	−1.42 (60)
PEN	+0.38 (60), +0.83 (60), +1.29 (irr.)	−1.02 (70), −1.39 (80), −1.80 (irr.)

^a Refers to oxidative processes. ^b Refers to reductive processes. ^c Irr. refers to an irreversible electrochemical step.

on one of the pyrene units. This situation is entirely in keeping with the above assignment of the cyclic voltammograms. The LUMO associated with ACC is distributed over the styryl-dipyrrin without real penetration onto the DTC units while LUMO(1) appears to be localized on one of the styryl-DTC fragments and is two-fold degenerate (Fig. S5, ESI†). A logical pattern is now apparent for PEN, with the first reduction step being associated with ExBOD and the second with BODIPY (Fig. 1). The third reductive step can now be assigned to the irreversible reduction of the tolane-like spacer unit, this being unique to the assembled supermolecule, while the next components in line for reduction are the two DTC fragments. The LUMO includes an important contribution from the styryl arms and reaches the first thiophene ring.

The HOMO localized on ACC is essentially centred on one of the TPA fragments (Fig. S5, ESI†), although it stretches onto the attached thiophene ring, and is essentially two-fold degenerate. This finding tends to confirm the above assertion that the

observed $E_{1/2}$ value of +0.38 V vs. SCE is due to one-electron oxidation of a terminal TPA unit. According to the MO description, the next component to be oxidized will be ExBOD. Here, the corresponding HOMO reaches onto the styryl arms but not onto the appended DTC units. Thus, one-electron oxidation of ExBOD can be assigned an $E_{1/2}$ value of +0.83 V vs. SCE for ACC. The third wave recognized in the cyclic voltammograms can be attributed to one-electron oxidation of the styryl-DTC fragments and occurs with $E_{1/2}$ of +1.00 V vs. SCE. For the supermolecule PEN, the first oxidation step is clearly associated with the terminal TPA units (Fig. 1), as occurs with ACC. The next oxidative process can be safely assigned to one-electron oxidation of the styryl-dipyrrin fragment present in ExBOD. The corresponding $E_{1/2}$ value becomes +0.83 V vs. SCE, exactly as found for ACC. According to the MO descriptors, the two overlapping peaks centred at around 1.3 V vs. SCE can be attributed to the successive one-electron oxidation of the DTC fragment and the conventional BODIPY unit, respectively.

Absorption and emission spectroscopy

The absorption spectrum recorded for PEN in CH_2Cl_2 solution shows a rich variety of optical transitions stretching across the entire visible range and into the near-UV region (Fig. 2). These transitions can be assigned on the basis of spectra recorded for the reference compounds, with assistance from the scientific literature. Firstly, the absorption transitions associated with ExBOD can be observed at relatively low energy, with the 0,0 band being located at 813 nm and with a pronounced vibronic shoulder at 750 nm. There is essentially no spectral shift between spectra recorded for ACC and PEN over the wavelength region from 550 to 900 nm, thereby indicating that the two BODIPY-based chromophores are not in strong electronic communication. No doubt, the orthogonal phenyl rings help in keeping these chromophores in mutual electronic isolation.

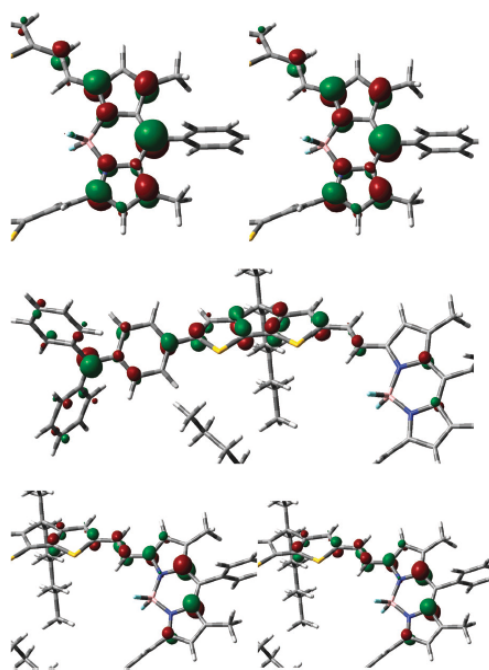


Fig. 1 Kohn-Sham representations of LUMO(1) (upper left panel), LUMO (upper right panel), HOMO (centre panel), HOMO(−1) (lower left panel) and HOMO(−3) (lower right panel) for fragments of PEN at an isodensity of 0.02.

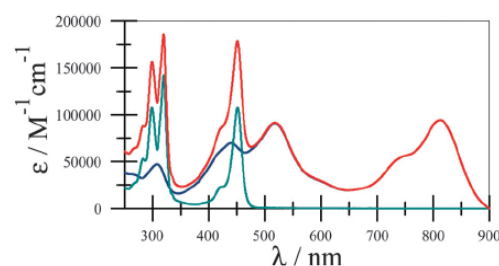


Fig. 2 Absorption spectra recorded for PEN (red curve), ACC (blue curve) and DON (cyan curve) in CH_2Cl_2 solution.

The conventional BODIPY dye has a significant absorption transition centred at 502 nm for DON and at 504 nm for PEN. This transition can be seen clearly in the spectrum recorded for PEN, although there is a pronounced spectral overlap with transitions localized on ExBOD. The terminal pyrene chromophores exhibit a series of strong absorption transitions in the near-UV region, giving rise to sharp absorption bands at 276, 286, 351 and 371 nm for PEN (Fig. 2). Again, it has to be stressed that these bands are contaminated by weaker absorption due to ExBOD and, to a lesser extent, by BODIPY. It is not possible to clearly identify optical transitions associated with either TPA or DTC chromophores, although these are known²⁶ from earlier studies conducted with the relevant molecular fragments.

Fluorescence can be observed from PEN in CH₂Cl₂ solution following excitation into any of the various chromophores (Fig. 3). Thus, excitation at 750 nm gives rise to a relatively weak emission centred at about 910 nm that agrees closely with that recorded for ACC under the same conditions. The fluorescence quantum yield (Φ_F), measured in CH₂Cl₂ at room temperature, is 0.013 while the singlet-excited state lifetime (τ_S) measured at 900 nm is 230 ps. The excitation spectrum is in fairly good agreement with the optical absorption spectrum recorded across the entire visible range, although the corresponding spectrum is less than perfect in the region around 500 nm. Both Φ_F (=0.011) and τ_S (=260 ps) are closely comparable to values recorded for ACC in CH₂Cl₂ solution. In contrast, fluorescence from the BODIPY unit, which is clearly evident at around 515 nm for DON in CH₂Cl₂ solution (Fig. S6, ESI†) where Φ_F = 0.57 and τ_S = 3.7 ns, can hardly be resolved from the baseline. As a crude estimate, emission from the BODIPY fragment present in PEN corresponds to a Φ_F value in the region of 10^{-4} while τ_S (<30 ps) is too short to be resolved by the conventional time-correlated, single photon counting methodology. No emission could be attributed to the pyrene fragments,²⁷ despite the fact that ethynylpyrene emits strongly in the region around 400–440 nm.

An interesting feature of the emission spectra recorded for PEN in CH₂Cl₂ solution at room temperature relates to the pronounced hot fluorescence band seen at ca. 690 nm (Fig. 3 inset). For these experiments, the excitation wavelength was 480 nm,

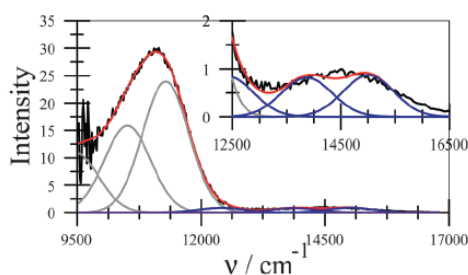


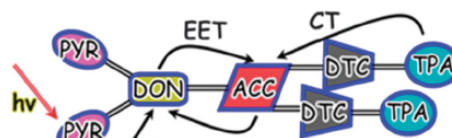
Fig. 3 Fluorescence spectrum recorded for PEN in CH₂Cl₂ solution (black curve) and the best fit to a series of Gaussian-shaped vibronic components, with the combined fit shown in red and the individual bands shown in grey. The inset shows the same pattern for the hot emission bands.

corresponding to the preferential absorption by the BODIPY unit. The same hot emission is seen for ACC under the same conditions. Spectral curve-fitting analysis, based on the assumption of Gaussian-shaped components, indicates that the spontaneous fluorescence emitted by ExBOD has a major vibronic component of ca. 800 cm⁻¹ (Fig. 3 inset). The same value is recovered for both PEN and ACC and is independent of the excitation wavelength. The hot emission observed for PEN following excitation into the BODIPY unit corresponds to a vibronic mode of ca. 1460 cm⁻¹. Now, the energy gap between 0,0 vibrational levels for S₁ states associated with the donor and the acceptor is 7540 cm⁻¹ but EET is more likely to populate the S₂ state of the acceptor, since the relevant energy gap is reduced to 565 cm⁻¹. The remaining excess excitation energy will be lost due to rapid intramolecular vibrational cooling and it is here that the 1460 cm⁻¹ mode could play an important role.

Charge transfer involving the terminal ExBOD unit

Analysis of the cyclic voltammetry results, taken together with the optical absorption and fluorescence data, argues against the occurrence of light-induced charge transfer between the two BODIPY-based chromophores following selective excitation into ExBOD. This situation is confirmed by the observation that both Φ_F and τ_S remain insensitive to the presence of the appended BODIPY unit. Thus, although emission from the ExBOD fragment in both ACC and PEN appears to be heavily quenched, it is not because of interaction with the nearby BODIPY unit. Instead, quenching of the excited-singlet state of ExBOD, in both molecules, is likely to arise from charge transfer from the terminal TPA group (Scheme 2). There is a modest thermodynamic driving force (ΔG = -0.15 eV) for this process in CH₂Cl₂ solution and the interspersed DTC fragment might be expected to function as an effective conduit²⁸ for intramolecular charge transfer along the molecular axis. This is because the spacer unit is also redox active and could promote through-bond charge transfer by way of superexchange interactions.²⁹ It is also important to stress that earlier work³⁰ has described such light-induced charge transfer in somewhat related molecular architectures.

Pump-probe (FWHM = 120 fs) transient absorption spectroscopy with excitation at 420 nm carried out with ACC in CH₂Cl₂ solution showed the rapid formation of the S₁ state associated with the ExBOD chromophore (Fig. 4). This assignment can be made on the basis of the pronounced bleaching at 815 nm and the appearance of stimulated emission at 900 nm. Decay of the S₁ state follows first-order kinetics, with a lifetime of 225 ± 25 ps,



Scheme 2 Simplistic representation of the various events that follow from selective excitation into one of the pyrene units: EET and CT refer, respectively, to electronic energy transfer and light-induced charge transfer.

to restore the pre-pulse baseline. There is no obvious indication for transient formation of charge-separated species and, in particular, the TPA radical cation cannot be detected in the spectral window at around 740 nm where it is known³¹ to display a broad but weak absorption band. The indication, therefore, is that charge recombination ($\Delta G = -1.30$ eV) occurs too quickly for significant build-up of any transient species. In fact, charge recombination is likely to be promoted by super-exchange interactions with the bridging DTC unit. Similar results were observed with PEN in CH_2Cl_2 solution following laser excitation at 420 nm.

Electronic energy transfer along the molecular axis

Previous work¹⁹ has established that rapid EET occurs from pyrene to BODIPY in several disparate molecular dyads of comparable structure to DON. Such EET is usually quantitative and this is certainly the case for DON. The excitation spectrum agrees well with the absorption spectrum across the region where the pyrene chromophores absorb strongly and this is highly suggestive of efficacious intramolecular EET. We presume that the absence of fluorescence from the pyrene units present in PEN is also because of highly effective EET across the ethynylene bond. This process has been studied in detail^{9,19} in simpler molecular structures, where the timescale for intramolecular EET is on the order of a few ps. There is every indication that the same situation holds for both DON and PEN.

A careful comparison of excitation and absorption spectra recorded for PEN in CH_2Cl_2 leads us to the conclusion that intramolecular EET from BODIPY to ExBOD accounts for about 85% of the fate of the first-excited state. Since fluorescence from S_1 is unimportant for PEN, in contrast to DON where $\Phi_F = 0.57$, it follows that an additional nonradiative process competes with EET. According to the results of the cyclic voltammetry experiments, there is a modest thermodynamic driving force ($\Delta G = -0.19$ eV) for light-induced charge transfer from ExBOD to the first-excited singlet state of BODIPY in CH_2Cl_2 solution. In fact, this is the only allowed charge-transfer process

between the two main chromophores. It seems likely that this reaction is responsible for the incomplete match between excitation and absorption spectra. In principle, the occurrence of intramolecular charge transfer can be scrutinised³⁰ by pump-probe transient absorption spectroscopy but it is essentially impossible to isolate a suitable excitation wavelength in the case of PEN. This is because of the strong spectral overlap between BODIPY and ExBOD in the region around 500 nm, together with the difficulty to generate certain excitation wavelengths. As such, we have not been able to confirm this competition for PEN.

The situation is improved when the experiment involves recording time-resolved fluorescence following excitation at 500 nm with a short duration (FWHM = 110 ps) laser diode. Under these conditions, approximately 60% of absorbed photons enter the BODIPY chromophore, with the remaining 40% being partitioned to the ExBOD unit. The latter emits in the far red region but shows no appreciable fluorescence in the wavelength range around 530 nm. Monitoring at this wavelength (Fig. 5), which is close to the peak of the emission expected for BODIPY, allows determination of the singlet-excited state lifetime of the latter emitter to be 22 ± 6 ps. The rather large uncertainty arises because of the limited temporal resolution available under these experimental conditions. Taking due account of the comparative excitation spectra, it is now possible to estimate rate constants for intramolecular EET ($k_{\text{EET}} = 3.9 \times 10^{10} \text{ s}^{-1}$) and charge transfer ($k_{\text{CT}} = 7 \times 10^9 \text{ s}^{-1}$) from the first-excited state of BODIPY to ExBOD.

Photochemical stability

In order to explore the possibilities for developing artificial light-harvesting antennae based on molecular arrays³² such as PEN, attention has been given to the inherent photostability of the ExBOD chromophore.³³ Thus, a solution of ACC in deaerated CH_2Cl_2 was exposed to simulated sunlight delivered using a 450 W solar illuminator. At early stages of the reaction, the chromophore bleaches slowly under exposure to white light (Fig. 6). A series of isosbestic points is evident during this phase of illumination and

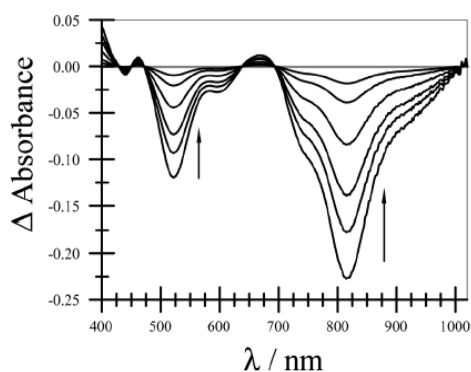


Fig. 4 Differential transient absorption spectra recorded following excitation of ACC in deaerated CH_2Cl_2 solution with a short laser pulse at 420 nm: individual traces (average of 100 shots) were recorded at delay times of 0, 55, 110, 215, 350 and 550 ps.

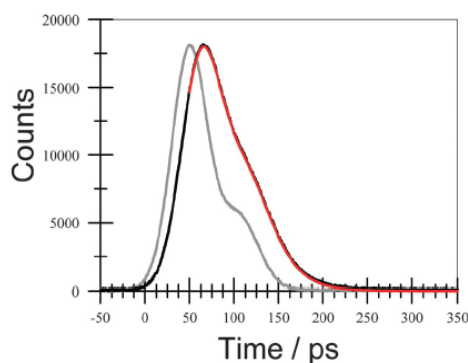


Fig. 5 Time-resolved fluorescence decay curve recorded for PEN in CH_2Cl_2 following excitation at 500 nm. The instrumental response function is shown as a grey curve while the fit to the experimental data is shown as a red curve. Emission was detected at 530 ± 25 nm.

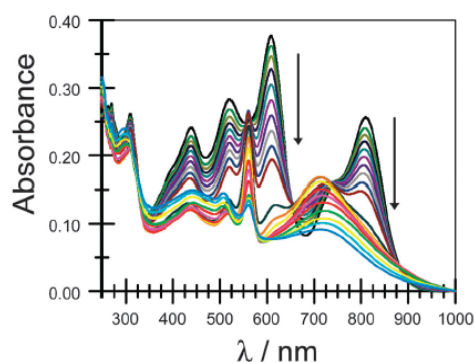


Fig. 6 Effect of continuous illumination with white light on the absorption spectrum recorded for ACC in deaerated CH_2Cl_2 . The arrows indicate the initial stage of bleaching. Spectra were recorded at regular time intervals over the course of eight hours.

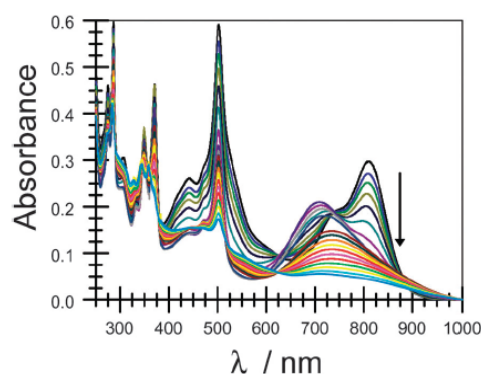


Fig. 7 Effect of continuous illumination with white light on the absorption spectrum recorded for PEN in deaerated CH_2Cl_2 . Spectra were recorded at regular intervals over a period of ten hours.

similar bleaching rates are found across the entire visible spectral range. Under typical illumination conditions, the initial rate of bleaching is *ca.* 5 nM min^{-1} . At any given wavelength, the bleaching process gives a poor fit to first-order kinetics but shows much better correlation with an autocatalytic mechanism as shown in Fig. S7 (ESI†).³⁴ In the latter case, a product formed during early stages of photolysis enhances the rate of bleaching. Fitting the experimental data to such a mechanism³⁴ across the entire wavelength range allows calculation of the inherent rate constant (k_0) to be 0.0012 min^{-1} and the rate constant for autocatalysis (k_c) to be $0.0018 \mu\text{M}^{-1} \text{ min}^{-1}$. New products are apparent by way of a broad absorption peak centred at around 720 nm and a sharp absorption band centred at 560 nm. These two absorption bands form at the same rate, which agrees with the rate of bleaching of the ExBOD chromophore and, as such, are considered to be the primary products of the bleaching reaction. On continuing the illumination, both products begin to fade at a relatively fast rate to leave a broad absorption band stretching from about 650 to 350 nm. This secondary bleaching step only proceeds once the bleaching of ExBOD is complete. Both absorption bands bleach *via* approximately first-order kinetics with the same rate constant (k_b) of 0.0025 min^{-1} .

The absorption band seen at around 720 nm has the general appearance of a charge-transfer transition while that at 560 nm is what might be expected for an expanded BODIPY derivative possessing limited π -conjugation.²² Our analysis, however, does not allow identification of the products. An interesting feature of this progressive bleaching chemistry is that both 560 nm and 720 nm absorbing species remain fluorescent so that the ability to sensitise a solar cell or photochemical reaction is not lost and the optical bandgap remains very similar at around 1.4 eV. Furthermore, bleaching of the ultimate product is extremely slow when compared to a solution of Texas Red, the latter being our recommended standard for photochemical bleaching.

Turning our attention to the full array, PEN, in deaerated CH_2Cl_2 solution, it is apparent that illumination with white

light causes bleaching of the ExBOD chromophore (Fig. 7). As for the control compound, the initial bleaching step corresponds to an autocatalytic reaction (Fig. S8, ESI†).³⁴ Analysis across the entire spectral window allows derivation of k_0 and k_c , respectively, to be 0.0012 min^{-1} and $0.0049 \mu\text{M}^{-1} \text{ min}^{-1}$. It will be recognised that whereas k_0 remains identical to that found for ACC, the corresponding rate constant for autocatalysis is considerably faster (*i.e.*, almost a factor of 3-fold) for PEN than for ACC despite the fact that bleaching is associated with the ExBOD chromophore in both cases. It can also be seen from the spectral traces that bleaching of ExBOD gives rise to the same charge-transfer absorption band at 710 nm but there is no indication for formation of the absorption band centred at 560 nm. Bleaching of the 710 nm absorption band can be approximated to a first-order process with a rate constant of 0.0032 min^{-1} . Again, this is faster than observed with ACC ($k_b = 0.0025 \text{ min}^{-1}$), which might be a consequence of the increased photon flux due to the improved light-harvesting characteristics of PEN compared to ACC. At 502 nm, where both ACC and DON make significant contributions to the total absorbance, the early segment of the bleaching reaction agrees perfectly with autocatalytic bleaching of ExBOD. On longer time scales, the BODIPY chromophores undergo slow bleaching by approximately first-order kinetics with a rate constant of 0.0019 min^{-1} . It is not practical to monitor bleaching rates for the pyrene chromophore because of the build-up of a permanent product in the near-UV region. The latter species, which remains fluorescent, bleaches very slowly under white-light illumination.

Attempts were made to follow the bleaching process for PEN using 700 MHz ^1H -NMR spectroscopy in a dilute solution (*ca.* 10^{-4} M). From the data (see Fig. S3 ESI† for a representative example) some general conclusions can be drawn but the product is a complex mixture of compounds. It appears that the DON part of the PEN chromophore is not damaged at a significant level, according to the analysis of the diagnostic signal of the pyrene moiety at 8.63 ppm in CD_2Cl_2 . The most fragile part of the molecule, as might be expected, is the ACC

fragment which undergoes major modifications of the β -pyrrolic protons. This situation most likely reflects an attack of the vinylic system. Several new products are formed as can be testified by the presence of at least three new singlets at around 6.0 ppm and the new peaks likely assigned, in light of reference compounds, to the dithiocyclopentane fragments. The high intensity of the latter peaks attests to the presence of several products displaying similar molecular frameworks.

Conclusions

This work considers the electrochemical, photophysical and photochemical properties of a large supermolecule built up by logical positioning of individual subunits. The assembled array absorbs across the entire visible spectral range and in the near-IR region. Essentially, more than 99% of the absorbed photonic energy is converted into heat in less than 1 ns. There are many molecular assemblies that degrade excitation energy into heat but an attractive feature of PEN is that it absorbs over a very wide spectral range. As such, it possesses the main attributes needed for an organic-based photochemical heat engine, provided the material is sufficiently stable under prolonged exposure to sunlight. A key feature of this molecular array is that photodegradation occurs *via* a series of steps leading to a gradual loss of performance. Each of these bleaching steps decreases the fraction of solar light that can be harvested but does not curtail the solar heating process. The net result is that the array functions for extended periods, especially when dispersed in an inert polymer.

The compound displays a rich variety of electrode-active reactions, together with highly efficacious intramolecular EET along the molecular axis. The ExBOD-based acceptor enters into charge-transfer reactions with the terminal amine units, no doubt promoted by super-exchange interactions involving the interspersed dithiocyclopentane unit, so that fluorescence is kept to a modest level. On exposure to sunlight, photons can enter the system at any of the principle chromophores but inevitably reach the ExBOD site and thereby promote the charge-transfer reaction. The quantum yield for this process is *ca.* 90%, although the rate is modest, and leads to a transient state possessing around 1.3 eV of redox energy. This charge-transfer state deactivates quickly, at least relative to its rate of formation, thereby serving the purpose of an effective photochemical molecular heating system.

Acknowledgements

We thank Newcastle University and ECPM-Strasbourg for financial support of this work. Further funding from EPSRC (Seed Corn Fund) and CNRS is gratefully acknowledged. We are grateful to Dr Corrine Wills for recording the NMR traces during photobleaching and to Dr Anna Gakamsky (Edinburgh Photonics) for recording the far-red emission spectra and lifetimes.

Notes and references

- 1 B. Alberts, A. Johnson, J. Lewis, M. Raff, K. Roberts and P. Walker, *Mol. Biol. Cell*, Garland Science, New York, ch. 14, 2002.
- 2 J. Fajer, D. C. Brune, M. S. Davis, A. Forman and L. D. Spaulding, *Proc. Natl. Acad. Sci. U. S. A.*, 1975, 72, 4956–4960.
- 3 J. S. Hsiao, B. P. Krueger, R. W. Wagner, T. E. Johnson, J. K. Delaney, D. C. Mauzerall, G. R. Fleming, J. S. Lindsey, D. F. Bocian and R. J. Donohue, *J. Am. Chem. Soc.*, 1996, 118, 11181–11193; H. E. Song, C. Kirmaier, J. K. Schwartz, E. Hindin, L. H. Yu, D. F. Bocian, J. S. Lindsey and D. Holten, *J. Phys. Chem. B*, 2006, 110, 19121–19130.
- 4 J. Iehl, J. F. Nierengarten, A. Harriman, T. Bura and R. Ziessel, *J. Am. Chem. Soc.*, 2012, 134, 831–845; R. Ziessel, G. Ulrich, A. Haeferle and A. Harriman, *J. Am. Chem. Soc.*, 2013, 135, 11330–11344.
- 5 Y. Nakamura, N. Aratani and A. Osuka, *Chem. Soc. Rev.*, 2007, 36, 831–845; J. Yang, M. C. Yoon, H. Yoo, P. Kim and D. Kim, *Chem. Soc. Rev.*, 2012, 41, 4808–4826; I. W. Hwang, N. Aratani, A. Osuka and D. Kim, *Bull. Korean Chem. Soc.*, 2005, 26, 19–31.
- 6 A. N. Macpherson, P. A. Liddell, D. Kuciauskas, D. Tatman, T. Gillbro, D. Gust, T. A. Moore and A. L. Moore, *J. Phys. Chem. B*, 2002, 106, 9424–9433; C. Roger, M. G. Muller, M. Lysetska, Y. Miloslavina, A. R. Holzwarth and F. Wurthner, *J. Am. Chem. Soc.*, 2006, 128, 6542–6543.
- 7 M. J. Leonardi, M. R. Topka and P. H. Dinolfo, *Inorg. Chem.*, 2012, 51, 13114–13122; H. Imahori, *J. Phys. Chem. B*, 2004, 108, 6130–6143.
- 8 M. S. Choi, T. Yamazaki, I. Yamazaki and T. Aida, *Angew. Chem., Int. Ed.*, 2004, 43, 150–158; F. Wurthner, T. E. Kaiser and C. R. Saha-Moeller, *Angew. Chem., Int. Ed.*, 2011, 50, 3376–3410; H. Tamiaki, T. Miyatake, R. Tanikaga, A. R. Holzwarth and K. Schaffner, *Angew. Chem., Int. Ed. Engl.*, 1996, 35, 772–774.
- 9 R. Ziessel and A. Harriman, *Chem. Commun.*, 2011, 47, 611–631.
- 10 M. R. Wasielewski, *Acc. Chem. Res.*, 2009, 42, 1910–1921; M. R. Wasielewski, *J. Org. Chem.*, 2006, 71, 5051–5066; V. Balzani, A. Credi and M. Venturi, *ChemSusChem*, 2008, 1, 26–58; D. Nocera, *Acc. Chem. Res.*, 2012, 45, 767–776; S. Fukuzumi, *Phys. Chem. Chem. Phys.*, 2008, 10, 2283–2297.
- 11 Y. Nakamura, N. Aratani and A. Osuka, *Chem. Soc. Rev.*, 2007, 36, 831–845; N. Aratani, D. Kim and A. Osuka, *Acc. Chem. Res.*, 2009, 42, 1922–1934; D. M. Guldi, H. Imahori, K. Tamaki, Y. Kashiwagi, H. Yamada, Y. Sakata and S. Fukuzumi, *J. Phys. Chem. A*, 2004, 108, 541–548.
- 12 A. Harriman and J.-P. Sauvage, *Chem. Soc. Rev.*, 1996, 25, 41–46; J.-P. Collin, A. Harriman, V. Heitz, F. Odobel and J.-P. Sauvage, *Coord. Chem. Rev.*, 1996, 148, 63–69.
- 13 D. M. Guldi, *Chem. Soc. Rev.*, 2002, 31, 22–36; F. D'Souza and O. Ito, *Coord. Chem. Rev.*, 2005, 249, 1410–1422; L. Hammarström, *Curr. Opin. Chem. Biol.*, 2003, 7, 666–673; K. J. Elliott, A. Harriman, L. Le Pleux, Y. Pellegrin, E. Blart, C. R. Mayer and F. Odobel, *Phys. Chem. Chem. Phys.*, 2009, 11, 8767–8773.

- 14 M. R. Wasielewski, *Chem. Rev.*, 1992, 92, 435–461; D. Gust, T. A. Moore and A. L. Moore, *Acc. Chem. Res.*, 2001, 34, 40–48; D. Gust, T. A. Moore and A. L. Moore, *Acc. Chem. Res.*, 2009, 42, 1890–1898.
- 15 L. C. Sun, L. Hammarstrom, B. Akermark and S. Styring, *Chem. Soc. Rev.*, 2001, 30, 36–49; T. S. Balaban, *Acc. Chem. Res.*, 2005, 38, 612–623.
- 16 A. Harriman and R. Ziessel, *Chem. Commun.*, 1996, 1707–1716; M. H. V. Huynh, D. M. Dattelbaum and T. J. Meyer, *Coord. Chem. Rev.*, 2005, 249, 457–483.
- 17 F. D'Souza, P. M. Smith, M. E. Zandler, A. L. McCarty, M. Itou, Y. Akari and O. Ito, *J. Am. Chem. Soc.*, 2004, 126, 7898–7907; B. Rybtchinski, L. E. Sinks and M. R. Wasielewski, *J. Am. Chem. Soc.*, 2004, 126, 12268–12269.
- 18 G. Kodis, C. Herrero, R. Palacios, E. Marino-Ochoa, S. Gould, L. de la Garza, R. van Grondelle, D. Gust, T. A. Moore and A. L. Moore, *J. Phys. Chem. B*, 2004, 108, 414–425; R. Ballardini, A. Credi, M. T. Gandolfi, F. Marchioni, S. Silvi and M. Ventura, *Photochem. Photobiol. Sci.*, 2007, 6, 345–356.
- 19 A. Harriman, L. J. Mallon and R. Ziessel, *Chem. – Eur. J.*, 2008, 14, 11461–11473; A. Harriman, G. Izzet and R. Ziessel, *J. Am. Chem. Soc.*, 2006, 128, 10868–10875; C. Goze, G. Ulrich, L. J. Mallon, D. B. Allen, A. Harriman and R. Ziessel, *J. Am. Chem. Soc.*, 2006, 128, 10231–10239; R. Ziessel, C. Goze, G. Ulrich, M. Cesario, P. Retailleau, A. Harriman and J. P. Rostron, *Chem. – Eur. J.*, 2005, 11, 7366–7378.
- 20 R. Ziessel, P. Retailleau, K. J. Elliott and A. Harriman, *Chem. – Eur. J.*, 2009, 15, 10369–10374; M. E. El-Khouly, S. Fukuzumi and F. D'Souza, *ChemPhysChem*, 2014, 15, 30–47; W.-J. Shi, M. E. El-Khouly, K. Ohkubo, S. Fukuzumi and D. K. P. Ng, *Chem. – Eur. J.*, 2013, 19, 11332–11341; F. D'Souza, A. W. Amin, M. E. El-Khouly, N. K. Subbaiyan, M. E. Zandler and S. Fukuzumi, *J. Am. Chem. Soc.*, 2012, 134, 654–664; A. Eggenspieler, A. Takai, M. E. El-Khouly, K. Ohkubo, C. P. Gros, C. Bernhard, C. Goze, F. Denat, J. M. Barbe and S. Fukuzumi, *J. Phys. Chem. A*, 2012, 116, 3889–3898.
- 21 C. Lambert and G. Noll, *Synth. Met.*, 2007, 139, 57–62.
- 22 R. Ziessel, S. Rihn and A. Harriman, *Chem. – Eur. J.*, 2010, 16, 11942–11953.
- 23 A. Sutter and R. Ziessel, *Synlett*, 2014, 1466–1472.
- 24 G. Ulrich, R. Ziessel and A. Harriman, *Angew. Chem., Int. Ed. Engl.*, 2008, 47, 1184–1201.
- 25 J. L. Sessler, Y. Kubo and A. Harriman, *J. Phys. Org. Chem.*, 1992, 5, 644–648.
- 26 Y. Li, L. Xue, H. Xia, B. Xu, S. Wen and W. Tian, *J. Polym. Sci., Part A: Polym. Chem.*, 2008, 46, 3970–3984.
- 27 A. Harriman, M. Hissler and R. Ziessel, *Phys. Chem. Chem. Phys.*, 1999, 1, 4203–4211; A. C. Benniston, A. Harriman, D. J. Lawrie and S. A. Rostron, *Eur. J. Org. Chem.*, 2004, 2272–2276.
- 28 K. E. Linton, M. A. Fox, L. O. Palsson and M. R. Bryce, *Chem. – Eur. J.*, 2015, 21, 3997–4007.
- 29 M. N. Paddon-Row, *Aust. J. Chem.*, 2003, 56, 729–748.
- 30 T. Roland, E. Heyer, L. Liu, A. Rue, S. Ludwigs, R. Ziessel and S. Haacke, *J. Phys. Chem. C*, 2014, 118, 24290–24301.
- 31 M. Oyama, N. Nozaki and S. Okazaki, *Anal. Chem.*, 1991, 63, 1387–1392.
- 32 R. Ziessel, G. Ulrich, A. Haefele and A. Harriman, *J. Am. Chem. Soc.*, 2013, 135, 11330–11344.
- 33 A. Harriman, P. Stachelek, A. Sutter and R. Ziessel, *Photochem. Photobiol. Sci.*, 2015, 14, 1100–1109.
- 34 F. Mata-Perez and J. F. Perez-Benito, *J. Chem. Educ.*, 1987, 64, 925–927.

Solvent-Driven Conformational Exchange for Amide-Linked Bichromophoric BODIPY Derivatives

■ Dyes/Pigments

Solvent-Driven Conformational Exchange for Amide-Linked Bichromophoric BODIPY Derivatives

Shrikant Thakare,^[b] Patrycja Stachelek,^[a] Soumyaditya Mula,^[c] Ankush B. More,^[b] Subrata Chattopadhyay,^[c] Alok K. Ray,^[d] Nagaiyan Sekar,^[b] Raymond Ziessel,^[e] and Anthony Harriman^{*[a]}

Abstract: The fluorescence lifetime and quantum yield are seen to depend in an unexpected manner on the nature of the solvent for a pair of tripartite molecules composed of two identical boron dipyrromethene (BODIPY) residues attached to a 1,10-phenanthroline core. A key feature of these molecular architectures concerns the presence of an amide linkage that connects the BODIPY dye to the heterocyclic platform. The secondary amide derivative is more sensitive to environmental change than is the corresponding tertiary amide. In general, increasing solvent polarity, as measured by the static dielectric constant, above a critical threshold

tends to reduce fluorescence but certain hydrogen bond accepting solvents exhibit anomalous behaviour. Fluorescence quenching is believed to arise from light-induced charge transfer between the two BODIPY dyes, but thermodynamic arguments alone do not explain the experimental findings. Molecular modelling is used to argue that the conformation changes in strongly polar media in such a way as to facilitate improved rates of light-induced charge transfer. These solvent-induced changes, however, differ remarkably for the two types of amide.

Introduction

The amide bond plays a special role in biochemistry—it provides the key structural features needed to assemble helical peptides and folded proteins.^[1,2] Indeed, the amide carbonyl function is less electrophilic than in ketones, aldehydes and carboxylic acids, while sp^2 hybridisation renders the nitrogen atom non-basic.^[3] This last point is well illustrated by the fact that protonation of amides in acidic media occurs at the oxygen atom. In general, the amide group persists in two tautomeric forms; namely, the amide and iminol structures.^[4] However, the amide form is generally considered as a set of

zwitterionic resonance structures (Scheme 1). In each case, both *trans* and *cis* forms are possible. The partial double-bond character imposed on the central C–N bond helps position the atoms around the amide bond such that they reside in the same plane and provides a high (i.e., 10–25 kcal mol^{−1}) barrier for internal rotation.^[4d] In most proteins, the amide-*trans* tautomer (Scheme 1) is the more stable species, but the corresponding amide-*cis* form has been clearly recognised by X-ray crystallography. Indeed, the amide-*cis* tautomer is often found in simple amides, such as formamide and *N*-methylacetamide.^[5] Much less information is available regarding the possible occurrence of amide-iminol tautomerism for the amide bond (Scheme 1), although this situation is interesting from the theoretical viewpoint.^[6] Such transformations, which require a large structural rearrangement, might be more easily accomplished in solution, especially in the presence of hydrogen-bonding solvents. It is also significant that the amide oxygen atom is a good hydrogen-bond acceptor, while the nitrogen atom is an effective hydrogen-bond donor. This aspect of amide chemistry is of crucial importance in terms of establishing the secondary structures of proteins, enzymes, bacteria, viruses and so forth and has been studied in great detail.^[7]

The amide bond, although relatively small, might be expected to help dictate the global structures of large organic molecules and even supramolecular entities.^[8] This realisation takes on additional importance when allowance is made for the fact that the amide linkage can be sensitive to changes in the local environment. We now report bichromophoric molecules, BAB(H) and BAB(ET), wherein two identical boron dipyrromethene (BODIPY) dyes are appended at the 2,9-positions of

[a] P. Stachelek, Prof. Dr. A. Harriman
Molecular Photonics Laboratory, School of Chemistry
Newcastle University, Bedson Building, Newcastle upon Tyne, NE1 7RU (UK)
E-mail: anthony.harriman@ncl.ac.uk

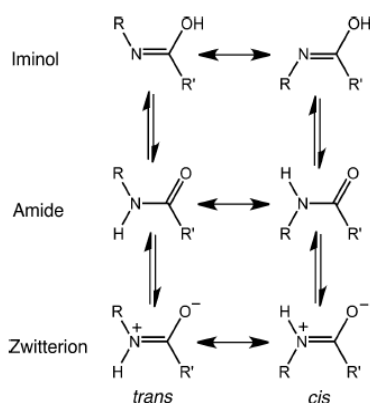
[b] S. Thakare, A. B. More, Prof. N. Sekar
Department of Dyestuff Technology, Institute of Chemical Technology
Mumbai 400019 (India)

[c] Dr. S. Mula, Prof. S. Chattopadhyay
Bio-Organic Division, Bhabha Atomic Research Centre
Mumbai 400085 (India)

[d] Prof. A. K. Ray
Laser and Plasma Technology Division, Bhabha Atomic Research Centre
Mumbai 400085 (India)

[e] Dr. R. Ziessel
Laboratoire de Chimie Organique et Spectroscopies Avancées (LCOSA)
Ecole Européenne de Chimie, Polymères et Matériaux
Université de Strasbourg, 25 rue Becquerel
67087 Strasbourg Cedex 02 (France)

Supporting information for this article can be found under <http://dx.doi.org/10.1002/chem.201602354>.



Scheme 1. Major tautomeric and resonance forms of the amide bond; the positive charge assigned to the nitrogen atom should not be taken literally, since the overall electronic charge at this site is likely to remain negative.

a 1,10-phenanthroline residue by way of amide connectors (Figure 1). Such BODIPY dyes are highly fluorescent markers^[9] that, at least in the case of monomeric dyes, are insensitive to the nature of the surrounding medium, temperature or pressure.^[10] The specific intention of this work is to explore whether the amide bond, which constitutes less than 3 % of the total solvent-accessible surface area of the supermolecule, can exert control over the molecular geometry. It might be noted that there is a complete library of BODIPY derivatives bearing aryl hydrocarbons attached directly to the dipyrin backbone or through the pseudo-*meso*-position,^[9] but none of these structures use an amide spacer as the means by which to interconnect the terminals.

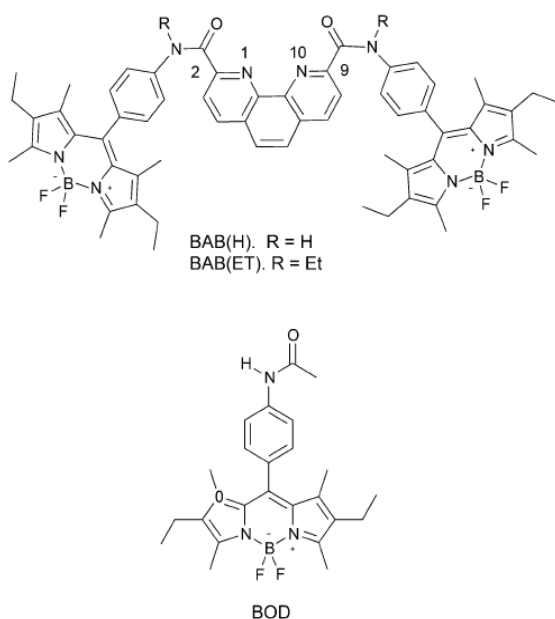


Figure 1. Molecular formulae of the new BODIPY-based bichromophores, BAB(H) and BAB(ET), and of the control compound, BOD.

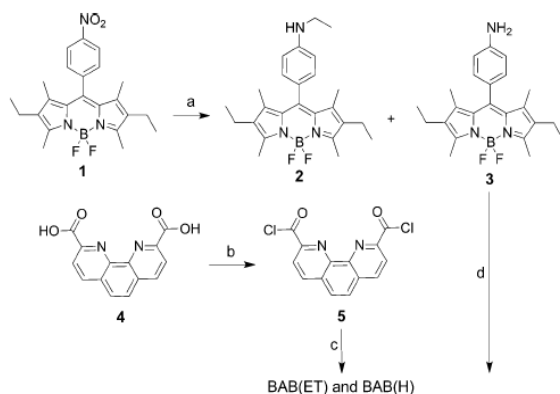
Our strategy is based on the realisation that the BODIPY dyes are likely to be strongly fluorescent when embedded in a solvent reservoir.^[11] Rotations around the connecting units should ensure that the two BODIPY dyes remain mutually independent and it might be noted that NMR spectra are fully consistent with this notion. In the event that the amide connector responds to changes in the nature of the surrounding solvent, the molecular conformation might be expected to change in such a way that the two BODIPY fluorophores are brought into closer proximity. In turn, this effect should be visualised by a change in the overall fluorescence output. The idea behind using 1,10-phenanthroline is to make use of its well-known ability^[12] to complex cations from solution, including protons. It is also apparent that repulsion between lone-pairs on the carbonyl and aza-nitrogen atoms should help establish the molecular conformation. If successful, this approach could be adapted to generate related structural changes brought about by external or internal triggering so that the kinetics for the folding and/or unfolding steps might be monitored. Such information could be helpful in terms of better understanding the critical issues of protein denaturation^[13] and unfolding.^[14]

Results and Discussion

Synthesis and characterisation

Synthesis of the target bichromophoric molecules BAB(ET) and BAB(H), which differ only in terms of the substitution pattern at the amide sites, was aided by earlier work^[15] which explored the catalytic hydrogenation of the corresponding mononuclear BODIPY derivative, **1**, bearing a *meso*-4-nitrophenyl group. Thus, the Pd-catalysed hydrogenation of **1** in a mixture of dichloromethane and ethanol at 25 °C gave the expected amino-BODIPY **3** as the only product. However, when the reaction was carried out in a mixture of acetonitrile and ethanol at 70 °C, dye **2** was the major product along with a small amount of **3** (2:3 = 95:5) (Scheme 2). Apparently, the initially formed **3** is readily transformed to **2** by an in situ reaction with CH₃CN.^[16] Compound **3** was acetylated with acetyl chloride in CH₂Cl₂ to obtain the control compound, BOD, in 81 % yield (Figure 1 and Scheme 2). The target compounds BAB(ET) and BAB(H) were synthesised by reacting 1,10-phenanthroline-2,9-diacetyl chloride^[17] with **2** and **3**, respectively. After workup and purification by flash chromatography, the desired compounds were isolated in 42% and 52% yield, respectively (Scheme 2).

The target compounds were characterised fully by NMR spectroscopy, giving well-defined spectra. For example, in the case of dye BAB(H), aromatic protons of the 1,10-phenanthroline unit appear as two different sets of signals. Protons of the central aromatic ring resonate as a singlet at 8.04 ppm, whereas the other aromatic protons exhibit two doublets at 8.57 and 8.74 ppm. The methyl groups of the BODIPY moieties resonate as singlets at 1.35 and 2.50 ppm, while the ethyl groups resonate as quartets (2.22 ppm) and triplets (0.91 ppm). The aromatic phenyl protons of the two BODIPY units are found as doublets at 7.33 and 8.11 ppm with the expected 4-proton integration for each signal. A diagnostic signal is provided by



Scheme 2. Synthetic scheme for preparation of dyes **2**, **3**, BAB(ET), BAB(H) and BOD. Reagents and conditions: a) H_2 , 10% Pd/C (10%), H_2O , EtOH/ CH_3CN (1:1), 70 °C (for **2**) and H_2 , 10% Pd/C (10%), H_2O , CH_2Cl_2 /EtOH (1:1), 25 °C (for **3**); b) SOCl_2 , reflux, 24 h; c) **2** (for BAB(ET))/**3** (for BAB(H)), Et_3N , CH_2Cl_2 , 25 °C, 24 h; d) CH_3COCl , CH_2Cl_2 , 25 °C, 12 h.

the N–H proton which is found as a singlet at 10.88 ppm. The ^{13}C NMR spectra present the expected 4 and 15 signals for the alkyl and aromatic carbon atoms, respectively. The amide carbonyl signal is found at 162.1 ppm in CDCl_3 .

Electrochemistry

Cyclic voltammetry studies were carried out for the target compounds, BOD, BAB(ET) and BAB(H), in both CH_2Cl_2 and CH_3CN with tetra-*N*-butylammonium hexafluorophosphate as the supporting electrolyte and the main results are summarised in Table 1. The control compound, BOD, exhibits quasi-reversible one-electron oxidation and reduction steps with half-wave potentials of +0.95 V and –1.40 V versus SCE, respectively, that can be assigned to formation of the corresponding π -radical cation and anion, respectively (Figure 2).^[18] The amide function has no effect on the reduction potentials and does not make a direct contribution to the cyclic voltammograms. The two solvents give comparable results. For BAB(ET), similar oxidation and reduction processes are observed, with much the same half-wave potentials to those noted for the control compound, and there are no undue effects associated with the bridging 1,10-phenanthroline unit. With the bichromophore, however, both processes involve the quasi-reversible transfer of two electrons. That the two electrons are transferred at the same potential is taken as testimony to the fact that the BODIPY units do not interact in an electronic sense.

Although BAB(H) displays similar behaviour to that noted for BAB(ET), there is indication for the one-electron reduction of the 1,10-phenanthroline-based bridge at about –1.6 V versus SCE (Figure 2). The appearance of this wave is attributed to internal hydrogen bonding between the aza-N atom and the amide proton. In fact, this situation was confirmed by IR spectroscopy. The significance of these results is that light-induced charge transfer between the BODIPY units and the bridging 1,10-phenanthroline unit is thermodynamically unfavourable,

Table 1. Electrochemical data recorded for the target BODIPY-based dyes in CH_2Cl_2 .^[a]

Compound	E_{ox}^0 [V] (ΔE [mV])	E_{red}^0 [V] (ΔE [mV])
BOD	+0.57 (32)	–1.77 (74)
BAB(ET)	+0.61 (66)	–1.69 (70)
BAB(H)	+0.60 (82)	–1.69 (62); –1.98 (78)

[a] Half-wave potentials determined by cyclic voltammetry in deoxygenated CH_2Cl_2 , containing 0.1 M TBAPF₆, at a solute concentration of 1.5 mM at 25 °C. Potentials were standardised using ferrocene (Fc) as an internal reference and the half-wave potentials are reported relative to the Fc/Fc^+ couple. Error in half-wave potentials is ± 15 mV.

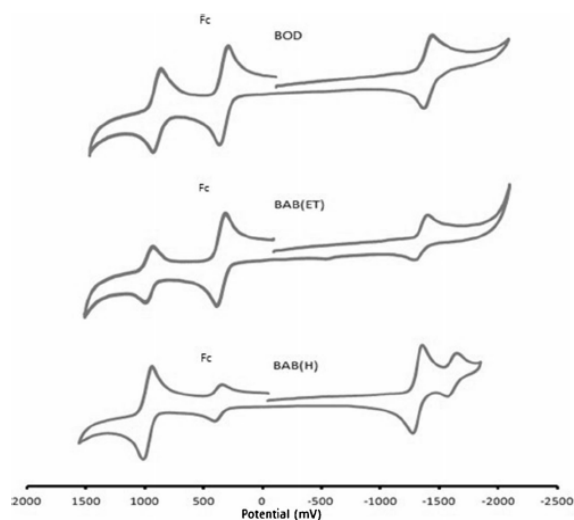


Figure 2. Typical cyclic voltammograms recorded for the target compounds (ca. 2 mM) in de-aerated CH_2Cl_2 containing background electrolyte. Note Fc refers to ferrocene used as internal standard. The lower axis corresponds to mV versus SCE.

even in polar solvents. The electrochemistry also indicates that there is no electronic interaction between the appended BODIPY residues.

Photophysical properties

The absorption and fluorescence spectra recorded for the control compound, BOD, in tetrahydrofuran (THF) at room temperature are entirely in accord with what might be expected for a conventional BODIPY dye.^[9] The absorption maximum (λ_{max}) lies at 523 nm while the emission maximum (λ_{em}) is found at 536 nm. Both values are unremarkable when considered in terms of related BODIPY derivatives.^[19] Moreover, both the fluorescence quantum yield ($\Phi_{\text{F}}=0.80$) and excited-singlet-state lifetime ($\tau_{\text{S}}=5.9$ ns) are in line with values recorded for structurally related dyes.^[9,19] There is excellent agreement between absorption and excitation spectra and the time-resolved emission decay profiles are well described by mono-exponential fits. Changes in solvent polarity have little effect on these

various parameters, although the absorption and emission maxima do respond slightly to changes in solvent polarisability.^[20] Spectral properties recorded for the bichromophores under identical conditions are closely comparable to those recorded for BOD (Table 2, Figure 3). Thus, we can conclude that there are no undue electronic effects associated with either the amide linker or the 1,10-phenanthroline spacer. In THF, the quantum yields and excited-state lifetimes recorded for BAB(ET) and BAB(H) are comparable to those found for BOD, although fluorescence is decreased slightly, especially for BAB(H) (Table 2). For the two bichromophores, excitation and absorption spectra are in close agreement and time-resolved decay curves remain mono-exponential over at least three half-lives. The presence of molecular oxygen does not affect the derived properties, while changes in solvent polarity have only minimal effect on the absorption and emission spectral maxima and on the band half-widths.

Table 2. Comparison of the photophysical properties determined for the target compounds in THF at room temperature.						
Compound	λ_{max} [nm]	λ_{fl} [nm]	Φ_{F}	τ_{S} [ns]	SS [cm ⁻¹] ^[a]	k_{rad} [$\times 10^8$ s ⁻¹] ^[b]
BOD	523	536	0.80	5.9	465	1.38
BAB(H)	522	540	0.73	5.4	640	1.40
BAB(ET)	524	538	0.75	5.5	500	1.40

[a] SS refers to the Stokes' shift for normalised spectra. [b] Radiative rate constant calculated from the Strickler–Berg expression.

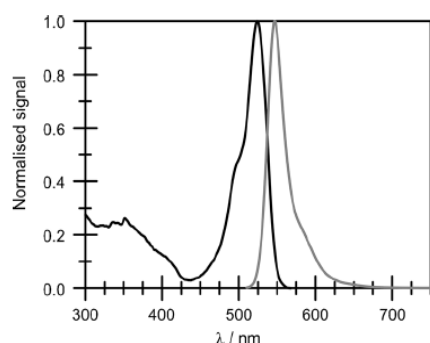


Figure 3. Normalised absorption (black curve) and fluorescence (grey curve) spectra recorded for BAB(H) in THF at room temperature.

The photophysical properties of the tertiary amide derivative, BAB(ET), were recorded in a range of organic solvents of differing dielectric constant, ϵ_{s} , and the results are summarised in Table 3. The variation in Φ_{F} is small across the range of solvents, despite ϵ_{s} changing from 2 to 47, and there is no noticeable influence of hydrogen-bond donor solvents. On close scrutiny, it seems that there is a gradual decrease in Φ_{F} with increasing solvent polarity, but the effect is shallow and certain solvents do not follow the generic pattern. The excited-state lifetime measured in the same series of solvents decreases with increasing solvent polarity in much the same manner as

found for the quantum yield. However, in polar solvents ($\epsilon_{\text{s}} > 10$) the quality of the statistical fit to a mono-exponential decay falls below the satisfactory level.^[21] This fit can be judged best in terms of the randomness of the weighted residuals,^[22] but is also evident in an increased chi-squared parameter (χ^2) and in the Durbin–Watson term (note: χ^2 is given in Table 3). Inclusion of a short-lived (i.e., < 1 ns) or long-lived (i.e., > 10 ns) component did not improve the quality of the fit. However, analysis of the decay curves as dual-exponential fits with lifetimes in the range of 5–7 ns and 1–3 ns gave superior (i.e., more random) residuals and χ^2 parameters closer to unity. Furthermore, the fractional contribution (A_1) of the shorter-lived component (τ_1) was found to increase in significance with increasing solvent polarity (see Supporting Information). Although the two lifetimes are too close for unique solutions to be extracted from these fits, the dual-exponential behaviour appears to better represent the situation in polar solution. Even so, certain hydrogen-bond acceptor solvents, specifically *N,N*-diethylformamide, *N,N*-diethylacetamide and dimethylsulfoxide, appear to behave anomalously.

At relatively low levels of precision, the dual-exponential or stretched-exponential fits give an adequate representation of the time-resolved emission decay profiles. At higher levels of precision, these fits become less satisfactory in terms of the randomness of the residuals and it is necessary to add a third exponential term. Even so, unique solutions could not be recovered from data collected over different time scales or count rates. An additional problem is that the derived lifetimes are too similar for accurate analysis. Under such conditions, it is impossible to justify the use of two or three discrete lifetimes

Table 3. Effect of solvent dielectric constant on the photophysical properties of BAB(ET) as recorded at room temperature.

Solvent	ϵ_{s}	Φ_{F}	τ_{S} [ns] ^[a]	k_{rad} [$\times 10^8$ s ⁻¹]	χ^2 ^[b]
toluene	2.43	0.78	5.74	1.36	0.95
dibutyl ether	3.18	0.83	6.85	1.21	0.92
diethyl ether	4.33	0.86	6.35	1.35	1.05
CHCl ₃	4.89	0.85	6.45	1.32	1.07
ethyl acetate	6.02	0.82	6.60	1.24	1.06
MTHF	7.47	0.79	6.60	1.20	0.99
THF	7.58	0.75	5.85	1.28	0.96
CH ₂ Cl ₂	9.02	0.78	6.17	1.26	1.12
heptyl cyanide	13.0	0.68	6.10	1.12	1.30
valeronitrile	20.0	0.58	6.00	0.97	1.43
acetone	21.4	0.67	6.00	1.12	1.12
ethanol	24.3	0.48	5.60	0.86	1.39
butyronitrile	24.6	0.55	5.90	0.93	1.52
nitropropane	27.3	0.46	5.55	0.83	1.87
propionitrile	28.9	0.44	5.60	0.79	1.51
DEF ^[c]	29.0	0.66	6.05	1.09	1.09
chloroacetonitrile	30.0	0.51	4.85	1.05	1.73
methanol	33.6	0.43	4.15	1.04	1.87
acetonitrile	37.5	0.35	3.35	1.05	2.20
DEA ^[d]	38.3	0.66	5.65	1.17	1.32
DMSO ^[e]	46.7	0.64	5.74	1.11	1.28

[a] Lifetime of the excited-singlet state based on a single-exponential fit. [b] Reduced chi-squared parameter associated with the single-exponential fit. [c] DEF = *N,N*-Diethylformamide. [d] DEA = *N,N*-Diethylacetamide. [e] DMSO = Dimethylsulfoxide.

as opposed to a continuous distribution of lifetimes. Certainly, the molecular structure is not suggestive of several discrete conformations because of what might be considered facile rotations. This situation is not uncommon in fluorescence spectroscopy, especially with regards to biologically relevant materials, and has led to the introduction of the maximum entropy method^[23] (MEM). This analytical approach, modified to increase reliability about the zero-time shift,^[24] allows recovery of the shape of distributions of lifetimes. The MEM method allows determination of the coefficients of an exponential series of pre-set lifetimes isolated from correlation effects and instrumental oscillations.

Using a variety of time ranges for each sample, it proved possible to recover reproducible lifetime distributions for BAB(ET) in polar and weakly polar solvents. In each case, the longer-lived species gave a lifetime of around 4–6 ns, while the shorter-lived component was in the region of 1–2 ns (Figure 4a). There was no evident correlation between mean lifetime and solvent polarity, but the total contribution of the shorter-lived species, integrated as a Gaussian profile, increased progressively with increasing ϵ_s (see Supporting Information). Thus, based on the MEM analysis, there appears to be a wide variety of slowly interconverting conformers that fall into two loose families, which differ in terms of the relative radiative probability of the BODIPY fluorophores.

It might be important to stress that ϵ_s is not the only means for expressing solvent polarity^[25] and, in fact, several alternatives are available. These include Reichardt's empirical ET(30) parameter,^[26] the Kirkwood factor,^[27] and the Catalan SPP^[28] and SB^[29] factors. It is not the purpose of the present investigation to critically compare these solvent descriptors, but it should be emphasised that similar behaviour is noted in all cases with regards to the polarity effect on fluorescence probability.

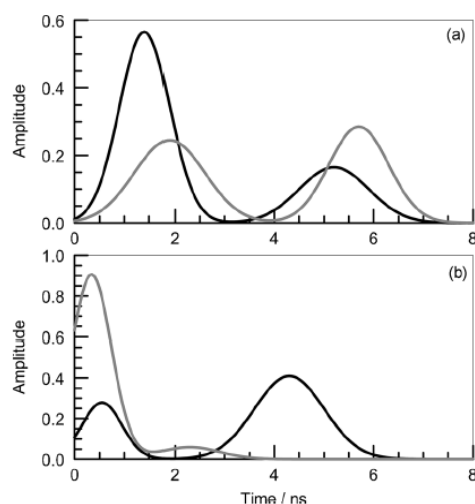


Figure 4. Maximum entropy method plots derived by fitting the deconvoluted emission decay curves for a) BAB(ET) and b) BAB(H) in butyronitrile (grey curve) and acetonitrile (black curve). See the text and Table 5 for the derived parameters.

An increased level of solvent sensitivity is displayed by BAB(H) across the same series of solvents (Table 4). In general, increasing ϵ_s tends to decrease Φ_F , although the overall behaviour is non-linear and again there are a few anomalous solvents, which were identified as being acetone ($\epsilon_s=21.4$), *N,N*-diethylformamide ($\epsilon_s=29$), *N,N*-diethylacetamide ($\epsilon_s=38.3$) and dimethylsulfoxide ($\epsilon_s=46.7$) and are hydrogen-bond acceptors. As such, these solvents might be expected to form a hydrogen bond with the amide proton and thereby perturb the molecular conformation. Otherwise, protic and aprotic solvents follow a common trend and there is no indication that solvent attachment to the aza-N atoms is important in the fluorescence quenching process. In mixtures of THF ($\epsilon_s=7.6$) and acetonitrile ($\epsilon_s=37.5$), Φ_F decreases progressively with increasing mole fraction of acetonitrile, while that for BOD, used as the control, shows no such effect (Figure 5).

Table 4. Effect of solvent dielectric constant on the photophysical properties of BAB(H) as recorded at room temperature.

Solvent	ϵ_s	Φ_F	τ_s [ns] ^[a]	k_{rad} [$\times 10^8$ s ⁻¹]	χ^2 ^[b]
toluene	2.43	0.60	4.19	1.43	1.02
dibutyl ether	3.18	0.65	4.50	1.44	0.96
diethyl ether	4.33	0.71	5.15	1.38	0.97
CHCl ₃	4.89	0.73	5.52	1.32	1.10
ethyl acetate	6.02	0.74	5.23	1.41	1.08
MTHF	7.47	0.73	4.88	1.50	1.18
THF	7.58	0.73	5.36	1.36	1.14
CH ₂ Cl ₂	9.02	0.63	5.40	1.17	1.38
heptyl cyanide	13.0	0.66	5.20	1.27	1.53
valeronitrile	20.0	0.56	5.14	1.10	1.82
acetone	21.4	0.50	5.18	0.97	1.48
ethanol	24.3	0.46	4.60	1.00	1.94
butyronitrile	24.6	0.44	4.55	0.97	2.11
nitropropane	27.3	0.39	3.57	1.11	1.82
propionitrile	28.9	0.23	1.96	1.12	2.35
DEF ^[c]	29.0	0.48	4.85	1.00	1.60
chloroacetonitrile	30.0	0.21	1.91	1.10	2.28
methanol	33.6	0.19	1.00	1.90	2.35
acetonitrile	37.5	0.07	0.74	0.95	3.10
DEA ^[d]	38.3	0.42	3.92	1.07	2.23
DMSO ^[e]	46.7	0.12	0.90	1.33	1.93

[a] Lifetime for the excited-singlet state as recovered from single-exponential fits. [b] Reduced chi-squared parameter associated with the singlet-exponential fits. [c] DEF = *N,N*-diethylformamide. [d] DEA = *N,N*-diethylacetamide. [e] DMSO = dimethylsulfoxide.

As above, the fluorescence decay curves recorded for BAB(H) could be analysed satisfactorily in terms of mono-exponential fits in non-polar (i.e., $\epsilon_s < 8$) solvents. However, with increasing solvent polarity the quality of the exponential fit was seen to worsen; this judgement was based^[21] on the reduced chi-squared parameters (χ^2 in Table 4) and the randomness^[22] of the weighted residuals. Furthermore, the radiative rate constant ($k_{rad} = \Phi_F/\tau_s$) adopts a strong dependence on solvent polarity that does not seem justified.^[30] The quality of the fit improved on inclusion of a second component, corresponding to a species with a shorter lifetime, but analysis of different decay profiles recorded for the same solvent on differing time bases

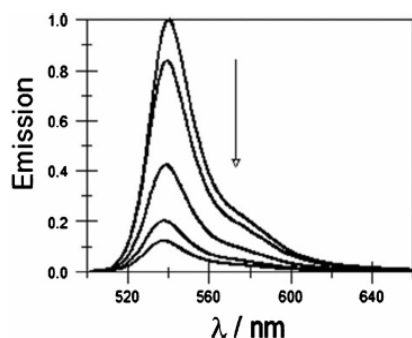


Figure 5. Effect of solvent composition on the fluorescence intensity recorded for BAB(H). The arrow indicates the direction of increasing mole fraction of acetonitrile in the mixture with THF; individual spectra refer to acetonitrile mole fractions of 0, 0.44, 0.61, 0.76 and 1.0.

did not return unique lifetime values. Again, data collected at high precision required analysis in terms of three discrete lifetimes.

Using the MEM analytical approach, it was possible to realise reproducible fits to two broad distributions of lifetimes in polar and weakly polar solvents (Figure 4b). The shorter-lived distribution had a mean lifetime of about 0.5 ns, while the second series correspond to a mean lifetime of about 3 ns (Table 5). The total contribution of the shorter component increased in more polar solvents but the mean lifetime did not correlate with ϵ_s . We are led to the conclusion that the reduced quantum yield arises from increased population of a family of bichromophores more susceptible to intramolecular fluorescence quenching. The nature of the solvent determines the extent of this population but there is no relationship between the level of quenching inherent to that family and the solvent polarity.

Table 5. Summary of the parameters derived from the MEM-based analysis of the time-resolved emission data collected for BAB(H) in polar solvents at room temperature.

Solvent	ϵ_s	τ_A [ns] ^[a]	τ_B [ns]	A_1	χ^2 ^[b]
CH ₂ Cl ₂	9.02	1.80	5.1	0.14	1.51
heptyl cyanide	13.0	0.84	5.5	0.14	1.47
valeronitrile	20.0	0.30	4.85	0.16	1.90
acetone	21.4	1.45	3.9	0.09	1.15
ethanol	24.3	1.00	3.65	0.10	1.44
butyronitrile	24.6	0.55	4.3	0.28	1.09
nitropropane	27.3	0.23	3.75	0.25	1.68
propionitrile	28.9	0.33	3.65	0.45	1.47
chloroacetonitrile	30.0	0.27	2.5	0.48	1.36
methanol	33.6	1.10	0.65	0.80	1.90
acetonitrile	37.5	0.34	2.3	0.91	1.15
DMSO ^[c]	46.7	0.80	2.9	0.95	1.33

[a] Mean lifetime for the shorter-lived component derived from fitting the distribution to a Gaussian profile. [b] Reduced chi-squared parameter associated with the fit between simulated and experimental decay curves. [c] DMSO = dimethylsulfoxide.

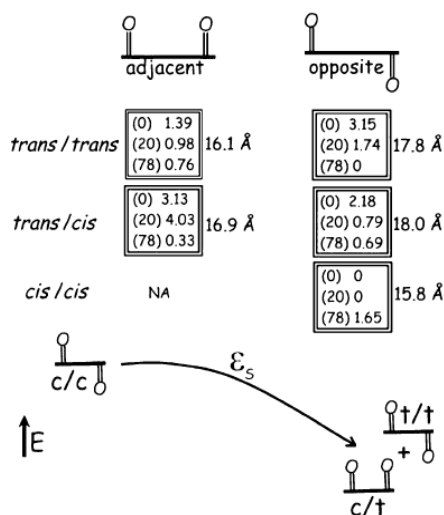
Fluorescence quenching

In consideration of the fluorescence quenching mechanism, we draw attention to the similar qualitative behaviour of the two compounds, but note that fluorescence quenching is much more pronounced for BAB(H) than for BAB(ET). The two bichromophores exhibit comparable optical spectroscopy and electrochemistry such that the disparate quenching level displayed in any given solvent cannot be ascribed to thermodynamic effects. The only chemical difference between the compounds relates to the substitution pattern around the amide linker. These linkers are not in electronic communication with the excited state localised on the BODIPY chromophore, suggesting that their role in the quenching event is to perturb the molecular conformation. We can also eliminate light-induced charge transfer between BODIPY and 1,10-phenanthroline as playing an important role, since such processes are thermodynamically unfavourable, unless the latter unit is protonated. Consideration of the cyclic voltammograms and taking due allowance for the excitation energy of the BODIPY chromophore, as derived from the intersection of normalised absorption and fluorescence spectra, indicates that light-induced charge transfer between the two BODIPY units is weakly exergonic in CH₂Cl₂. Indeed, the thermodynamic driving force ($-\Delta G_{CS}$) is 50 meV in the absence of electrostatic effects. This mechanism remains the most likely cause of the observed emission quenching in the target bichromophores and it is well established^[31] that the thermodynamics for light-induced charge transfer are sensitive to the nature of the solvent. It might be mentioned that other molecules containing two BODIPY-based chromophores have been observed to show excimer emission,^[32] dimerisation^[33] and light-induced charge transfer^[34] in fluid solution.

Based on existing theoretical principles,^[31,35,36] the effects of changes in solvent polarity and mutual separation distance between the reactants on ΔG_{CS} were simulated. The results are compiled in the Supporting Information in terms of driving force, solvent re-organisation energy and overall activation energy. At any given separation distance, ΔG_{CS} decreases sharply with increasing ϵ_s , but the general effect tends to saturate at moderate dielectric constant (i.e., $\epsilon_s > 10$). Similarly, at a given ϵ_s , ΔG_{CS} decreases with decreasing separation distance, but tends towards a plateau as R_{CC} exceeds about 10 Å. Similar effects are found for the activation energy, which requires knowledge of the re-organisation energy. Most of the change is expected to occur for weakly polar solvents at quite short separations.^[36,37] Although charge-transfer quenching will become more significant in polar solvents, the calculated changes in thermodynamic effects cannot explain the solvent-induced variations in fluorescence seen for these bichromophores. There are no differences in ΔG_{CS} between BAB(ET) and BAB(H), but the level of fluorescence quenching is quite disparate. Taking into account the MEM-derived results, we can conclude that there must be an accompanying solvent-induced structural change^[38] and we now examine this possibility using molecular modelling.

Molecular modelling studies (DFT, B3 LPY, 6-31G(d,p)) were undertaken with a view to better understand the mechanism of light-induced electron transfer in the two bichromophores. Starting firstly with BAB(ET), model calculations indicate that the carbonyl groups are hindered from adopting a planar orientation with the 1,10-phenanthroline unit because of steric crowding. Instead, the lowest energy configuration has the two carbonyl groups sitting almost perpendicular to the plane of the 1,10-phenanthroline nucleus. This gives rise to two interconvertible species; namely, the opposite structure having oxygen atoms pointing away from each other and the adjacent structure having the oxygen atoms pointing in the same direction (Scheme 3). For structures generated in vacuo, each amide group adopts the *cis* geometry, with the opposite form providing the more stable species. The same situation holds for structures calculated in a solvent reservoir of $\epsilon_s = 20$. However, in weakly polar solvents, there is increased likelihood that one of the carbonyl groups adopts the *trans* geometry. In water, the lowest energy conformation has both carbonyl groups existing as the *trans* species, although the mixed *trans/cis* geometry is only marginally less stable in polar media. This matrix of computed structures is illustrated in Scheme 3 and it might be stressed that it is not possible to generate a reasonable geometry for the hypothetical *cis/cis* species in the adjacent form because of severe steric crowding.

Calculations made for $\epsilon_s = 20$ suggest the presence of several barriers for rotation of the carbonyl unit around the plane of the 1,10-phenanthroline residue. Thus, starting from the adjacent *trans/trans* geometry and rotating a single carbonyl



Scheme 3. Effect of solvent polarity on the computed energies for the various conformers predicted for BAB(ET). The upper panel shows energies in kcal mol⁻¹ and B-B separation distances for opposite and adjacent species; the values given in parenthesis are the solvent dielectric constants. The lower panel shows the anticipated structural evolution as the dielectric constant increases.

group, the first barrier to be encountered relates to the ethyl group moving into space occupied by the *meso*-phenyl ring of the second BODIPY unit. This barrier is slightly less than 20 kcal mol⁻¹, but can be reduced by concerted motion of the opposing phenyl ring. A more substantial barrier is raised by close approach of the ethyl-CH₂ group to the H3 atom of the aza-aromatic unit, followed by a less severe clash between the ethyl-CH₃ group and the same proton; these barriers are essentially insurmountable at ambient temperature and restrict the direction through which the carbonyl group can oscillate between opposite and adjacent sites (Figure 6a).

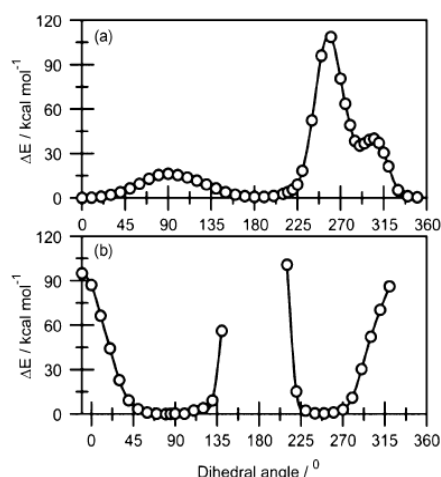


Figure 6. Rotational barriers computed for progressive twisting of one of the carbonyl groups present in BAB(ET) in a solvent reservoir with dielectric constant equal to 20. Panel a) refers to the all-*trans* form with zero degrees representing the opposite form. Panel b) refers to the *cis-trans* species with rotation around the *cis*-amide. Here, the energy-minimised geometry corresponds to a dihedral angle of 80°.

For the mixed *cis/trans* species, the carbonyl groups show only a minor preference for the opposite configuration, the difference in energy between opposite and adjacent species being only a few kcal mol⁻¹ at $\epsilon_s = 20$. Full rotation around the *cis*-amide is not possible because of severe steric clashes. The energy-minimised geometry has the carbonyl group on the *cis*-amide lying 85° to the plane of the 1,10-phenanthroline residue. Rotation in one direction causes the BODIPY unit to fold back onto the 1,10-phenanthroline nucleus, while rotation in the other direction brings the phenyl ring on the *cis*-amide into contact with the 1,10-phenanthroline H3 atom (Figure 6b). With the carbonyl groups in the adjacent configuration, rotation brings the BODIPY unit into contact with the ethyl group on the other amide. Interconversion between the opposite and adjacent configurations is possible only with concerted movement of the other BODIPY-based arm.

Similar calculations were performed for isomerisation of the amide group, starting with the *trans/trans* species with the adjacent configuration. Allowing rotation in one direction, an energy profile for isomerisation around the C-N bond^[39]

shows the maximum barrier of about 20 kcal mol^{-1} occurring at 90° , as might be expected.^[40] As the solvent polarity increases, the barrier height is raised^[41] for *trans*-to-*cis* isomerization, but decreases for the reverse step by a few kcal mol^{-1} for $\epsilon_s = 40$. Rotation in the opposite direction imposes an insurmountable barrier, in excess of $100 \text{ kcal mol}^{-1}$, which arises from steric clashes between the two BODIPY units (Figure 7). The corresponding *cis* isomer cannot be reached by this route. A similar barrier was observed for isomerisation from the opposite configuration, although here the *cis* isomer is the more favoured product in moderately polar solvents.

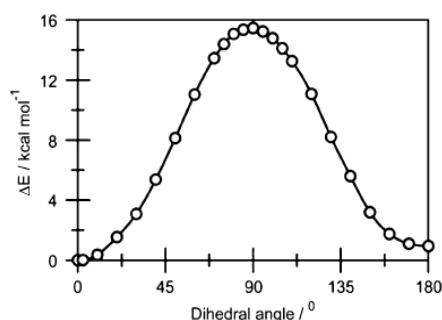


Figure 7. Rotational barrier computed for isomerisation of an amide group for BAB(ET) in a solvent reservoir with dielectric constant equal to 20. Zero degrees corresponds to the *cis*-geometry.

Molecular dynamics simulations made for the all-*trans* tautomer in a bath of water molecules ($50 \times 50 \times 50 \text{ Å}^3$)^[42] using the AMBER-03 force field^[43] indicate that the main structural motions relate to fluctuation of the carbonyl group around its connection to the 1,10-phenanthroline nucleus. At 250 K, there is no suggestion for isomerisation of the amide bond on the time scale of the simulations. Likewise, the carbonyl group does not alternate between adjacent and opposite configurations. The all-*cis* species oscillates around the mean geometry without switching to the *trans* form, at least on short simulations. As such, the two BODIPY units sample many different mutual orientations but remain at crude B–B separations of about 14–20 Å, regardless of starting geometry. None of these migratory pathways brings the BODIPY units into direct contact.

Computational studies made with BAB(H)

Attention now turns to the bichromophore built around secondary amide linkages. In order to avoid repulsion between lone pairs localised on O and aza-N atoms, the preferred dihedral angle for the carbonyl group and the heterocycle is about 90° . This configuration might be stabilised by hydrogen bonding between the carbonyl O atom and an *ortho*-phenyl-H atom.^[44] Again, there exists the possibility for opposite and adjacent forms, but these possess similar heats of formation and give rise to comparable distances between the appended BODIPY residues. The energy-minimised geometry has the amide bond

in the *trans* configuration^[45] for all solvent polarities. However, the energy difference between the all-*trans* and *cis/trans* species becomes negligible at high dielectric constant. As such, in highly polar solvents we would expect to attain almost equal populations of the all-*trans* and *cis/trans* species.

An energy profile^[46] for rotation of the carbonyl group around the connection with the 1,10-phenanthroline nucleus, while retaining the *trans* geometry, shows a modest barrier due to repulsion between the lone-pairs on carbonyl group and aza-N atom (Figure 8a). The height of this barrier decreases

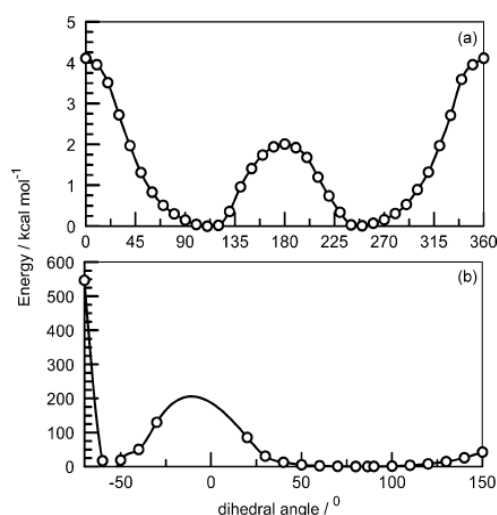


Figure 8. Rotational barriers calculated for motion of the carbonyl group around the 1,10-phenanthroline nucleus for a) the all-*trans* and b) all-*cis* geometries.

es in polar solvents and amounts to about 4 kcal mol^{-1} for $\epsilon_s = 20$. Clearly, this dihedral angle will cover a wide variance under ambient conditions. There are small differences in the calculated energies of the adjacent and opposite configurations, with increased solvent polarity moving the equilibrium position in favour of the former. This has a small effect on the average distance between the two BODIPY residues, but these units remain well separated in all cases for the *trans*-geometry.

The corresponding *cis*-amide^[47] in the mixed *cis/trans* species positions the carbonyl group orthogonal to the heterocycle. Rotation in one direction is blocked by steric clashes between the two BODIPY residues (Figure 8b). In the other direction, rotation is blocked by clashes between the phenyl ring and the 1,10-phenanthroline H3 atom. As such, the *cis* species has the propensity to bring the two BODIPY units into unusually close proximity.

The barrier for isomerisation of the amide bond is calculated^[48] to be about 15 kcal mol^{-1} for $\epsilon_s = 20$, but steric crowding between the two BODIPY residues prevents formation of the all-*cis* species. Calculations made for BAB(H) in vacuo give a barrier for isomerisation of about 32 kcal mol^{-1} , but this falls to slightly less than 15 kcal mol^{-1} in polar solvent. In fact, the

barrier height^[49] becomes almost independent of solvent polarity for $\epsilon_s > 10$. We might expect that isomerisation will be too slow to be competitive with decay of the excited singlet state, but can take place for the ground state. Furthermore, in non-polar solvents, the all-*trans* species will dominate, but a mixture of all-*trans* and *cis/trans* species should abound in solvents of higher polarity. The *trans* species can sample a wide variety of configurations through rotation of the carbonyl group, but the *cis* species experiences more restricted rotation. This situation seems to be in good accord with the MEM analysis in terms of there being two distinct groups of conformers.^[50]

Relationship between fluorescence quenching and molecular structure

We raise the hypothesis that the only viable mechanism able to account for the observed solvent effect on the emission properties of the BODIPY unit in these bichromophores is light-induced charge transfer^[31,34,51] between the terminal dyes. As such, it is instructive to enquire if the proposed changes in molecular conformation can explain the experimental observations. For BAB(ET), the two BODIPY units are held apart under all reasonable conditions to such an extent that through-space charge transfer^[52] is unlikely to compete effectively with the inherent radiative and nonradiative decay routes. Fluorescence quenching is ineffectual for this compound, except in strongly polar media. Polar solvents promote conversion of the *cis* species to the corresponding *trans* tautomer. Our modelling studies would suggest that, in strongly polar media, the bichromophore should persist as a mixture of all-*trans* and *cis/trans* isomers. Combining this result with the fluorescence behaviour, we can speculate that the *trans* geometry provides a better conduit^[53] for through-bond charge transfer. The long pathway,^[54] together with the modest thermodynamic driving force, means emission quenching will be kept at a minimum, as is observed. The mean difference between the two sets of emission lifetimes, taken together with the lifetime of the control compound, translates to a ratio of rate constants for charge-separation of twofold in favour of the *trans*-amide.

There is, in fact, ample evidence to indicate that the *trans* geometry provides a better pathway for super-exchange interactions in many different types of molecular bridge.^[55–58] This is attributed to improved electronic coupling and nicely explains the observations made with BAB(ET). The computational studies suggest that the all-*cis* species will predominate in non-polar solvents and also in weakly polar media. Strongly polar solvents, however, trigger the switch to the *trans* geometry and we would expect to see increased population of the *trans/cis* species in the more polar solvents. Isomerisation is unlikely to be competitive with inherent deactivation of the excited state. Instead, illumination of the ground-state equilibrium will produce a distribution of geometries that does not interconvert on the existing time scale. This situation would equate to two families of conformers, each displaying a range of non-radiative rate constants representing the mean geometry at the

moment of excitation. In turn, this would lead to the type of distributed lifetimes consistent with the MEM analysis.

Quite unexpectedly, there are major structural differences between BAB(ET) and BAB(H) caused by internal steric crowding and/or electronic effects. Fluorescence quenching becomes more significant for BAB(H), although the thermodynamic driving force is the same as that for BAB(ET) and there is a similar sensitivity towards solvent polarity. Calculations made for BAB(H) predict that the *trans* geometry is favoured in all solvents, this being the opposite situation to that found for BAB(ET), but polar solvent promotes transformation to the *cis* isomer. In non-polar solvents, we would expect to see only the all-*trans* species. Increasing the solvent polarity raises the possibility for finding the *trans/cis* species.

By analogy to BAB(ET), increasing the contribution of the *cis* species might be expected to extinguish through-bond charge separation. This would restore fluorescence. However, for BAB(H) the *cis/trans* species has the two BODIPY units close together, contact being possible in the extreme case, while rotation around one of the carbonyl groups further reduces the edge-to-edge separation (Figure 9). As such, the *cis* isomer can be expected to promote through-space, light-induced charge separation^[57] between the two BODIPY units. This situation would introduce a short-lived component into the decay records in polar solvents. Since each isomer samples a variety of conformations, the lifetime distributions provided by the MEM analysis appear to mirror the solvent-induced conformational change.

It might be noted that transient absorption spectral studies did not indicate the formation of an intermediate species with a lifetime longer than that of the excited-singlet state. Thus, laser excitation of BAB(ET) in deaerated CH₃CN at 400 nm indicated the presence of the S₁ state immediately after the pulse. This species is recognised by strong bleaching of the lowest-energy absorption transition centred at around 525 nm, together with weak absorption bands at higher and lower energy. There is an accompanying contribution from stimulated fluorescence. The signal decays with an approximate lifetime of 3.0 ± 0.7 ns to restore the pre-pulse baseline. Although the decay kinetics are not strictly mono-exponential, global analysis of the transient spectra recorded at different time delays showed only the S₁ state to be present. The same conclusion was reached for BAB(H) in CH₃CN, for which the recovery of the transient bleaching signal at 525 nm could be analysed as the sum of two exponential terms, with lifetimes of 0.4 ± 0.1 (80%) and 2.1 ± 0.5 ns (20%). Again, no transient species could be observed. This behaviour is not unusual and indicates that subsequent charge recombination occurs on a faster time scale than does light-induced charge transfer.^[59] The former process will be assisted by electrostatic attractive forces that should minimise separation between the two BODIPY units.

Conclusions

This work has shown that the amide linkage provides for multiple molecular conformations that differ in terms of their pro-

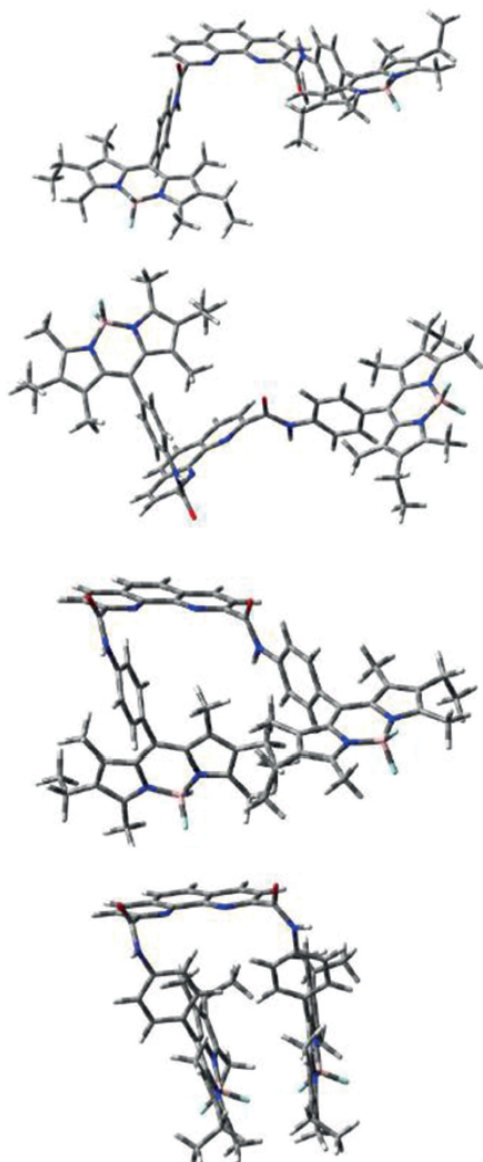


Figure 9. Snapshots of molecular conformations representing the important distributions for all-*trans* (uppermost panel), mixed-*cis/trans* (central panels), and all-*cis* (lower panel) geometries for BAB(H) in solution.

pensity to promote either through-bond or through-space charge transfer. In addition to isomerisation around the central C–N amide bond, structural complications arise from electronic interactions between the carbonyl O atom and the aza-N atom of the 1,10-phenanthroline unit. Indeed, the BODIPY-based arms attached to the heterocyclic linker provide a crude cavity wherein hydrogen-bonding and steric interactions further restrict conformational freedom to such an extent that the two target compounds appear structurally distinct. This situation is exemplified by the realisation that BAB(ET) adopts the *cis*-ge-

ometry while BAB(H) takes up the *trans*-geometry. These various conformations influence the quantum yield for fluorescence from the BODIPY appendages, but quenching is kept to a minimum by limited thermodynamics. It seems likely that these effects could be greatly amplified by appropriate choice of the terminals. Thus, the amide linkage might offer some unusual opportunities to switch between emissive and dark states under suitable stimulation. This situation is made possible because the absolute energies of the various tautomers are quite comparable, while rotational barriers will impose kinetic limitations at the excited-state level.

Experimental Section

Experimental details for the synthesis of the target compounds are provided as part of the Supporting Information. Solvents used for the spectroscopic studies were obtained from commercial sources and were checked for fluorescent impurities before use. Absorption spectra were recorded with a Hitachi U-3310 spectrophotometer while emission spectra were recorded with a Hitachi F-4500 spectrophotometer. Fluorescence spectra were recorded for optically dilute solution, the absorbance being less than 0.1 at the excitation wavelength, and were fully corrected for any instrumental imperfections. Fluorescence quantum yields were recorded relative to monomeric BODIPY derivatives already reported in the literature. Emission lifetimes were recorded via time-correlated, single photon counting methodologies using a short duration laser diode emitting at 505 nm for excitation. Quantum chemical calculations were made with TURBOMOLE and are described in more detail in the Supporting Information.

Acknowledgements

We thank Newcastle University, BRNS (BARC), and ECPM-Strasbourg for their financial support of this work. Dr. J. G. Knight (Newcastle University) is acknowledged for many helpful discussions on the chemistry of the amide bond.

Keywords: BODIPY • boron • charge transfer • conformational exchange • dyes/pigments • fluorescence • isomerisation

- [1] D. Whitford, *Proteins: Structure and Function*, Wiley, Chichester, 2005.
- [2] N. Seward, H.-D. Jakubke, *Peptides: Chemistry and Biology*, 2nd ed., Wiley-VCH, Weinheim, 2009.
- [3] E. Iglesias, L. Montenegro, *J. Chem. Soc. Faraday Trans.* **1996**, 92, 1205–1212.
- [4] a) D. B. Brown, M. B. Robin, R. D. Burbank, *J. Am. Chem. Soc.* **1968**, 90, 5621–5622; b) D. P. Fairlie, T. C. Woon, W. A. Wickramasinghe, A. C. Willis, *Inorg. Chem.* **1994**, 33, 6425–6428; c) C. R. Kemnitz, M. J. Loewen, *J. Am. Chem. Soc.* **2007**, 129, 2521–2528; d) E. M. Duffy, D. L. Severance, W. L. Jorgensen, *J. Am. Chem. Soc.* **1992**, 114, 7535–7542; e) J. Zhang, M. W. Germann, *Biopolymers* **2011**, 95, 755–762.
- [5] a) H. B. Schlegel, P. Gund, E. M. Fluder, *J. Am. Chem. Soc.* **1982**, 104, 5347–5351; b) K. B. Wiberg, P. R. Rablen, D. J. Rush, T. A. Keith, *J. Am. Chem. Soc.* **1995**, 117, 4261–4270.
- [6] K. Kamiya, M. Boero, K. Shiraishi, A. Oshiyama, *J. Phys. Chem. B* **2006**, 110, 4443–4450.
- [7] S. H. Gellman, G. P. Dado, G. B. Liang, B. R. Adams, *J. Am. Chem. Soc.* **1991**, 113, 1164–1173.
- [8] P. J. Cragg, *Supramolecular Chemistry: From Biological Inspiration to Bio-medical Applications*, Springer, Dordrecht, 2010.

- [9] a) A. Loudet, K. Burgess, *Chem. Rev.* **2007**, *107*, 4891–4932; b) G. Ulrich, R. Ziessel, A. Harriman, *Angew. Chem. Int. Ed.* **2008**, *47*, 1184–1201; *Angew. Chem.* **2008**, *120*, 1202–1219; c) N. Boens, V. Leen, W. Dehaen, *Chem. Soc. Rev.* **2012**, *41*, 1130–1172; d) A. Kamkaew, S. H. Lim, H. B. Lee, L. V. Kiew, L. Y. Chung, K. Burgess, *Chem. Soc. Rev.* **2013**, *42*, 77–88; e) H. Lu, J. Mack, Y. Yanga, Z. Shen, *Chem. Soc. Rev.* **2014**, *43*, 4778–4823.
- [10] a) M. A. H. Alamiry, E. Bahaidarah, A. Harriman, J. H. Olivier, R. Ziessel, *Pure Appl. Chem.* **2013**, *85*, 1349–1365; b) A. Harriman, R. Ziessel, *Photochem. Photobiol. Sci.* **2010**, *9*, 960–967.
- [11] a) R. Ziessel, G. Ulrich, A. Harriman, *New J. Chem.* **2007**, *31*, 496–501; b) A. C. Benniston, G. Copley, *Phys. Chem. Chem. Phys.* **2009**, *11*, 4124–4130; c) M. Gupta, S. Mula, M. Tyagi, T. K. Ghanty, S. Murudkar, A. K. Ray, S. Chattopadhyay, *Chem. Eur. J.* **2013**, *19*, 17766–17772.
- [12] J. Rosenthal, A. B. Nepomnyashchii, J. Kozhukh, A. J. Bard, S. J. Lippard, *J. Phys. Chem. C* **2011**, *115*, 17993–18001.
- [13] V. Muñoz, L. Serrano, *Nature Struct. Biol.* **1994**, *1*, 399–409.
- [14] A. Ben-Naim, *Adv. Biol. Chem.* **2013**, *3*, 29–39 and references therein.
- [15] a) S. Mula, G. Ulrich, R. Ziessel, *Tetrahedron Lett.* **2009**, *50*, 6383–6388; b) S. Mula, K. Elliott, A. Harriman, R. Ziessel, *J. Phys. Chem. A* **2010**, *114*, 10515–10522.
- [16] a) H. Sajiki, T. Ikawa, K. Hirota, *Org. Lett.* **2004**, *6*, 4977–4980; b) R. Nacario, S. Kotakonda, D. M. D. Fouchard, L. M. V. Tillekeratne, R. A. Hudson, *Org. Lett.* **2005**, *7*, 471–474.
- [17] a) C. J. Chandler, L. W. Deady, J. A. Reiss, *J. Heterocycl. Chem.* **1981**, *18*, 599–601; b) D. Manna, S. Mula, A. Bhattacharyya, S. Chattopadhyay, T. K. Ghanty, *Dalton Trans.* **2015**, *44*, 1332–1340.
- [18] a) R. Ziessel, L. Bonardi, P. Retailleau, G. Ulrich, *J. Org. Chem.* **2006**, *71*, 3093–3102; b) T. Bura, R. Ziessel, *Tetrahedron Lett.* **2010**, *51*, 2875–2879; c) N. Shivan, S. Mula, T. K. Ghanty, S. Chattopadhyay, *Org. Lett.* **2011**, *13*, 5870–5873.
- [19] a) J. Karolin, L. B. A. Johansson, L. Strandberg, T. Ny, *J. Am. Chem. Soc.* **1994**, *116*, 7801–7806; b) A. Burghart, H. J. Kim, M. B. Welch, L. H. Thorsen, J. Reibenspies, K. Burgess, F. Bergstrom, L. B. A. Johansson, *J. Org. Chem.* **1999**, *64*, 7813–7819; c) H. Sunahara, Y. Urano, H. Kojima, T. Nagano, *J. Am. Chem. Soc.* **2007**, *129*, 5597–5604; d) K. K. Jagtap, N. Shivan, S. Mula, D. B. Naik, S. K. Sarkar, T. Mukherjee, D. K. Maity, A. K. Ray, *Chem. Eur. J.* **2013**, *19*, 702–708.
- [20] W. W. Qin, M. Baruah, M. Van der Auweraer, F. C. De Schryver, *J. Phys. Chem. A* **2005**, *109*, 7371–7384.
- [21] D. V. O'Connor, D. Phillips, *Time-Correlated Single Photon Counting*, Academic Press, New York, **1979**.
- [22] K. Santra, J. C. Zhan, X.-Y. Song, E. A. Smith, N. Vaswani, J. W. Petrich, *J. Phys. Chem. B* **2016**, *120*, 2484–2490.
- [23] A. Siemiarczuk, B. D. Wagner, W. R. Ware, *J. Phys. Chem.* **1990**, *94*, 1661–1666.
- [24] R. Esposito, G. Mensitieri, S. de Nicola, *Analyst* **2015**, *140*, 8138–8147.
- [25] A. R. Katritzky, D. C. Fara, H. Yang, K. Tamm, T. Tamm, M. Karelson, *Chem. Rev.* **2004**, *104*, 175–198.
- [26] C. Reichardt, *Chem. Rev.* **1994**, *94*, 2319–2358.
- [27] Y. Q. Zhou, G. Stell, *J. Chem. Phys.* **1992**, *96*, 1507–1515.
- [28] J. Catalán, V. López, P. Pérez, R. Martín-Villamil, J.-G. Rodríguez, *Liebigs Ann.* **1995**, *241*–252.
- [29] J. Catalán, C. Díaz, V. López, P. Pérez, J. L. G. De Paz, J.-G. Rodríguez, *Liebigs Ann.* **1996**, *1785*–1794.
- [30] S. J. Strickler, R. A. Berg, *J. Chem. Phys.* **1962**, *37*, 814–822.
- [31] a) M. R. Wasielewski, *Chem. Rev.* **1992**, *92*, 435–461; b) R. Ziessel, B. D. Allen, D. B. Rewinska, A. Harriman, *Chem. Eur. J.* **2009**, *15*, 7382–7393.
- [32] a) M. A. H. Alamiry, A. C. Benniston, G. Copley, A. Harriman, D. Howgego, *J. Phys. Chem. A* **2011**, *115*, 12111–12119; b) N. Saki, T. Dinc, E. U. Akkaya, *Tetrahedron* **2006**, *62*, 2721–2725; c) H. L. Qi, J. J. Teesdale, R. C. Pupillo, J. Rosenthal, A. J. Bard, *J. Am. Chem. Soc.* **2013**, *135*, 13558–13566.
- [33] a) A. Harriman, L. J. Mallon, B. Stewart, G. Ulrich, R. Ziessel, *Eur. J. Org. Chem.* **2007**, 3191–3198; b) A. N. Kursunlu, *Tetrahedron Lett.* **2015**, *56*, 1873–1877; c) R. Misra, B. Dhokale, T. Jadhav, S. M. Mobin, *New J. Chem.* **2014**, *38*, 3579–3585; d) S. Choi, J. Bouffard, Y. Kim, *Chem. Sci.* **2014**, *5*, 751–755; e) A. B. Nepomnyashchii, M. Broering, J. Ahrens, A. J. Bard, *J. Am. Chem. Soc.* **2011**, *133*, 8633–8645.
- [34] a) M. T. Whited, N. M. Patel, S. T. Roberts, K. Allen, P. I. Djurovich, S. E. Bradforth, M. E. Thompson, *Chem. Commun.* **2012**, *48*, 284–286; b) A. C. Benniston, G. Copley, A. Harriman, D. Howgego, R. W. Harrington, W. Clegg, *J. Org. Chem.* **2010**, *75*, 2018–2027.
- [35] P. F. Barbara, T. J. Meyer, M. A. Ratner, *J. Phys. Chem.* **1996**, *100*, 13148–13168.
- [36] a) D. Rehm, A. H. Weller, *Isr. J. Chem.* **1970**, *8*, 259–271; b) D. Rehm, A. H. Weller, *Ber. Bunsen-Ges.* **1969**, *73*, 834–839; c) A. H. Weller, *Z. Phys. Chem.* **1982**, *133*, 93–98.
- [37] G. King, A. Warshel, *J. Chem. Phys.* **1990**, *93*, 8682–8692.
- [38] T. Otsu, K. Ishii, T. Tahara, *Nat. Commun.* **2015**, *6*, 7685.
- [39] A. G. Martínez, E. T. Vilar, A. G. Fraile, P. Martínez-Ruiz, *J. Phys. Chem. A* **2002**, *106*, 4942–4950.
- [40] S. Samdal, *J. Mol. Struct.* **1998**, *440*, 165–174.
- [41] Y. A. Mantz, H. Gerard, R. Iftimie, G. J. Martyna, *J. Phys. Chem. B* **2006**, *110*, 13523–13538.
- [42] V. Lounnas, S. K. Ludemann, R. C. Wade, *Biophys. Chem.* **1999**, *78*, 157–182.
- [43] C. G. Ricci, A. S. de Andrade, M. Mottin, P. A. Netz, *J. Phys. Chem. B* **2010**, *114*, 9882–9893.
- [44] D. A. Dixon, K. D. Dobbs, J. J. Valenti, *J. Phys. Chem.* **1994**, *98*, 13435–13439.
- [45] E. Beausoleil, W. D. Lubell, *J. Am. Chem. Soc.* **1996**, *118*, 12902–12908.
- [46] M. A. Leiva, R. G. E. Morales, V. Vargas, *J. Phys. Org. Chem.* **1996**, *9*, 455–458.
- [47] G. Fischer, *Chem. Soc. Rev.* **2000**, *29*, 119–127.
- [48] Y. K. Yang, H. S. Park, *J. Mol. Struct. THEOCHEM* **2004**, *676*, 171–176.
- [49] A. Radzicka, L. Pedersen, R. Wolfenden, *Biochemistry* **1988**, *27*, 4538–4541.
- [50] F. B. Dias, M. Knaapila, A. P. Monkman, H. D. Burrows, *Macromolecules* **2006**, *39*, 1598–1606.
- [51] J. M. Gialmo, A. V. Gusev, M. R. Wasielewski, *J. Am. Chem. Soc.* **2002**, *124*, 8530–8532.
- [52] V. Bandi, H. B. Gobeze, P. A. Karr, F. D'Souza, *J. Phys. Chem. C* **2014**, *118*, 18969–18982.
- [53] a) R. M. Williams, *Photochem. Photobiol. Sci.* **2010**, *9*, 1018–1026; b) B. P. Paulson, L. A. Curtiss, B. Bal, G. L. Closs, J. R. Miller, *J. Am. Chem. Soc.* **1996**, *118*, 378–387; c) A. M. Oliver, D. C. Craig, M. N. Paddon-Row, J. Kroon, J. W. Verhoeven, *Chem. Phys. Lett.* **1988**, *150*, 366–373.
- [54] A. M. Brun, A. Harriman, V. Heitz, J.-P. Sauvage, *J. Am. Chem. Soc.* **1991**, *113*, 8657–8663.
- [55] A. C. Benniston, A. Harriman, *Chem. Soc. Rev.* **2006**, *35*, 169–179.
- [56] M. N. Paddon-Row, *Aust. J. Chem.* **2003**, *56*, 729–748.
- [57] K. Pettersson, J. Wiberg, T. Ljungdahl, J. Martensson, B. Albinsson, *J. Phys. Chem. A* **2006**, *110*, 319–326.
- [58] A. Harriman, V. Heitz, J.-P. Sauvage, *J. Phys. Chem.* **1993**, *97*, 5940–5946.
- [59] a) K. J. Elliott, A. Harriman, L. Le Pleux, Y. Pellegrin, E. Blart, C. R. Mayer, F. Odobel, *Phys. Chem. Chem. Phys.* **2009**, *11*, 8767–8773; b) A. Harriman, K. J. Elliott, M. A. H. Alamiry, L. Le Pleux, M. Severac, Y. Pellegrin, E. Blart, C. Fosse, C. Cannizzo, C. R. Mayer, F. Odobel, *J. Phys. Chem. C* **2009**, *113*, 5834–5842.

Received: May 17, 2016

Published online on ■■■■■, 0000

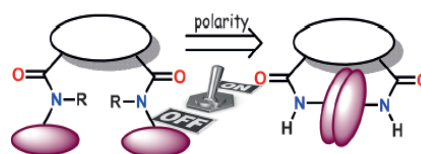
FULL PAPER

Dyes/Pigments

S. Thakare, P. Stachelek, S. Mula,
A. B. More, S. Chattopadhyay, A. K. Ray,
N. Sekar, R. Ziessel, A. Harriman*



Solvent-Driven Conformational
Exchange for Amide-Linked
Bichromophoric BODIPY Derivatives



Solvent has its finger on the trigger:
Polar solvent triggers a conformational
change from *cis*- to *trans*-geometries for
a tertiary amide-bridged molecular

dyad, but the exact opposite situation is
found for the corresponding secondary
amide-bridged bichromophore (see
scheme).

Electronic Communication in Closely-Connected BODIPY-Based Bi-Chromophores.

Electronic Communication in Closely-connected BODIPY-based Bi-chromophores

Patrycja Stachelek and Anthony Harriman*

Molecular Photonics Laboratory, School of Chemistry, Bedson Building, Newcastle University, Newcastle upon Tyne, NE1 7RU, United Kingdom

ABSTRACT: A small series of closely-spaced, bichromophoric boron dipyrromethene (BODIPY) derivatives has been examined by optical spectroscopy and compared to the corresponding mononuclear dyes. The compounds vary according to the site of attachment and also by the nature of alkyl or aryl substituents incorporated into the dipyrin backbone. Excitonic coupling splits the lowest-energy absorption transition in each case, but to highly variable degrees. There are also marked changes in the fluorescence quantum yields across the series, but much less variation in the excited state lifetimes. After comparing different models, it is concluded that the ideal dipole approximation gives a crude qualitative representation of the observed splitting of the absorption transition, but the extended dipole approach is not applicable to these systems. Agreement is substantially improved by employing a model that takes into account the dihedral angle between the planes of the two dipyrin units. The large variation in radiative rate constants, and those for the accompanying non-radiative processes, are accountable in terms of electronic coupling and/or intensity borrowing between the two excitonic states. In all cases, the dihedral angle between the two BODIPY units plays a key role.

INTRODUCTION

The so-called "special pair" plays a critical role in natural photosynthesis,¹ being both the ultimate acceptor for photons absorbed by the light-harvesting machinery and the primary electron donor for subsequent charge separation.^{2,3} Strong coupling between the two chromophores, which are chemically identical but subjected to slightly disparate environments, favors exciton/charge delocalization around what is effectively a molecular dimer.^{4,5} Apart from experimental and theoretical studies aimed at better appreciating the nuances of the special pair, considerable attention has been given to the detailed spectroscopic examination of artificial molecular dimers.⁶⁻¹⁰ Notable among such studies have been dimers formed from porphyrins,¹¹ nucleobases,¹² aryl mono- and diimides,¹³ and aryl hydrocarbons.¹⁴ Many more studies have addressed the electronic properties of intermolecular¹⁵ and intramolecular excimers.¹⁶ It is recognized that the degree of electronic coupling between the two chromophores depends on the separation distance,¹⁷ their mutual orientation¹⁸ and the nature of the local environment.¹⁹ The same factors govern electrostatic interactions and are seen in the Förster theory²⁰ for electronic energy transfer. Kasha²¹ integrated these features into one of the first coherent discussions of excitonic interactions in molecular dimers and classified the orientations into several major groupings. Refinements to the general theory have been made by Gouterman,²² Davydov,²³ Katz,²⁴ and Shipman²⁵ and their coworkers, although the basic framework introduced by Kasha²¹ remains intact for dimers formed from relatively small molecules. It seems doubtful that the same approach can be applied to molecular interactions in conducting

polymers²⁶ or compact crystals,²⁷ where the nearest neighbor principle is often invoked.

Tremendous interest has been shown, over the past decade or so, in the photophysical properties of the boron dipyrromethene (BODIPY) family of dyes.²⁸ These highly fluorescent compounds have found important applications in many diverse fields and continue to attract attention.²⁹⁻³¹ In certain circumstances, BODIPY dyes will aggregate in the form of either fluorescent or non-emissive entities as has been well demonstrated by Johansson et al.³² In addition, various covalently-linked BODIPY bichromophores have been reported. The latter include both face-to-face³³ and side-by-side analogues³⁴ wherein the photophysical properties are controlled by the molecular topology. Notable among these systems are the tilted molecular dimers described by Harriman et al.³⁵ and the adjacent dimers reported by Bröring et al.³⁶ We now expand the library of known BODIPY-based bichromophores to include a series of side-by-side derivatives. In most cases, the two BODIPY units are connected via a solitary C-C bond so that the mutual orientation is set by any peripheral groups and by the position of attachment. This strategy permits subtle structural effects to be examined in fluid solution using optical spectroscopy. Particular attention has been given to understanding excitonic coupling in those bichromophores where the individual transition dipole moment vectors are in-line but out-of-plane. This allows examination of how the molecular alignment, measured by way of the central dihedral angle, affects the degree of excitonic interaction along the molecular axis.

RESULTS and DISCUSSION

MATERIALS

The compounds examined in this work are illustrated in Charts 1-3 and comprise a series of chromophores based on the BODIPY nucleus and their complementary bichromophores. It might be noted that most of the compounds lack a phenylene ring at the *meso*-position and, therefore, are not to be regarded as putative molecular-scale rotors.³⁷ In certain cases, the *meso*-position is without substitution but it should be realized that the substitution pattern differs throughout the series and this effect causes minor perturbation of the optical spectra. Two of the compounds possess an aryl group at each of the 3,5-positions which, at least in the case of B3, introduces severe steric hindrance for internal rotation occurring within the bichromophore. The corresponding single chromophoric analogues, M1-M3 (Chart 1) are required as spectroscopic reference compounds. A second set of bichromophores (Chart 3) involves more sterically encumbered derivatives that carry a tolyl group at the pseudo-*meso*-position and at the 3-position (compound P1). When both the 3- and 5-positions are blocked with an aryl substituent, the coupling reaction proceeds selectively at the 2-position, providing access to compound P2.

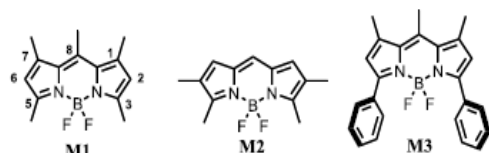


Chart 1. Molecular formulae of the relevant single chromophore analogues used as spectroscopic markers.

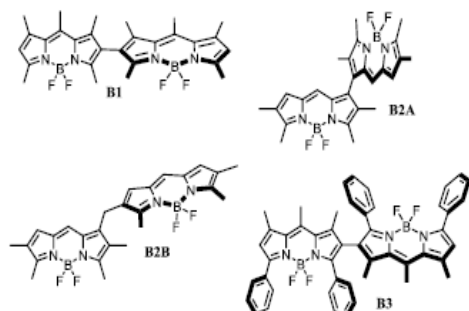


Chart 2. Molecular formulae of the bichromophores prepared via oxidative homo-coupling reactions.

Synthetic details³⁸⁻⁴⁰ for these compounds have been published previously and the compounds were further purified by TLC prior to measurement of their photophysical properties. Some of the bichromophores (Chart 2) have also been reported previously.⁴⁰ These compounds are reasonably soluble in common organic solvents and are not prone to aggregation under our experimental conditions. Crystal structures have been reported for B1, B3 and P1 while M1 is well known⁴¹ in the literature. Authenticity of the remaining bichromophores was established by high-resolution ¹H- and ¹³C-NMR spectroscopy before starting the experiment.

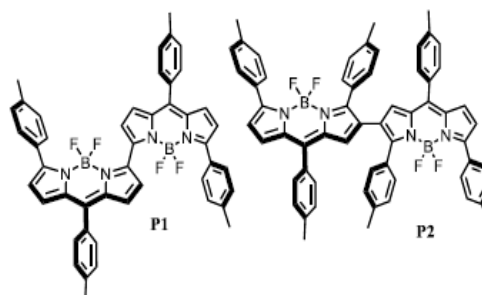


Chart 3. Molecular formulae for the two sterically-encumbered bichromophores prepared by oxidative homo-coupling. Note these compounds bear a tolyl group at the pseudo-*meso*-position.

REFERENCE COMPOUNDS

The photophysical properties of the isolated chromophores were measured in 2-methyltetrahydrofuran (MTHF) solution and the derived parameters are summarized in Table 1. The important terms relate to absorption (λ_{MAX}) and fluorescence (λ_{FLU}) maxima in solution, the Stokes' shift ($\Delta\lambda_{\text{SS}}$) derived after spectral deconvolution into Gaussian components, and the molar absorption coefficient (ϵ_{MAX}) for the lowest-energy absorption transition. Variations in ϵ_{MAX} are offset by comparison of the corresponding oscillator strengths (f), which take into account the relative width of the absorption bands. The derived values are quite similar across the series, although there are minor spectral variations. It might be noted that aryl substitution at the dipyrin periphery leads to a markedly increased $\Delta\lambda_{\text{SS}}$ while the substitution pattern perturbs the spectral properties, as can be seen by comparing data for M1 and M2.

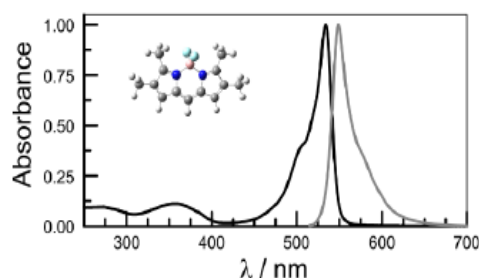


Figure 1. Normalized absorption (black curve) and fluorescence (gray curve) spectra recorded for M2 in MTHF solution at ambient temperature. The inset gives the energy-minimized structure computed for the ground state.

Also compiled are the fluorescence quantum yields (Φ_{F}), excited-singlet state lifetimes (τ_{S}), and the corresponding radiative rate constants (k_{RAD}) calculated from the Strickler-Berg expression.⁴² Fluorescence decay profiles were mono-exponential in each case and excellent agreement was found between excitation and absorption spectra. Typical absorption and fluorescence profiles are shown in Figure 1 for reference purposes while all the spectra are collected in the Supporting Information. Peak maxima are dependent on the substitution pattern, especially if aryl groups are attached to the dipyrin core, but the overall properties remain within reasonably close limits. Furthermore, the results tabulated here remain in good agreement with those reported²⁸⁻³¹ elsewhere in the literature for related conventional BODIPY dyes and it should be

stressed that, in the main, these dyes are highly fluorescent and free from problems of aggregation.

The emission properties hardly change on cooling to 77K, other than a slight spectral blue-shift and a narrowing of the optical bandwidth for the transition. At room temperature, the absorption and emission spectra could be well reproduced by summation of ca. five Gaussian-shaped components of common half-width (see Supporting Information). This allows calculation of the low-frequency vibronic mode ($h\omega$) that accompanies the optical transition (Table 1). This value ranges from 530 to 800 cm^{-1} and corresponds, in generic terms, to large-scale torsional motion of the dipyrin backbone. It is interesting to note that aryl substitution at the dipyrin core induces a significant increase in the mean value. There is also a marked variation in the Huang-Rhys factor (S) derived⁴³ by fitting the emission spectrum. This value falls markedly on aryl substitution due to increased π -conjugation between the dipyrin and the aryl substituent. Indeed, there is a clear correlation between S and both λ_{MAX} and λ_{FLU} . The same effect is not seen when the aryl group is placed at the *meso*-position.

Table 1. Summary of the photophysical properties of the control compounds measured in MTHF solution at room temperature.

Property	M1	M2	M3
$\lambda_{\text{MAX}} / \text{nm}$	495	534	549
$\epsilon_{\text{MAX}} / \text{M}^{-1}\text{cm}^{-1}$	93,470	75,830	62,090
$f^{(a)}$	0.50	0.45	0.50
$\lambda_{\text{FLU}} / \text{nm}$	508	549	591
$\Delta S S / \text{cm}^{-1}$	510	505	1,275
Φ_F	0.94	0.91	0.87
τ_S / ns	5.6	5.5	6.4
$k_{\text{RAD}} / 10^8 \text{ s}^{-1 (b)}$	1.70	1.65	1.35
$h\omega / \text{cm}^{-1 (c)}$	580	530	800
S	0.58	0.42	0.23

(a) Oscillator strength calculated for the lowest-energy transition. (b) Radiative rate constant calculated from the Strickler-Berg expression. (c) Low-frequency vibronic mode coupled to nonradiative decay as derived from spectral deconstruction.

Quantum chemical calculations (DFT/B3LYP-6-31G(d)) carried out for the various control compounds indicate that, as might be expected, both HOMO and LUMO are distributed around the dipyrin core; Figure 2 gives a typical example while distribution patterns for all the control compounds are provided as part of the Supporting Information. It is apparent that the BF_2 unit plays no significant role in determining the electronic properties of either HOMO or LUMO. Interestingly, the *meso*-carbon atom has an important function for the LUMO but is much less significant for the HOMO. These computational studies show that the dipyrin core is planar in each case (See Table S1) and that the compounds are highly symmetrical. Computed oscillator strengths and transition dipole moments are sensitive to the nature of the substituents while the calculated wavelengths for the first-allowed absorption transitions are reasonably close to the experimental values (see Table S2). The phenyl rings are held at an average dihedral angle of ca. 50° to the plane of the dipyrin nucleus for the ground-state structures but these appended groups are free to rotate over a wide range (see Supporting Information). The ability of the HOMO/LUMO to off-load electron density to the aryl substituent depends on the relevant

dihedral angle,⁴⁴ as might be expected (See Supporting Information).

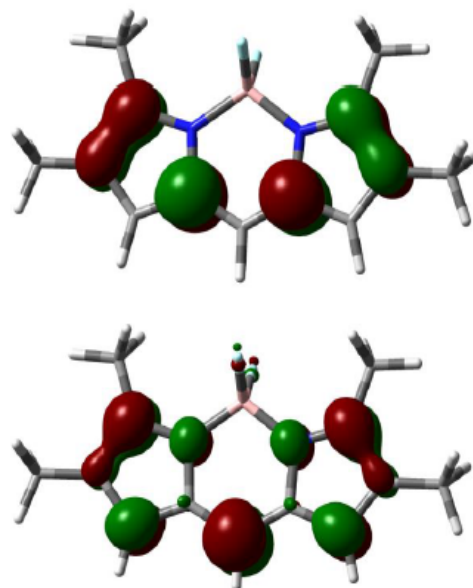


Figure 2. Kohn-Sham representations of the HOMO (upper panel) and LUMO (lower panel) computed for M2 in a solvent reservoir corresponding to a dielectric constant of 10.

ROTATION AROUND THE CONNECTING BOND

In order to obtain information about the likely molecular conformations of the bichromophores in solution, a series of DFT calculations (B3LYP-aug-cc-pVTZ) was made for the ground-state molecules; the results are provided as part of the Supporting Information. For B1, the two BODIPY units are held at an average dihedral angle of 72° but gyration about this position is essentially unhindered over a wide variance. Full rotation about the connecting C-C bond is unlikely, however, since the methyl groups impose severe steric crowding at 0° and 180° . Instead, the dihedral angle can vary between 40° and 140° with little resistance, although there is a slight barrier to attaining the mutually orthogonal geometry (Figure 3). Similar conclusions are drawn for B2A, where the average dihedral angle between the two BODIPY residues is reduced to 57° at the ground-state level. Again, steric crowding between the substituents hinders attainment of planar geometries, for 180° the problem is caused by the *meso*-hydrogen atoms, but there is a much reduced barrier for rotation around 0° . For this derivative, the mean dihedral angle lies within the range 30° to 90° .

The indirectly linked bichromophore B2B has more internal flexibility and the mean dihedral angle between the two BODIPY units is 50° at the ground state. Steric clashes between the methyl group and the second BODIPY unit introduce a substantial barrier for full rotation, while again there is a minor obstacle to attaining the orthogonal geometry. Nonetheless, the dihedral angle can vary widely and is expected to cover the range 40° to 140° at ambient temperature. Molecular dynamics simulations (MDS) carried out in a reservoir of water molecules are consistent with the above results but indicate a much narrower distribution of accessible geometries, with typical variance of 11° around the energy-minimized structure.

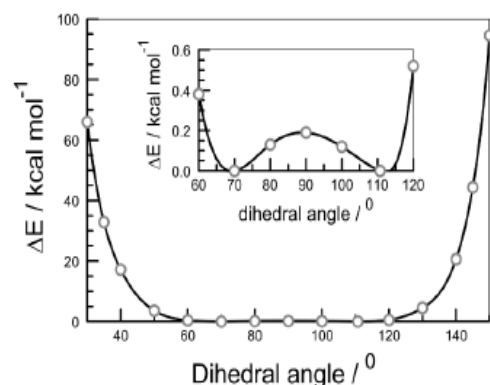


Figure 3. Effect of dihedral angle between the two BODIPY units on the total energy of the molecule calculated for B1 in a solvent reservoir. The inset gives an expansion of the region where the BODIPY units approach an orthogonal geometry.

The bichromophore possessing aryl substituents at the lower rim of the dipyrin unit is more prone to steric inhibition for rotation around the C-C connection. This situation serves to restrict the range over which the dihedral angle is likely to oscillate at room temperature. Thus, for B3 the preferred dihedral angle is ca. 76° but mutual gyration covers a fairly wide variance. The main steric problems are caused by clashes between the ancillary phenyl rings on the one hand and clashes between a phenyl ring and the 5-methyl group on the other. As above, the general findings were confirmed by MDS studies using periodic boundary conditions ($50 \times 50 \times 50 \text{ \AA}^3$) with a water reservoir. Here, the variation around the starting geometry was less than 10° .

The two analogues bearing *meso*-tolyl groups prefer to maintain the dipyrin units in an almost perpendicular geometry, dihedral angles being 66° and 64° respectively for P1 and P2. Both structures show slight curvature in line with the X-ray data.⁴¹ Full rotation around the connecting linkage is blocked by steric clashes between the fluorine atoms for P1 and by fluorine-tolyl interactions for P2. In the main, the structural data agree well with that derived from the crystal structures while MDS studies indicate highly restricted rotation around the connecting bonds. Further details are provided in the Supporting Information.

PHOTOPHYSICS OF THE BICHROMOPHORES

Absorption and fluorescence spectra were recorded for the bichromophores in MTHF at room temperature and the main findings are summarized in Table 2. Examples of the spectra are provided as Figure 4. In each case, absorption and emission spectra are red shifted with respect to the corresponding control compound while the fluorescence quantum yields are lowered by a significant factor. The excited-singlet state lifetimes are shortened relative to the control compounds but to a less extent than noted for the quantum yields. As a consequence there is a marked variation in the corresponding radiative rate constants. These are reduced relative to the control compounds but are now surprisingly sensitive to the structure of the bichromophore. In particular, compounds B1 and B3 remain reasonably emissive but the other compounds in the series are weakly fluorescent. As before, there is good agreement between absorption and excitation spectra and, throughout the series, the fluorescence decay profiles were well represented by single-exponential fits. The fluorescence spectra sharpen and undergo a slight blue shift on cooling to 77K but there are no major spectral changes.

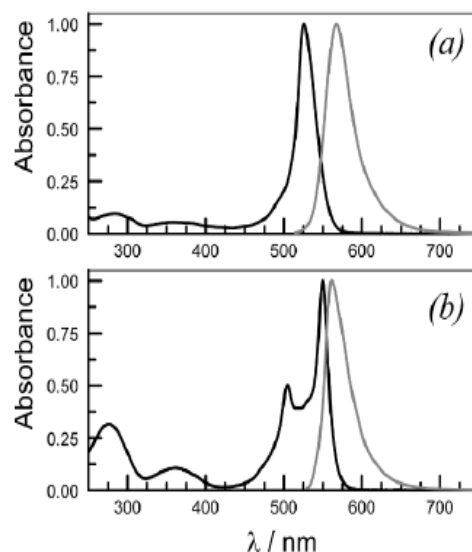


Figure 4. Comparison of absorption (black curve) and fluorescence (gray curve) spectra recorded for (a) B1 and (b) B2B in MTHF solution at ambient temperature.

At room temperature, a low-frequency vibronic mode ($h\nu_L$) of around 700 cm^{-1} promotes nonradiative deactivation of the excited-singlet state (Table 2). The magnitude of this vibronic mode remains comparable to that derived for the relevant control compound. Except for B2B, the bichromophores exhibit a smaller Huang-Rhys (*S*) factor⁴³ than found for the control compound (Table 2). This is taken as being indicative of increased π -conjugation at the excited-state level for the bichromophoric derivatives. This is not the case for B2B, where the conjugation is broken by the sp^3 -connecting carbon atom and the derived *S* value is close to what might be anticipated for the corresponding control compound.

Absorption spectra recorded for the bichromophoric compounds in MTHF display increased oscillator strengths, as might be expected, and are red-shifted compared to spectra recorded for the control compounds. In fact, the oscillator strengths are roughly twice that of the control compound. Most notably for B2B, the absorption spectra display the characteristic features of excitonic splitting due to close electronic interaction between the two dipyrin units.²¹⁻²⁵ A comprehensive curve-fitting analysis based on the assumption of Gaussian-shaped components allows estimation of the splitting energy by assigning 0.0 transition energies for the lower (E_{10}) and upper (E_{20}) transitions (Table 3). The magnitude of the splitting ($\Delta\epsilon$) varies from 530 cm^{-1} for B1 to $1,630 \text{ cm}^{-1}$ for B2B. It is also evident that the relative intensities of these two transitions (A_{10} and A_{20}) vary across the series,⁴⁵ this point is exemplified by the ratio (*N*) of integrated absorption intensities for the two transitions; note, these intensities take into account any vibronic bands associated with the 0,0 transition. The spectra are complicated by the appearance of strong vibrational satellites accompanying the main transitions and the corresponding low-frequency modes associated with upper- ($h\nu_1$) and lower-energy ($h\nu_2$) transitions are collected in Table 3. These latter values are somewhat sensitive to the nature of the bichromophore and tend to increase for the lower transition. Figure 5 illustrates the scope of this spectral analysis, while fitted spectra for all the bichromophores are included in the Supporting Information.

Table 2. Summary of spectroscopic properties determined for the bichromophores in MTHF solution at room temperature.

Property	B1	B2A	B2B	B3	P1	P2
$\lambda_{\text{ABS}} / \text{nm}$	526	558	557	584	691	634
$\varepsilon_{\text{MAX}} / \text{M}^{-1}\text{cm}^{-1}$	154,955	79,700	139,105	157,615	67,500	92,250
f	0.91	0.94	0.94	0.93	0.85	1.00
$\lambda_{\text{FLU}} / \text{nm}$	563	600	565	628	770	712
Φ_{F}	0.40	0.090	0.072	0.40	0.13	0.15
$\tau_{\text{S}} / \text{ns}$	3.8	1.9	1.8	4.0	3.4	2.1
$\Delta_{\text{SS}} / \text{cm}^{-1}$	825	1,085	365	890	690	935
$k_{\text{RAD}} / 10^8 \text{ s}^{-1}$	1.05	0.47	0.40	1.0	0.38	0.71
$k_{\text{NR}} / 10^8 \text{ s}^{-1}$	1.6	4.8	5.4	1.5	2.6	4.1
S	0.35	0.31	0.61	0.24	0.16	0.26
$h\omega_{\text{L}} / \text{cm}^{-1} \text{ (a)}$	740	735	540	725	480	425
$\nu_{\text{FLU}} / \text{cm}^{-1} \text{ (b)}$	17,690	16,925	17,825	16,010	13,005	13,900

(a) Low-frequency vibronic mode accompanying nonradiative decay of the excited-singlet state as derived from spectral curve fitting. (b) Maxima derived for the emission spectral profiles on the basis of spectral curve fitting.

Table 3. Parameters derived by spectral curve fitting of the absorption spectra recorded for the bichromophores in MTHF solution at room temperature.

Property	B1	B2A	B2B	B3	P1	P2
$E_{1,0} / \text{cm}^{-1}$	19,040	19,035	19,820	17,795	14,290	15,695
$E_{2,0} / \text{cm}^{-1}$	18,515	18,010	18,190	16,900	13,695	14,835
$\Delta\varepsilon / \text{cm}^{-1}$	525	1,025	1,630	895	1,485	860
$A_{1,0} / \%$	73.0	56.8	44.8	78.6	70.1	70.7
$A_{2,0} / \%$	27.0	43.2	55.2	21.4	29.9	29.3
$N_{\text{EXPT}} \text{ (a)}$	2.71	1.32	0.81	3.68	2.34	2.41
$N_{(1)} \text{ (b)}$	0.04	1.83	2.36	0.02	1.24	0.06
$N_{(2)} \text{ (c)}$	2.97	1.55	1.02	3.98	2.25	2.06
$h\omega_1 / \text{cm}^{-1} \text{ (d)}$	640	550	590	705	595	660
$h\omega_2 / \text{cm}^{-1} \text{ (e)}$	720	695	500	900	705	770
$\Phi / ^\circ$	71.4	57.1	72.0	75.9	66.0	64.1
$\theta / ^\circ$	1.8	60.2	52.8	1.0	52.2	5.9
$V_{\text{OB}} / \text{cm}^{-1}$	800	500	855	930	800	975
$V_{\text{XTD}} / \text{cm}^{-1}$	8,700	2,300	1,100	6,650	3,150	10,250
$V_{\text{N}} / \text{cm}^{-1}$	400	105	55	465	60	485
$V_{\text{NP}} / \text{cm}^{-1}$	535	55	420	640	3.5	620
$V_{\text{ANG}} / \text{cm}^{-1}$	580	1,105	1,670	685	1,285	690

(a) Ratio of integrated absorption transition intensities for direct absorption to the upper and lower excitonic bands as derived by experiment. (b) The above ratio calculated on the basis of Equation 1. (c) The above ratio calculated from Equation 1 but with the dihedral angle, Φ , replacing the angle between the transition dipole moment vectors and the corresponding distance vectors. (d) Low-frequency vibronic mode associated with direct absorption to the upper-lying excitonic state. (e) Low-frequency vibronic mode associated with direct absorption to the lower-lying excitonic state.

EXCITONIC COUPLING WITH THE BICHROMOPHORES

According to the excitonic coupling theory developed first by Kasha²¹ but extended by many others,²²⁻²⁵ interaction between the transition dipole moment vectors associated with the two dipyrin units causes a two-fold splitting of the excited-singlet state. The ratio of the relative intensities,⁴⁵ N , of the two absorption transi-

tions is expected to depend on the mutual alignment of the respective transition dipole moment vectors. In the case of perfectly aligned chromophores, one or other of these transitions is forbidden due to accidental cancellation of the transition dipole moments. Furthermore, fluorescence should occur exclusively from the lower-energy state since rapid internal conversion will be promoted by the small energy gap⁴⁶ between the two states. The vectors run down the long molecular axis of the dipyrin backbone and, in most

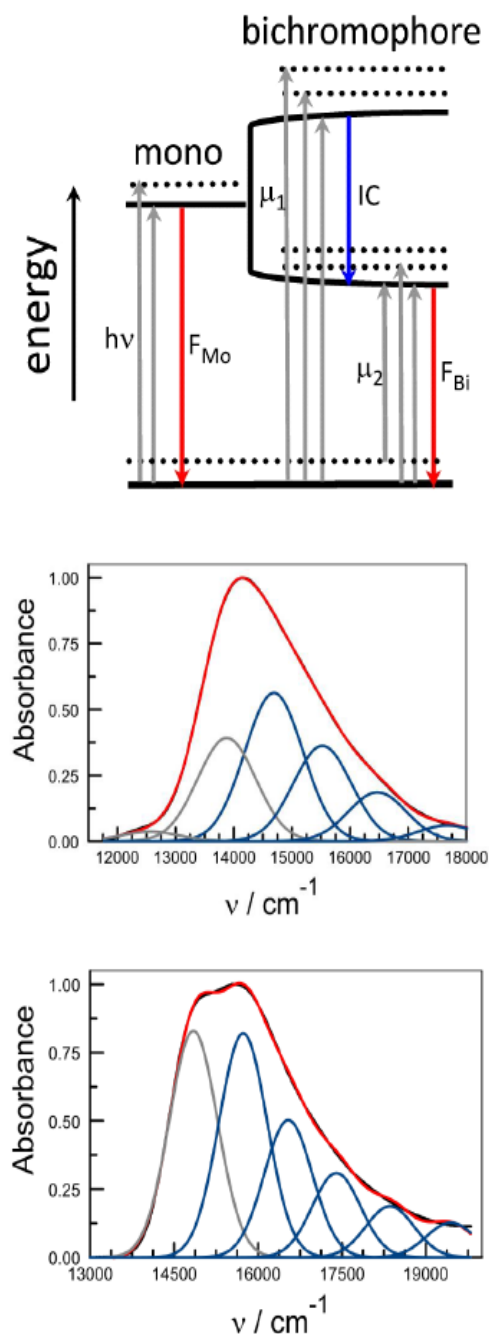


Figure 5. Examples of excitonic splitting of the lowest-energy absorption transition for the bichromophores in MTHF solution. The upper panel illustrates the model used for the spectral analysis while the experimental (black curve) and constructed (red curve) spectra are shown for P1 (central panel) and P2 (lower panel). Each spectrum is deconstructed into a series of Gaussian-shaped components corresponding to absorption to the higher-energy state (blue curves) and the lower-energy state (gray curves). The peak splitting ($\Delta\epsilon$) is taken as the energy gap between adjacent gray and blue curves.

cases, the two vectors run parallel to the distance vector connecting the centers of the chromophores (Figure 6). Because of steric constraints, however, the in-line transition dipole moment vectors lie out-of-plane. As such, it is instructive to enquire if the level of excitonic interaction is sensitive to the dihedral angle between the dipyrin units for these particular geometries. To do so, we first employ Equation 1, where μ_M refers to the transition dipole moment of the corresponding monochromatic dye, to calculate the relative strengths (N) of the two absorption transitions. The geometry parameter, θ , refers to the mean angle between the transition dipole moment vectors and the distance vector connecting the centers of the chromophores (Figure 6).

$$N = \frac{\mu_1}{\mu_2} = \frac{\sqrt{2}\mu_M \sin\theta}{\sqrt{2}\mu_M \cos\theta} \quad (1)$$

This equation is intended for use with oblique geometries, but for B1, B3 and P2 the transition dipole moment vectors are essentially parallel. These compounds, therefore, are predicted to exhibit a value for N that is significantly less than unity (Table 3); in other words, absorption to the lower-energy transition (A_1) is strongly favored relative to direct absorption to the higher-energy state (A_2). This situation is at odds with the experimental data (NEXPT) and, in fact, there is poor agreement between calculated and observed N values (Table 3). The vectors are almost orthogonal for B2B such that absorption should be primarily to the lower-energy state but, as above, this expectation does not give a proper representation of the experiment. Compounds B2A and P1 adopt an oblique geometry and agreement between calculated and observed N values is somewhat improved, but still poor (Table 3).

Notably, replacing θ in Equation 1 with the corresponding dihedral angle (Φ) between the respective dipyrin units leads to vastly improved agreement for the in-line bichromophores (Table 3 and Figure 6). This points towards a strong angular dependence for N . Indeed, the revised expression accurately predicts the ratio of the transition moments for each of the in-line compounds, although it should be stressed that the dihedral angle is subject to a variance of around $\pm 10^\circ$ in fluid solution at ambient temperature, according to the MDS studies. Even for the two oblique geometries, the insistence on a strong angular dependence leads to a better correlation between calculated and observed N values. This is not to say, however, that there is an important contribution from through-bond excitonic coupling.⁴⁶⁻⁴⁸

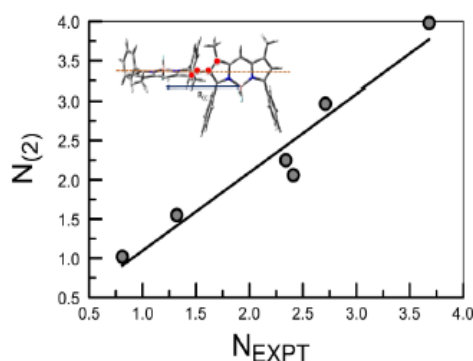


Figure 6. Comparison between the experimentally determined ratio of integrated absorption intensities for upper- and lower-energy transitions and the value calculated from Equation 1 with the dihedral angle replacing the angle between the transition dipole moment vectors and the distance vector. The inset illustrates the dihedral angle using red dots to signify the four carbon atoms.

It might be noted that the DFT calculations support the idea of weak interactions between the two BODIPY-based units in these bichromophores. This is evidenced by the observation that the molecular orbitals are clearly associated with each chromophore, rather than being delocalized over the entire super-molecule. There is little, if any, coupling at the ground-state level, despite the close proximity of the two units. Coupling occurs at the excited-state level to give the observed excitonic splitting.

Excitonic coupling theory²¹ predicts that the extent of the splitting of the lowest-energy absorption band ($\Delta\epsilon$) depends on the magnitude of the transition dipole moment (μ_M) of the mononuclear dye and the average distance (R_{CC}) between the centers of the respective transition dipole moment vectors (Equation 2).⁴⁹ Here, κ refers to the orientation factor representing the mutual alignment of the two vectors. In his original study, Kasha²¹ identified three key orientations in addition to the aligned geometry. Within the confines of the ideal dipole approximation,⁵⁰ these relate to oblique, inclined and non-planar arrangements of the transition dipole moment vectors (see Supporting Information for a full description of the methodology, including tabulation of the structural parameters). For an oblique geometry, the orientation factor (κ_{OB}) depends on the angle (α_{DD}) between the two dipole moment vectors and on the mean angle (θ) between each vector and the distance vector connecting the two dipole centers according to Equation 3. A similar relationship²¹ holds for the inclined geometry, where κ_{IN} is obtained from Equation 4. Exciton splitting for the non-planar geometry makes use of an orientation factor (κ_{NP}) based on the angle between the two molecular planes as illustrated by way of Equation 5. We can now calculate splitting energies for each of the three projected orientations and compare the results with the experimental data (Table 3).

$$V_{IDA} = \frac{\mu_M^2 \kappa}{4\pi\epsilon_0 R_{CC}^3} = \beta \kappa \quad (2)$$

$$\kappa_{OB} = \cos\alpha_{DD} + 3\cos^2\theta \quad (3)$$

$$\kappa_{IN} = 1 - 3\cos^2\theta \quad (4)$$

$$\kappa_{NP} = \cos\alpha_{DD} - 3\cos^2\Phi \quad (5)$$

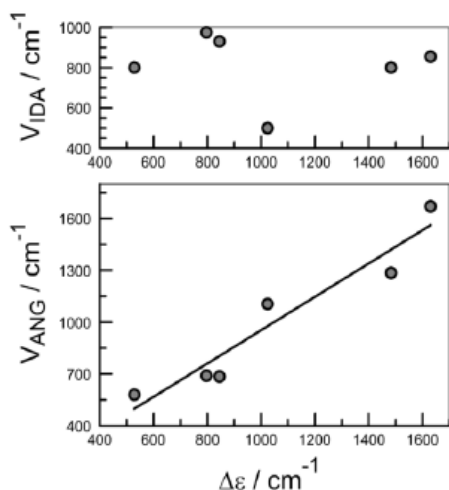


Figure 7. Correlation between the experimentally derived peak splitting, $\Delta\epsilon$, and that calculated for a strong angular effect according to Equation 6. The upper panel shows the same correlation for the peak splitting according to the ideal dipole approximation (Equations 2-5).

None of the above orientations accurately describes the molecular geometries of the target bichromophores and the various equations fail to reproduce the experimental splitting energies. No single orientation works for all the compounds and even taking the best agreement for each individual compound does not give a reasonable qualitative trend. Replacing the point sources with extended dipoles running the length of the transition dipole moment vector⁵¹ gives rise to splitting energies (V_{XTD}) much higher than the experimental results (Table 3). Here, the problem is caused by the unusually close proximity of one pair of coordinates. Although useful in many intermolecular dimers,⁵² the extended dipole method seems inappropriate for the bichromophores studied here.

Also collected in Table 3 are the peak separations (V_{ANG}) calculated from the respective dihedral angles (Φ) between the two dipyrin planes (Equation 6). This approach leads to excellent quantitative agreement between calculated and observed splitting energies (Figure 7). In turn, this points to a strong angular dependence for excitonic coupling in these systems and it might be argued that through-bond interactions could play an important role. The results obtained with B2B, however, appear to be inconsistent with this notion. This is because the sp^3 -hybridized carbon atom present in the connecting unit will restrict through-bond interactions by imposing an additional resistance.⁵³ In fact, B2B shows the largest splitting energy and the shortest center-to-center separation distance. Nonetheless, inclusion of an angular dependence dramatically improves the agreement between experiment and calculation for these particular compounds.

$$V_{ANG} = \beta(3 - \cos^2\Phi) \quad (6)$$

It seems appropriate to enquire if the same treatment could be applied to quantify the splitting of the oxidation and reduction peaks observed in the cyclic voltammograms recorded for these bichromophores. Unfortunately, some of these processes are electrochemically irreversible and therefore it is questionable if meaningful calculations can be attempted. For the successive one-electron reduction steps, which are split in each case because of electrostatic repulsion, there is reasonable qualitative agreement between the peak splitting and the size of the excitonic splitting found for the absorption spectra. This finding suggests that there is a similar angular dependence for the Coulombic effects associated with the electrochemistry.

One remaining issue relates to the large variation in the k_{RAD} values found for the various bichromophores in fluid solution. For mononuclear BODIPY-based dyes, k_{RAD} depends on the magnitude of the vibronic transition moment density and the average energy of the excited singlet state,^{42,54} usually denoted by the emission maximum (ν_{FLU}). For the bichromophoric dyes, the expression needs to be modified to allow for the fact that only the lower-energy excitonic state emits. As such, we might expect the following relationship to hold for the bichromophores (Equation 7):

$$k_{RAD} = \frac{32\pi^2 n^3}{3h} \nu_{FLU}^3 |\mu_L|^2 \quad (7)$$

Here, n is the refractive index of the solvent and μ_L is the transition dipole moment for direct absorption to the lowest-energy exciton state. The experimental k_{RAD} values do not correlate with Equation 7 and, if anything, the trend is opposite to the predicted fit (Figure 8). Replacing μ_L with the overall transition dipole moment ($\mu_T = \mu_L + \mu_U$) does not improve the quality of the fit. Somewhat unexpectedly, it was noted that k_{RAD} increases progressively with decreasing energy gap, $\Delta\epsilon$, between the two excitonic states. This situation might be indicative of coupling between the two states and is reminiscent of earlier work by Verhoeven et al.⁵⁵ where it was reported that certain compounds displaying charge-recombination fluorescence were prone to intensity borrowing from an upper-lying excited state. Indeed, by modifying the expression for the radiative rate constant derived by Verhoeven et al.⁵⁵ for

the specific case of interest (Equation 8), it becomes possible to greatly improve the correlation between k_{RAD} and the energy gap parameter, γ (Figure 8a). Here, V^* refers to the electronic matrix element for coupling between the two excitonic states. This situation is consistent with intensity borrowing from the upper-lying excitonic state by the emissive state. To the best of our knowledge, this consideration has not been raised previously, although the situation is familiar for intramolecular charge-recombination fluorescence.⁵⁶

$$k_{\text{RAD}} = \frac{32\pi^2 n^3 (V^*)^2 v_{\text{FLU}}^2}{3h (\Delta\varepsilon - v_{\text{FLU}})^2} = \frac{32\pi^2 n^3}{3h} \gamma \quad (8)$$

Along similar lines, the corresponding rate constant for nonradiative decay (k_{NR}) does not exhibit the anticipated exponential dependence⁵⁷ on the amount of energy to be dissipated during the process. We have taken v_{FLU} as being representative of this latter term. Instead, it is found that k_{NR} shows a crude exponential dependence on the energy gap between the two excitonic states, $\Delta\varepsilon$ (Figure 8b). The rate of radiationless decay tends to increase as this energy gap increases. This is the opposite of the situation found for k_{RAD} and, as a consequence, the fluorescence quantum yield shows a strong dependence on the extent of splitting between the two excitonic states. The effect observed for k_{NR} implies some mild stabilization of radiationless deactivation by way of mixing with the upper-lying excitonic state. Most likely, this overall behavior involves weak charge-transfer interactions such that state mixing introduces some degree of polarity into the lower-lying excitonic state. Indeed, in other BODIPY-based bichromophores, symmetry breaking has been observed under illumination.⁵⁸ We have not been able to detect long-lived charge-separated states in our systems but the involvement of mild charge-transfer interactions is a strong possibility.

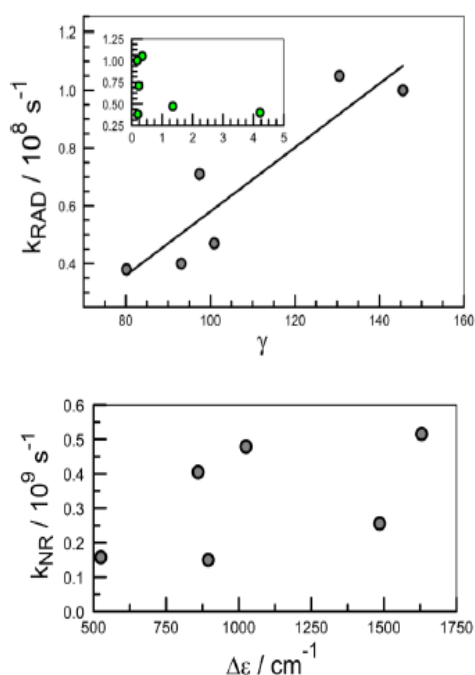


Figure 8. (a) The upper panel shows a plot of the rate constant for radiative decay of the excited-singlet state vs the energy gap factor γ as described in Equation 8 (see Supporting Information for details). The inset shows the corresponding relationship between k_{RAD} and the energy factor in the absence of coupling to the upper-lying

excitonic state. (b) The lower panel shows a plot of the rate constant for nonradiative decay of the excited-singlet state vs the energy gap between the two excitonic states.

CONCLUDING REMARKS

Numerous studies have addressed important issues relating to excitonic coupling in bichromophoric molecules, many of which have been built around the BODIPY nucleus.^{32–36,58} Such compounds are important as simple models for the photosynthetic special pair^{1–3} but more significantly as a means by which to extend the opto-electronic properties of emissive dyes. The bichromophore might be considered to provide a facile way to increase the Stokes shift,³⁶ for subsequent applications in cytometry, microscopy and photon concentrators. Related compounds have been proposed for electro-generated chemiluminescent probes.^{40,59,60} In this contribution we have examined the optical properties of bichromophores that do not fall naturally into the categories identified by Kasha²¹ during his pioneering work on excitonic coupling. In certain cases, the transition dipole moment vectors appear to be aligned in a parallel manner and this should eliminate direct absorption to one or other of the two excitonic states. This is not seen experimentally because, in our case, the dihedral angle between the planes extended by the chromophores is not close to zero. This introduces a strong angular dependence for the optical properties that might be further exploited to optimize the molecular electronic properties. An interesting observation to emerge from this work is that the fluorescence quantum yield is sensitive to the extent of splitting of the excitonic bands. Again, this effect might be manipulated to obtain new dyes with advanced optical properties.

ASSOCIATED CONTENT

Supporting Information. Contains experimental details and information about the computed geometries for all compounds, Kohn-Sham orbital representations, absorption and emission spectra for the dyes, tabulated output from the DFT calculations, plots of how the dihedral angle affects the total energy of the system, deconstructed spectra showing the underlying Gaussian components, explanations of the alignment of the transition dipole moment vectors and plots for k_{NR} vs energy gap. This material is available free of charge via the Internet at <http://pubs.acs.org>.

AUTHOR INFORMATION

Corresponding Author

*Professor Anthony Hariman. e-mail: anthony.hariman@ncl.ac.uk. Tel: +44 191 2088660.

Author Contributions

All authors have given approval to the final version of the manuscript.

Funding Sources

Newcastle University

ACKNOWLEDGMENT

We thank Newcastle University for financial support of this work, including the award of a Research Scholarship to PS. We also thank Dr. Raymond Ziessel (ECPM-Strasbourg) for providing samples of the BODIPY-based derivatives used in this work.

ABBREVIATIONS

DFT, density functional theory; NMR, nuclear magnetic resonance spectroscopy; TLC, thin-layer chromatography.

REFERENCES

1. Lockhart, D. J.; Boxer, S. G. Stark Effect Spectroscopy of Rhodospirillum rubrum and Rhodospirillum rubrum Reaction Centers. *Proc. Natl. Acad. Sci.* 1988, 85, 107-111.
2. Bixon, M.; Jortner, J.; Michel-Beyerle, M. E. On the Mechanism of the Primary Charge Separation in Bacterial Photosynthesis. *Biochim. Biophys. Acta* 1991, 1056, 301-315.
3. Arnett, D. C.; Moser, C. C.; Dutton, P. L.; Scherer, N. F. The First Events in Photosynthesis: Electronic Coupling and Energy Transfer Dynamics in the Photosynthetic Reaction Center from Rhodospirillum rubrum. *J. Phys. Chem. B* 1999, 103, 2014-2032.
4. Cho, H. S.; Song, N. W.; Kim, Y. H.; Jeoung, S. C.; Hahn, S.; Kim, D.; Kim, S. K.; Yoshida, N.; Osuka, A. Ultrafast Energy Relaxation Dynamics of Directly Linked Porphyrin Arrays. *J. Phys. Chem. A* 2000, 104, 3287-3298.
5. Womick, J. M.; Moran, A. M. Vibronic Enhancement of Exciton Sizes and Energy Transport in Photosynthetic Complexes. *J. Phys. Chem. B* 2011, 115, 1347-1356.
6. Baderschneider, S.; Scherf, U.; Köhler, J.; Hildner, R. Influence of the Conjugation Length on the Optical Spectra of Single Ladder-type (p-phenylene) Dimers and Polymers. *J. Phys. Chem. A* 2016, 120, 233-240.
7. Tait, C. E.; Neuhaus, P.; Anderson, H. L.; Timmel, C. R. Triplet State Delocalization in a Conjugated Porphyrin Dimer Probed by Transient Electron Paramagnetic Resonance Techniques. *J. Am. Chem. Soc.* 2015, 137, 6670-6679.
8. Wu, Y. L.; Frascioni, M.; Gardner, D. M.; McGinigal, P. R.; Schneebeli, S. T.; Wasielewski, M. R.; Stoddart, J. F. Electron Delocalization in a Rigid Cofacial Naphthalene-1,8:4,5-bis(dicarboximide) Dimer. *Angew. Chem., Int. Ed.* 2014, 53, 9476-9481.
9. Takai, A.; Gros, C. P.; Barbe, J. M.; Guillard, R.; Fukuzumi, S. Enhanced Electron-Transfer Properties of Cofacial Porphyrin Dimers Through π - π Stacking. *Chem. Eur. J.* 2009, 15, 3110-3122.
10. Satake, A.; Kobuke, Y. Artificial Photosynthetic Systems: Assemblies of Slipped Cofacial Porphyrins and Phthalocyanines Showing Strong Electronic Coupling. *Org. Biomol. Sci.* 2007, 5, 1679-1691.
11. Gouterman, M.; Holten, D.; Lieberman, E. Exciton Coupling in μ -Oxo Scandium Dimers. *Chem. Phys.* 1977, 25, 139-153.
12. Voityuk, A. A.; Jortner, J.; Bixon, M.; Rosch, N. Electronic Coupling Between Watson-Crick Pairs for Hole Transfer and Transport in Desoxyribonucleic Acid. *J. Chem. Phys.* 2001, 114, 5614-5620.
13. Clark, A. E.; Qin, C. Y.; Li, A. D. Q. Beyond exciton theory: A Time-Dependent DFT and Franck-Condon Study of Perylene Diimide and its Chromophoric Dimer. *J. Am. Chem. Soc.* 2007, 129, 7586-7595.
14. Li, J.; Liu, Y.; Qian, Y.; Li, L.; Xie, L.; Shang, J.; Yu, T.; Yi, M.-D.; Huang, W. Describing Curved-Planar π - π Interactions Modelled by Corannulene, Pyrene and Coronene. *Phys. Chem. Chem. Phys.* 2013, 15, 12694-12701.
15. Scholes, G. D.; Ghiggino, K. P. Electronic Interactions and Interchromophore Excitation Transfer. *J. Phys. Chem.* 1994, 98, 4580-4590.
16. Winnik, F. M. Photophysics of Pre-associated Pyrenes in Aqueous Polymer-Solutions and in Organized Media. *Chem. Rev.* 1993, 93, 587-614.
17. Harriman, A.; Zissel, R. Making Photoactive Molecular-scale Wires. *Chem. Comm.* 1996, 1707-1716.
18. Sakata, Y.; Ysue, H.; O'Neil, M. P.; Wiederecht, G. P.; Wasielewski, M. R. Effect of Donor-Acceptor Orientation on Ultrafast Electron Transfer and Dark Charge Recombination in Porphyrin-Quinone Molecules. *J. Am. Chem. Soc.* 1994, 116, 6904-6909.
19. Kubar, T.; Elstner, M. What Governs the Charge Transfer in DNA? The role of DNA Conformation and Environment. *J. Phys. Chem. B* 2008, 112, 8788-8798.
20. Förster, T. Intermolecular Energy Transference and Fluorescence. *Ann. Phys.* 1948, 2, 55575.
21. Kasha, M. Energy Transfer Mechanisms and the Molecular Exciton Model for Molecular Aggregates. *Radiat. Res.* 1963, 20, 55-70.
22. Selensky, R.; Holten, D.; Windsor, M. W.; Paine, J. B.; Dolphin, D.; Gouterman, M.; Thomas, J. C. Excitonic Interactions in Covalently-linked Porphyrin Dimers. *Chem. Phys.* 1981, 60, 33-46.
23. Davydov, A. S. Theory of Molecular Excitons. McGraw-Hill, New York, 1962.
24. Shipman, L. L.; Cotton, T. M.; Norris, J. R.; Katz, J. J. Analysis of Visible Absorption Spectrum of Chlorophyll-a Monomer, Dimer and Oligomers in Solution. *J. Am. Chem. Soc.* 1976, 98, 8222-8230.
25. Shipman, L. L.; Norris, J. R.; Katz, J. J. Quantum Mechanical Formalism for Computation of Electronic Spectral Properties of Chlorophyll Aggregates. *J. Phys. Chem.* 1976, 80, 877-882.
26. Scholes, G. D.; Rumbles, G. Excitons in Nanoscale Systems. *Nature Mater.* 2006, 5, 683-696.
27. Yoshida, H.; Sato, N. Crystallographic and Electronic Structures of Three Different Polymorphs of Pentacene. *Phys. Rev. B* 2008, 77, 235205.
28. Ulrich, G.; Zissel, R.; Harriman, A. The Chemistry of Fluorescent Bodipy Dyes: Versatility Unsurpassed. *Angew. Chem., Int. Ed.* 2008, 47, 1184-1201.
29. Loudet, A.; Burgess, K. BODIPY Dyes and Their Derivatives: Syntheses and Spectroscopic Properties. *Chem. Rev.* 2007, 107, 4891-4932.
30. Boens, N.; Leen, V.; Dehaen, W. Fluorescent Indicators Based on BODIPY. *Chem. Soc. Rev.* 2012, 41, 1130-1172.
31. Zissel, R.; Ulrich, G.; Harriman, A. The Chemistry of Bodipy: A New El Dorado for Fluorescent Tools. *New J. Chem.* 2007, 31, 496-501.
32. Karolin, J.; Johansson, L. B. Å.; Strandberg, L.; Ny, T. Fluorescence and Absorption Spectroscopic Properties of Dipyrrometheneboron Difluoride (BODIPY) Derivatives in Liquids, Lipid Membranes, and Proteins. *J. Am. Chem. Soc.* 1994, 116, 7801-7806.
33. Saki, N.; Dinc, T.; Alkaya, E. U. Excimer Emission and Energy Transfer in Cofacial Boradiazaindacene (BODIPY) Dimers Built on a Xanthene Scaffold. *Tetrahedron* 2006, 62, 2721-2725.
34. Bergstrom, F.; Mikhalyov, I.; Hagglof, P. Dimers of Dipyrrometheneboron Difluoride (BODIPY) With Light Spectroscopic Applications in Chemistry and Biology. *J. Am. Chem. Soc.* 2002, 124, 196-204.
35. Benniston, A. C.; Copley, G.; Harriman, A.; Howeggo, D.; Harrington, R. W.; Clegg, W. Cofacial Boron Dipyrromethene (Bodipy) Dimers: Synthesis, Charge Delocalization, and Exciton Coupling. *J. Org. Chem.* 2010, 75, 2018-2027.
36. Bröring, M.; Krueger, R.; Link, S.; Kleeberg, C.; Koehler, S.; Xie, X.; Ventura, B.; Flamigni, L. Bis(BF₂)-2,2'-bidipyrins (Bis-BODIPYs): Highly Fluorescent BODIPY Dimers with Large Stokes Shifts. *Chem. Eur. J.* 2008, 14, 2976-2983.
37. Alamiry, M. A. H.; Benniston, A. C.; Harriman, A.; Stewart, B.; Zhi, Y.-G. A Molecular Rotor Based on an Unhindered Boron Dipyrromethene (Bodipy) Dye. *Chem. Mater.* 2008, 20, 4024-4032.
38. Rihn, S.; Erdem, M.; de Nicola, A.; Retaillieu, P.; Zissel, R. Phenylidene(III) Bis(trifluoroacetate) (PIFA)-promoted Synthesis of Bodipy Dimers Displaying Unusual Redox Properties. *Org. Lett.* 2011, 13, 1916-1919.
39. Poirel, A.; de Nicola, A.; Retaillieu, P.; Zissel, R. Oxidative Coupling of 1,7,8-Unsubstituted BODIPYs: Synthesis and Electrochemical and Spectroscopic Properties. *J. Org. Chem.* 2012, 77, 7512-7525.
40. Nepomnyashchii, A. B.; Bröring, M.; Ahrens, J.; Bard, A. J. Synthesis, Photophysical, Electrochemical, and Electrogenetic Chemiluminescence Studies. Multiple Sequential Electron Transfers in BODIPY Monomers, Dimers, Trimers, and Polymer. *J. Am. Chem. Soc.* 2011, 133, 8633-8645.
41. Arbeloa, F. L.; Arbeloa, T. L.; Arbeloa, I. L. Electronic Spectroscopy of Pyrromethene 546. *J. Photochem. Photobiol. A: Chem.* 1999, 121, 177-182.
42. Strickler, S. J.; Berg, R. A. Relationship between Absorption Intensity and Fluorescence Lifetime of Molecules. *J. Chem. Phys.* 1962, 3, 814-822.
43. Huang, K.; Rhys, A. Theory of Light Absorption and Nonradiative Transitions in F-Centres. *Proc. Roy. Soc. A: Math. Phys.* 1950, 204, 406-423.
44. Karlsson, J. K. G.; Harriman, A. Origin of Red-Shifted Optical Spectra Recorded for aza-BODIPY Dyes. *J. Phys. Chem. A* 2016, 120, 2537-2546.

45. Thorley, K. J.; Würthner, F. Synthesis and Properties of a Covalently Linked Angular Perylene Imide Dimer. *Org. Lett.* **2012**, *14*, 6290-6193.
46. Ibrayev, N. K.; Yeroshina, S. A.; Ishchenko, A. A.; Mushkalo, I. L. Investigation of Conformational and Electron Properties of Biscyanine Dyes. *Mol. Cryst. Liq. Cryst.* **2005**, *427*, 451-459.
47. Ahrens, J.; Boeker, B.; Brandhorst, K.; Funk, M.; Bröring, M. Sulfur-Bridged BODIPY DYEmers. *Chem. Eur. J.* **2013**, *19*, 11382-11395.
48. Sun, D.; Rosokha, S. V.; Kochi, J. K. Donor-Acceptor (Electronic) Coupling in the Precursor Complex to Organic Electron Transfer: Intermolecular and Intramolecular Self-exchange Between Phenothiazine Redox Centers. *J. Am. Chem. Soc.* **2004**, *126*, 1388-1401.
49. Spiegel, J. D.; Kleinschmidt, M.; Larbig, A.; Tatchen, J.; Marian, C. M. Quantum-Chemical Studies on Excitation Energy Transfer Processes in BODIPY-based Donor-Acceptor Systems. *J. Chem. Theory Comput.* **2015**, *11*, 4316-4327.
50. Alamiry, M. A. H.; Hagon, J. P.; Harriman, A.; Bura, T.; Ziesse, R. Resolving the contribution due to Forster-type intramolecular electronic energy transfer in closely coupled molecular dyads. *Chem. Sci.* **2012**, *3*, 1041-1048.
51. Czikkely, V.; Forsterling, H. D.; Kuhn, H. Extended Dipole Model for Aggregates of Dye Molecules. *Chem. Phys. Lett.* **1970**, *6*, 207-210.
52. Marguet, S.; Markovitsi, D.; Millie, P.; Sigal, H.; Kumar, S. Influence of Disorder on Electronic Excited States: An Experimental and Numerical Study of Alkylthiotriphenyl Columnar Phases. *J. Phys. Chem. B* **1998**, *102*, 4697-4710.
53. Oliver, A. M.; Craig, D. C.; Paddon-Row, M. N.; Kroon, J.; Verhoeven, J. W. Strong Effects of the Bridge Configuration on Photoinduced Charge Separation in Rigidly Linked Donor-Acceptor Systems. *Chem. Phys. Lett.* **1988**, *150*, 366-373.
54. Birks, J. B. Radiative Lifetime Anomalies. *Zeitschrift Phys. Chem. Frankfurt*. **1976**, *101*, 91-104.
55. Bixon, M.; Jortner, J.; Verhoeven, J. W. Lifetimes for Radiative Charge Recombination in Donor-Acceptor Molecules. *J. Am. Chem. Soc.* **1994**, *116*, 7349-7355.
56. Harriman, A.; Hissler, M.; Ziessel, R. Photophysical Properties of Pyrene-(2,2'-bipyridine) Dyads. *Phys. Chem. Chem. Phys.* **1999**, *1*, 4203-4211.
57. Englman, R.; Jortner, J. Energy Gap Law for Radiationless Transitions in Large Molecules. *Mol. Phys.* **1970**, *18*, 145-170.
58. Whited, M. T.; Patel, N. M.; Roberts, S. T.; Allen, K.; Djurovich, P. I.; Bradforth, S. E.; Thompson, M. E. Symmetry-Breaking Intramolecular Charge Transfer in the Excited State of meso-Linked BODIPY Dyads. *Chem. Commun.* **2012**, *48*, 284-286.
59. Qi, H.; Teesdale, J. J.; Pupillo, R. C.; Rosenthal, J.; Bard, A. J. Synthesis, Electrochemistry, and Electrogenated Chemiluminescence of Two BODIPY-appended Bipyridine Hologues. *J. Am. Chem. Soc.* **2013**, *135*, 13558-13566.
60. Rosenthal, J.; Neponmyashchii, A. B.; Bard, A. J.; Lippard, S. J. Synthesis, Photophysics, Electrochemistry and Electrogenated Chemiluminescence of a Homologous Set of BODIPY-appended Bipyridine Derivatives. *J. Phys. Chem. C* **2011**, *115*, 17993-18001.

